Faculty of Aerospace Engineering

Fixed-Wing UAV Integrated Navigation with Low-Cost IMU/GPS

B. A. Hummelink

January 14, 2011

TU Delft Delft University of Technology

Challenge the future

Fixed-Wing UAV Integrated Navigation with Low-Cost IMU/GPS

Master of Science Thesis

For obtaining the degree of Master of Science in Aerospace Engineering
at Delft University of Technology

B. A. Hummelink

January 14, 2011

Faculty of Aerospace Engineering · Delft University of Technology

Delft University of Technology

Delft University Of Technology
Department Of
Control and Simulation

The undersigned hereby certify that they have read and recommend to the Faculty of Aerospace Engineering for acceptance a thesis entitled **"Fixed-Wing UAV Integrated Navigation with Low-Cost IMU/GPS"** by **B. A. Hummelink** in partial fulfillment of the requirements for the degree of **Master of Science**.

Dated: January 14, 2011

Readers:

prof. dr. ir. J. A. Mulder

dr. Q. P. Chu

dr. G. C. H. E. de Croon

ir. C. de Wagter

ir. J. H. Breeman

Preface

This thesis report is the result of the graduation work on the subject of integrated navigation applied to fixed-wing unmanned aerial vehicles with low-cost IMU/GPS. This report contains the master thesis graduation work performed at the faculty of Aerospace engineering, department Control and Simulation. This report focuses on the application of different sensor configurations, sensor modeling and simulation, state observability theory and state identification.

I would like to thank Prof. dr. ir. J. A. Mulder for the inspiring environment I am working in. I would also like to thank dr. ir. Q. P. Chu for his advice and assistance during the last years. Furthermore, I would like to thank my supervisors of the Aerospace Software and Technologies Institute (ASTI), ir. C. de Wagter, dr. G. C. H. E. de Croon and dr. ir. E. de Weerdt for their contribution and insightful discussions over the last year. I would also like to thank ir. J. H. Breeman of the National Aerospace Laboratory (NLR) for taking part in the exam comity.

A big thanks to ir. M. P. de Graaf for reading the entire report and improving the readability.

I would like to extend my thanks to the Simona Graduate comity, student rooms Sim004 and Sim008. The "off-topic thesis moments" during the past year have made the graduation time enjoyable.

Delft, University of Technology — Bart Hummelink
January 14, 2011

Contents

List of Figures

List of Tables

Acronyms

A/D	Analog to Digital
AC	Angle Correction
ASTI	Aerospace Software and Technologies Institute
ATC	Air Traffic Control
C/A	Coarse/ Acquisition signal
CEP	Circular Error of Probability
DCM	Direction Cosine Matrix
DOF	Degree of Freedom
ECEF	Earth-Centered-Earth-Fixed
EGM-96	Earth Gravitational Model, 1996
EKF	Extended Kalman Filter
EOM	Equations of Motion
GA	General Aviation
GLONASS	Global Navigation Satellite System
GN&C	Guidance, Navigation and Control
GPS	Global Position System
IEKF	Iterated Extended Kalman Filter
IFOG	Interferometric Fiber-Optical Gyroscope
IMU	Inertial Measuring Unit
INS	Inertial Navigation System
ISA	International Standard Atmosphere
LTI	Linear-time Invariant System
LTV	Linear-time Varying System
MAV	Micro Aerial Vehicle
MEMS	Micro-Electro-Mechanical Systems
MIT	Massachusetts Institute of Technology
NAVSTAR	NAVigation by Satellite Time And Range

NED	North-East-Down
NGA	National Geospatial Agency
OCS	Operational Control Segment
PPS	Pulse-Per-Second
PPS	Precise Positioning Service
RLG	Ring Laser Gyroscopes
sINS	Strapdown Inertial Navigation System
SO(3)	Special Orthogonal Group
SPIRE	Space Inertial Reference Equipment
SVD	Singular-Value Decomposition
UAV	Unmanned Aerial Vehicle
VTOL	Vertical Take-off and Landing
WGS-84	World Geodetic System, 1984
WMM	World Magnetic Model 2000

List of Symbols

Greek Symbols

α	Angle of attack
β	Side-slip angle
ΔT	Temperature difference
η	Observability degree
γ	Maximum allowable observability degree
γ	Flight path angle
Λ	Diagonal matrix containing eigenvalues
Ω	Rotational matrix
ϕ	Roll angle
ψ	Yaw angle
σ	Standard deviation
σ	Singular value
Σ	Summation sign
Σ	Diagonal matrix containing singular values
θ	Pitch angle

Roman Symbols

A	System matrix of a state space system
A_x	Specific force component along the body X-axis
A_y	Specific force component along the body Y-axis
A_z	Specific force component along the body Z-axis

B	Input matrix of a state space system
b	Bias
C	Measurement matrix of a state space system
$\mathbb{C}$	Set of all complex numbers
D	Direct feed-trough matrix of a state space system
d	Distance
e	Noise
e_c	Correlated noise
e_d	Dither noise
e_ω	White noise
e_q	Quantization noise
e_r	Random walk noise
F	Jacobians of the dynamics equation
G	System noise input matrix
g	Gravitational acceleration
H	Jacobians of the observer equation
i	Imaginary number
$L_f(h)$	Lie derivative of scalar function h with respect to vector field $\underline{f}$
$\mathcal{O}$	Observability matrix
p	Rotational rate around the body X-axis
PR	Pseudo-range
q	Rotational rate around the body Y-axis
R	Rotational matrix
r	Rotational rate around the body Z-axis
r	Rank
$\mathbb{R}$	Set of all real numbers
S_T	Temperature linear scale factor
t	Time vecotor
u	Velocity component in X-direction
V	Total airspeed
VR	Vibration rectification factor
v	Velocity component in Y-direction
w	Velocity component in Z-direction

$\mathbb{Z}$	Set of all integers

Subscripts

$_A$	Accelerometer variable
$_{am}$	Axis misalignment
$_B$	Quantity in a body-fixed reference frame
$_E$	Quantity in an Earth reference frame
$_{GPS}$	GPS variable
$_m$	Measurement quantity
$_{rw}$	Random walk
$_{sm}$	Sensor-to-sensor misalignment
$_T$	True value
$_u$	User
$_\omega$	Gyroscopic variable

Superscripts

^{T}	Transpose operator
$^\wedge$	Estimation of a variable
$^\sim$	Error of a variable

Summary

Today, there is an increase in the use of Unmanned Aerial Vehicles (UAV's), for applications that can be considered dull, dirty or dangerous when compared to those applications of conventional aircraft or helicopters. To further increase the use of UAV's, their navigation filters must be robust and reliable. The trend in current autopilot development is defined by the ever decreasing size of vehicles leading to the creation of miniature Inertial Navigation Systems (INS) with low cost, low grade sensors. Small flying vehicles have fast dynamics requiring higher control rates and higher dynamic ranges with minimal available onboard computational capacities. Sensor and processing limitations have consequences for the achievable navigation performance. This in turn poses limits on the minimal vehicle stability, weather conditions and trajectory smoothness. The most important aspect and thesis goal is to guarantee the navigation filter solution robustness during all flight maneuvers. A navigation filter is an integration algorithm that provides a navigation solution on the vehicle's state vector from sensor data. This thesis focuses on one UAV platform in particular, namely small fixed-wing UAV's. One of the main challenges with designed navigation filters is that they can be theoretically stable but the outcome can sometimes not be used. In practice, the navigation filter outcome can give a diverging solution while theoretically stable. The goal of this thesis is to define the minimal requirements of sensors and other hardware for an INS such that the stabilization requirements posed by the vehicle dynamics and size can be satisfied. With the requirements stated, smaller and more dynamic fixed-wing UAV's can be stabilized based on the integrated navigation solution.

The developed observability analysis tool is able to provide a quantitative analysis on the state observability that can be used to analyze different systems or sensor configurations. The observability matrix is composed of the system and observer dynamics. The system dynamics is based on the Inertial Measuring Unit (IMU) prediction of the system states, the observer equations correspond to the observer dynamics. A non-linear local observability analysis has been performed to calculate the observability matrix. The traditional Singular-Values Decomposition (SVD) algorithm provides the singular values of an observability matrix in a decreasing order and indicates the rank of the system. The rank of the observability matrix corresponds to the number of observable system states, the SVD can however not directly link the singular values to the system states. To overcome this problem a different

matrix decomposition is used that is able to directly couple the singular values to the system states. This developed matrix decomposition algorithm is based on the QR factorization, called QRsvd. With this algorithm it is possible to quantitatively indicate the observability (degree) of each system state.

An analysis into the physical properties of fixed-wing aircraft kinematics resulted in new insight into the movement of flying vehicles. Based on the derived kinematics together with the coupling of an IMU, GPS receiver and fixed-wing aircraft kinematics this resulted in new physical insight. This resulted in three angle correction (AC) equations that can be used as additional attitude/heading angle observers to the conventional IMU/GPS integration. With these three additional observers, the three orientation angles become instantaneously observable. Without the AC equations, a rotational rate constraint is always present to integrate the IMU with GPS. GPS receivers and IMU are separate, self-contained subsystems with different updating frequencies and processing times. Resulting clock differences are called time synchronization errors and result in filter estimation problems. A time synchronization requirement is derived, which is a function of changes in vehicle accelerations and filter innovation. The time synchronization requirement is proportional to the magnitude of the change in vehicle accelerations $|\underline{a}'|$ and negatively proportional to the magnitude of the identification filter innovation. Vehicles with fast dynamics, like fixed-wing UAV's, can have larger changes in vehicle accelerations magnitude, resulting in a more stringent time synchronization requirement.
Based on performed simulations and verification with flight test data, it can be concluded that the improved IMU/GPS filter with AC equations can provide a stable long-term navigation solution with accurate short-term performance, by using (Iterated) Extended Kalman filters. During the performed simulations the position states give the largest source of error, due to the large GPS position uncertainty. For the three orientation angles, the heading angle has a larger identification error compared to the pitch and roll angle. For the orientation angles, the influence of atmospheric wind on the identification performance is minimal except for the heading angle due to the presence of a side-slip angle β.

Coordinate transformations between the Earth, North-East-Down (NED) reference frame $\mathcal{F}_E$ and the body-fixed reference frame $\mathcal{F}_B$ can be performed using a rotational transformation matrix R_{BE}. The antisymmetric matrix R_{BE} holds special properties that can be utilized and fits in the category of Special Orthogonal Lie groups with a dimension of three, called $SO(3)$. Based on $SO(3)$ group properties, a non-linear complementary filter can be constructed that uses this matrix as a single state. The non-linear complementary filter on the $SO(3)$ group, can be used as an alternative to conventional Kalman state identification filters. For (I)EKF the heading angle is the largest source of error of the attitude/heading angles, this is also the case for the $SO(3)$ filter. Differences between the $SO(3)$ filter and (I)EKF are due to two aspects. The $SO(3)$ filter uses constant proportional and integrator gains, where Kalman gain matrices include process and observer uncertainties. The other source of differences can be found in the strong coupling between the individual attitude/heading angles for the non-linear SO(3) filter compared to (I)EKF.

Keywords: UAV sensor configurations, Kalman filtering, Lie derivatives, non-linear complementary filters on $SO(3)$, state identification, observability (degree) analysis, IMU sensor modeling, GPS receiver modeling

Chapter 1

Introduction

This MSc thesis report is called: Fixed-wing UAV integrated navigation with low-cost IMU/GPS. The following sections provide the framework for this report and underlying research. Section 1-1 provides the reports background and problem statement in section 1-2. Last section 1-3 gives the outline of the report.

1-1 Thesis Background

Navigation is an ancient skill that is mainly used for steering and following directions. Navigation is the determination of a vehicles position and velocity which is performed onboard. In the past, when people were sailing around the world, they needed to know their position to steer in the right direction and follow the route on a map. During those days the navigation of a ship was a difficult job and required special skills. Landmarks, the Sun and other stars and later self made maps were the only tools used by navigators to steer around the World. Today navigation is still as important as in the past with the difference that nowadays it has become much more accurate with diverse platforms and digital systems. The special navigator skills have been replaced by sensors, digital maps and other systems to navigate as safe and economically efficient as possible. Nowadays, with the increase in computer power, most calculations are done onboard by computers. With the use of computers the navigational data can also be used for other systems, for instance to improve vehicle stabilization performance. The ancient navigator has now been replaced by today's engineers who are responsible for the Guidance, Navigation and Control (GN&C) design and are more and more applied to other vehicles like airplanes, cars and missiles. One special type of navigation and vehicle stabilization application that is becoming important, is the use of Unmanned Aerial Vehicle (UAV) and in particular Micro Aerial Vehicle (MAV).

The trend in current autopilot development is determined by the decreasing size of vehicles leading to the creation of miniature Inertial Navigation System (INS) systems with affordable sensors. Smaller vehicles with increasing dynamics requiring higher control rates and higher dynamic ranges with minimal computational capacities. Sensor and computational capacities

limit the control performance and update rate. This has consequences for the minimal vehicle stability, maximal weather toughness and trajectory smoothness. The most important aspect is the robustness of the navigation filter solution. Without a well designed filter, the minimal vehicle navigation filter requirements cannot be met and the vehicle cannot be controlled. An important aspect in the design of a robust filter, is the problem of divergence. The designed filter is theoretically stable, but the outcome cannot be used to stabilize the vehicle, as the filter solution is diverging. This phenomenon of divergence is called filter saturation. Filter saturation usually occurs for badly designed filters with unobservable states. However, saturation can also occur for properly designed filters with theoretically fully observable states. The problem of filter saturation when the system is fully observable in theory, makes it a real challenge to predict onboard filter performance for flying applications under the constraint of minimal computational power and low grade sensors.

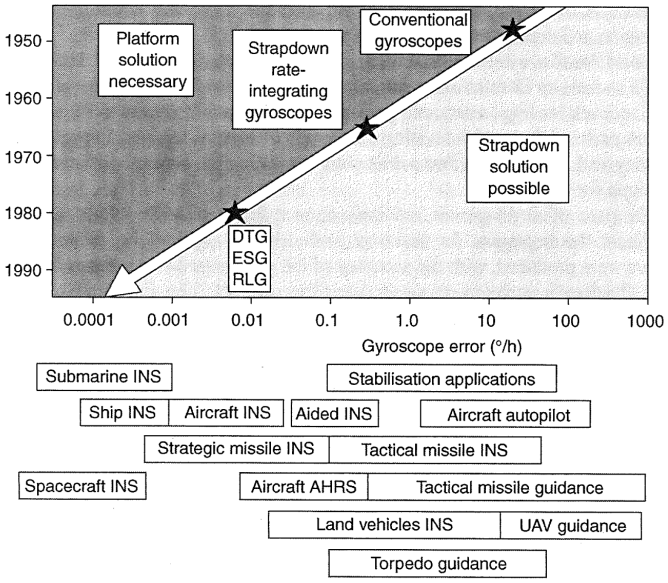

Figure 1-1: Overview on strapdown sensor development

Sources of error in INS are for instance due to gyroscopic and accelerometer sensor imperfections, wrong navigation system initialization and imperfections in the used online Earth gravity model. In most cases the largest sources of error come from the gyroscopic and accelerometer sensor imperfections. This can have many causes like mechanical imperfections, electronics, Analog to Digital (A/D) conversion or external factors like vibrations and temperature fluctuations. For gyroscopic sensors, the errors are in measuring the angular rate and integration to obtain angle information. The accelerometers have errors in measuring acceleration and are used for velocity and position estimation by means of integration. For both type of sensors the largest sources of error can usually be found in bias instability and scale-factor error. The required navigation performance will determine the selection of the specific inertial instruments in order to meet the mission requirements. For MAV applications the vehicles size and computational requirements limits this selection to MEMS sensor technology. Figure 1-1 gives an historic overview strapdown on sensor development with corresponding applications from (Titterton & Weston, 2009).

Figure 1-1 shows the accuracy required from the gyroscopes. From this figure can be seen

that the range of applications in which inertial navigation is used is extensive. In addition current application in the upcoming field of robots should be mentioned.
Figure 1-2 gives an overview of the predicted near term advantages in gyroscopic and accelerometer sensor performance in terms of bias instability. Micro-Electro-Mechanical Systems (MEMS) and Interferometric Fiber-Optical Gyroscope (IFOG) sensor technologies have the potential to replace the current systems that use Ring Laser Gyroscopes (RLG) and mechanical gyroscopes. The performance of MEMS is constantly improving, but is however pending on MEMS gyro development. The advantage of MEMS over other technologies is that MEMS technologies are low cost, small size, lightweight and have low power requirements. MEMS based sensor technology is expected to continuously improve in the near future. Although the basic principles of inertial navigation remain the same for most applications, the accuracy and associated computation effort varies widely.

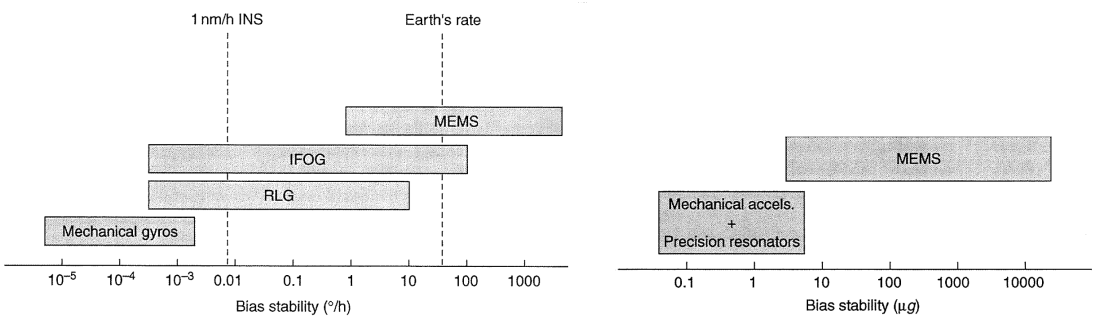

(a) Gyroscopic performance

(b) Accelerometer performance

Figure 1-2: Expected near term sensor performance

1-2 Problem Statement

To make way for continuation of further INS development, the problems occurring from low grade sensors, minimal available computation power and fast dynamics need to be solved. A standalone Inertial Measuring Unit (IMU), with gyroscopes and accelerometers, will drift over time due to bias instability. The sensor's output drifts over time and has as a consequence an upper bound on stabilization accuracy using inertial navigation alone. Various sensors have been used over the years to improve inertial navigation. For example, satellite navigation systems like Global Position System (GPS) or Global Navigation Satellite System (GLONASS), velocity meters, star trackers, magnetometers, radar, lidar and vision based systems. The use of GPS aiding has greatly improved the role of traditional navigation systems. GPS can constrain the long term bias error of inertial sensors. The scope of this research is limited to vehicle stabilization requirements using INS by means of MEMS technology applied to small fixed-wing UAV. Optical flow sensors or other vision-based systems that have high power and computational requirement are not treated in this report.

To be able to successfully continue the trend in miniaturizing INS, the problems faced with low grade sensors and fast vehicle dynamics must be solved. This development must be able to continue under the constrain of limited available onboard computational power. The navigation solution must be able to stabilize a typical small fixed-wing UAV, under

the constraints that are imposed by INS and UAV hardware and software. The navigation solution should perform as a stable and robust filter. Based on this, the following research goal is defined:

Define the minimal requirements of sensors and other hardware for an Inertial Navigation System (INS) such that the navigation filter requirements imposed by small fixed-wing Unmanned Aerial Vehicle (UAV) dynamics and size can be satisfied.

Based on this research goal several objectives are defined:

- Definition of the problems restricting the development of INS for smaller size vehicles with high dynamics and/or miniaturizing INS.
- Investigation of the minimal stabilization requirements related to vehicle dynamics and size and their influence on state estimation requirements.
- Definition of the lower bounds on hardware performance for INS such that stabilization requirements are met, linked to vehicle dynamics and size.
- Development/adjustment of (Kalman) filter implementation and testing these adjustments via simulations. Standard (Kalman) filter implementations are not applicable due to computational and saturation issues.
- Testing of the developed filter(s) at Aerospace Software and Technologies Institute (ASTI) using existing hardware.

The final objective houses the contest that the developed filter solutions are able to optimize the overall performance of the INS and are able to control an aircraft. The used aircraft will be a fixed-wing MAV, which is small and has fast dynamics.

1-3 Thesis Outline

This report consists of six parts. Part I provides a theoretical background on the relevant subjects used in this report. Chapter 2 gives a background on navigation in general, followed by chapter 3 about observability theory for different types of systems. Chapter 4 provides background on the topic of Kalman filtering. Chapters 2, 4 and most of chapter 3 provide an introduction on the different topics that are used in the later chapters, the experienced reader can choose to skip these chapters and start with part II on modeling.

Part II is about modeling and contains the used modeling tools. Chapter 5 contains theory and corresponding modeling about Inertial Measuring Unit (IMU). The same is done for GPS receivers in chapter 6. Chapter 7 describes an UAV modeling library that is used for building a Matlab/Simulink model of a dynamic non-linear 6-DOF fixed-wing UAV.

Part III contains different modeling tools and starts with the equations of motion for a standard loosely coupled IMU/GPS integration derived in chapter 8. Different sensor configurations are given in chapter 9. Chapter 10 gives new insight into aircraft kinematics resulting in a set of three angle corrections (AC) equations. The observability of different sensor configurations is analyzed in chapter 11 on a simulated trajectory by using the model of chapter 7. The results on different observers of chapter 11 are linked to the physical background of chapter 10 into chapter 12 leading to the creation of the optimal sensor configuration that forms a basis for the angle state identification filter.

Part IV gives the result of different identifications by means of simulations, the use of real UAV flight data and testing the developed IMU/GPS algorithm. Chapter 13 gives the result on the improved IMU/GPS with AC navigation filter simulation results, by using (Iterated) Extended Kalman filtering. Chapter 14 gives a different approach into identification filters, by means of the complementary non-linear filter on the Special Orthogonal Lie Group, $SO(3)$.

The conclusions and steps for future research in can be found in part V. Chapter 15 houses the conclusions of this thesis report and chapter 16 contains future research topics.

The appendices can be found in part VI and contain the underlying Jacobians of the observability studies and singular values corresponding to the observability analysis. The Aerosonde UAV simulation results and use of flight test data of part IV are also included in the appendices.

Part I

Theory

Chapter 2

Navigation Theory

This chapter provides a background into the subject of navigation. Section 2-1 gives an overview of different navigation systems and navigation in general. Section 2-2 is about the principle of the Global Positioning System (GPS). The last section 2-3 is about different types of integration between inertial and satellite navigation systems.

2-1 Navigation

The French physicist Foucault, mostly active in the field of optics, became famous for his understanding of the gyroscopic effect. In 1852 he measured the rotation of the Earth using nothing more than a spinning disk. He labeled it *gyroscope* from two Greek words: *Gyros* meaning *rotation* and *skopein* meaning *to view*. Nowadays, most gyroscopes still use this kind of spinning rotor principle. Figure 2-1(a) gives an illustration of one of the first built gyroscopes from the National Conservatory of Arts and Crafts museum in Paris. The gyroscope wheel is mounted in a double-axed gimbal, such that the gravity force acts on the wheel's center of mass with no torque acting on the wheel itself. With no torque applied to the wheel, the spinning wheel will always point in the same direction. As can be seen in figure 2-1(a), a second device is used to spin up the gyroscope wheel before it can be placed in the mounting. With magnification is was possible to measure Earth's rotation very accurately for that time.

One of the first developments in inertial navigation was performed by the Massachusetts Institute of Technology (MIT) Instrumentation Laboratory. They were asked by the US Air Force to develop inertial systems for the Thor and Titan missiles. In 1953 the lab demonstrated the feasibility of an autonomous inertial navigation for aircraft with a system called Space Inertial Reference Equipment (SPIRE). Professor Charles Stark Draper and his colleagues reduced the angular rate from $15°/hour$ to about $0.01°/hour$, (Draper, Wrigley, & Hovorka, 1960). The system has a height of 5 feet with a weight of 2.700 pounds and used gimbals to obtain navigation information. Figure 2-1(b) gives an impression of how big such early navigational devices were. The success led to further application in aircraft, missiles, spacecraft and ships.

Before the 1950's the world already saw a demonstration of inertial guidance trough the German V1 and V2. A step forward in guidance was taken by improving the system with sensor feedback.

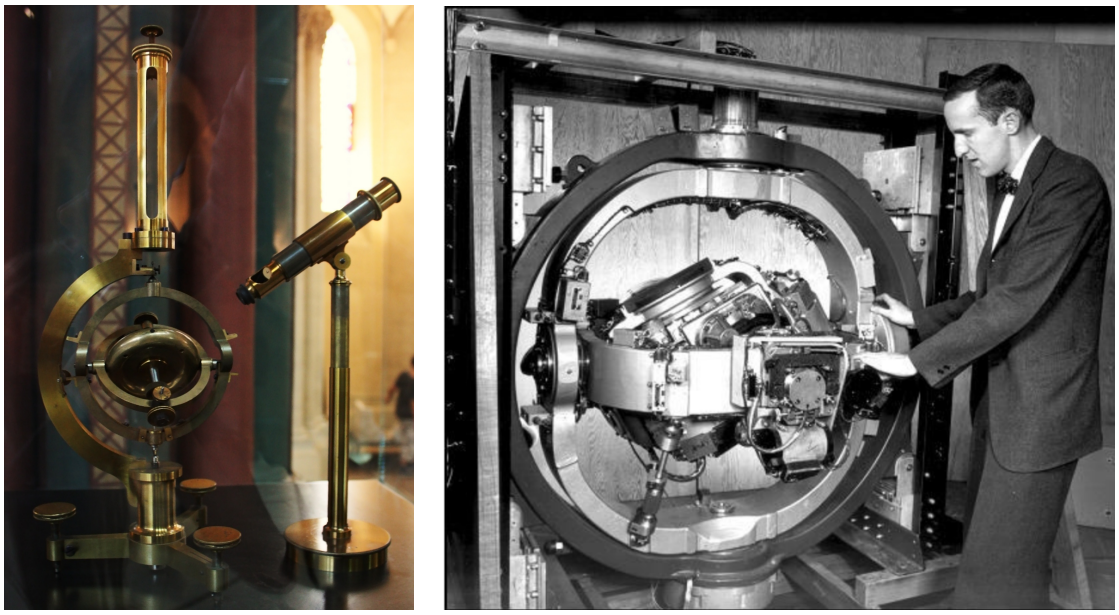

(a) Foucault's free spinning gyroscope (b) SPIRE system

Figure 2-1: Early type of gyroscopes

Navigation is defined as the determination of one's vehicle position and velocity. According to Newton, the motion of a rigid body will continue in a straight line when not exposed to external forces. Newtons 2^{nd} law also tells that external forces will result in accelerations. If somehow these forces could be measured, information about the vehicle accelerations can be obtained. If these accelerations are integrated, the velocities and positions are also known. The position, velocity and acceleration components along a precisely known set of axes make a nine-component vector, called the state vector. Accelerations can be measured by devices called accelerometers, usually three accelerometers are used to measure all three orthogonal components. Rotations are measured by gyroscopic sensors, called gyroscopes. Gyroscopes are used to determine the orientation of the acceleration vector. These sensors provide continues measurements of the current state of the vehicle. This principle is known as "dead reckoning", where the state vector is derived from a continuous series of measurements relative to an initial position. Due to the fact that dead reckoning systems give updates relative to an initial position, sensor errors will result in an increasing error over time, also known as "random walk." It is essential for inertial navigation systems to have an accurate initial position as the error will increase over time. The system must be reinitialized as the error will further increase and becomes too big for navigation purposes. The reinitialization can be done in many ways, for instance by using radio navigation systems, satellite navigation adding or magnetic sensors. Besides reinitialization different sensors can be integrated to compensate each other.

Gyroscopes and accelerometers provide the vehicles position, velocity and angle information,

however still no navigation information is provided. The different states of the state vector can be used to determine the position and orientation of the moving vehicle. However, different calculation steps are required which depend on the platform and sensors. For example a coordinate transformation can be required to integrate different measurements. Also the measured accelerations need to be compensated for gravity forces, since the accelerometers measure the total specific force in inertial space.

The state vector maps the translational and rotational motion of the vehicle. If the determination of the state vector is done on-board, it is called navigation. When calculated outside the vehicle, it is called surveillance or position location. Which is for instance used by Air Traffic Control (ATC) to monitor air traffic. Different platforms can be used for inertial navigation depending on the vehicles hardware and software requirements.

Different types of navigation systems exist. Besides "dead reckoning systems", systems that measure the state vector without regard to the path traveled by the vehicle in the past are called positioning systems. Examples of positioning systems are radio navigation systems, where ground stations send out radio signals which can be received by airborne vehicles to determine their position. Other examples are mapping navigation systems, by using visual images of the Earth's surface and celestial navigation based on the stars position. Figure 2-2 gives an overview of the different navigation systems.

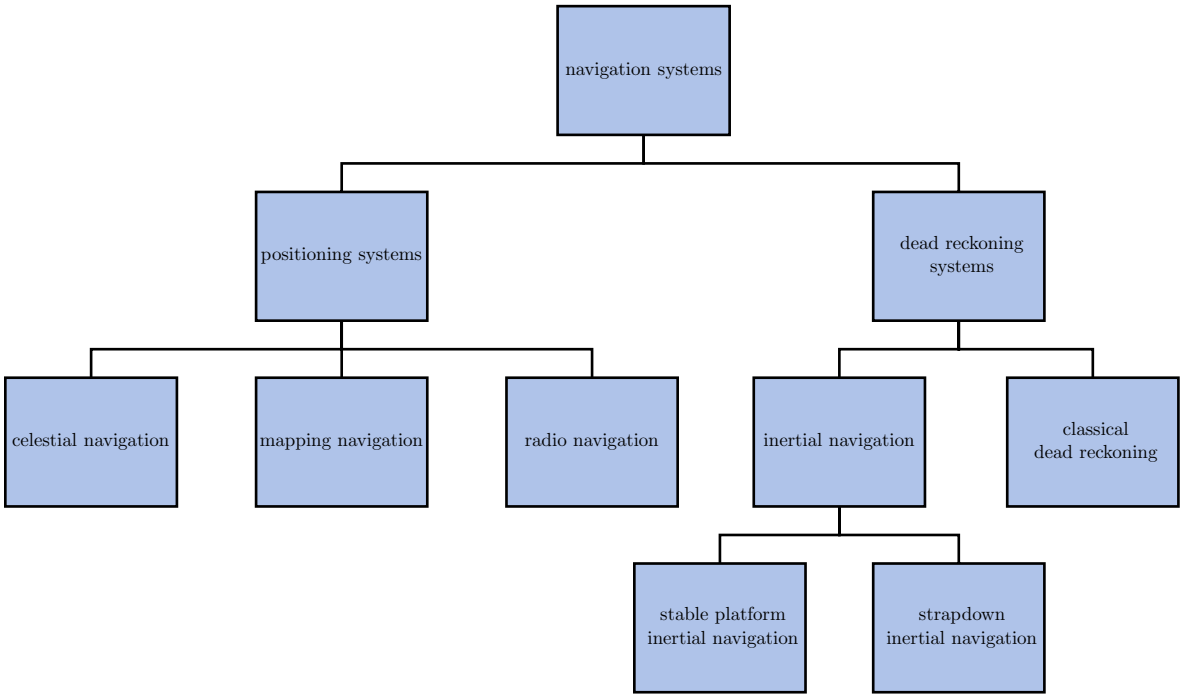

Figure 2-2: Overview of different navigation systems

Unlike positioning systems, dead reckoning systems use the information from the traveled path. The state vector is derived from a continuous series of measurements relative to an initial position. Position is calculated in the absence of direct position measurements. Position information is obtained by integrating estimated or measured ground speeds. The navigation information is usually given in discrete steps. In it most basic form, the position of a vehicle

is calculated from measuring the ground speed V_g and the true heading ψ_T, equation 2-1 from (Kayton & Fried, 1997).

$$\begin{array}{rclcrcl} V_{NORTH} & = & V_g \cos\psi_T, & & y - y_0 & = & \int_0^t V_{NORTH}\ dt \\ V_{EAST} & = & V_g \sin\psi_T, & & x - x_0 & = & \int_0^t V_{EAST}\ dt \end{array} \tag{2-1}$$

In equation 2-1, wind is neglected and $y - y_0$, $x - x_0$ are the east and north traveled distances during a discrete measurement interval. Note that this example is the most elementary form of dead reckoning navigation calculations, however even the more advanced navigation and stabilization algorithms still use this principle.

Due to the integration of measurement data, a disadvantage of dead reckoning systems is that they need to be re-initialized as small errors accumulate in time and result in increasing errors over time due to the integration of measurement data. The integration of measurement data causes the measurement noise to be accumulated. The most used type of dead reckoning systems, is the Inertial Navigation System or simply INS. Two types of INS exist: stable platform and Strapdown Inertial Navigation System (sINS). Classical dead reckoning systems are systems using solely air data sensors, compass or wind velocities. sINS are systems where the sensors are directly placed onto the vehicle to provide an analytical navigation platform. The sINS type of navigation system is used throughout the report and research.

2-2 Global Position System

Today two navigation satellite systems are operational namely the US Global Positioning System (GPS) and Russian GLONASS. The European system Galileo will be fully operational in the near future. Today the most used system is GPS by the US department of defense and is also called NAVigation by Satellite Time And Range (NAVSTAR). Originally designed to provide the US military with accurate information about position and velocity. In the 1990's when the system was fully operational, only certified military users were able to use the full extend of the system. Users that were not certified were not able to use the system to its full accuracy, up to a few years ago. Nowadays, this difference has been lifted which made the GPS a system that can now be used by both military and civilian users. Since this event, GPS has played an important role in many research topics regarding positioning. This interest and further development also leads to significant decrease in size and cost of GPS receivers. Today GPS receivers can be as small and cheap as a microchip of $20 instead of the early receivers that were in the range of $100.000.

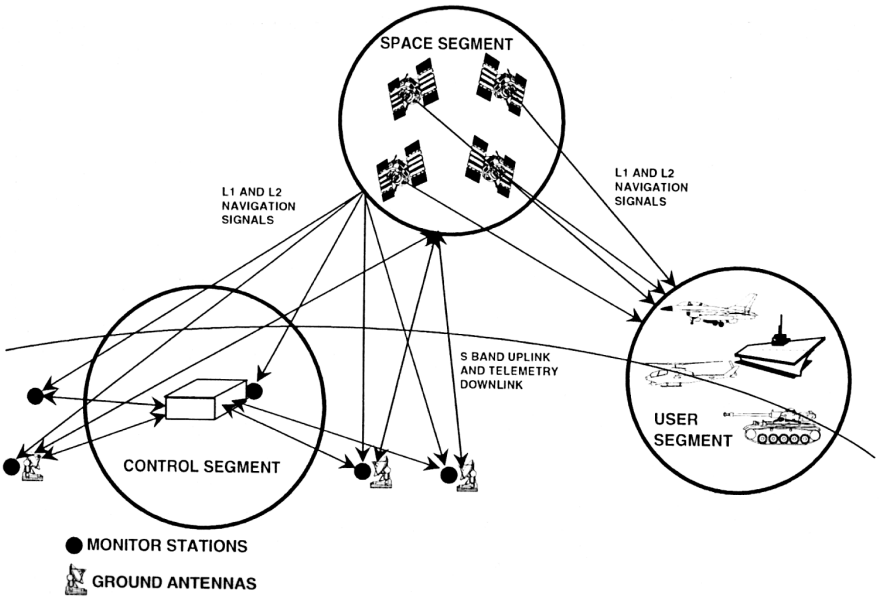

Figure 2-3: GPS system overview: Space, control and user segment

2-2-1 Principle of the Global Positioning System

The GPS consists of three main segments: Space, control and a user segment as can be seen in figure 2-3. The space segment consists of orbiting satellites that are sending out signals. These signals are received by both the user and the control segment. What distinguishes the control segment from the user segment is that the control segment can also upload information to the satellites.

The GPS space segment consists of 24 satellites in six orbital planes, plus a few extra satellites, which can take over damaged satellites if needed. The orbits are located at orbital planes

at 55 degrees to the equator in a near circular orbit at about 20.180 kilometer altitude. An impression of the satellite constellation is given in figure 2-4(a) from (Titterton & Weston, 2009). The spacing of the satellites is made as such that at least six satellites are visible to the user at all times. Each satellite transmits two signals using a carrier wave in the L band. The two carrier frequencies are equal to: $L1 = 1575.42$ MHz and $L2 = 1227.6$ MHz.

The control segment is made out of several stations all over the world to continuously track the GPS satellites and upload information if needed. The tracking task consists of monitoring and predicting satellite orbits, checking onboard atomic clocks and system integrity. Recently the National Geospatial Agency (NGA) has been adding monitoring sites in two phases to existing stations of the US Air Force sites in the Operational Control Segment (OCS). The additional sites give an improvement in combined clock and satellite monitoring. The master control station is located at Colorado Spring in the USA and three uploading station are located worldwide. Figure 2-4(b) gives an overview of the different monitor stations from (Schmidt, 2009). If needed, the clock correction parameters are uploaded when each satellite goes overhead of an uplink.

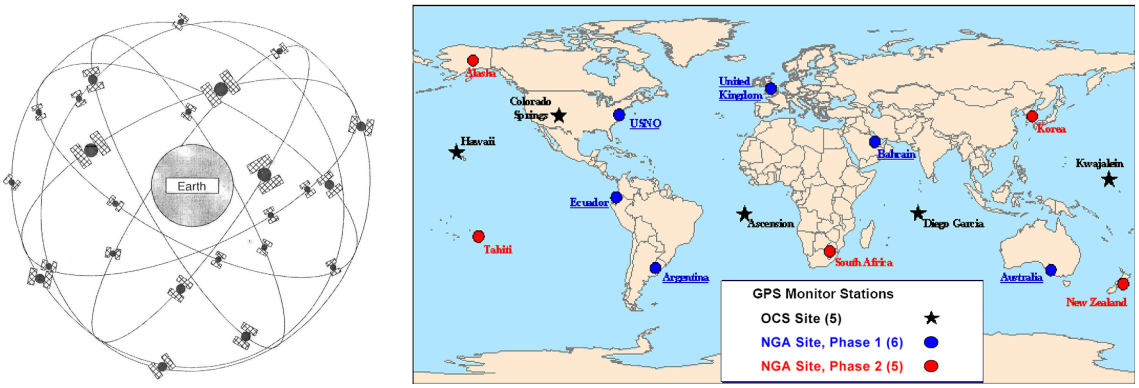

(a) GPS satellite constellation

(b) GPS control segment

Figure 2-4: GPS space and control segment

The user segment consists of a passive GPS receiver. A wide variety of light weight and compact GPS receivers are nowadays available for both civilian and military users. The information that is sent by the satellites contains two codes and the standard positioning service signal. One of the codes is the Coarse/ Acquisition signal (C/A), which is now available to all users. Until May 2000, this signal was deliberately degraded, which is still possible by the US government. When the signal is degraded, the positioning accuracy drops to the order of 100m. This code is only transmitted onto the $L1$ carrier wave. The other code is the Y-code for the Precise Positioning Service (PPS) or simply precision P-code at 10.23 MHz that modulates both $L1$ and $L2$ carries waves. The Y-code gives access to the PPS and is restricted for military purposes. The PPS is the most precise and timing service. Whether the P-code and/ or Y-code are used, the principle of positioning remains the same for all satellite navigation systems which are based on timing.
Electro-magnetic signals are broadcasted by satellites which are received by a user. The difference in sending and receiving time can be used to determine the pseudo-range (PR) between the satellite and user. The pseudo-range is the basis for the user's location on Earth.

In theory three satellites are needed to obtain an unambiguous position fix as can be seen in figure 2-5.

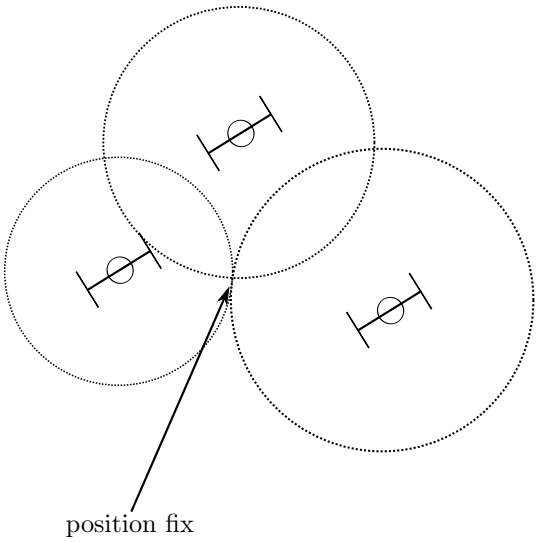

Figure 2-5: Principle of satellite navigation

In practice, a fourth satellite is added to obtain a good position fix. Due to the quality of the receiver clock. The system depends on very precise time measurements, the receiver clock isn't as accurate as the satellite's atomic clock. A time difference of only 10 ns will result in a distance error of 3 m due to the fact that the signals are traveling at the speed of light. The fourth satellite is used to correct for the receivers clock error. Equation 2-2 is used to calculate the pseudo-range (PR), where R stands for the distance between each satellite $_i$ and the user $_u$. The user's clock error is denoted by the symbol Δt_u, where c stands for the speed of light. The sum of various errors is indicated by ϵ_{PR_i}. More about different error sources be found in subsection 2-2-2.

$$\begin{aligned} &PR_i = R_i + c\Delta t_u + \epsilon_{PR_i} \\ &\text{with:} \\ &R_i = \sqrt{(x_{s_i} - x_u)^2 + (y_{s_i} - y_u)^2 + (z_{s_i} - z_u)^2} \end{aligned} \tag{2-2}$$

Using the Doppler shift, the frequency shift of the satellite signal due to the satellites relative velocity to the user, given in equation 2-3. The moving observers are the orbiting satellites f_s and GPS receiver f_r, causing a change in frequency Δf. The change in frequency can be rewritten as the time derivative of the pseudo-range $\dot{PR}$ as defined in equation 2-2, also called pseudo-range rate or simply range rate. The range rate, can be calculated by using equation 2-4. The range rate allows the user velocity to be calculated with a higher accuracy compared to the user position, which is usually one order of magnitude better. The term $c\Delta t_u$ indicates the drift of the user receiver clock.

$$\Delta f = f_r - f_s = \frac{\dot{PR}_i f_s}{c} \tag{2-3}$$

$$\dot{PR}_i = \frac{\underline{x}_{s_i} - \underline{x}_u}{R_i} (v_{s_i} - v_u) + c\Delta t_u \tag{2-4}$$

2-2-2 Sources of Error

As mentioned in the previous section, the user receiver clock is the largest source of error and is the reason that not three, but four satellites are used for satellite navigation. The second clock used for satellite navigation are the atom clocks of the satellites. Despite that these clocks are very accurate, they are not perfect and may still show small errors over a long period of time. The monitoring stations, part of the control segment described in subsection 2-2-1, have many functions. Their functions are to detect and correct possible satellite clock errors and to predict future satellite orbits. Wrong orbit estimations and differences in theoretical and real satellite orbits are called ephemeris error.

In case a satellite signal partially bounces against buildings or other large objects, the GPS receiver receives mixed signals, called multipath effects. The result is that the received signal is not the shortest distance to the sending satellite. A solution is to use a receiver with a cutoff angle such that the reflected signals are not received. Other solutions may consist of a receiver placement which is out of range of any reflected signals. Besides reflected signals, electromagnetic signals can also be affected by objects between the users receiver and satellites. The affected signals tend to be delayed due to the traveling through objects. This phenomenon is called signal attenuation and may lead to errors in satellite navigation.

When a satellite signal travels through the Earth's ionosphere, the signal may be influenced by free ions. The free ions will cause the signal to delay, where the amount of delay is dependent on the density of the ionic particles and orbit elevation. The ionosphere delay can be compensated by using the Y-code which gives access to the PPS. The PPS is transmitted onto the satellite signal and only available for restricted military users. Besides the free ions located in the ionosphere, the troposphere can also be a source of signal delay depending on density and elevation. The troposphere houses different temperatures and water vapor concentrations. When summarizing, the main factors contributing to errors in satellite navigation are the following:

- User receiver clock error.
- Satellite clock error.
- Satellite ephemeris.
- Multipath effects.
- Signal attenuation.
- Ionosphere delays.
- Troposphere delays.

2-3 INS/GPS Integration

Over the years, the integration of inertial and satellite navigation systems has shown to have a positive influence on the overall navigational performance. INS take advantage of complementary properties of the individual components to create a system that provides a better navigational solution. The integration of inertial navigation with satellite data from for instance GPS or GLONASS, or in the future Galileo when fully operational, has been researched for many years. This report only considers GPS. Different integrations of inertial and satellite navigation have been explored over many years, which all have in common that the individual components are aiding one another. Inertial navigation tends to have low noise, but shows large drift over time due to the accumulating error. Satellite systems on the other hand are not effected by long term drift problems, however they tend to have larger short term noise and bias properties. The error characteristics of both type of systems are totally different. INS shows low noise and long-term drift divergence, figure 2-6 gives an example of the position estimation for a coupled or uncoupled INS/GPS. From figure 2-7 can be seen that the 3D position error shows a 2^{nd} order trend. When the INS is coupled with a GPS receiver, the position update resets the accumulated position error. Satellite systems show large noise and very little drift. Satellite navigation systems provide pseudo-range and pseudo-range rate measurements to calculate position and velocity, as can be found in section 2-2 for GPS. INS measures specific force acceleration, which needs to be compensated for gravity and resolved in a predefined known frame of reference. Besides these constraints, the accelerometer measurement data needs to be integrated twice to obtain position data. By integrating INS with satellite navigation, different measurement data are combined into a single algorithm to provide a navigational solution. Table 2-1 gives the general comparison of inertial and satellite navigation systems.

Table 2-1: Comparison of inertial and satellite navigation systems

	Advantages	Disadvantages
Inertial navigation systems	Measurement at high frequency. Provides both translational and rotational data. Autonomous system.	Unbounded errors (long term drift). Required knowledge of gravity.
Satellite navigation systems	Errors are bounded.	Signals at low frequency No (easy) attitude information. Many sources of error; satellite orbit, ionic decay, receiver time delay, etc.

Different inertial and satellite integrating architectures are possible, depending on the required navigational data, available computational power and whether or not the GPS updates are added to an existing system. In the coming sections, the most important systems architectures are explained. In general four different system architectures for INS/GPS integration are distinguished:

- Uncoupled, the GPS data is used to reset the INS position estimation at fixed intervals,

subsection 2-3-1.

- Loosely coupled, the INS and GPS position and velocity estimations are compared, the result is corrected with a (Kalman) filter, subsection 2-3-2.
- Tightly coupled, the GPS pseudo-range and pseudo-range rate measurements are compared with their INS estimates, the result is corrected with a (Kalman) filter, subsection 2-3-3.
- Deep integration, the GPS signal tracking function is integrated together with INS measurements into a single algorithm, subsection 2-3-4.

It should be noted that a good integration is important between inertial and satellite navigation to obtain an accurate and stable navigation solution. Enhancement of the navigation solution is strongly dependent on the integration, and is not mainly dependent on the quality and properties of one of the two elements.

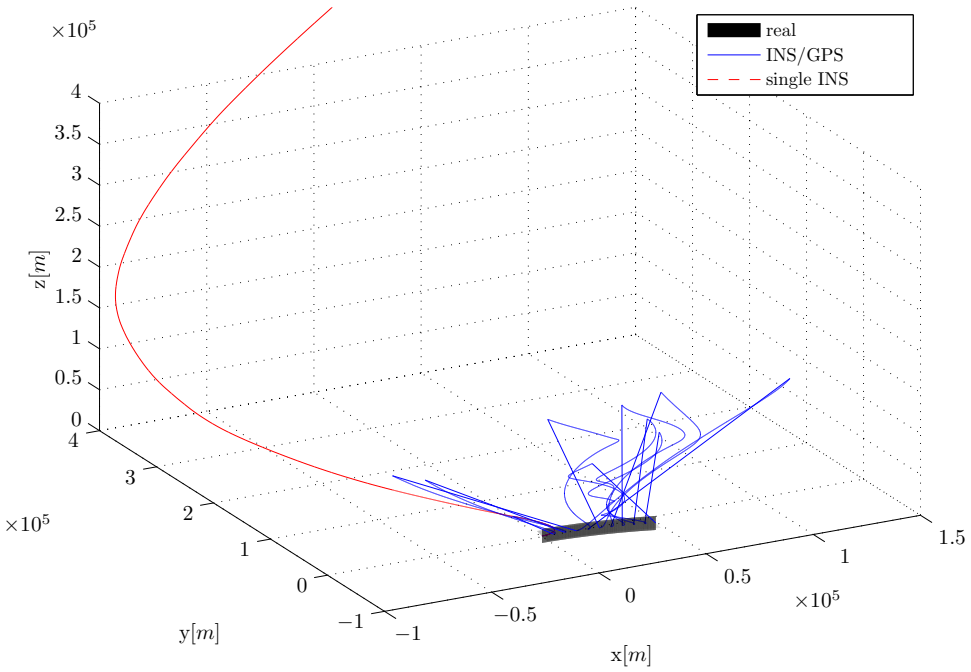

Figure 2-6: INS/GPS integration, 3D position

2-3-1 Uncoupled

The most elementary integration between inertial and satellite navigational measurements is when both systems remain uncoupled. The estimated position (and velocity) measurements from satellite navigation are used to reset the estimated values from inertial navigation. Due to the fact that inertial navigation drifts over time due to accumulation of small errors, this long term drift is compensated by the satellite navigation system that doesn't have this

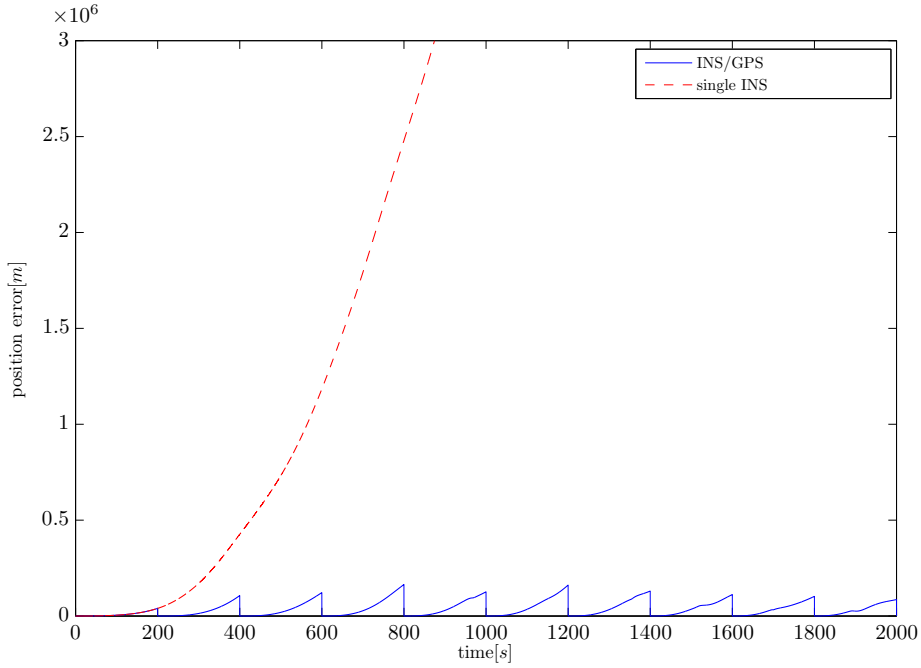

Figure 2-7: 3D position error propagation

long term divergence property. The two systems operate independently and provide system redundancy. If one of the systems fails to operate, the other system can provide the necessary measurements. The advantage of this type of integration is that one of the two can easily be added to an existing system, because their is no interaction between the two. Another advantage is that the integration asks for little or no extra computational power. The added signal simply replaces the other signal at a predefined interval.

2-3-2 Loosely Coupled

For uncoupled inertial and satellite systems, both systems operate separately. This same principle holds for loosely coupled INS/GPS systems. The GPS receiver continues to work autonomously, while aiding the INS. The two systems function in cascade, where the GPS provides position and velocity measurements to correct the INS estimations. The redundant system can function as an integrity monitor of the integrated navigation solution and report filter failures, for instance during filter saturation. This is possible due to the fact that the GPS receiver has its own Kalman filter to provide position and velocity information. Next to monitoring, the combined filter can overrule the existing navigation solution to provide filter recovery.

The advantages of a loosely coupled architecture next to integrity monitoring are redundancy and a relative easy implementation. One of the two systems can take over in case of failure of the other. Like for the uncoupled case, a system can be added to an existing system, however the integration of the two systems asks for more effort when compared to uncoupled integration. The filter, responsible for the sensor fusion, needs to be designed properly depending

on the two separate navigation systems and vehicle properties.

The integration is usually performed by using a Kalman filter. A qualitative overview of the different aspects can be found in figure 2-8 from (Schmidt, 2009). In the overview the integration provides estimates of the INS error which are used to correct the estimated position and velocity. Other derived states from the position and velocity can also be corrected in the same manner. The GPS receiver on the other hand can use the INS to provide a faster acquisition.

One of the disadvantages of using this type of integration is the difference in processing time of inertial and satellite navigational systems. When comparing a GPS receiver to a gyroscope or accelerometer, the processing time of the GPS receiver is much larger. This difference causes the GPS receiver output to be delayed, which makes it difficult to integrate the two outputs into one integration filter. Besides the difference in processing time, the sensors provide their output data at different time steps. The GPS receiver needs more time to calculate the position and velocity and is dependent on the number of available satellites. For instance when a different satellite is used for the first time to obtain a position fix using at least four satellites, this is a so called "difficult solution" and takes more processing time. This makes the sensor integration more difficult to design and as a result the filter measurement update interval becomes important.

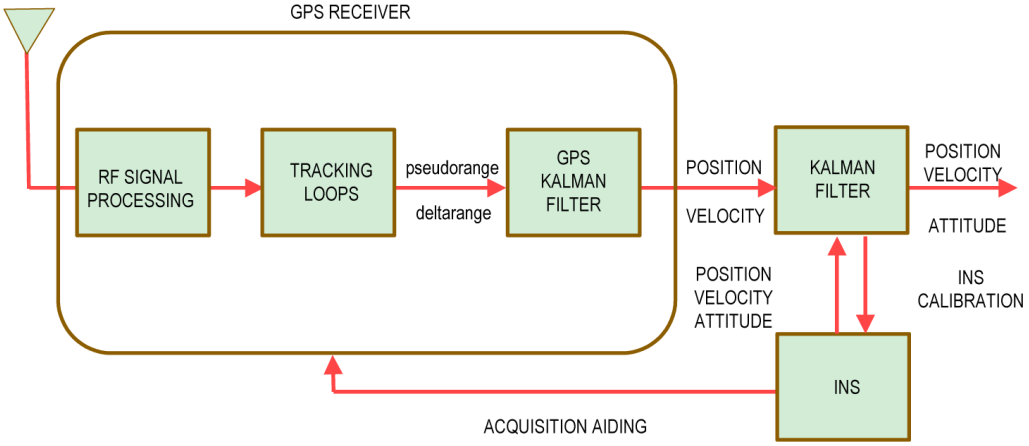

Figure 2-8: Loosely coupled INS/GPS integration architecture

2-3-3 Tightly Coupled

Tightly coupled, or closely coupled, INS/GPS integrations use a more integrated approach when compared to uncoupled or loosely couped architectures. The independent GPS Kalman filter becomes part of the INS/GPS integration Kalman filter as can be seen in figure 2-9 from (Schmidt, 2009) when comparing to figure 2-8 for the loosely coupled case. The pseudo-range and pseudo-range rate measurements from the GPS receiver are now directly used to estimate or correct the INS solution.

Like for the loosely coupled concept, timing is important when integrating the individual measurements. Either the pseudo-range or the pseudo-range rate measurements can be used for the INS correction. In practice it is best to use both since the two measurement are

complimentary. Pseudo-range comes from the GPS code-tracking loop, the pseudo-range rate comes from the more accurate carrier-tracking loop. It should be noted that while the pseudo-range rate is more accurate, it is also less robust. The benefits of tightly coupled integration comes mostly from the fact that the two Kalman filters, one for the GPS receiver and one for the integration, are replaced by a singular INS/GPS integration filter. Statistical problems due to the structure of two Kalman filters are eliminated. The big advantage is also that no longer a minimum of four visible satellites is required to obtain a position fix. GPS measurements can be used with less information, however the accuracy will be less when compared to using four or more satellites.
Tight coupling is also better when compared to loosely coupled integrations in jamming environments. The single satellite lock is more robust, compared to the minimum requirement of four satellites to calculate a position fix. However, during long term loss of GPS satellites it will be INS that becomes the dominant factor in navigation solution accuracy.

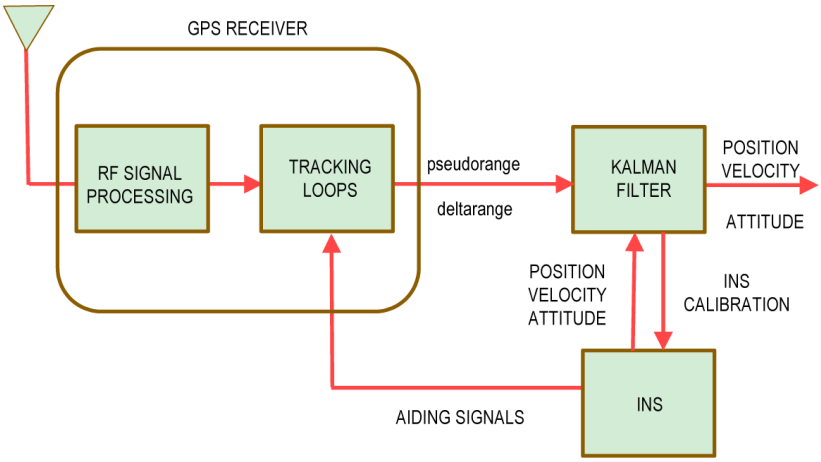

Figure 2-9: Tightly coupled INS/GPS integration architecture

2-3-4 Deep Integration

Deep integration, also called ultra-tight integration uses the GPS signal tracking. Deep integration methods are still under development, although papers have been published on this topic that show a lot of promise, their is no fully working hardware implementation available. A theoretical example can be found in (Li & Wang, 2005). Figure 2-10 shows a diagram of a deep integration architecture from (Titterton & Weston, 2009). Like the tightly coupled integration, deep integration does not need a minimum of four visible satellites. However more satellites improve the navigation solution. By using the GPS signals together, the tracking of each individual signal is aided by the others, besides the INS data. This type of integration uses a single algorithm, which has some advantages when compared to other types of integration.

Less independent quantities are tracked when using the same data, which results in an improvement of the effective signal to noise ratio. When more satellites are tracked, the improvement becomes greater. Next to this, the reacquisition of a signal due to a (short) interruption becomes much faster. Also a change in visible satellites, causing a “difficult solution” fix, becomes less of a problem due to the fact that each satellite signal is tracked individually.

These potential improvements will probably come at the expense of increasing complexity. Deep integration needs more computational power and tight time synchronization. Also accurate INS data is required to maintain a tracking loop lock, as is indicated in figure 2-10 by the arrows connecting the integrated Kalman filter with a (code) correlator.

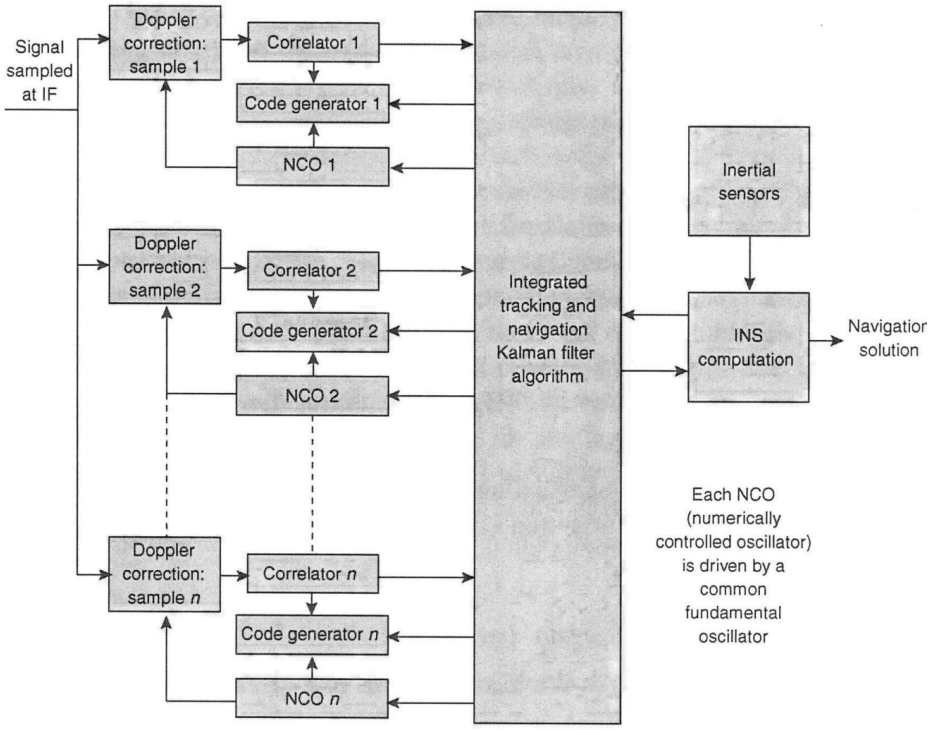

Figure 2-10: Deep integration INS/GPS architecture

Chapter 3

Observability Theory

This chapter provides a background about observability, which can be used to analyze different types of systems and sensor configurations as can be found in chapter 11. Section 3-1 gives observability theory for a Linear-time Invariant System (LTI), section 3-2 does the same for a Linear-time Varying System (LTV). Next to linear systems, also non-linear systems are addressed in section 3-3. Section 3-4 gives matrix algebra about matrix decompositions that can assist in analyzing observability matrices or matrices in general. Leading to the derived singular-value matrix decomposition algorithm where the singular values are given in state structured order. Last section 3-5 is about observability degree, used for measuring observability in a quantitative way and can be used to analyze different observers.

3-1 Observability of LTI Systems

Observability is a measure to how many states of a system can be seen by looking at the system output. Expression 3-1 gives the definition of a standard LTI system from (Olsder & van der Woude, 2005).

$$\begin{aligned} \underline{\dot{x}}(t) &= A\underline{x}(t) + B\underline{u}(t) \\ \underline{y}(t) &= C\underline{x}(t) + D\underline{u}(t) \end{aligned} \tag{3-1}$$

The observability matrix $\mathcal{O}$ for the pair (C,A) can be obtained by using equation 3-2. The number of observable states is equal to the rank n of the observability matrix, or shortly $\text{rank}(\mathcal{O})$.

$$\mathcal{O} = \begin{bmatrix} C \\ CA \\ CA^2 \\ \vdots \\ CA^{n-1} \end{bmatrix} \tag{3-2}$$

All states of the state vector $\underline{x}$ are observable when: $\text{rank}(\mathcal{O}) = n$, with n equal to the number of states of state vector $\underline{x}$. This is given in definition 3.1 from (Olsder & van der Woude, 2005).

Definition 3.1

The LTI system (A,B,C,D) is observable if a finite time $t_1 > 0$ exists such that for each admissible input function $\underline{u}$, it follows from $\underline{y}(t, \underline{x}_0, \underline{u}) = \underline{y}(t, \underline{x}_1, \underline{u})$ for all $t \in [0, t_1]$, with $\underline{x}_0 = \underline{x}_1$.

From a practical point of view, definition 3.1 can be interpreted as: A LTI system (A,B,C,D) is observable if $\underline{x}_0$ can be constructed from $\underline{u}$ and $\underline{y}$ for $t_1 > 0$. When a system is found to be fully observable, theorem 3.1 holds some properties for the pair (A,C). This theorem is found in (Olsder & van der Woude, 2005) and houses properties about the system eigenvalues.

Theorem 3.1

If the pair (A,C) is observable then:

- $\text{rank} \begin{pmatrix} sI - A \\ C \end{pmatrix} = n$, for all s in $\mathbb{C}$.
- $\text{rank} \begin{pmatrix} sI - A \\ C \end{pmatrix} = n$, for all eigenvalues of matrix A.

If the initial state $\underline{x}_0$ cannot be determined, the system is called unobservable. When only part of the system can be determined, this means the rank of the system is smaller then the number of states, this part of the system is observable. The unobservable part corresponds to the kernel (null-space) of pair (A,C), which is built of unobservable modes. Next to the system property of observability, a somewhat weaker system property can be applied to unobservable modes, called detectability. Definition 3.2 gives the definition on detectability for a LTI. If a system contains unobservable modes, these modes might still be detectable and the system is stable.

Definition 3.2

Detectability: The LTI system (A,B,C,D) is detectable if there exists a real matrix K such that the $real(\lambda) < 0, \forall \lambda$ of $A - KC$.

3-2 Observability of LTV Systems

In practice systems are time-invariant by approximation. Due to modeling errors or particular systems properties, the system dynamics change over time. In LTI systems, the system matrices A,B,C,D are assumed to be time invariant. If the matrices change over time, a different system description exists namely Linear-time Varying Systems (LTV). Expression 3-3 gives a standard LTV system in continuous-time, from (Olsder & van der Woude, 2005).

$$\begin{aligned} \dot{\underline{x}}(t) &= A(t)\underline{x}(t) + B(t)\underline{u}(t) \\ \underline{y}(t) &= C(t)\underline{x}(t) + D(t)\underline{u}(t) \end{aligned} \tag{3-3}$$

When considering a continuous-time LTV as defined in 3-3 on an interval $[t_0, t_1]$ the observability matrix $\mathcal{O}(t)$ can be determined with equation 3-4.

$$\mathcal{O}(t) = \begin{bmatrix} N_0(t) \\ N_1(t) \\ N_2(t) \\ \vdots \\ N_{n-1}(t) \end{bmatrix} \tag{3-4}$$

Where:

$$\begin{aligned} N_0(t) &= C(t) \\ N_{k+1} &= N_k(t)A(t) + \tfrac{d}{dt}N_k(t), \qquad \text{with } k = 0, 1, 2, \ldots, n-2 \end{aligned}$$

Continuous-time systems like LTV propagate through time, however in practice this is not always the case. Systems might be sample based and can best be described in discrete-time. Continuous-time LTV differ from discrete-time LTV and their corresponding observability properties. Expression 3-5, gives a standard discrete-time LTV system, from (Olsder & van der Woude, 2005).

$$\begin{aligned} \underline{x}(k+1) &= A(k)\underline{x}(k) + B(k)\underline{u}(k) \\ \underline{y}(k) &= C(k)\underline{x}(k) + D(k)\underline{u}(k) \end{aligned} \tag{3-5}$$

When considering a discrete-time LTV as defined in expression 3-5, on an interval $[t_0, t_1]$, the observability matrix differs from the continuous-time observability matrix $\mathcal{O}(t)$. The discrete-time observability matrix $\mathcal{O}[t_0, t_1]$ is defined by expression 3-6 on interval $[t_0, t_1]$. The observability matrix is built on the number of samples k used on the applicable interval.

If a discrete-time system used turns out to be a LTI instead of LTV, the A and C matrices are no longer varying and equation 3-6 reduces to the a LTI system, as given in equation 3-2. It should be noted that for both continuous- and discrete-time LTI systems that use equation 3-2 to determine their global observability, the system matrices A and C will in most cases

be different. The latter is due to the fact that the system and observer dynamics are modeled differently when using continuous- or discrete-time.

$$\begin{bmatrix} y(t_0) \\ y(t_0+1) \\ y(t_0+2) \\ \vdots \\ y(t_1-1) \end{bmatrix} = \underbrace{\begin{bmatrix} C(t_0) \\ C(t_0)A(t_0) \\ C(t_0+1)A(t_0+1)A(t_0) \\ \vdots \\ C(t_1-1)A(t_1-2)\cdots A(t_0) \end{bmatrix}}_{\mathcal{O}[t_0,t_1]} \cdot(t_0) \tag{3-6}$$

When comparing LTV to LTI systems, different types of observability can be considered due to the fact that the system matrices A and C are continuous- or discrete-time. Three different types of observability can be defined from (Rhee, Abdel-Hafez, & Speyer, 2004): Instantaneous observability as is defined in definition 3.3, complete observability as is defined in definition 3.4 and differential observability as defined in definition 3.5.

Definition 3.3

The LTV system $(A(t), B(t), C(t), D(t))$ is instantaneous observable on an interval $[t_0, t_1]$ if the state $\underline{x}(t)$ can be determined instantaneously from observation of the system output $\underline{y}(t)$.

Definition 3.4

The LTV system $(A(t), B(t), C(t), D(t))$ is complete observable on an interval $[t_0, t_1]$ if any initial state $\underline{x}_0$ at t_0 can be determined from knowledge of the system output $\underline{y}(t)$ over interval $[t_0, t_1]$.

Definition 3.5

The LTV system $(A(t), B(t), C(t), D(t))$ is differentially observable on an interval $[t_0, t_1]$ if it is completely observable on every subinterval on $[t_0, t_1]$.

Definitions 3.3, 3.4 and 3.5 are given in continuous-time as can be found in (Rhee et al., 2004). The distinction on different local observability, as described in these definitions, also holds for discrete-time LTV. Instantaneous observability is the strongest property when compared to complete and differential observability. If a LTV is instantaneously observable, the state $\underline{x}(t)$ can always be determined instantaneously from observing the system output and its derivatives. Complete and differential observability only requires the system state to be observable during a finite time interval. This is an important property as the system observability may change during a finite time interval. The distinction between complete and differential observability disappears when the matrices A and C are analytic, as is described in (Silverman & Meadows, 1967). Definitions 3.3, 3.4 and 3.5 can be rephrased in terms of their rank properties into lemma 3.1, 3.2 and 3.3 which can be found in (Rhee et al., 2004).

Lemma 3.1

The LTV system $(A(t), B(t), C(t), D(t))$ is instantaneously observable on an interval $[t_0, t_1]$ if $\mathcal{O}(t)$ has rank n for all $t \in [t_0, t_1]$.

Lemma 3.2

The LTV system $(A(t), B(t), C(t), D(t))$ is complete observable on an interval $[t_0, t_1]$ if and only if $\mathcal{O}(t)$ has rank n for some $t \in [t_0, t_1]$.

Lemma 3.3

The LTV system $(A(t), B(t), C(t), D(t))$ is differentially observable on an interval $[t_0, t_1]$ if and only if $\mathcal{O}(t)$ does not have rank less than n on any subinterval of $[t_0, t_1]$.

3-3 Observability of Non-Linear Systems

Linear systems are a linear approximation of real systems. Nonetheless in practice most physical processes are non-linear by nature. Besides linear systems, as described in section 3-1 and 3-2, also non-linear system descriptions exist. Equation 3-7 gives a standard non-linear system, where $\underline{f}$ corresponds to the non-linear state equation which is similar to the matrix A and B of a linear system. The linear matrix C is replaced by the non-linear observer equation $\underline{h}$. When using linear systems, the system matrices are the result of partial derivatives, when linearizing around a certain point.

$$\begin{aligned} \dot{\underline{x}}(t) &= \underline{f}\left(\underline{x}(t), \underline{u}(t), t\right) \\ \underline{y}(t) &= \underline{h}\left(\underline{x}(t), t\right) \end{aligned} \tag{3-7}$$

When using non-linear systems, the observability analysis differs from linear systems. The local observability of non-linear systems can be analyzed used Lie derivatives. Lie derivatives represent the derivative of a scalar function along a vector field. Like for LTV systems, observability is a local system property for non-linear systems depending on the system and observer dynamics. To analyze local observability, first the definition of distinguishability is required. Distinguishability is defined in definition 3.6, which can be found in (Hedrick & Girard, 2005).

Definition 3.6

For the non-linear system $\left(\underline{f}\left(\underline{x}(t), \underline{u}(t), t\right) \underline{h}\left(\underline{x}(t), t\right)\right)$ two states $\underline{x}_0$ and $\underline{x}_1$ are distinguishable if there exists an input function $\underline{u}^*$ such that: $\underline{h}(\underline{x}_0) \neq \underline{h}(\underline{x}_1)$.

When two states $\underline{x}_0$ and $\underline{x}_1$ are found to be distinguishable in accordance with definition 3.6, the local system observability at local state $\underline{x}_0$ and input $\underline{u}^*$ can be analyzed by using the following definition, definition 3.7 from (Hedrick & Girard, 2005). The definition can also by interpreted from a more practical perspective: "If the sensor readings are different, the states are different."

Definition 3.7

The non-linear system $\left(\underline{f}\left(\underline{x}(t), \underline{u}(t), t\right) \underline{h}\left(\underline{x}(t), t\right)\right)$ is locally observable at $\underline{x}_0$ if there exists a neighborhood of $\underline{x}_0$ such that every $\underline{x}$ in that neighborhood is other than $\underline{x}_0$, such that:

$$\underline{x}_0 \neq \underline{x}_1 \;\Rightarrow\; \underline{y}_0 \neq \underline{y}_1$$

Local observability for non-linear systems can best be analyzed by using Lie derivatives. Equation 3-8 gives the Lie derivative definition from (Hedrick & Girard, 2005) of a scalar function h with respect to vector field $\underline{f}$.

$$L_f h = \nabla h \cdot \underline{f} = \frac{\partial h}{\partial x}\underline{f} = \sum_{i=1}^{n} \frac{\partial h}{\partial x_i} f_i \tag{3-8}$$

Where:

$$\begin{array}{ll} \underline{f}: & \mathbb{R}^n \to \mathbb{R}^n \text{ be a vector field in } \mathbb{R}^n \\ h: & \mathbb{R}^n \to \mathbb{R} \text{ be a smooth scalar function} \end{array}$$

Equation 3-8 can be worked out in equation 3-9 to calculate the first-order Lie derivatives.

$$L_f^1(h) = \left[\frac{\partial h}{\partial x_1}, \ldots, \frac{\partial h}{\partial x_n}\right] \begin{bmatrix} f_1(x) \\ f_2(x) \\ \vdots \\ f_n(x) \end{bmatrix} \tag{3-9}$$

By definition holds that the zero-order Lie derivative is equal to the function itself: $L_f^0(h) = h$. Also higher-order Lie derivatives can be derived, equation 3-10 gives a second-order derivative of h with respect to vector field $\underline{f}$.

$$L_f^2(h) = \frac{\partial}{\partial x}\left[L_f^1(h)\right]\underline{f} = \frac{\partial}{\partial x}\left[\frac{\partial h}{\partial x}\underline{f}\right]\underline{f} \tag{3-10}$$

Equation 3-10 can be generalized into the following expression 3-11.

$$L_f^n(h) = \frac{\partial}{\partial x}\left[L_f^{n-1}(h)\right]\underline{f} \tag{3-11}$$

Equation 3-12 gives the expression to calculate the local observability of $(\underline{x}_0, \underline{u}^*)$ using up to 4^{th} order Lie derivatives, by using equation 3-11.

$$\begin{aligned} \mathcal{O}(\underline{x}_0, \underline{u}^*) = & \begin{bmatrix} H(\underline{x}) \\ H(\underline{x})F(\underline{x},\underline{u}) \\ H(\underline{x})[F(\underline{x},\underline{u})]^2 \\ H(\underline{x})[F(\underline{x},\underline{u})]^3 \\ H(\underline{x})[F(\underline{x},\underline{u})]^4 \\ \vdots \\ H(\underline{x})[F(\underline{x},\underline{u})]^{n-1} \end{bmatrix}_{\underline{x}_0,\underline{u}^*} + \begin{bmatrix} \emptyset^{p\times n} \\ E(\underline{x},\underline{u}) \\ E(\underline{x},\underline{u})F(\underline{x},\underline{u}) \\ E(\underline{x},\underline{u})[F(\underline{x},\underline{u})]^2 \\ E(\underline{x},\underline{u})[F(\underline{x},\underline{u})]^3 \\ \vdots \\ E(\underline{x},\underline{u})[F(\underline{x},\underline{u})]^{n-2} \end{bmatrix}_{\underline{x}_0,\underline{u}^*} + \\ & \begin{bmatrix} \emptyset^{p\times n} \\ \emptyset^{p\times n} \\ D(\underline{x},\underline{u}) \\ D(\underline{x},\underline{u})F(\underline{x},\underline{u}) \\ D(\underline{x},\underline{u})[F(\underline{x},\underline{u})]^2 \\ \vdots \\ D(\underline{x},\underline{u})[F(\underline{x},\underline{u})]^{n-3} \end{bmatrix}_{\underline{x}_0,\underline{u}^*} + \begin{bmatrix} \emptyset^{p\times n} \\ \emptyset^{p\times n} \\ \emptyset^{p\times n} \\ C(\underline{x},\underline{u}) \\ C(\underline{x},\underline{u})F(\underline{x},\underline{u}) \\ \vdots \\ C(\underline{x},\underline{u})[F(\underline{x},\underline{u})]^{n-4} \end{bmatrix}_{\underline{x}_0,\underline{u}^*} \end{aligned} \tag{3-12}$$

Where:

$$
\begin{aligned}
\underline{f}: \quad & \mathbb{R}^n \to \mathbb{R}^n \text{ be a vector field in } \mathbb{R}^n \\
h: \quad & \mathbb{R}^n \to \mathbb{R} \text{ be a smooth scalar function} \\
H\left(\underline{x}\right) = \quad & \frac{\partial h(\underline{x})}{\partial \underline{x}} \\
F\left(\underline{x},\underline{u}\right) = \quad & \frac{\partial \underline{f}(\underline{x},\underline{u})}{\partial \underline{x}} \\
E\left(\underline{x},\underline{u}\right) = \quad & \begin{bmatrix} \underline{f}^T \frac{\partial (dh_1)^T}{\partial \underline{x}} \\ \vdots \\ \underline{f}^T \frac{\partial (dh_n)^T}{\partial \underline{x}} \end{bmatrix} \\
D\left(\underline{x},\underline{u}\right) = \quad & \begin{bmatrix} \left(\underline{f}^T \frac{\partial (dh_1)^T}{\partial \underline{x}}\right)^T \underline{f} \\ \vdots \\ \left(\underline{f}^T \frac{\partial (dh_n)^T}{\partial \underline{x}}\right)^T \underline{f} \end{bmatrix} \\
C\left(\underline{x},\underline{u}\right) = \quad & \begin{bmatrix} \left\{\left(\underline{f}^T \frac{\partial (dh_1)^T}{\partial \underline{x}}\right)^T \underline{f}\right\} \underline{f} \\ \vdots \\ \left\{\left(\underline{f}^T \frac{\partial (dh_n)^T}{\partial \underline{x}}\right)^T \underline{f}\right\} \underline{f} \end{bmatrix}
\end{aligned}
$$

The first term of the second order Lie derivatives $E\left(\underline{x},\underline{u}\right)$, represents the second order derivative of smooth scaler function h, which is equal to 0. The same holds for the first and second term of the third order Lie derivatives $D\left(\underline{x},\underline{u}\right)$. Also the first up to the third terms for the fourth order Lie derivatives $C\left(\underline{x},\underline{u}\right)$ are equal to 0.

3-4 Matrix Decompositions

To analyze observability of different systems, as described in the previous sections for different type of systems, it is useful to include matrix decompositions. The different observability matrices $\mathcal{O}$ for the different types of systems are: Equation 3-2 for LTI systems, equation 3-4 for LTV systems or equation 3-12 for non-linear systems. Matrix decompositions can assist in the analysis of observability matrices. A basic matrix decomposition is the eigenvalue decomposition. For instance when taking a eigenvalue decomposition of a matrix $A \epsilon \mathbb{R}^{m \times n}$ with n linearly independent eigenvectors. When these eigenvectors are put together into a matrix V, expression 3-13 holds, where Λ contains the eigenvalues of matrix A along its diagonal.

$$AV = V\Lambda \tag{3-13}$$

When the eigenvalues of matrix A are assumed to be linearly independent, the following theorem 3.2 holds from (Verhaegen & Verdult, 2007).

Theorem 3.2

Eigenvalue decomposition: Any matrix $A \epsilon \mathbb{R}^{m \times n}$, with n linearly independent eigenvalues can be decomposed as:

$$A = V\Lambda V^{-1}$$

Where: $\Lambda \epsilon \mathbb{R}^{n \times n}$ is a diagonal matrix containing the eigenvalues of the matrix A and the columns of the matrix $V \epsilon \mathbb{R}^{n \times n}$ are the corresponding eigenvectors.

It is important to note that theorem 3.2 only holds when matrix A has n linearly independent eigenvectors. An other matrix decomposition is the Singular-Value Decomposition (SVD), described in theorem 3.3 from (Verhaegen & Verdult, 2007).

Theorem 3.3

Singular-value decomposition: Any matrix matrix $A \epsilon \mathbb{R}^{m \times n}$ can be decomposed as:

$$A = U\Sigma V^T$$

Where: $U \epsilon \mathbb{R}^{m \times m}$ and $V \epsilon \mathbb{R}^{n \times n}$ are orthogonal matrices and $\Sigma \epsilon \mathbb{R}^{m \times n}$ has its only non-zero elements along the diagonal. These elements σ_i are ordered such that:

$$\sigma_1 \geqslant \sigma_2 \geqslant \ldots \geqslant \sigma_r > \sigma_{r+1} = \sigma_k = 0$$

Where: $r = rank(A)$ and $k = min(m, n)$.

The matrix Σ contains non-zero values σ_i along its diagonal, these values are called singular values of matrix A. The orthogonal matrices U and V contain the left and right singular vectors of A. The transpose of matrix V can be replaced with V^H if the matrix contains

complex numbers, where V^H represent the conjugate transpose of V. The singular-value decomposition of a matrix can be performed in different ways. When a matrix $A \epsilon \mathbb{R}^{m \times n}$ has rank r, such that $r < m$ and $r < n$ the SVD can be calculated by using equation 3-14, from (Verhaegen & Verdult, 2007).

$$A = [U_1 \; U_2] \begin{bmatrix} \Sigma_1 & 0 \\ 0 & 0 \end{bmatrix} \begin{bmatrix} {V_1}^T \\ {V_2}^T \end{bmatrix} \tag{3-14}$$

Where:

$$\begin{aligned} &U_1 \; \epsilon \; \mathbb{R}^{m \times r} \\ &U_2 \; \epsilon \; \mathbb{R}^{m \times (m-r)} \\ &\Sigma_1 \; \epsilon \; \mathbb{R}^{r \times r} \\ &V_1 \; \epsilon \; \mathbb{R}^{n \times r} \\ &V_2 \; \epsilon \; \mathbb{R}^{n \times (n-r)} \end{aligned}$$

From equation 3-14 four different subspaces can be identified, these subspaces relate to the kernel (null-space) and range (column-space) of matrix $A \epsilon \mathbb{R}^{m \times n}$ with rank r:

$$\begin{aligned} \text{range}(A) &= \text{range}(U_1) \\ \ker(A^T) &= \text{range}(U_2) \\ \text{range}(A^T) &= \text{range}(V_1) \\ \ker(A) &= \text{range}(V_2) \end{aligned}$$

Next to the four different subspaces the number of singular values of matrix A, put together in Σ_1, corresponds to the rank r. Each non-zero value on the diagonal of Σ_1 corresponds to an eigenvalue of A. When a matrix has rank r that is smaller to the number of columns m or rows n, this corresponds to zero diagonal elements of Σ_1. The SVD is a numerically robust factorization, the computations are not sensitive to rounding errors.
Next to the singular-value and eigenvalue decomposition, there is one other important matrix decomposition namely the QR factorization given in theorem 3.4, from (Verhaegen & Verdult, 2007).

Theorem 3.4

QR factorization: Any matrix matrix $A \epsilon \mathbb{R}^{m \times n}$ can be decomposed as:

$$A = QR$$

Where: $Q \epsilon \mathbb{R}^{m \times m}$ is an orthogonal matrix and $R \epsilon \mathbb{R}^{m \times n}$ is upper-triangular, augmented with columns on the right for $n > m$ or augmented with zero rows at the bottom for $m > n$.

When a matrix $A \epsilon \mathbb{R}^{m \times n}$ has rank r, such that $r < m$ and $r < n$. The QR factorization can be performed by using equation 3-15, from (Verhaegen & Verdult, 2007).

$$A = [Q_1 \; Q_2] \begin{bmatrix} R_1 & R_2 \\ 0 & 0 \end{bmatrix} \tag{3-15}$$

Where:

$$Q_1 \in \mathbb{R}^{m\times r}$$
$$Q_2 \in \mathbb{R}^{m\times(m-r)}$$
$$R_1 \in \mathbb{R}^{r\times r}$$
$$R_2 \in \mathbb{R}^{r\times(n-r)}$$

The bottom zero rows below R_1 and R_2 in expression 3-15 account for the number of rows $m-r$ of matrix A. Like for the SVD, different subspaces can be identified for the QR factorization, each with its relation to the kernel and column space of matrix $A \in \mathbb{R}^{m\times n}$ with rank r:

$$\begin{aligned}\text{range}(A) &= \text{range}(Q_1)\\ \ker(A^T) &= \text{range}(Q_2)\\ \text{range}(A^T) &= \text{range}(R_1^T)\end{aligned}$$

The SVD and QR factorizations can be used to determine the column space and kernel of a matrix by decomposition. The corresponding rank of a matrix is equal to the number of independent columns and rows. These particular properties can be utilized when analyzing observability matrices. In both theorems a matrix $A \in \mathbb{R}^{m\times n}$ is used, matrix A can be replaced by an observability matrix $\mathcal{O}$ for a LTI system, $\mathcal{O}(t)$ for a continuous-time LTV, $\mathcal{O}[t_0, t_1]$ for a discrete-time LTV or $\mathcal{O}(\underline{x}_0, \underline{u}^*)$ for a non-linear system. The number of singular values σ_i corresponds to which states are observable based on the used observability matrix. Theorem 3.3 can be used to decompose $\mathcal{O}$ into a SVD, resulting in equation 3-16 when $\mathcal{O}$ has rank r such that $r < m$ and $r < n$.

$$\mathcal{O} = U\Sigma V^T = [U_1\ U_2]\begin{bmatrix}\Sigma_1 & 0\\ 0 & 0\end{bmatrix}\begin{bmatrix}V_1{}^T\\ V_2{}^T\end{bmatrix} \tag{3-16}$$

Like for the SVD, the same can be done for a QR decomposition. Using theorem 3.4, an observability matrix $\mathcal{O}$ can be decomposed into a QR factorization, resulting in equation 3-17 when $\mathcal{O}$ has rank r such that $r < m$ and $r < n$.

$$\mathcal{O} = QR = [Q_1\ Q_2]\begin{bmatrix}R_1 & R_2\\ 0 & 0\end{bmatrix} \tag{3-17}$$

When performing a SVD, the corresponding singular values σ_i are given in structured decreasing order, starting with the highest value. This decreasing order has the disadvantage that it is no longer possible to directly link a singular value to its corresponding state. When analyzing different observers, corresponding to different sensor configurations, this makes it difficult to analyze observer performance for individual states. The decreasing order of the SVD is usually not the same as compared to the numbering order of the system states. To avoid this problem a QR factorization can be used to determine the singular values of an observability matrix $\mathcal{O}$. Expression 3-16 and 3-17 can be set equal when the same $\mathcal{O}$ is used. The orthogonal matrix $U \in \mathbb{R}^{m\times m}$ with the left hand-side eigenvectors is equal to $Q \in \mathbb{R}^{m\times m}$ as defined in equation 3-18. The product $\Sigma_1 V \in \mathbb{R}^{m\times n}$ is equal to $R \in \mathbb{R}^{m\times n}$ as defined in equation 3-19.

$$U = Q \tag{3-18}$$

$$\begin{bmatrix} \Sigma_1 & 0 \\ 0 & 0 \end{bmatrix} \begin{bmatrix} V_1{}^T \\ V_2{}^T \end{bmatrix} = \begin{bmatrix} R_1 & R_2 \\ 0 & 0 \end{bmatrix} \tag{3-19}$$

From expression 3-19 it can be seen that the singular values matrix Σ_1 together with the right hand-side singular vectors V form the matrix R from the QR factorization. Both Σ_1 and R are $\mathbb{R}^{m \times n}$, the singular values σ_i are the only non-zero elements along the diagonal of Σ_1, equal to the rank r and observable states of $\mathcal{O}$. The non-zero elements correspond to the non-zero eigenvalues of $\mathcal{O}$ and the zero elements correspond to the zero eigenvalues. Figure 3-1 gives an overview of a singular-value decomposition algorithm by using QR. The R matrix is upper-triangular, augmented with columns on the right for $n > m$ or augmented with zero rows at the bottom if $m > n$. The algorithm uses "s" as QR input and s_{new} as the QR factorization output matrix R. The upper-triangular part of s with possible non-zero eigenvalues can be extracted with the "triu.m" Matlab-function. The extracted upper-triangular part, denoted by e is used to calculate the error. When the error is below a threshold "$error_{tol}$", the last step is to sign correct the diagonal terms of s_{new} by taking the absolute value. The complete algorithm "QRsvd.m" can be found in appendix C, listing C-1.

A disadvantage of QR factorization is that it is more sensitive to numerical instability compared to SVD. The SVD can best be used to determine the rank since it is not sensitive to rounding errors. After the rank has been determined with SVD, the singular values can be linked to the corresponding states by using the QRsvd algorithm. When using real or simulated sensor data usually no discontinuities or sharp edges are present due to the presents of noise, the QRsvd algorithm will not run into numerical problems. It is advised that after the rank is determined by SVD, the QRsvd algorithm is used to quantitatively analyze the observability of the known observable states.

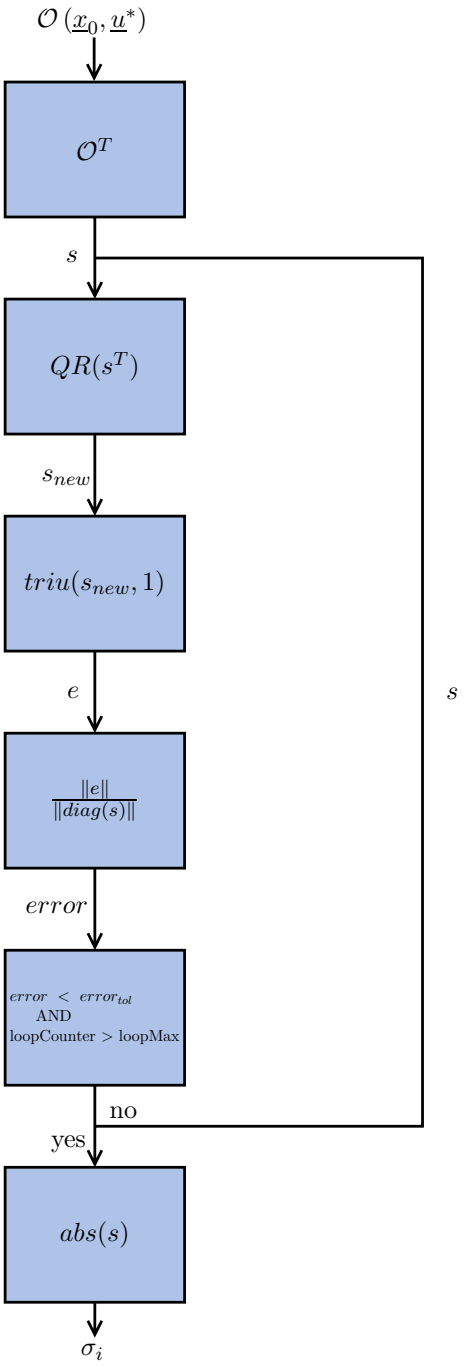

Figure 3-1: QRsvd Algorithm

3-5 Observability Degree

The observability degree is a measure to quantify the observability of individual system states. The observable degree η_k of different system states can be analyzed based on the matrix decompositions of the observability matrix $\mathcal{O}$, as described section 3-4. The observability degree acts as a ratio between the observability of individual system states. Furthermore, this ratio can be used to determine which states are "good" or "bad" observable. This ratio can be used to measure the performance of different observers, and to determine if an observer is ill-conditioned to observe particular states. Ill-conditioned observers usually results in high observability degree. Definition 3.8 gives the definition of observability degree. Besides measuring observer performance, the observability degree can be used to predict potential estimation filter problems for particular system states, an example can be found in (Long, Yong-yuan, & Ji-chao, 2008). A higher observability degree is likely to give a higher Kalman filter error for that particular state as the observer has difficulty to observe that specific part of the system. Likewise, a low observability degree will give good Kalman filter performance as those states are well observed. When designing a Kalman filter is it advised to take an appropriate value as maximum allowable degree of observability γ as defined in definition 3.8 when performing the observability analysis to know a-priory which states are likely to give high errors and filtering problems.

Definition 3.8

The observability degree is defined as the ratio between singular values:

$$\eta_k = \frac{\sigma_{max}}{\sigma_i}, \qquad \text{for } i = 1,\ 2,\ \ldots, n$$

Where: η_k is the observability degree of the k^{th} state, σ_i are the singular values with σ_{max} as the maximum singular value. The maximum degree of observability is defined as:

$$\gamma = \max\{\eta_k\}$$

Where: γ is the maximum allowable degree of observability, which can be used as an initial condition.

Chapter 4

Kalman Filtering

This chapter gives a background on Kalman Filtering, that is used for state identification of chapter 13. Section 4-1 gives an introduction into the subject of Kalman filtering. Section 4-2 gives the conventional Kalman filter framework for state estimation. Section 4-3 gives an extension on Kalman filtering when using non-linear systems, Extended Kalman Filter (EKF). The last section 4-4 gives an improvement to the EKF, the Iterated Extended Kalman Filter (IEKF).

4-1 Introduction

Kalman filtering has its origin in the 1960's when published by Rudolf E. Kalman. This new approach into linear filtering can be found in (Kalman, 1960) and has its application in many scientific fields. In essence, Kalman filtering produces estimations of measurement values by predicting its values using a set of mathematical equations. The estimation is performed by predicting its value together with its uncertainty, by computing an average of the predicted and measured value. The measured values are given by observers and are used to correct the predicted values. Kalman filtering is powerful in many aspects; it supports state estimation of past, present and future measurements. Besides states it can estimate system parameters when part of the modeled system is unknown or even both, called dual estimation. This report mainly focuses on state estimation using MEMS sensors applied to fixed-wing UAVs. Figure 4-1 gives the principle of state and parameter identification.

4-2 State Identification Kalman Filters

Different types of systems can be used when applying Kalman filter theory. The conventional Kalman filter uses linear filter theory and can only be applied to linear systems. Section 4-3 gives an extension for non-linear systems, using Jacobians.

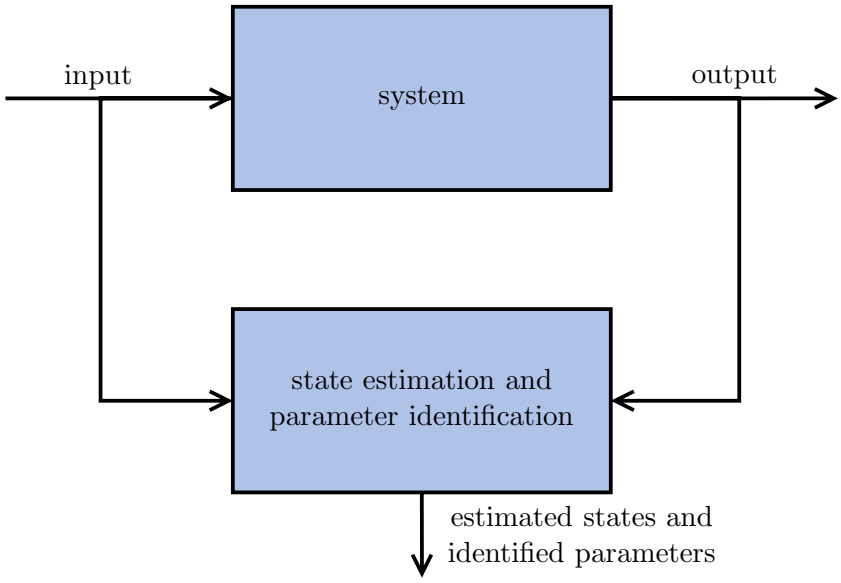

Figure 4-1: Principle of state and parameter identification

A description on the standard discrete linear time-varying (LTV) system can be found in section 3-2, expression 3-3, which is used to describe the observability of linear time-varying systems. The standard LTV systems does not include the system's noise properties, for Kalman filtering the system and input noise properties are essential and should be included. Expression 4-1 form (Simon, 2006) gives a more general form of linear discrete-time varying systems.

$$\begin{aligned} \underline{x}(k+1) &= \Phi(k)\underline{x}(k) + \Psi(k)\underline{u}(k) + \underline{w}(k) \\ \underline{z}(k+1) &= H(k+1)\underline{x}(k+1) + D(k+1)\underline{u}(k) + \underline{v}(k+1) \end{aligned} \tag{4-1}$$

The matrix $\Phi(k)$ is the system transition matrix, the input distribution matrix $\Psi(k)$ with time varying parameters. The output observer dynamics $H(k+1)$ represents the sensor dynamics between the state vector $\underline{x}$ and measured quantities $\underline{z}$. The factor $D(k+1)\underline{u}(k)$ represents sensor feedback with the observer. When assumed that the input and observer are decoupled, $D(k+1)\underline{u}(k)$ can be left out. The process noise $\underline{w}(k)$ and measurement noise $\underline{v}(k+1)$ are assumed to be white mean Gaussian, uncorrelated with known constant covariance matrices Q and R as defined in expressions 4-2 and 4-3. In practice sensors usually have biases, are correlated and have time varying noise properties. If this is the case, sensor biases can be added as additional states or parameters to the state vector. With added bias states, the estimation performance increases. A disadvantage of a larger state vector, is that the required computational power also increases.

$$\underline{w} \sim N(0, Q) \tag{4-2}$$

$$\underline{v} \sim N(0, R) \tag{4-3}$$

The goal is to estimate the state vector $\underline{x} \epsilon \mathbb{R}^n$ based on predefined knowledge of the system and observer dynamics and availability of measurements $\underline{z}$. The error between the true state $\underline{x}$ and the estimate $\hat{\underline{x}}$ is defined in expression 4-4.

$$\underline{e} = \underline{x} - \hat{\underline{x}} \tag{4-4}$$

The mean of the state vector is defined as follows: $E\{\underline{x}(k+1)\} = \hat{\underline{x}}(k+1 \mid k)$. The notation "$k+1 \mid k$" is to indicate an a priori estimate and "$k+1 \mid k+1$" is to indicate an a posteriori estimate. These two notations are used to indicate different Kalman filter steps. The two corresponding error covariances are in expressions 4-5 and 4-6.

$$P(k+1 \mid k) = E\left\{[\underline{x}(k+1) - \hat{\underline{x}}(k+1 \mid k)][\underline{x}(k+1) - \hat{\underline{x}}(k+1 \mid k)]^T\right\} \tag{4-5}$$

$$P(k+1 \mid k+1) = E\left\{[\underline{x}(k+1) - \hat{\underline{x}}(k+1 \mid k+1)][\underline{x}(k+1) - \hat{\underline{x}}(k+1 \mid k+1)]^T\right\} \tag{4-6}$$

The goal of the Kalman filter is to find the state estimate $\hat{\underline{x}}(k+1 \mid k+1)$. The estimated state vector is a linear combination of the a priori estimate $\hat{\underline{x}}(k+1 \mid k)$ and measurement correction $\hat{\underline{z}}(k+1 \mid k+1)$. To perform the linear combination, the state estimate $\hat{\underline{x}}(k+1 \mid k)$ is multiplied by the measurement dynamics $H(k+1)$, as can be seen in expression 4-7. The difference between the measurement $\underline{z}(k+1 \mid k+1)$ and predicted measurement $H(k+1)\hat{\underline{x}}(k+1 \mid k)$ is multiplied with a Kalman gain matrix $K(k+1)$ and added to the predicted state $\hat{\underline{x}}(k+1 \mid k)$. The difference between $\hat{\underline{z}}(k+1 \mid k+1)$ and $H(k+1)\hat{\underline{x}}(k+1 \mid k)$ is called the residual of the measurement innovation.

$$\hat{\underline{x}}(k+1 \mid k+1) = \hat{\underline{x}}(k+1 \mid k) + K(k+1)\left[\hat{\underline{z}}(k+1 \mid k+1) - H(k+1)\hat{\underline{x}}(k+1 \mid k)\right] \tag{4-7}$$

The equations of expression 4-1 must be combined with expression 4-7 to construct a Kalman filter. The first equation of 4-1 represents the prediction step, the second equation the innovation equation where observer measurements correct the prediction step. First the state is predicted called one step ahead prediction, expression 4-8 together with the covariance matrix results in equation 4-9 from (Simon, 2006). The initial state $\hat{\underline{x}}_0$ and covariance P_0 are applied when first performing a step update.

$$\hat{\underline{x}}(k+1 \mid k) = \Phi(k)\hat{\underline{x}}(k \mid k) + \Psi(k)\underline{u}(k), \qquad \hat{\underline{x}}(0 \mid 0) = \hat{\underline{x}}_0 \tag{4-8}$$

$$P(k+1 \mid k) = \Phi(k)P(k \mid k)\Phi^T(k) + Q(k), \qquad P(0 \mid 0) = P_0 \tag{4-9}$$

As previously mentioned, the Kalman filter uses a prediction step together with a correction. These two steps form a type of Feedback control, where the Kalman gain is the gain onto the

residual. The Kalman gain is given in expression 4-10. The Kalman gain uses the covariance estimation during the prediction, expression 4-9.

$$K(k+1) = P\left(k+1 \mid k\right) H^T(k+1)\left[H(k+1)P\left(k+1 \mid k\right) H^T(k+1) + R(k+1)\right]^{-1} \quad (4\text{-}10)$$

A measurement update step can be performed by working out expression 4-7 by using expression 4-10 together with expression 4-7, resulting in expression 4-11.

$$\begin{aligned}\underline{\hat{x}}\left(k+1 \mid k+1\right) = \underline{\hat{x}}\left(k+1 \mid k\right) + P\left(k+1 \mid k\right) H^T(k+1)[H(k+1) \\ P\left(k+1 \mid k\right) H^T(k+1) + R(k+1)]^{-1}\left[\underline{z}(k+1 \mid k+1) - H(k+1)\underline{\hat{x}}\left(k+1 \mid k\right)\right]\end{aligned} \quad (4\text{-}11)$$

Together with the measurement update of expression 4-11, the covariance matrix $P\left(k+1 \mid k+1\right)$ of the state estimation error vector can use the information obtained during the correction step, expression 4-12.

$$P\left(k+1 \mid k+1\right) = \left[I - K(k+1)H(k+1)\right] P\left(k+1 \mid k\right) \quad (4\text{-}12)$$

To implement the Kalman filter, the measurement covariance noise R is required and is usually obtained prior to implementation. This is usually done by taking off-line measurements, where the process is observed during filter operation. Knowing the variance of the measurement noise before operation, will improve the filter performance and stability. The process noise covariance matrix Q is more difficult to determine as usually no direct process state observers are available. A simple or uncertain process model can best be used by selecting high Q values to account for process uncertainty. The individual process states, which are usually influenced by input noise, can be tuned individually by selecting higher or lower values on the diagonal of Q. Off diagonal terms of matrix Q represent process noise coupling effects between individual states. When a process model is very uncertain or caused by noisy measurements, it can still produce reliable filter output as high uncertainties are included in the calculation of the covariance matrix P and Kalman gain K. The disadvantage of selecting high process noise covariances is that the filter performance and convergence decreases. The filter parameters R and Q should be tuned properly to improve the filter performance. The R matrix can best be selected based on the noise level of observer noises. Under the constraint that the matrices R and Q are kept constant, the estimation covariance P and Kalman gain K will stabilize and converge to constant values. When the latter is the case, these parameters can be determined by using off-line filtering when looking at their steady-state values.

In practice, equation 4-12 can lead to numerical round-off errors and results in a updated covariance matrix $P\left(k+1 \mid k+1\right)$ that is not symmetrical and positive-semi definite. As an alternative, equation 4-13 can be used which is the result of multiplying expression 4-12 with $P\left(k+1 \mid k+1\right)$ at the left and $P\left(k+1 \mid k\right)$ at the right.

$$\begin{aligned}P\left(k+1 \mid k+1\right) &= \left[I - K(k+1)H(k+1)\right] P\left(k+1 \mid k\right) \cdot \\ &\quad \left[I - K(k+1)H(k+1)\right]^T + K(k+1)R(k+1)K^T(k+1)\end{aligned} \quad (4\text{-}13)$$

If the covariance matrix of the state estimation error $P(k+1 \mid k+1)$, expression 4-12 leads to numerical instability, the covariance matrix can be forced to be symmetric. This can be done by taking the transpose of the covariance matrix and divide this the sum by 2, expression 4-14 from (Simon, 2006). This expression does usually not result in better filter convergence, but increases the filters numerical robustness. Also square root forms may compensate for instability during calculations, which are usually the result of inverting singular matrices. More about square root and alternate forms of Kalman filtering can be found in (Simon, 2006). The Kalman filter assumes that the process and measurements noise are Gaussian bases. This may however not be the case in practice, if so a particle or Bayesian filter framework should be chosen. More about different attitude filtering methods can be found in (Markley, Crassidis, & Cheng, 2005).

$$P = \frac{P + P^T}{2} \tag{4-14}$$

4-3 Extended Kalman Filter

In the previous section 4-2, the traditional Kalman filter was used to estimate the state vector $\underline{x}$, by using a linear discrete stochastic time-varying system description. In practice, the process and measurements equations are usually non-linear. The linear Kalman filter theorem can be extended for non-linear systems by linearizing around the mean and covariance, which is referred to as the Extended Kalman Filter (EKF). The EKF uses first order partial derivatives to linearize non-linear dynamical systems at each time step to estimate the state vector $\underline{x}$. Expression 4-15 gives a general non-linear system. In expression 4-15 $\underline{f}$ represents the aircraft kinematics, G the system noise input matrix with $\underline{w}$ the input noise. Together this gives the non-linear state equation, the first row of expression 4-15 indicated by $\underline{\dot{x}}(t)$. The non-linear observer equation $\underline{h}$, together with the measurement noise $\underline{v}$ and measurement noise dynamics D this gives the measurement equation $\underline{z}$.

Linearizing and discretization of the state equation $\underline{\dot{x}}(t)$ around a point $[\underline{x}(t), \underline{u}(t)]$ is required, since the state equation has time-varying non-linear parameters, the linearized state equation needs to be recalculated during each step $\underline{x} = \underline{\hat{x}}(k|k)$.

$$\begin{aligned} \underline{\dot{x}}(t) &= \underline{f}\left[\underline{x}(t), \underline{u}(t), t\right] + G\left[\underline{x}(t), t\right] \underline{w}(t) && \underline{x}(0) = \underline{x}_0 \\ \underline{z}_m(t) &= \underline{h}\left[\underline{x}(t), \underline{u}(t), t\right] && \\ \underline{z}(t) &= \underline{z}_m(t) + D\left[\underline{x}(t), t\right] \underline{v}(t) && k = 1, 2, \ldots \end{aligned} \tag{4-15}$$

To use EKF, some of the expressions of the previous section 4-2 needs to be rewritten. The one step ahead prediction for non-linear systems can be obtained by integrating the non-linear state equation of expression 4-15 with the one step earlier estimate of the state vector, expression 4-16.

$$\underline{\hat{x}}\left(k+1 \mid k\right) = \underline{\hat{x}}\left(k \mid k\right) + \int_{t_k}^{t_{k+1}} \underline{f}\left(\underline{x}(t), \underline{u}(t), t\right) dt \tag{4-16}$$

The covariance matrix is calculated in the same way as for the linear Kalman filter, expression 4-9 with the difference of a linearization step. Expression 4-17 and 4-18 gives the linearization

of the non-linear state equation $\underline{f}\left[\underline{x}(t), \underline{u}(t), t\right]$ and system noise matrix $G\left[\underline{x}(t), t\right]$, by using Jacobians.

$$F(k) = \frac{\partial \underline{f}\left(\underline{x}(t), \underline{u}(t), t\right)}{\partial \underline{x}(t)}\Big|_{\underline{x}=\underline{\hat{x}}(k|k)} \tag{4-17}$$

$$G(k) = \frac{\partial G\left(\underline{x}(t), t\right)}{\partial \underline{x}(t)}\Big|_{\underline{x}=\underline{\hat{x}}(k|k)} \tag{4-18}$$

Expression 4-19 gives the error covariance matrix $P\left(k+1 \mid k\right)$ of the prediction step by using discrete time linearized system dynamics $\Phi(k)$ and input dynamics $\Gamma(k)$.

$$P\left(k+1 \mid k\right) = \Phi(k) P\left(k \mid k\right) \Phi^T(k) + \Gamma(k) Q(k) \Gamma^T(k) \tag{4-19}$$

The same linearization should be done of the observer equation $\underline{h}\left[\underline{x}(t), \underline{u}(t), t\right]$, of expression 4-15 at sample k. Expressions 4-20 and 4-21 give the observer and observer noise linearization.

$$H(k) = \frac{\partial \underline{h}\left(\underline{x}(t), \underline{u}(t), t\right)}{\partial \underline{x}(t)}\Big|_{\underline{x}=\underline{\hat{x}}(k|k)} \tag{4-20}$$

$$D(k) = \frac{\partial D\left(\underline{x}, (t)\right)}{\partial \underline{x}(t)}\Big|_{\underline{x}=\underline{\hat{x}}(k|k)} \tag{4-21}$$

Resulting in the Kalman gain matrix, expression 4-22.

$$\begin{aligned} K(k+1) = {} & P\left(k+1 \mid k\right) H^T(k+1) \\ & \left[H(k+1) P\left(k+1 \mid k\right) H^T(k+1) + D(k+1) R(k+1) D(k+1)^T\right]^{-1} \end{aligned} \tag{4-22}$$

Measurement update equation, expression 4-23.

$$\underline{\hat{x}}\left(k+1 \mid k+1\right) = \underline{\hat{x}}\left(k+1 \mid k\right) + K(k+1)\left[\underline{z}(k+1) - H(k+1)\underline{\hat{x}}\left(k+1 \mid k\right)\right] \tag{4-23}$$

Covariance matrix update, expression 4-24.

$$\begin{aligned} P\left(k+1 \mid k+1\right) = {} & \left[I - K(k+1)H(k+1)\right] P\left(k+1 \mid k\right) \\ & \left[I - K(k+1)H(k+1)\right]^T + K(k+1)\left(D(k+1)R(k+1)D(k+1)^T\right) K^T(k+1) \end{aligned} \tag{4-24}$$

When there is no measurement observer noise, captured in $D(k+1)$ the term "$K(k+1)\left[D(k+1)R(k+1)D(k+1)^T\right]K^T(k+1)$" becomes: $K(k+1)R(k+1)K^T(k+1)$. Expression 4-24 can be rewritten into expression 4-25.

$$\begin{aligned} P\left(k+1 \mid k+1\right) = {} & \left[I - K(k+1)H(k+1)\right] P\left(k+1 \mid k\right) \\ & \left[I - K(k+1)H(k+1)\right]^T + K(k+1)R(k+1)K^T(k+1) \end{aligned} \tag{4-25}$$

4-4 Iterated Extended Kalman Filter

The extended Kalman filter described in the previous section 4-3, contains linearization around the observer dynamics

$$\underline{h}\left[\underline{x}(t), \underline{u}(t), t\right]$$

. This linearization, equation 4-20, can be extended to obtain a better state estimate of the observer dynamics. For many observers the non-linearities present cannot be neglected and need to be included in dynamics models. To ensure stability, the perturbed state vector must be small, meaning the initial condition of the EKF should be close to the optimal solution. By recalculating the Kalman gain and measurement update steps of equations 4-22 and 4-23, a better state estimate around the linearized observer dynamics can be obtained by reiteration.

The one stage ahead estimation remains the same and is now reiterated around $\underline{\hat{x}}\left(k+1 \mid k\right) = \eta_1$ from the prediction step, to partially compensate for non-linearities. The prediction is calculated the same as for the EKF, expression 4-16. Kalman gain $K(k+1)$ is now recalculated at each iteration together with the measurement update, resulting in equation 4-26 and 4-27. During every iteration the linearization of the observer dynamics $H(k+1)$ is repeated to obtain a better observer linearization.

$$K(k+1) = P\left(k+1 \mid k\right) H^T(k+1)\left[H(k+1)P\left(k+1 \mid k\right) H^T(k+1) + R(k+1)\right]^{-1} \quad (4\text{-}26)$$

Measurement update equation 4-23 is rewritten into equation 4-27. The measurement state update $\underline{\hat{x}}\left(k+1 \mid k+1\right)$, has been replaced with a dummy variable η_2.

$$\eta_2 = \underline{\hat{x}}\left(k+1 \mid k\right) + K(k+1)\left[z(k+1) - h(\eta_1) - H(k+1)\underline{\hat{x}}\left(k+1 \mid k\right) - \eta_1\right] \quad (4\text{-}27)$$

Last two equations 4-26 and 4-27 can be repeated for a maximum number of iterations or until the error is below a tolerance $|\varepsilon_{crit}|$, equation 4-28.

$$\varepsilon = \frac{\eta_2 - \eta_1}{\eta_2}, \qquad \text{repeated while} |\varepsilon| > |\varepsilon_{crit}| \quad (4\text{-}28)$$

When the iteration stopping criteria is reached of equation 4-28 or after a finite number of steps, the variable η_2 becomes the final state estimation $\underline{\hat{x}}\left(k+1 \mid k+1\right)$. After the measurement update has been performed, the covariance matrix of state estimation error vector of equation 4-13 can be calculated, expression 4-29.

$$\begin{aligned} P\left(k+1 \mid k+1\right) &= \left[I - K(k+1)H(k+1)\right] P\left(k+1 \mid k\right) \\ &\left[I - K(k+1)H(k+1)\right]^T + K(k+1)\left(D(k+1)R(k+1)D(k+1)^T\right) K^T(k+1) \end{aligned} \quad (4\text{-}29)$$

Part II

Modeling

Chapter 5

Inertial Measuring Unit Modeling

This chapter is about the modeling of Inertial Measuring Unit (IMU) gyroscopes and accelerometers sensors. The developed sensor simulation tool in this chapter can be used to convert the UAV output states of chapter 7 to MEMS based IMU sensor output signals. Section 5-1 gives a short background about a Micro-Electro-Mechanical Systems (MEMS) based IMU. Sections 5-2 up to 5-7 describe the individual sensor properties as can be found in (Abdel-Hafez, 2009). Last section 5-8 summarizes the individual IMU characteristics.

5-1 Introduction

Throughout this chapter IMU sensors consist of three gyroscopic and accelerations sensors to sense angular rates and accelerometers in all three directions. Furthermore it is assumed that the IMU is based on MEMS technology. MEMS can best be seen as a system-on-a-chip. Such a system is the complete integration of electronic, mechanical, sensors and actuator elements by means of micro fabrication technology. The electronic components are made using conventional integrated circuit technology, the micromechanical components using micromachining technology. The combination of these two technologies makes it possible to create complete systems on a single chip. MEMS devices can be used for navigational purposes, the microsensors function as the systems eyes with the microelectronics as the brains of the system. These devices are used more and more on smaller and cheaper platforms. When compared to conventional inertial instruments, MEMS improves many features that constrain the use of inertial instruments on smaller platforms, like cost, size and power consumption. The reduction in size brings other challenges to obtain good measurements when compared to conventional instruments. A decrease in sensitivity together with an increase in thermal sensitivity and noise. With changing temperature, the mechanical properties of the system are expected to change resulting in lower accuracy and sensitivity. One other aspect is the effect of time delays, it is assumed that no time delays are present. For the final signal modeling of chapter 7, a GPS receiver is also included. For the GPS receiver modeling of chapter 6, time delays are considered between IMU and GPS receivers. GPS receivers usually

need more processing time, when compared to MEMS based IMU and result in time delay between IMU and GPS signals. For this reason time delays are only applied to GPS receiver modeling as they are larger. The following sections 5-2 to 5-8 will go into more detail about MEMS based IMU sensor properties and how they can properly be modeled.

5-2 Random Walk

A described in chapter 2 most dead-reckoning navigation systems experience an accumulation of error. This increase in error over time, due to a continuous series of measurements relative to an initial position is called drift. This increase in error is called a random walk, meaning the calculated position is going to "walk away" in a random fashion from the true value. A random walk can best be seen as an integrated zero mean Gaussian. The change in individual noise samples will cause fluctuations around a zero mean. If these individual samples are summed up over time, the accumulated signal will show an increase/ decrease result around zero, figure 5-1 shows the integration step. The noise $e \, \epsilon \, N(0,1)$ has a standard normal distribution with a mean around zero and a standard deviation $\sigma = 1$, the magnitude of the random walk b can be increased by multiplication for modeling purposes.

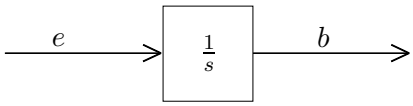

Figure 5-1: Random walk

Figure 5-2 gives an example of a random walk by using a Gaussian around zero with a standard deviation of 1. Subfigure 5-2(a) gives the Gaussian noise, with the resulting random walk in subfigure 5-2(b).

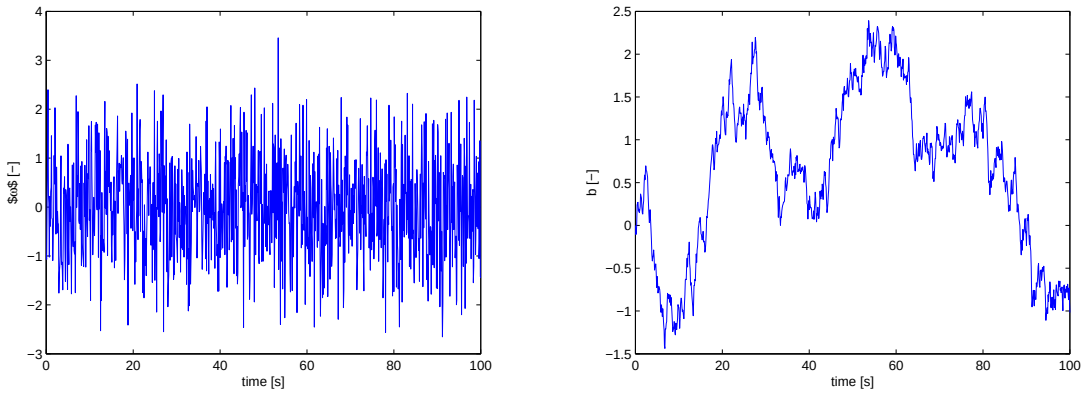

(a) Standard Gaussian around zero

(b) Random walk bias

Figure 5-2: Example of random walk bias by integrating a Gaussian around zero

5-3 Axis Misalignment

A placed sensor package onto a platform never coincides completely with the vehicle axes of orientation. The axis misalignment between the sensor axis of sensitivity and the body axis can be described by looking at the angle in between. Figure 5-3 gives an example of a single axis misalignment, resulting in a rotation angle θ around the z-axis. When using an IMU with 3 orthogonal sensors, a Direction Cosine Matrix (DCM) can best be used as is explained in more detail in 8-2. With the DCM the sensor package orientation can be transformed to the virtual misaligned frame of reference, corresponding to the axis misalignment.

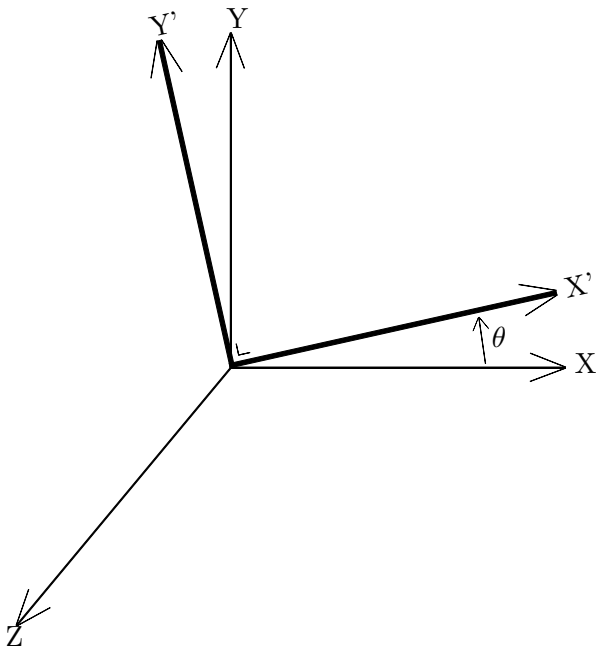

Figure 5-3: Rotation around z-axis with an angle θ

Equation 5-1 gives the axis misalignment rotational matrix R_{am} using three misalignment angles ϕ_{am}, θ_{am} and ψ_{am}. Equation 5-2 gives the simulated acceleration measurements $\underline{A}_m$ including axis misalignment by multiplying the true values with the misalignment DCM matrix. Equations 5-1 and 5-2 also hold for gyroscopic sensor axis misalignment, as can be found in (Abdel-Hafez, 2009).

$$R_{am}\left(\phi_{am},\theta_{am},\psi_{am}\right)=\begin{bmatrix}\cos\theta_{am}\cos\psi_{am} & \sin\phi_{am}\sin\theta_{am}\cos\psi_{am}- & \cos\phi_{am}\sin\theta_{am}\cos\psi_{am}+\\ & \cos\phi_{am}\sin\psi_{am} & \sin\phi_{am}\sin\psi_{am}\\ \cos\theta_{am}\sin\psi_{am} & \sin\phi_{am}\sin\theta_{am}\sin\psi_{am}+ & \cos\phi_{am}\sin\theta_{am}\sin\psi_{am}-\\ & \cos\phi_{am}\cos\psi_{am} & \sin\phi_{am}\cos\psi_{am}\\ -\sin\theta_{am} & \sin\phi_{am}\cos\theta_{am} & \cos\phi_{am}\cos\theta_{am}\end{bmatrix} \tag{5-1}$$

$$\underline{A}_m = R_{am}\left(\phi_{am},\theta_{am},\psi_{am}\right)\underline{A}_{true} \tag{5-2}$$

5-4 Sensor-to-Sensor Misalignment

IMU consists of three separate gyroscopic and three accelerometer sensors. Both sets have three orthogonal placed sensors to measure in all three directions. The sensors are manufactured in an orthogonal fashion, however in practice small deviations are usually present. These small deviation causes (small) measurement errors by sensors orthogonal to the axis of orientation, called sensor-to-sensor misalignment. Like for the axis misalignment errors of section 5-3, sensor-to-sensor misalignment errors can be included by using a DCM matrix for transforming the true values to a virtual frame of reference. The virtual frame of reference represents the misaligned frame of reference. The rotational matrix R_{sm} uses three angles ϕ_{sm}, θ_{sm} and ψ_{sm} to calculate the non-orthogonal influence on the sensor performance. Equation 5-3 represents the corresponding DCM matrix as is described in section 8-2. Equation 5-4 gives the acceleration $\underline{A}_m$ computation to include sensor-to-sensor misalignment. Both equations 5-3 and 5-4 also hold for gyroscopic sensors.

$$R_{sm}\left(\phi_{sm},\theta_{sm},\psi_{sm}\right)=\begin{bmatrix} \cos\theta_{sm}\cos\psi_{sm} & \sin\phi_{sm}\sin\theta_{sm}\cos\psi_{sm}- & \cos\phi_{sm}\sin\theta_{sm}\cos\psi_{sm}+ \\ & \cos\phi_{sm}\sin\psi_{sm} & \sin\phi_{sm}\sin\psi_{sm} \\ \cos\theta_{sm}\sin\psi_{sm} & \sin\phi_{sm}\sin\theta_{sm}\sin\psi_{sm}+ & \cos\phi_{sm}\sin\theta_{sm}\sin\psi_{sm}- \\ & \cos\phi_{sm}\cos\psi_{sm} & \sin\phi_{sm}\cos\psi_{sm} \\ -\sin\theta_{sm} & \sin\phi_{sm}\cos\theta_{sm} & \cos\phi_{sm}\cos\theta_{sm} \end{bmatrix} \tag{5-3}$$

$$\underline{A}_m = R_{sm}\left(\phi_{sm},\theta_{sm},\psi_{sm}\right)\underline{A}_{true} \tag{5-4}$$

5-5 Temperature Influence

A change in temperature over time, called temperate flux, influences the performance of a MEMS based IMU. It causes two kinds of performance degradation, a linear scale factor S and a bias term b. Linear scale factor errors as defined in expression 5-5 are in the range of 200 ppm to 1400 ppm according to (Geiger & Bartholomeyczik, 2008). The temperature influence on the sensor bias is the same as for the random walk of section 5-2 with the addition of a multiplication factor to include the linear scale factor. Both effects are modeled as a factor times a temperature difference ΔT. It is assumed for simulation purposes that both gyroscopes and accelerometers are calibrated when there is no temperature difference $\Delta T = 0$.

$$S_T = lsf\Delta T \tag{5-5}$$

$$b_{\Delta T} = b_T\Delta T. \tag{5-6}$$

Besides a linear scale factor and bias, additional higher order terms can be added to simulate the influence of temperature more accurately, for instance non-linear scale factors and axis misalignment of a function of temperature changes. An example about temperature polynomial fitting and IMU sensor calibration can be found in (De Wagter, 2004).

5-6 External Vibration Source

MEMS based IMU's are very sensitive to external factors. Besides temperature influences as described in the previous section, also vibrations have an influence on the sensor output. MEMS based sensors are influenced by internal or external vibrational sources. An example of a vibrational source usually present is the UAV's engine. This is usually a fixed-propeller rotating at a high frequency. The engine vibrations are passed through to the vehicles body and are sensed by the IMU. Due to the vehicles body, engine and other components, the vibrations are changed. While the IMU can always be placed on vibrations dampers, the sensors will always sense some kind of vibration due to their high sensitivity. The influence of vibrations on the sensor performance can best be modeled as Gaussian noise. For accelerometers, the vibrations will be sensed as a source of acceleration and are combined in the measurement noise. The gyroscopes are influenced by vibrations in a different way due to the fact that gyroscopes measure angular rates instead of accelerations. This can be modeled by using a vibration rectification factor VR_ω, as defined in equation 5-7 from (Geiger & Bartholomeyczik, 2008). Typical values are about 0.02 $^o/h/g^2$ according to (Geiger & Bartholomeyczik, 2008), usually some information is included in the manufacturing datasheet.

$$\underline{\omega}_m = \underline{\omega}_{true} + \mathrm{VR}_\omega F_{vibrations} \tag{5-7}$$

5-7 Measurement Noise

The total measurement noise e is a combination of white noise e_ω, correlated noise e_c, random walk e_{rw}, quantization error e_q and dither noise e_d as summarized in equation 5-8. When a sensor signal is passed through a low-pass filter, it becomes correlated to the properties of the low-pass filter, which is used to filter out high frequency white noise. The random walk is due to integration of the white noise. Quantization errors are due to analog-digital (AD) converters. The input signal is analog and basically a continuous set of values, which is digitalized to a discrete set. Dither is an intentionally added noise term to randomize quantization errors and noise at discrete frequencies. To include the effect of an external vibration source on the accelerometers, this can best be modeled as white noise e_ω with a Gaussian deviation σ equal to 0.25 - 0.5g to model the engine vibration source.

$$e = e_\omega + e_c + e_{rw} + e_q + e_d \tag{5-8}$$

Additional sources could be added to equation 5-8 like acoustic rectification error which usually starts to occur above sound levels of 140 dB. During normal operations such sound levels are not reached and these effects can be neglected.

5-8 IMU Modeling

The individual IMU properties, described in sections 5-2 to 5-7, can be summarized to give an accurate description of how accelerometer and gyroscopic sensor data is being sensed by MEMS based sensors. It is assumed that MEMS IMU are used, the true sensor signal is multiplied and added by different properties to obtain a realistic IMU measurement. The term $\underline{b}_{RW}$ is a 3D vector, to simulate a random walk in all three orthogonal sensitivity axes. Equations 5-9 and 5-10 give the accelerometer and gyroscopic output. Some terms have an added subscript $_A$ or $_\omega$ to indicate differences between accelerometer and gyroscopic sensors. These two equations are used in this report when simulating IMU output signals. As can be found in chapter 13 about different identification simulations.

$$\underline{A}_m = [1 - R_{am_A} R_{sm_A}]\, \underline{A}_{true} + \underline{b}_{RW_A} + \Delta T\,(lsf_A + b_{T_A}) + e_A \tag{5-9}$$

$$\underline{\omega}_m = [1 - R_{am_\omega} R_{sm_\omega}]\, \underline{\omega}_{true} + \underline{b}_{RW_\omega} + \Delta T\,(lsf_\omega + b_{T_\omega}) + \mathrm{VR}_\omega F_{vibrations} + e_\omega \tag{5-10}$$

Accelerometers equation 5-9, with $\underline{A}_{true}$ being the true vehicle accelerations, subscript $_m$ being the measured value, b being a sensor bias value and e being sensor noise. The accelerometer equation 5-9 is split up into the three orthogonal directions: $\underline{A} = [A_x A_y A_z]^T$ resulting in equation 5-11.

$$\begin{aligned} A_{x_t true} &= A_{x_m} - b_{A_x} - e_{A_x} \\ A_{y_t true} &= A_{x_m} - b_{A_y} - e_{A_y} \\ A_{z_t true} &= A_{y_m} - b_{A_z} - e_{A_z} \end{aligned} \tag{5-11}$$

The bias terms [b_{A_x},b_{A_y},b_{A_z}] are a function of the axis and sensor-to-sensor misalignment properties, random walk and temperature. The sensor noise terms [e_{A_x},e_{A_y},e_{A_z}] are a function of external vibration sources and measurement noise. The gyroscopic equation 5-10, with $\underline{\omega}_{true}$ being the true value, $_m$ being the measured value, b being a sensor bias value and e being sensor noise. The gyroscopic equation 5-10 is split up into the three orthogonal directions: $\underline{\omega} = [p\ q\ r]^T$ resulting in equation 5-12.

$$\begin{aligned} p_{true} &= p_m - b_p - e_p \\ q_{true} &= q_m - b_q - e_q \\ r_{true} &= r_m - b_r - e_r \end{aligned} \tag{5-12}$$

The bias terms [b_p,b_q,b_r] are a function of the axis and sensor-to-sensor misalignment properties, random walk and temperature. The sensor noise terms [e_p,e_q,e_r] are a function of external vibrations sources and measurement noise.

Chapter 6

GPS Receiver Modeling

This chapter is about the modeling of GPS receivers. Section 6-1 is about the processing time that is usually present with GPS receivers. The sections 6-2 and 6-3 are about position and velocity modeling. More about GPS itself and satellite navigation in general can be found in section 2-2.

6-1 GPS Receiver Processing Time

GPS satellite signals can be received by GPS receivers. The data received from a minimum of four satellites is processed and transmitted to other systems. Processing of received GPS satellite signals takes time called processing time. This processing time is about $0.25 - 0.40[s]$ for most GPS receivers with an integrated Kalman filter for signal processing. The receivers output provides the user with its position and velocity. The total time is dependent on the fact that the position calculation is an "easy" or a "difficult" position fix. For instance, when a new satellite is flying over, its takes more calculation time. It is assumed that position and velocity calculation needs the same processing time for each update. For the modeling of processing time, it is assumed that the receivers processing time is Gaussian based with a mean at $0.25[s]$ and a standard deviation of 10%. This can be implemented by taking a data sample which occurred at $0.25 \pm 0.025[s]$ in the past. Figure 6-1 displays an example on processing time delay by using a signal time step of $\mathrm{dt} = 0.01[s]$. The processing time delay array index is rounded off to the nearest array index. The rounded sample is to simulate a GPS receiver output. Figure 6-1(a) shows the raw processing time estimation, figure 6-1(b) gives the sample rounded time delay.

6-2 GPS Position Modeling

The received GPS position is modeled as the original position signal with the addition of a noise term and a processing time delay as described in section 6-1. The noise term combines

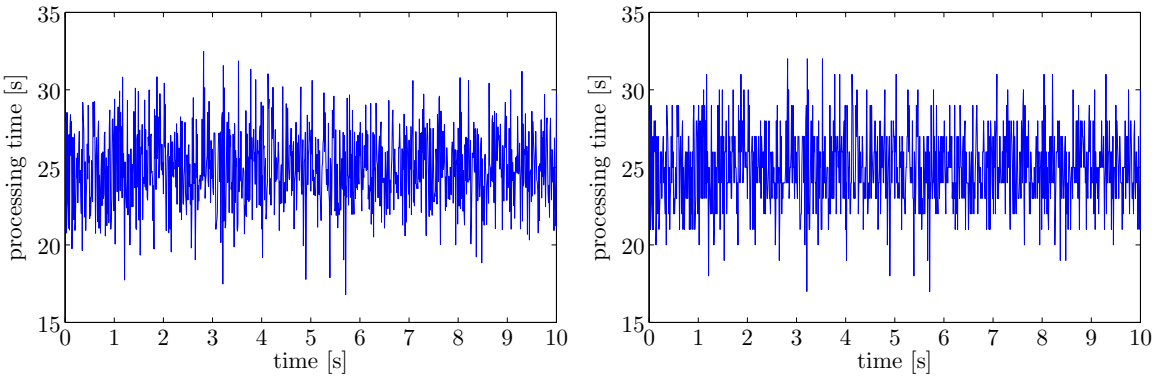

(a) Original time delay (b) Sample rounded time delay

Figure 6-1: GPS processing time, using a time step of 0.01 [s]

several satellite navigation sources of error as described in section 2-2. The noise terms are modeled as a white Gaussian, with a standard deviation σ. Besides noise terms, some sources of error show a bias effect. The absolute satellite navigation error is dependent on many factors. Table 6-1 gives a typical example on GPS position error budget, from (Schmidt, 2009). Based on this table the total error is about 10.3 meters, this is consistent with normal operation where the Circular Error of Probability (CEP) is about 10 meter in horizontal direction and about 15 meter in vertical direction. The error is usually higher in vertical direction due to satellite ephemeris 6.4 instead of 1.4 meter, performed by the control segment. The vertical direction has a higher uncertainty due to differences in theoretical and real satellite orbit height estimation.

Table 6-1: GPS position error budget

GPS noise-like range errors	1σ values [m]
Multipath	0.6
receiver noise	0.3
RMS noise	0.7
Total noise	**1.6**
GPS bias-like range errors	1σ values [m]
Satellite ephemeris	1.4 - 6.4
Satellite clock	3.4
Atmospheric residual	0.2
RMS bias-like error	3.7
Total bias	**8.7 - 13.7**

The modeling of a GPS position is performed in two parts. The total bias term is modeled as a sphere around the real position, by using cylindrical coordinates. Two angles θ_b and ϕ_b, are randomly varied between 0 and 2π $[rad]$, the three radius terms $[b_x b_y b_z]$ can be chosen separately to represent different bias errors. Figure 6-2 gives an impression of the 3D position bias error. Besides bias, noise $[e_{x_{GPS}} e_{y_{GPS}} e_{z_{GPS}}]$ must be added to include the error noise of table 6-1. Equation 6-1 gives the equations to model GPS position, including bias and noise.

The second part to accurately model GPS receiver position output is to include processing time. This can be done by taking a position value at an earlier time step, as explained in section 6-1.

$$\begin{array}{rclcll} x_{GPS} & = & x_{real} & + & b_x \cos\theta_b \sin\phi_b & + & e_{x_{GPS}} \\ y_{GPS} & = & y_{real} & + & b_y \sin\theta_b \sin\phi_b & + & e_{y_{GPS}} \\ z_{GPS} & = & z_{real} & + & b_z \sin\theta_b & + & e_{z_{GPS}} \end{array} \tag{6-1}$$

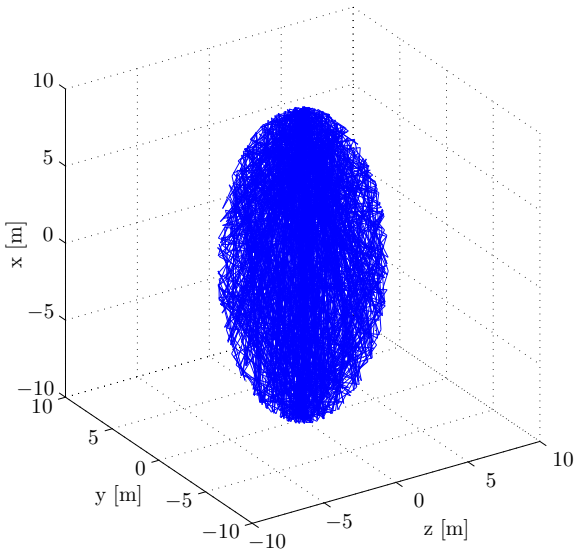

Figure 6-2: GPS position error modeling

6-3 GPS Velocity Modeling

The GPS velocity components are a result of measuring the Doppler shift between the satellites and user receiver as described in section 2-2. The accuracy of the GPS velocity is usually much higher when compared to GPS position, about one order of magnitude. For modeling purposes, it is assumed that the clock drift of the users receiver and satellites can be neglected. The satellite clock drift is measured and corrected by the GPS control segment at regular intervals. The users clock drift is in practice relatively small compared to the user receiver noise. Equation 6-2 expresses the GPS velocity modeling in all three directions, the noise has values in the order of 0.01 $[m/s]$.

$$\begin{aligned} u_{GPS_m} &= u_{GPS} + e_{u_{GPS}} \\ v_{GPS_m} &= v_{GPS} + e_{v_{GPS}} \\ w_{GPS_m} &= w_{GPS} + e_{w_{GPS}} \end{aligned} \tag{6-2}$$

Chapter 7

Aeronautical Simulation Library

The fixed-wing UAV model that is used in this report is based on the Aeronautical Simulation (AeroSim) Matlab/Simulink library from Unmanned Dynamics, LLC. The AeroSim blockset is a Simulink block library that can be used for development of non-linear 6-DOF UAV models. It is commercial software that can be downloaded free of charge for academic purposes. Section 7-1 is about the library itself and section 7-2 describes the Simulink model that is used in chapter 13 when performing simulations.

7-1 AeroSim Library Block Reference

The AeroSim library includes different blocks that are required to build 6-DOF aircraft Matlab/Simulink models, for instance for a UAV model. This section gives an overview of the different elements used for building theUAV model. The main library can be found in figure 7-1 which includes subfolders for different variants of the model elements with a total of 103 blocks. This section gives a quick overview of the different blocks and how they interact with each other. A more extensive description including all mathematical equations can be found the AeroSim Blockset user's guide, which can be downloaded from `http://www.u-dynamics.com/aerosim/`.

The actuator block contains generic models of electro-mechanical actuators. These models are very useful for conducting stability and performance analysis of autopilots and closed loop systems. The library provides simple actuators with 1^{st} order dynamics to more complicated 2^{nd} order dynamics. Both type of actuator models use a transfer function combined with a user defined range on input signal and actuator deflections together with a maximum actuation rate. The latter being the maximum speed at which the actuator can move. Next to actuator dynamics, a digital-to-analog converter block can be implemented to model realistic signal processing.

The aerodynamics block consists of the required blocks to create a full non-linear 6-DOF aerodynamic model aerodynamic derivatives. The aerodynamic force block computes the total aerodynamic force on the airframe by using the aerodynamic force coefficients and

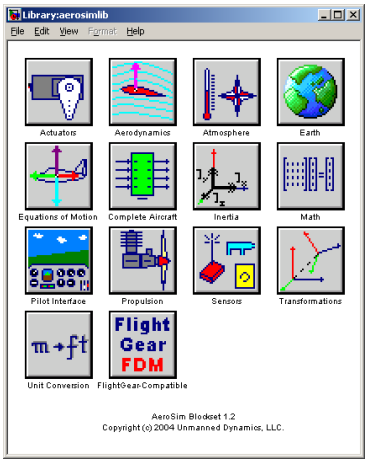

Figure 7-1: AeroSim library 1.2

dynamic pressure. These coefficients come from other aerodynamic sub-blocks, that compute aerodynamic coefficients, dynamic pressure and wind-axes velocities. The output from the aerodynamic force block should go into the total acceleration and total moment block to obtain the total force and moment, an example is given in figure 7-2(a). The same holds for the aerodynamic moment block, which is also depending on other elements to calculate the final aerodynamic moments as is illustrated in figure 7-3. The wind-axes block computes the wind-axes velocities based on the wind speed and ground speed. The wind-axes velocities are outputted by the total airspeed V_T, the angle of attack α, the side-slip angle β and the Mach number.

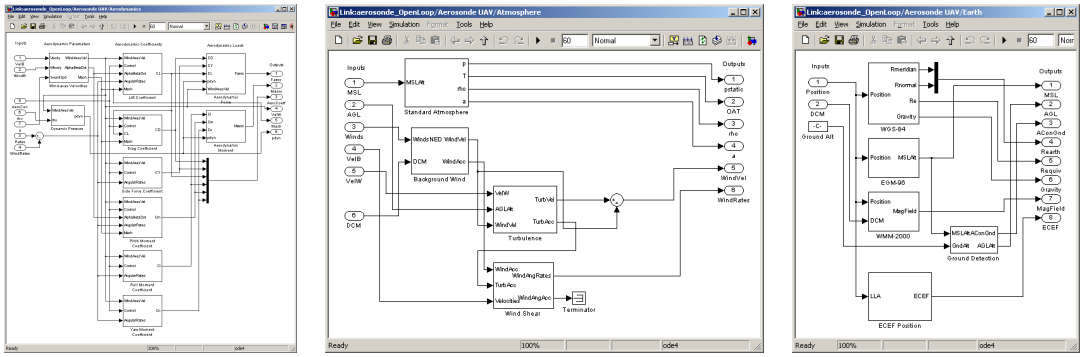

(a) Aerodynamic sub-block (b) Atmosphere sub-block (c) Earth coordinate frame sub-block

Figure 7-2: Subblocks of the complete aircraft model

The atmosphere library simulates the local air using air parameters and wind effects. Figure 7-2(b) gives an example of a complete atmospheric block. The atmosphere block calculates the altitude together with the static pressure, outside air temperature, air density and speed of sound. The background wind velocity components are calculated in a body-fixed frame of reference by the wind block. This block can be used as wind input for the atmosphere model

for turbulence, wind shear or the aerodynamics.

The block called "Earth" contains blocks to model the Earth's shape, gravity and magnetic field. The WGS-84 block computes the local Earth radius and gravity using WGS-84 Earth coefficients, the World Geodetic System, 1984 (WGS-84) coordinate system is the reference coordinate system used by the GPS systems to calculate positions. The Earth is modeled as an ellipsoid, where the 84 stands for the systems last revision in 1984. The EGM-96 block can compute the sea level with respect to the Earth elliptical WGS-84 model. The Earth Gravitational Model, 1996 (EGM-96) block uses an geoid undulation model of the Earth. Geoid undulation includes the difference in altitude between the theoretical ellipsoid shape and actual mean sea level caused by the non-uniformity of the Earth's gravitational potential. The output from the EGM-96 block is used by the ground detection block to compute the aircraft altitude above the ground level. If flying below ground level, a boolean flag is used to stop the simulation. The World Magnetic Model 2000 (WMM) block can be used to calculate the Earth magnetic field components according to the WMM-2000. This can for instance be used when simulating a three axis magnetometer sensor.

Various types of propulsion are included in the propulsion library, that can virtually be mounted onto the model. Propulsion can also be left out in case of modeling a glider. The fixed-pitch propeller uses a look-up table for obtaining the current advance ratio which is defined as the ratio between the forward flight speed and the speed of the rotor tip. The block also provides the propulsion force and other propulsion dynamics. Besides the propeller engine a piston engine is also included in the library. The piston engine also uses a look-up table, including tables for fuel flow and engine power at sea-level, both are a function of the number of rotations and manifold pressure. The fixed-pitch propeller and the piston engine are included in the General Aviation (GA) propulsion block to provide the engine torque by using the current engine shaft rotation speed, atmospheric conditions and airspeed. Next to the engine torque, also the propulsion forces and moments are calculated that act onto the aircraft.

The library also contains extensions to include sensor properties and some predefined mathematical operations. Also flight gear compatible software to interface the Simulink model with flight gear software is available. Together with pilot interface blocks which allow the user to interact with the aircraft model including a joystick connection and visual instruments. These additions can be used to include a pilot in the loop, to use for instance for experiments. Besides the individual element, complete 6-DOF aircraft models which already contain all of the sub-models as described above can be selected. Figure 7-3(a) gives an example of such a complete non-linear 6-DOF UAV model, figure 7-3(b) gives a simplified overview of the different elements that are used in the Simulink model. The next section 7-2 gives a more detailed explanation about the final UAV model that is used for simulations, chapter 13.

7-2 Fixed-Wing AeroSim UAV Model

The developed UAV model, will be used to simulate different trajectories. This section gives a general overview of the used Simulink model to simulate a small fixed-wing UAV. Figure 7-4 gives an overview of the UAV model. The block UAV dynamics houses the dynamics, figure 7-3 gives the complete Simulink model and model structure. Behind the Simulink model a

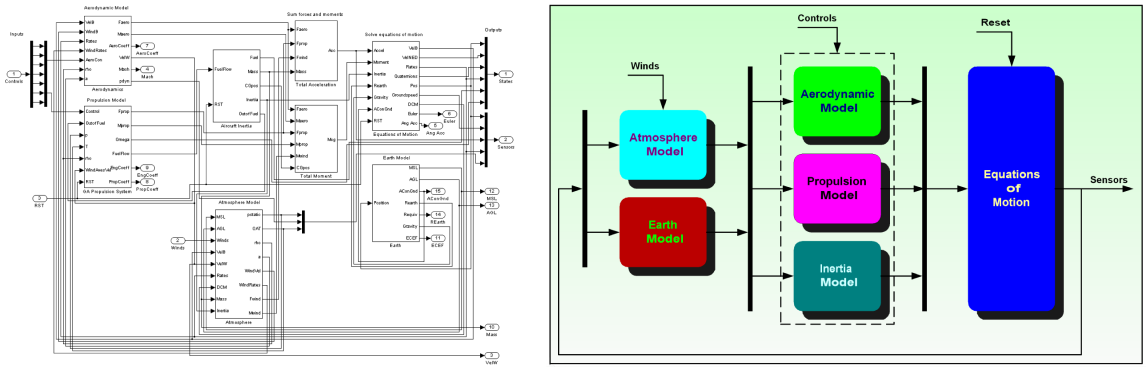

(a) Complete Simulink aircraft model

(b) Simplified internal structure diagram

Figure 7-3: Complete aircraft model

parameter file defines the aerodynamic properties, see appendix B-1. Besides aerodynamics, also engine properties and inertia can be defined. The used model has a single propeller introducing an unbalanced roll moment. This roll moment is stabilized by a lateral autopilot, called a wing leveler. The bank angle ϕ is multiplied with a proportional-integral (PI) and then feed back to the ailerons δ_a. Besides lateral control, a longitudinal control law is implemented to control the UAV's forward airspeed. It uses a proportional-integral-derivative control law (PID) times the error between the forward airspeed and desired forward airspeed $u_{command}$. The output signal of the PID is feed back to control the UAV elevator δ_e. This longitudinal control law is needed, to obtain stable simulations. Without it the aircraft can become unstable in longitudinal direction and can flip over during fast dynamic maneuvers. The lateral and longitudinal controllers are implemented to control the UAV model during simulations, otherwise the UAV model might become unstable because of its fast dynamics. While these controllers have a stabilizing effect on the UAV dynamics, it can still perform fast dynamic maneuvers and represent a small fixed-wing UAV. The engine inputs that can be given to model are the mixture and ignition. These two parameters are best set constant, as a small fixed-wing UAV uses a single propeller. The engine thrust can be changed by using a different throttle setting. The model also has the option to include a flap setting and to trim the model. The output states of the UAV dynamics block are saved before they are send to an IMU/GPS sensor simulation tool as described in chapters 5 and 6. The sensor simulation tool block also includes the addition of simulated atmospheric gust to the output velocity states. An impression of the Simulink model is given in figure 7-5. The simulations of appendices B to F use the UAV model described in this chapter.

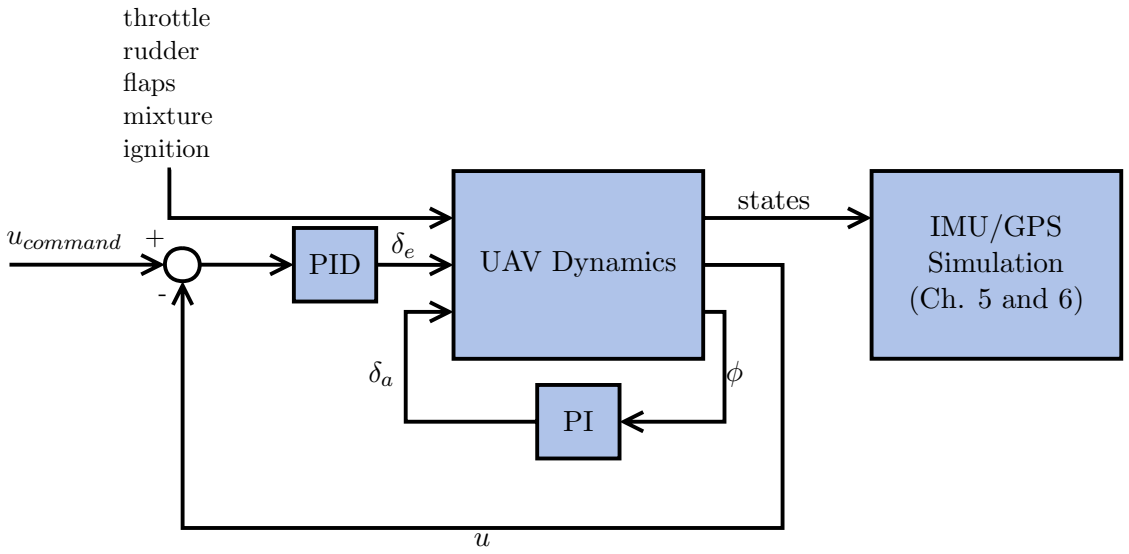

Figure 7-4: Schematic overview Aerosonde UAV model

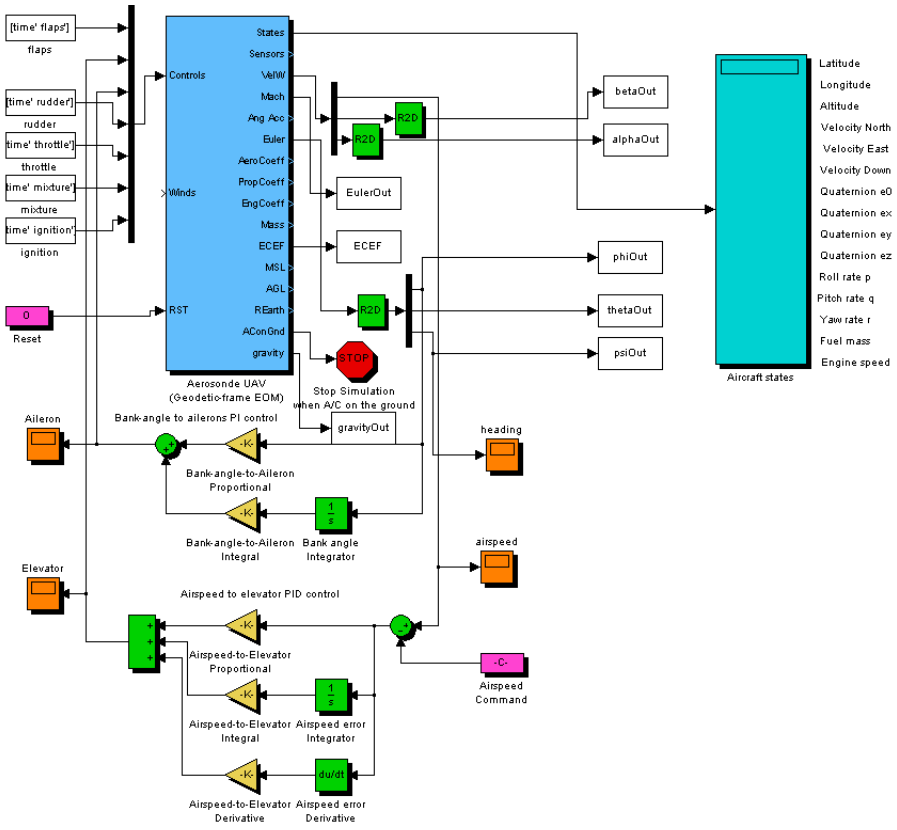

Figure 7-5: Simulink UAV model

Part III

Sensor Configurations

Chapter 8

Equations of Motion

This chapter houses the Equations of Motion (EOM) derived for a loosely coupled INS/GPS sensor integration. Section 8-1 contains a description of the two used reference frames, with the coordinate transformation in section 8-2. Section 8-3 gives the rational rate of a general 3D rotational vector. The equations of motion are derived in section 8-4 with some assumption in section 8-5, with the final result in section 8-6.

8-1 Introduction

When analyzing the motion of a flying object, several reference frames can be used. In this report two reference frames are used to describe the motion of an UAV, namely the body-fixed reference frame $\mathcal{F}_B$ and Earth-fixed frame of reference $\mathcal{F}_E$. The Earth-fixed reference frame is a local North-East-Down (NED) frame of reference, placed at a specific height above the Earth surface. These two reference frames are used throughout this chapter when deriving the EOM.

The body-fixed frame of reference ($GX_BY_BZ_B$) is defined as an orthogonal right-handed axis system with the origin at the vehicle center of gravity G. The X_B-axis is the symmetry plane of orientation and points into the direction of flight. The vertical Z_B-axis points downwards to the ground and also lies in the symmetry plane. The Y_B-axis coincides with the right wing, perpendicular to the symmetry plane. Figure 8-1(a) gives an illustration of $\mathcal{F}_B$ from (Mulder, van Staveren, van der Vaart, & de Weerdt, 2007).

The Earth-fixed frame of reference ($OX_EY_EZ_E$) is like $\mathcal{F}_B$ defined as an orthogonal right-handed axis system, but with a different origin. The origin O can be chosen at an arbitrary height or at ground level. The X_E-axis is directed to the North, the Y_E-axis directed to the East. Perpendicular to the Earth's surface lies the Z_E-axis. For an Earth-fixed reference frame $\mathcal{F}_E$ it is assumed that the Earth is flat and non-rotating, as illustrated in figure 8-1(b).

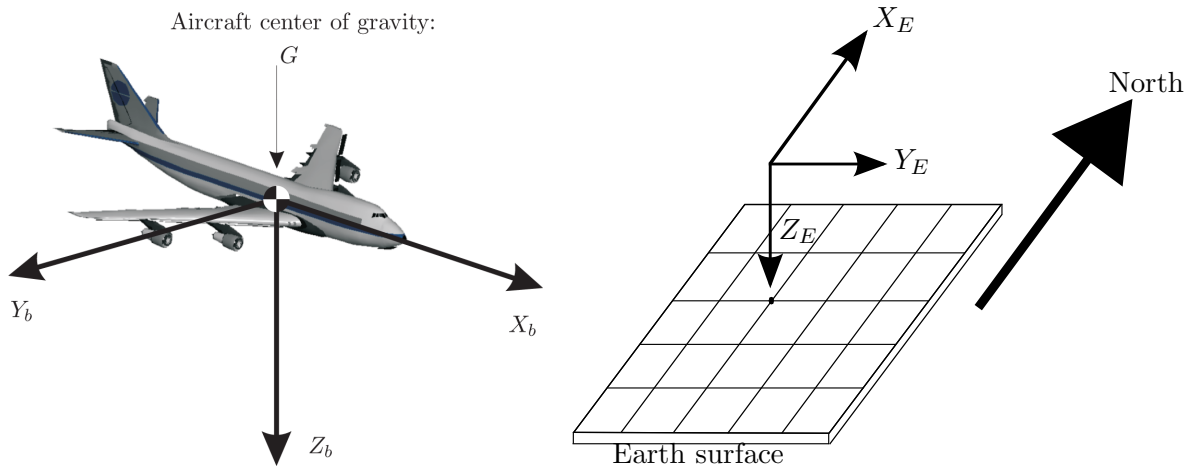

(a) Body-fixed reference frame $\mathcal{F}_B$ (b) Earth-fixed reference frame $\mathcal{F}_E$

Figure 8-1: $\mathcal{F}_B$ and $\mathcal{F}_E$ reference frames

8-2 Transformations between Reference Frames

The two reference frames of section 8-1 are most commonly used when describing the movement of a flying vehicle. The transformation from a body-fixed reference frame to an Earth-fixed reference frame is performed by using three consecutive rotations, called Euler angles. Rotation with a roll angle ϕ about the X-axis, can be calculated by using expression 8-1.

$$R_{BE}(\phi) = \begin{bmatrix} 1 & 0 & 0 \\ 0 & \cos\phi & \sin\phi \\ 0 & -\sin\phi & \cos\phi \end{bmatrix} \tag{8-1}$$

Rotation with a pitch angle θ about the Y-axis, can be calculated by using expression 8-2.

$$R_{BE}(\theta) = \begin{bmatrix} \cos\theta & 0 & -\sin\theta \\ 0 & 1 & 0 \\ \sin\theta & 0 & \cos\theta \end{bmatrix} \tag{8-2}$$

Rotation with a heading angle ψ about the Z-axis, can be calculated by using expression 8-3.

$$R_{BE}(\psi) = \begin{bmatrix} \cos\psi & \sin\psi & 0 \\ -\sin\psi & \cos\psi & 0 \\ 0 & 0 & 1 \end{bmatrix} \tag{8-3}$$

The Euler angles of expressions 8-1, 8-2 and 8-3 can be combined for a complete coordinate transformation. The transformation, transforms a given set of coordinates from a body-fixed reference frame $\mathcal{F}_B$ to an Earth-fixed reference frame $\mathcal{F}_E$ using the three angles. The coordinate transformation is defined as follows: $\mathcal{F}_E = R_{BE}(\phi, \theta, \psi)\,\mathcal{F}_B$, where $R_{BE}(\phi, \theta, \psi)$ is the transformation matrix. This particular transformation matrix is also called a Direction

Cosine Matrix (DCM) as is given in expression 8-4, which can for instance be found in (Mulder et al., 2007).

$$R_{BE}(\phi,\theta,\psi) = \begin{bmatrix} \cos\theta\cos\psi & \sin\phi\sin\theta\cos\psi - \cos\phi\sin\psi & \cos\phi\sin\theta\cos\psi + \sin\phi\sin\psi \\ \cos\theta\sin\psi & \sin\phi\sin\theta\sin\psi + \cos\phi\cos\psi & \cos\phi\sin\theta\sin\psi - \sin\phi\cos\psi \\ -\sin\theta & \sin\phi\cos\theta & \cos\phi\cos\theta \end{bmatrix} \tag{8-4}$$

8-3 Rotational Rate of a Vector

The rotational rate of an object can be described by using a 3-dimensional rotational vector as: $\underline{\omega}(t) = \begin{bmatrix} \omega_1(t) \\ \omega_2(t) \\ \omega_3(t) \end{bmatrix}$. When the rotational rate is measured with three orthogonal gyroscopes in $\mathcal{F}_B$ it can be converted to $\mathcal{F}_E$ by taking the crossproduct of the eigenvectors in $\mathcal{F}_B$ with the rotational vector $\underline{\omega}$, as given with expression 8-5.

$$\Omega[\underline{\omega}(t)] = \left\{ \begin{bmatrix} \omega_1(t) \\ \omega_2(t) \\ \omega_3(t) \end{bmatrix} \times \begin{bmatrix} 1 \\ 0 \\ 0 \end{bmatrix} \right\}, \left\{ \begin{bmatrix} \omega_1(t) \\ \omega_2(t) \\ \omega_3(t) \end{bmatrix} \times \begin{bmatrix} 0 \\ 1 \\ 0 \end{bmatrix} \right\}, \left\{ \begin{bmatrix} \omega_1(t) \\ \omega_2(t) \\ \omega_3(t) \end{bmatrix} \times \begin{bmatrix} 0 \\ 0 \\ 1 \end{bmatrix} \right\} \tag{8-5}$$

Equation 8-5 can be worked out into expression 8-6.

$$\Omega[\underline{\omega}(t)] = \begin{bmatrix} 0 & -\omega_3(t) & \omega_2(t) \\ \omega_3(t) & 0 & -\omega_1(t) \\ -\omega_2(t) & \omega_1(t) & 0 \end{bmatrix} \tag{8-6}$$

In expression 8-6, $\Omega[\underline{\omega}(t)]$ is the result of the crossproduct of the rotational vector $\underline{\omega}(t)$ with the $\mathcal{F}_B$ unit vectors, resulting in the skewsymmetric matrix Ω. Figure 8-2 gives a graphical representation of the rotational vector. The rotational matrix Ω can be used to obtain the body rotational rate, or time derivative of the transformation matrix $\dot{R}_{BE}$, to indicate the rate of change of $R_{BE}(\phi,\theta,\psi)$ between $\mathcal{F}_B$ and $\mathcal{F}_E$ as given in expression 8-7.

$$\dot{R}_{BE}(\phi,\theta,\psi) = R_{BE}(\phi,\theta,\psi)\,\Omega[\underline{\omega}(t)] \tag{8-7}$$

When taking $\underline{\omega}(t)$=$[p,q,r]^T$ as indicated in figure 8-2, the resulting crossproduct is $\Omega = [q-r, r-p, p-q]^T$. The vector $\underline{v} = [1,1,1]^T$ is a linear combination of the eigenvectors $[1,0,0]$, $[0,1,0]$ and $[0,0,1]$.

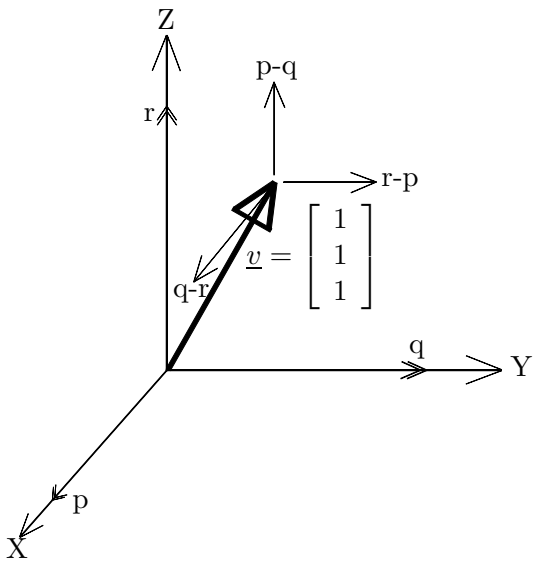

Figure 8-2: Crossproduct of a rotational vector $[p,q,r]^T$

8-4 Equations of Motion

The position of an aircraft's center of gravity (cg) relative to an Earth-fixed frame of reference $\mathcal{F}_E$ can be calculated by using the DCM of expression 8-4. When including the wind components $\underline{W} = [W_x W_y W_z]^T$, this results in expression 8-8.

$$\begin{bmatrix} \dot{x} \\ \dot{y} \\ \dot{z} \end{bmatrix}_E = R_{BE}(\phi, \theta, \psi) \begin{bmatrix} u \\ v \\ w \end{bmatrix}_B + \begin{bmatrix} W_x \\ W_y \\ W_z \end{bmatrix}_E \tag{8-8}$$

When the IMU is not placed at the vehicle's center of gravity (cg), but at a distance $\underline{d}$=$[d_x,d_y,d_z]^T$ relative to the true cg, this results in extra acceleration terms, lateral and rotational. Equation 8-9 gives the additional accelerations measured together with the specific forces.

$$\begin{bmatrix} A_{IMU_x} \\ A_{IMU_y} \\ A_{IMU_z} \end{bmatrix} = \begin{bmatrix} A_x \\ A_y \\ A_z \end{bmatrix} + \begin{bmatrix} \dot{p} \\ \dot{q} \\ \dot{r} \end{bmatrix} \times \begin{bmatrix} d_x \\ d_y \\ d_y \end{bmatrix} + \begin{bmatrix} p \\ q \\ r \end{bmatrix} \times \left(\begin{bmatrix} p \\ q \\ r \end{bmatrix} \times \begin{bmatrix} d_x \\ d_y \\ d_y \end{bmatrix} \right) \tag{8-9}$$

During flight is it possible that the center of gravity changes and as a consequence also the distance $\underline{d}$ between the aircraft center of gravity and the origin of sensitivity of the accelerometers. During flight it is assumed that the vehicle is a rigid body and can be described by using a single rotational matrix Ω. The three orthogonal gyroscopes measure Ω into its three rotational components. When assuming a rigid body, the rotation is the same for the entire vehicle and the gyroscopes can be placed at every point onto the vehicle. When compared to accelerometers, the sensors location is important as described in expression 8-9, gyroscopes do not have this problem. However in practice an aircraft is never a perfect rigid

body. Therefore when placing rotational sensors, the sensors should be placed at positions without the presence of large bending modes.

The forces that act onto an aircraft can be seen as three body forces X, Y and Z. The body forces consists of aerodynamic forces together with engine forces and possible atmospheric forces. Equation 8-10 describes the three body forces onto an aircraft.

$$\begin{bmatrix} X \\ Y \\ Z \end{bmatrix} = m\underline{a} + m\Omega\left[\underline{\omega}(t)\right]\underline{v} + m\underline{g} \tag{8-10}$$

In expression 8-10, $\underline{a}$ contains the acceleration components or time derivatives of the vehicles velocity components, $[\dot{u},\dot{v},\dot{w}]^T$. The mass is indicated with m and the gravity vector $\underline{g}$. The term $m\Omega\left[\underline{\omega}(t)\right]\underline{v}$ is worked out in expression 8-11, by using expression 8-6.

$$m\Omega\left[\underline{\omega}(t)\right] = \begin{bmatrix} m\left[qw - rv\right] \\ m\left[ru - pw\right] \\ m\left[pv - qu\right] \end{bmatrix} \tag{8-11}$$

When gravity is unknown in local body-fixed coordinates $\mathcal{F}_B$, it can be calculated by multiplying the gravity vector in Earth reference coordinates $\underline{g}_E(t)$ with the skewsymmetric matrix as a function of the rotational vector $\Omega[\underline{\omega}(t)]$, as can be found in (Batista, Silvestre, & Oliveira, 2009). The same skewsymmetric matrix $\Omega[\underline{\omega}(t)]$ of expression 8-6 is used, resulting in expression 8-12 where the rate of change of the local gravity vector $\underline{\dot{g}}_B(t)$ in can be $\mathcal{F}_B$ determined.

$$\underline{\dot{g}}_B(t) = \Omega[\underline{\omega}(t)]\underline{g}_E(t) \tag{8-12}$$

When assuming that gravity is constant with factor g_0 and is pointing downwards in $\mathcal{F}_E$, the gravity vector becomes $\underline{g}_E(t) = [0\ 0\ -g_0]^T$. Expression 8-12 can be rewritten in expression 8-13.

$$\begin{bmatrix} \dot{g}_x \\ \dot{g}_y \\ \dot{g}_z \end{bmatrix}_B = \begin{bmatrix} 0 & -\omega_3(t) & \omega_2(t) \\ \omega_3(t) & 0 & -\omega_1(t) \\ -\omega_2(t) & \omega_1(t) & 0 \end{bmatrix} \begin{bmatrix} 0 \\ 0 \\ -g_0 \end{bmatrix}_E \tag{8-13}$$

Expression 8-13 can be worked out in expression 8-14.

$$\begin{bmatrix} \dot{g}_x \\ \dot{g}_y \\ \dot{g}_z \end{bmatrix}_B = \begin{bmatrix} -\omega_2(t)g_0 \\ \omega_1(t)g_0 \\ 0 \end{bmatrix}_B \tag{8-14}$$

To obtain the change in attitude and heading angles $[\dot{\phi},\dot{\theta},\dot{\psi}]$, a 3-2-1 rotational sequence can be used as is given in (Mulder et al., 2007). The rotational sequence uses expressions 8-1, 8-2 and 8-3 resulting in expression 8-15.

$$\begin{bmatrix} p \\ q \\ r \end{bmatrix} = \begin{bmatrix} \dot{\phi} \\ 0 \\ 0 \end{bmatrix} + R_{BE}(\phi)\begin{bmatrix} 0 \\ \dot{\theta} \\ 0 \end{bmatrix} + R_{BE}(\phi,\theta)\begin{bmatrix} 0 \\ 0 \\ \dot{\psi} \end{bmatrix} \tag{8-15}$$

When filling in the rotational matrices $R_{BE}(\phi)$ and $R_{BE}(\theta)$ into expression 8-15 this results in expression 8-16.

$$\begin{bmatrix} p \\ q \\ r \end{bmatrix} = \begin{bmatrix} \dot{\phi} \\ 0 \\ 0 \end{bmatrix} + \begin{bmatrix} 1 & 0 & 0 \\ 0 & \cos\phi & \sin\phi \\ 0 & -\sin\phi & \cos\phi \end{bmatrix} \begin{bmatrix} 0 \\ \dot{\theta} \\ 0 \end{bmatrix} + \begin{bmatrix} 1 & 0 & 0 \\ 0 & \cos\phi & \sin\phi \\ 0 & -\sin\phi & \cos\phi \end{bmatrix} \begin{bmatrix} \cos\theta & 0 & -\sin\theta \\ 0 & 1 & 0 \\ \sin\theta & 0 & \cos\theta \end{bmatrix} \begin{bmatrix} 0 \\ 0 \\ \dot{\psi} \end{bmatrix} \tag{8-16}$$

Expression 8-16 can be workout into expression 8-17.

$$\begin{bmatrix} p \\ q \\ r \end{bmatrix} = \begin{bmatrix} \dot{\phi} \\ 0 \\ 0 \end{bmatrix} + \begin{bmatrix} 0 & 0 & 0 \\ 0 & \dot{\theta}\cos\phi & 0 \\ 0 & -\dot{\theta}\sin\phi & 0 \end{bmatrix} + \begin{bmatrix} 0 & 0 & -\dot{\psi}\sin\theta \\ 0 & 0 & \dot{\psi}\sin\phi\cos\theta \\ 0 & 0 & \dot{\psi}\cos\phi\cos\theta \end{bmatrix} \tag{8-17}$$

Expression 8-17 can be rewritten into expression 8-18.

$$\begin{bmatrix} p \\ q \\ r \end{bmatrix} = \begin{bmatrix} 1 & 0 & -\sin\theta \\ 0 & \cos\phi & \sin\phi\cos\theta \\ 0 & -\sin\phi & \cos\phi\cos\theta \end{bmatrix} \begin{bmatrix} \dot{\phi} \\ \dot{\theta} \\ \dot{\psi} \end{bmatrix} \tag{8-18}$$

To obtain the time derivatives of the Euler angles $[\dot{\phi},\dot{\theta},\dot{\psi}]^T$, expression 8-18 needs to be inverted resulting in expression 8-19.

$$\begin{bmatrix} \dot{\phi} \\ \dot{\theta} \\ \dot{\psi} \end{bmatrix} = \begin{bmatrix} 1 & \sin\phi\tan\theta & \cos\phi\tan\theta \\ 0 & \cos\phi & -\sin\phi \\ 0 & \frac{\sin\phi}{\cos\theta} & \frac{\cos\phi}{\cos\theta} \end{bmatrix} \begin{bmatrix} p \\ q \\ r \end{bmatrix} \tag{8-19}$$

8-5 Assumptions

An IMU usually contains three accelerometers and three gyroscopic sensors, as described in chapter 5. Which are modeled with expressions 5-11 and 5-12 as the true specific force is equal to the measured value $_m$, minus a bias $_b$ and noise term $_e$. This is summarized for the accelerometers in expression 8-20 regarding specific forces and for the gyroscopes in expression 8-21 for the angular rates. More about MEMS based IMU modeling can be found in chapter 5.

$$\underline{A} = \begin{bmatrix} A_x \\ A_y \\ A_z \end{bmatrix} = \begin{bmatrix} A_{x_m} - b_{A_x} - e_{A_x} \\ A_{x_m} - b_{A_y} - e_{A_y} \\ A_{y_m} - b_{A_z} - e_{A_z} \end{bmatrix} \tag{8-20}$$

$$\underline{\omega} = \begin{bmatrix} p \\ q \\ r \end{bmatrix} = \begin{bmatrix} p_m - b_p - e_p \\ q_m - b_q - e_q \\ r_m - b_r - e_r \end{bmatrix} \tag{8-21}$$

Gravity is assumed known and modeled as a 3D-vector, using three vector components $[g_x, g_y, g_z]^T$. When using an Earth-fixed navigation frame $\mathcal{F}_E$, this can be seen as a constant vector pointing downwards to the Earth's center of gravity. This vector can be converted from $\mathcal{F}_E$ to $\mathcal{F}_B$ using the transpose of rotational transformation matrix R_{BE}^T, as described in section 8-2 resulting in expression 8-22.

$$\begin{bmatrix} g_x \\ g_y \\ g_z \end{bmatrix}_B = R_{BE}^T(\phi, \theta, \psi) \begin{bmatrix} 0 \\ 0 \\ g_z \end{bmatrix}_E \tag{8-22}$$

Equation 8-22 can be worked out in expression 8-23.

$$\begin{bmatrix} g_x \\ g_y \\ g_z \end{bmatrix}_B = \begin{bmatrix} \cos\theta\cos\psi & \cos\theta\sin\psi & -\sin\theta \\ \sin\phi\sin\theta\cos\psi - \cos\phi\sin\psi & \sin\phi\sin\theta\sin\psi + \cos\phi\cos\psi & \sin\phi\cos\theta \\ \cos\phi\sin\theta\cos\psi + \sin\phi\sin\psi & \cos\phi\sin\theta\sin\psi - \sin\phi\cos\psi & \cos\phi\cos\theta \end{bmatrix} \begin{bmatrix} 0 \\ 0 \\ g_z \end{bmatrix}_E \tag{8-23}$$

Expression 8-23 is workout in expression 8-24, where the assumed gravity constant g_z in $\mathcal{F}_E$ has been replaced by g_0.

$$\begin{bmatrix} g_x \\ g_y \\ g_z \end{bmatrix}_B = \begin{bmatrix} -g_0\sin\theta \\ g_0\sin\phi\cos\theta \\ g_0\cos\phi\cos\theta \end{bmatrix}_B \tag{8-24}$$

When gravity is assumed to be a constant vector the time derivative is zero, $\dot{\underline{g}} = 0$ and constantly pointing downwards, only two angles ϕ and θ are required. This can be concluded from expression 8-24 where the third angle, the heading angle ψ is perpendicular to the direction of the gravity vector.

8-6 Final Equations of Motion

The individual equations of motion of the previous sections can be summarized into one set of equations. Equation 8-8 is used to describe the position update, expressions 8-10, 8-11 and 8-24 for velocity update and expression 8-19 for updating the Euler angles. It is assumed that a calibrated IMU is used, such that the measured accelerometer values are compensated by using expression 8-9. The IMU biases b and noise e are included, the time derivatives are assumed to be zero and the same holds for the wind components $\underline{W} = [W_x, W_y, W_z]^T$. The total kinematic aircraft expressions results in expression 8-25.

$$
\begin{aligned}
\dot{x} &= [u\cos\theta + (v\sin\phi + w\cos\phi)\sin\theta]\cos\psi - (v\cos\phi - w\sin\phi)\sin\psi + W_x \\
\dot{y} &= [u\cos\theta + (v\sin\phi + w\cos\phi)\sin\theta]\sin\psi + (v\cos\phi - w\sin\phi)\cos\psi + W_y \\
\dot{z} &= -u\sin\theta \ + (v\sin\phi + w\cos\phi)\cos\theta + W_z \\
\dot{u} &= A_{x_m} - b_{A_x} - e_{A_x} + (r_m - b_r - e_r)v - (q_m - b_q - e_q)w - g_0\sin\theta \\
\dot{v} &= A_{y_m} - b_{A_y} - e_{A_y} + (p_m - b_p - e_p)w - (r_m - b_r - e_r)u + g_0\sin\phi\cos\theta \\
\dot{w} &= A_{z_m} - b_{A_z} - e_{A_z} + (q_m - b_q - e_q)u - (p_m - b_p - e_p)v + g_0\cos\phi\cos\theta \\
\dot{\phi} &= p_m - b_p - e_p + (q_m - b_q - e_q)\sin\phi\tan\theta + (r_m - b_r - e_r)\cos\phi\tan\theta \\
\dot{\theta} &= (q_m - b_q - e_q)\cos\phi - (r_m - b_r - e_r)\sin\phi \\
\dot{\psi} &= (q_m - b_q - e_q)\tfrac{\sin\phi}{\cos\theta} + (r_m - b_r - e_r)\tfrac{\cos\phi}{\cos\theta} \\
\dot{b}_{A_x} &= 0 \\
\dot{b}_{A_y} &= 0 \\
\dot{b}_{A_z} &= 0 \\
\dot{b}_p &= 0 \\
\dot{b}_q &= 0 \\
\dot{b}_r &= 0 \\
\dot{W}_x &= 0 \\
\dot{W}_y &= 0 \\
\dot{W}_z &= 0
\end{aligned}
\tag{8-25}
$$

Chapter 9

Sensor Configurations

This chapter discusses different sensor configurations that can be mounted onto a MAV. The different sensor configurations are described in section 9-1. Four sensor configurations are selected in section 9-2 that focuses on attitude/ heading stabilization. These four configurations are used in chapter 11 for observability analysis, next chapter 10 gives possible improvements by means of physical analysis.

9-1 Different Sensor Configurations

This chapter describes different sensor configurations applicable for a small fixed-wing UAV. The most elementary configuration, sensor configuration 1, described in subsection 9-1-1, uses only an IMU. This configuration forms the basis for the other sensor configurations. As a general rule, it can be said that when more sensors are added, more information of the UAV becomes available. The following subsections describe possible sensor configurations, with a goal to stabilize a fixed-wing UAV. The latter is translated into the requirement of having full knowledge of all three orientation angles of a UAV during all flight conditions. Because the IMU can only provide noisy biased estimations, additional sensors are added. For each sensor configuration one additional sensor is added to the IMU. Each of the following 8 subsections describe a sensor configuration with the corresponding properties.

9-1-1 1: Solely IMU

The use of an IMU, using three orthogonal gyroscopic sensors and three orthogonal accelerometers, provides information on the vehicles 6-DOF. As mentioned in chapter 8, the gyroscopes can be integrated to obtain all three orientation angles. The accelerometers give the vehicle accelerations, together with an onboard gravity model the vehicles specific forces, or non-gravitational forces can be determined. Integration of the accelerations gives velocities, twice integration gives the vehicles position. When properly calibrated, an IMU has low short term

noise and biases, measured at a high frequency. The integration steps will cause noise amplification and result in increasing bias errors with respect to the real velocity, position and orientation angles. For a long period of time, the increasing bias will result in an increasing estimation error, as each new estimation is based on the previous estimation step plus the current measurement.

The sole use of an IMU for navigation purposes is valid for a short period of time and is dependent on the sensor technology, calibration and temperature sensitivity. For a long period of time additional sensors are needed to compensate accumulated errors. The sensor configurations of the following subsections use the IMU as a basis with additional sensors to cope with the long-term stabilization problem. To summarize, sensor configuration 1 solely using an IMU uses the following sensors:

- 3 gyroscopes, output quantities: rotational rates p, q and r.
- 3 accelerometers, output quantities: specific forces A_x, A_y and A_z.

9-1-2 2: IMU + GPS

An IMU as described in sensor configuration 1 can be used to predict all basic nine states; position (3), velocity (3) and angles (3). These states should provide all necessary information to stabilize and navigate a flying vehicle. However, over period of time the increasing bias error will result in divergence. When implemented into a Kalman filter, the IMU information can be used for the prediction step. Due to sensor noise, biases and integration errors other sensors are added to aid the IMU. A combined navigation solution becomes more accurate when the prediction errors are compensated. The first sensor configuration, sensor configuration config 1, uses an IMU that consists of three orthogonal gyroscopes and three orthogonal accelerometers to measure the rotational rates and accelerations in all three directions. The sensor data can be fused together to obtain the vehicles' orientation angles, velocity and position in a reference frame. The used reference frame can for example be an Earth-Centered-Earth-Fixed (ECEF) or a local North-East-Down (NED) frame of reference.

Equation 9-1 gives the definition of a GPS position observer in an Earth-fixed reference frame $\mathcal{F}_E$, which can be ECEF or NED. Beside the 3D-position, the GPS receiver can also provide the vehicles' velocity components u_E, v_E and w_E. The GPS receiver information can be used to correct long-term IMU errors as shown in section 2-3, about integrating inertial and satellite navigation systems. The IMU position estimate is the result of two times integration of acceleration signals and is likely to contain some errors. Both position and velocity IMU prediction are measured in a body-fixed frame of reference $\mathcal{F}_B$. The position and velocity information needs to be transformed to an Earth-fixed reference frame $\mathcal{F}_E$ to fuse them together with the GPS receiver output.

$$\underline{y} = \begin{bmatrix} x_{GPS} \\ y_{GPS} \\ z_{GPS} \end{bmatrix}_E = \begin{bmatrix} x \\ y \\ z \end{bmatrix}_B \tag{9-1}$$

The GPS position measurements does not need to be transformed as the aircraft's position is measured as a point, with the exception of a reference position or altitude above the

Earths' surface. Equation 9-2 gives the GPS velocity observer equations with the coordinate transformation $\mathcal{F}_E = R_{BE}\mathcal{F}_B$. Where the used transformation matrix R_{BE} transforms the body-fixed velocities to $\mathcal{F}_E$ using the three orientation angles. The GPS velocities are the total velocity and contain wind components $\underline{W} = [W_x\ W_y\ W_z]$, if present.

$$\underline{y}_E = \begin{bmatrix} [u\cos\theta + (v\sin\phi + w\cos\phi)\sin\theta]\cos\psi - (v\cos\phi - w\sin\phi)\sin\psi + W_x \\ [u\cos\theta + (v\sin\phi + w\cos\phi)\sin\theta]\sin\psi + (v\cos\phi - w\sin\phi)\cos\psi + W_y \\ -u\sin\theta + (v\sin\phi + w\cos\phi)\cos\theta + W_z \end{bmatrix}_B \tag{9-2}$$

To summarize, sensor configuration 2 uses the following sensors and receivers:

- 3 gyroscopes, output quantities: rotational rates p, q and r.
- 3 accelerometers, output quantities: specific forces A_x, A_y and A_z.
- GPS receiver, output quantities: 3D position x, y and z, velocity u, v and w.

9-1-3 3: IMU + GPS + Magnetometer

Sensor configuration 3 is the same as configuration 2, with three additional magnetometers. The magnetometers are added to measure the Earth magnetic field and use this information to give an estimate of the aircrafts heading angle with respect to the Earth magnetic North direction. The obtained magnetic heading information can be used to correct the IMU heading estimation and complement the GPS velocity based gyroscopes bias estimation. The difference in gyroscopic angle estimation and magnetometer angles holds information about the gyroscopic biases. The output of the magnetometer is used as an observer of the vehicle heading angle by using the Earth magnetic field M, as is defined in equations 9-3. The difference between the true north and the magnetic north, is called the magnetic declination.

$$\begin{bmatrix} M_x \\ M_y \\ M_z \end{bmatrix} = R_{be}(\phi,\theta,\psi) \begin{bmatrix} \cos\gamma & 0 & -\sin\gamma \\ 0 & 1 & 0 \\ \sin\gamma & 0 & \cos\gamma \end{bmatrix} \begin{bmatrix} M \\ 0 \\ 0 \end{bmatrix} \tag{9-3}$$

The magnetometer measurements give angle information based on the Earth magnetic field in body-fixed reference frame $\mathcal{F}_B$. With the rotational matrix R_{BE} this can be transformed to $\mathcal{F}_E$, where γ is the tilt angle of the local magnetic field as is given in expression 9-3. If three magnetometers are mounted perpendicular to each other, the magnetic vector can be reconstructed. From the magnetic vector, the heading angle can be estimated. This results in observer equation 9-4, where the heading angle is calculated by using expression 9-3. The factor D_m represents the magnetic declination angle between true and magnetic North, which is nowadays about 11.5°. The triad of magnetometers allows for the construction of a three dimensional magnetic vector, two angles and magnitude. Besides the heading angle, also the pitch angle can be estimated. During normal flight conditions, the downward magnetic component is very small, resulting in bad pitch angle estimations. For very large pitch angles the downward components becomes larger and a better estimation can be obtained. It should however be noted that in practice a three directional magnetometer can always provide

heading information as long as the Earth magnetic field is measured. Onboard electronics and systems can degrade the sensor data, resulting in a bad estimation.

$$y_\psi = D_m \left[\ \psi_m \ \right] \tag{9-4}$$

To summarize, sensor configuration 3 uses the following sensors and receivers:

- 3 gyroscopes, output quantities: rotational rates p, q and r.
- 3 accelerometers, output quantities: specific forces A_x, A_y and A_z.
- GPS receiver, output quantities: 3D position x, y and z, velocity u, v and w.
- 3 directional magnetometer, output quantities: heading angle ψ.

9-1-4 4: IMU + GPS + Barometer

The previously described IMU/GPS sensor configuration 2 can be extended with a barometer, that measures the static atmospheric pressure. As mentioned in section 2-2, the GPS satellite ephemeris source of error results in less accurate vertical position estimation when compared to horizontal estimations. With the use of an additional sensor for the altitude, the vertical position estimation can be improved. The barometer altitude is based on the relative atmospheric pressure between the measured and reference pressure altitude. The measured atmospheric pressure needs to be converted to a reference pressure altitude setting, usually International Standard Atmosphere (ISA). The pressure measurements are affected by weather, as the barometric pressure can suddenly change during rough weather conditions. As a consequence, the barometric pressure sensor can only be used for low frequency corrections. The main source of error is usually the conversion between pressure and altitude. To summarize, sensor configuration 4 uses the following sensors and receivers:

- 3 gyroscopes, output quantities: rotational rates p, q and r.
- 3 accelerometers, output quantities: specific forces A_x, A_y and A_z.
- GPS receiver, output quantities: 3D position x, y and z, velocity u, v and w.
- Barometer pressure altitude, output quantity: barometric pressure P.

9-1-5 5: IMU + GPS + Airspeed Aiding

The previously described IMU/GPS sensor configuration 2 can be extended with airspeed aiding. Airspeed aiding is a type of air data sensor that measures the dynamic pressure of a moving vehicle together with the static atmospheric pressure. The difference between the measured pressures holds the true airspeed V_T. This can be interpreted as the aircrafts velocity seen from a moving air particle. The true airspeed is equal to vectorial sum of the individual velocity components u, v and w as defined in observer expression 9-5.

$$y = V_T = \sqrt{u^2 + v^2 + w^2} \tag{9-5}$$

Airspeed aiding will especially improve the velocity estimation during conditions with much wind and turning maneuvers. The GPS velocity update frequency is usually lower when compared to airspeed aiding sensors. During situations with low atmospheric winds, airspeed aiding will usually outperform GPS velocity corrections. To summarize, sensor configuration 5 uses the following sensors and receivers:

- 3 gyroscopes, output quantities: rotational rates p, q and r.
- 3 accelerometers, output quantities: specific forces A_x, A_y and A_z.
- GPS receiver, output quantities: 3D position x, y and z, velocity u, v and w.
- Total velocity air data sensor, output quantity: true airspeed V_T.

9-1-6 6: IMU + GPS + V_T, α, β Sensors

Sensor configuration 6 is the same as configuration 5, with two additional air data sensors. The air data sensors measure the angle of attack α, side-slip angle β and true airspeed V_T. Figure 9-1 gives the definition of the two angles together with the true airspeed. These three sensors provide additional measurements which can be used as additional observers. Equation 9-6 gives the corresponding equations, derived from figure 9-1.

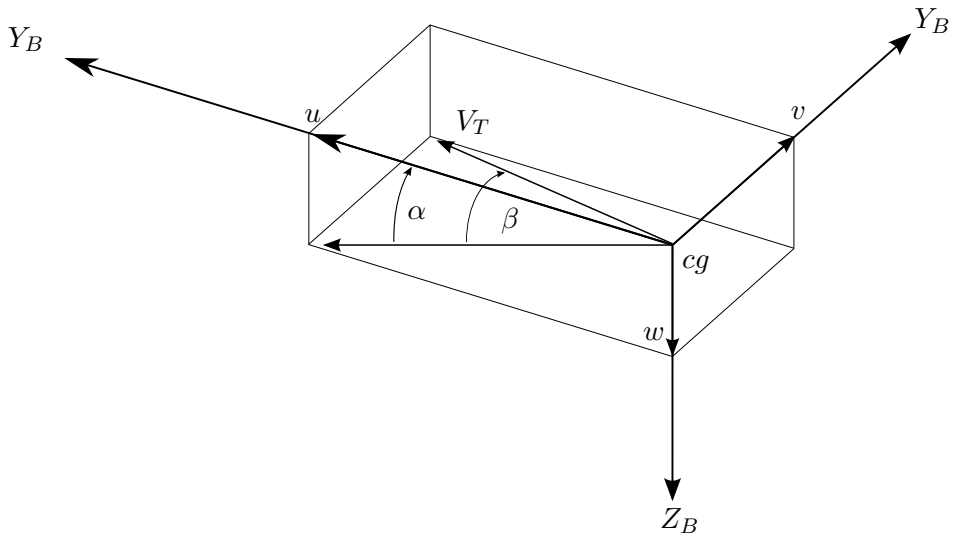

Figure 9-1: Definition of angle of attack α, side-slip angle β and true airspeed V_T

$$\underline{y} = \begin{bmatrix} \alpha \\ \beta \\ V_T \end{bmatrix} = \begin{bmatrix} \arctan(\frac{w}{u}) \\ \arctan\left(\frac{v}{\sqrt{u^2+w^2}}\right) \\ \sqrt{u^2+v^2+w^2} \end{bmatrix} \tag{9-6}$$

The true airspeed as described in sensor configuration 5, provides adequate airspeed aiding to GPS velocities during windy or high turning situations. With the angle of attack and side-slip angle sensors, the direction of the true airspeed vector is known. From this all three body-fixed velocity components can be derived.

The air data sensors measure the true velocity of the vehicle as seen from a moving air particle, including any possible wind components. Together with the velocity output from the GPS receiver, the wind components become observable. The IMU velocity prediction can be corrected by using either the GPS velocities or the three air data sensors. When using both type of sensors also the wind components can be estimated, as the redundant velocity observer can be used to indicate the difference in IMU velocity prediction error and atmospheric wind. To summarize, sensor configuration 6 uses the following sensors and receivers:

- 3 gyroscopes, output quantities: rotational rates p, q and r.
- 3 accelerometers, output quantities: specific forces A_x, A_y and A_z.
- GPS receiver, output quantities: 3D position x, y and z, velocity u, v and w.
- Air data sensors, output quantities: α, β and V_T.

9-1-7 7: IMU + Multiple GPS with Carrier Phase

This sensor configuration is the same as configuration 2, with the addition of multiple GPS receivers. When four GPS receivers are placed onto a vehicle, all receive GPS satellite signals. By using the geometry between the receivers, information about the vehicle attitude can be derived. Usually the measurements from all receivers are fused together, where a single algorithm calculates the attitude. Expression 9-7 gives the observer equation.

$$\underline{y} = \begin{bmatrix} \phi_{GPS} \\ \theta_{GPS} \\ \psi_{GPS} \end{bmatrix} \tag{9-7}$$

Different algorithms and procedures exist to obtain the orientation angles by using multiple GPS receivers, an example can be found in (Wendel, Meister, Mönikes, & Trommer, 2006) using time-differenced carrier phase measurements. Most algorithms need a minimal baseline length between the receivers, determined by the carrier phase signal, to be able to calculate the orientation angles. Sensor configuration 7 uses the following sensors and receivers:

- 3 gyroscopes, output quantities: rotational rates p, q and r.
- 3 accelerometers, output quantities: specific forces A_x, A_y and A_z.
- GPS receiver, output quantities: 3D position x, y and z, velocity u, v and w.
- GPS phase measurements, output quantities: 3 orientation angles ϕ, θ and ψ.

Possible extensions to the orientation angles estimation can be the receiver clock error and receiver clock error drift. The GPS receiver outputted position and velocity are based on the pseudo-range and pseudo-range rate. With a correct estimation of user clock error and drift, the pseudo-range and pseudo-range rate can be calculated more accurately.

9-1-8 8: IMU + Multiple GPS with Carrier Phase + V_T, α, β Sensors

Sensor configuration 8 is a combination of the configurations 6 and 7. By using GPS carrier phase measurements, a correction on the IMU predicted orientation angles and an estimation of the gyroscopic biases can be made. The combined use of the GPS velocities output together with three air data sensors, the true airspeed, angle of attack and side-slip, can be used to correct the IMU velocity predictions and estimate atmospheric wind velocities. Also all six IMU biases can be estimated. To summarize, sensor configuration 8 uses the following sensors and receivers:

- 3 gyroscopes, output quantities: rotational rates p, q and r.
- 3 accelerometers, output quantities: specific forces A_x, A_y and A_z.
- GPS receiver, output quantities: 3D position x, y and z, velocity u, v and w.
- GPS phase measurements, output quantities: 3 orientation angles ϕ, θ and ψ.
- Air data sensors, output quantities: α, β and V_T.

9-2 Selection

The goal of this report is to describe sensor configurations that can stabilize a fixed-wing UAV during all phases of flight. To be able to stabilize a flying vehicle, information on all three orientation angles, roll angle ϕ, pitch angle θ and heading angle ψ is required. The traditional integration between inertial and satellite navigation systems is represented by sensor configuration 2, IMU/GPS integration. Sensor configuration 2 forms the basis, as the biased IMU predictions can be corrected by a different set of unbiased measurements. The other sensor configurations are all extensions to sensor configuration 2.

Sensor configuration 3, 4 and 5 all have a sensor extension for one particular state. Configuration 3 improves the heading angle estimation by means of magnetometers, configuration 4 the vertical position estimation by using a barometer and configuration 5 velocity estimation with the use of airspeed aiding. With the exception of sensor configuration 3, these three configurations give no additional information about the vehicles orientation. The magnetic heading angle can be used as an additional heading angle observer to the GPS velocity based heading angle estimation. The focus of this report is on the stabilization of flying vehicles, sensor configuration 4 and 5 can be used for navigation purposes.

Sensor configuration 6 can be used to correct all velocity estimations and holds information about the vehicles orientation. It should however be further investigated how accurate the derived orientation angles and atmospheric wind estimations are. The same holds for sensor configuration 7, where the quality of the calculated orientation angles is mainly dependent on the integration algorithm. Sensor configuration 8 will provide most information as the most sensors are used. Chapter 10 analyzes the physical properties of flying vehicles together with the coupling of individual sensors such that additional information of the vehicle can be obtained. The following sensor configuration are used in the following two chapters. The physical analysis of chapter 10 into additional kinematic relations between flying vehicles together with the coupling of individual sensors such that additional information of the vehicle's orientation angles can be obtained. Together with the observability analysis of chapter 11, the following sensor configurations are investigated:

- Sensor configuration 2, IMU + GPS
- Sensor configuration 6, IMU + GPS + V_T, α, β
- Sensor configuration 7, IMU + multiple GPS with Carrier Phase
- Sensor configuration 8, IMU + V_T, α, β + multiple GPS with Carrier Phase

Chapter 10

Physical Properties of Aircraft Kinematics

This chapter is about improving the sensor fusion of a loosely coupled IMU/GPS integration by adding kinematic observers, starting with the derivation of the motion of a particle in inertial space seen from a local reference frame in section 10-1. The derived kinematic equations are applied to rigid bodies in section 10-2. Based on the derived kinematics together with the coupling of IMU, GPS receiver and fixed-wing aircraft kinematics this results in new physical insight. Section 10-3 gives the possible use of additional attitude/heading expressions to improve navigation filter performance, resulting in three angle correction (AC) equations. The last section 10-4 is about specific forces estimation with the use of GPS velocity derivatives.

10-1 Kinematics in Non-Inertial Reference Frames

Newton's laws of motion can be applied to the domain of reference frames. Different reference frames can be used to describe the motion of a flying vehicle. This section describes the general kinematic formulation and movement of a particle within the context of moving reference frames.

Figure 10-1 describes the relative motion of a reference frame with origin B and coordinate axes xyz to an inertial frame with coordinate axes XYZ and origin O. The unit vectors $\underline{\hat{i}}$, $\underline{\hat{j}}$, $\underline{\hat{k}}$ represent the moving axes, and the unit vectors $\underline{\hat{I}}$, $\underline{\hat{J}}$, $\underline{\hat{K}}$ the moving axes of the inertial frame of reference O. An inertial reference frame is fixed in space, any reference frame attached to the Earth, for instance the Earth reference frame $\mathcal{F}_E$ of chapter 8, is strictly speaking not an inertial reference frame. Nevertheless, during short times and small disturbances the assumption of a coordinate system attached to the Earth being an inertial coordinate system is valid. The linear velocity and acceleration of the xyz coordinate system are given by $\underline{v}_B$ and $\underline{a}_B$. The angular velocity of xyz coordinate frame is denoted by $\underline{\omega}$.

Consider the particle P with respect to the inertial system given by vector $\underline{r}_P$, as given in figure 10-2. The particle P is seen by an observer in the local moving xyz coordinate system.

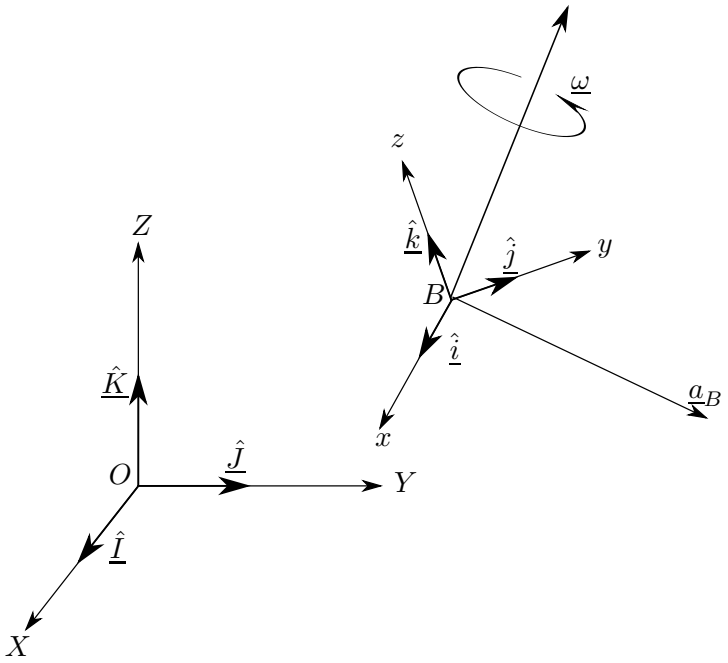

Figure 10-1: Relative motion of the local coordinate frame B with respect to inertial frame of reference O

Position $\underline{r}_{rel}$ is the position of particle P relative to the moving coordinate system xyz. The position of P with respect to the XYZ inertial coordinate system is represented by the vector $\underline{r}_P$. The position vector $\underline{r}_P$ can be obtained by combining the position vectors $\underline{r}_B$ and $\underline{r}_{rel}$. The position vector $\underline{r}_{rel}$ of particle P as seen from the xyz coordinate system, is defined by expression 10-1.

$$\underline{r}_{rel} = x(t)\hat{\underline{i}} + y(t)\hat{\underline{j}} + z(t)\hat{\underline{k}} \tag{10-1}$$

The time derivative of the position of particle P: $\frac{d\underline{r}_{rel}}{dt}$ with respect to the coordinate system xyz is defined with expression 10-2.

$$\underline{v}_{rel} = \dot{x}\hat{\underline{i}} + \dot{y}\hat{\underline{j}} + \dot{z}\hat{\underline{k}} \tag{10-2}$$

The same can be done for the acceleration of particle P with respect to the xyz coordinate system, resulting in expression 10-3.

$$\underline{a}_{rel} = \ddot{x}\hat{\underline{i}} + \ddot{y}\hat{\underline{j}} + \ddot{z}\hat{\underline{k}} \tag{10-3}$$

The position of particle P with respect to the inertial frame O is given in expression 10-4 as can be seen in figure 10-2 from the two position vectors $\underline{r}_B$ and $\underline{r}_{rel}$ connecting the particle P to the inertial frame via the local moving frame of reference B.

$$\underline{r}_P(t) = \underline{r}_B(t) + \underline{r}_{rel}(t) \tag{10-4}$$

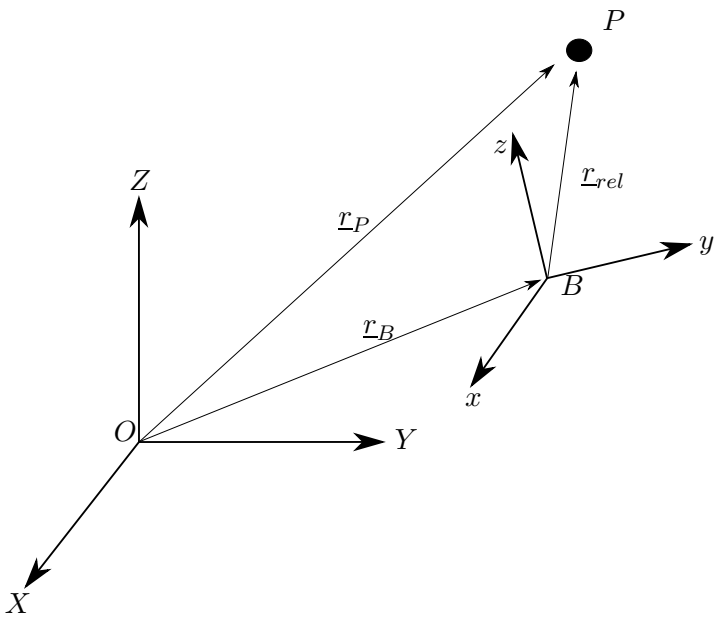

Figure 10-2: Motion of a particle P in an inertial frame, as seen by the local and moving coordinate frame B

The velocity of P defined in inertial space, $\underline{v}_P$, can be obtained by taking the time derivative of the position vector of P, as defined in expression 10-4. This results in expression 10-5.

$$\underline{v}_P = \frac{d\underline{r}_P}{dt} = \frac{d\underline{r}_B}{dt} + \frac{d\underline{r}_{rel}}{dt} \tag{10-5}$$

The first term of expression 10-5 is given in expression 10-6, as the time derivative of the absolute position between local frame of reference B and inertial frame O.

$$\frac{d\underline{r}_B}{dt} = \underline{v}_B \tag{10-6}$$

The second term of expression 10-5 can be obtained by applying the chain rule, expression 10-7.

$$\frac{d\underline{r}_{rel}(t)}{dt} = \frac{dx}{dt}\underline{\hat{i}} + \frac{dy}{dt}\underline{\hat{j}} + \frac{dz}{dt}\underline{\hat{k}} + \frac{d\underline{\hat{i}}}{dt}x + \frac{d\underline{\hat{j}}}{dt}y + \frac{d\underline{\hat{k}}}{dt}z \tag{10-7}$$

Expression 10-7 holds 2 sets of terms, the first three terms represent the translation of the xyz coordinate frame with respect to the inertial frame O. During pure translation, when $\underline{\omega} = 0$ with respect to the XYZ inertial coordinate system, the orientation of xyz does not change with respect to XYZ. This results in constant unit vectors $\underline{\hat{i}}$, $\underline{\hat{j}}$ and $\underline{\hat{k}}$, with zero time derivatives. During pure translation, expression 10-7 results in expression 10-8 by using the first three terms of expression 10-7.

$$\frac{d\underline{r}_{rel}(t)}{dt} = \frac{dx}{dt}\underline{\hat{i}} + \frac{dy}{dt}\underline{\hat{j}} + \frac{dz}{dt}\underline{\hat{k}} = \underline{v}_{rel} \tag{10-8}$$

During rotation of the xyz coordinate system with angular velocity $\underline{\omega}$, the orientation of the local coordinate frame xyz changes resulting in different local unit vectors $\underline{\hat{i}}$, $\underline{\hat{j}}$ and $\underline{\hat{k}}$. The resulting time derivatives of the unit vectors are the result of the crossproduct between the angular velocity $\underline{\omega}$ and the local unit vectors. Expression 10-9 gives the time derivatives of all three unit vectors.

$$\begin{aligned} \dot{\underline{\hat{i}}} &= \underline{\omega} \times \underline{\hat{i}} \\ \dot{\underline{\hat{j}}} &= \underline{\omega} \times \underline{\hat{j}} \\ \dot{\underline{\hat{k}}} &= \underline{\omega} \times \underline{\hat{k}} \end{aligned} \tag{10-9}$$

The last three terms of expression 10-7 result in expression 10-10, by using the result of expression 10-9. The scalar coordinates x, y and z are combined in one vector relative position vector $\underline{r}_{rel}$ between particle P and local frame of reference B.

$$\frac{d\underline{r}_{rel}(t)}{dt} = \underline{\omega} \times \underline{r}_{rel} \tag{10-10}$$

Expressions 10-8 and 10-10 can be combined into one expression for describing the combined translation and rotation of a particle P with respect to the inertial frame O, resulting in final velocity $\underline{v}_P$ expression 10-11. This expression also includes the velocity of the local xyz coordinate frame $\underline{v}_B$ with respect to the inertial reference O as given in expression 10-6.

$$\underline{v}_P = \underline{v}_B + \underline{v}_{rel} + \underline{\omega} \times \underline{r}_{rel} \tag{10-11}$$

Expression 10-11 can be interpreted as the velocity corresponding to the movement of the xyz coordinate system together with the translation and rotation of particle P as seen from the local xyz coordinate system with respect to the XYZ coordinate system. The vectors $\underline{r}_{rel}$ and $\underline{v}_{rel}$ are relative vectors between the local moving xyz coordinate system and particle P. The vectors $\underline{v}_B$ and $\underline{\omega}$ are absolute vectors in inertial space.

The acceleration $\underline{a}_P$ of particle P with respect to both reference frames can be obtained by differentiating expression 10-11, resulting in expression 10-12.

$$\underline{a}_P = \frac{d\underline{v}_P}{dt} = \frac{d\underline{v}_B}{dt} + \frac{d\underline{v}_{rel}}{dt} + \frac{d\left(\underline{\omega} \times \underline{r}_{rel}\right)}{dt} \tag{10-12}$$

Three terms are present in expression 10-12, the first one is the acceleration of the local xyz coordinate system with respect to the inertial reference system O, resulting in expression 10-13. This acceleration is the absolute acceleration of moving reference frame B in inertial space. The second term is the time derivative of the relative velocity between particle P and local reference frame B. This quantity can be obtained by using the same procedure as for the time derivative of the relative motion $\frac{d\underline{r}_{rel}}{dt}$ of expression 10-7 by applying superposition. Superposition is applied by looking at the translation and rotation between particle P and local reference frame B, resulting in expression 10-14.

$$\frac{d\underline{v}_B}{dt} = \underline{a}_B \tag{10-13}$$

$$\frac{d\underline{v}_{rel}}{dt} = \underline{\omega} \times \underline{v}_{rel} + \underline{a}_{rel} \tag{10-14}$$

The third term of expression 10-12 can be expanded by using the chain rule, resulting in expression 10-15.

$$\frac{d\left(\underline{\omega} \times \underline{r}_{rel}\right)}{dt} = \left(\frac{d\underline{\omega}}{dt}\right) \times \underline{r}_{rel} + \underline{\omega} \times \left(\frac{d\underline{r}_{rel}}{dt}\right) \tag{10-15}$$

The first term expression 10-15 corresponds to the crossproduct of the time derivative of the angular velocity vector of the local frame of reference B with the position vector $\underline{r}_{rel}$ between the particle P and local reference frame B, denoted by $\dot{\underline{\omega}}$. The second term can be obtained by using superposition and with the result of expressions 10-8 and 10-10, resulting in expression 10-16.

$$\underline{\omega} \times \left(\frac{d\underline{r}_{rel}}{dt}\right) = \underline{\omega} \times \left(\underline{v}_{rel} + \underline{\omega} \times \underline{r}_{rel}\right) \tag{10-16}$$

With expression 10-16 the third time derivative of expression 10-12 can be obtained, resulting in expression 10-17.

$$\underline{\omega} \times \left(\frac{d\underline{r}_{rel}}{dt}\right) = \dot{\underline{\omega}} \times \underline{r}_{rel} + \underline{\omega} \times \underline{v}_{rel} + \underline{\omega} \times \left(\underline{\omega} \times \underline{r}_{rel}\right) \tag{10-17}$$

Together with the derived expressions 10-13, 10-14 and 10-17, the total acceleration of a particle P seen from a moving local frame of reference B with respect to an inertial frame of reference O can be made, resulting in expression 10-18.

$$\underline{a}_P = \underline{a}_B + 2\left(\underline{\omega} \times \underline{v}_{rel}\right) + \underline{a}_{rel} + \dot{\underline{\omega}} \times \underline{r}_{rel} + \underline{\omega} \times \left(\underline{\omega} \times \underline{r}_{rel}\right) \tag{10-18}$$

The quantity $\underline{a}_{rel}$, was previously defined in expression 10-3 as the acceleration between particle P and moving frame of reference B. Expression 10-18 gives the kinematic expression of the acceleration of a particle P from a moving frame of reference B with respect to the inertial frame of reference O. It must be emphasized that both frames of reference observe the same particle, however by using different descriptions. Up till now there has been no mentioning of what causes the motion or what forces act on the particle P. Following section 10-2 explains the motion of rigid bodies under external forces by using the derived kinematic expression 10-18.

10-2 Motion of Rigid Bodies

The derived kinematic expressions 10-11 for velocity and 10-18 for acceleration describe the general motion of a particle P with respect to a moving reference frame B in inertial space. The particle P with mass m is now placed in the origin of the moving frame of reference B with coordinate system xyz attached to it, called a rigid body. At any instant the angular velocity of the rigid body is specified as $\underline{\omega}$ and its corresponding angular acceleration $\underline{\alpha}$. The motion of P is relative to an inertial coordinate system, denoted by origin O and coordinate system XYZ. Figure 10-3 displays the two frames of reference with the rigid body.

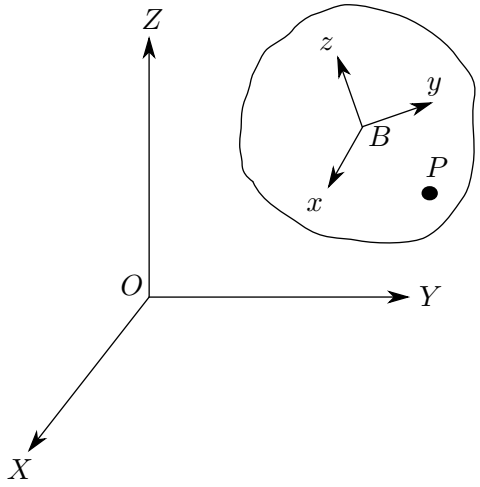

Figure 10-3: Motion of a rigid body with the center of gravity at the center of the local frame of reference B with respect to inertial frame of reference O

Expressions 10-19 and 10-20 are repeated below of section 10-1, which describe the velocity and acceleration of P. Point P is now located somewhere on the rigid body, relative to a constant position to the frame of reference B.

$$\underline{v}_P = \underline{v}_B + \underline{v}_{rel} + \underline{\omega} \times \underline{r}_{rel} \tag{10-19}$$

$$\underline{a}_P = \underline{a}_B + 2\left(\underline{\omega} \times \underline{v}_{rel}\right) + \underline{a}_{rel} + \underline{\alpha} \times \underline{r}_{rel} + \underline{\omega} \times \left(\underline{\omega} \times \underline{r}_{rel}\right) \tag{10-20}$$

Expressions 10-19 and 10-20 describe the general motion of a particle in inertial space as seen from a moving frame of reference B. When using these expression to describe the absolute motion of origin B, only the absolute kinematic quantities should be considered. The kinematic quantities in inertial space are the following:

- $\underline{v}_B$, absolute velocity of local reference frame with origin B.
- $\underline{a}_B$, absolute acceleration of local reference frame with origin B.
- $\underline{\omega}$, angular velocity of xyz coordinate system of local reference frame with origin B.

- $\underline{\alpha}$, angular acceleration of xyz coordinate system of local reference frame with origin B.

The mentioned absolute quantities result in the following two expressions 10-21 and 10-22, from (Török, 2000) to describe the velocity and acceleration of any point P with position vector $\underline{r}$ located on the body. The position of point P is fixed on the body and the relative velocity becomes $\underline{v}_{rel} = 0$. The last term of expression 10-20, $\underline{\omega} \times (\underline{\omega} \times \underline{r}_{rel})$, can be rewritten when $\underline{r}_{rel}$ remains constant into $\underline{\omega} \times \underline{v}_B$. This results in expression 10-22.

$$\underline{v}_P = \underline{v}_B + \underline{\omega} \times \underline{r} \tag{10-21}$$

$$\underline{a}_P = \underline{a}_B + \underline{\alpha} \times \underline{r}_B + \underline{\omega} \times \underline{v}_B \tag{10-22}$$

When assumed that a force $\underline{\mathrm{F}}$ is acting on point P of the rigid body with mass m, Newton's second law holds in inertial space, expression 10-23.

$$\underline{F} = m\underline{a}_P \tag{10-23}$$

When substituting the derived acceleration of expression 10-22 into expression 10-23, this results in expression 10-24.

$$\underline{F} = m\underline{a}_B + m\left(\underline{\alpha} \times \underline{r}_B\right) + m\left[\underline{\omega} \times \left(\underline{\omega} \times \underline{r}_B\right)\right] \tag{10-24}$$

Expression 10-24 can be rewritten into 10-25 when dividing all terms by the mass m. The final expression 10-25 will be used in the next section 10-3 when deriving kinematic relations, applied to flying vehicles.

$$\frac{\underline{F}}{m} = \underline{a}_B + \underline{\alpha} \times \underline{r}_B + \underline{\omega} \times \underline{v}_B \tag{10-25}$$

10-3 Kinematics Applied to Flying Vehicles

The derived expression 10-25 of section 10-2 can be applied to aircraft, where the resulting force $\underline{F}$ is composed of resulting body forces and gravitational forces. The two forces are given in expression 10-26 with respect to inertial frame of reference O as defined in figure 10-3. There are two forces acting on the aircraft, the body forces $\underline{F}_{body} = [X, Y, Z]$ holding the aerodynamic, atmospheric and engine forces and the gravity force $\underline{F}_g$ representing the gravitational forces between the aircrafts and Earth's masses.

$$\underline{F} = \underline{F}_{body} + \underline{F}_g \tag{10-26}$$

Expression 10-26 can be substituted into expression 10-25. This results in expression 10-27, where the gravitational acceleration $\underline{a}_g$ is replacing the gravitational force $\underline{F}_g$ when divided by mass m.

$$\frac{\underline{F}_{body}}{m} + \underline{a}_g = \underline{a}_B + \underline{\alpha} \times \underline{r}_B + \underline{\omega} \times \underline{v}_B \tag{10-27}$$

The change in gravity vector orientation between local $\mathcal{F}_B$ and Earth frame of reference $\mathcal{F}_E$ as derived in chapter 8, the equations of motions. When assuming that gravity is a constant vector pointing downwards in $\mathcal{F}_E$, three angles are required $\underline{\theta} = [\phi, \theta, \psi]$ to describe the gravity vector orientation in $\mathcal{F}_B$, expression 8-24. Expression 10-27 can be worked out in expression 10-28 together with expression 8-24.

$$\begin{bmatrix} \frac{X}{m} \\ \frac{Y}{m} \\ \frac{Z}{m} \end{bmatrix} + \begin{bmatrix} g_0 \sin\theta \\ -g_0 \sin\phi \cos\theta \\ -g_0 \cos\phi \cos\theta \end{bmatrix} = \begin{bmatrix} a_{B_x} \\ a_{B_y} \\ a_{B_z} \end{bmatrix} + \begin{bmatrix} \alpha_y r_z - \alpha_z r_y \\ \alpha_z r_x - \alpha_x r_z \\ \alpha_x r_y - \alpha_y r_x \end{bmatrix} + \begin{bmatrix} \omega_y v_{B_z} - \omega_z v_{B_y} \\ \omega_z v_{B_x} - \omega_x v_{B_z} \\ \omega_x v_{B_y} - \omega_y v_{B_x} \end{bmatrix} \tag{10-28}$$

The following subsections give the derivations of additional Angle Correction (AC) expressions as kinematic observers, by using the force equilibrium equation 10-28.

10-3-1 Pitch Angle Estimation

During the prediction step of a state identification filter, the pitch angle θ is predicted by using the pitch angle derivative $\dot{\theta}$ as derived in chapter 8, expression 8-25. The pitch angle kinematic equation of 8-25, is repeated in expression 10-29. From this expression can be seen that the pitch angle time derivative calculation uses angular rates q and r together with the roll angle ϕ. The angular rates are assumed to be measured by gyroscopes together with sensor noises e and biases b.

$$\dot{\theta} = (q_m - b_q - e_q)\cos\phi - (r_m - b_r - e_r)\sin\phi \tag{10-29}$$

Besides the pitch angle kinematic equation, the pitch angle is found in more kinematic equations. The force equilibrium equation 10-28 will be used in this section to find additional expressions to estimate θ. The first row of expression 10-28 is repeated below in expression 10-30 is used in the following part to find relations to describe θ.

$$\frac{X}{m} + g_0 \sin\theta = a_{B_x} + (\alpha_y r_z - \alpha_z r_y) + \left(\omega_y v_{B_z} - \omega_z v_{B_y}\right) \tag{10-30}$$

When assuming that accelerometers can measure specific forces, the force terms of expression 10-30 can be grouped together into one specific force equation. Expression 10-31 gives the specific force equation, where the resulting specific force in forward direction A_x can be measured with an accelerometer.

$$A_x = \frac{X}{m} - (\alpha_y r_z - \alpha_z r_y) \tag{10-31}$$

The measured acceleration contains the specific force together with the gravitational acceleration. Knowledge about the gravitational field is required to extract the specific forces. The mechanical terms that are used in expression 10-30 can be renamed to a more conventional flight dynamics notation. The term a_{B_x} is equal to the time derivative of the velocity in forward direction and is usually denoted by $\dot{u}$. The velocity components v_{B_y} and v_{B_z}, can be replaced by v_B and w_B. When rewriting, expression 10-30 results in 10-32.

$$\dot{u}_B = A_x - g_0 \sin\theta + r v_B - q w_B \tag{10-32}$$

Equation 10-32 shows the expression that is used to predict the derivative of the forward velocity $\dot{u}$ in a body-fixed reference frame, coming from the equations of motion, from expression 8-25 where the angular rates are measured by the onboard gyroscopic sensors and the specific forces by the accelerometers.

$$\dot{u} = A_{x_m} - b_{A_x} - e_{A_x} + (r_m - b_r - e_r)v - (q_m - b_q - e_q)w - g_0 \sin\theta \tag{10-33}$$

Equation 10-33 can be used to obtain an additional expression of the pitch angle. The physical interpretation about the relation between of the forward velocity derivative $\dot{u}$ and the term "$g_0 \sin(\theta)$" of expression 10-33 can be seen as follows: A change in pitch angle results in different specific forces acting onto an aircraft in $\mathcal{F}_B$, as a result of different gravitational orientation on the aircraft as the orientation between $\mathcal{F}_B$ and $\mathcal{F}_E$ changes. The difference in specific forces due to a different gravitational orientation, as sensed by the onboard accelerometers, can be used to calculate changes in pitch angle orientation. The gravity vector is assumed to be pointing downwards in $\mathcal{F}_E$, with a constant factor g_0. The first step to obtain a relation between the pitch angle and change in gravitational orientation, is to rewrite expression 10-33 into 10-34 by putting $\sin\theta$ at the left hand side of the equal sign.

$$\sin\theta = \frac{A_{x_m} - b_{A_x} - e_{A_x}}{g_0} + \frac{(r_m - b_r - e_r)v}{g_0} - \frac{(q_m - b_q - e_q)w}{g_0} - \frac{\dot{u}}{g_0} \tag{10-34}$$

Equation 10-34 can be rewritten into 10-35 to obtain θ.

$$\theta = \arcsin\left(\frac{A_{x_m} - b_{A_x} - e_{A_x}}{g_0} + \frac{(r_m - b_r - e_r)v}{g_0} - \frac{(q_m - b_q - e_q)w}{g_0} - \frac{\dot{u}}{g_0}\right) \tag{10-35}$$

From expression 10-35 can be seen that four terms determine the pitch angle. The first term includes the specific force in X-direction in $\mathcal{F}_B$, the second and third term are Coriolis accelerations which are the result of $\underline{\omega} \times \underline{v}$. The fourth term relates to changes in forward velocity in $\mathcal{F}_B$. To investigate the influence of the individual terms of expression 10-35 with respect to θ, the simulation of appendix D has been used. For the simulation a generic flight maneuver is simulated, where a 360° left turn is simulated followed by a 360° right turn and a 10° doublet input on the rudder combined with different throttle settings. The simulation results together with all output states can be found in appendix D. For each of the following cases kinematic terms of expression 10-35 are used. During the simulation, only the true states are considered, the sensor biases and noises have been left out. This has been done to qualitatively indicate the kinematic properties of each individual term, when including realistic sensor signals the kinematic relations become overshadowed by noise and biases. Expression 10-35 can be rewritten into expression 10-36 when leaving out the IMU biases and noise.

$$\theta = \arcsin\left(\frac{A_x}{g_0} + \frac{r \cdot v}{g_0} - \frac{q \cdot w}{g_0} - \frac{\dot{u}}{g_0}\right) \tag{10-36}$$

Besides looking at kinematic terms, cases can be investigated where terms are put together. Combining the first and fourth term of expression 10-36, results in expression 10-37. By combining the specific force in X-direction in $\mathcal{F}_B$, A_x, with the change in forward velocity $\dot{u}$, it is expected that the detection in change of gravity vector orientation with respect to $\mathcal{F}_E$ improves.

$$\theta = \arcsin\left(\frac{A_x - \dot{u}}{g_0}\right) \tag{10-37}$$

From expression 10-36 and 10-37, different cases on pitch angle estimation can be investigated:

1. $\theta_1 = \arcsin\left(\frac{A_x}{g_0}\right)$
2. $\theta_2 = \arcsin\left(\frac{r \cdot v}{g_0}\right)$
3. $\theta_3 = \arcsin\left(-\frac{q \cdot w}{g_0}\right)$
4. $\theta_4 = \arcsin\left(-\frac{\dot{u}}{g_0}\right)$
5. $\theta_5 = \arcsin\left(\frac{A_x - \dot{u}}{g_0}\right)$

Each case is plotted during the simulation of appendix D together with the true pitch angle θ_{true}, in the figures 10-4 to 10-8. Besides the pitch angle estimation, the estimation error is also included.

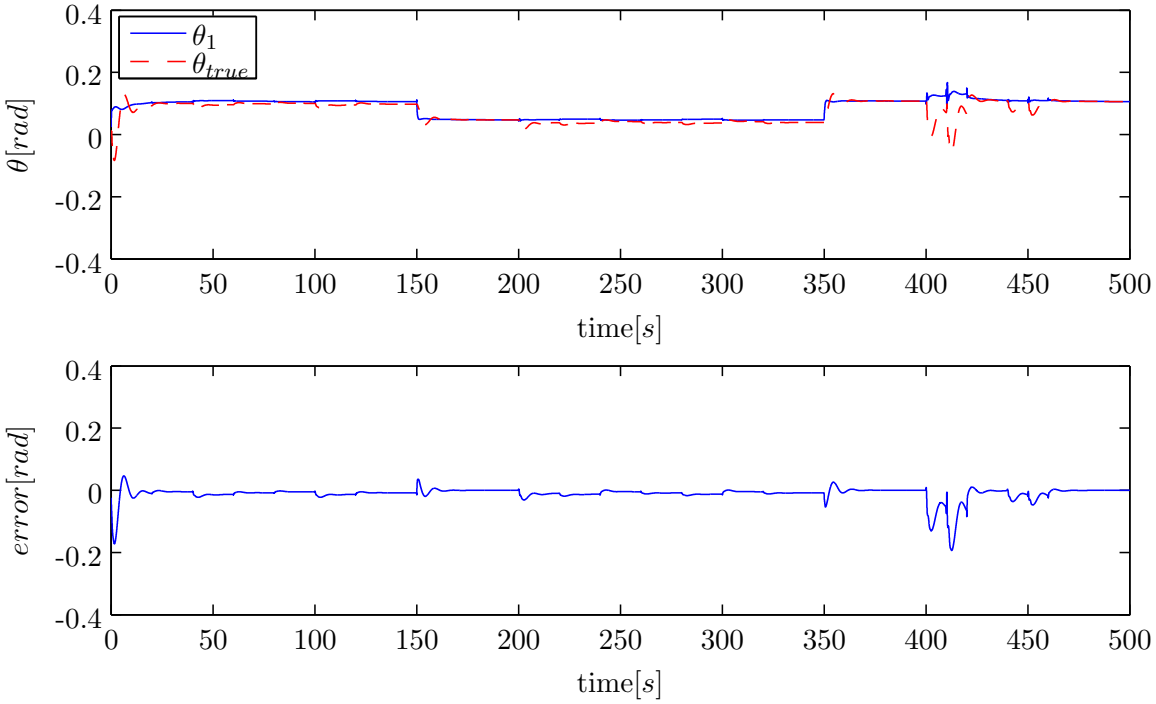

Figure 10-4: Pitch angle estimation, simulation results on case 1

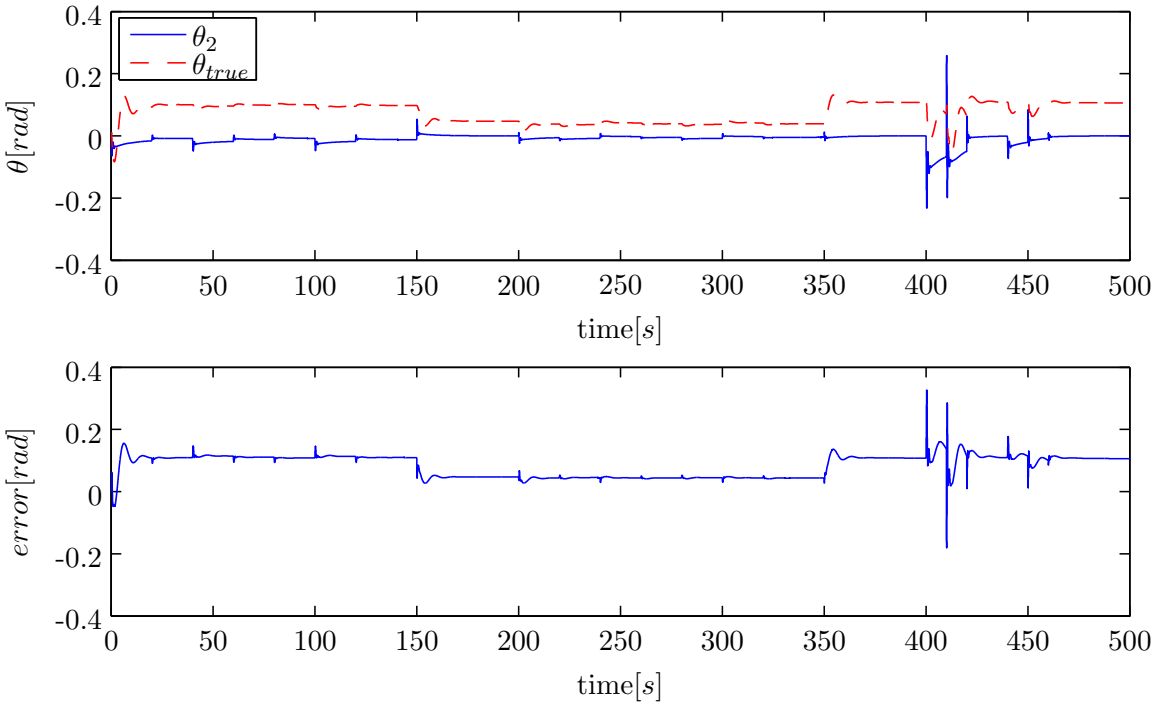

Figure 10-5: Pitch angle estimation, simulation results on case 2

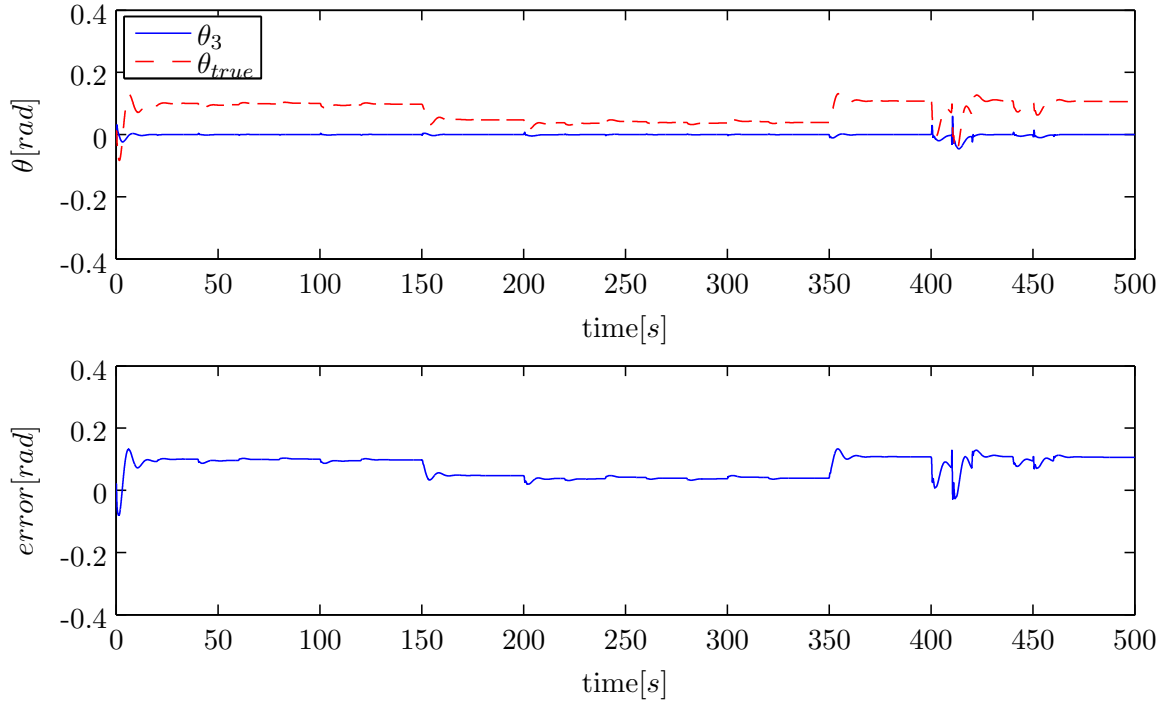

Figure 10-6: Pitch angle estimation, simulation results on case 3

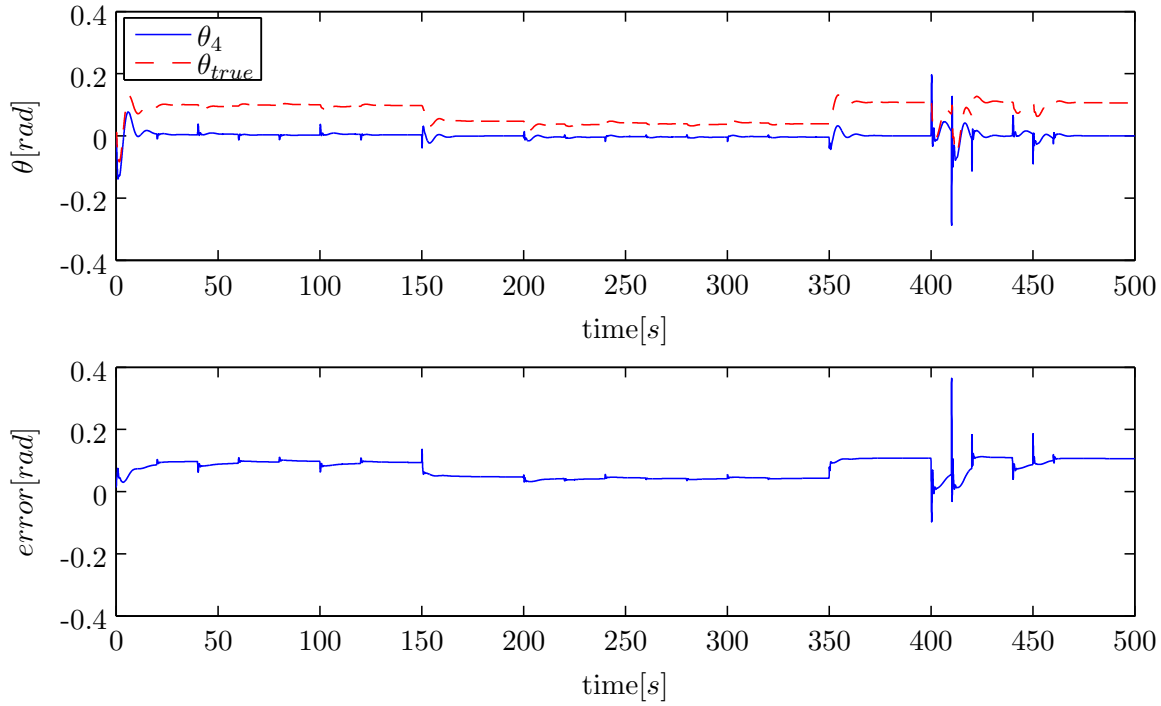

Figure 10-7: Pitch angle estimation, simulation results on case 4

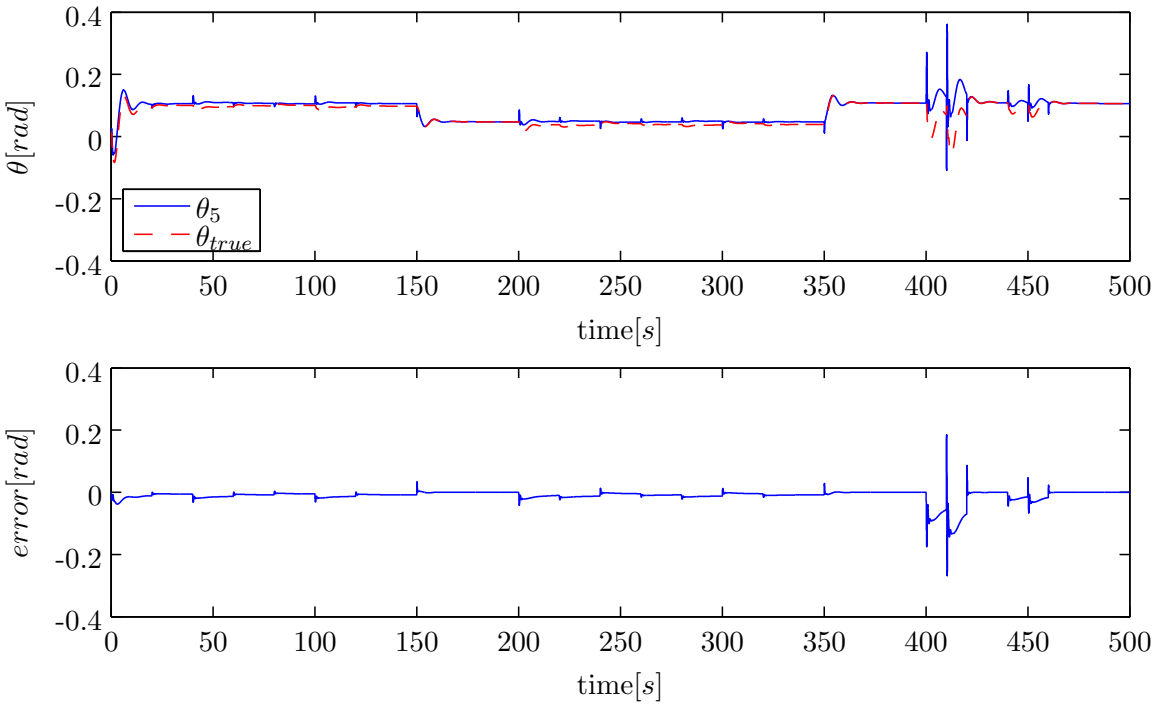

Figure 10-8: Pitch angle estimation, simulation results on case 5

From the figures 10-4 to 10-8 can be seen that θ_1 and θ_5 follow the general trend of the true pitch angle during the simulation. During the turning and change of throttle setting, the estimate follows the true pitch angle. When a sudden change in rudder setting is applied, doublet at 400 seconds, the direction of the gravity vector suddenly changes during a short period. To capture the dynamic changes solely using the direction of the gravity vector is inadequate. From the figures can be seen that the error increases during the doublet input. It can be concluded that case 1 and 5 give a good estimation of the pitch angle, solely acting on the change in orientation of the gravity vector. Cases 2 and 3 include Coriolis acceleration terms, which only include rotational changes and show large amplitudes during the rudder doublet input at 400 seconds. They do however not follow the change in throttle setting. Case 4 captures dynamic changes, based on changes in forward velocity. This result is a static error during a change in throttle setting, as can be seen from figure 10-7.

Case 1 and case 5 do not differ much from each other. Caused by the fact that the specific force A_x and derivative of the forward velocity $\dot{u}$ in $\mathcal{F}_B$ are strongly correlated. By including the change in forward velocity, case 5 gives a better pitch angle estimation compared to case 1. The improvement comes from including longitudinal changes, resulting in a different forward velocity, captured by the time derivative of the forward velocity $\dot{u}$ as can be seen in figure 10-8. Case 5 has however still difficulties when coping with fast dynamic changes as no Coriolis terms are included. A disadvantage of using cases 2 and 3 is that the body velocities v and w are obtained by integrating the specific forces obtained by the accelerometers, the velocity estimations contain a lot of noise due to the integration step and will result in a bad estimate. The obtained GPS velocities have a time delay with the IMU and cannot be used to correct these fast dynamic changes as the velocities are obtained later when compared to

the angular rates p and r.
Besides the previous described cases, the pitch angle can be derived by looking at the aircraft as a pendulum, where the gravity vector is pointing downwards with small deviations. This results in expression 10-38. This expression is based on the difference in gravitational orientation between $\mathcal{F}_B$ and $\mathcal{F}_E$, assuming a constant 3D vector that is pointing downwards in $\mathcal{F}_E$.

$$\theta_{\text{pen}} = \arctan\left(\frac{g_{x_B}}{\sqrt{{g_{y_B}}^2 + {g_{z_B}}^2}}\right) \tag{10-38}$$

When an aircraft is moving at a constant speed, assuming a difference in gravity orientation is the only change of the aircraft. The change in gravity orientation in $\mathcal{F}_B$ is the only force acting onto the aircraft. When assumed that gravity is the only force acting on the aircraft besides the aircraft body forces, it is the only source of change in specific forces sensed by the accelerometers in $\mathcal{F}_B$. Under this assumption, equation 10-38 can be rewritten into expression 10-39 from (Lai, Jan, & Hsiao, 2010).

$$\theta_{\text{pen}} = \arctan\left(\frac{A_x}{\sqrt{{A_y}^2 + {A_z}^2}}\right) \tag{10-39}$$

During maneuvers, the assumption that changes in gravitational orientation are the only source of changes in specific forces acting on the aircraft in $\mathcal{F}_B$, no longer holds and expression 10-39 is no longer valid. During the performed simulation of appendix D, the pitch angle estimation results are given in figure 10-9, estimation errors are due to the presence of other forces then gravity. The errors come from the fact that other forces are not included and the accelerometers sense only total accelerations. Extreme maneuvers are not included in the performed simulation of figures 10-4 to 10-9, maximum turning accelerations are about $\pm 1 m/s^2$, so the influence of specific forces is limited and figure 10-9 gives the same pitch angle estimation compared to case 1 or 5. During small changes and slow maneuvers the pendulum based expression 10-38 can be used as an alternative of case 1 or 5. The simulation shows the same estimation results. However, if fast dynamic turning maneuvers with higher accelerations are present, which are not uncommon for a small fixed-wing UAV, expression 10-39 cannot be used or constraints should be added.

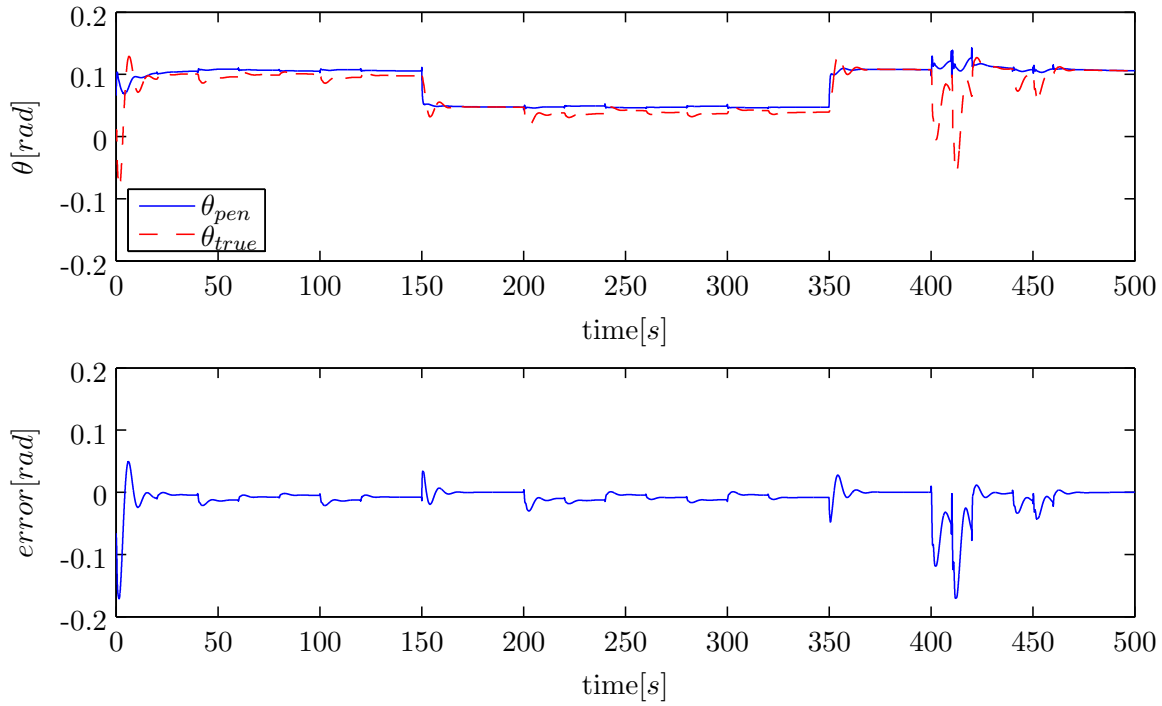

Figure 10-9: Pitch angle estimation, simulation results on pendulum case

Pitch angle estimation based on velocity components

The total velocity vector of a flying vehicle, contains the magnitude and direction of the aircrafts velocity. Information about the vehicles orientation can be obtained by utilizing the properties of vectors. Velocity in $\mathcal{F}_E$ can be obtained by using the GPS receiver velocity measurements. The pitch angle θ can be estimated by using the forward u_B and vertical w_B speed components. Estimations using only u and w, assume that the pitch angle is a function of the flight path angle γ and angle of attack α, as defined in equation 10-40 from basic airplane performance (Ruijgrok, 1996). Equation 10-40 is based on the physics of figure 10-10.

$$\theta = \gamma + \alpha \tag{10-40}$$

An aircraft with forward speed u follows a flight path, denoted by flight path angle γ. The flight path is the movement of an aircraft as seen from a moving air particle. The actual trajectory can be obtained with a GPS receiver, the GPS velocity components u_{GPS} and w_{GPS} can be used to make an estimation of γ as can be seen from figure 10-10 by using a North-East-Down (NED) frame of reference in $\mathcal{F}_E$ as described in chapter 8. This results in expression 10-41 for a GPS measured flight path angle γ_{GPS}.

$$\gamma_{GPS} = \arctan\left(\frac{-w_{GPS}}{u_{GPS}}\right) \tag{10-41}$$

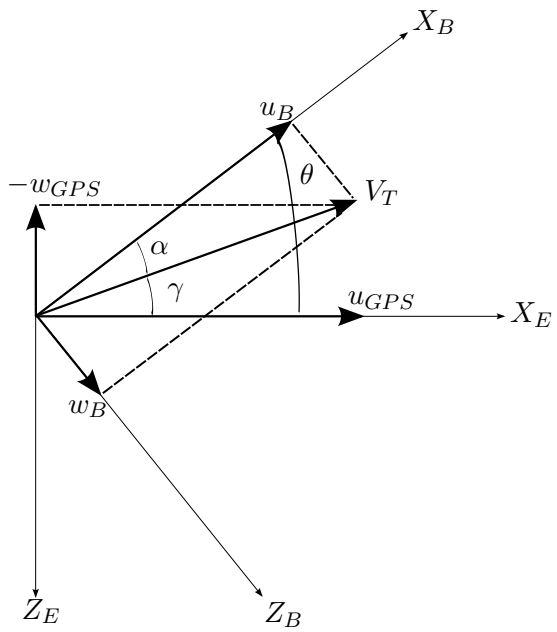

Figure 10-10: Pitch angle dynamics

Expression 10-41 can be used to perform an estimation of θ when neglecting the angle the attack α, resulting in expression 10-42. Expression 10-42 is the first GPS based pitch angle estimation case θ_{GPS1}.

$$\theta_{GPS1} = \arctan\left(\frac{-w_{GPS}}{u_{GPS}}\right) \tag{10-42}$$

Expression 10-42 can be extended into expression 10-43, when adding an angle of attack air data sensor, called an α sensor.

$$\theta_{GPS2} = \arctan\left(\frac{-w_{GPS}}{u_{GPS}}\right) + \alpha \tag{10-43}$$

Besides using an angle of attack sensor, α can also be estimated with the body-fixed velocity components u_B and w_B as indicated in figure 10-10. The angle of attack is equal to: $\alpha = \arctan\left(\frac{w_B}{u_B}\right)$. This results in the third theta estimation θ_{GPS3} by using velocity components, expression 10-44.

$$\theta_{GPS3} = \arctan\left(\frac{-w_{GPS}}{u_{GPS}}\right) + \arctan\left(\frac{w_B}{u_B}\right) \tag{10-44}$$

Based on expressions 10-42, 10-43 and 10-44 three GPS velocity based pitch angle estimations can be made:

- $\theta_{GPS1} = \arctan\left(\frac{-w_{GPS}}{u_{GPS}}\right)$
- $\theta_{GPS2} = \arctan\left(\frac{-w_{GPS}}{u_{GPS}}\right) + \alpha$

- $\theta_{GPS3} = \arctan\left(\frac{-w_{GPS}}{u_{GPS}}\right) + \arctan\left(\frac{w_B}{u_B}\right)$

Figures 10-11, 10-12 and 10-13 give the results of the three velocity based pitch angle estimation cases using the simulation of appendix D. The estimation error angles are not included, instead a zoomed figure on the estimation is added.

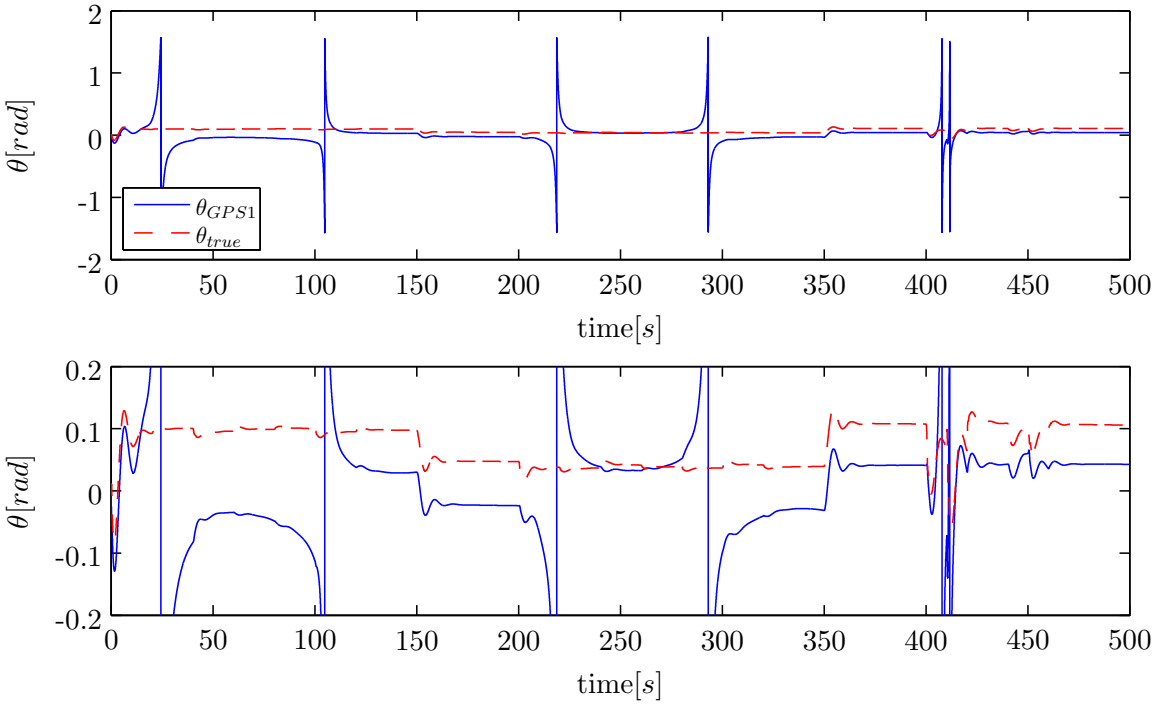

Figure 10-11: Pitch angle estimation, simulation results on GPS case 1

From figures 10-11 to 10-13 can be seen that GPS cases 2 and 3 give the same estimation results. From this can be concluded that there is no need of an extra α sensor, when there is a good velocity estimation. For some angles the estimation error becomes really large, as the angle between the two velocity components approaches $\pm 90°$. These high peaks needs to be filtered out, for instance using a low-pass filter or posing constraints. The forward velocity component u_{GPS} in $\mathcal{F}_E$ can go to zero during turning maneuvers, resulting in a small denominator of $\frac{-w_{GPS}}{u_{GPS}}$. The closer u_{GPS} goes to zero, the larger the resulting outcome of $\frac{-w_{GPS}}{u_{GPS}}$ becomes and the closer arctan $\left(\frac{-w_{GPS}}{u_{GPS}}\right)$ reaches $\pm\frac{\pi}{2}$, as the angle approaches $\pm 90°$.

The problem of u_{GPS} going to zero can also be solved by taking the forward body-fixed velocity component u_B instead of u_{GPS}. From figure 10-10 can be seen that these two velocities are not the same, the difference is a function of the flight path angle in between. Estimation errors as a result of the flight path angle are to be expected. Expression 10-45 gives the modified expression 10-44, by using both GPS and body-fixed velocity components.

$$\theta = \arctan\left(\frac{-w_{GPS}}{u_B}\right) + \arctan\left(\frac{w_B}{u_B}\right) \tag{10-45}$$

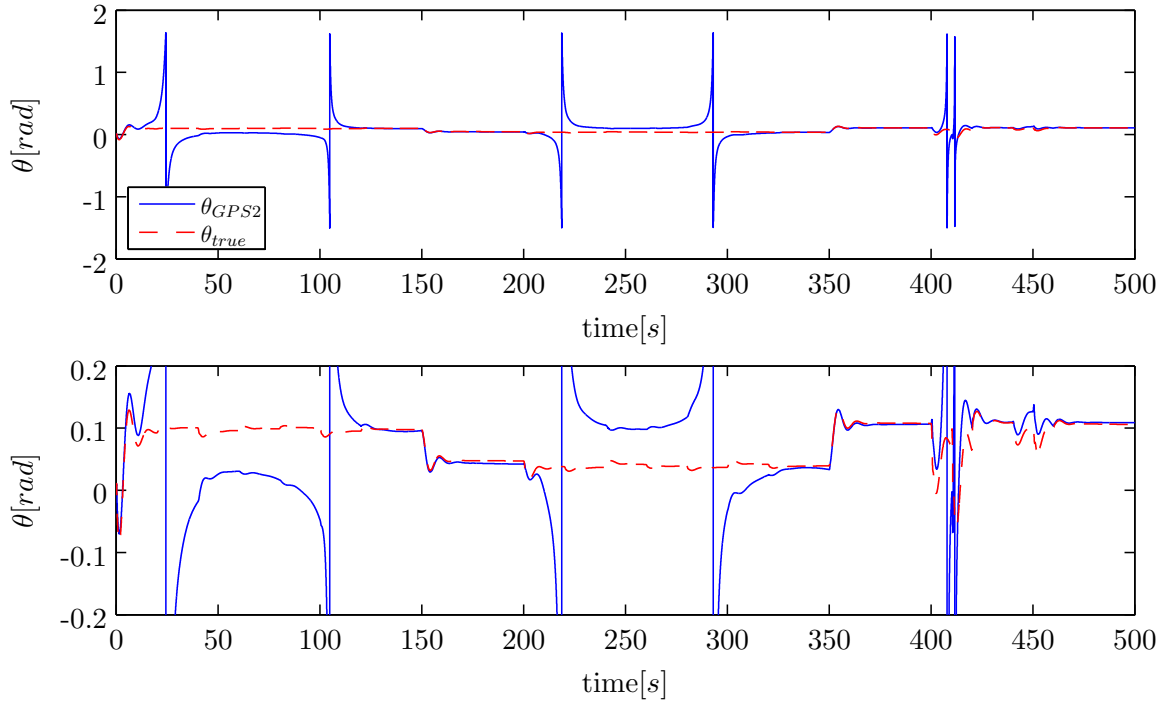

Figure 10-12: Pitch angle estimation, simulation results on GPS case 2

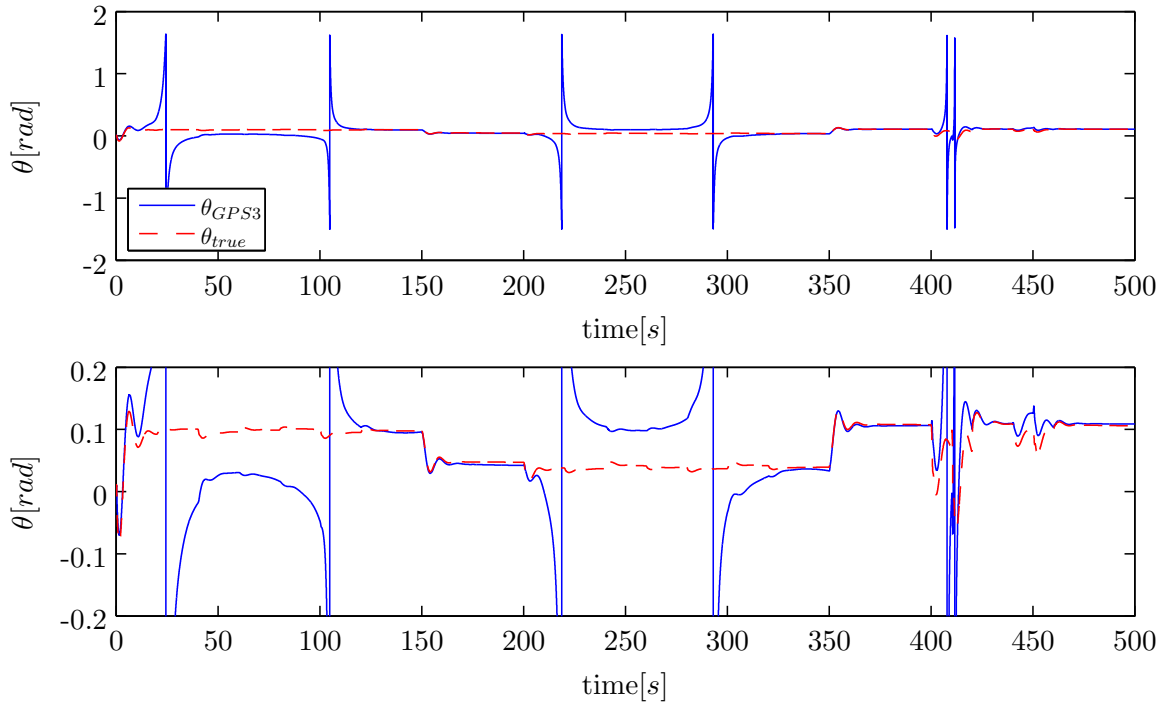

Figure 10-13: Pitch angle estimation, simulation results on GPS case 3

Expression 10-45 has the same denominator and can be rewritten into expression 10-46. Figure 10-14 gives the fourth velocity based theta estimation θ_{GPS4} during simulation together with the estimation error. From figure 10-14 can be seen that case 4 is about the same compared to GPS cases 2 and 3 where the former does not have large peaks, as long as u_B does not go to zero. The main advantage of using u_B instead of u_{GPS}, is that the denominator no longer reaches zero and no peaks are present. From figure 10-14 can also be seen that the error due to the difference in flight path angle, results in small estimation errors. The error becomes larger during dynamic maneuvers, for example the rudder doublet input at 400 seconds, as can be seen in figure 10-14. From this can be concluded that changing u_{GPS} to u_B shows big improvement.

$$\theta_{GPS4} = \arctan\left(\frac{w_B - w_{GPS}}{u_B}\right) \tag{10-46}$$

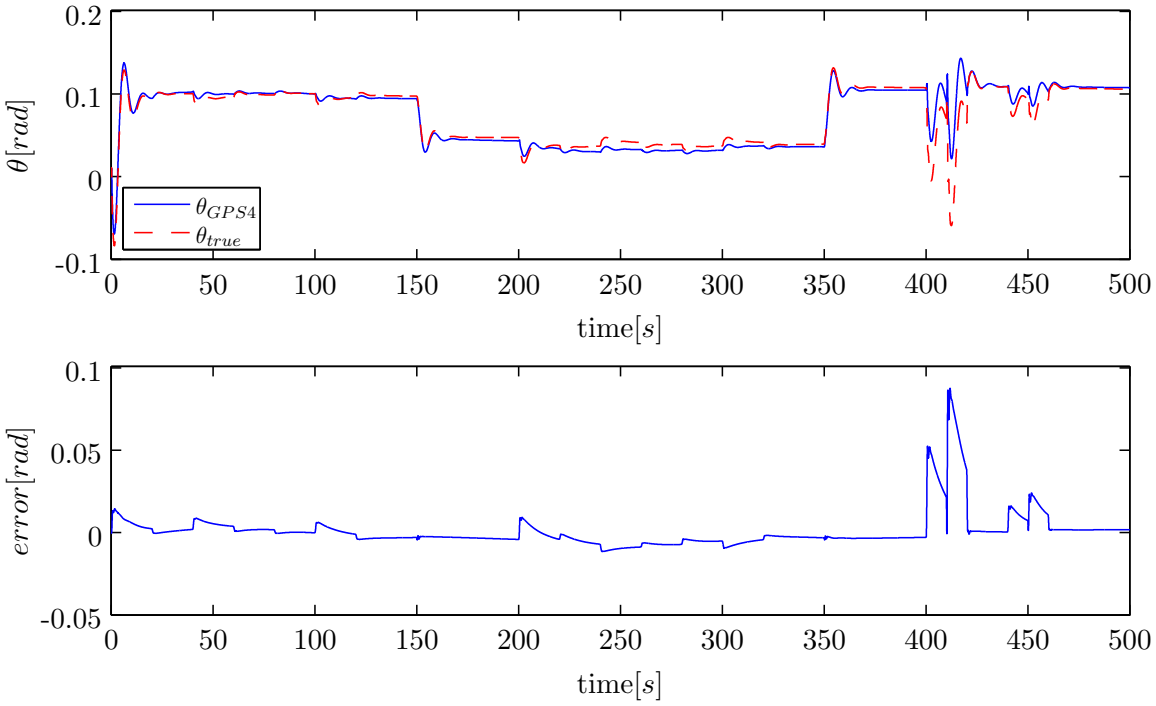

Figure 10-14: Pitch angle estimation, simulation results on GPS case 4

10-3-2 Roll Angle Estimation

Like the pitch angle of the previous subsection 10-3-1, the roll angle is predicted by using an angular kinematic equation of chapter 8, the time derivative of the roll angle $\dot{\phi}$. Equation 8-25 uses gyroscopic sensor measurements together with the pitch and roll angle, as repeated in expression 10-47 below.

$$\dot{\phi} = p_m - b_p - e_p + (q_m - b_q - e_q)\sin\phi\tan\theta + (r_m - b_r - e_r)\cos\phi\tan\theta \tag{10-47}$$

From expression 10-47 can be seen that the roll angle derivative is calculated by using angular rates p, q and r. Besides the roll angle kinematic equation, the roll angle is found in more kinematic equations. The derived force equilibrium equation 10-28 can be used to find additional roll angle expressions. The second and third row both contain a term ϕ and are repeated below, expression 10-48.

$$\begin{bmatrix} \frac{Y}{m} \\ \frac{Z}{m} \end{bmatrix} + \begin{bmatrix} -g_0\sin\phi\cos\theta \\ -g_0\cos\phi\cos\theta \end{bmatrix} = \begin{bmatrix} a_{B_y} \\ a_{B_z} \end{bmatrix} + \begin{bmatrix} \alpha_z r_x - \alpha_x r_z \\ \alpha_x r_y - \alpha_y r_x \end{bmatrix} + \begin{bmatrix} \omega_z v_{B_x} - \omega_x v_{B_z} \\ \omega_x v_{B_y} - \omega_y v_{B_x} \end{bmatrix} \tag{10-48}$$

Like for the pitch angle of subsection 10-3-1 it is assumed that the accelerometer can measure specific forces. Expression 10-49 gives the specific force equations, by using expression 10-48 where the resulting specific forces A_y and A_z can be measured by accelerometers.

$$\begin{bmatrix} A_y \\ A_z \end{bmatrix} = \begin{bmatrix} \frac{Y}{m} \\ \frac{Z}{m} \end{bmatrix} - \begin{bmatrix} \alpha_z r_x - \alpha_x r_z \\ \alpha_x r_y - \alpha_y r_x \end{bmatrix} \tag{10-49}$$

The measured accelerations contain besides specific forces also gravitational forces. Knowledge about the gravitational field is required to extract the specific forces. The kinematic terms that are used in expression 10-49 can be renamed to a more conventional flight dynamics notation. The terms a_{B_y} and a_{B_z} are equal to the time derivatives of the velocity in lateral and downward direction, $\dot{v}_B$ and $\dot{w}_B$. The same holds for the velocity components: v_{B_x}, v_{B_y} and v_{B_z} and can replaced by u, v and w. Expression 10-48 can rewritten into 10-50, by using expression 10-49.

$$\begin{bmatrix} \dot{v}_B \\ \dot{w}_B \end{bmatrix} = \begin{bmatrix} A_y \\ A_z \end{bmatrix} - \begin{bmatrix} -g_0\sin\phi\cos\theta \\ -g_0\cos\phi\cos\theta \end{bmatrix} + \begin{bmatrix} \omega_z v_{B_x} - \omega_x v_{B_z} \\ \omega_x v_{B_y} - \omega_y v_{B_x} \end{bmatrix} \tag{10-50}$$

Equation 10-50 is used to predict the lateral and downward velocity, by using their time derivatives $\dot{v}$ and $\dot{w}$ and can be rewritten in equations 10-51 and 10-52. These equations are used to predict the derivative of the lateral and downward velocity in a body-fixed reference frame, coming from the equations of motion, expression 8-25, where the angular rates ω_x, ω_y, ω_z are assumed to be measured by the onboard gyroscopic sensors p, q, r.

$$\dot{v} = A_{y_m} - b_{A_y} - e_{A_y} + (p_m - b_p - e_p)w - (r_m - b_r - e_r)u + g_0\cos\theta\sin\phi \tag{10-51}$$

$$\dot{w} = A_{z_m} - b_{A_z} - e_{A_z} + (q_m - b_q - e_q)u - (p_m - b_p - e_p)v + g_0 \cos\theta \cos\phi \tag{10-52}$$

Both equations 10-51 and 10-52 include a term with ϕ and can be rewritten to construct additional roll angle estimations. Expressions 10-51 and 10-52 can be rewritten into 10-53 and 10-54 to get ϕ at the left-hand side of the equal sign.

$$\sin\phi = -\frac{A_{y_m} - b_{A_y} - e_{A_y}}{g_0 \cos\theta} - \frac{(p_m - b_p - e_p)w}{g_0 \cos\theta} + \frac{(r_m - b_r - e_r)u}{g_0 \cos\theta} + \frac{\dot{v}}{g_0 \cos\theta} \tag{10-53}$$

$$\cos\phi = -\frac{A_{z_m} - b_{A_z} - e_{A_z}}{g_0 \cos\theta} - \frac{(q_m - b_q - e_q)u}{g_0 \cos\theta} + \frac{(p_m - b_p - e_p)v}{g_0 \cos\theta} + \frac{\dot{w}}{g_0 \cos\theta} \tag{10-54}$$

From expression 10-53, ϕ can be obtained resulting in expression 10-55.

$$\phi = \arcsin\left(-\frac{A_{y_m} - b_{A_y} - e_{A_y}}{g_0 \cos\theta} - \frac{(p_m - b_p - e_p)w}{g_0 \cos\theta} + \frac{(r_m - b_r - e_r)u}{g_0 \cos\theta} + \frac{\dot{v}}{g_0 \cos\theta}\right) \tag{10-55}$$

The roll angle can also be obtained from expression 10-54, resulting in expression 10-56.

$$\phi = \arccos\left(-\frac{A_{z_m} - b_{A_z} - e_{A_z}}{g_0 \cos\theta} - \frac{(q_m - b_q - e_q)u}{g_0 \cos\theta} + \frac{(p_m - b_p - e_p)v}{g_0 \cos\theta} + \frac{\dot{w}}{g_0 \cos\theta}\right) \tag{10-56}$$

For both expressions 10-55 and 10-56, holds that four kinematic terms determine the roll angle. Both expressions use the same kind of kinematic terms and are very similar, except for the "arcsin" and "arccos" functions. The first terms are accelerations, corresponding to lateral and downward direction in $\mathcal{F}_B$: A_y corresponds to v and A_z corresponds to w. The second and third terms relate to Coriolis acceleration, as a result of $\underline{\omega} \times \underline{v}$. The fourth and last term relate to changes in velocity components. To investigate the influence of the individual terms for both expressions, a simulation has been performed. The same simulation of appendix D as for the pitch angle expressions of section 10-3-1 is used. A generic flight maneuver is performed, where a 360° left turn is followed by a 360° right turn and a 10° rudder doublet together with different throttle settings. The simulation results together with all individual states can be found in appendix D. During the simulation, the sensor noise and biases have been left out and the true accelerations and angular rates are used. Only the true values are considered to qualitatively indicate the kinematic properties with realistic sensor signals the kinematic relations are overshadowed by noise and biases. Expressions 10-55 and 10-56 can be rewritten into 10-57 and 10-58 when leaving out biases and noise.

$$\phi = \arcsin\left(-\frac{A_y}{g_0 \cos\theta} - \frac{p \cdot w}{g_0 \cos\theta} + \frac{r \cdot u}{g_0 \cos\theta} + \frac{\dot{v}}{g_0 \cos\theta}\right) \tag{10-57}$$

$$\phi = \arccos\left(-\frac{A_z}{g_0 \cos\theta} - \frac{q \cdot u}{g_0 \cos\theta} + \frac{p \cdot v}{g_0 \cos\theta} + \frac{\dot{w}}{g_0 \cos\theta}\right) \tag{10-58}$$

From expression 10-57 and 10-58, 8 cases are investigated as follows:

1. $\phi_1 = \arcsin\left(-\frac{A_y}{g_0 \cos\theta}\right)$
2. $\phi_2 = \arcsin\left(-\frac{p \cdot w}{g_0 \cos\theta}\right)$
3. $\phi_3 = \arcsin\left(\frac{r \cdot u}{g_0 \cos\theta}\right)$
4. $\phi_4 = \arcsin\left(\frac{\dot{v}}{g_0 \cos\theta}\right)$
5. $\phi_5 = \arccos\left(-\frac{A_z}{g_0 \cos\theta}\right)$
6. $\phi_6 = \arccos\left(-\frac{q \cdot u}{g_0 \cos\theta}\right)$
7. $\phi_7 = \arccos\left(\frac{p \cdot v}{g_0 \cos\theta}\right)$
8. $\phi_8 = \arccos\left(\frac{\dot{w}}{g_0 \cos\theta}\right)$

Each case is plotted during the simulation in figure 10-15 to 10-22 with the true roll angle. The estimation error is calculated for each case with respect to the true roll angle.

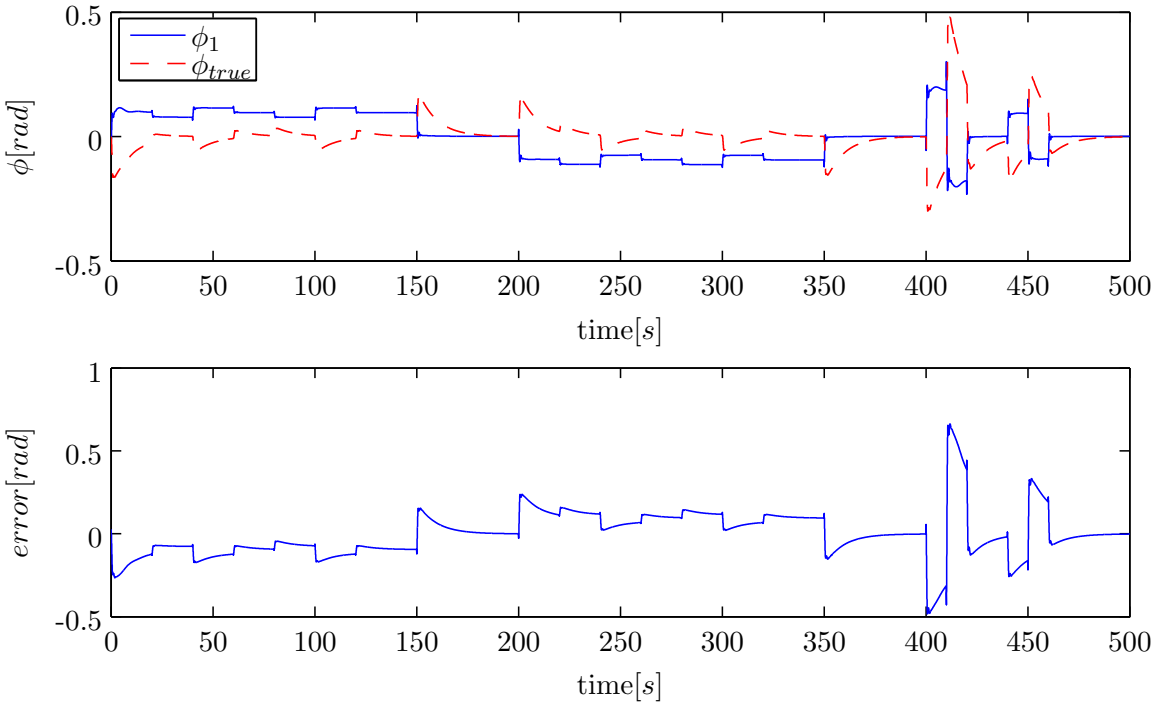

Figure 10-15: Roll angle estimation, simulation results on case 1

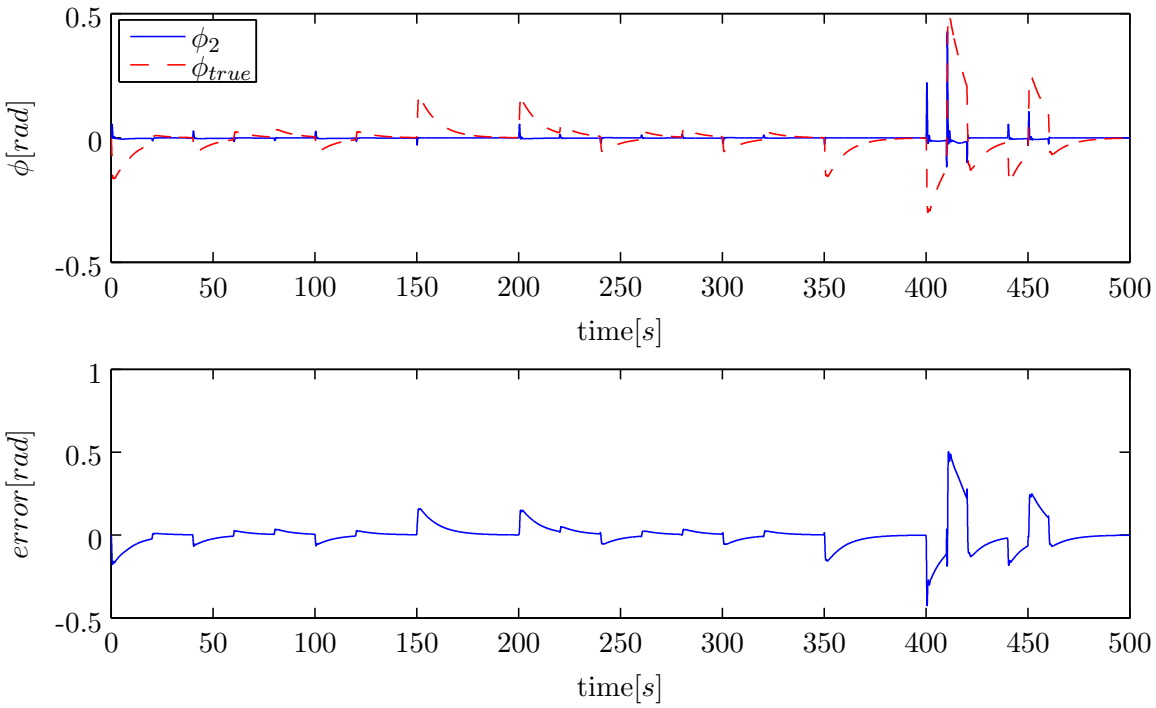

Figure 10-16: Roll angle estimation, simulation results on case 2

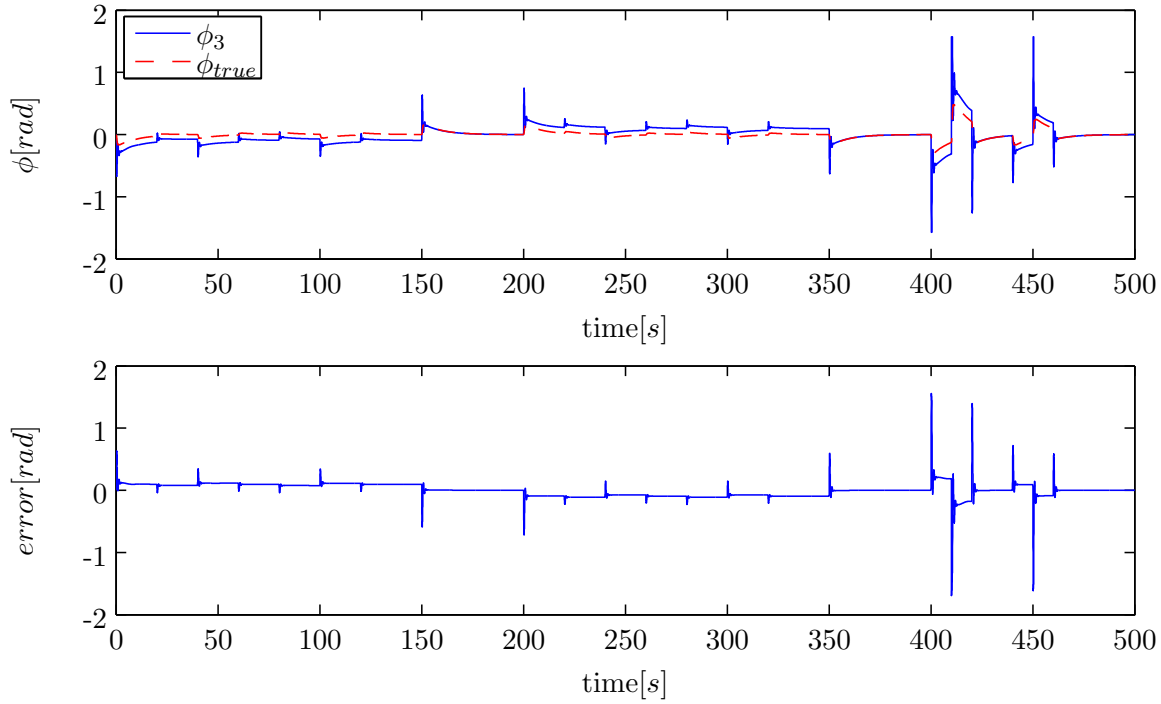

Figure 10-17: Roll angle estimation, simulation results on case 3

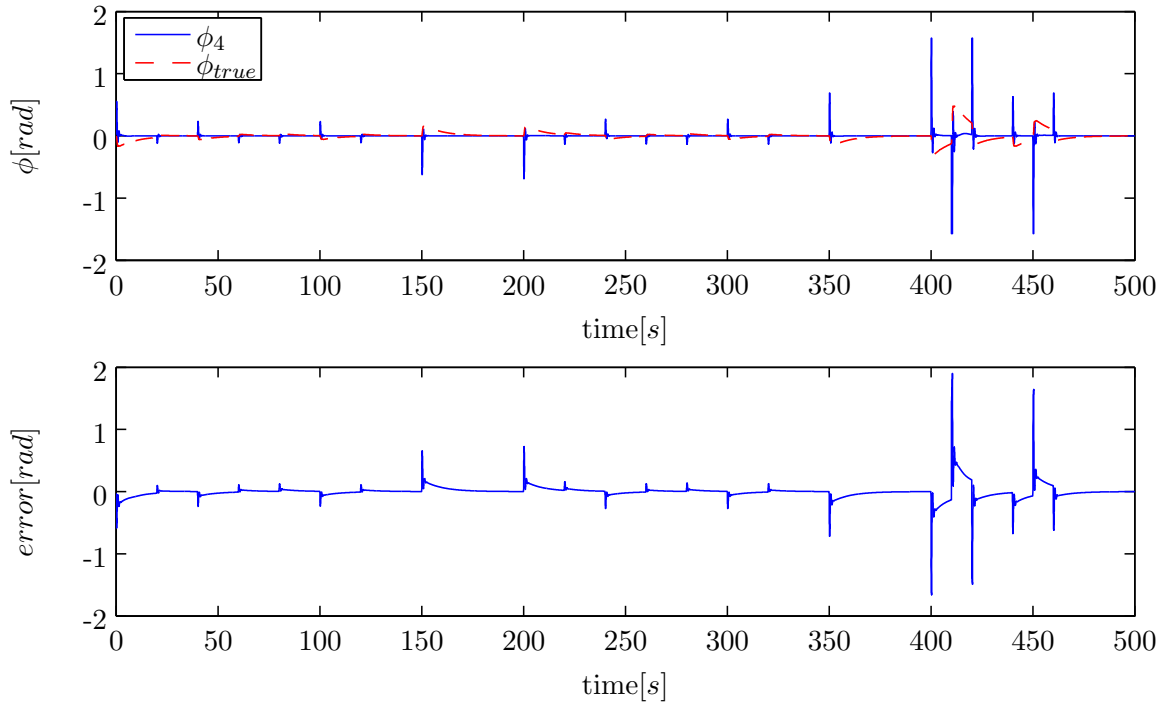

Figure 10-18: Roll angle estimation, simulation results on case 4

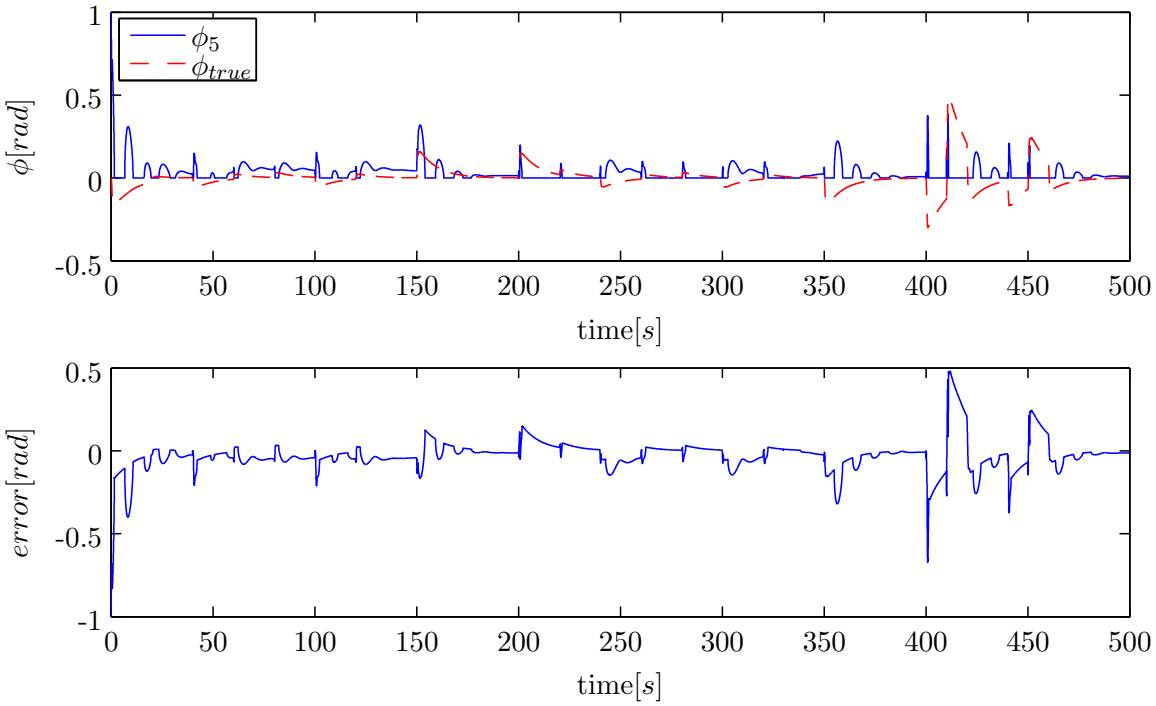

Figure 10-19: Roll angle estimation, simulation results on case 5

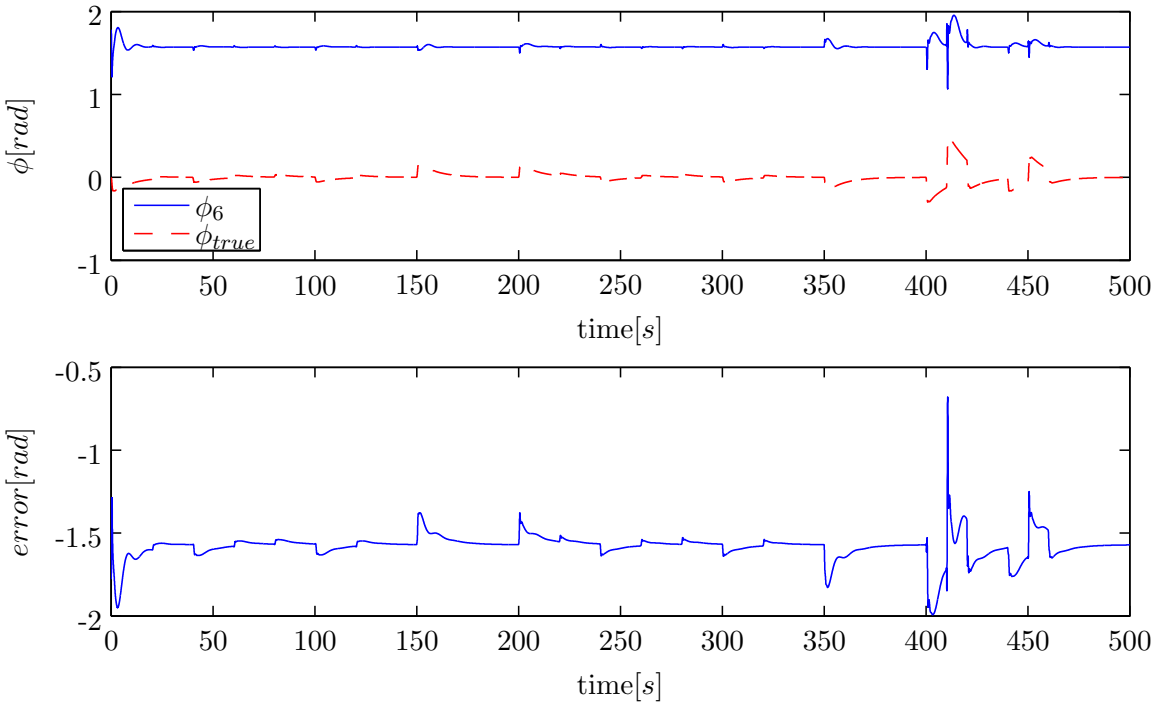

Figure 10-20: Roll angle estimation, simulation results on case 6

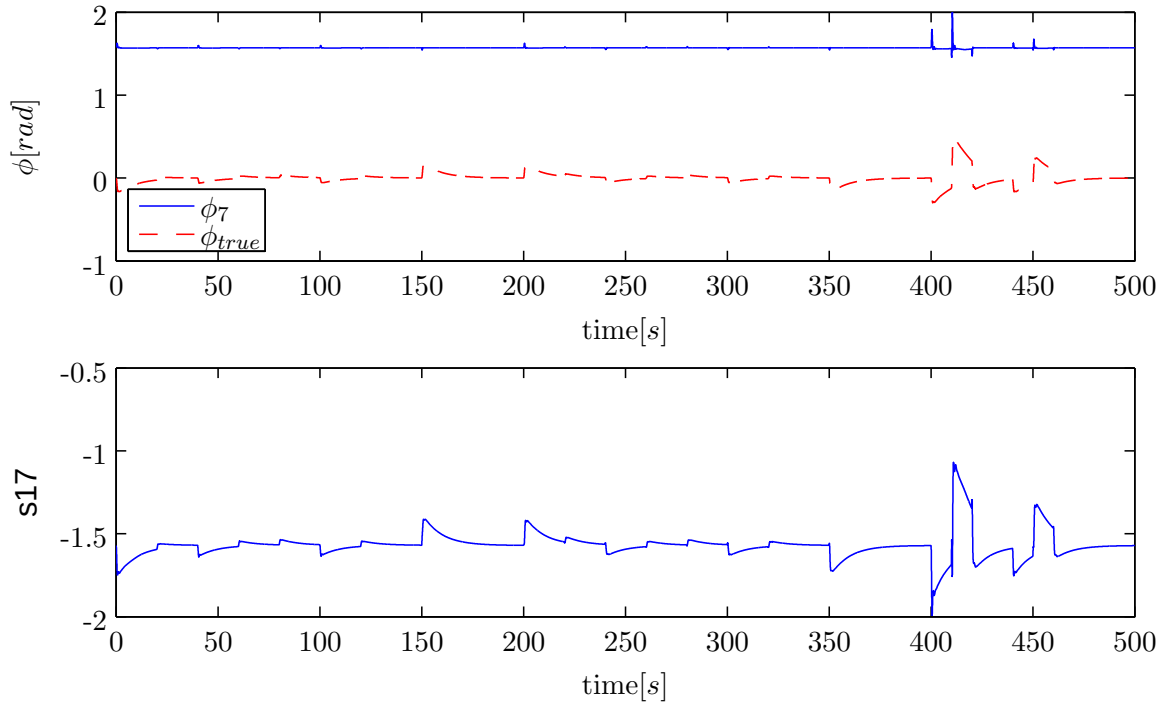

Figure 10-21: Roll angle estimation, simulation results on case 7

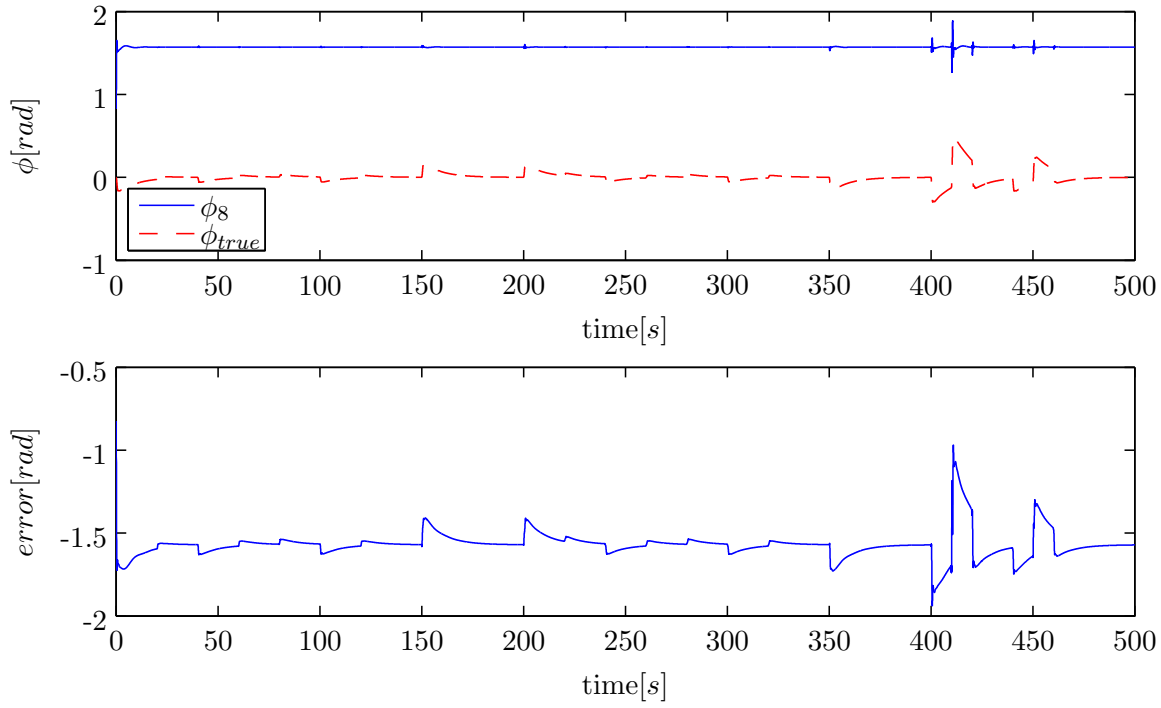

Figure 10-22: Roll angle estimation, simulation results on case 8

From figures 10-19 to 10-22 can be concluded that by using arccos can give numerical problems, coming from the fact that $\arccos(0) = \frac{\pi}{2}$. The roll angle of a fixed-wing aircraft is usually around zero for a stable flying aircraft, this may lead to numerical difficulties when implementing observers that make use of arccos. For large roll angles, this is however not a problem if the $\frac{\pi}{2}$ error is compensated. Arcsin properties hold that $\arcsin(0) = 0$ and goes to $\pm\infty$ when going to ± 1. When arcsin reaches ± 1, this means that the numerator becomes equal to the term "$g_0 \cos\theta$". From a more physical perspective this means that the aircraft has a roll angle close to $\pm 90°$.

Case 1 and 5 corresponds to lateral and downward velocity derivatives, where only high peaks are present due to sudden changes. Case 4 and 8 show similar results as A_y, $\dot{v}$ and A_z, $\dot{w}$ are closely related. Coriolis acceleration terms, present in the cases 2, 3, 6 and 7, follow the general direction of the roll angle during the simulation and have difficulties when coping with sudden dynamic changes. The use of arccos gives problems and arcsin can only be used for small angles. For the final roll angle estimation none of the cases are explicitly used, the Coriolis terms are however strongly present. Cases 1 and 5 hold the specific forces, as sensed by the onboard accelerometers, in Y_B and Z_B direction together with the expressions that hold the Coriolis terms. Expressions 10-57 and 10-58 can be rewritten such that both arcsin and arccos are removed and the dominant kinematic terms are present.
Estimating the roll angle can also be done by combining the properties of the individual cases. Figure 10-23 displays an aircraft making a coordinated roll turn. The force equilibrium is given in equation 10-59 by using the geometry of figure 10-23.

$$L \sin\phi = mV\omega \tag{10-59}$$

Assuming that the roll angle is constant with a constant turning rate ω together with small angles, $\sin\phi \approx \phi$ and $L \approx mg_0$, expression 10-59 can be rewritten into expression 10-60.

$$mg_0\phi = mV\omega \tag{10-60}$$

Expression 10-60 can be rewritten in expression 10-61.

$$\phi = \frac{mV}{mg_0}\omega \tag{10-61}$$

The magnitude of the total velocity V can be estimated by using the magnitude of the total GPS velocity vector in $\mathcal{F}_E$: $\underline{V}_{GPS} = \sqrt{u_{GPS}^2 + v_{GPS}^2 + w_{GPS}^2}$. When assuming that the turning rate ω can be measured with the yaw gyroscope r, this leads to expression 10-62.

$$\phi = \frac{\sqrt{u_{GPS}^2 + v_{GPS}^2 + w_{GPS}^2}}{g_0} r \tag{10-62}$$

Expression 10-62 assumes a constant turn rate, without accelerations. In practice, aircraft usually experience coupled maneuvers where both angular rates and accelerations are present. The specific forces in Y_B- and Z_B-direction, present in case 1 and 5, can be added to expression 10-62. The angle between A_y and A_z represents forces due to turning, which are usually

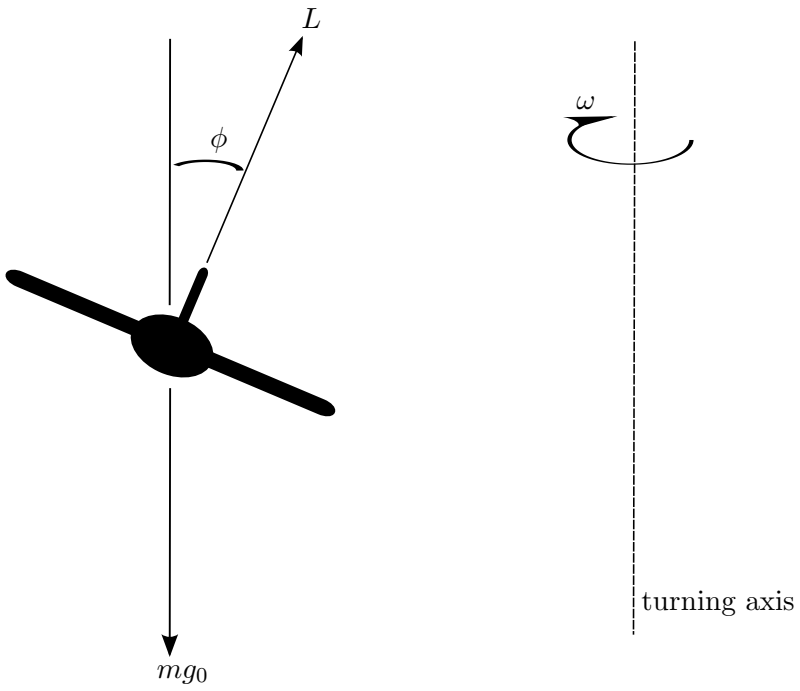

Figure 10-23: Roll angle during a constant turn

present during combined turning and rolling. With the addition of the specific forces, the dynamic part can be added to the static roll angle estimation of expression 10-62. This results in roll angle estimation case 9, ϕ_9 of expression 10-63.

$$\phi_9 = \frac{\sqrt{u_{GPS}^2 + v_{GPS}^2 + w_{GPS}^2}}{g_0} r + \arctan\left(\frac{A_y}{A_z}\right) \tag{10-63}$$

Figure 10-24 gives the result of expression 10-63 the during generic simulation of appendix D. From the figure can be concluded that the roll angle estimation follows the true roll angle and gives the best roll angle estimation when looking at case 1 to 9. Some peaks are still present during fast changes, which can be filtered out by using a low-pass filter. Estimation case 9 includes the turning accelerations present in case 1 and 5 together with the static turning relation of expression 10-63.

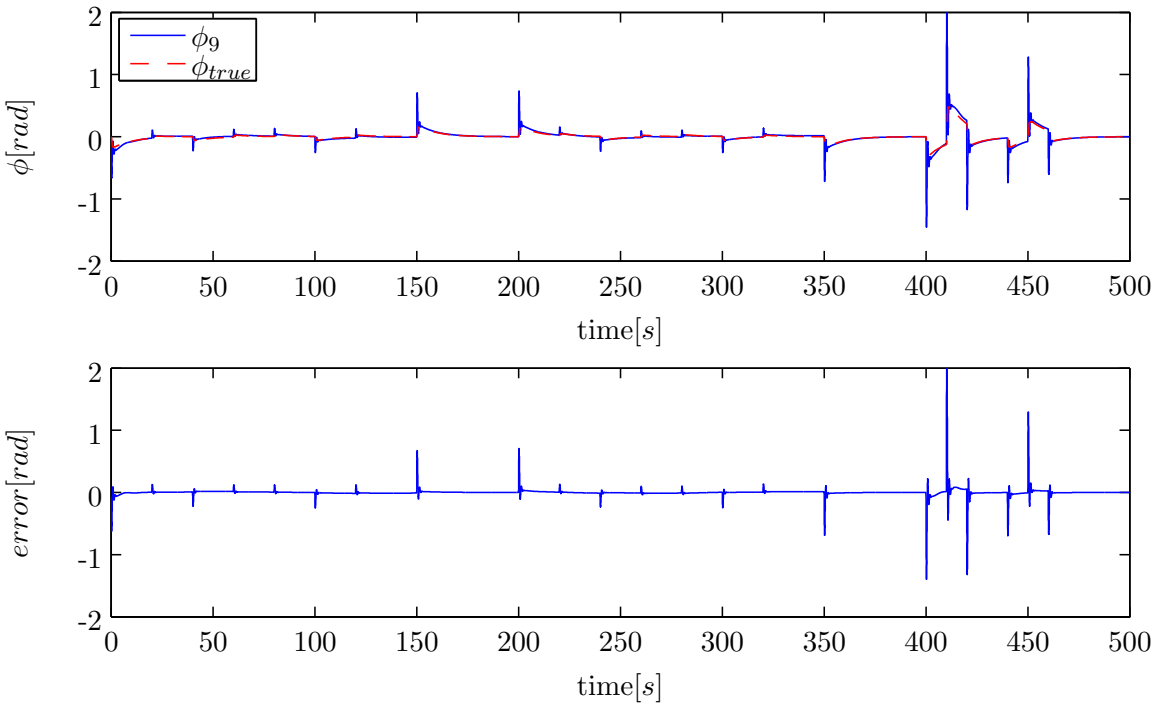

Figure 10-24: Roll angle estimation, simulation results on case 9

10-3-3 Heading Angle Estimation

Like the pitch and roll angles of the previous subsections, the heading angle ψ is also calculated by using angular rates of the gyroscopic sensors, as derived in chapter 8 equation 8-25. Additional heading angle expressions should be performed in a different manner as ψ is not present in the derived kinematic expression in the beginning of this section, equation 10-28. The heading angle can be estimated by calculating the angle between the forward and lateral velocity components u_E and v_E. With the use of additional sensors to an IMU, the heading angle can be estimated differently as by using gyroscopes. Expression 10-64 uses the velocity components in $\mathcal{F}_E$, obtained from a GPS receiver. This expression follows the vehicle in $\mathcal{F}_E$ as can be seen from a non-moving observer on the ground, called ground track.

$$\psi_1 = \arctan\left(\frac{v_{GPS}}{u_{GPS}}\right) \tag{10-64}$$

Figure 10-25 gives the heading angle estimation of expression 10-64 by using the same generic fixed-wing UAV simulation of appendix D as for the pitch and roll angle of the previous subsections. The error between the true and estimated heading angle comes from the fact that the side-slip angle β is not included in expression 10-64. The difference in real and estimated heading angle is small as can be seen in figure 10-25. From the error between the real and estimated heading angle from figure 10-25 can be concluded that side-slip is a function of the rudder magnitude. Meaning there is an influence of the rudder deflection on the side-slip. The side-slip angle is the angle between the heading angle and true ground track, which is provided by the GPS receiver. Expression 10-65 gives the definition on true ground track and heading angle from (Mulder et al., 2007).

$$\psi - \beta = \psi_{\text{ground track}} \tag{10-65}$$

The GPS velocity heading angle estimation can be improved by including the electronic rudder input signal E_{δ_r}. Expression 10-66 includes a linear relation between the rudder input signal and the side-slip angle, where the factor "-1.15" is a 1^{st} order model dependent fit. The first order approximation can be extended to a higher order linearization, to improve accuracy. From figure 10-26 can be seen that the modified heading angle estimation denoted with heading angle case 2 ψ_2, results in expression 10-66.

$$\psi_2 = \arctan\left(\frac{v_{GPS}}{u_{GPS}}\right) - 1.15E_{\delta_r} \tag{10-66}$$

Expression 10-66 only holds when there is no wind present. In practice side-slip is usually present and can result in large angles and differences between the heading and ground track angle. Expression 10-67 gives the definition of the side-slip angle from (Mulder et al., 2007). This problem can be solved with the addition of a slide slip angle sensor or β-sensor. The sensor can also compensate for the change in heading due to atmospheric wind.

$$\beta = \arcsin\left(\frac{v_B}{\underline{V}}\right) \tag{10-67}$$

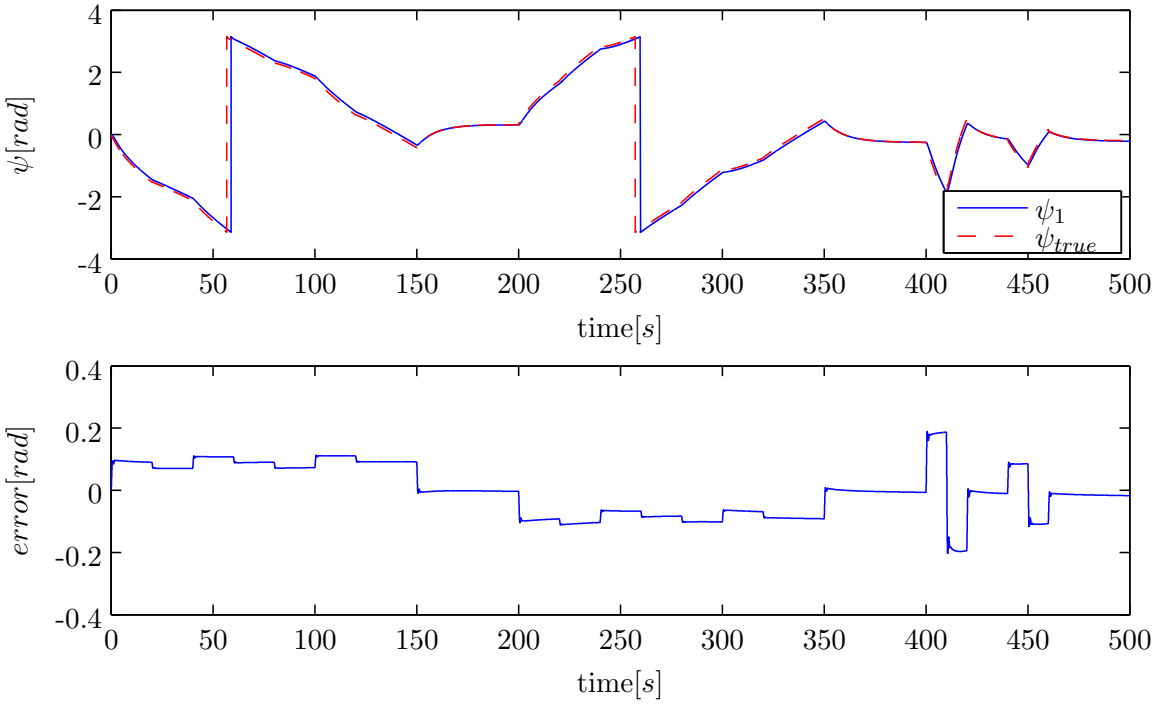

Figure 10-25: Heading estimation, simulation results on case 1

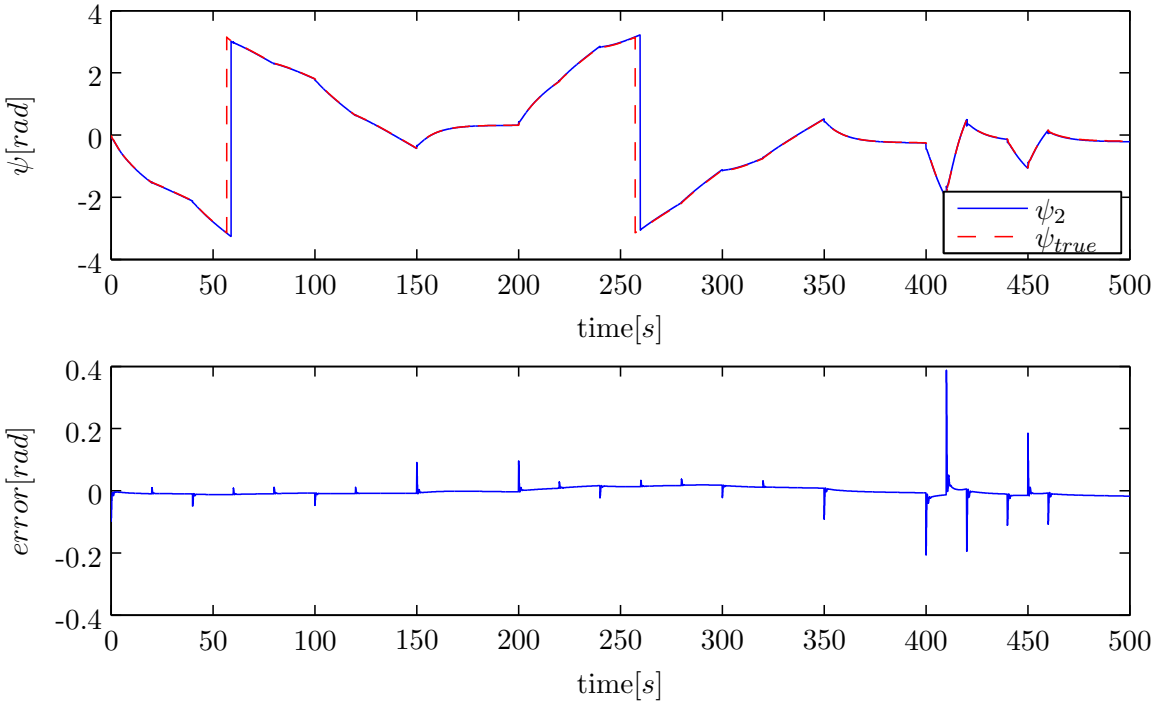

Figure 10-26: Heading estimation, simulation results on case 2

The velocity vector $\underline{V} = \sqrt{(u_{GPS}^2 + v_{GPS}^2 + w_{GPS}^2)}$ in expression 10-67 can be measured with a GPS receiver, like for the roll angle. This results in the third heading estimation ψ_3 of expression 10-68. This estimation is simulated in figure 10-27 by using the generic simulation of appendix D together with the true heading angle.

$$\psi_3 = \arctan\left(\frac{v_{GPS}}{u_{GPS}}\right) - \arcsin\left(\frac{v_B}{\sqrt{u_{GPS}^2 + v_{GPS}^2 + w_{GPS}^2}}\right) \tag{10-68}$$

From the simulation results of figure 10-27 can be seen that the side-slip error of estimation case 1 is not present. The estimation error peaks which are present in case 2, as the result of a change in rudder setting are also not present. The side-slip estimation provides a better estimation as compared to linking the rudder signal to the side-slip. With estimation case 3, the side-slip is estimated using body-fixed velocity components resulting in an better estimation.

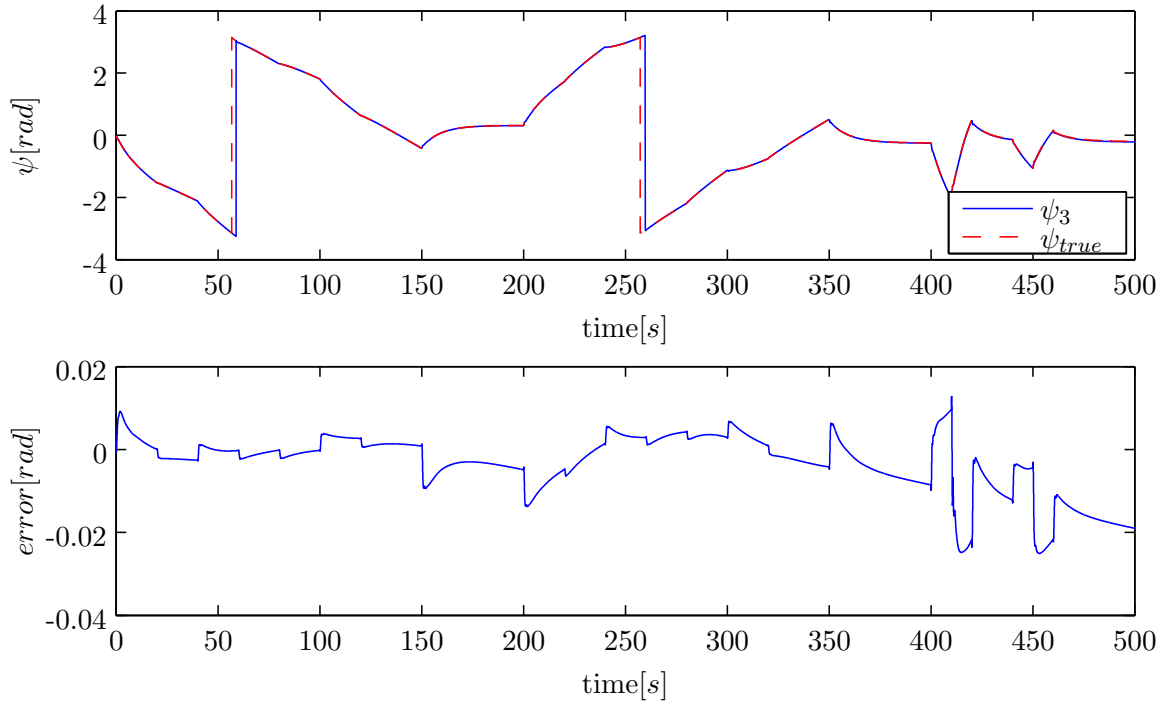

Figure 10-27: Heading estimation, simulation results on case 3

10-3-4 Conclusion

The different investigated cases of the previous subsections use the derived kinematic expressions of the first 2 sections to derive additional orientation angle relations. The physical relations combine kinematic properties of fixed-wing aircraft kinematics with onboard IMU sensors and GPS receivers.

For the developed pitch angle approximation of subsection 10-3-1, two cases can best be considered as additional observers. These cases are defined as case 5 and GPS case 4, repeated below in expressions 10-69 and 10-70 as the two final pitch angle estimations. GPS case 4 is dependent on GPS velocity measurements with estimated body-fixed velocity components. The body-fixed velocities are the result of accelerometer integration or can be obtained by transforming GPS velocity measurements from $\mathcal{F}_E$ to $\mathcal{F}_B$ by using a rotational matrix that uses all three orientation angles as described in chapter 8.

Some additional situations should be mentioned that are not part of the simulation of appendix D, used for deriving the pitch angle observers. Situations where the longitudinal flight dynamics as displayed in figure 10-10 are different. When an aircraft stalls, the pitch angle is usually very large together with the angle of attack, while the flight path angle is pointing downwards. The same holds during landing, the throttle setting is very low and as a result the altitude is decreasing while having a positive pitch angle. The velocity components are still in the same direction and it is expected that expression 10-70 still holds, however larger estimation errors are expected. When there is a large wind coming to the front of the aircraft, the aircraft might move in backwards direction seen in $\mathcal{F}_E$ resulting in a negative u_{GPS}. The forward velocity component u_B is still in forward direction as the aircraft is moving in forward direction, seen from a moving air particle that is part of the wind coming towards the aircraft. This is also the reason that the aircraft still has a positive lift vector and can stay in the air. When this is the case, the pitch angle estimation will differ from the real angle. Beforehand knowledge of the wind direction and magnitude is required to avoid this problem.

The second pitch angle estimation uses GPS velocity components. When strong wind is present, expression 10-70 will have some estimation errors. Figure 10-29 and 10-28 give the pitch angle estimation simulation results, using the generic simulation of appendix D. The simulation is the same as used for subsection 10-3-1 when deriving the correction angles, only this time with realistic sensor signals including biases, noises and the presence of wind. From figure 10-29 can be concluded that expression 10-69 gives the same estimation as in figure 10-8 when using realistic sensor signals. Expression 10-70 gives however different estimation result as can be seen in figure 10-28 when compared to figure 10-14. Due to the presence of atmospheric wind, the flight path angle estimation using body-fixed and Earth reference velocity components $\gamma = \frac{-w_{GPS}}{u_B}$ is no longer correct as the angle is different as a result of wind. It can be concluded that $\hat{\theta}_2$ is a less practical estimation when compared to $\hat{\theta}_1$ during windy conditions. The first pitch angle estimation $\hat{\theta}_1$ is the final pitch angle observer equation.

$$\hat{\theta}_1 = \arcsin\left(\frac{A_x - \dot{u}}{g_0}\right) \tag{10-69}$$

$$\hat{\theta}_2 = \arctan\left(\frac{w_B - w_{GPS}}{u_B}\right) \tag{10-70}$$

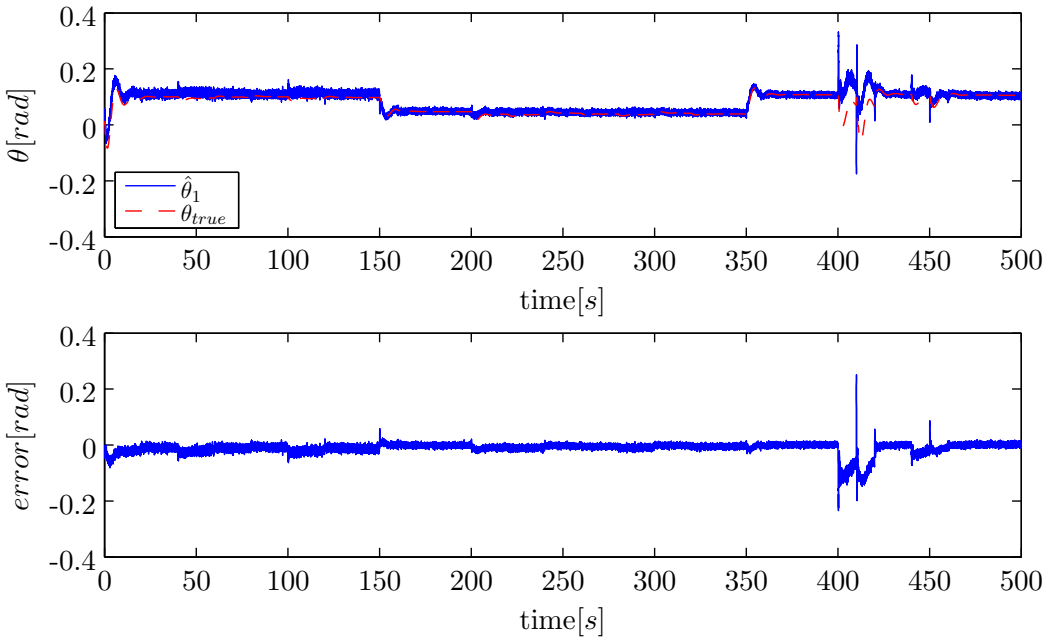

Figure 10-28: Final pitch angle estimation case 1, using realistic sensors and atmospheric wind

The roll angle estimation case 9 derived in subsection 10-3-2, is composed of the turning accelerations A_y and A_z together with the static roll angle estimation of expression 10-63. Case 9 is repeated in expression 10-71 as the final roll angle estimation $\hat{\phi}$. Figure 10-30 gives the simulation results using the generic simulation of appendix D, using realistic sensor signals together with the presents of atmospheric wind. From figure 10-30 can be seen that the influence of noise and biases are limited as the mean of the estimation corresponds with the true roll angle. The influence of wind is present in the estimation as the total GPS velocity magnitude changes. The magnitude is multiplied with the angular yaw rate r and the influence of changes in velocity magnitude becomes smaller. From a physical point of view the influence of wind on the roll angle is limited as the corresponding turning axis origin changes and not the roll angle itself, as displayed in figure 10-23. This physical aspect is shown in figure 10-30 due to the fact that no bias errors are present for the angle estimation. From this can be concluded that the influence of atmospheric wind is very limited to the roll angle estimation and that the estimation can be used as an additional angle observer.

$$\hat{\phi} = \frac{\sqrt{u_{GPS}^2 + v_{GPS}^2 + w_{GPS}^2}}{g_0} r + \arctan\left(\frac{A_y}{A_z}\right) \tag{10-71}$$

The heading angle expression of subsection 10-3-3 uses a GPS receiver to determine the velocity components to estimate the heading angle. The third heading angle estimation case ψ_3, is repeated in expression 10-72 as the final heading angle estimation. From figure 10-31 can be seen that the presence of wind influences the angle estimation performance, when compared to figure 10-27.

The difference in ground track and heading angle ψ increases due to the presence of atmospheric wind. The GPS velocity components in $\mathcal{F}_E$ include the influence of the wind velocities

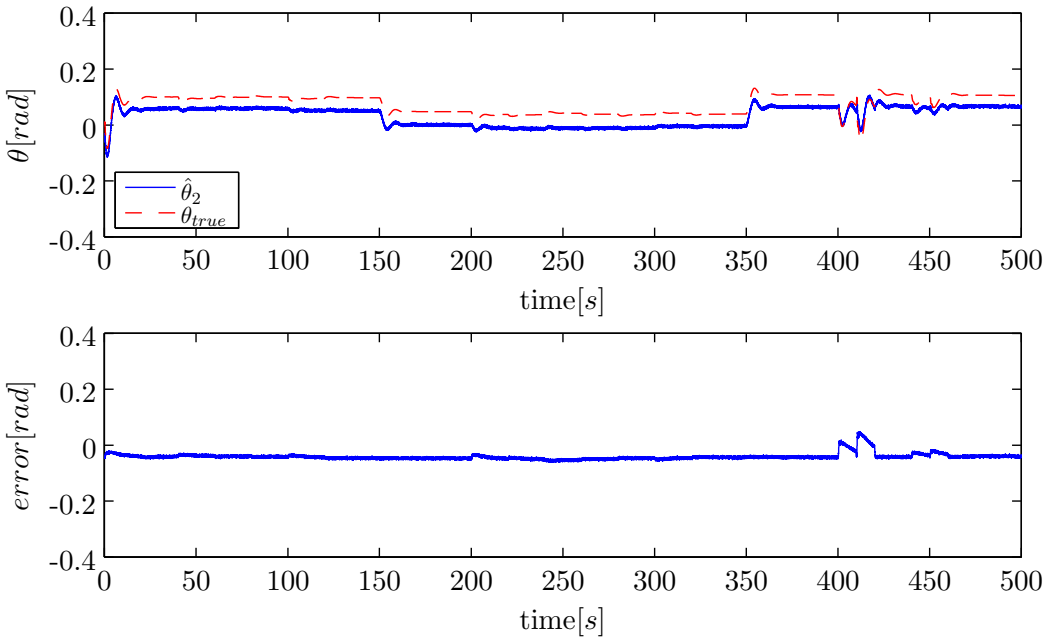

Figure 10-29: Final pitch angle estimation case 2, using realistic sensors and atmospheric wind

since the total velocity vector is measured. The side-slip angle β estimation, the second term of expression 10-72, is insufficient during the presence of wind. While despite that the estimation is not perfect, the heading angle estimation can still be used as an additional angle observer as the estimation errors are bounded. Different sensors like a magnetometer, side-slip β sensor or thermopile sensors can also be added to increase the accuracy during windy conditions.

The disadvantage of adding more sensors is the time synchronization between individual components, which will be explained in more detail in section 13-1. Time synchronization errors will be present as each individual component has its own update frequency and processing time. There is a constraint, under which expression 10-72 must be used, which is maintaining a minimum velocity. An example of simulating responses during minimum flying velocities together with wind is not present in the used simulation and doesn't show up in figure 10-31, it can however not be ignored. If the aircrafts' velocity becomes very small, the angle between the lateral and forward velocity components become overshadowed by the GPS receiver noise and becomes difficult to estimate. The estimated heading angle can suddenly turn out to be in opposite direction. If a minimum velocity constraint is applied to expression 10-72 to avoid these situations, a robust and long-term stable angle correction is be made. When the lateral body-fixed velocity v_B is badly estimated or when the side-slip can be assumed small, the second term of expression 10-72 can be left out.

$$\hat{\psi} = \arctan\left(\frac{v_{GPS}}{u_{GPS}}\right) - \arcsin\left(\frac{v_B}{\sqrt{u_{GPS}^2 + v_{GPS}^2 + w_{GPS}^2}}\right) \tag{10-72}$$

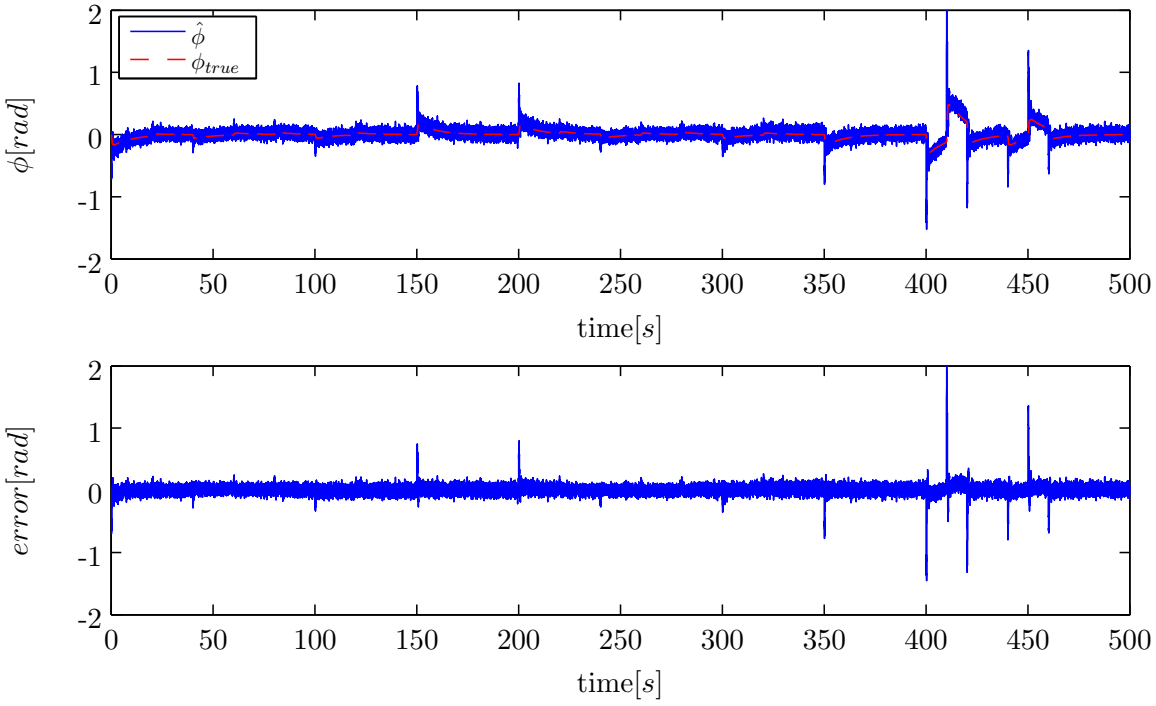

Figure 10-30: Final roll angle estimation, using realistic sensors and atmospheric wind

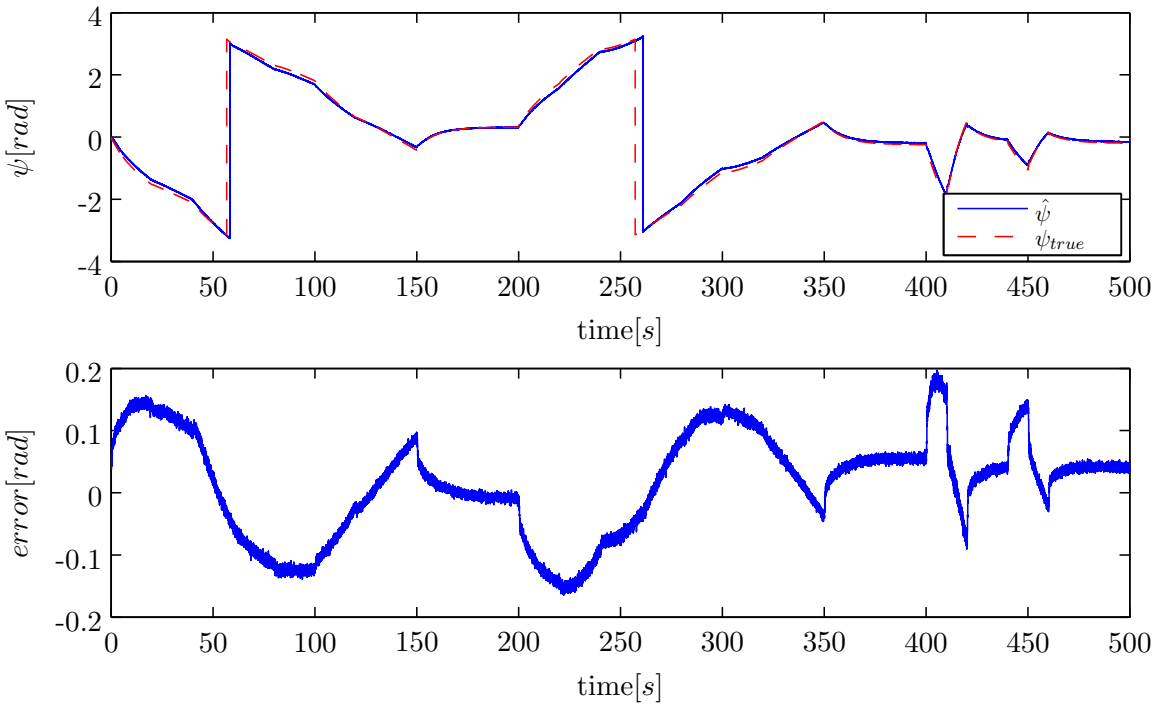

Figure 10-31: Final heading angle estimation, using realistic sensors and atmospheric wind

10-4 GPS Accelerations

The previous sections focused on deriving kinematic expressions by combining fixed-wing aircraft kinematics with an IMU and GPS receiver. The expressions started by deriving the kinematics of a particle in inertial space seen from a local moving frame of reference. This has led to the derivation of the final AC equations of subsection 10-3-4. This section uses a different approach to derive additional expressions to complement the IMU/GPS sensor integration.

The provided GPS receiver velocities can be considered as an accurate unbiased measurement. As was previously mentioned in section 2-2 about GPS satellite navigation, the frequency shift of the satellite signals due to the satellite's relative velocity to the user receiver, called Doppler shift. The GPS velocities are unbiased with low signal noise and some processing time due to onboard signal integration of the individual satellite signals.

10-4-1 ECEF to NED Coordinate Transformation

The GPS receiver velocities are in the Earth-Centered-Earth-Fixed (ECEF) Cartesian coordinate frame of reference. The origin of the ECEF frame of reference (0,0,0) is the Earth's center of gravity. The $X-$, $Y-$ and $Z-$axis remain fixed, the Earth is considered to be non-rotating. The Z-axis points to the North pole, and the XY-plane coincides with the equatorial plane, as indicated in figure 10-32. When neglecting the Earth's rotations, it can be assumed that ECEF is an inertial frame of reference with coordinate system XYZ attached to the Earth's center of gravity (0,0,0). When this assumption holds, the GPS velocities are assumed to be in inertial space. When differentiating the GPS velocities, the resulting GPS accelerations can provide the vehicles accelerations. Under the assumption that the GPS velocities are obtained in inertial space, the obtained accelerations provide the vehicle's specific forces in inertial space.

Figure 10-32 shows the ECEF together with the local North-East-Down (NED) frame of reference. By obtaining the GPS velocity derivatives in ECEF, the obtained accelerations should be transformed to local body-fixed coordinates in a local body-fixed frame of reference $\mathcal{F}_B$ to integrate them with the IMU accelerations. To derive the required transformation, between ECEF and $\mathcal{F}_B$, the derived expression 10-28 from section 10-3 is taken as a starting point. This expression is repeated below, expression 10-73. The specific forces A_x, A_y and A_z consist of the body forces divided by the vehicle's mass m and are assumed to be in inertial space.

$$\begin{bmatrix} A_x \\ A_y \\ A_z \end{bmatrix}_B + \underline{a}_g = \begin{bmatrix} \dot{u}_{GPS} \\ \dot{v}_{GPS} \\ \dot{w}_{GPS} \end{bmatrix}_{ECEF} \tag{10-73}$$

The three acceleration components $\underline{a}_{ECEF} = [\dot{u}_{GPS}, \dot{v}_{GPS}, \dot{w}_{GPS}]$ in expression 10-73 are the assumed accelerations in inertial space. When assuming that the ECEF is an inertial frame of reference, the accelerations are the absolute accelerations of the local reference frame. When this assumption holds, fictitious forces can be left out. An example of fictitious forces that can be left out are the Coriolis forces, as a result of $\underline{\omega} \times \underline{v}_{rel}$, where $\underline{v}_{rel}$ are the relative velocities

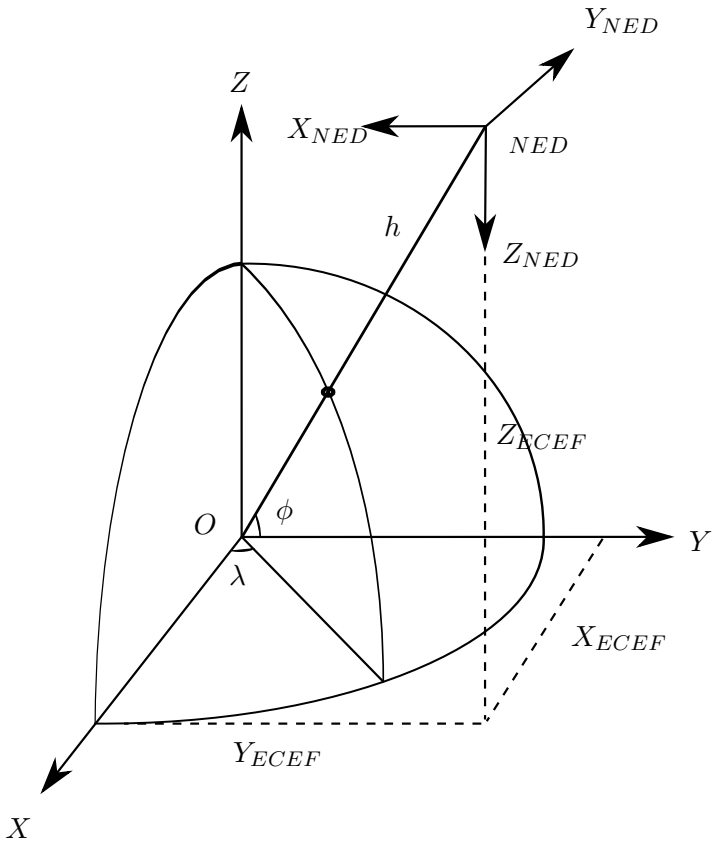

Figure 10-32: Earth-Centered-Earth-Fixed (ECEF) and North-East-Down (NED) frame of reference

between the vehicle and local frame of reference. To apply expression 10-73, the gravity vector needs to be converted to $\mathcal{F}_B$ together with the accelerations obtained by differentiating the GPS velocities. The GPS accelerations $\underline{\dot{v}}_{GPS}$ need to be converted to the local NED frame of reference before transformed to $\mathcal{F}_B$. This means two transformations are required, namely a transformation between ECEF and NED, $R_{ECEF,NED}$ and a transformation from NED to $\mathcal{F}_B$, $R_{NED,B}$. Expression 10-73 can be rewritten into 10-74 when including the required transformation matrices.

$$\underline{A}_B = R_{NED,B}\ R_{ECEF,NED}\ \underline{\dot{v}}_{GPS} - R_{NED,B}\underline{g}_{NED} \tag{10-74}$$

To transform the GPS accelerations from ECEF to body-fixed coordinates and to use expression 10-74, the required transformation matrices $R_{ECEF,NED}$ and $R_{NED,B}$ need to be derived. From figure 10-32 can be seen that three angles are required to make the transformation between ECEF and NED. The two latitude ϕ and longitude λ angles can be calculated by using expressions 10-75 and 10-76.

$$\phi = \arctan\left(\frac{Z_{ECEF}}{\sqrt{X_{ECEF}^2 + Y_{ECEF}^2}}\right) \tag{10-75}$$

$$\lambda = \arctan\left(\frac{Y_{ECEF}}{X_{ECEF}}\right) \tag{10-76}$$

The third required angle is to correct the differences in Z-axis orientation in ECEF and NED. This angle is assumed to be constant, resulting in the matrix transformation definition of expression 10-77.

$$\underline{\dot{v}}_{GPS,NED} = R_{ECEF,NED}(\phi, \lambda, -90^\circ)\underline{\dot{v}}_{GPS,ECEF} \tag{10-77}$$

In ECEF the Z-axis Z_{ECEF} is pointing in upward direction, while in NED Z_{NED} is pointing downwards as can be seen in figure 10-32. The difference in Z-axis orientation in ECEF and NED is a fixed angle of 90 degrees. Expression 10-78 defines the required transformation matrix.

$$R_{ECEF,NED}(-90^\circ) = \begin{bmatrix} \cos 90^\circ & 0 & \sin 90^\circ \\ 0 & 1 & 0 \\ -\sin 90^\circ & 0 & \cos 90^\circ \end{bmatrix} \tag{10-78}$$

Rotational matrix using latitude angle ϕ, expression 10-79.

$$R_{ECEF,NED}(\phi) = \begin{bmatrix} \cos\phi & 0 & \sin\phi \\ 0 & 1 & 0 \\ -\sin\phi & 0 & \cos\phi \end{bmatrix} \tag{10-79}$$

Rotational matrix using longitude angle λ, expression 10-80.

$$R_{ECEF,NED}(\lambda) = \begin{bmatrix} \cos\lambda & \sin\lambda & 0 \\ -\sin\lambda & \cos\lambda & 0 \\ 0 & 0 & 1 \end{bmatrix} \tag{10-80}$$

By combining expressions 10-78, 10-79 and 10-80, the ECEF to NED transformation matrix $R_{ECEF,NED}(\phi, \lambda, -90^\circ)$ of expression 10-77 can be worked out. The result is the final transformation matrix of expression 10-81, that can directly transform GPS acceleration in ECEF to NED.

$$\begin{bmatrix} \dot{u}_{GPS} \\ \dot{v}_{GPS} \\ \dot{w}_{GPS} \end{bmatrix}_{NED} = \begin{bmatrix} -\sin\phi\cos\lambda & -\sin\phi\sin\lambda & \cos\phi \\ -\sin\lambda & \cos\lambda & 0 \\ -\cos\phi\cos\lambda & -\cos\phi\sin\lambda & -\sin\phi \end{bmatrix} \begin{bmatrix} \dot{u}_{GPS} \\ \dot{v}_{GPS} \\ \dot{w}_{GPS} \end{bmatrix}_{ECEF} \tag{10-81}$$

Expression 10-81 can also be written out, resulting in expression 10-82.

$$\begin{aligned} \dot{u}_N &= -\dot{u}_{ECEF}\sin\phi\cos\lambda - \dot{v}_{ECEF}\sin\phi\sin\lambda + \dot{w}_{ECEF}\cos\phi \\ \dot{v}_E &= -\dot{u}_{ECEF}\sin\lambda + \dot{v}_{ECEF}\cos\lambda \\ \dot{w}_D &= -\dot{u}_{ECEF}\cos\phi\cos\lambda - \dot{v}_{ECEF}\cos\phi\sin\lambda - \dot{w}_{ECEF}\sin\phi \end{aligned} \tag{10-82}$$

The second rotational matrix, $R_{NED,B}(\phi,\theta,\psi)$ transforms the accelerations from local NED coordinates to body-fixed frame of reference $\mathcal{F}_B$. This transformation is equal to the used transformation of chapter 8, expression 8-23. It is assumed that gravity is constant and pointing downwards in NED. Together with the coordinate transformation $R_{NED,B}$, the vehicles specific forces can finally be obtained. The result is expression 10-83, by working out expression 10-74. It should however be noted, that expression 10-83 can only transform GPS velocities and its time derivatives. Expressions 10-83 and 10-82 cannot be used to transform GPS positions from ECEF to NED. The Earth surface is not a perfect ellipsoid as indicated in figure 10-32, the surface is a complex surface and accurate knowledge of the Earth's gravity is required to define its shape. To transform GPS positions from ECEF to NED, a geodetic coordinate transformation is required. The geodetic coordinate transformation will compensate for the differences in height in the Earth's reference ellipsoid and real geoid. The Earth radius of curvature and height above the ellipsoid should be included, for instance by using the WGS84 reference ellipsoid to make this transformation.

$$\begin{bmatrix} A_x \\ A_y \\ A_z \end{bmatrix}_B = \begin{bmatrix} \cos\theta\cos\psi & \cos\theta\sin\psi & -\sin\theta \\ \sin\phi\sin\theta\cos\psi - \cos\phi\sin\psi & \sin\phi\sin\theta\sin\psi + \cos\phi\cos\psi & \sin\phi\cos\theta \\ \cos\phi\sin\theta\cos\psi + \sin\phi\sin\psi & \cos\phi\sin\theta\sin\psi - \sin\phi\cos\psi & \cos\phi\cos\theta \end{bmatrix} \cdot \begin{bmatrix} \dot{u}_N \\ \dot{v}_E \\ \dot{w}_D \end{bmatrix} - \begin{bmatrix} -g_0\sin\theta \\ g_0\sin\phi\cos\theta \\ g_0\cos\phi\cos\theta \end{bmatrix}_B \quad (10\text{-}83)$$

With the derived expressions 10-82 and 10-83, it is possible to transform GPS velocity derivatives from ECEF to $\mathcal{F}_B$. Before this coordinate transformation can be made, first the GPS accelerations need to calculated from GPS velocities. These can be calculated by differentiating the GPS velocity signals. While the GPS velocities provide good measurements on the vehicles velocity, the receiver signals still contain noise. When differentiating a noisy signal, the noise is amplified. To overcome the problem of differentiating signals with noise, different solutions exist.

By using a moving average over a finite number of samples, high frequency errors can be filtered out. The simulation of appendix E, small turns Aerosonde UAV, is used to simulate the estimation of specific forces by using GPS accelerations. This simulation simulates a series of left and right turns with a small turning radius. This simulation is different form the generic simulation, used in the previous sections. Due to the larger specific forces, this simulation is preferred from the generic simulation. Figures 10-33 and 10-34 give the results on differentiating the GPS velocity signals over a moving average of 10 and 50 samples. The blue line represents the simulated GPS accelerations by differentiating the simulated received GPS velocities. The red lines are the real specific forces. From the figures can be seen, that the more samples are used, the lower the signal noise becomes. Using more samples to average out the differentiated signal, means that less high frequency noise is present. A disadvantage of using more samples is that more phase is introduced, resulting in a larger time delay.

Figures 10-35 and 10-36 use the results of signal differentiation of figures 10-33 and 10-34. In these two figures, the real specific forces are added to show the differences between the estimated and real specific forces. Depending on the desired accuracy on specific force esti-

mation, more samples to average the signal can be chosen. From figure 10-36 can be seen that by using 50 samples gives a good specific force estimation, with little high frequency noise.

Besides the moving average method, the signal can also be modified by using a low pass filter. A type of digital filter is used to perform the low pass filtering of the differentiated signal, called a butterworth filter. The applied filter is a 2^{nd} order low pass butterworth filter. Two different cutoff frequencies are used, 0.2 and 0.01 $[rad/s]$. The simulation of appendix E is used to simulate the working of a butterworth filter. Figures 10-37 and 10-38 give the results on low pass filtering the obtained GPS accelerations, where the red lines represent the real specific forces. From the two figures can be seen that using a lower cutoff frequency results in less high frequency noise. Like for the moving average method, also for a butterworth filter holds that using a lower cutoff frequency results in larger phase and time delay.

Figures 10-39 and 10-40 use the results of low pass filtering the GPS accelerations of figures 10-37 and 10-38 by means of a butterworth filter. From figure 10-40 can be seen that the specific force estimation by using a cutoff frequency of 0.01 $[rad/s]$ gives a good estimation with very little high frequency noise. Figure 10-40 also shows the presence of time delay, which is particularly visible for the A_x and A_y specific force estimation.

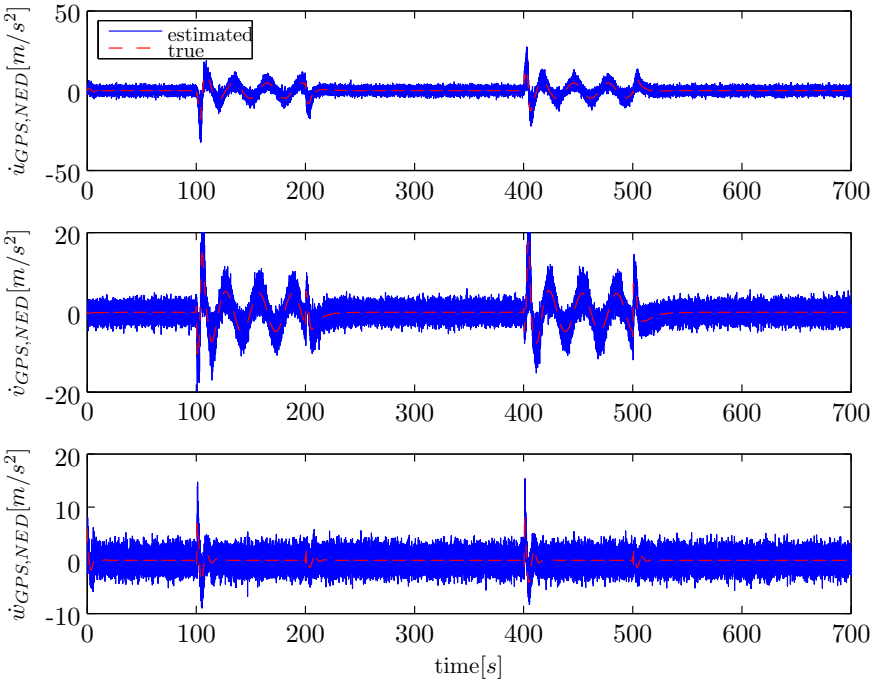

Figure 10-33: GPS velocity derivatives using a moving average over 10 samples

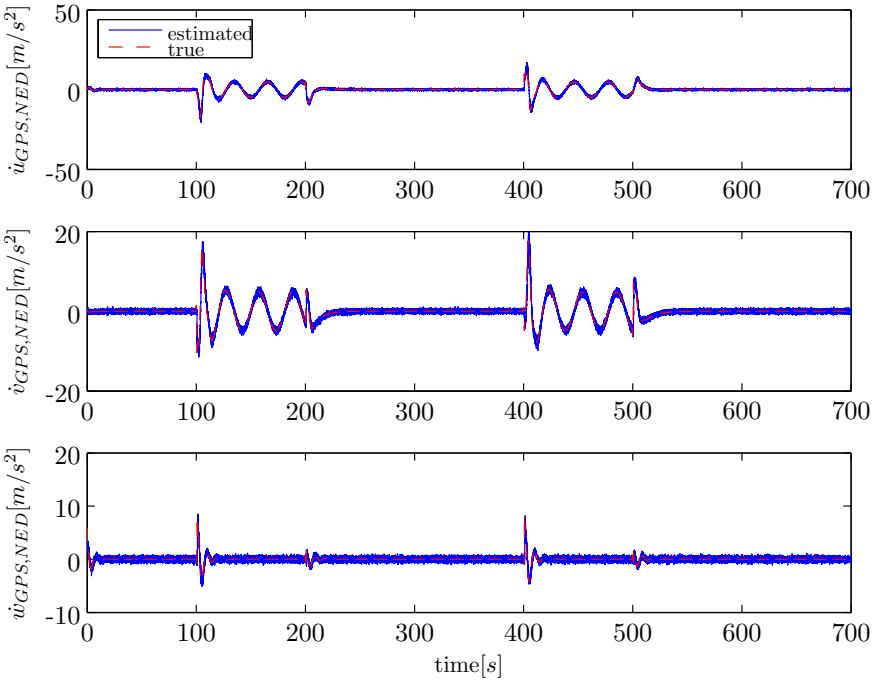

Figure 10-34: GPS velocity derivatives using a moving average over 50 samples

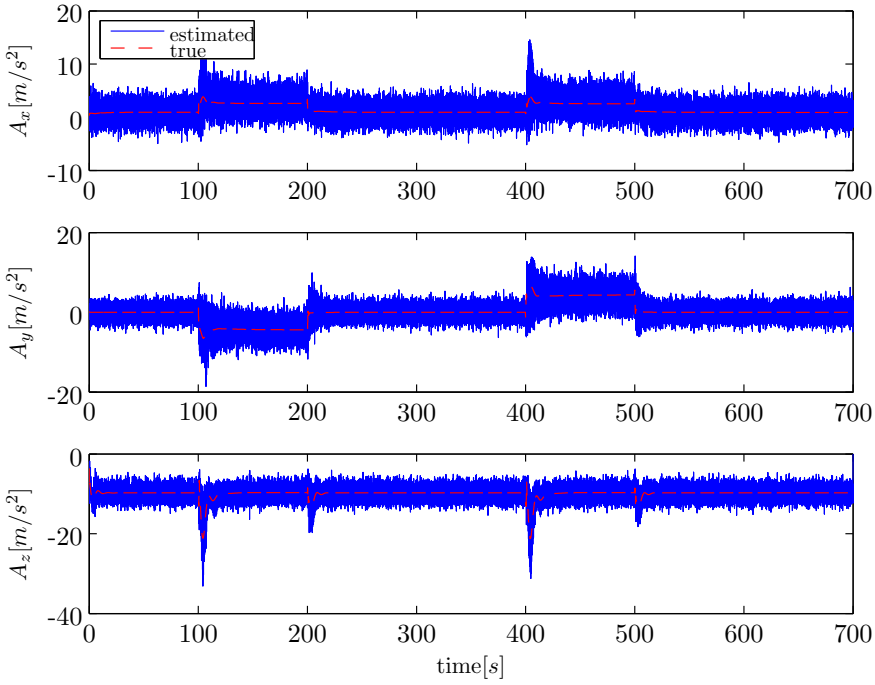

Figure 10-35: Estimated specific forces by GPS velocity derivatives using a moving average over 10 samples

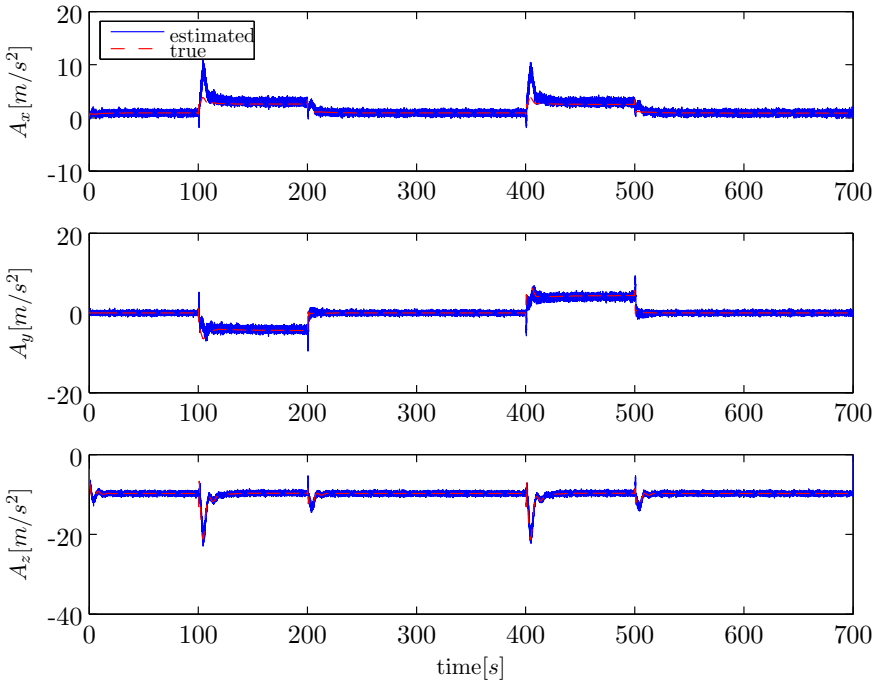

Figure 10-36: Estimated specific forces by GPS velocity derivatives using a moving average over 50 samples

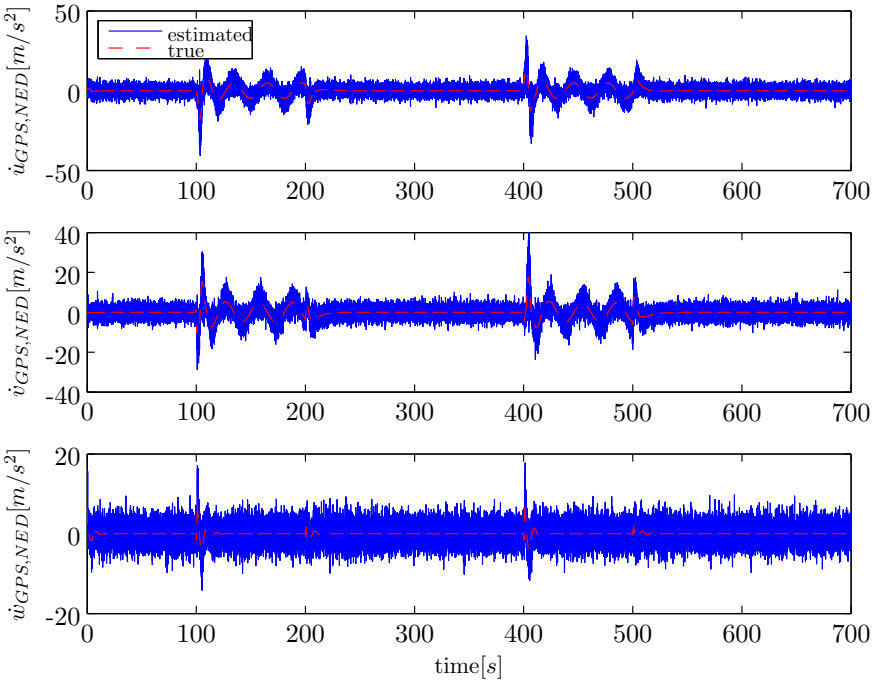

Figure 10-37: GPS velocity derivatives using a 2^{nd} order butterworth filter with a cutoff frequency of 0.2 $[rad/s]$

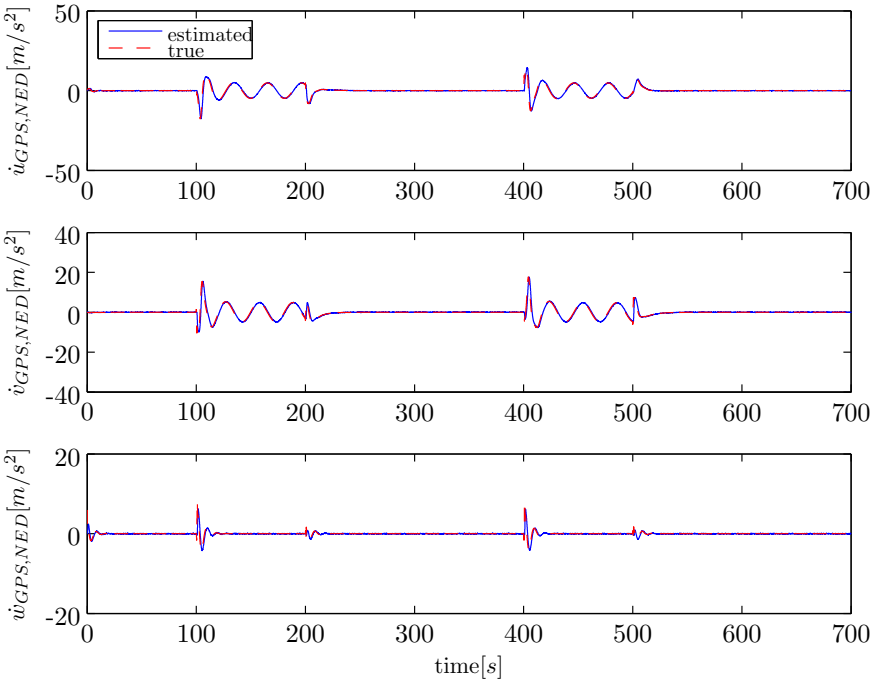

Figure 10-38: GPS velocity derivatives using a 2^{nd} order butterworth filter with a cutoff frequency of 0.01 $[rad/s]$

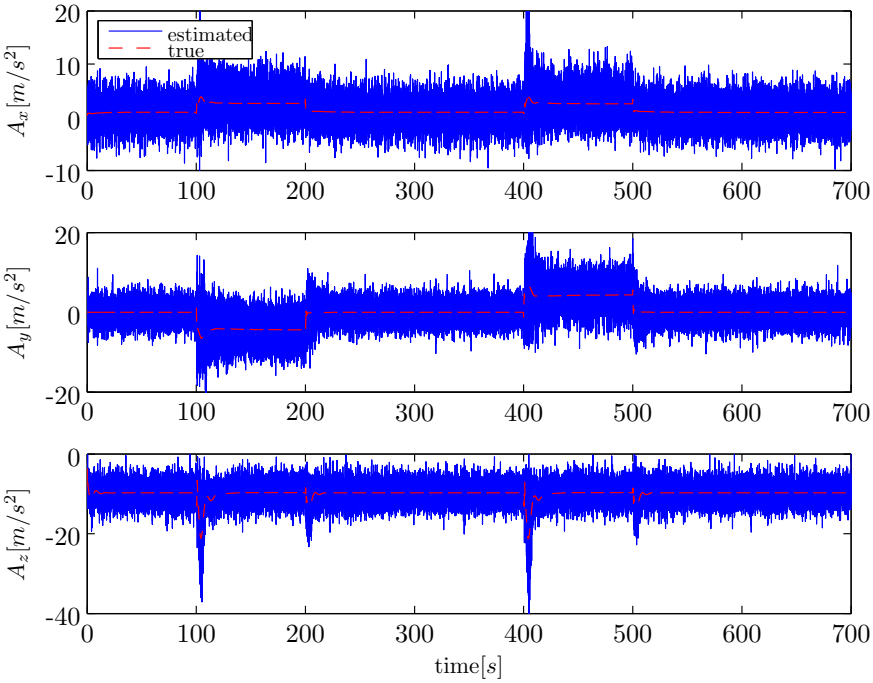

Figure 10-39: Estimated specific forces by GPS velocity derivatives using a 2^{nd} order butterworth filter with a cutoff frequency of 0.2 $[rad/s]$

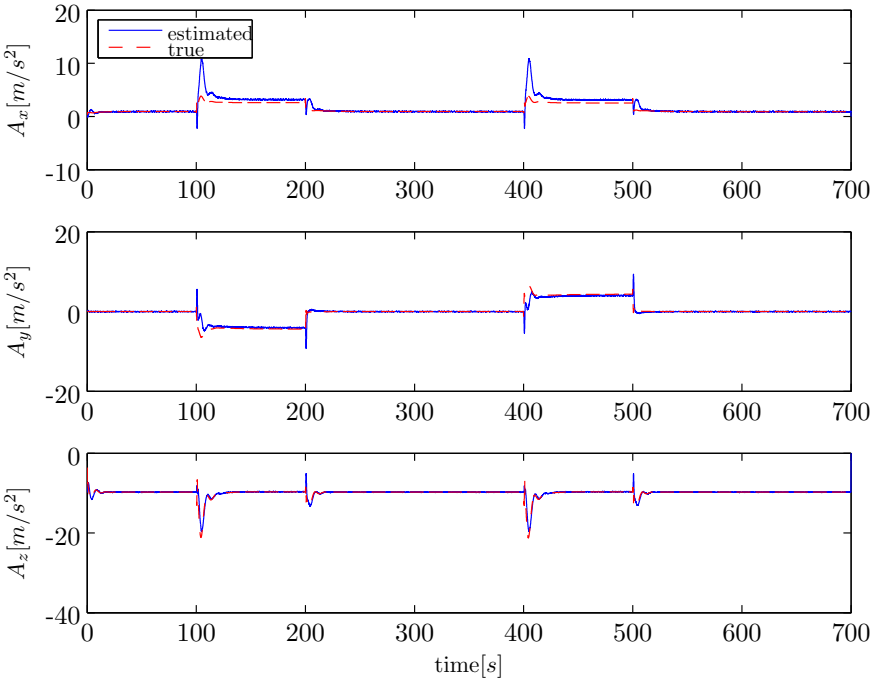

Figure 10-40: Estimated specific forces by GPS velocity derivatives using a 2^{nd} order butterworth filter with a cutoff frequency of 0.01 $[rad/s]$

10-4-2 Conclusion

The derived expression of the previous subsection 10-4-1 can convert GPS accelerations from ECEF to local body-fixed coordinates. This conversion can be used to estimate the vehicle's specific forces. Expression 10-84 below gives the transformation for converting GPS velocity derivatives to specific forces.

$$\begin{bmatrix} A_x \\ A_y \\ A_z \end{bmatrix}_B = \begin{bmatrix} \cos\theta\cos\psi & \cos\theta\sin\psi & -\sin\theta \\ \sin\phi\sin\theta\cos\psi - \cos\phi\sin\psi & \sin\phi\sin\theta\sin\psi + \cos\phi\cos\psi & \sin\phi\cos\theta \\ \cos\phi\sin\theta\cos\psi + \sin\phi\sin\psi & \cos\phi\sin\theta\sin\psi - \sin\phi\cos\psi & \cos\phi\cos\theta \end{bmatrix} \cdot \begin{bmatrix} \dot{u}_N \\ \dot{v}_E \\ \dot{w}_D \end{bmatrix} - \begin{bmatrix} -g_0\sin\theta \\ g_0\sin\phi\cos\theta \\ g_0\cos\phi\cos\theta \end{bmatrix}_B \quad (10\text{-}84)$$

The GPS velocity derivatives are calculated using expression 10-85.

$$\begin{aligned} \dot{u}_N &= -\dot{u}_{ECEF}\sin\phi\cos\lambda - \dot{v}_{ECEF}\sin\phi\sin\lambda + \dot{w}_{ECEF}\cos\phi \\ \dot{v}_E &= -\dot{u}_{ECEF}\sin\lambda + \dot{v}_{ECEF}\cos\lambda \\ \dot{w}_D &= -\dot{u}_{ECEF}\cos\phi\cos\lambda - \dot{v}_{ECEF}\cos\phi\sin\lambda - \dot{w}_{ECEF}\sin\phi \end{aligned} \quad (10\text{-}85)$$

The advantage of using expression 10-84 with respect to the derived equations of motion of chapter 8, is that no fictitious forces are required. When assuming that the GPS velocity derivatives are obtained in inertial space, the Coriolis forces as a result of $\underline{\omega} \times \underline{v}_{rel}$ can be left out. The GPS accelerations give an unbiased estimation of the aircrafts specific forces. Next to estimating the vehicle's specific forces, this estimation can also used to correct the IMU accelerometer biases, or the attitude/ heading angles.

Figures 10-33 to 10-40 show that the accuracy of the specific force estimation is mainly dependent on the applied differentiating technique of the GPS velocities. Two methods were discussed, the moving average and the 2^{nd} order low pass butterworth filter. The use of a butterworth filter results in better filtering out of high frequency noise, while having a lower phase delay. From this can be concluded that the 2^{nd} order butterworth filter should be chosen over the moving average method. When the described method is implemented into a navigation filter, the time delay due to GPS receiver processing time and filtering should be compensated for. The butterworth cutoff frequency should be chosen as such that a compromise between high frequency noise cancellation and time delay is reached.

Chapter 11

Observability Analysis of Different Sensor Configurations

This chapter shows the results of a theoretical study on the observability of different sensor configurations. The used four sensor configurations are described in chapter 9. Theory on observability as described in chapter 3 together with the QRsvd-algorithm, is used to perform the corresponding analysis. The sensor configurations are analyzed in section 11-2. The angle correction improvements of chapter 10 to an IMU/GPS integration is analyzed in section 11-3. Observability conclusions can be found in section 11-4 based on the results of sections 11-2 and 11-3.

11-1 Introduction

Before Kalman filtering can be used to perform a state estimation on a UAV or navigation algorithms in general, it is necessary to analyze the underlying sensor configuration and properties. The sensor configuration and designed filter must be able to observe the states that are to be estimated by means of an identification filter. If not, the filter will not function properly and give a diverging outcome. Observability of system states determines if a Kalman filter will converge or diverge, because unobservable states cannot be corrected and may give unbounded errors. The corresponding observability degree, as defined in section 3-5, is a measure to quantify the observability of individual system states and indicates if a state is "easy" or "difficult" to observe. A high observability degree indicates that a state is difficult to observe, the lower the value the easier to observe and a converging filter is usually guaranteed. The observability degree can be used to quantitatively analyze the performance of different observers and provides a measure of convergence when a state estimate is reached. High observability degrees means little state information is available and more filter cycles are required to obtain an adequate state estimation. It is advised that before using a Kalman filter or any other type of filter, the observability (degree) of the system states is investigated.

The focus of the following sections is on the observability analysis regarding the attitude/ heading angles, as the main goal of this report is to stabilize fixed-wing UAVs. As mentioned in chapter 9 not all sensor configurations will be used for the observability analysis. Section 11-3 will analyze the influence on state observability by using the three angle correction equations, as derived in chapter 10. To summarize, the different sensor configurations of chapter 9 that will be analyzed in the following sections:

- Sensor configuration 2, subsection 9-1-2.
- Sensor configuration 6, subsection 9-1-6.
- Sensor configuration 7, subsection 9-1-7.
- Sensor configuration 8, subsection 9-1-8.

11-2 Observability Analysis on Different Sensor Configurations

This section contains the results of an analytical observability analysis on the different sensor configurations that were described in section 9-2. The analytical analysis of this section provides qualitative observability results on individual states for the different sensor configurations using SVD. Table 11-1 summarizes the individual sensor configurations.

Table 11-1: Sensor configurations used for the observability analysis

Sensor type	Quantity	Config 2	Config 6	Config 7	Config 8
Accelerometers	A_x	√	√	√	√
	A_y	√	√	√	√
	A_z	√	√	√	√
Gyroscopes	p	√	√	√	√
	q	√	√	√	√
	r	√	√	√	√
GPS position	x_{GPS}	√	√	√	√
	y_{GPS}	√	√	√	√
	z_{GPS}	√	√	√	√
GPS velocity	u_{GPS}	√	√	√	√
	v_{GPS}	√	√	√	√
	w_{GPS}	√	√	√	√
Air data senors	α		√		√
	β		√		√
	V_T		√		√
GPS angles	GPS_ϕ			√	√
	GPS_θ			√	√
	GPS_ψ			√	√

The observability analysis is performed by using the fixed-wing UAV model of chapter 7, the model simulation parameters can be found in appendix B. The simulation results can

be found in appendix D. The simulated trajectory consists of three parts, a 360° left turn, followed by a 360° right turn and ended with two rudder doublets of 10° and 5°. The analytical observability analysis is performed by using non-linear system observability theory for non-linear systems as described in section 3-3. The required state and observer Jacobians for the observability matrix $\mathcal{O}$ can be found in appendix A, which are based on the equations of motion expression 8-25 of chapter 8. The observer equations 9-1, 9-2, 9-6 and 9-7 for the different sensor configurations are used as observers. The local observability matrix $\mathcal{O}\left(\underline{x}_0, \underline{u}^*\right)$ for non-linear systems is calculated by using equation 3-12, which can be found in section 3-3, up to 4^{th} order Lie derivatives are used. Including higher order terms results in an increase of required computational power, with no increase in observability accuracy. Appendix C gives the observability values for all four configurations during the simulation.

For the observability analysis three cases are analyzed. A normal flight condition where all sensors receive measurement data. Secondly, a situation where the vehicle's rotational rates are zero, $\underline{\omega} = 0$, and as a consequence the attitude/ heading angles remain constant. Thirdly no vehicle accelerations, $\underline{A} = 0$, where as a consequence the vehicle velocities remain constant. These last two cases can be used to see which states become unobservable if the gyroscopes or accelerometers do not provide measurements during such maneuvers. The two additional cases are implemented by changing the appropriate state values after the performed simulation to zero or a constant value. Table 11-2 gives the observability results for each sensor configuration for the three described cases.

Table 11-2: Observable states of different sensor configurations, based on the simulation results of appendix D

states	Config 2			Config 6			Config 7			Config 8		
		$\underline{\omega}=0$	$\underline{A}=0$		$\underline{\omega}=0$	$\underline{A}=0$		$\underline{\omega}=0$	$\underline{A}=0$		$\underline{\omega}=0$	$\underline{A}=0$
x	√	√	√	√	√	√	√	√	√	√	√	√
y	√	√	√	√	√	√	√	√	√	√	√	√
z	√	√	√	√	√	√	√	√	√	√	√	√
u	√	√	√	√	√	√	√	√	√	√	√	√
v	√	√	√	√	√	√	√	√	√	√	√	√
w	√	√	√	√	√	√	√	√	√	√	√	√
ϕ	√	√	√	√	√	√	√	√	√	√	√	√
θ	√	√	√	√	√	√	√	√	√	√	√	√
ψ	√	√	√	√	√	√	√	√	√	√	√	√
b_{A_x}	√	√	√	√	√	√	√	√	√	√	√	√
b_{A_y}	√	√	√	√	√	√	√	√	√	√	√	√
b_{A_z}	√		√	√	√	√	√	√	√	√	√	√
b_p				√	√	√	√	√	√	√	√	√
b_q				√	√	√	√	√	√	√	√	√
b_r				√	√	√	√	√	√	√	√	√
W_x										√	√	√
W_y										√	√	√
W_z										√	√	√
rank	12	11	12	15	15	15	15	15	15	18	18	18

The observability result of table 11-2 indicate whether or not a state is observable. Observable states are indicated by "√", unobservable states are left blank. The results differ for the individual sensor configurations. By adding more sensors more and more information

becomes available, which results in more observable states. For sensor configuration 2 it can be concluded from the table that the position (3), velocity (3), angles (3) together with two accelerometer biases b_{A_x} and b_{A_y} angle are always observable. These states are not maneuver dependent when there is zero rotation rate $\underline{\omega} = 0$ or acceleration $\underline{A} = 0$, the states remain observable.

Sensor configuration 1 shows changing observability results for b_{A_z} with different vehicle maneuvers. From table 11-2 can be concluded that sensor configuration 2 and 3 do not have this property. The position (3), velocity (3), angles (3) and IMU biases (6) states are always observable, independent on vehicle rotations or accelerations. These 15 states are called instantaneously observable as defined in lemma 3.1 for configuration 6 and 7. With the additional air data sensors, additional information about the vehicle's orientation is obtained. This information can be used to estimate all IMU biases. As a result, the third accelerometer bias b_{A_z} becomes instantaneously observable. The same result is obtained by measuring the attitude/ heading angles with the use of multiple GPS receivers. Obtaining attitude/heading information using multiple GPS receivers is not treated in this report. From an observability point of view, it results in the same observability as using three air data sensors. While the number of observable states is the same, the quality and filter performance of sensor configuration 6 and 7 may differ. This is depends on the sensor hardware and software properties. The state identification and filter results will differ for the two configurations and further investigation is required to make a distinction between the two.

Sensor configuration 8 uses both air data sensors and multiple GPS receiveers as additions to sensor configurations 2. With the addition of these sensors to the IMU sensor and GPS receiver, also the wind components $\underline{W}$ become observable. These three states are not maneuver dependent and are instantaneously observable since the rank is always 18, as defined in lemma 3.1. The information from the set of GPS receivers can be combined with the gyroscope output to estimate the gyroscope biases. The same can be done with the air data sensors as is shown with sensor configuration 2. This extra velocity information can also be used together with the velocity estimations from the accelerometers and GPS velocity to provide information on the individual wind components.

11-3 Observability Analysis on Improved IMU/GPS Sensor Configuration

Sensor configuration 2, as described in subsection 9-1-2, can be improved by using additional equations instead of adding more sensors to increase its observability rank. The three angle correction (AC) expressions derived in chapter 10 can increase the observability by utilizing fixed-wing aircraft kinematics together with sensor properties. The increase in observability is artificially, since no additional sensor are used. To summarize, the modified sensor configuration 2 with three AC equations as defined as follows:

- 3 gyroscopes, output quantities: rotational rates p, q and r.
- 3 accelerometers, output quantities: specific forces A_x, A_y and A_z.
- GPS receiver, output quantities: 3D position x, y and z, velocity u, v and w.

- Three AC observers, output quantities: 3 orientation angles ϕ_{AC}, θ_{AC} and ψ_{AC}.

The analyzed state observability is performed in a quantitative manner. The observability degree as described in section 3-5, can be used to indicate differences between "good" and "bad" observable states. The expression to calculate the observability degree is repeated below, expression 11-1. The largest singular value during the simulated trajectory is the forward velocity component u, which is taken as σ_{max}. The other states observability degree η_k are relative to u. Larger observability degrees mean these individual states are more difficult to observe compared to u.

$$\eta_k = \frac{\sigma_{max}}{\sigma_i}, \qquad \text{for } i = 1,\ 2,\ \ldots, n \tag{11-1}$$

Table 11-3 gives the observability degree of the sensor configuration 2. Table 11-4 gives the observability degree of the improved sensor configuration 2, including the angle correction equations. The same simulation is used as in the previous observability analysis, the Generic Aerosonde UAV simulation of appendix D. A normal flight condition case where all sensors receive measurement data. Secondly, a situation where the vehicles rotational rates are zero, $\underline{\omega} = 0$, and as a consequence the attitude/ heading angles remain constant. Thirdly, no vehicle accelerations, $\underline{A} = 0$, where as a consequence the vehicle velocities remain constant. These two cases can be used to see which states become unobservable if the gyroscopes or accelerometers do not receive measurements. The observability results for both sensor configurations can be found in appendix C-6 for all three cases. Large observability degree values mean unobservable states and have been left out, indicated by "$> 10^{15}$."

From table 11-3 can be seen that some states can be become "badly" observable during zero rotations, because of a high observability degree. These states are the heading angle and two of the accelerometer biases b_{A_x} and b_{A_y}. These three states are likely to diverge during zero rotational rates $\underline{\omega} = 0$ maneuvers. In section 11-2 was concluded that one of the accelerometer biases b_{A_z} becomes unobservable during zero rotational rates and as a result the corresponding observability degree is higher then 10^{15}. States having relatively high observability degrees are observable, however are still difficult to estimate when implemented into an identification filter as very little information is available. High observability degrees, values of η larger then 10^{10}, are present for the heading angle and accelerometer biases. This means that these states become practically unobservable during zero rotational rate maneuvers.

The zero acceleration case $\underline{\mathrm{A}} = 0$, has no significant influence on the state observability degree. The previous section 11-2 showed that the number of observable states doesn't change. This holds for both sensor configurations. For the improved sensor configuration 2 + AC, the zero rotational rate constraint is no longer present. The additional angle observers have the same results as adding three air data sensor or a three GPS receiver angle configuration, of previous section 11-2. The heading angle and accelerometer biases are now instantaneously observable according to lemma 3.1. The corresponding observability degrees have lower values, meaning that the observability of these states has been improved.

Table 11-3: Observability degree η_k results of different states for sensor configuration 2

states		$\underline{\omega} = 0$	$\underline{A} = 0$
x	2.07E+002 ± 1.41E+003	1.77E+002 ± 2.28E+000	2.07E+002 ± 1.41E+003
y	2.07E+002 ± 1.41E+003	1.77E+002 ± 2.28E+000	2.07E+002 ± 1.41E+003
z	2.07E+002 ± 1.41E+003	1.77E+002 ± 2.28E+000	2.07E+002 ± 1.41E+003
u[1]	1.00E+000 ± 0.00E+000	1.00E+000 ± 0.00E+000	1.00E+000 ± 0.00E+000
v	2.72E+000 ± 9.97E-002	2.75E+000 ± 2.59E-002	2.72E+000 ± 9.97E-002
w	3.37E+000 ± 4.08E+000	3.28E+000 ± 3.20E-002	3.37E+000 ± 4.08E+000
ϕ	3.74E+000 ± 7.81E+000	3.63E+000 ± 2.29E-001	3.74E+000 ± 7.81E+000
θ	4.29E+000 ± 2.63E+001	3.62E+000 ± 2.07E-001	4.29E+000 ± 2.63E+001
ψ	3.66E+001 ± 2.95E+001	6.89E+012 ± 1.54E+015	3.66E+001 ± 2.95E+001
b_{A_x}	5.52E+001 ± 1.97E+002	1.58E+013 ± 3.54E+015	5.52E+001 ± 1.97E+002
b_{A_y}	6.30E+001 ± 3.27E+002	5.12E+011 ± 1.14E+014	6.30E+001 ± 3.27E+002
b_{A_z}	1.49E+003 ± 7.25E+003	$> 10^{15}$	1.49E+003 ± 7.25E+003
b_p	$> 10^{15}$	$> 10^{15}$	$> 10^{15}$
b_q	$> 10^{15}$	$> 10^{15}$	$> 10^{15}$
b_r	$> 10^{15}$	$> 10^{15}$	$> 10^{15}$
W_x	$> 10^{15}$	$> 10^{15}$	$> 10^{15}$
W_y	$> 10^{15}$	$> 10^{15}$	$> 10^{15}$
W_z	$> 10^{15}$	$> 10^{15}$	$> 10^{15}$
rank	12	11	12

Table 11-4: Observability degree η_k results of different states for sensor configuration 2 plus angle correction equations

states		$\underline{\omega} = 0$	$\underline{A} = 0$
x	1.88E+002 ± 4.55E+002	1.77E+002 ± 2.28E+000	1.88E+002 ± 4.55E+002
y	1.88E+002 ± 4.55E+002	1.77E+002 ± 2.28E+000	1.88E+002 ± 4.55E+002
z	1.88E+002 ± 4.55E+002	1.77E+002 ± 2.28E+000	1.88E+002 ± 4.55E+002
u[2]	1.00E+000 ± 0.00E+000	1.00E+000 ± 0.00E+000	1.00E+000 ± 0.00E+000
v	2.72E+000 ± 9.97E-002	2.75E+000 ± 2.58E-002	2.72E+000 ± 9.97E-002
w	3.31E+000 ± 1.42E+000	3.28E+000 ± 3.19E-002	3.31E+000 ± 1.42E+000
ϕ	3.62E+000 ± 2.72E+000	3.62E+000 ± 2.29E-001	3.62E+000 ± 2.72E+000
θ	3.92E+000 ± 8.48E+000	3.62E+000 ± 2.08E-001	3.92E+000 ± 8.48E+000
ψ	3.60E+001 ± 1.35E+001	5.09E+001 ± 8.06E-001	3.60E+001 ± 1.35E+001
b_{A_x}	5.24E+001 ± 6.46E+001	4.92E+001 ± 1.42E+001	5.24E+001 ± 6.46E+001
b_{A_y}	5.85E+001 ± 1.05E+002	5.60E+001 ± 1.21E+001	5.85E+001 ± 1.05E+002
b_{A_z}	2.25E+002 ± 1.65E+002	1.68E+002 ± 2.19E+000	2.25E+002 ± 1.65E+002
b_p	3.11E+003 ± 8.16E+003	3.02E+003 ± 7.26E+001	3.11E+003 ± 8.16E+003
b_q	3.55E+003 ± 9.24E+003	3.48E+003 ± 7.47E+001	3.55E+003 ± 9.24E+003
b_r	4.14E+003 ± 1.12E+004	4.62E+003 ± 1.44E+002	4.14E+003 ± 1.12E+004
W_x	$> 10^{15}$	$> 10^{15}$	$> 10^{15}$
W_y	$> 10^{15}$	$> 10^{15}$	$> 10^{15}$
W_z	$> 10^{15}$	$> 10^{15}$	$> 10^{15}$
rank	15	15	15

[1] u is taken as σ_{max}, as a consequence the observability degree is 1.00 ± 0.00
[2] u is taken as σ_{max}, as a consequence the observability degree is 1.00 ± 0.00

11-4 Conclusion

From the analytical observability study performed in section 11-2, can be concluded that the observability of observable states is not dependent on whether the vehicle has acceleration. From table 11-2 can be seen that the observable states of each sensor configuration remain observable during case 3, zero accelerations $\underline{A} = 0$ maneuvers. When a vehicle is not accelerating, the IMU accelerometers do not receive acceleration information and no estimation of the vehicles' velocity and position using the IMU can be made. When an IMU is coupled with a GPS receiver, the GPS position and velocity information can assist the accelerometer during zero acceleration maneuvers such that the states remain observable. From table 11-2 can be concluded that this conclusion holds for all the investigated sensor configurations, as they are all based on a IMU/GPS integration.

From the observability analysis of section 11-2 can also be concluded that next to the assisting function of the GPS receiver to the IMU, the obtained GPS receiver information can be used to correct the accelerometer biases, as can be seen from table 11-2. The time derivatives of the GPS position and velocity can be used to make an estimation of the vehicle accelerations. The derived vehicle accelerations are in the GPS receiver NED frame of reference $\mathcal{F}_E$. The IMU accelerometer signals are in the body-fixed reference frame $\mathcal{F}_B$. The conversion between $\mathcal{F}_E$ and $\mathcal{F}_B$ can be performed by a rotational matrix, using all three orientation angles. When converting the GPS velocity derivatives from $\mathcal{F}_E$ to $\mathcal{F}_B$, by using a rotational matrix the GPS velocities can be used to correct the IMU accelerometer biases.

During maneuvers with zero angular rates, the accelerometer bias b_{A_z} becomes unobservable for sensor configuration 2 as the state is no longer observable. This can be seen from table 11-2 for case 2 where $\underline{\omega} = 0$. From section 11-3 can be concluded that the other two accelerometer biases b_{A_x} and b_{A_y}, together with the heading angle ψ, also become unobservable as the corresponding observability degrees have very high values. The observability degrees for case 2 have values that are larger then 10^{10}, as can be seen in table 11-3. The reason why the accelerometer biases together with the heading angle become unobservable is due to the rotational matrix, used for transforming the position and velocity states between $\mathcal{F}_B$ and $\mathcal{F}_E$. All three orientation angles are required for the rotational matrix $R_{BE}(\phi, \theta, \psi)$ to fuse the GPS velocities and positions with the accelerometer based predictions. During maneuvers with zero rotational rates, no knowledge of the three orientation angles is available and the conversion between reference frames cannot be made.

For the sensor configurations 6, 7 and 8 can be concluded from table 11-2 that the observable states are instantaneously observable as defined by lemma 3.1 in section 3-2. The observable states remain observable for case 2 during zero rotational rates $\underline{\omega} = 0$ and for case 3 for zero accelerations $\underline{A} = 0$.

From table 11-4 in section 11-3, can be concluded that the observability improvement due to the use of three AC equations has the same effect as adding three air data sensors or using multiple GPS receivers for attitude/ heading estimation. Sensor configuration 2 with the addition of three AC equations has an observability rank of 15, which is the same as for configuration 6 and 7. With the three AC equations, the rank of sensor configuration 2 has increased from 12 to 15, meaning all IMU biases are observable. Together with the increase in observability rank the observable states have become instantaneously observable, as defined in lemma 3.1 of section 3-2. The latter means that the zero rotational rate constraint is no

longer present. This can be concluded from table 11-4 as the observability degree does not change for case 2 when $\underline{\omega} = 0$.

Chapter 12

Combining Physical and Observability Analyses Results

The last two chapters, chapters 10 and 11, provided insight into improving the sensor fusion of an IMU/GPS sensor configuration from different perspectives. Chapter 10 focused on improvement by means of adding kinematic observers by combining fixed-wing aircraft kinematics together with an onboard IMU and GPS receiver. Chapter 11 performed a mathematical observability analysis of different sensor configurations. This chapter combines the results of the obtained physical insight and observability analyses. Section 12-1 provides conclusions as a result of combining the observability analysis with the obtained physical insight. The second and last section 12-2 gives the final angle correction (AC) equations, which are used in the next chapter 13 for different state identification simulations.

12-1 Results

Chapter 10 provided insight into the kinematics of fixed-wing flying vehicles. The derived kinematic expression explains the motion of a particle P in inertial space, as seen from a local moving frame of reference. This expression is used to describe the motion of a rigid body in inertial space. With the derived kinematic expression, different physical relations on the three orientation angles were investigated. This led to the design of different expressions to estimate the attitude/heading angles. The goal of chapter 10 was to find additional kinematic relations that could provide information on the three orientation angles to improve the IMU predictions. With a better and more robust estimation of the orientation angles, the vehicle can be stabilized better. The IMU predictions use the angular rates p, q and r provided by the gyroscopes, to make an estimation by means of integrating the angular rates as described in chapter 8. To be able to correct the increasing error in gyroscopic estimations, the AC equations need to be independent from the gyroscopic estimations. In the perfect case, none of the gyroscopes provided angular rates are present in the AC equations. For the AC equations design, the influence of different kinematic terms was examined by means of simulation. By

using the generic UAV simulation of appendix D, the influence of different kinematic elements was determined.

For the pitch angle estimation the physical analysis has led to the fact that a change in local orientation in $\mathcal{F}_B$ of the gravity vector can be used to make a pitch angle estimation. This estimation is valid over a long period of time. The absence of Coriolis terms, results in less accurate pitch angle estimations during the presence of fast dynamics. The only fast dynamic component that can be included is the time derivative of the body-fixed velocity in forward direction $\dot{u}_B$. The absence of Coriolis forces in the pitch angle AC equation is the largest source of error. Besides the change in local gravity vector orientation, the pitch angle can also be estimated using velocity components. The total velocity vector can be used to obtain information on the vehicle's pitch angle. This estimation is however more sensitive to windy conditions, because the obtained GPS velocities include wind components while the estimation based on the local gravity vector orientation does not. Also the use of GPS velocities means that the estimation will have a time delay with respect to the IMU prediction.

For the roll angle this has led to an estimation that includes both static and dynamic roll angle components. When making a constant turn without accelerations, the roll angle is equal to the total velocity vector times the angular rate around the Z-axis. During a real flight, this is however not the case and turning accelerations are present. The angle between the specific force in lateral A_y and downward A_z direction provides the resulting turning forces. By adding the dynamic part to the static estimation, an adequate roll angle estimation can be made. It should be noted that the angular rate r, provided by an IMU gyroscope, is used twice. This is however not a problem, since the roll angle is estimated by directly using the gyroscope and not by integration.

The heading angle can be estimated by taking the angle between the lateral and forward GPS velocity components. This angle is the absolute angle, as seen from a non-moving observer on the ground, called ground track. This means that the side-slip angle β is also part of the estimated heading angle, as the ground track is defined as the heading angle plus the side-slip angle. In the presence of large wind velocities, the side-slip angle can become very large and may result in bad heading estimations. When the latter is the case, this is the largest source of estimation error. Since this estimation uses GPS velocities, time latency is present between the IMU and GPS signals.

The goal of the observability analysis was to quantitatively indicate the relative difference between observers, in terms of "good" or "bad" state observers. The observability analysis uses the developed singular values tool of chapter 3, where the singular values of the observability matrix are directly linked to each particular state. From the observability analysis was concluded that the traditional IMU/GPS configuration can have unobservable states during zero rotational rates maneuvers. This sensor configuration requires the aircraft to rotate, because the received GPS velocities need to be transformed to the body-fixed frame of reference. From the physical analyses it was concluded that with the additional AC equations, this rotational rate constraint no longer holds as the predicted gyroscopic angle predictions can always be corrected. Due to the three AC equations, all six IMU biases become instantaneously observable. During zero rotation rates $\underline{\omega} = 0$ and zero acceleration $\underline{A} = 0$ maneuvers with the extension of the three AC equations, the singular values remain of the same order of magnitude. The IMU biases together with the heading angle are now instantaneously observable in

a quantitative way, as the observability degrees remain of the same order of magnitude.

While all six IMU biases are observable, it will still be difficult to estimate the gyroscopic biases. To make an accurate estimation on the gyroscopic biases, unbiased measurements are required. The AC equations are not unbiased as was concluded from chapter 10 and the bias estimation will not be accurate. The derived AC expressions give a long-term stable estimation, however may contain a short-term bias. The short-term bias estimation will most likely be time-varying as a result of errors in the AC expressions together with the gyroscopic bias and possible some time latency between the IMU and GPS receiver.

The observability results show that the improvement due to the AC equations has the same result as adding three air data sensors or the use of multiple GPS receivers for attitude/ heading estimations. It should be noted that from an observability point of view this gives the same results in terms of state observability based on the singular values. The actual performance during state identification will probably differ, as will be investigated in more detail in chapter 13 when performing different simulations.

Next to the improvement of the AC equations on the three orientation angles, it was also concluded that the IMU accelerometer biases are observable. Section 10-4 derived a possible method to make an estimation on the vehicle's specific forces by using GPS velocity measurements. This section showed the required transformation matrices to transform the GPS velocities from the assumed inertial frame of reference ECEF to the local NED frame of reference. Next step is to transform the velocities from NED to body-fixed velocities by using all three orientation angles.

When neglecting the Earth's rotation the GPS velocity derivatives can be assumed measured in inertial space, the specific forces can be calculated directly without any fictitious forces. The improvement of the three AC equations results in the fact that the orientation angles are instantaneously observable, which is required to make one of the two coordinate transformations. The rotational rate constraint is in accordance with the physics derived in section 10-4. This section shows that all three orientation angles, roll, pitch and heading angle are required to make the transformation between NED and the body-fixed frame of reference. This means that the zero rotational rate constraint is no longer present and that the developed method can always be used, as long as there is a GPS fix. From section 10-4 was concluded that when using this method, the largest source of error is due to the GPS accelerations. The GPS velocity signals need to be differentiated to obtain the GPS accelerations, which will contain high frequency noise. The best method is the use of a low pass butterworth filter. A 2^{nd} order filter with two different cutoff frequencies has been used in section 10-4. From this was concluded that the butterworth cutoff frequency should be chosen as a compromise between the allowable time delay and required cancellation of high frequency noise.

12-2 Final Sensor Configuration

The previous section 12-1 combined the results from the physical and observability analyses. Both analyses showed that the derived AC equations have a positive influence on the attitude/ heading angle estimations and vehicle stabilization. Based on this result it can be concluded that adding the three AC equations improves the loosely coupled IMU/GPS sensor configuration. This sensor configurations can be summarized as follows:

- 3 gyroscopes, output quantities: rotational rates p, q and r.
- 3 accelerometers, output quantities: specific forces A_x, A_y and A_z.
- GPS receiver, output quantities: 3D position x, y and z, velocity u, v and w.
- Three AC observers, output quantities: 3 orientation angles ϕ_{AC}, θ_{AC} and ψ_{AC}.

Bases on the derived equations of motion of chapter 8, expression 12-1 below can be used for the state prediction step. Expression 12-2 provides observers for all nine IMU prediction residuals, based on sensor configuration 2 of chapter 9 together with the three derived AC equations.

The derived AC equations are based on the generic UAV simulation of appendix D. This simulation is based on a generic flight maneuvers, left and right turns together with doublet rudder inputs. Different situations may however occur during real flight, the following chapter 13 includes different simulations. The small turns simulation of appendix E simulates more dynamic turning where the derived AC equations are expected to have difficulties observing the orientation angles. The large turns simulation of appendix F is a test for long-term stability and lasts for about 40 minutes. A slow 360° left turn is followed by a slow 360° right turn. During the two turns the lateral specific force A_x is almost non-existent. With an almost zero specific force in lateral direction, the provided gyroscopic estimation on the orientation angles will slowly drift away.

The second part of the simulations of chapter 13 will be about the usage of real flight data. This real flight data will be used to validate the conclusions made on the result of the performed simulations. The flight data can also be used to see if the developed UAV, IMU sensor and GPS receiver simulation tools give realistic simulations.

Besides the Kalman filter technique on state identification as described in chapter 4, also the use of non-linear complementary filters is investigated. Chapter 14 describes the working of one particular non-linear complementary filter. This non-linear filter is based on the transformation matrix R_{BE} between a local body-fixed and Earth frame of reference. This transformation matrix contains all three orientations angles, required to stabilize a flying vehicle. The principle is the same as for the Kalman filter, first a prediction is made where the residuals are corrected using observers. Difference with respect to Kalman filters are in the observer gain calculation. Also the complementary filter does not require linearization at each step. The same simulations of appendices D to F and flight data of appendix G are used to analyze the stability and performance of the non-linear complementary filter.

$$
\begin{aligned}
\dot{x}_B &= [u_B \cos\theta + (v_B \sin\phi + w_B \cos\phi)\sin\theta]\cos\psi - (v_B \cos\phi - w_B \sin\phi)\sin\psi \\
\dot{y}_B &= [u_B \cos\theta + (v_B \sin\phi + w_B \cos\phi)\sin\theta]\sin\psi + (v_B \cos\phi - w_B \sin\phi)\cos\psi \\
\dot{z}_B &= -u_B \sin\theta \ + (v_B \sin\phi + w_B \cos\phi)\cos\theta \\
\dot{u}_B &= A_{x_m} + r_m v_B - q_m w_B - g_0 \sin\theta \\
\dot{v}_B &= A_{y_m} + p_m w_B - r_m u_B + g_0 \sin\phi \cos\theta \\
\dot{w}_B &= A_{z_m} + q_m u_B - p_m v_B + g_0 \cos\phi \cos\theta \\
\dot{\phi} &= p_m + q_m \sin\phi \tan\theta + r_m \cos\phi \tan\theta \\
\dot{\theta} &= q_m \cos\phi - r_m \sin\phi \\
\dot{\psi} &= q_m \tfrac{\sin\phi}{\cos\theta} + r_m \tfrac{\cos\phi}{\cos\theta}
\end{aligned}
\tag{12-1}
$$

$$
\begin{aligned}
x_{GPS} &= x_B \\
y_{GPS} &= y_B \\
z_{GPS} &= z_B \\
u_{GPS} &= [u_B \cos\theta + (v_B \sin\phi + w_B \cos\phi)\sin\theta]\cos\psi - (v_B \cos\phi - w_B \sin\phi)\sin\psi \\
v_{GPS} &= [u_B \cos\theta + (v_B \sin\phi + w_B \cos\phi)\sin\theta]\sin\psi + (v_B \cos\phi - w_B \sin\phi)\cos\psi \\
w_{GPS} &= -u_B \sin\theta \ + (v_B \sin\phi + w_B \cos\phi)\cos\theta \\
\phi_{AC} &= \tfrac{\sqrt{u_{GPS}^2 + v_{GPS}^2 + w_{GPS}^2}}{g_0} r_m + \arctan\left(\tfrac{A_{y_m}}{A_{z_m}}\right) \\
\theta_{AC} &= \arcsin\left(\tfrac{A_{x_m}}{g_0}\right) \\
\psi_{AC} &= \arctan\left(\tfrac{v_{GPS}}{u_{GPS}}\right)
\end{aligned}
\tag{12-2}
$$

Part IV

Simulation

Chapter 13

State Identification Simulations

The sensor configuration of previous chapter 12 is the result of a physical and observability analysis. This chapter simulates the working of this sensor configuration to see if it can stabilize a fixed-wing aerial vehicle. Section 13-1 addresses one particular aspect, namely time synchronization errors that can occur during sensor integration. The simulation results of appendix D to F are given in section 13-2. Simulations using real flight data of appendix G are given in section 13-3.

13-1 Time Latency Compensation and Implementation

As mentioned, in chapter 6 a GPS receiver has a relatively large processing time, due to the internal processing filter. The received satellite data needs to be processed into position and velocity information. This processing time is usually more compared to an IMU or other sensors. When using data from individual sensors with different processing data, the sensor fusion algorithm must be properly designed, as described in (Ding, Wang, Li, Mumford, & Rizos, 2008). Figure 13-1 gives an example of time delay on a GPS receiver velocity, from appendix D. The output data from the receiver is delayed by a time step dt with respect to the true velocity component in $\mathcal{F}_E$.

Time synchronization between GPS and INS measurements, is a problem when using an integrated INS/GPS sensor fusion algorithm. The GPS receiver and INS are separate, self-contained subsystems with different frequencies and processing times. The resulting clock difference could result in discrepancies during the sensor fusion. Dependent on the amount of information available from the sensors, different time synchronization techniques can be used. Next to the processed position and velocity data, also the 1 Pulse-Per-Second (PPS) is available for some GPS receivers. The 1PPS electrical signal indicates the turnover time of each second. The 1PPS can be used as a timing reference to synchronize the GPS signals with the IMU. External clock references or separate hardware timers can also be used, since the 1PPS signal is not available for all GPS receivers.

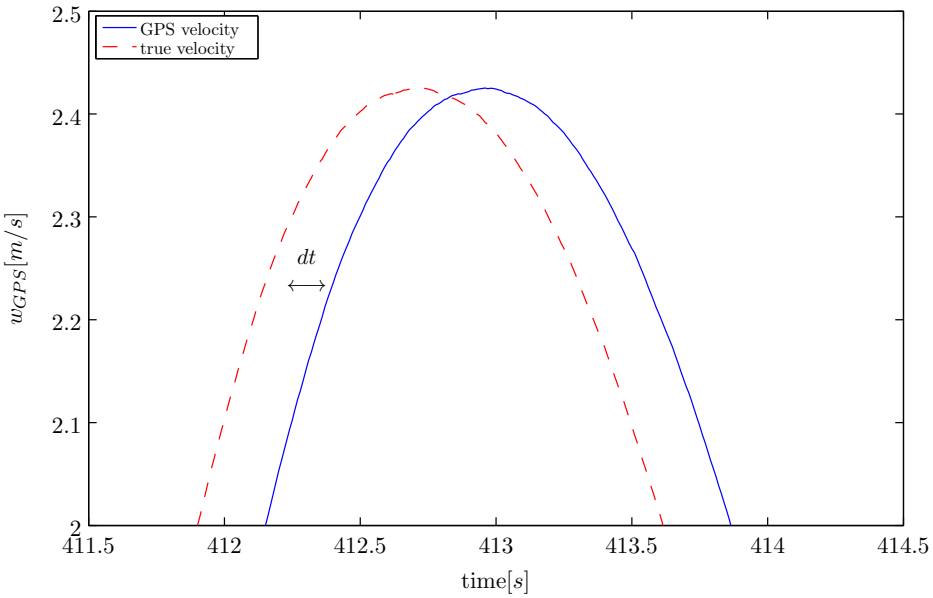

Figure 13-1: Example on sensor time delay, zoom of figure D-9

The sensor output usually goes through internal pre-processing components before there are used by the fusion algorithm. The pre-processing includes A/D convention, raw data sampling manipulation and possible some low- or high-pass filtering. Timing synchronization, which for instance uses the 1PPS signal, can be used to time-tag individual signals. The 1PPS signal can define the beginning of each second, which can be used to synchronize the GPS receiver signals to the other IMU signals. Time synchronization can also be improved by adding an additional state to the integration filter, as can be found in (Skog & Händel, 2010).

Before any sensor time delay compensation technique is used, data buffers are needed. The data buffers are required to interpolate the IMU data, to make it coincide with GPS data. The asynchronous measurement sampling of the IMU and GPS comes from the fact that both signals are running at different frequencies. Interpolation is needed to reduce the misalignment, due to fact that the IMU usually runs at higher frequencies. Especially with high grade IMU, the innovation magnitude is smaller, time synchronization becomes more important to adequately calibrate IMU with GPS data. Easy solutions, without using data interpolation, make use of down sampling IMU signals such that it coincides with the GPS receiver frequency. This reduces the total system accuracy as a lower sampling frequency is used. However, lower time synchronization accuracy is usually sufficient when applied to low grade INS/GPS systems. When dealing with platforms having fast dynamics, the time synchronization requirement becomes more important as the innovation may take place too late with respect to the prediction step. Example of timing modules, both for analogue and digital interfaces can be found in (Ding et al., 2008).

The influence of time synchronization errors on the total system accuracy can vary. To determine the influence of the propagation of a time latency error, an expression can be derived by looking at the observer equations. Starting with the output observer $\underline{z}(t)$ equation,

as given in expression 13-1, defined in continuous time.

$$\underline{z}(t) = \underline{r}_{GPS}(t) - \left(\underline{r}_{IMU}(0) + \int \underline{v}_{IMU}(0) + \iint \underline{a}(t)\right) \tag{13-1}$$

In expression 13-1, $\underline{r}_{GPS}(t)$ represents the GPS receiver update measurement and $\underline{r}_{IMU}(0)$, $\underline{v}_{IMU}(0)$ as the IMU initial position and velocity. The measured acceleration is assumed to be time-varying and is denoted by $\underline{a}(t)$. It is assumed that the initial IMU based position and velocity are known and a time synchronization error Δt exits between the GPS receiver and IMU sensor. The time synchronization error can be implemented into expression 13-1, resulting in the baltered observer equation $\underline{\tilde{z}}(t)$ of expression 13-2.

$$\underline{\tilde{z}}(t) = \underline{r}_{GPS}(t) - \left(\underline{r}_{IMU}(0) + \int \underline{v}_{IMU}(0) + \iint \underline{a}(t+\Delta t)\right) \tag{13-2}$$

The time synchronization error Δt can both be positive or negative, as such it is treated as a constant at time t. By taking the Taylor expansion of the IMU measurements of expression 13-2, the altered observer equation $\underline{\tilde{z}}(t)$ can be rewritten into expression 13-3.

$$\underline{\tilde{z}}(t) = \underline{r}_{GPS}(t) - \left(\underline{r}_{IMU}(0) + \int \underline{v}_{IMU}(0) + \iint \underline{a}(t) + \iint \left(\underline{a}'(t)\Delta t\right)\right) \tag{13-3}$$

Expression 13-3 can be rewritten into 13-4, using expression 13-1.

$$\underline{\tilde{z}}(t) = \underline{z}(t) - \iint \left(\underline{a}'(t)\Delta t\right) \tag{13-4}$$

The last term $\iint (\underline{a}'(t)\Delta t)$ can be seen as a constant time synchronization observer error, from now on denoted by $\underline{\zeta}$. The magnitude of $\underline{\zeta}$ is a function of the change in vehicle accelerations or "jerk." The jerk term $\underline{a}'(t)$ represents the vehicle dynamics, which can be seen as a constant during one innovation update assuming that the time synchronization error during one measurement update is constant. The combined influence of the change in vehicle acceleration and time delay, represented by $\underline{\zeta}$, can be implemented into the measurement update equation. When using the Kalman filter framework of chapter 4, the measurement update equation 4-7 becomes expression 13-5.

$$\begin{aligned}\underline{\hat{x}}\,(k+1 \mid k+1) = \underline{\hat{x}}\,(k+1 \mid k) + K(k+1)[&\underline{\hat{z}}\,(k+1 \mid k+1) \\ &- \underline{\zeta}\,(k+1) - H(k+1)\underline{\hat{x}}\,(k+1 \mid k)]\end{aligned} \tag{13-5}$$

From expression 13-5, the state estimation error vector $\underline{\varepsilon}$ can be extracted. The error $\underline{\varepsilon}$ is a result of the time synchronization observer error, $\underline{\zeta}(k+1)$ during one measurement update. Expression 13-6 gives the state estimation error vector of each innovation.

$$\underline{\varepsilon} = \underline{\hat{x}}\,(k+1 \mid k+1) - \underline{x}(k \mid k) \tag{13-6}$$

Expression 13-6 can be rewritten into expression 13-7, by using the result of expression 13-5.

$$\underline{\varepsilon} = -K(k+1)\underline{\zeta}(k+1) \tag{13-7}$$

From expression 13-7 can be concluded that the Kalman gain matrix $K(k+1)$ distributes the time synchronization error to the individual system states $\underline{x}$, according to the covariance estimation and observer dynamics. The required time synchronization accuracy can be calculated with expression 13-5 as long as the following constraint is met: $|\underline{\zeta}(k+1)| \ll |\underline{\hat{z}}\,(k+1 \mid k+1) - H(k+1)\underline{\hat{x}}\,(k+1 \mid k)\,|$. This constraint means that the Kalman filter innovation should be much smaller then the defined constant time synchronization observer error $\underline{\zeta}(k+1)$. If this constraint is met together with the assumption that the time estimation error due to the internal IMU data processing latency can be neglected, expression 13-8 can be used to estimate the required magnitude of the time synchronization observer error $|\Delta t|$. This expression comes from expression 13-4, requiring a small time synchronization error compared to the change in vehicle dynamics.

$$|\Delta t| \ll \frac{|\underline{\hat{z}}\,(k+1 \mid k+1) - H(k+1)\underline{\hat{x}}\,(k+1 \mid k)\,|}{|\iint \underline{a}'(t)|} \tag{13-8}$$

From expression 13-8 can be seen that the sensor fusion requirement on time synchronization accuracy is dependent on the Kalman filter innovation. This dependency is negative proportional, a smaller magnitude in filter innovation will result in a more stringent time synchronization requirement. This dependency is largely influenced by the IMU accuracy. From a practical point of view this can be interpreted as: The time latency requirement becomes more stringent with an increase in IMU accuracy and calibration. It can be concluded that when using low grade IMU, MEMS based sensors, this requirement becomes more flexible. This conclusion does however not hold when there is a large change in vehicle dynamics as the time synchronization accuracy is proportional to the vehicle dynamics. Represented by the jerk $\underline{a}'(t)$ in the denominator of expression 13-8.

When applied to fixed-wing UAV's or other vehicles with fast dynamics, the time synchronization requirement is proportional to the magnitude of the jerk $\underline{a}'$ and negatively proportional to the filter innovation. From this can be concluded that the time synchronization accuracy is dependent on both the filter innovation magnitude and change in vehicle accelerations. Exact calculations on sensor fusion time synchronization accuracy requirements is usually difficult due to errors in gyroscopic and accelerometer measurements together with errors in the used gravity model. To obtain the general influence of time synchronization errors on the IMU/GPS sensor integration, the small turns simulation op appendix E is used together with expression 13-8. To use expression 13-8, the exact accelerometer signals are used without signal noise and biases. Figure 13-2(a), shows the sum of absolute magnitudes of the jerk vector during the small turns simulation. These are calculated by taking the sum of the time derivatives of the accelerations at each time step. The large peaks in figure 13-2(a) are due to exact jerk calculations, which are not realistic values. The absence of accurate actuator dynamics in the used UAV model results in these large peaks, as no actuator time delays are included. Figure 13-2(b) shows a detail on the change in acceleration during the beginning of the first turn, this part will be used to estimate the time synchronization requirement. From figure 13-2(b) can be seen that a change in acceleration of 20 $[m/s^3]$ can be present. Assuming

that the GPS receiver runs a 5 Hz, double integration of a value of 20 $[m/s^3]$ at 0.2 $[s]$ gives a speed error of 2.0 $[m/s]$. When the innovation error is assumed to be 0.20 $[m]$, assuming a perfect GPS receiver and IMU with no signal noise or biases. These two values can be divided by each other as explained in expression 13-8, resulting in a time synchronization error of $\Delta t = 0.2[s]$. Based on the research of (Ding et al., 2008) a factor of 10 should be applied to the right hand side of expression 13-8. This results in a time synchronization requirement of 0.02 seconds. This requirement is based on the small turns simulation of appendix E and an innovation magnitude of 20 centimeters using a GPS receiver with an update rate of 5 Hz.

During the simulations of the next section 13-2 the IMU signals are placed into a buffer before the IMU/GPS sensor integration is made. The buffer time is dependent on the GPS receiver time latency, as explained based on the 1PPS signal. During the simulations, the GPS receiver time delay has been set to $0.25 \pm 0.025[s]$, as explained in chapter 6. The IMU signals and rest of the simulation runs at 100 Hz, the derived time synchronization requirement of 0.02 $[s]$ corresponds to 2 IMU samples. The latter means that the simulated GPS receiver and IMU signals should be synchronized within this requirement of 2 samples. The IMU signals are assumed to have no time delays, however in practice usually some small delay is present due to onboard IMU signal processing. If in practice the time synchronization requirement becomes so stringent that it is smaller than one sample time, this requires the IMU data to be interpolated to ensure that the IMU/GPS measurements coincide at each epoch.

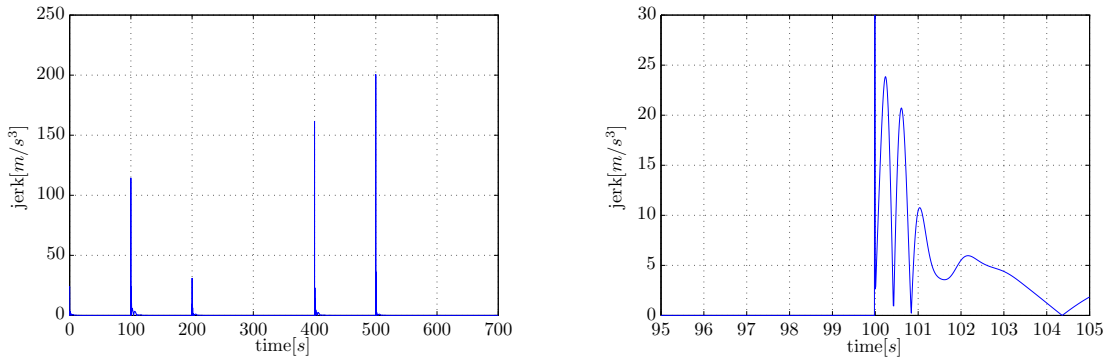

(a) Change in accelerations

(b) Detail on change in accelerations

Figure 13-2: Sum of change in vehicle accelerations, small turns simulation of appendix E

13-2 Identification Results of Simulations

The improved sensor configuration of section 12-2 is tested by using three simulations. The generic simulation of appendix D has already been used throughout the report. The second simulation is a test for short-term performance by means of small turns with a fast turning rate, appendix E. The third and last simulation is a test for long-term stability where little dynamics are present for a long period of time, as can be seen in appendix F. All three simulations are performed and analyzed with and without the presence of gust. Two state identification algorithms are applied, the Extended Kalman Filter (EKF) and Iterated Extended Kalman Filter (IEKF). This brings a total of 12 simulation cases, three simulations, each is performed by using two identification algorithms, each with and without the presence of gust. The simulation results on the use of the non-linear complementary identification filter on the $SO(3)$ group is treated in chapter 14, by using the same simulations as in this chapter. The simulation results of appendix D to F are summarized in tables 13-1, 13-2 and 13-3 for all 12 cases. For each case, the identification errors are calculated by taking the absolute difference between the simulated outcome and the real states. Each table entry contains the average error and standard deviation. Figures 13-3 to 13-11 give a statistical graph on the mean and variance of the simulation results. The time history of each state can be found in appendix D to F together with the identification error.

From the state identification results in table 13-1 to 13-3, can be seen that the differences between EKF and IEKF results are small. The IEKF algorithm can partially compensate for non-linearities in the observer dynamics by reiteration. Linearization errors are present due to errors in the first order derivatives. The first order derivatives or Jacobians are required for the Kalman filter, as explained in chapter 4. The improvement in state identification using the IEKF compared to EKF is not significant, as the observer dynamics non-linearities are not the largest source of error. The general trend in the simulation results is that the IEKF shows lower identification errors, this is however not a significant improvement. The improvement in IEKF over EKF is the largest during the presence of fast dynamics. This can be seen during the doublet input of the generic simulation at 400 seconds and during the small turns simulation. Without the presence of highly dynamic maneuvers, the difference is almost zero. During the large turns simulation of appendix F the difference in EKF and IEKF identification algorithms is almost non-existent.

As a general observation, the presence of gust has a negative influence on state identification. From the observability analysis of chapter 11 was concluded that the wind velocities remain unobservable for the improved IMU/GPS sensor configuration. The position and velocity estimations are affected the most as the wind velocities are not part of the specific forces sensed by the onboard IMU. From the EKF identification results on the generic simulation in figure D-13 and D-19 can be seen that the presence of gust results in a constant position error. This position error due to gust is present for all three position states, as can be seen in table 13-1 and figures 13-3 to 13-5. The gust effect is present for both EKF and IEKF, while the IEKF performs slightly better. The reason why IEKF performs slightly better, is because the IEKF is able to partially correct the non-linearity errors in the observer dynamics by means of reiterating the observer equations. These errors are smaller compared to the presence of gust, as can be seen in table 13-1 where the state estimation errors are larger when gust is present. From this can be concluded that the presence of gust influences the identification performance, resulting in larger position and velocity estimation errors.

For the orientation angles, the influence of gust on the identification performance is minimal. The largest difference in the presence of gust on the orientation angles, is the heading angle. The heading angle is also the largest source of error of the orientation angles. The presents of gust on the heading angle results in the presence of a side-slip angle β. The side-slip angle is defined as the difference between the ground track and heading angle. The difference is compensated by the AC heading angle equation, based on the GPS velocities u_{GPS} and v_{GPS}, explained in more detail in section 10-3-3. The influence of gust is the largest for dynamic maneuvers, as can be seen from table 13-2 and figures 13-6 to 13-8 on the small turns simulation. The error in the heading angle estimation increases the most during the presence of gust, compared to the generic and large turns simulation.
The roll angle is less influenced by the presence of gust, as can be seen in the identification result tables below. The difference in identification error between the situation with gust and without gust is for the roll angle less then 1 degree. This means that the influence of gust on the roll angle identification can be neglected. The pitch angle is partly influenced by gust, as a result of the flight path angle γ, as was previously concluded from 10-10. The gust in downward direction w_E is about 1 $[m/s]$. While the influence of gust is larger on the pitch angle when compared to the roll angle, it is still within 1 degree difference for the small turns simulation.

The small turns simulation, of appendix E results are displayed below in table 13-2 and figures 13-6 to 13-8. This simulation is a test for short-term performance with high turning dynamics. It was already concluded that IEKF results in slightly better results, compared to EKF. Also the presence of gust influences the results negatively. The state identification errors are the largest for this simulation as the simulated maneuver is the most dynamic of the three simulations. The position and velocity errors are of the same order of magnitude, compared to the generic and large turns simulation. For all simulations holds that the heading angle is the largest source of error for the orientation angles, also for the small turns simulation. Next the presence of gust has a large influence on the heading angle. The error in attitude angles, pitch and roll angle is smaller when compared to the heading angle, due to the better correcting function of the derived AC equations. From this can be concluded that the improved IMU/GPS configuration with the AC equations can provide an accurate short-term navigation solution during a small turns simulation.

The results of the large turn simulation of appendix F are displayed in table 13-3 and figures 13-9 to 13-11. This simulation takes about 40 minutes of simulated flight and is a test on long-term filter stability during very slow turning dynamics. From appendix F can be seen that the identification filter is able to remain stable over a long period of time. From table 13-3 can be seen that IEKF shows no significant improvement compared to EKF. Like for the generic and small turns simulation, the heading angle is the largest source of error for the three orientation angles. From a performance point of view, this simulation should result in the lowest identification errors. From the identification results of table 13-3 can be seen that this statement holds for the orientation angles. The difference in position and velocity identification results are small compared to the other two simulations. This is due to the fact that the identification performance on position and velocity states is mainly determined by the IMU and GPS receiver performance. From the results on the large turns simulation can be concluded that the improved IMU/GPS with AC equations sensor configuration is able to provide a stable and long-term navigation solution.

Table 13-1: Identification results generic simulation of appendix D

	EKF		IEKF	
states	gust	no gust	gust	no gust
x [m]	28.74 ± 4.85	4.30 ± 1.90	28.15 ± 5.76	4.37 ± 1.86
y [m]	8.70 ± 3.78	3.24 ± 1.98	8.57 ± 3.62	3.23 ± 1.96
z [m]	17.60 ± 3.78	2.31 ± 1.55	17.84 ± 4.65	2.34 ± 1.53
u [m/s]	2.28 ± 0.90	0.11 ± 0.15	2.33 ± 0.91	0.11 ± 0.13
v [m/s]	2.10 ± 1.08	1.69 ± 0.90	2.09 ± 1.41	1.80 ± 0.92
w [m/s]	1.32 ± 0.56	0.31 ± 0.23	1.38 ± 0.58	0.32 ± 0.20
ϕ [deg]	0.71 ± 0.73	0.48 ± 0.72	0.70 ± 0.76	0.49 ± 0.73
θ [deg]	1.49 ± 0.87	0.67 ± 0.58	1.55 ± 0.89	0.69 ± 0.57
ψ [deg]	6.14 ± 3.25	4.19 ± 2.38	6.39 ± 3.99	4.46 ± 2.44

Table 13-2: Identification results small turns simulation of appendix E

	EKF		IEKF	
states	gust	no gust	gust	no gust
x [m]	28.28 ± 5.14	5.11 ± 3.32	27.85 ± 6.05	5.29 ± 3.30
y [m]	10.25 ± 3.78	2.98 ± 2.26	10.15 ± 3.90	2.99 ± 2.26
z [m]	14.55 ± 3.54	6.10 ± 3.10	14.23 ± 3.47	5.67 ± 2.95
u [m/s]	2.32 ± 0.84	0.47 ± 0.52	2.36 ± 0.84	0.48 ± 0.55
v [m/s]	2.43 ± 2.79	1.53 ± 1.90	2.22 ± 2.25	1.56 ± 1.93
w [m/s]	2.08 ± 1.43	0.62 ± 0.96	1.85 ± 1.22	0.61 ± 0.97
ϕ [deg]	1.60 ± 1.79	1.55 ± 1.62	1.34 ± 1.69	1.49 ± 1.60
θ [deg]	2.60 ± 2.80	1.99 ± 1.97	2.09 ± 2.37	1.93 ± 2.00
ψ [deg]	8.53 ± 6.38	4.50 ± 5.49	8.50 ± 5.46	4.34 ± 5.50

Table 13-3: Identification results large turns simulation of appendix F

	EKF		IEKF	
states	gust	no gust	gust	no gust
x [m]	24.05 ± 5.16	6.24 ± 4.22	24.03 ± 5.20	6.25 ± 4.21
y [m]	5.02 ± 4.02	9.44 ± 7.01	5.02 ± 4.02	9.44 ± 7.01
z [m]	20.92 ± 12.64	11.14 ± 10.06	20.96 ± 12.66	11.17 ± 10.08
u [m/s]	1.84 ± 0.84	0.70 ± 0.59	1.84 ± 0.84	0.70 ± 0.59
v [m/s]	0.43 ± 0.25	0.41 ± 0.25	0.43 ± 0.25	0.41 ± 0.25
w [m/s]	1.73 ± 1.07	0.92 ± 0.84	1.72 ± 1.08	0.92 ± 0.85
ϕ [deg]	0.90 ± 0.60	0.65 ± 0.48	0.90 ± 0.60	0.65 ± 0.48
θ [deg]	1.00 ± 0.63	0.65 ± 0.49	1.03 ± 0.65	0.65 ± 0.49
ψ [deg]	4.02 ± 1.99	2.13 ± 1.54	4.01 ± 2.00	2.13 ± 1.54

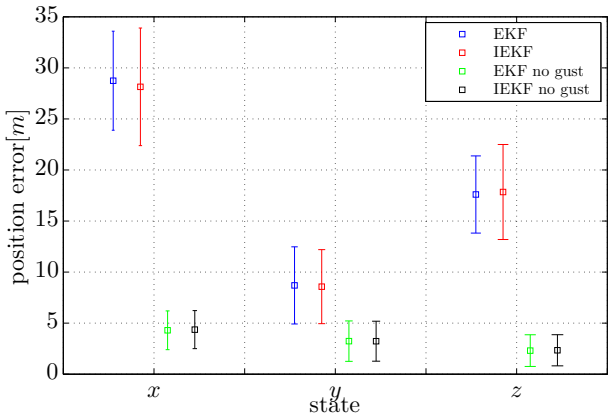

Figure 13-3: Error statistics for the position states, generic simulations

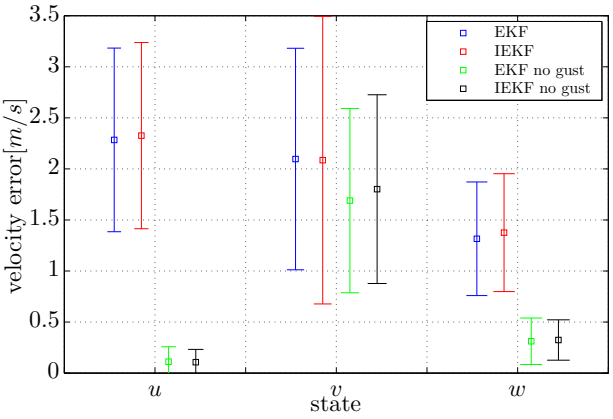

Figure 13-4: Error statistics for the velocity states, generic simulations

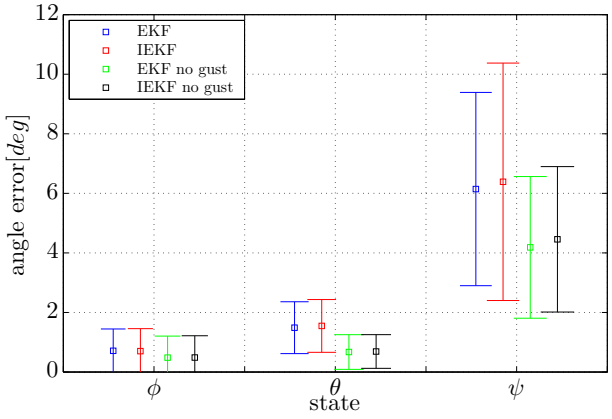

Figure 13-5: Error statistics for the attitude/heading states, generic simulations

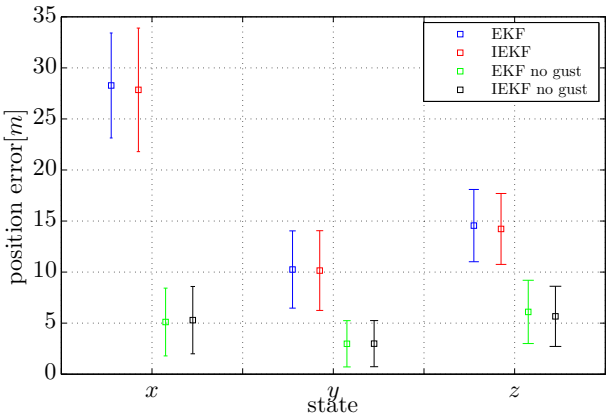

Figure 13-6: Error statistics for the position states, small turns simulations

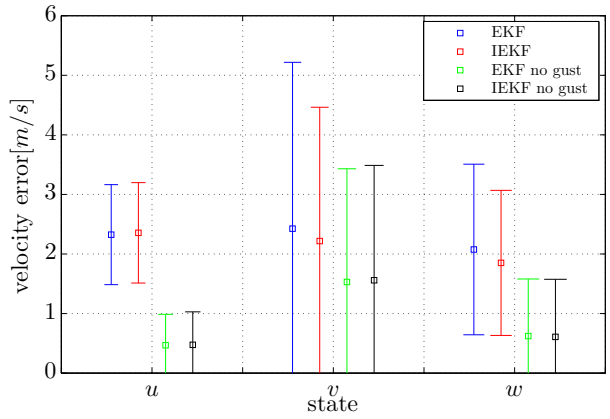

Figure 13-7: Error statistics for the velocity states, small turns simulations

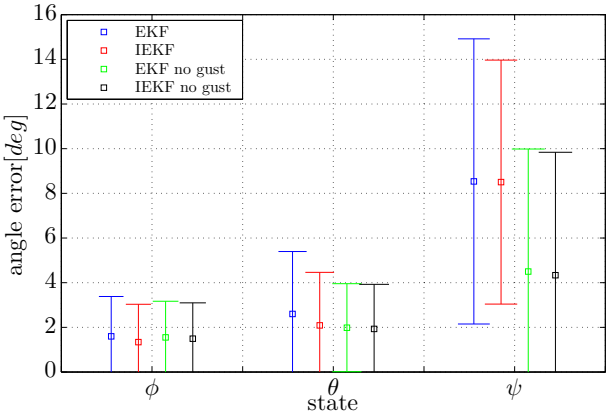

Figure 13-8: Error statistics for the attitude/heading states, small turns simulations

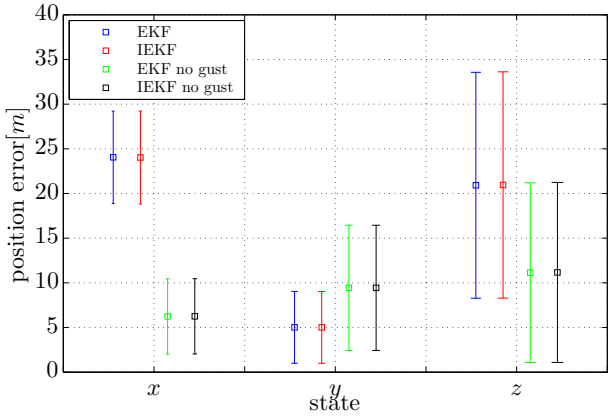

Figure 13-9: Error statistics for the position states, large turns simulations

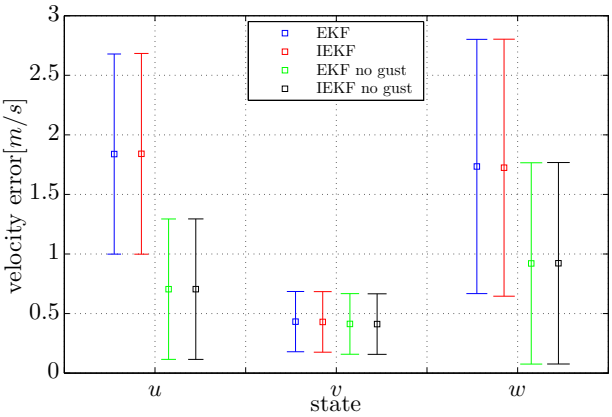

Figure 13-10: Error statistics for the velocity states, large turns simulations

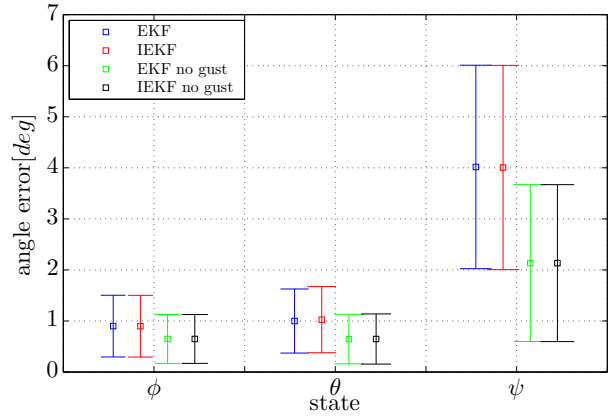

Figure 13-11: Error statistics for the attitude/heading states, large turns simulations

13-3 Identification Results of Flight Data

From the simulations of the previous section 13-2 was concluded that the improved IMU/GPS sensor configuration can provide an accurate and stable navigation filter. Based on the small turns simulation, an accurate short-term navigation solution can be provided during dynamic maneuvers. From the large turns simulation was concluded that the algorithm gives a long-term stable filter solution. The results of previous section are based on simulation, where the identification filter together with the IMU and GPS receiver are based on simulated signals. The advantage of using simulations is that all information is available, and the performance of the identification algorithms can easily be determined. This section uses real flight test data to determine the IMU/GPS sensor configuration performance. The flight test data can be found in appendix G together with the identification results, using EKF and IEKF. The results on the SO(3) identification filter are treated in chapter 14. The performance of the (I)EKF identification is analyzed together with the Xsens' onboard algorithm output. The difference between the Xsens output is a measure for performance, it is not the absolute performance as the Xsens is not a perfect sensor package. The difference is a function of errors in the Xsens output and identification errors of the improved IMU/GPS algorithm. Besides the difference in performance, the used flight data sets do not contain all the recorded data. The data was recorded at 100Hz, however during the post processing it turned out that not every recorded line could be used. During the post processing a "checksum" of each recorded line is performed, where each line is scanned to see if all recorded bites are correct and accounted for. The post processing resulted in about 25% of useful recorded data lines.

Differences in flight maneuvers between the simulation of section 13-2 and the recorded flight logs are visible. During the test flight, the roll angle can become larger or smaller then 90 degrees. During such maneuvers the derived expression for the roll angle no longer holds, as the assumption that the specific force in Z_B-direction including the gravity force is pointing downwards, is no longer valid. When the measured specific force A_z by the accelerometers has a positive value meaning the specific force is in upward direction. As a result the roll angle centripetal force, calculated by $\arctan\left(\frac{A_y}{A_z}\right)$, lays in a quadrant above the aircraft. Expression 13-9 gives the AC equation for roll angles larger then 90 degrees. The same can be done for roll angles smaller then -90 degrees, resulting in expression 13-10. The specific force measurement in downward direction A_z, provided by the onboard IMU acts as the trigger together with the specific force in lateral direction A_y. A positive A_z with a positive A_y should use expression 13-10. During maneuvers with positive A_z with negative A_y expression 13-9 should be used.

$$\hat{\phi}_{>90^\circ} = \frac{\sqrt{u_{GPS}^2 + v_{GPS}^2 + w_{GPS}^2}}{g_0} r + \arctan\left(\frac{A_y}{A_z}\right) + \pi \tag{13-9}$$

$$\hat{\phi}_{<-90^\circ} = \frac{\sqrt{u_{GPS}^2 + v_{GPS}^2 + w_{GPS}^2}}{g_0} r + \arctan\left(\frac{A_y}{A_z}\right) - \pi \tag{13-10}$$

Like for the roll angle, the pitch angle AC expression is also based on Euler angles and also has the $\pm 90^\circ$ singularity. During one of the performed test flights, LOG00042 of appendix section G-2 the pitch angle reaches $\pm 90^\circ$, due to fast climbing and descending. The same quadrant correction as for the roll angle is required. If the magnitude of the specific force in

forward direction A_x becomes equal to the gravitational constant, the pitch angle becomes larger then 90 degrees.

From the results of table 13-4 and figure 13-12 can be seen that the difference between the Xsens and IEKF is smaller, compared to Xsens and EKF. It was concluded in the previous section 13-2 that the IEKF performs better due to the partially compensation of non-linearities in the observer dynamics. Based on the smaller difference between IEKF and Xsens, it can be concluded that this is also the case for the performed simulation of the log files of appendix G. The identification results of the orientation angles can be analyzed with the output of the Xsens onboard identification filter. This does not hold for the estimated position and velocity states, with one exception being the height. From the figures in appendix G can be seen that the predicted height z_B is equal to the barometer height during all phases of flight. From the simulations of the previous section 13-2 was concluded that the heading angle is the largest source of error of the three orientation angles. From table 13-4 can be seen that this is also the case for the used flight test log files. The larger error in orientation angles compared to the simulation of the previous chapter comes from the fact that no innovation is present during the first 400 to 600 samples. This is due to the lack of a GPS fix, this aspect is not included during the simulation of previous section. If is the first simulation part is not taken into account, the result would be closer to the simulation results of the previous section 13-2.

As a general remark it should be mentioned that the identification differences between Xsens and (I)EKF results is also due to the fact that the (I)EKF simulations could only use 25% of the measurement data. If more data points would be used, the performance would probably improve.

Table 13-4: Identification results, indicated values are the differences between the simulation and onboard Xsens of appendix G

	LOG00039		LOG00042		LOG00050	
states	EKF	IEKF	EKF	IEKF	EKF	IEKF
ϕ [deg]	6.49 ± 7.12	5.26 ± 6.26	8.91 ± 9.90	6.99 ± 8.31	6.65 ± 6.70	4.81 ± 5.91
θ [deg]	3.82 ± 4.07	2.47 ± 3.03	6.50 ± 9.29	4.24 ± 5.31	3.42 ± 3.66	2.40 ± 3.30
ψ [deg]	19.06 ± 15.27	18.48 ± 14.87	25.02 ± 30.39	28.33 ± 33.04	33.45 ± 33.95	31.92 ± 34.36

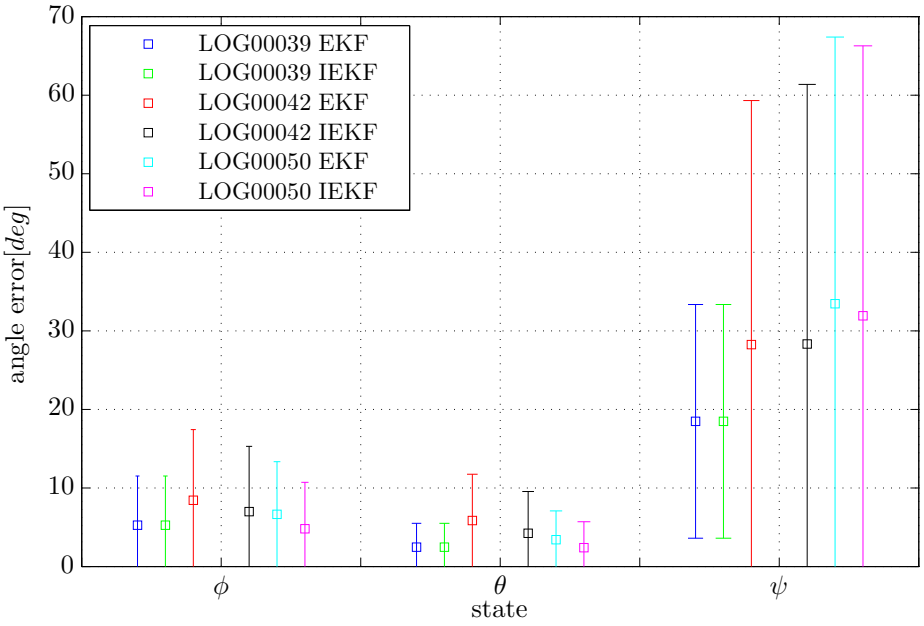

Figure 13-12: Error statistics for the attitude/heading states, flight data files

Chapter 14

Complementary Filter on the Special Orthogonal Group

Previous chapter 13 showed the results on the improved IMU/GPS sensor configuration by using conventional (I)EKF identification algorithms. This chapter does the same, only with a different type of identification filter. The applied filter is the non-linear complementary filter on the special orthogonal group. The special orthogonal group with dimension three is called $SO(3)$. The $SO(3)$ group is the transformation matrix R_{BE} between a body-fixed $\mathcal{F}_B$ and Earth frame of reference $\mathcal{F}_E$. Section 14-1 describes the background of the filter framework and unique properties of the $SO(3)$ group. The simulation results of appendix D to F can be found in section 14-2. The last section 14-3 contains the identification results using real flight data of appendix G.

14-1 Non-linear Complementary Filter on the SO(3) Group

Traditional filtering makes use of (Extended) Kalman filters although they perform well, it is proposed to apply a different approach into identification filters, namely by using non-linear complementary filtering. Non-linear filters retain the non-linear system dynamics, compared to Kalman filters that require Jacobians for linearization. Non-linear observers are especially useful since they keep non-linear observer dynamics. The complementary filters that are described in the work of Mahony, exploit the use of deterministic observer kinematics posed on a special Lie group, called Special Orthogonal Group or $SO(3)$. Recent work of Mahony can be found in (Mahony & Hamel, 2008) and (Mahony, Hamel, & Pflimlin, 2005). This $SO(3)$ group represents the rotational transformation matrix R_{BE} between a body-fixed $\mathcal{F}_B$ and an Earth reference frame $\mathcal{F}_E$. This rotational matrix equals the Direction Cosine Matrix (DCM) of chapter 8 and contains relative vehicle attitude and heading information between the two reference frames that can be used for navigational purposes.

Three types of complementary filters can be used, figure 14-1 gives an impression of a general non-linear observer on $SO(3)$. The factor k represents a proportional controller gain which

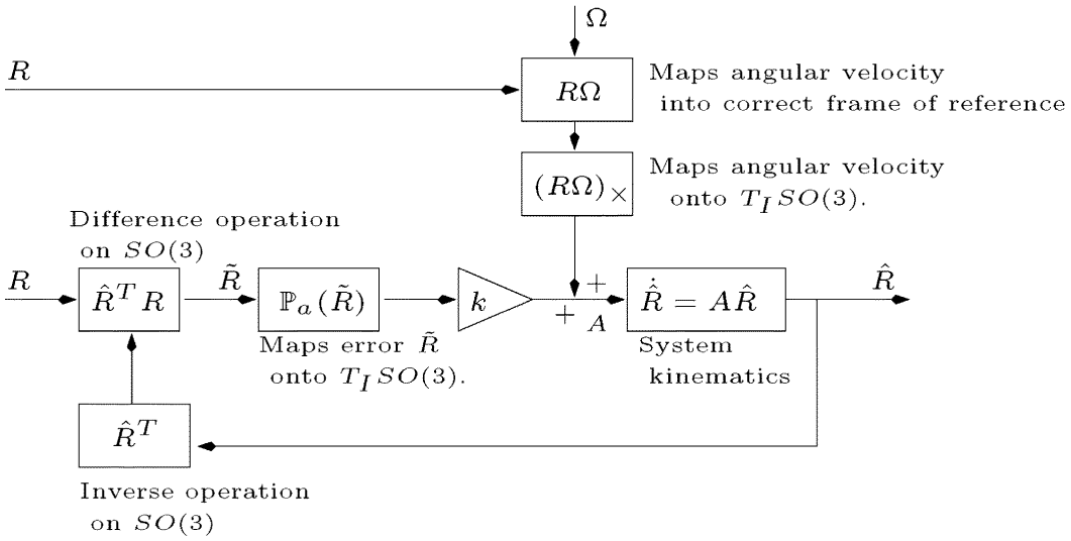

Figure 14-1: General form of a complementary filter on $SO(3)$

can be extended to a PID to include an integrator and differentiator. Passive and direct complementary filters uses the reconstructed measurement matrix R directly on the $SO(3)$ geometry from sensor outputs to express the estimation error matrix $\tilde{R}$. Differences between passive and direct complementary filtering are in the reconstruction steps. The third type of filter is the explicit complementary filter which uses the direct and untreated sensor measurements, where the relative contribution of individual sensors can be adjusted by using different weights of the proportional gain vector $\underline{k}$. All three mentioned types of complementary filters are based on figure 14-1. Equation 14-1 gives the kinematic equation, where $R \, \epsilon \, \mathbb{R}^{3\times3}$ is the DCM matrix and $\dot{R}$ is the time derivative, to calculate the next estimate. The anti-symmetric matrix $\Omega \, \epsilon \, \mathbb{R}^{3\times3}$ denotes the rotational matrix containing the measured angular rates $[p, q, r]$ from gyroscopic sensors.

$$\dot{R} = R\Omega \tag{14-1}$$

The $SO(3)$ group has some special properties, the associated Lie-algebra is a set of anti-symmetric matrices. To explain the Lie-algebra, the matrix $A \, \epsilon \, \mathbb{R}^{3\times3}$ is taken as an example. One special property is that the negative of the matrix transpose is equal to A, as given in equation 14-2.

$$SO(3) = \left\{ A \, \epsilon \, \mathbb{R}^{3x3} | A = -A^T \right\} \tag{14-2}$$

Two special matrix operators are included in the complementary filter of figure 14-1, which are also present when using passive, direct or explicit complementary filters. The operator vex: $SO(3) \rightarrow \mathbb{R}^3$ represent the inverse of the Ω_{X} operator. For any three dimensional vector $\underline{v} \, \epsilon \, \mathbb{R}$ holds $\Omega_{\mathrm{X}} v = \Omega \times v$, is the vector crossproduct as defined in equation 14-3.

$$\begin{aligned} \mathrm{vex}\,(\Omega_x) &= \Omega, \quad \Omega \, \epsilon \, \mathbb{R}^3 \\ \mathrm{vex}\,(A)_x &= A, \quad A \, \epsilon \, SO(3) \end{aligned} \tag{14-3}$$

The following expression 14-4 gives the *vex* operator on the skew-symmetric matrix Ω that holds the vehicle's rotational rates. This operator can be used to extract the off-diagonal terms, in this case representing the rotational angles of rotational vector $\underline{\omega} = [\omega_1(t)\omega_2(t)\omega_3(t)]^T$.

$$\Omega\left[\underline{\omega}(t)\right] = \begin{bmatrix} 0 & -\omega_3(t) & \omega_2(t) \\ \omega_3(t) & 0 & -\omega_1(t) \\ -\omega_2(t) & \omega_1(t) & 0 \end{bmatrix}, \qquad \text{vex}\left(\Omega\left[\underline{\omega}(t)\right]\right) = \begin{bmatrix} \omega_1(t) \\ \omega_2(t) \\ \omega_3(t) \end{bmatrix} \tag{14-4}$$

The second matrix operator $\mathbb{P}_a(\tilde{R})$, the skew-symmetric projection operator in matrix space, is defined in equation 14-5. This projection matrix operator, projects the skew-symmetric error matrix $\hat{R}$ into square matrix space. This operation is required to obtain the individual rotational error elements using the *vex* operator of expression 14-3. The obtained results of these two expression 14-3 and 14-5: $vex\left[\frac{1}{2}\left(H - H^T\right)\right]$ gives the three rotational errors element of expression 14-4: $[\omega_{e_1}(t), \omega_{e_2}(t), \omega_{e_3}(t)]^T$, written out in expression 14-6.

$$\mathbb{P}_a(H) = \frac{1}{2}\left(H - H^T\right) \tag{14-5}$$

$$\mathbb{P}_a(H) = \frac{1}{2}\left(\begin{bmatrix} 0 & \omega_{e_3}(t) & -\omega_{e_2}(t) \\ -\omega_{e_3}(t) & 0 & \omega_{e_1}(t) \\ \omega_{e_2}(t) & -\omega_{e_1}(t) & 0 \end{bmatrix} - \begin{bmatrix} 0 & -\omega_{e_3}(t) & \omega_{e_2}(t) \\ \omega_{e_3}(t) & 0 & -\omega_{e_1}(t) \\ -\omega_{e_2}(t) & \omega_{e_1}(t) & 0 \end{bmatrix}\right) \tag{14-6}$$

Expression 14-6 results in expression 14-7.

$$\mathbb{P}_a(H) = \begin{bmatrix} 0 & 0 & \omega_{e_2}(t) \\ \omega_{e_3}(t) & 0 & 0 \\ 0 & \omega_{e_1}(t) & 0 \end{bmatrix} \tag{14-7}$$

Next step after the $\mathbb{P}_a(\tilde{R})$ operator, is to multiply the error elements time a proportional gain vector $\underline{K_P}$ where each element can tuned individually. The obtained error can also be integrated to make a bias estimation. The goal of the estimated attitude matrix $\hat{R}\ \epsilon\ SO(3)$ is to be equal or as close to the real rotational matrix R. The estimation can be multiplied with the transpose, equal to its inverse according to equation 14-2, which should approach an identity matrix I_3. This multiplication provides the estimation error matrix $\tilde{R}$ as given in expression 14-8.

$$\tilde{R} = \hat{R}^T R \ \rightarrow \ I_3 \tag{14-8}$$

The matrix operator $\mathbb{P}_a$ is performed on the error matrix $\tilde{R}$, the off-diagonal terms should converge to zero and the matrix should approach the identify matrix I_3 when the difference between the estimated attitude $\hat{R}$ and true value of matrix R becomes smaller. Expression 14-8 can be reformulated into equation 14-9 to clearly indicate that the estimation error matrix

$\tilde{R}$ converges to the identity matrix I_3, when the estimated attitude matrix $\hat{R}$ approaches the true value of matrix R.

$$\hat{R} \ \rightarrow \ R \Leftrightarrow \tilde{R} \ \rightarrow \ I_3 \tag{14-9}$$

As a result of expression 14-9, the complementary non-linear filter design can be simplified to find the correct kinematics of $\hat{R}$ such that $\tilde{R} \rightarrow I_3$. The non-linear Passive Complementary Filter (PCF) can be summarized in expression 14-10, from (Mahony & Hamel, 2008). The matrix R_{AC} indicates the innovation rotational matrix, based on the derived AC equations of chapter 10.

$$\begin{aligned} \dot{\hat{R}} &= \hat{R}\left[\Omega + \underline{\hat{b}} + \underline{\omega}_e\right] \\ \underline{\omega}_e &= \underline{K}_P \text{vex}\left[\mathbb{P}_a(\tilde{R})\right] \\ \underline{\hat{b}} &= \underline{K}_I \int \underline{\omega}_e \\ \tilde{R} &= \hat{R}^T R_{AC} \end{aligned} \tag{14-10}$$

The bias estimation $\underline{\hat{b}}$ is a function of the IMU gyroscopes together with the observer error, in this case based on the AC equations. The gain vectors $\underline{K}_P$ and $\underline{K}_I$ can be tuned individually. High gains means large corrections on the gyroscopes input matrix Ω, low gains means less innovation or influence of the R_{AC} matrix. Figure 14-2 shows the block diagram of the passive complementary filter on $SO(3)$.

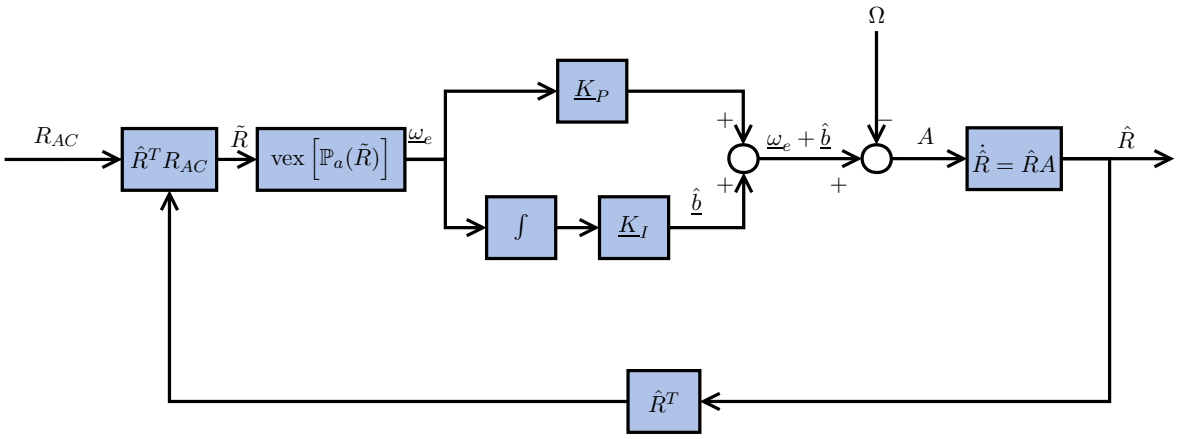

Figure 14-2: Block diagram of the passive complementary filter on $SO(3)$

14-2 Simulation Results Filter on the SO(3) Group

This section uses the non-linear complementary filter on the Special Orthogonal group $SO(3)$. This identification filter differs from the 9 state (I)EKF of previous chapter 13. Instead of having 9 state equations and 9 observers, the $SO(3)$ utilizes special matrix properties and associated Lie-algebra. Based on special matrix properties, the transformation matrix R_{BE} that holds all vehicle attitude and heading information between a body-fixed $\mathcal{F}_B$ and an Earth frame of reference $\mathcal{F}_E$, is used as a single matrix state. In principle this is the only required navigation information to stabilize an aircraft as all three orientation angles are available. While other filters, like for instance the 9 state filter of section 12-2, provide additional position and velocity information, only the three orientation angles are required to stabilize a fixed-wing UAV. Expression 14-11 gives the input matrix Ω, containing the three rotational rates p, q and r which are provided by the gyroscopes.

$$\Omega = \begin{bmatrix} 0 & -r & q \\ r & 0 & -p \\ -q & p & 0 \end{bmatrix} \tag{14-11}$$

The residual matrix $\tilde{R}$, as displayed in figure 14-2, is calculated by multiplying the estimation matrix $\hat{R}$ with a correction matrix R_{AC}. Where R_{AC} is based on the three AC equations. Expression 14-12 gives the definition of the R_{AC} matrix, based on the three AC observers.

$$R_{AC}\left(\phi_{AC}, \theta_{AC}, \psi_{AC}\right) = \begin{bmatrix} \cos\theta_{AC}\cos\psi_{AC} & \sin\phi_{AC}\sin\theta_{AC}\cos\psi_{AC} - \cos\phi_{AC}\sin\psi_{AC} & \cos\phi_{AC}\sin\theta_{AC}\cos\psi_{AC} + \sin\phi_{AC}\sin\psi_{AC} \\ \cos\theta_{AC}\sin\psi_{AC} & \sin\phi_{AC}\sin\theta_{AC}\sin\psi_{AC} + \cos\phi_{AC}\cos\psi_{AC} & \cos\phi_{AC}\sin\theta_{AC}\sin\psi_{AC} - \sin\phi_{AC}\cos\psi_{AC} \\ -\sin\theta_{AC} & \sin\phi_{AC}\cos\theta_{AC} & \cos\phi_{AC}\cos\theta_{AC} \end{bmatrix} \tag{14-12}$$

The sensor configuration of expressions 14-11 and 14-12 uses the angular rates of the gyroscopes to provide an estimate. The AC equations provide the innovation matrix to correct any errors by the gyroscopic prediction. Like for the conventional (I)EKF filters, the simulations of appendix D to F are used to analyze the performance and stability of the $SO(3)$ filter. The time history for all simulations can be found in the appendices, the results are summarized in table 14-1 and figures 14-3 to 14-5 below.

Due to the multiplication and (co)sine operators on the attitude/ heading angles in the estimation matrix $\hat{R}$, the three individual angles have a strong correlation. This strong correlation is also present in the simulation results. The small turns simulation contains maneuvers that are the most dynamic. From table 14-1 and figure 14-4 can be seen that the difference in identification result is smaller for each individual orientation angle. From the simulation results of chapter 13 was concluded that the heading has the largest error when compared to the pitch and roll angle. This also holds for the $SO(3)$ filter, however the difference between the heading and attitude angles is smaller. The strong correlation between the three angles has a positive influence on the heading angle. The latter is also partly the reason that the identification results on the pitch and roll angles are different compared to the Kalman filter. The most important reason for the difference in identification results with

respect to Kalman filters are the gains. The $SO(3)$ filter uses constant gains $\underline{K_P}$ and $\underline{K_I}$, compared to the Kalman gain $K(k)$ where process and observer uncertainties are taken into account. Uncertainties in position and velocity states, result in larger entries of the covariance matrix $P(k|k)$. The larger position and velocity uncertainties result in lower Kalman gains. The position and velocity Kalman gains are a function of their process uncertainties in the covariance matrix calculation. Also the influence of gust is larger on the position and velocity states, compared to the attitude/heading angles. Since the $SO(3)$ filter does not need the position and velocity states, the influence of gust is less on the pitch and roll angle. The influence of gust remains strongly present on the heading angle. The presence of gust results in a side-slip angle β, as the gyroscopic prediction differs form the real ground track. The small turns simulation together with the generic simulation provides accurate identification results. This holds during and without the presence of gust. Based from this can be concluded that the $SO(3)$ filter can provide an accurate short-term solution during dynamic maneuvers.

From the large turns simulation of appendix F can be seen that the $SO(3)$ filter remains stable over a long period of time. The maneuver of a very slow left and right turn can be estimated by the $SO(3)$ filter and remains stable during the simulation. Like for the generic and small turns simulations, the heading angle is also the largest source of error during the large turns simulation. The identification performance of the pitch and roll angle is comparable to that of the generic simulation, the heading angle is slightly better estimated. Based on this can be concluded that the $SO(3)$ filter can provide a stable long-term identification filter. Also the influence of gust on the heading angle is smaller compared to the (I)EKF identification results of table 13-3 due to the strong coupling of the three orientation angles.

Table 14-1: Identification results non-linear $SO(3)$ filter

	Generic		Small turns		Large turns	
states	gust	no gust	gust	no gust	gust	no gust
ϕ [deg]	1.29 ± 0.98	1.25 ± 0.87	3.79 ± 3.34	3.55 ± 3.33	1.31 ± 0.85	1.29 ± 0.84
θ [deg]	1.21 ± 0.82	1.16 ± 0.77	5.37 ± 4.07	5.71 ± 4.24	0.92 ± 0.59	0.89 ± 0.55
ψ [deg]	6.42 ± 5.36	5.00 ± 2.76	8.53 ± 7.05	7.90 ± 7.47	3.95 ± 1.85	2.50 ± 1.89

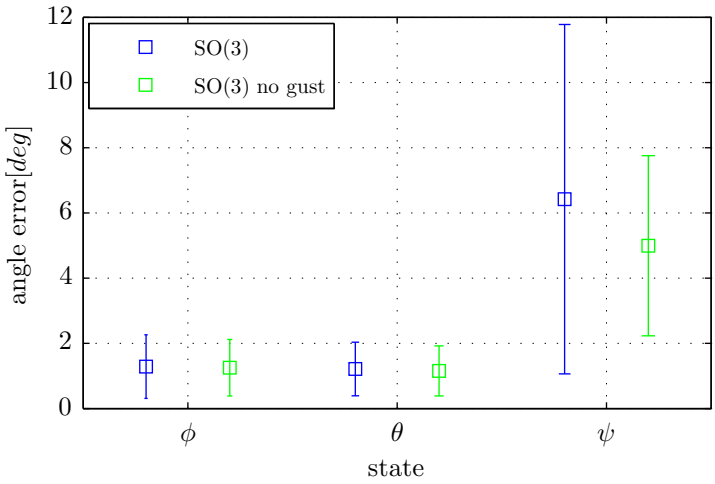

Figure 14-3: Error statistics for the attitude/heading states, generic simulations

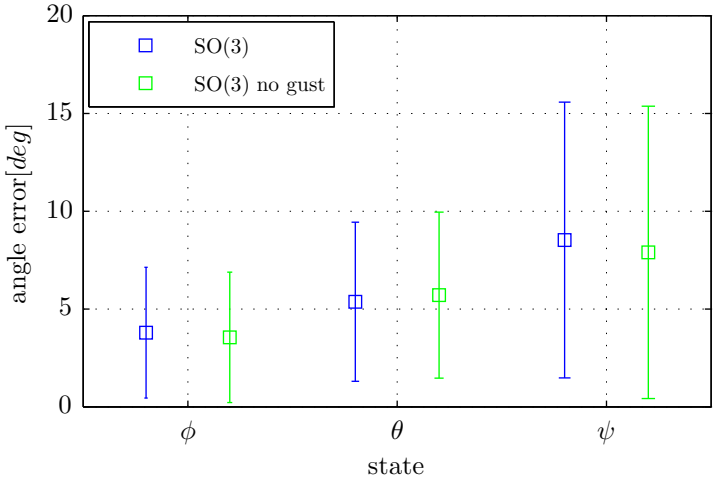

Figure 14-4: Error statistics for the attitude/heading states, small turns simulations

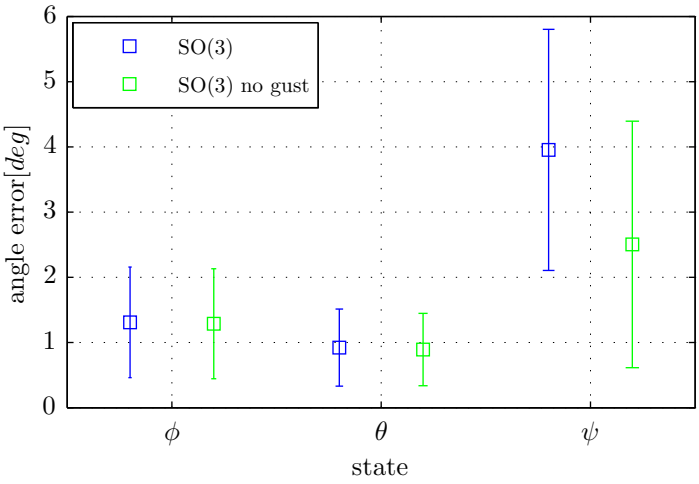

Figure 14-5: Error statistics for the attitude/heading states, large turns simulations

14-3 Flight Data Results Filter on the SO(3) Group

From the simulations of the previous section 14-2 was concluded that the improved IMU/GPS sensor configuration can provide an accurate and stable identification by using a non-linear $SO(3)$ filter. Based on the results of the small turns simulation, it was concluded that an accurate short-term solution during the presence of high vehicle dynamics can be provided. The large turns simulation showed that the $SO(3)$ filter does not only provide an accurate, but also a long-term stable solution. The results of the previous section 14-2 are based on simulations, using simulated IMU and GPS receiver signals, which were fed into the $SO(3)$ identification filter. This section will analyze the $SO(3)$ filter performance on the improved IMU/GPS sensor configuration by using real flight data. The flight data can be found in appendix G with the identification results using $SO(3)$ together with the (I)EKF results. The performance of the $SO(3)$ filter is analyzed together with the Xsens' onboard algorithm and the (I)EKF results of previous chapter 13. As explained in chapter 13, during the performed test flight the pitch and roll angles can become larger and smaller than 90 degrees. The same $\pm 90^\circ$ Euler angle singularity compensation as in expressions 13-9 and 13-10 is applied. The difference between the identification output of the $SO(3)$ and the onboard Xsens filter is not the exact identification error, as the onboard Xsens algorithm also contains errors. Besides any differences in performance, it should be noted that only 25% of the recorded data lines can be used. The performed post processing "sumcheck" routine called on the flight data files resulted in 25% of complete recorded lines.

The identification results can be found in appendix G and summarized in table 14-2 and figure 14-5 below. As a general result it can be concluded that the $SO(3)$ identification results differ more with the Xsens output compared to the (I)EKF results. From this can be concluded that the $SO(3)$ filter gives less accurate results when compared the (I)EKF identifications. From the simulations of previous section 14-2 was already concluded that the heading angle is the least accurate orientation angle. The strong coupling between the three angles can lead to less accurate pitch and roll angle estimations due to a larger heading angle estimation error. As a result of this strong coupling the pitch and roll angle are estimated less accurate, due to the heading angle.

The estimation differences are the largest for logfile LOG00042, which is also the case for the (I)EKF simulations. The larger difference in $SO(3)$ estimation results and Xsens are due to the larger presence of gust. From the trajectories flown in figure G-1 for LOG00039, figure G-15 for LOG00042 and figure G-29 for LOG00050 can be seen that the flown circles are drifting away for LOG00042. The movement of the circles' middle points of the flown circular trajectory indicates the strong presence of gust. The strong presence of gust results in a large side-slip angle β. This angle has a negative influence on the heading angle estimation. This explains the larger error, also present for the (I)EKF identifications. Due to the strong coupling of the attitude angles with the heading angles via the estimation matrix R, the bad heading angle estimation also results in worse pitch and roll angle estimations. From this can be concluded that due to the strong internal coupling of the $SO(3)$ filter, the least accurate angle estimation influences the other angles. During maneuvers with fast vehicle dynamics or presence of gust, the badly estimated heading angle results in less accurate pitch and roll attitude angles.

Table 14-2: Identification results non-linear $SO(3)$ filter, indicated values are the differences between the simulation and onboard Xsens

states	LOG00039	LOG00042	LOG00050
ϕ [deg]	8.88 ± 7.23	12.23 ± 14.39	7.51 ± 8.31
θ [deg]	6.04 ± 6.10	6.56 ± 6.72	5.61 ± 8.33
ψ [deg]	22.55 ± 18.36	30.36 ± 27.21	23.99 ± 28.13

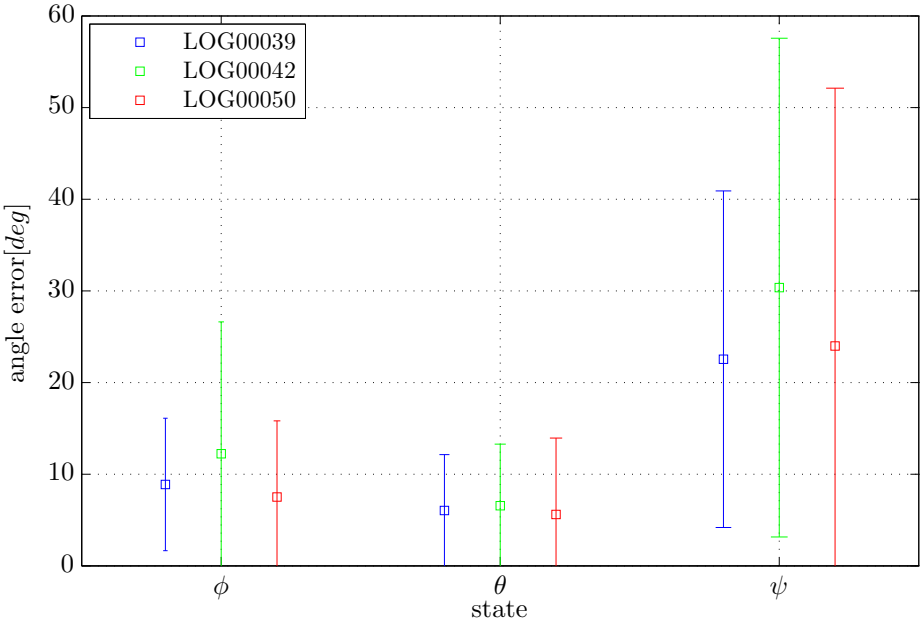

Figure 14-6: Error statistics for the attitude/heading states, flight data files

Part V

Conclusions and Recommendations

Chapter 15

Conclusions

From the performed theoretical observability and physical analyses, the following conclusions can be drawn:

- From the analytical observability analysis can be concluded that the observability of observable system states is not influenced during zero acceleration maneuvers $\underline{A} = 0$, as long as the GPS receiver remains to have a fix. When a flying vehicle is equiped with an integrated IMU/GPS configuration, the IMU receives no acceleration information from the accelerometers during zero acceleration maneuvers. The GPS position and velocity can be used to identify the position and velocity states.
- During zero rotational rate maneuvers $\underline{\omega} = 0$, the heading angle ψ together with all three accelerometer biases (b_{A_x}, b_{A_y}, b_{A_z}) become unobservable due to zero entries in the transformation matrix R_{BE}, needed to transform states from an Earth reference frame to a body-fixed frame of reference. The required attitude/ heading angles for the R_{BE} matrix to integrate the GPS velocity and position with IMU measurements are zero. This is concluded from the observability analysis where the input signals of IMU gyroscopes have been put to zero. In practice the input signals never become exactly zero and these states become badly observable depending on the closeness to zero and sensor noise.
- The derived angle correction (AC) equations from the physical analysis can improve a loosely coupled IMU/GPS configuration significantly in terms of state observability. The zero rotational rate maneuver constraint $\underline{\omega} = 0$, is no longer present and the heading angle becomes instantaneously observable. The AC equations utilize fixed-wing kinematics together with an onboard IMU and GPS receiver.

The performed studies have led to the development of three AC equations, resulting in instantaneously observable orientation angles and looseness of the zero rotation rate maneuver $\underline{\omega} = 0$ constraint. The theoretical results can be used as a starting point, based on the performed simulations and analysis of different state identification filters the following conclusion can be made:

- The influence of a time synchronization error Δt between individual sensors during sensor fusion, is a function of the change in vehicle acceleration $\underline{a}'$ and filter innovation. The time synchronization requirement is proportional to the magnitude of $|\underline{a}'|$ and negatively proportional to the magnitude of the filter innovation. Vehicles with fast dynamics, like fixed-wing UAV's, require a more stringent time synchronization requirement as the vehicle's acceleration can suddenly change with large magnitudes. When using low-cost, low-grade sensors with low frequency GPS receiver corrections, the innovation magnitude can increase. Larger innovation magnitudes are due to the low-update frequency of the GPS receiver, required for the innovation part. Larger innovation magnitudes can result in a less stringent time synchronization requirement, as they are negatively proportional. From this can be concluded that the time synchronization requirement becomes less important with low-cost sensors and is a compromise between changes in vehicle acceleration and filter innovation.

- Different simulations were performed to test the improved IMU/GPS sensor integration with AC equations. Based on the performed simulations, it can be concluded that the improved IMU/GPS sensor integration with AC equations can provide a stable long-term navigation solution with accurate short-term performance. During all simulations the position states give the largest source of estimation error, due to the large GPS position uncertainty. From the observability analysis was concluded that the wind components are unobservable and the position and velocities states are influenced during the presence of wind. The position and velocity estimations are effected the most by the wind components as the wind velocities are not part of the specific forces measured by the onboard IMU accelerometers. The largest source of error of the orientation angles, is the heading angle. For the orientation angles, the influence of wind on the identification performance is minimal except for the heading angle due to the presence of a side-slip angle β.

- The performed simulations show that the convergence of the Iterated Extended Kalman Filter (IEKF) identification algorithm is slightly better compared to the Extended Kalman Filter (EKF). The improvement is however not significant because the observer non-linearities are not the largest source of error, both algorithms show stable and accurate results. From this can be concluded that their is no need to reiterate the observer dynamics and the EKF identification algorithm should be chosen over the IEKF as it requires less computational power.

- The non-linear complementary filter on the Special Orthogonal group, $SO(3)$ filter, can be used as an alternative to conventional Kalman state identification filters. The special orthogonal group uses the transformation matrix R_{BE} between the body-fixed $\mathcal{F}_B$ and Earth reference frame $\mathcal{F}_E$. The transformation matrix is used as a single filter state. For (I)EKF filters, the heading angle is the largest source of error, which is also the case for the $SO(3)$ filter. This filter can be used as an alternative, any differences

in filter results are due to two aspects. The $SO(3)$ filter uses constant proportional and integrator gains, where the Kalman gain matrix $K(k)$ is based on process and observer uncertainties. The other source of differences is due to the strong coupling of the individual attitude/heading angles for the $SO(3)$ filter compared to (I)EKF.

- The developed Aerosonde UAV model is able to provide adequate fixed-wing UAV simulations with fast dynamics. Together with the IMU and GPS receiver simulations, realistic sensor simulations can be made. The developed sensor simulation tools can be used to analyze different sensor configurations and identification algorithms. The thesis report aims to link the navigation requirements of fixed-wing UAV's to minimal INS/GPS sensor requirements. The observability analysis together with the simulation of a fixed-wing UAV, IMU and GPS receiver simulation tools provide powerful insight in the performance of different sensor configurations and state identification algorithms. With these developed tools, new configurations can be tested on short-term performance, long-term stability and time synchronization errors. These tools can be useful for future research into new implementations and sensor configurations.

Chapter 16

Recommendations

Research into integrated navigation applied to fixed-wing Unmanned Aerial Vehicles (UAVs) with fast dynamics, with low-cost sensors can be improved by addressing the following topics:

- *Research into different INS/GPS integrations.* The sensor integration that has been used throughout this report is the loosely coupled integration between inertial and satellite navigation systems. This integration is mostly used in applications, however are known to have time latencies between the GPS receiver and IMU signals. The GPS receiver has an internal processing filter to obtain a position fix, resulting in a position and velocity update. The IMU doesn't need such a processing step resulting in a different processing time. Other integrations like tightly coupled or deep integration use a single integration filter between a GPS receiver and IMU. Investigation into these integrations with a focus on time synchronization errors between the individual sensors and receivers should be performed. The use of a single integration filter can provide new insight and improvement on time synchronization errors. Another advantage of tight or deep integration over the loosely coupled integration is that it can also work when the number of visible GPS satellites drops below four or during jamming environments.

- *Using other UAV platforms.* The angle correction (AC) equations have been developed for fixed-wing UAV, utilizing fixed-wing aircraft kinematics. This concept could also be applied to other platforms like quadrotor, helicopter, flapping wing, VTOL, etc. If the vehicle kinematics differ however a lot, the derived set a kinematic AC equations should also be changed accordingly.

- *Controller design on the non-linear complementary $SO(3)$ filter.* The output of the complementary non-linear filter on the Special Orthogonal group or $SO(3)$, differs from traditional Kalman filters. The $SO(3)$ filter uses the rotational transformation matrix R_{BE} between a body-fixed $\mathcal{F}_B$ and an Earth reference frame $\mathcal{F}_E$, where the Kalman filter directly provides the attitude/ heading angles together with additional states. The controller design for a $SO(3)$ filter differs, an initial implementation with existing controllers can be performed by extracting the angles from the R_{BE} matrix. This transformation can however be replaced by a controller that directly uses the transformation

matrix R_{BE}. A coupled matrix controller and $SO(3)$ filter should be able to provide better closed loop performance.

- *Implementation using real hardware.* Before the IMU/GPS sensor configuration with derived AC equations can be implemented in an onboard environment, an autopilot must be designed that can cope with uncertainties from the state estimation. Also the Direction Cosine Matrix (DCM) angle representation should be converted to quaternions. The physical meaning of Euler angles vanishes when using a quaternions representation, the advantage is that less calculation is required during each update. The DCM representation contains 9 matrix entries, when using quaternions only 4 elements are updated at each epoch.

- *Unobservable gust states.* To solve the large position and velocity estimation error problem, additional sensors are required to make the distinction between IMU prediction errors and wind velocities. The sole use of GPS velocities can correct the IMU velocity prediction, but these corrections are however insufficient to see any differences between IMU errors or wind velocities. When three air data sensors are added to measure the angle of attack α, side-slip angle β and total velocity V_T, a redundant set of all three velocity components is present. This set of additional velocity measurements can be used to identify any differences in velocity estimation errors between IMU accelerometer biases and wind velocities.

- *GPS velocity derivatives.* Besides the assisting and correcting function of the GPS receiver to the IMU position and velocity prediction, the GPS velocities can also be used to correct the accelerometer biases or orientation angles. The GPS velocities can be differentiated to accelerations in an Earth-Centered-Earth-Fixed (ECEF) reference frame. The GPS accelerations in ECEF can be compared to the IMU accelerations in a body-fixed reference frame $\mathcal{F}_B$, when using the required transformation matrices.

Part VI

Appendices

Appendix A

Jacobians

Jacobians of the state equation for $\underline{x} = (x, y, z, u, v, w, \phi, \theta, \psi)$:

$$F = \frac{\partial \underline{f}\,(\underline{x}, \underline{u})}{\partial \underline{x}} = \begin{bmatrix}
0 & 0 & 0 & \cos\theta\cos\psi & \sin\phi\sin\theta\cos\psi - \cos\phi\sin\psi & \cos\phi\sin\theta\cos\psi + \sin\phi\sin\psi & (v\cos\phi - w\sin\phi)\sin\theta\cos\psi - (-v\sin\phi - w\cos\phi)\sin\psi & (-u\sin\theta + (v\sin\phi + w\cos\phi)\cos\theta)\cos\psi & -(u\cos\theta + (v\sin\phi + w\cos\phi)\sin\theta)\sin\psi - (v\cos\phi - w\sin\phi)\cos\psi \\
0 & 0 & 0 & \cos\theta\sin\psi & \sin\phi\sin\theta\sin\psi + \cos\phi\cos\psi & \cos\phi\sin\theta\sin\psi - \sin\phi\cos\psi & (v\cos\phi - w\sin\phi)\sin\theta\sin\psi + (-v\sin\phi - w\cos\phi)\cos\psi & (-u\sin\theta + (v\sin\phi + w\cos\phi)\cos\theta)\sin\psi & (u\cos\theta + (v\sin\phi + w\cos\phi)\sin\theta)\cos\psi - (v\cos\phi - w\sin\phi)\sin\psi \\
0 & 0 & 0 & -\sin\theta & \sin\phi\cos\theta & \cos\phi\cos\theta & (v\cos\phi - w\sin\phi)\cos\theta & -u\cos\theta - (v\sin\phi + w\cos\phi)\sin\theta & 0 \\
0 & 0 & 0 & 0 & r_m - b_r & -q_m + b_q & 0 & -g\cos\theta & 0 \\
0 & 0 & 0 & -r_m + b_r & 0 & p_m - b_p & g\cos\theta\cos\phi & -g\sin\theta\sin\phi & 0 \\
0 & 0 & 0 & q_m - b_q & -p_m + b_p & 0 & -g\cos\theta\sin\phi & -g\sin\theta\cos\phi & 0 \\
0 & 0 & 0 & 0 & 0 & 0 & (q_m - b_q)\cos\phi\tan\theta - (r_m - b_r)\sin\phi\tan\theta & (q_m - b_q)\sin\phi(1+\tan^2\theta) + (r_m - b_r)\cos\phi(1+\tan^2\theta) & 0 \\
0 & 0 & 0 & 0 & 0 & 0 & -(q_m - b_q)\sin\phi - (r_m - b_r)\cos\phi & 0 & 0 \\
0 & 0 & 0 & 0 & 0 & 0 & \frac{(q_m - b_q)\cos\phi}{\cos\theta} + \frac{(r_m - b_r)\sin\phi}{\cos\theta} & \frac{(q_m - b_q)\sin\phi}{\cos^2\theta}\sin\theta - \frac{(r_m - b_r)\cos\phi}{\cos^2\theta}\sin\theta & 0 \\
0 & 0 & 0 & 0 & 0 & 0 & 0 & 0 & 0 \\
0 & 0 & 0 & 0 & 0 & 0 & 0 & 0 & 0 \\
0 & 0 & 0 & 0 & 0 & 0 & 0 & 0 & 0 \\
0 & 0 & 0 & 0 & 0 & 0 & 0 & 0 & 0 \\
0 & 0 & 0 & 0 & 0 & 0 & 0 & 0 & 0 \\
0 & 0 & 0 & 0 & 0 & 0 & 0 & 0 & 0 \\
0 & 0 & 0 & 0 & 0 & 0 & 0 & 0 & 0 \\
0 & 0 & 0 & 0 & 0 & 0 & 0 & 0 & 0 \\
0 & 0 & 0 & 0 & 0 & 0 & 0 & 0 & 0
\end{bmatrix} \tag{A-1}$$

Jacobians of the state equation for $\underline{x} = (b_{A_x}, b_{A_y}, b_{A_z}, p_m, q_m, r_n, W_x, W_y, W_z)$:

$$F = \frac{\partial \underline{f}\,(\underline{x}, \underline{u})}{\partial \underline{x}} = \begin{bmatrix}
0 & 0 & 0 & 0 & 0 & 0 & 1 & 0 & 0 \\
0 & 0 & 0 & 0 & 0 & 0 & 0 & 1 & 0 \\
0 & 0 & 0 & 0 & 0 & 0 & 0 & 0 & 1 \\
-1 & 0 & 0 & 0 & w & -v & 0 & 0 & 0 \\
0 & -1 & 0 & -w & 0 & u & 0 & 0 & 0 \\
0 & 0 & -1 & v & -u & 0 & 0 & 0 & 0 \\
0 & 0 & 0 & -1 & -\sin\phi\tan\theta & -\cos\phi\tan\theta & 0 & 0 & 0 \\
0 & 0 & 0 & 0 & -\cos\phi & \sin\phi & 0 & 0 & 0 \\
0 & 0 & 0 & 0 & -\frac{\sin\phi}{\cos\theta} & \frac{\cos\phi}{\cos\theta} & 0 & 0 & 0 \\
0 & 0 & 0 & 0 & 0 & 0 & 0 & 0 & 0 \\
0 & 0 & 0 & 0 & 0 & 0 & 0 & 0 & 0 \\
0 & 0 & 0 & 0 & 0 & 0 & 0 & 0 & 0 \\
0 & 0 & 0 & 0 & 0 & 0 & 0 & 0 & 0 \\
0 & 0 & 0 & 0 & 0 & 0 & 0 & 0 & 0 \\
0 & 0 & 0 & 0 & 0 & 0 & 0 & 0 & 0 \\
0 & 0 & 0 & 0 & 0 & 0 & 0 & 0 & 0 \\
0 & 0 & 0 & 0 & 0 & 0 & 0 & 0 & 0
\end{bmatrix} \tag{A-2}$$

Jacobians of the GPS position:

$$H = \frac{\partial \underline{h}}{\partial \underline{x}} = \begin{bmatrix} 1 & 0 & 0 & 0 & 0 & 0 & 0 & 0 & 0 & 0 & 0 & 0 & 0 & 0 & 0 & 0 & 0 & 0 \\ 0 & 1 & 0 & 0 & 0 & 0 & 0 & 0 & 0 & 0 & 0 & 0 & 0 & 0 & 0 & 0 & 0 & 0 \\ 0 & 0 & 1 & 0 & 0 & 0 & 0 & 0 & 0 & 0 & 0 & 0 & 0 & 0 & 0 & 0 & 0 & 0 \end{bmatrix} \tag{A-3}$$

Jacobians of the GPS velocity for $\underline{x} = (x, y, z, u, v, w, \phi, \theta, \psi)$:

$$H = \frac{\partial \underline{h}}{\partial \underline{x}} = \begin{bmatrix} 0 & 0 & 0 & \cos\theta\cos\psi & \begin{matrix}\sin\phi\sin\theta\cos\psi \\ -\cos\phi\sin\psi\end{matrix} & \begin{matrix}\cos\phi\sin\theta\cos\psi \\ +\sin\phi\sin\psi\end{matrix} & \begin{matrix}(v\cos\phi - w\sin\phi)\sin\theta\cos\psi \\ -(-v\sin\phi - w\cos\phi)\sin\psi\end{matrix} & (-u\sin\theta + (v\sin\phi + w\cos\phi)\cos\theta)\cos\psi & \begin{matrix}-(u\cos\theta + (v\sin\phi + w\cos\phi)\sin\theta)\sin\psi \\ -(v\cos\phi - w\sin\phi)\cos\psi\end{matrix} \\ 0 & 0 & 0 & \cos\theta\sin\psi & \begin{matrix}\sin\phi\sin\theta\sin\psi \\ +\cos\phi\cos\psi\end{matrix} & \begin{matrix}\cos\phi\sin\theta\sin\psi \\ -\sin\phi\cos\psi\end{matrix} & \begin{matrix}(v\cos\phi - w\sin\phi)\sin\theta\sin\psi \\ +(-v\sin\phi - w\cos\phi)\cos\psi\end{matrix} & (-u\sin\theta + (v\sin\phi + w\cos\phi)\cos\theta)\sin\psi & \begin{matrix}(u\cos\theta + (v\sin\phi + w\cos\phi)\sin\theta)\cos\psi \\ -(v\cos\phi - w\sin\phi)\sin\psi\end{matrix} \\ 0 & 0 & 0 & -\sin\theta & \sin\phi\cos\theta & \cos\phi\cos\theta & (v\cos\phi - w\sin\phi)\cos\theta & -u\cos\theta - (v\sin\phi + w\cos\phi)\sin\theta & 0 \end{bmatrix} \tag{A-4}$$

Jacobians of the GPS velocity for $\underline{x} = (b_{A_x}, b_{A_y}, b_{A_z}, p_m, q_m, r_n, W_x, W_y, W_z)$:

$$H = \frac{\partial \underline{h}}{\partial \underline{x}} = \begin{bmatrix} 0 & 0 & 0 & 0 & 0 & 0 & 1 & 0 & 0 \\ 0 & 0 & 0 & 0 & 0 & 0 & 0 & 1 & 0 \\ 0 & 0 & 0 & 0 & 0 & 0 & 0 & 0 & 1 \end{bmatrix} \tag{A-5}$$

Jacobians of the air data sensors, observer equation:

$$H = \frac{\partial \underline{h}}{\partial \underline{x}} = \begin{bmatrix} 0 & 0 & 0 & \frac{-w}{u^2\left(1+\frac{w^2}{u^2}\right)} & 0 & \frac{1}{u\left(1+\frac{w^2}{u^2}\right)} & 0 & 0 & 0 & 0 & 0 & 0 & 0 & 0 & 0 & 0 & 0 \\ 0 & 0 & 0 & \frac{-u\cdot v}{\left(u^2+w^2\right)^{1.5}\left(1+\frac{v^2}{u^2+w^2}\right)} & \frac{1}{\sqrt{\left(u^2+w^2\right)}\left(1+\frac{v^2}{u^2+w^2}\right)} & \frac{-u\cdot w}{\left(u^2+w^2\right)^{1.5}\left(1+\frac{v^2}{u^2+w^2}\right)} & 0 & 0 & 0 & 0 & 0 & 0 & 0 & 0 & 0 & 0 & 0 \\ 0 & 0 & 0 & \frac{u}{\sqrt{u^2+v^2+w^2}} & \frac{v}{\sqrt{u^2+v^2+w^2}} & \frac{w}{\sqrt{u^2+v^2+w^2}} & 0 & 0 & 0 & 0 & 0 & 0 & 0 & 0 & 0 & 0 & 0 \end{bmatrix} \tag{A-6}$$

Jacobians of the angle correction (AC) equations, observer equation:

$$H = \frac{\partial \underline{h}}{\partial \underline{x}} = \begin{bmatrix} 0 & 0 & 0 & 0 & 0 & 0 & 1 & 0 & 0 & 0 & 0 & 0 & 0 & 0 & 0 & 0 & 0 & 0 \\ 0 & 0 & 0 & 0 & 0 & 0 & 0 & 1 & 0 & 0 & 0 & 0 & 0 & 0 & 0 & 0 & 0 & 0 \\ 0 & 0 & 0 & 0 & 0 & 0 & 0 & 0 & 1 & 0 & 0 & 0 & 0 & 0 & 0 & 0 & 0 & 0 \end{bmatrix} \tag{A-7}$$

Jacobians of the GPS velocity derivatives, observer equations:

$$H = \frac{\partial \underline{h}}{\partial \underline{x}} = \begin{bmatrix} 0 & 0 & 0 & 0 & 0 & 0 & 0 & \begin{matrix}-\dot{u}_N\sin(\theta)\cos(\psi) - \dot{v}_E\sin(\theta)\sin(\psi) - \\ \dot{w}_D\cos(\theta) - g_0\cos(\theta)\end{matrix} & \begin{matrix}-\dot{u}_N\cos(\theta)\sin(\psi) + \dot{v}_E\cos(\theta)\cos(\psi)\end{matrix} & 0 & 0 & 0 & 0 & 0 & 0 & 0 & 0 & 0 \\ 0 & 0 & 0 & 0 & 0 & 0 & \begin{matrix}\dot{u}_N(\cos(\phi)\sin(\theta)\cos(\psi) + \sin(\phi)\sin(\psi)) + \\ \dot{v}_E(\cos(\phi)\sin(\theta)\sin(\psi) - \sin(\phi)\cos(\psi)) + \\ \dot{w}_D\cos(\phi)\cos(\theta) - g_0\cos(\phi)\cos(\theta)\end{matrix} & \begin{matrix}\dot{u}_N\sin(\phi)\cos(\theta)\cos(\psi) + \\ \dot{v}_E\sin(\phi)\cos(\theta)\sin(\psi) - \\ \dot{w}_D\sin(\phi)\sin(\theta) + g_0\sin(\phi)\sin(\theta)\end{matrix} & \begin{matrix}\dot{u}_N(-\sin(\phi)\sin(\theta)\sin(\psi) - \cos(\phi)\cos(\psi)) + \\ \dot{v}_E(\sin(\phi)\sin(\theta)\cos(\psi) - \cos(\phi)\sin(\psi))\end{matrix} & 0 & 0 & 0 & 0 & 0 & 0 & 0 & 0 & 0 \\ 0 & 0 & 0 & 0 & 0 & 0 & \begin{matrix}\dot{u}_N(-\sin(\phi)\sin(\theta)\cos(\psi) + \cos(\phi)\sin(\psi)) + \\ \dot{v}_E(-\sin(\phi)\sin(\theta)\sin(\psi) - \cos(\phi)\cos(\psi)) - \\ \dot{w}_D\sin(\phi)\cos(\theta) + g_0\sin(\phi)\cos(\theta)\end{matrix} & \begin{matrix}\dot{u}_N\cos(\phi)\cos(\theta)\cos(\psi) + \\ \dot{v}_E\cos(\phi)\cos(\theta)\sin(\psi) - \\ \dot{w}_D\cos(\phi)\sin(\theta) + g_0\cos(\phi)\sin(\theta)\end{matrix} & \begin{matrix}\dot{u}_N(-\cos(\phi)\sin(\theta)\sin(\psi) + \sin(\phi)\cos(\psi)) + \\ \dot{v}_E(\cos(\phi)\sin(\theta)\cos(\psi) + \sin(\phi)\sin(\psi))\end{matrix} & 0 & 0 & 0 & 0 & 0 & 0 & 0 & 0 & 0 \end{bmatrix} \tag{A-8}$$

Appendix B

Aerosonde UAV Simulation Parameters

B-1 Aerosonde Configuration Parameters

Listing B.1: Aerosonde configuration aerosondeConfig.m

```
% AIRCRAFT CONFIGURATION SCRIPT
%   Aerosonde UAV - sample model from AeroSim Library

%   Copyright 2002 Unmanned Dynamics, LLC
%   Revision: 1.0   Date: 05/13/2002

% Clear workspace
clear all;

% Name of the MAT-file that will be generated
cfgmatfile = 'aerosondecfg';

%%% AERODYNAMICS %%%
% Aerodynamic force application point (usually the aerodynamic center)[x y z]
rAC = [0.1425 0 0]; % m

%%% Aerodynamic parameter bounds %%%
% Airspeed bounds
VaBnd = [15 50]; % m/s
% Sideslip angle bounds
BetaBnd = [-0.05 0.05]; % rad
% Angle of attack bounds
AlphaBnd = [-0.05 0.05]; % rad

%%% Aerodynamic reference parameters %%%
% Mean aerodynamic chord
MAC = 0.189941; % m
% Wind span
b = 2.8956; % m
% Wing area
S = 0.55; % m^2

% ALL aerodynamics derivatives are per radian:
%%% Lift coefficient %%%
% Zero-alpha lift
CL0 = 0.23;
% alpha derivative
CLa = 5.6106;
% Lift control (flap) derivative
CLdf = 0.74;
% Pitch control (elevator) derivative
CLde = 0.13;
% alpha-dot derivative
CLalphadot = 1.9724;
% Pitch rate derivative
```

```
CLq = 7.9543;
% Mach number derivative
CLM = 0;

%%% Drag coefficient %%%
% Lift at minimum drag
CLmind = 0.23;
% Minimum drag
CDmin = 0.0434;
% Lift control (flap) derivative
CDdf = 0.1467;
% Pitch control (elevator) derivative
CDde = 0.0135;
% Roll control (aileron) derivative
CDda = 0.0302;
% Yaw control (rudder) derivative
CDdr = 0.0303;
% Mach number derivative
CDM = 0;
% Oswald's coefficient
osw = 0.75;

%%% Side force coefficient %%%
% Sideslip derivative
CYbeta = -0.83;
% Roll control derivative
CYda = -0.075;
% Yaw control derivative
CYdr = 0.1914;
% Roll rate derivative
CYp = 0;
% Yaw rate derivative
CYr = 0;

%%% Pitch moment coefficient %%%
% Zero-alpha pitch
Cm0 = 0.135;
% alpha derivative
Cma = -2.7397;
% Lift control derivative
Cmdf = 0.0467;
% Pitch control derivative
Cmde = -0.9918;
% alpha_dot derivative
Cmalphadot = -10.3796;
% Pitch rate derivative
Cmq = -38.2067;
% Mach number derivative
CmM = 0;

%%% Roll moment coefficient %%%
% Sideslip derivative
Clbeta = -0.13;
% Roll control derivative
Clda = -0.1695;
% Yaw control derivative
Cldr = 0.0024;
% Roll rate derivative
Clp = -0.5051;
% Yaw rate derivative
Clr = 0.2519;

%%% Yaw moment coefficient %%%
% Sideslip derivative
Cnbeta = 0.0726;
% Roll control derivative
Cnda = 0.0108;
% Yaw control derivative
Cndr = -0.0693;
% Roll rate derivative
Cnp = -0.069;
% Yaw rate derivative
Cnr = -0.0946;


%%% PROPELLER %%%
%Propulsion force application point (usually propeller hub) [x y z]
rHub = [0 0 0]; % m
% Advance ratio vector
J = [-1 0 0.1 0.2 0.3 0.35 0.4 0.45 0.5 0.6 0.7 0.8 0.9 1 1.2 2];
% Coefficient of thrust look-up table CT = CT(J)
CT = [0.0492 0.0286 0.0266 0.0232 0.0343 0.034 0.0372 0.0314 0.0254 0.0117 -0.005 -0.0156 -0.0203
    -0.0295 -0.04 -0.1115];
% Coefficient of power look-up table CP = CP(J)
CP = [0.0199 0.0207 0.0191 0.0169 0.0217 0.0223 0.0254 0.0235 0.0212 0.0146 0.0038 -0.005 -0.0097
    -0.018 -0.0273 -0.0737];
% Propeller radius
Rprop = 0.254; % m
% Propeller moment of inertia
Jprop = 0.002; % kg*m^2
```

```
%%% ENGINE %%%
% Engine rpm vector
RPM = [1500 2100 2800 3500 4500 5100 5500 6000 7000]; % rot per min
% Manifold pressure vector
MAP = [60 70 80 90 92 94 96 98 100]; % kPa

% Sea-level fuel flow look-up table fflow = fflow(RPM, MAP)
% RPM -> rows, MAP -> columns
FuelFlow = [
    31 32 46 53 55 57 65 73 82
    40 44 54 69 74 80 92 103 111
    50 63 69 92 95 98 126 145 153
    66 75 87 110 117 127 150 175 190
    83 98 115 143 148 162 191 232 246
    93 102 130 159 167 182 208 260 310
    100 118 137 169 178 190 232 287 313
    104 126 151 184 191 206 253 326 337
    123 144 174 210 217 244 321 400 408
]; % g/hr
% Sea-level power look-up table P = P(RPM, MAP)
% RPM -> rows, MAP -> columns
Power = [
    18.85 47.12 65.97 67.54 69.12 67.54 67.54 69.12 86.39
    59.38 98.96 127.55 149.54 151.74 160.54 178.13 200.12 224.31
    93.83 149.54 187.66 237.5 249.23 255.1 307.88 366.52 398.77
    109.96 161.27 245.57 307.88 326.2 351.86 421.5 491.14 531.45
    164.93 245.04 339.29 438.25 447.68 494.8 565.49 673.87 772.83
    181.58 245.67 389.87 496.69 528.73 571.46 662.25 822.47 993.37
    184.31 293.74 403.17 535.64 570.2 622.04 748.75 956.09 1059.76
    163.36 276.46 420.97 565.49 609.47 691.15 860.8 1130.97 1193.81
    124.62 249.23 417.83 586.43 645.07 762.36 996.93 1246.17 1429.42
]; % W
% Sea-level pressure and temperature at which the data above is given
pSL = 102300; % Pa
TSL = 291.15; % deg K
% Engine shaft moment of inertia
Jeng = 0.0001; % kg*m^2


%%% INERTIA %%%
% Empty aircraft mass (zero-fuel)
mempty = 8.5; % kg
% Gross aircraft mass (full fuel tank)
mgross = 13.5; % kg
% Empty CG location [x y z]
CGempty = [0.156 0 0.079]; % m
% Gross CG location [x y z]
CGgross = [0.159 0 0.090]; % m
% Empty moments of inertia [Jx Jy Jz Jxz]
Jempty = [0.7795 1.122 1.752 0.1211]; % kg*m^2
% Gross moments of inertia [Jx Jy Jz Jxz]
Jgross = [0.8244 1.135 1.759 0.1204]; % kg*m^2


%%% OTHER SIMULATION PARAMETERS %%%
% WMM-2000 date [day month year]
dmy = [13 05 2002];

% Save workspace variables to MAT file
save(cfgmatfile);

% Output a message to the screen
fprintf(strcat('\n Aircraft configuration saved as:\t', strcat(cfgmatfile),'.mat'));
fprintf('\n');
```

B-2 IMU, GPS Receiver and Environmental Properties

Table B-1: IMU sensor performance parameters

quantity	accelerometers	gyroscopes
scale factor over temperature, 1 σ	400-1400 $[ppm]$	200-1200 $[ppm]$
bias over temperature, 1 σ	0.5 - 2.0 $[mg]$	1.0 - 5.0 $[^\circ/h]$
random walk bias, $^\circ/\sqrt{h}$	0.2 $[^\circ/\sqrt{h}]$	0.2 $[^\circ/\sqrt{h}]$
axis misalignment, per axis	1 $[^\circ]$	1 $[^\circ]$
sensor-to-senor misalignment, per axis	0.1 $[^\circ]$	0.1 $[^\circ]$
vibration rectification error, 1 σ	-	0.02 $[^\circ/h/g^2]$
white noise (external source), 1 σ	0.25 $[g]$	1 $[^\circ/s]$

Table B-2: GPS receiver performance parameters

quantity	GPS position
constraint position bias	8.7-13.7[1] $[m]$
position noise, 1 σ	1.6 $[m]$
receiver time lag	0.25 [s] $\pm 0.025[s]$
quantity	GPS velocity
velocity noise, 1 σ	0.01 $[m/s]$
receiver time lag	0.25 [s] $\pm 0.025[s]$

Table B-3: Environmental properties during simulations

quantity	magnitude
ΔT	10°
Wind X-direction[2]	3 $[m/s]$ + 0.05 $[m/s/s]$
Wind Y-direction	1 $[m/s]$ + 0.05 $[m/s/s]$
Wind Z-direction	1 $[m/s]$ + 0.05 $[m/s/s]$

[1] Due to a difference in satellite ephemeris the position bias is usually higher in Z-direction
[2] The wind is modeled as a constant speed $[m/s]$ plus a random walk [m/s/s]

Appendix C

Observability Values

C-1 QRsvd.m

Listing C.1: QRsvd.m

```
function [s] = QRsvd(A,tol,loopMax)
% calculating the singular values in a state ordered way
% Si -> xi, each singular value corresponds to each state as defined
% in the observability matrix A
%
%
% syntax: S = QRsvd(A,tol,loopMax)
%
% singular values S are calculated for matrix A, with tolerance
% tol that is used while iterating
%
%
% 18/03/2010
% last updated: 18/08/2010
% Bart Hummelink, MSc thesis


% initialize
if ~exist('tol','var')   % if no tollerance is given
   tol = 10^-15;
end

if ~exist('','var')   % if no max # loops is given
   sizeA=size(A);
    loopMax=10*max(sizeA);
end


loopCounter=0;

u=eye(sizeA(1));
s=A';
v=eye(sizeA(2));


Error = 10^300;
% running
while Error > tol & loopCounter < loopMax;
    [q,s] = qr(s');

    e=triu(s,1);        % extracting values above diagonal
    E=norm(e(:));
    F=norm(diag(s));    % sum of singular values
    if F==0, F=1;end
    Error=E/F;
    loopCounter=loopCounter+1;
end

% correcting signs of singular values
```

```
ss = diag(s);                                                    51
s = zeros(sizeA(2));

for i = 1:length(ss)
    ssi = ss(i);
    s(i,i) = abs(ssi);                                           56
    if ssi<0
        u(:,i) = -u(:,i);
    end
end
                                                                 61
s = diag(s);
```

C-2 Singular Values Sensor Configuration 2

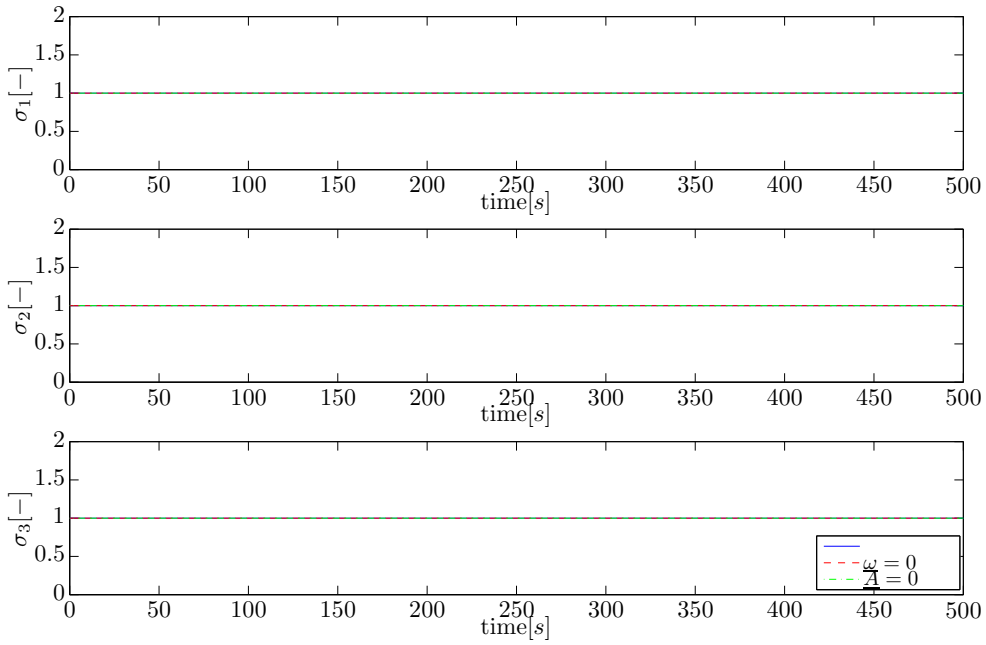

Figure C-1: Singular values states x, y and z sensor configuration 2

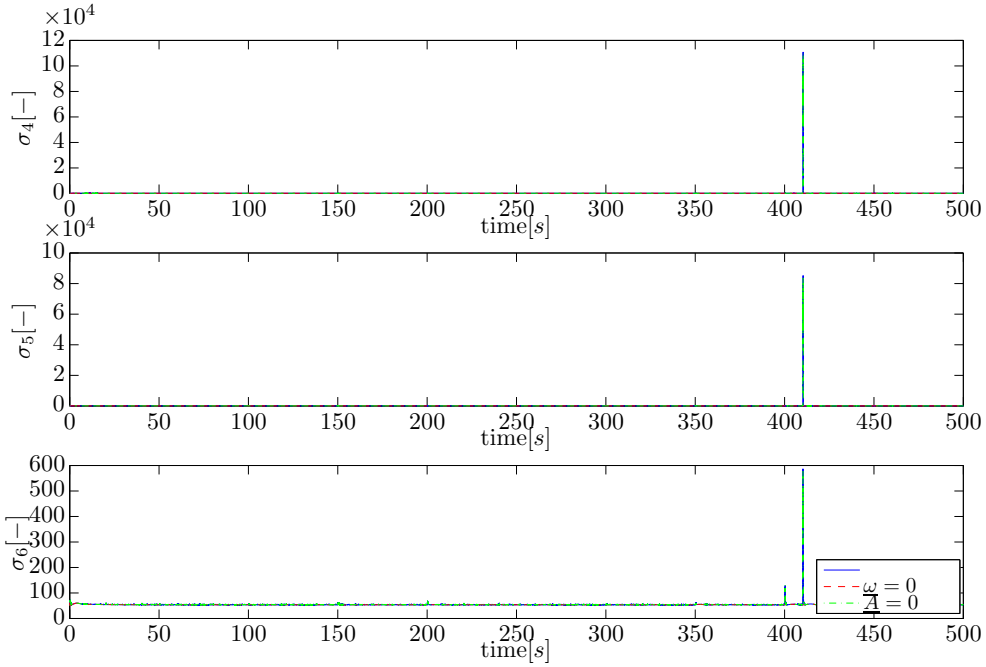

Figure C-2: Singular values states u, v and w sensor configuration 2

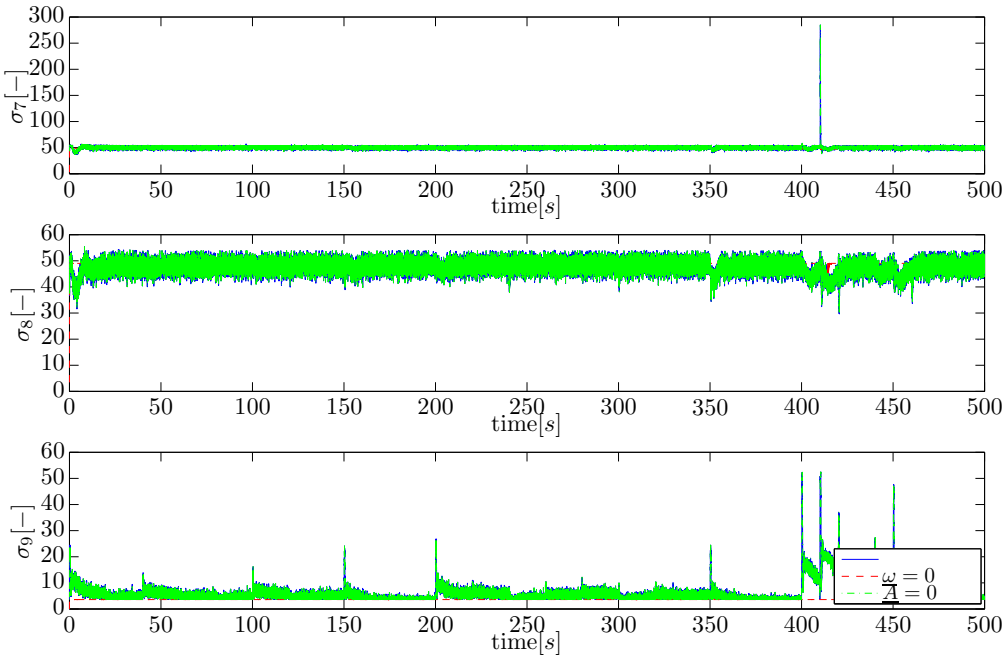

Figure C-3: Singular values states ϕ, θ and ψ sensor configuration 2

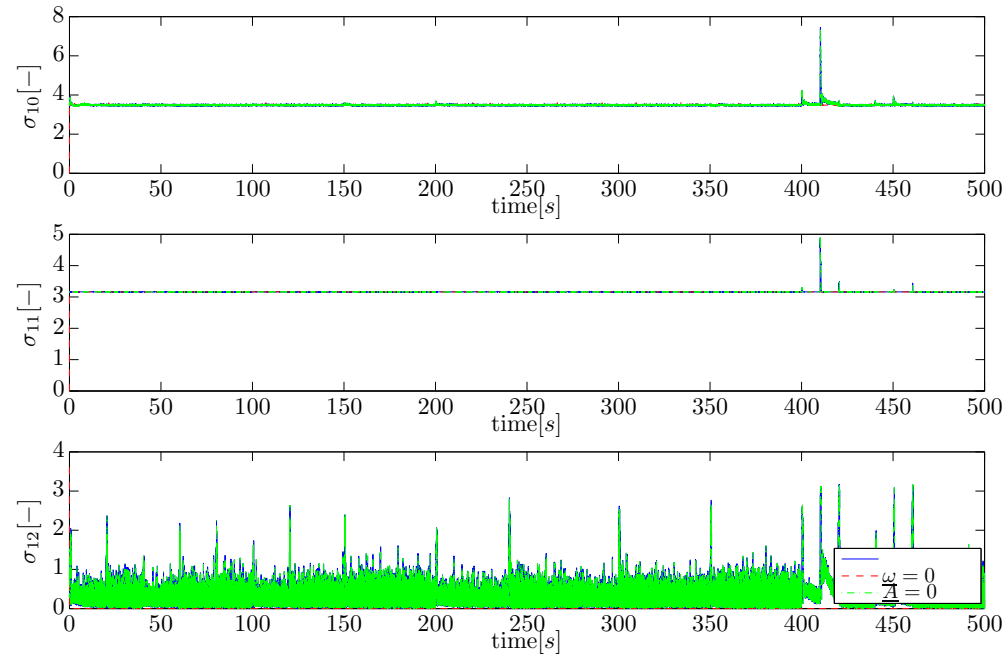

Figure C-4: Singular values states b_{A_x}, b_{A_y} and b_{A_z} sensor configuration 2

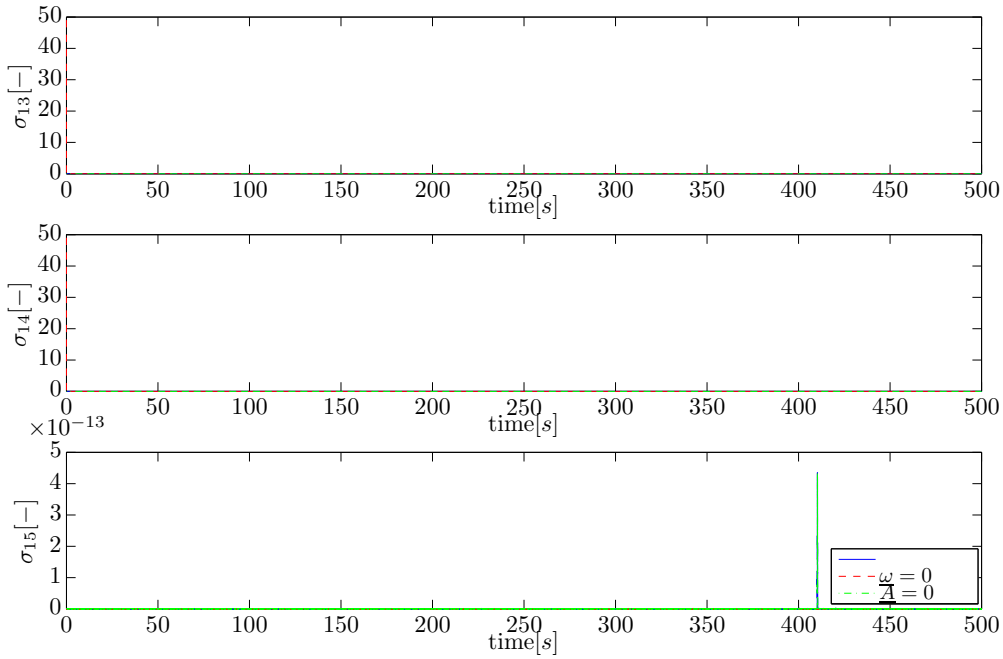

Figure C-5: Singular values states b_p, b_q and b_r sensor configuration 2

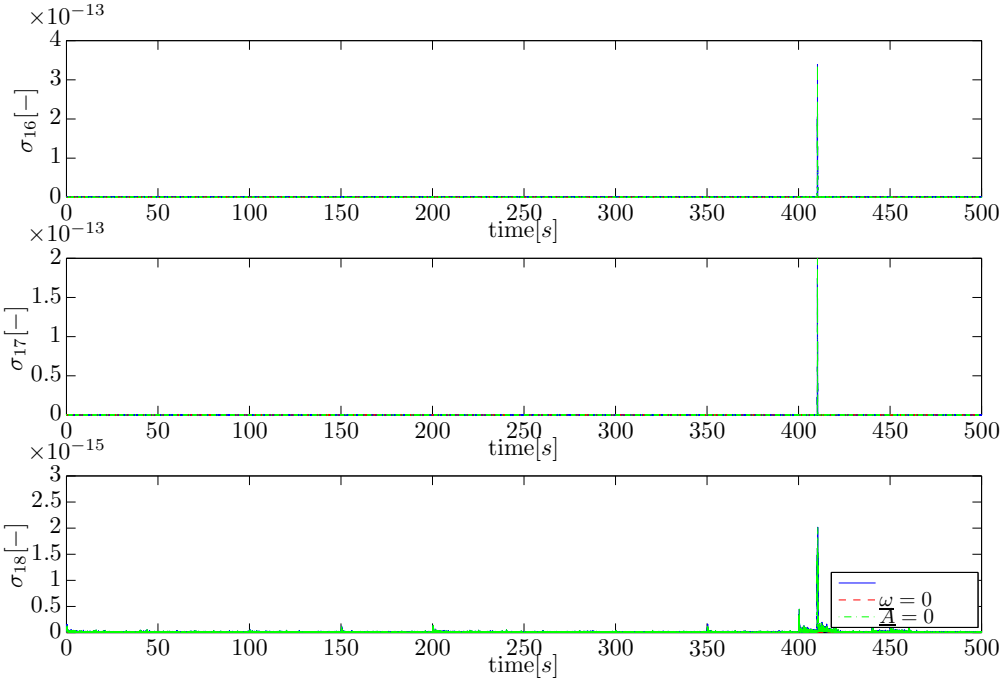

Figure C-6: Singular values states W_x, W_y and W_z sensor configuration 2

C-3 Singular Values Sensor Configuration 6

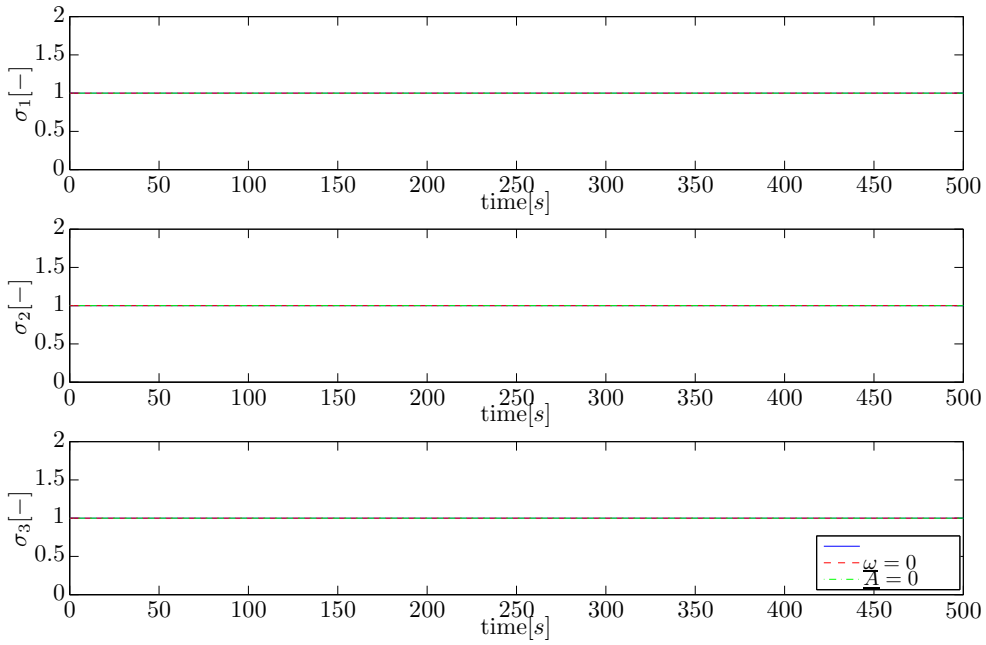

Figure C-7: Singular values states x, y and z sensor configuration 6

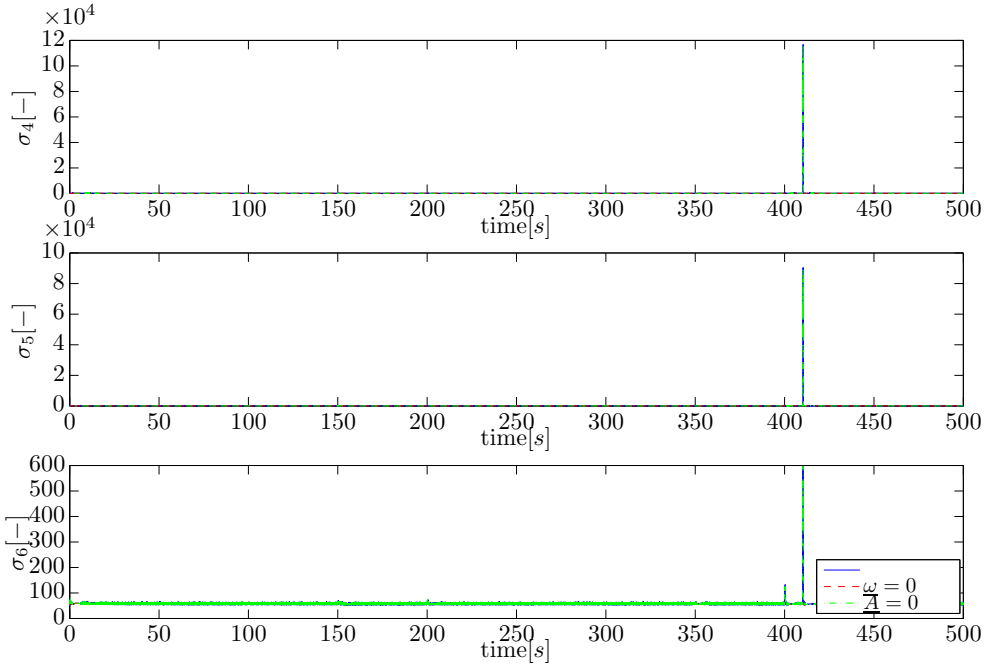

Figure C-8: Singular values states u, v and w sensor configuration 6

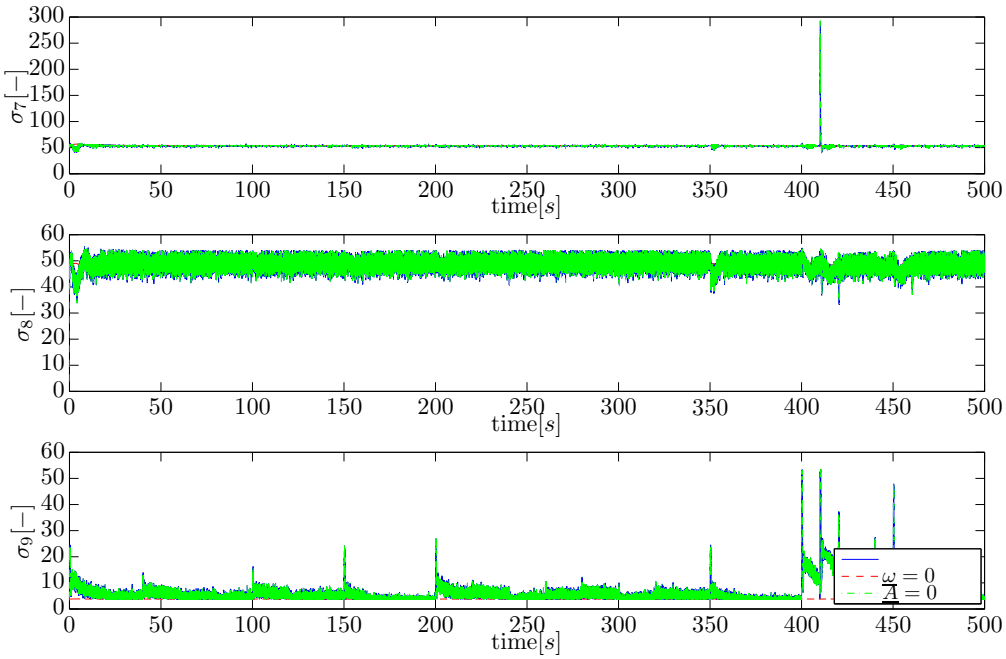

Figure C-9: Singular values states ϕ, θ and ψ sensor configuration 6

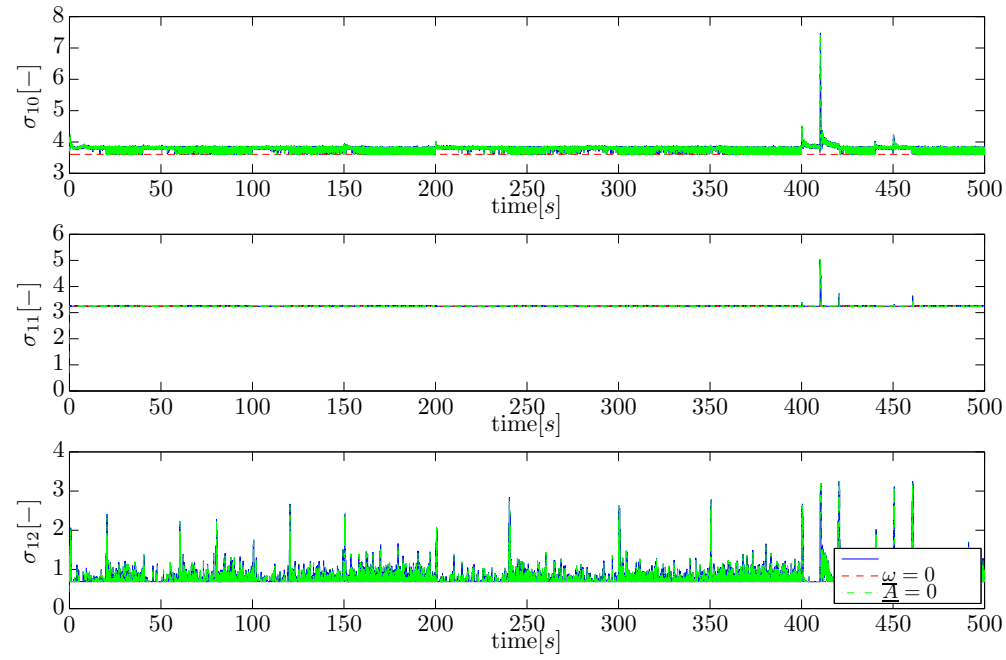

Figure C-10: Singular values states b_{A_x}, b_{A_y} and b_{A_z} sensor configuration 6

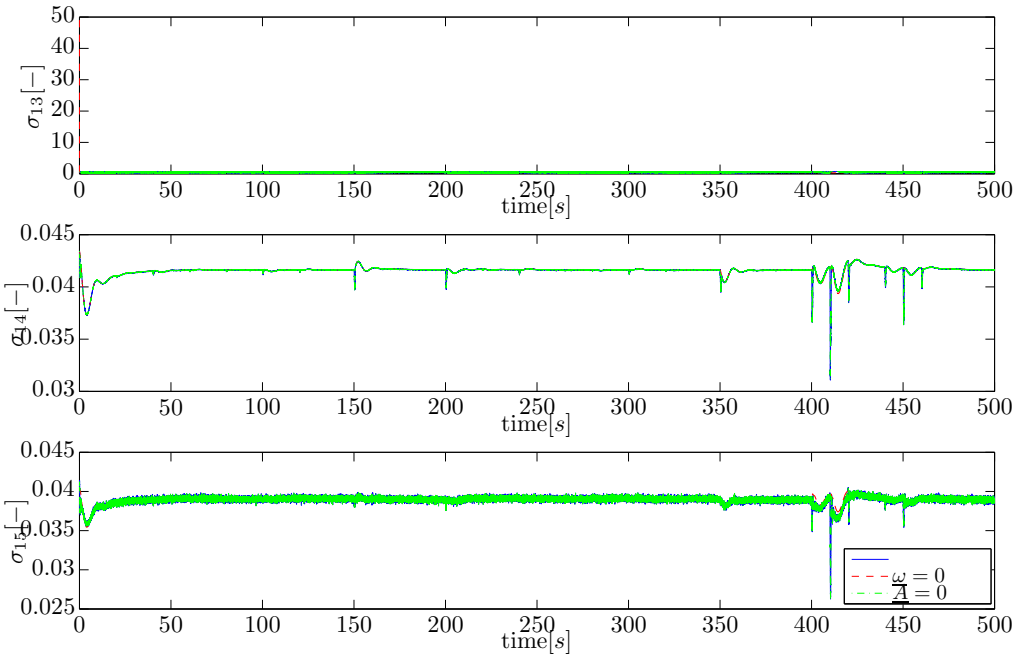

Figure C-11: Singular values states b_p, b_q and b_r sensor configuration 6

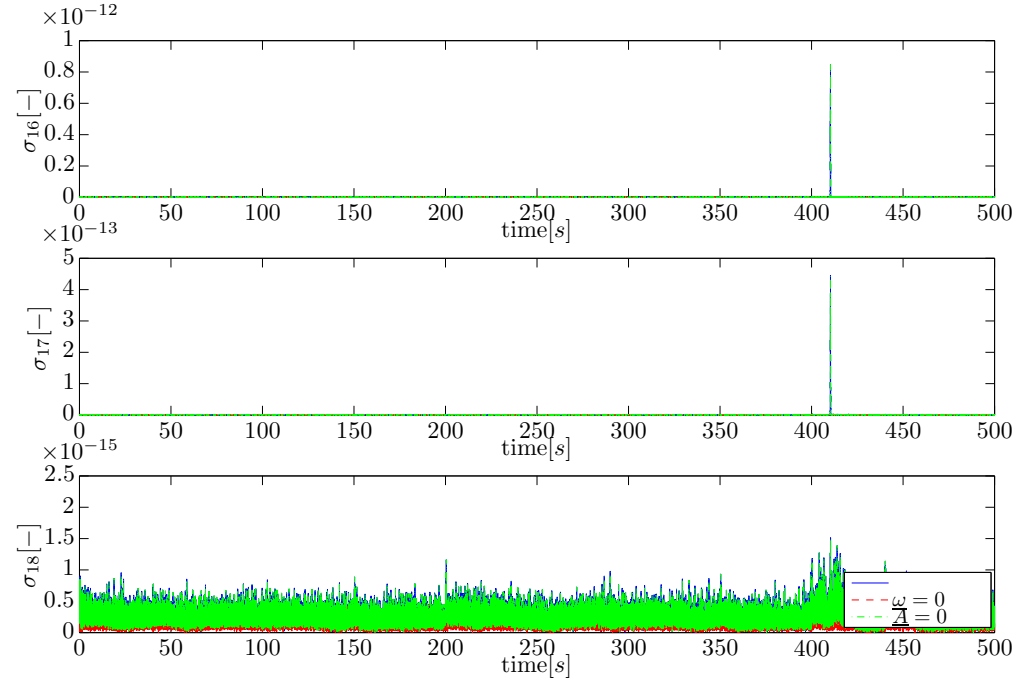

Figure C-12: Singular values states W_x, W_y and W_z sensor configuration 6

C-4 Singular Values Sensor Configuration 7

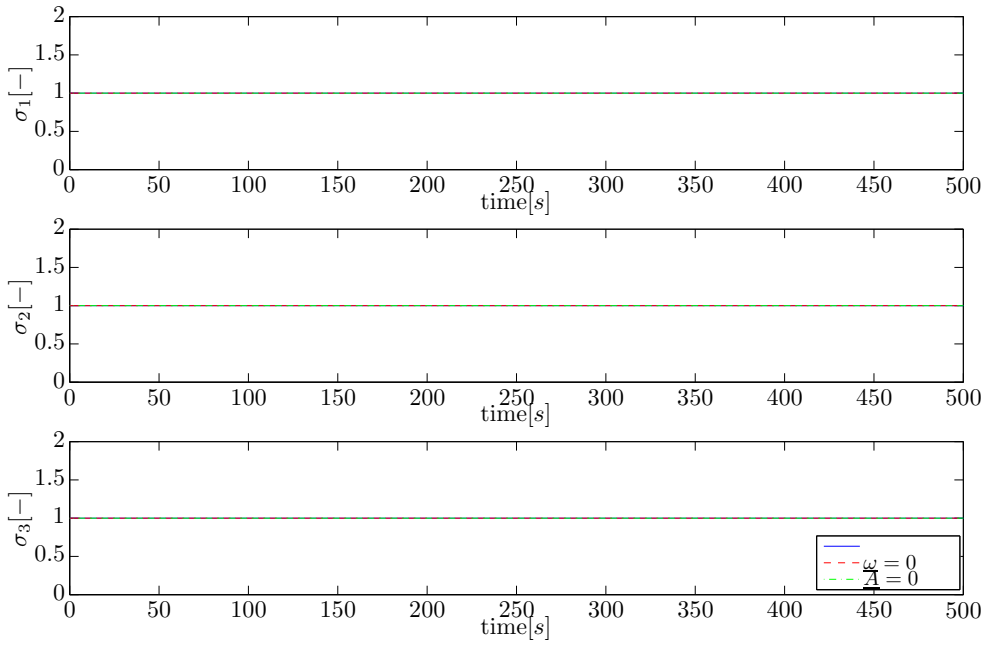

Figure C-13: Singular values states x, y and z sensor configuration 7

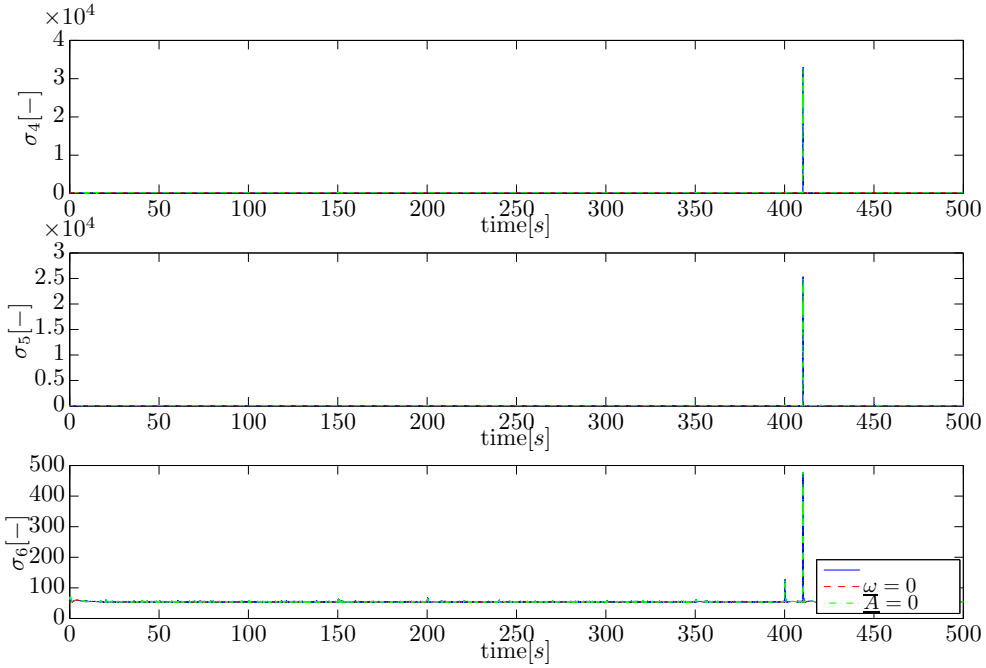

Figure C-14: Singular values states u, v and w sensor configuration 7

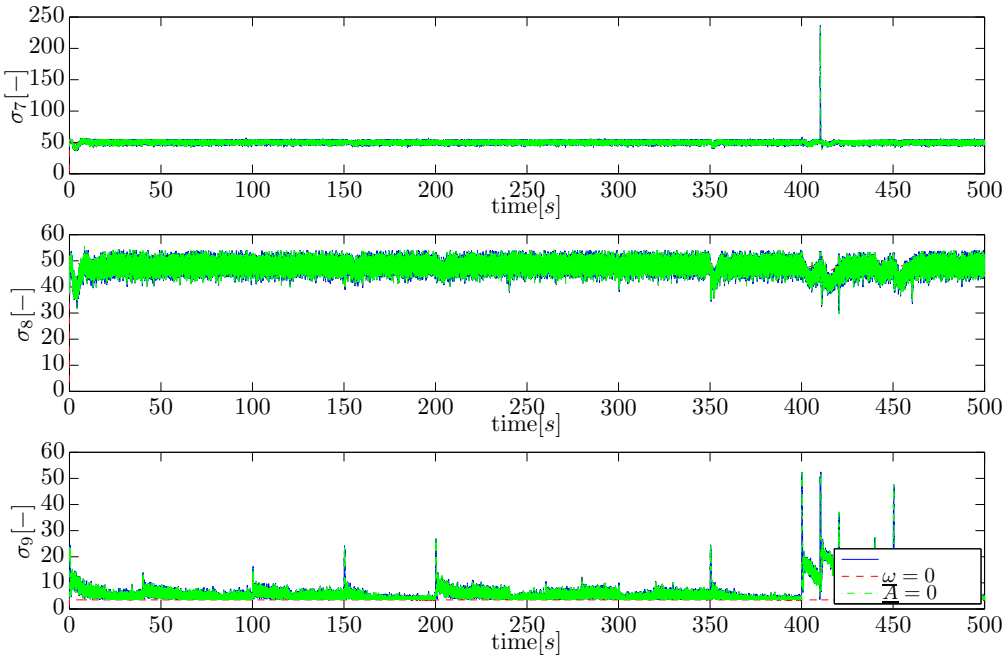

Figure C-15: Singular values states ϕ, θ and ψ sensor configuration 7

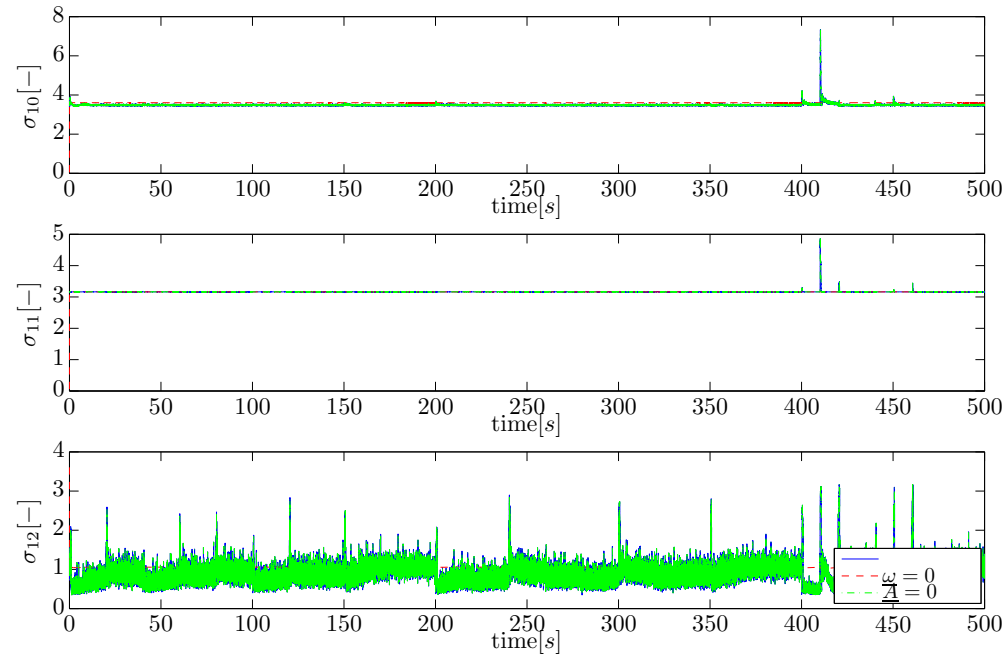

Figure C-16: Singular values states b_{A_x}, b_{A_y} and b_{A_z} sensor configuration 7

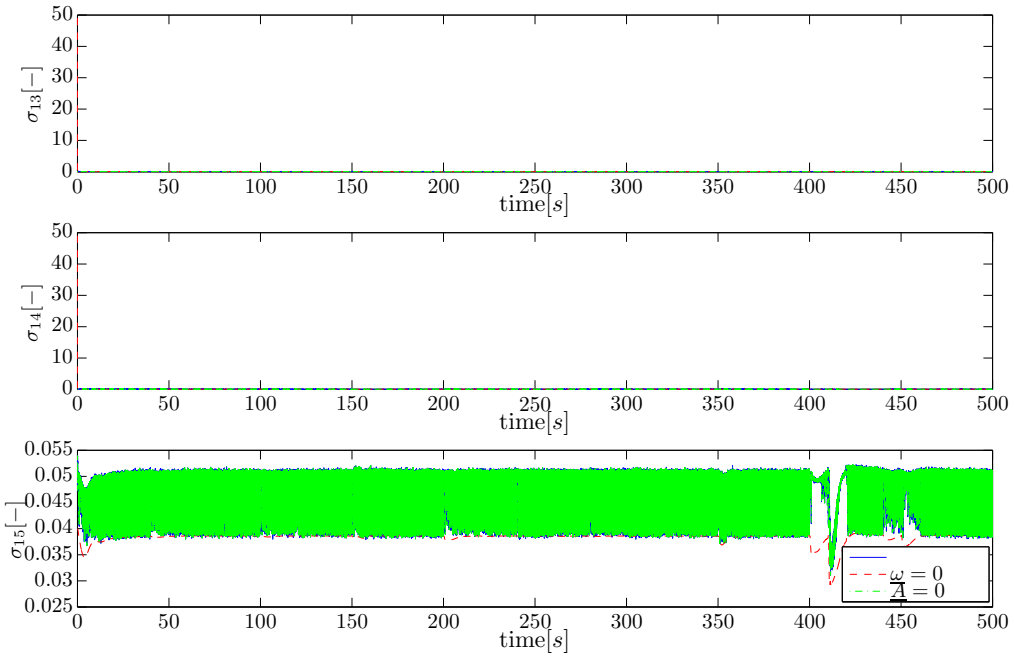

Figure C-17: Singular values states b_p, b_q and b_r sensor configuration 7

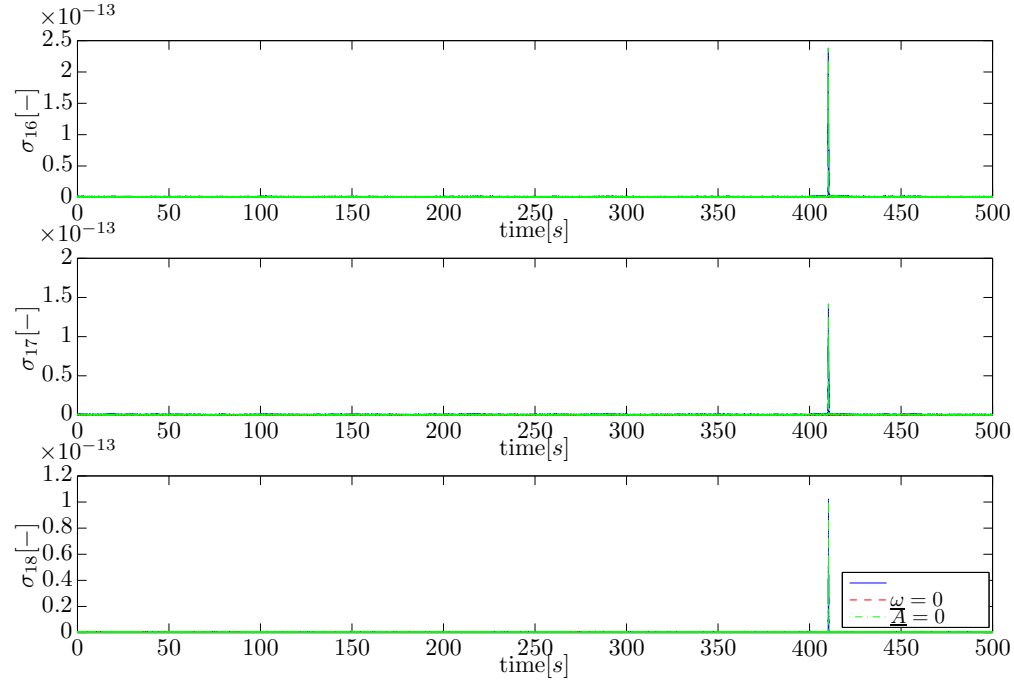

Figure C-18: Singular values states W_x, W_y and W_z sensor configuration 7

C-5 Singular Values Sensor Configuration 8

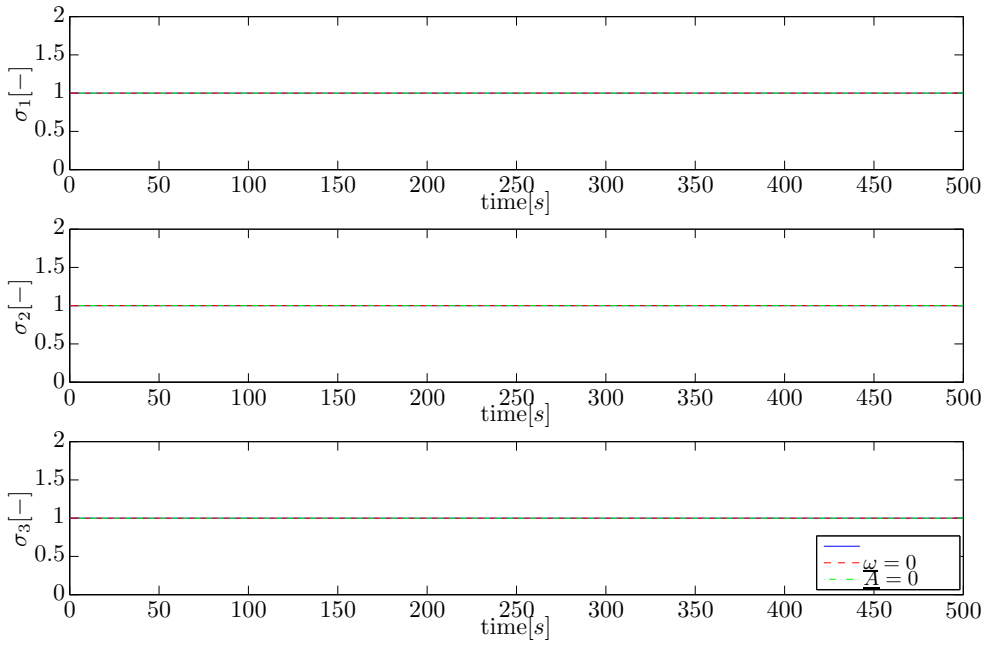

Figure C-19: Singular values states x, y and z sensor configuration 8

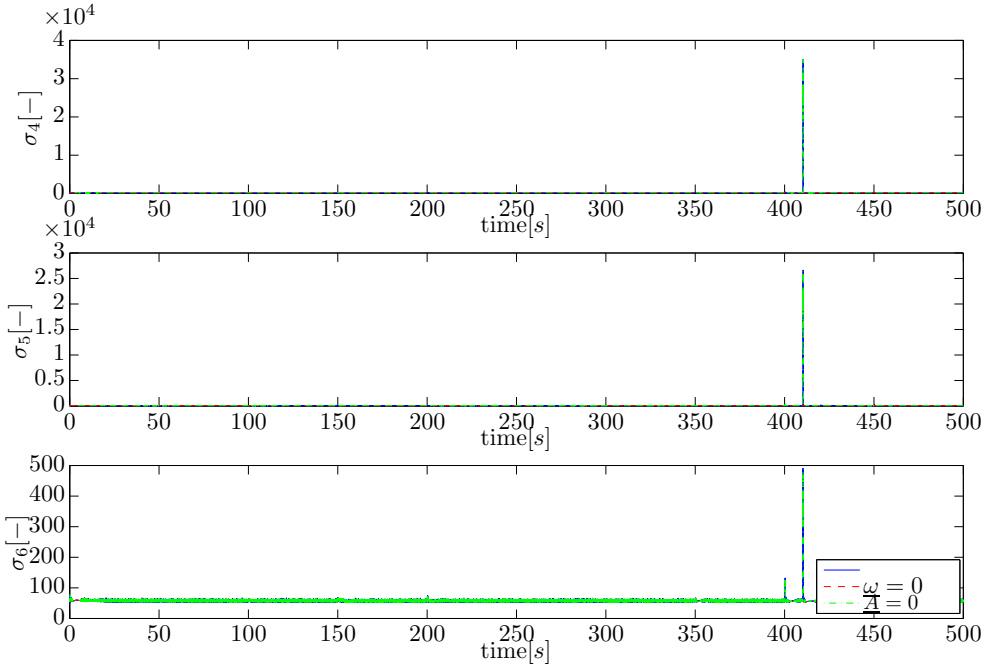

Figure C-20: Singular values states u, v and w sensor configuration 8

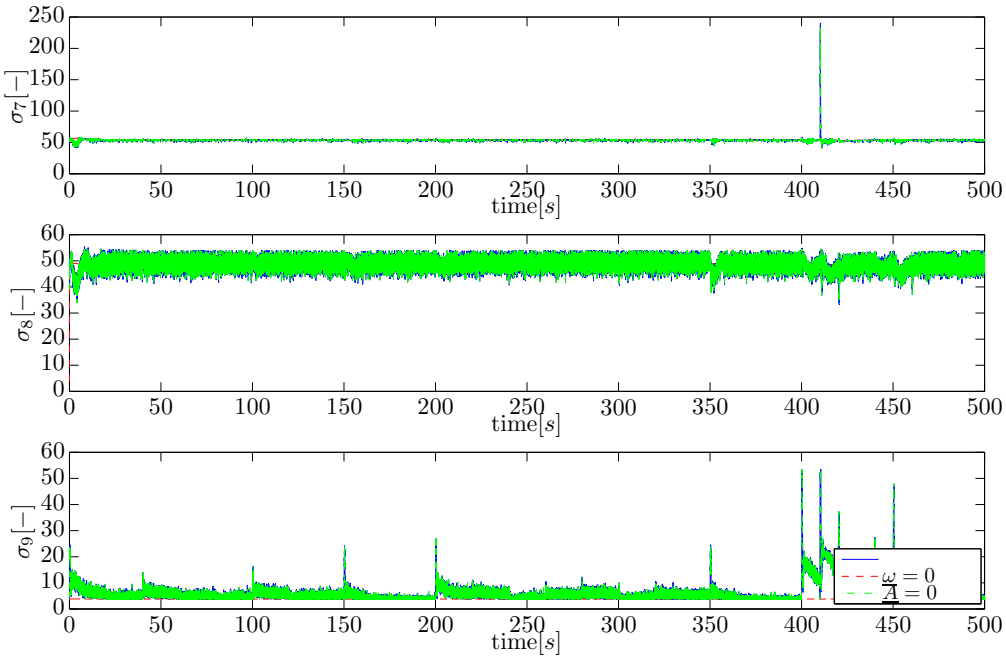

Figure C-21: Singular values states ϕ, θ and ψ sensor configuration 8

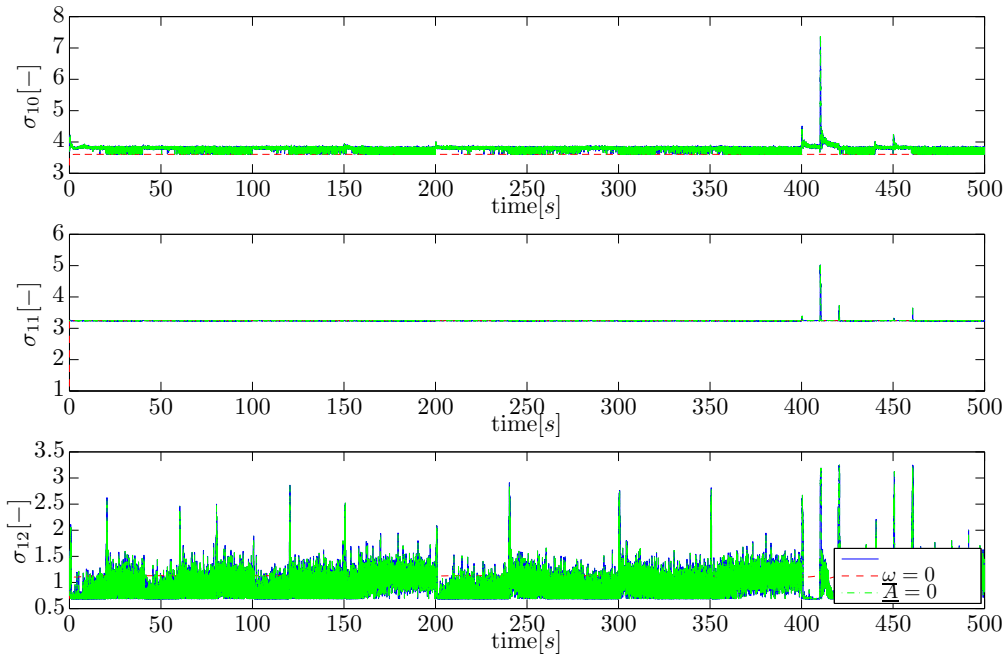

Figure C-22: Singular values states b_{A_x}, b_{A_y} and b_{A_z} sensor configuration 8

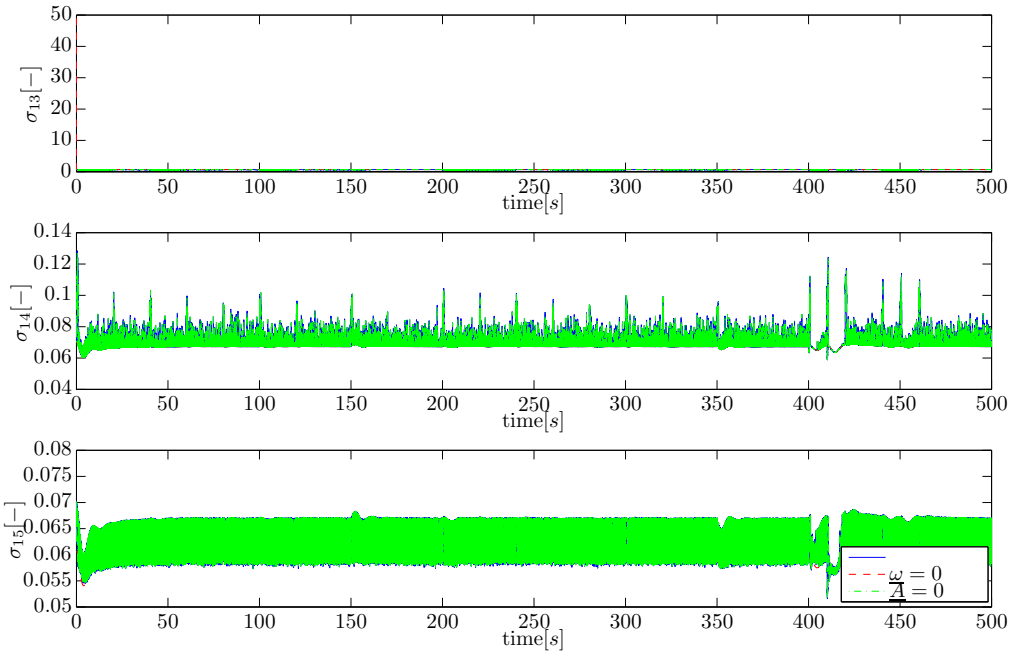

Figure C-23: Singular values states b_p, b_q and b_r sensor configuration 8

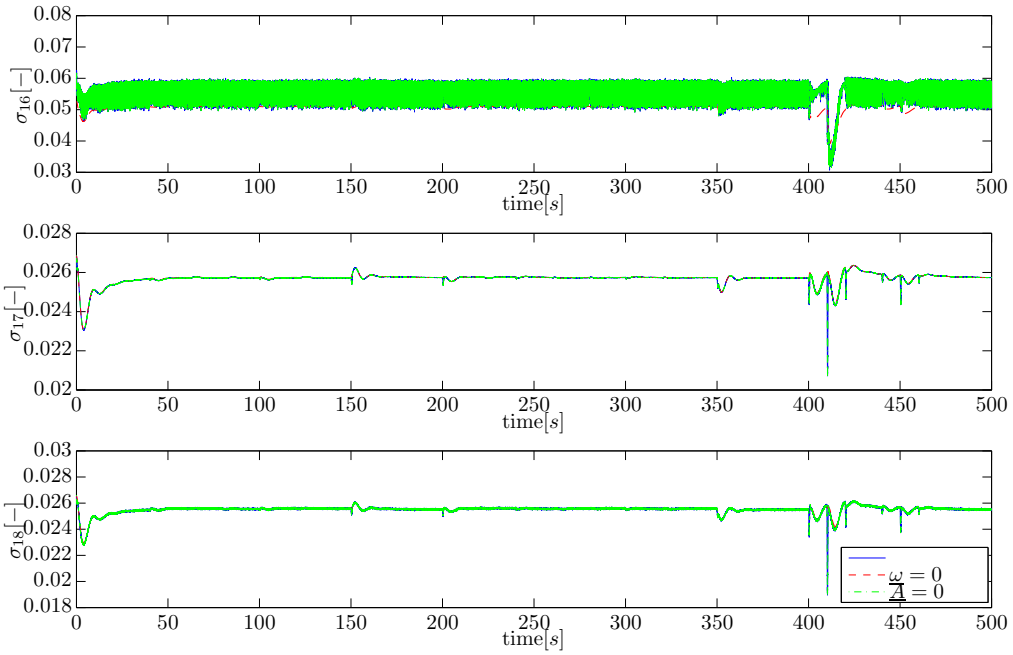

Figure C-24: Singular values states W_x, W_y and W_z sensor configuration 8

C-6 Singular Values Sensor Configuration 2 with Angle Correction

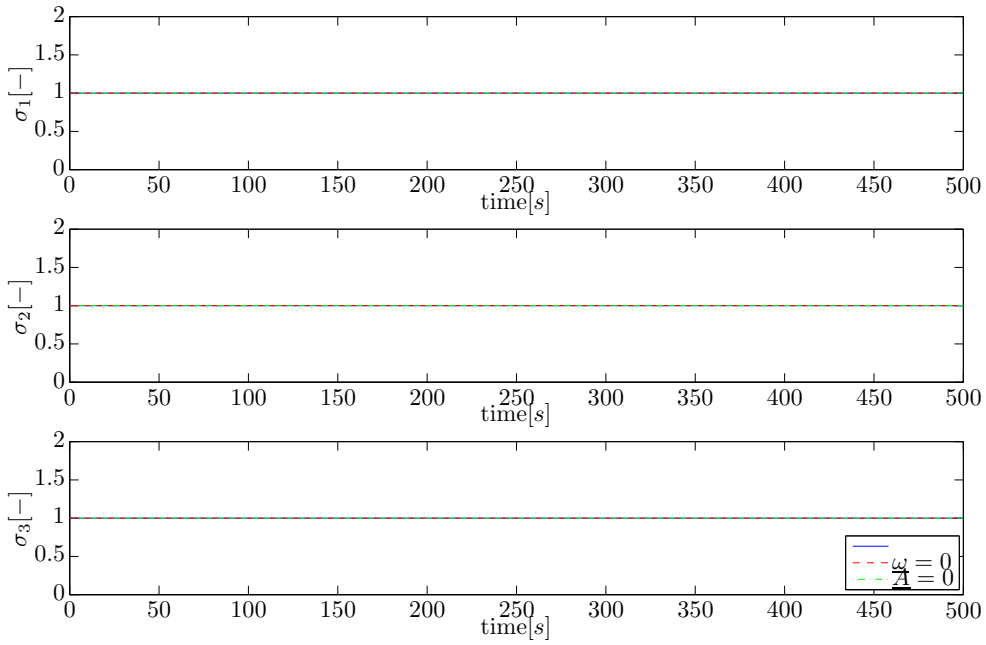

Figure C-25: Singular values states x, y and z sensor configuration 2 + AC

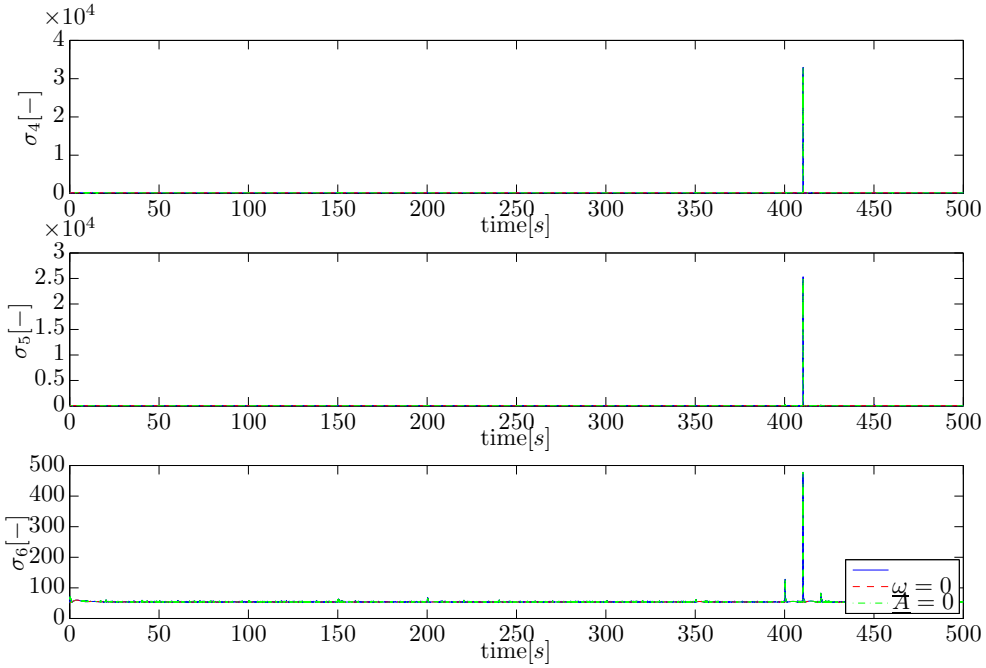

Figure C-26: Singular values states u, v and w sensor configuration 2 + AC

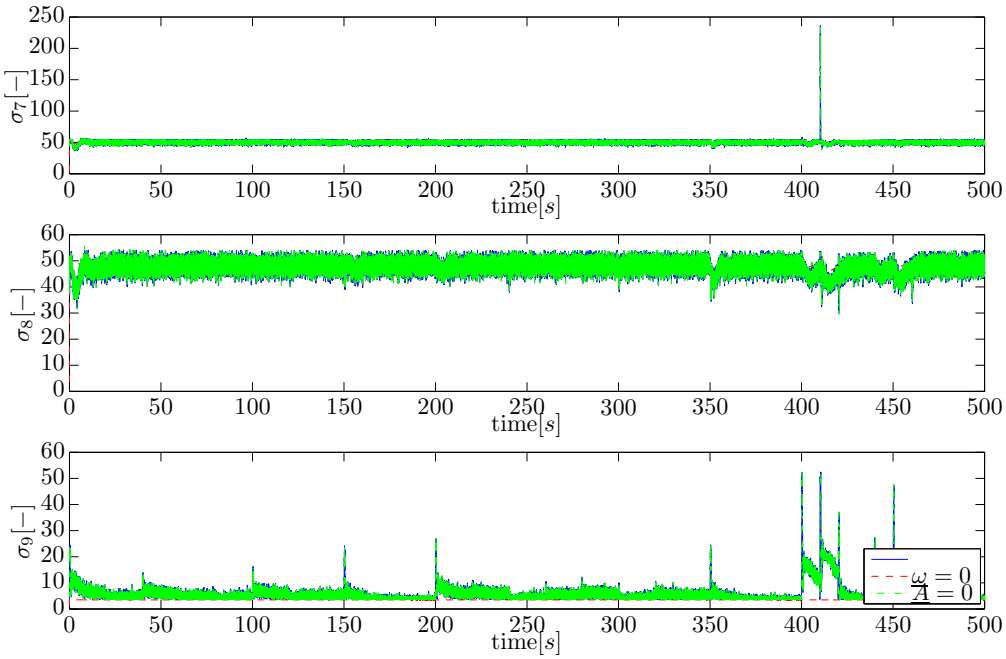

Figure C-27: Singular values states ϕ, θ and ψ sensor configuration 2 + AC

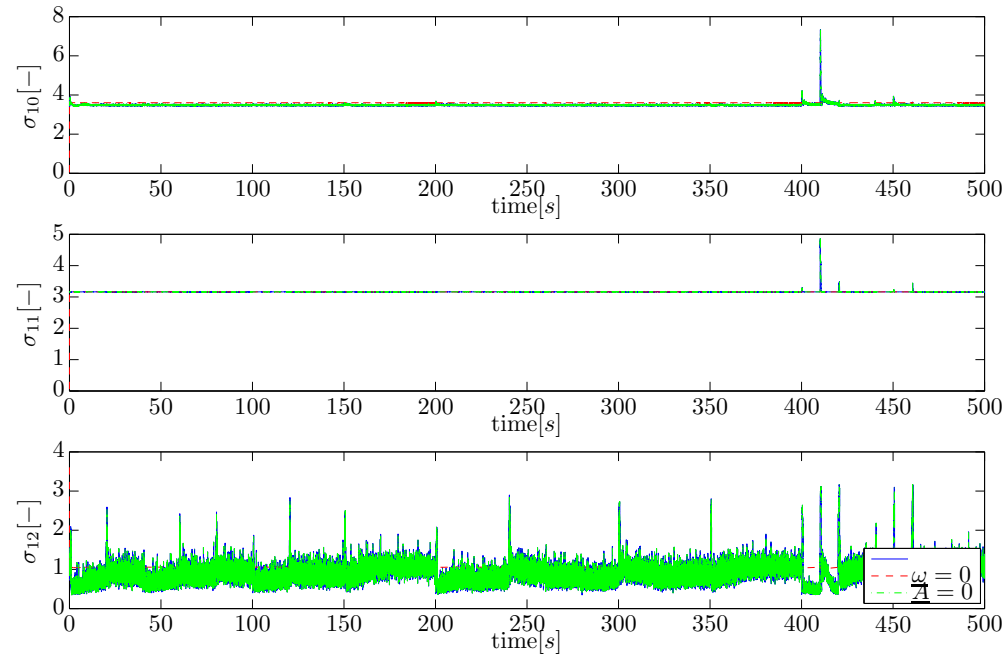

Figure C-28: Singular values states b_{A_x}, b_{A_y} and b_{A_z} sensor configuration 2 + AC

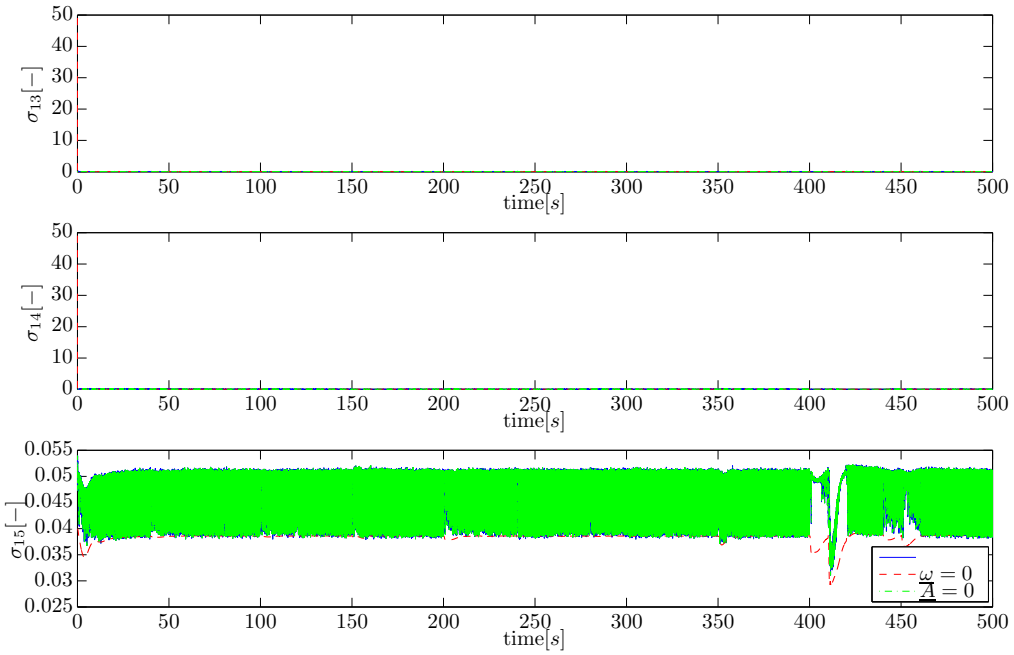

Figure C-29: Singular values states b_p, b_q and b_r sensor configuration 2 + AC

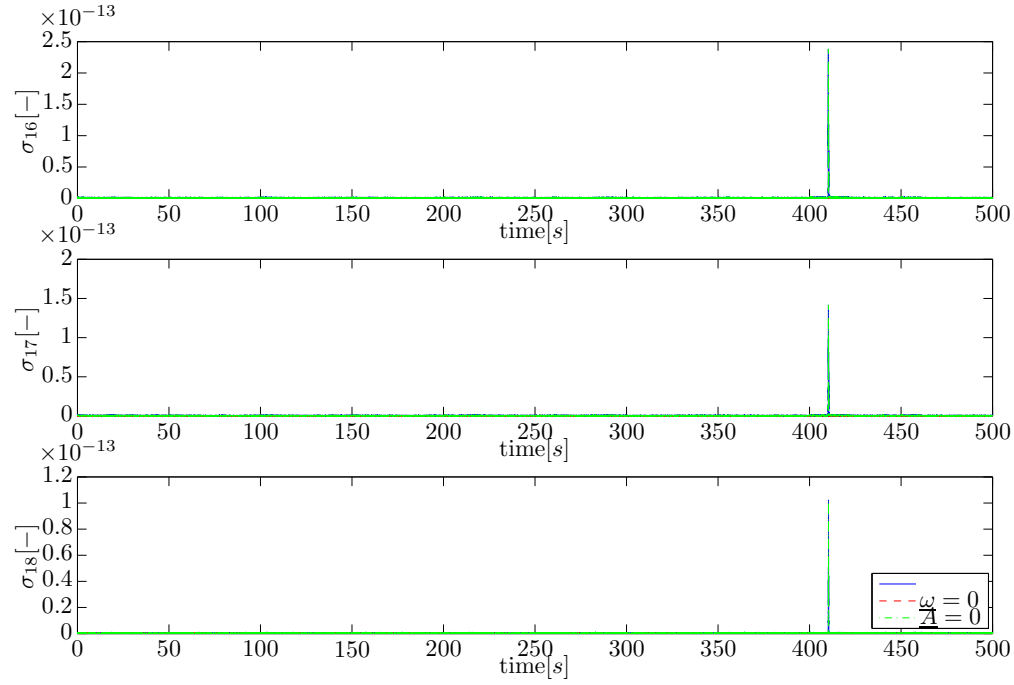

Figure C-30: Singular values states W_x, W_y and W_z sensor configuration 2 + AC

Appendix D

Generic Aerosonde UAV Simulations

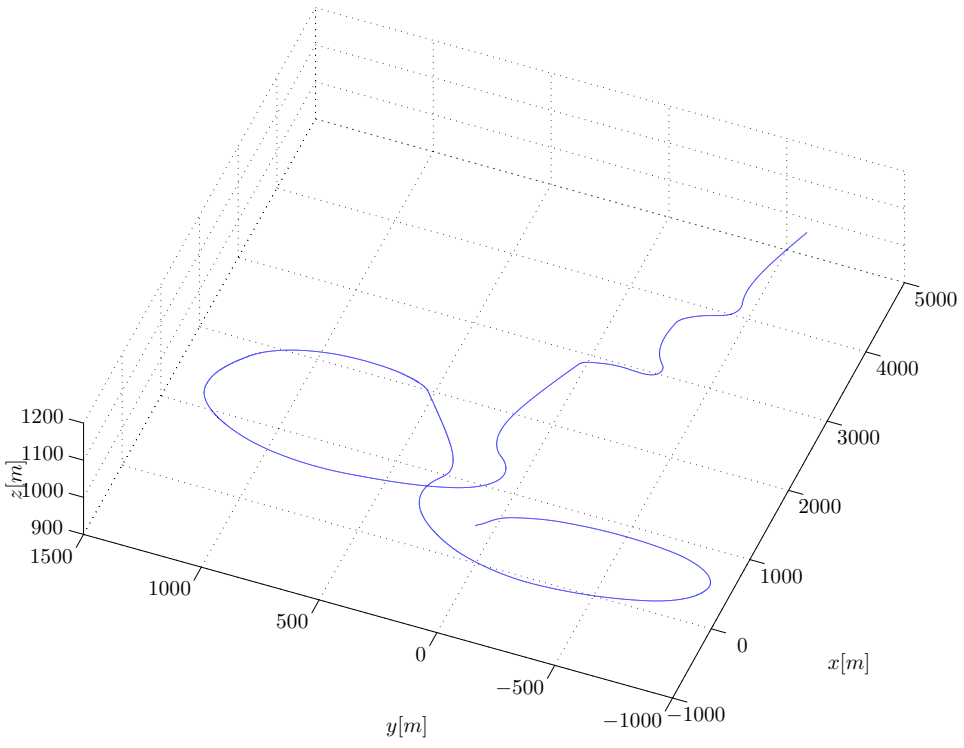

Figure D-1: 3D position, generic Aerosonde UAV simulation

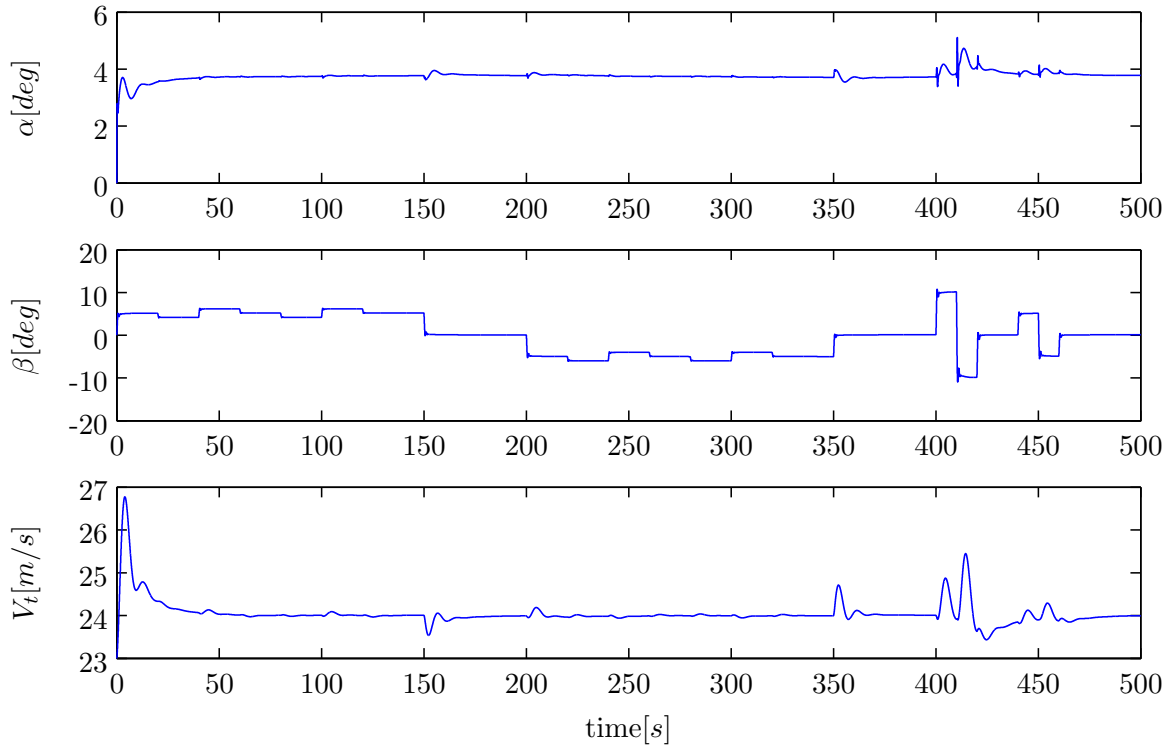

Figure D-2: Angle of attack α, side-slip angle β and true airspeed V_T

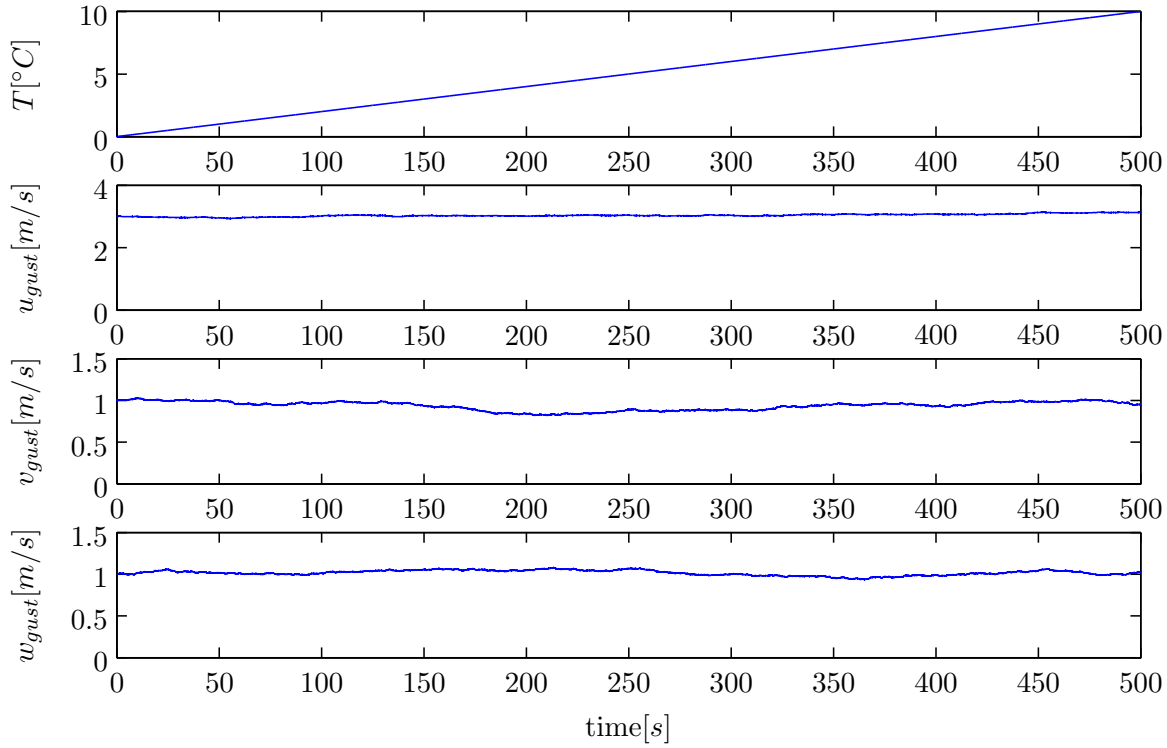

Figure D-3: Environmental properties, temperature and gust velocities in an Earth reference frame $\mathcal{F}_E$

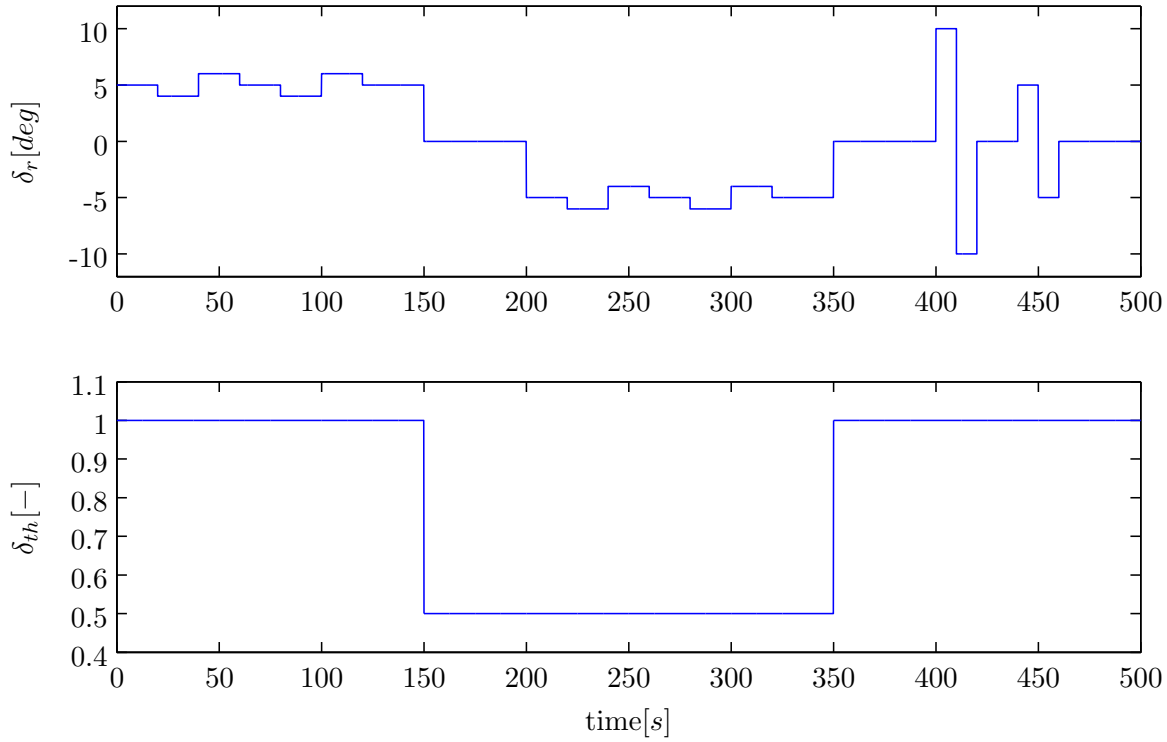

Figure D-4: Throttle and electric rudder input signal

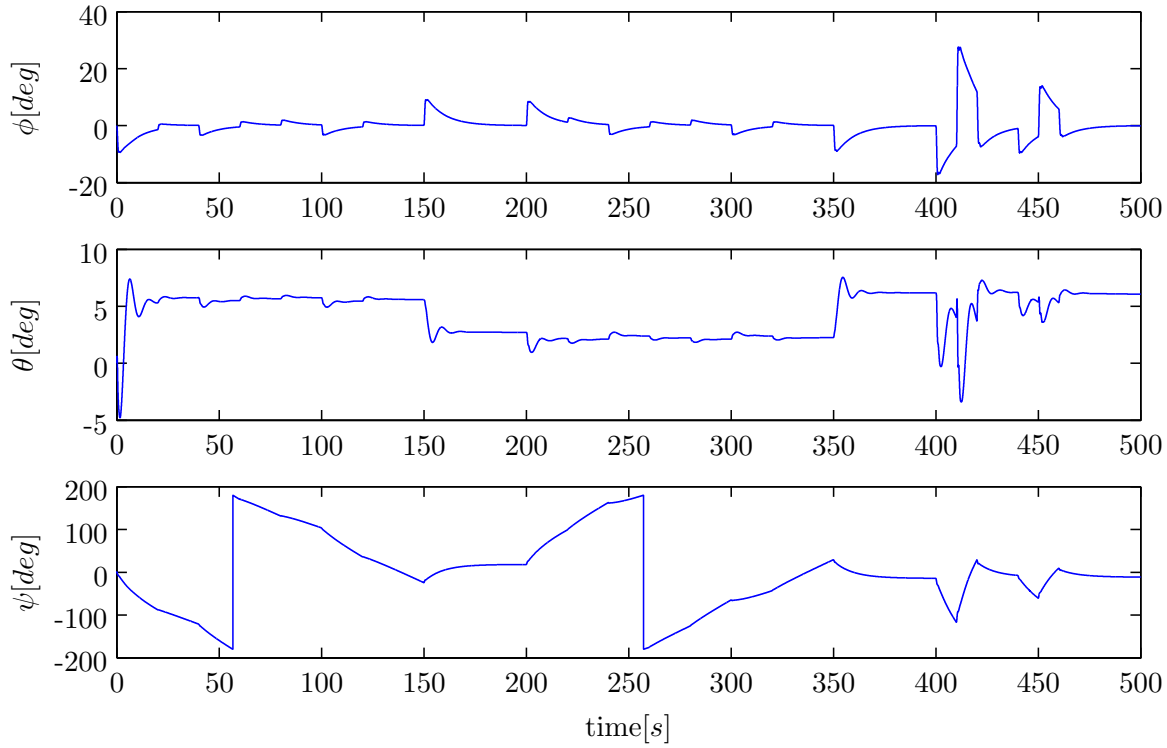

Figure D-5: Attitude and heading angles

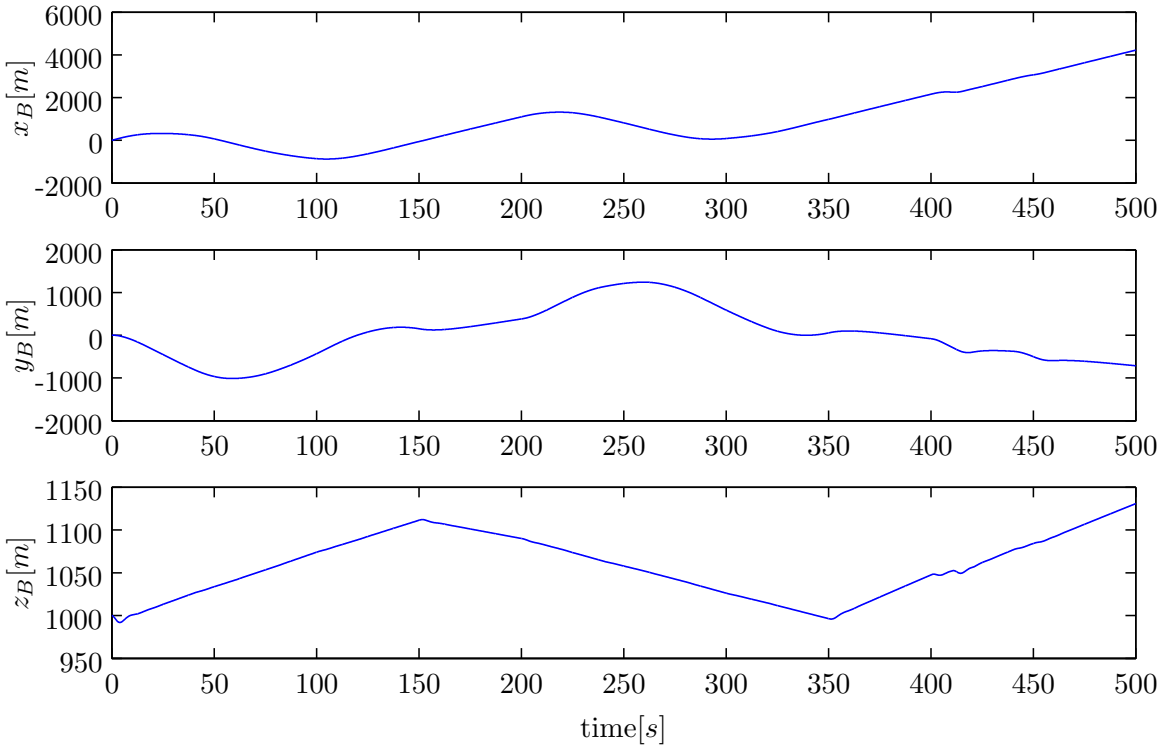

Figure D-6: Position in body-fixed reference frame $\mathcal{F}_B$

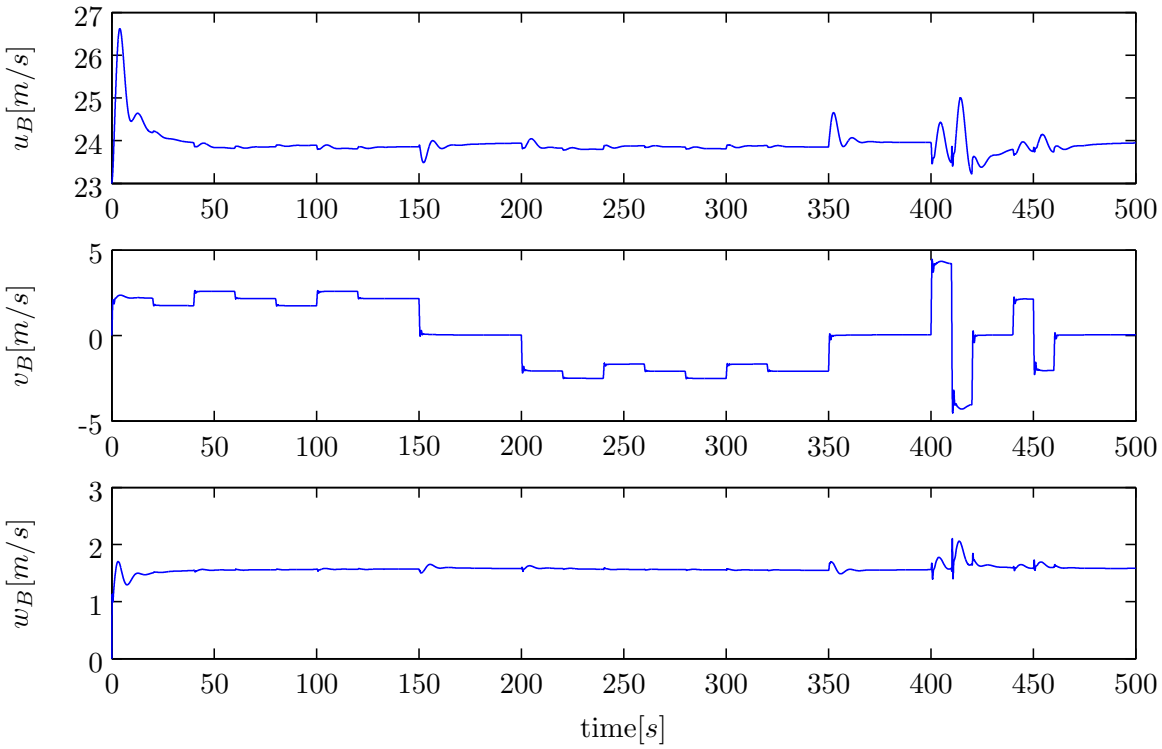

Figure D-7: Velocity in body-fixed reference frame $\mathcal{F}_B$

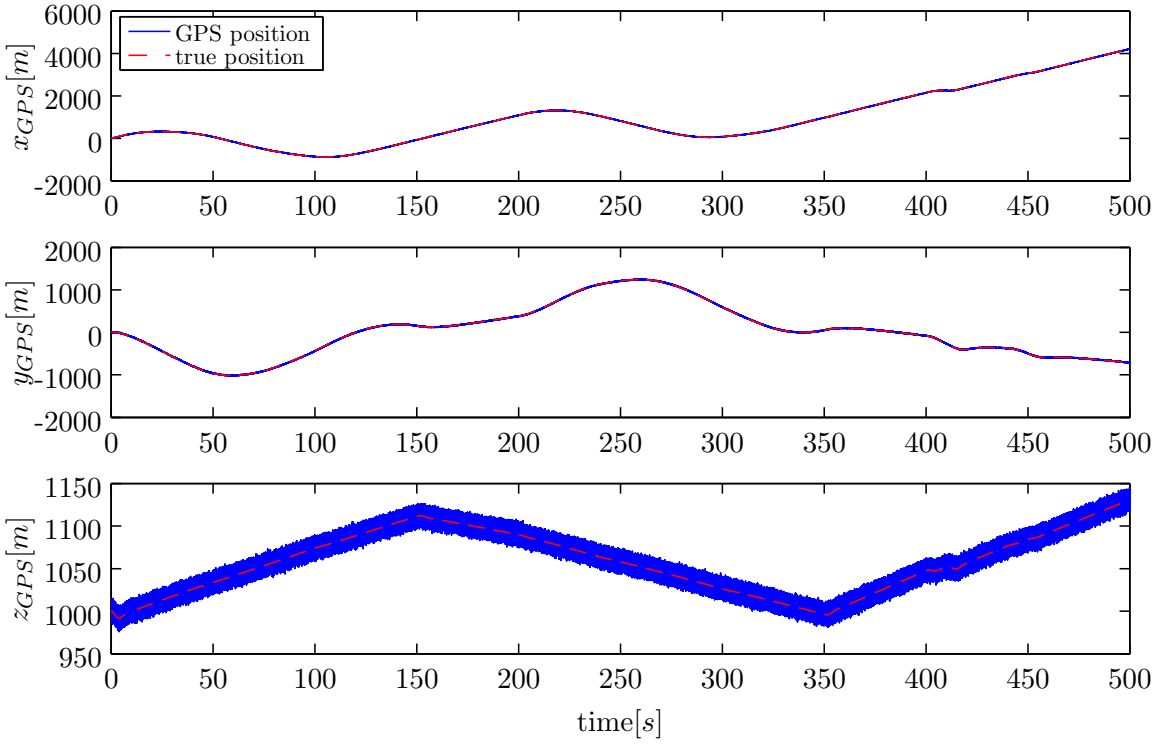

Figure D-8: GPS position in Earth reference frame $\mathcal{F}_E$

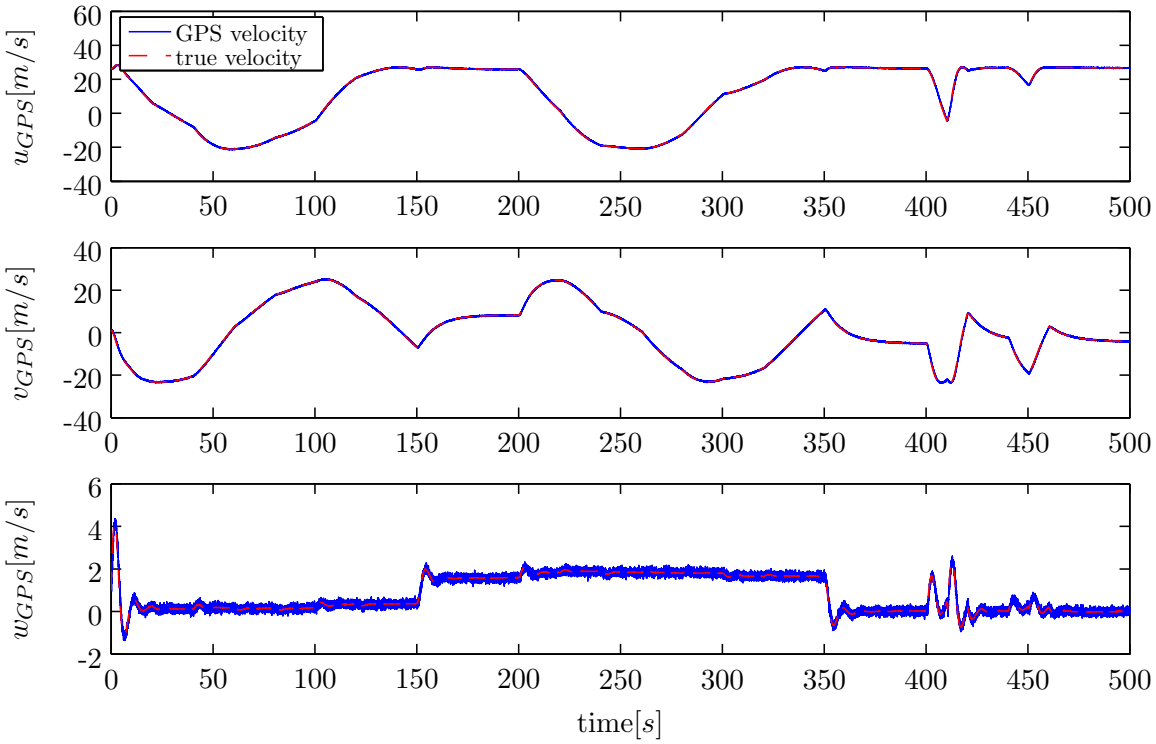

Figure D-9: GPS velocity in Earth reference frame $\mathcal{F}_E$

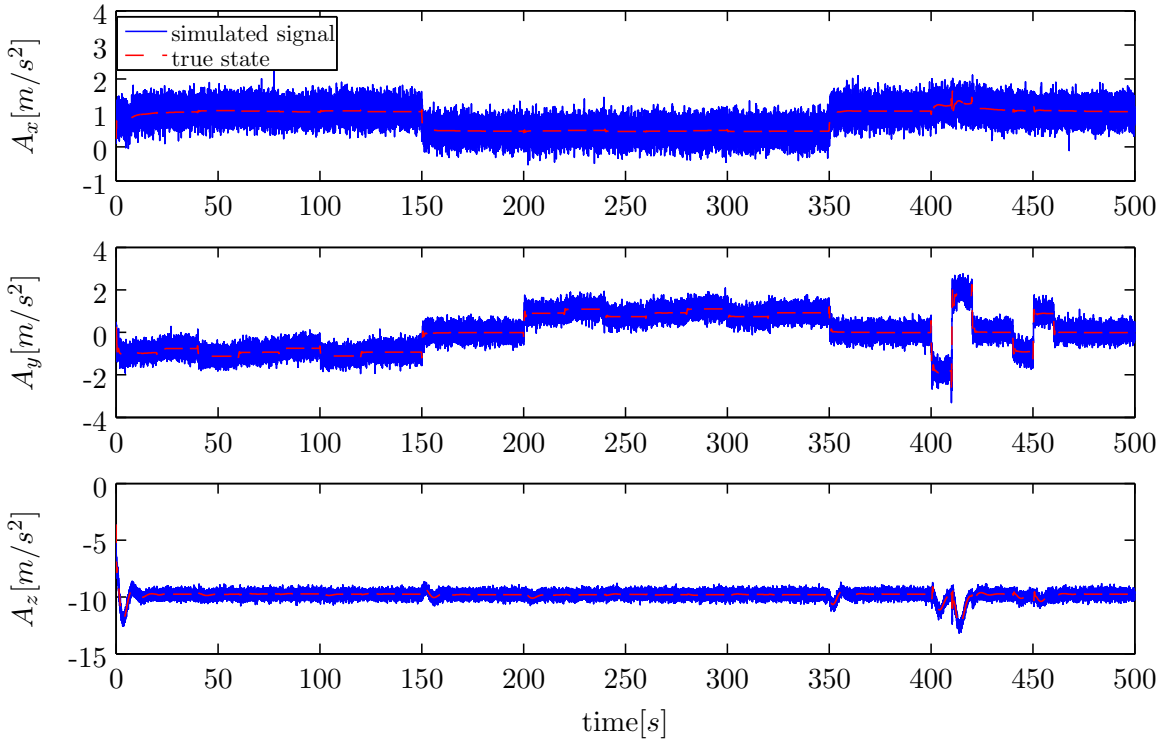

Figure D-10: Accelerometer signals

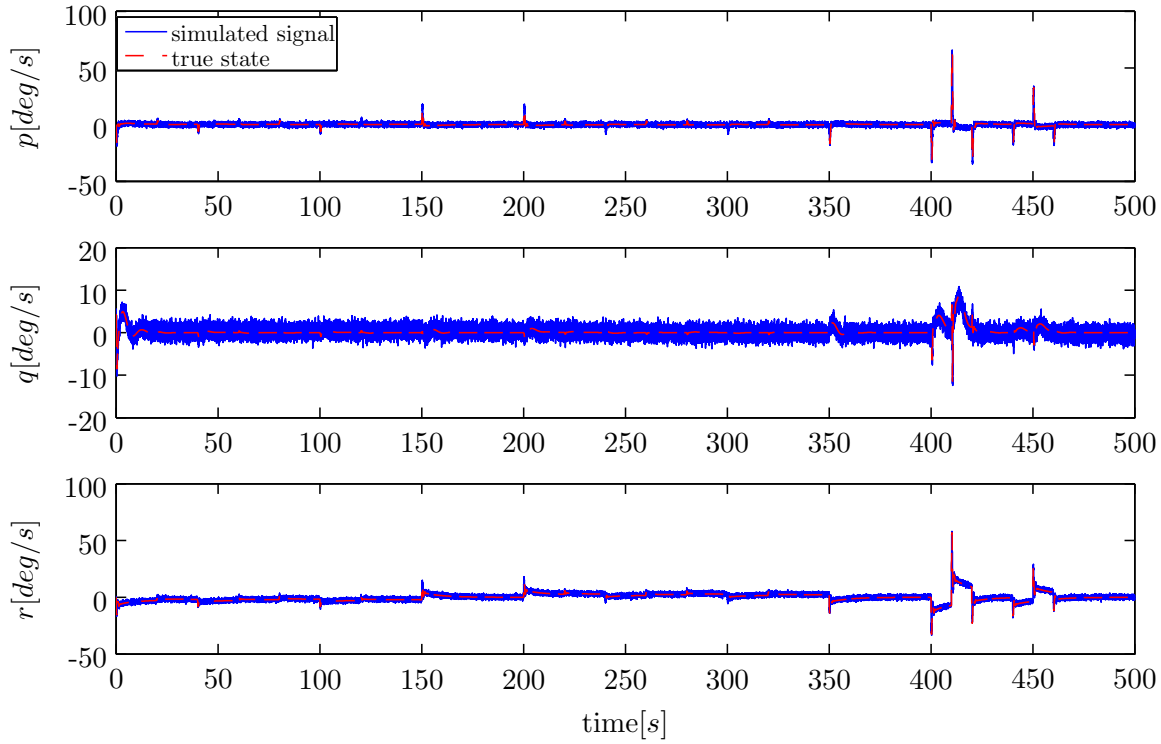

Figure D-11: Gyroscopic signals

D-1 Results EKF Identification

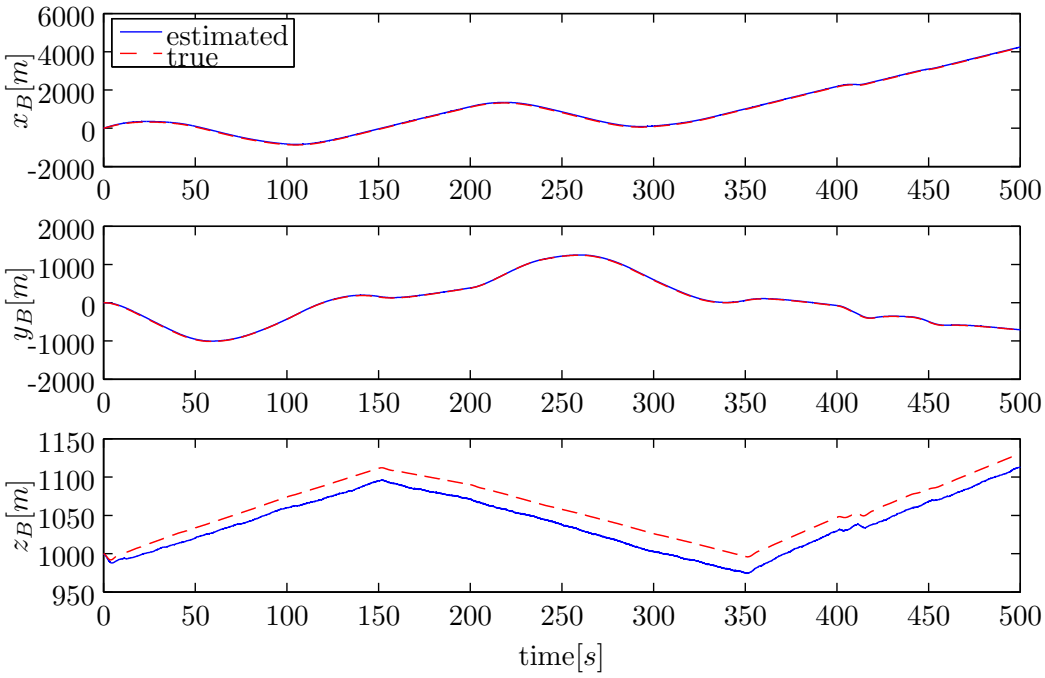

Figure D-12: Estimated position states EKF, generic Aerosonde UAV simulation

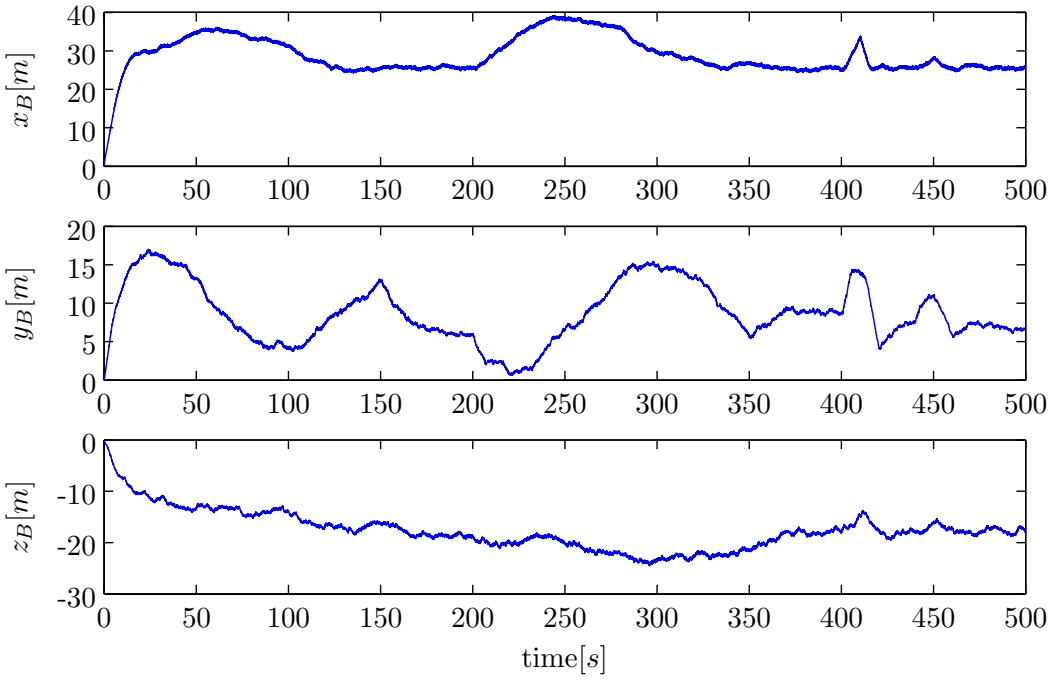

Figure D-13: Error position states EKF, generic Aerosonde UAV simulation

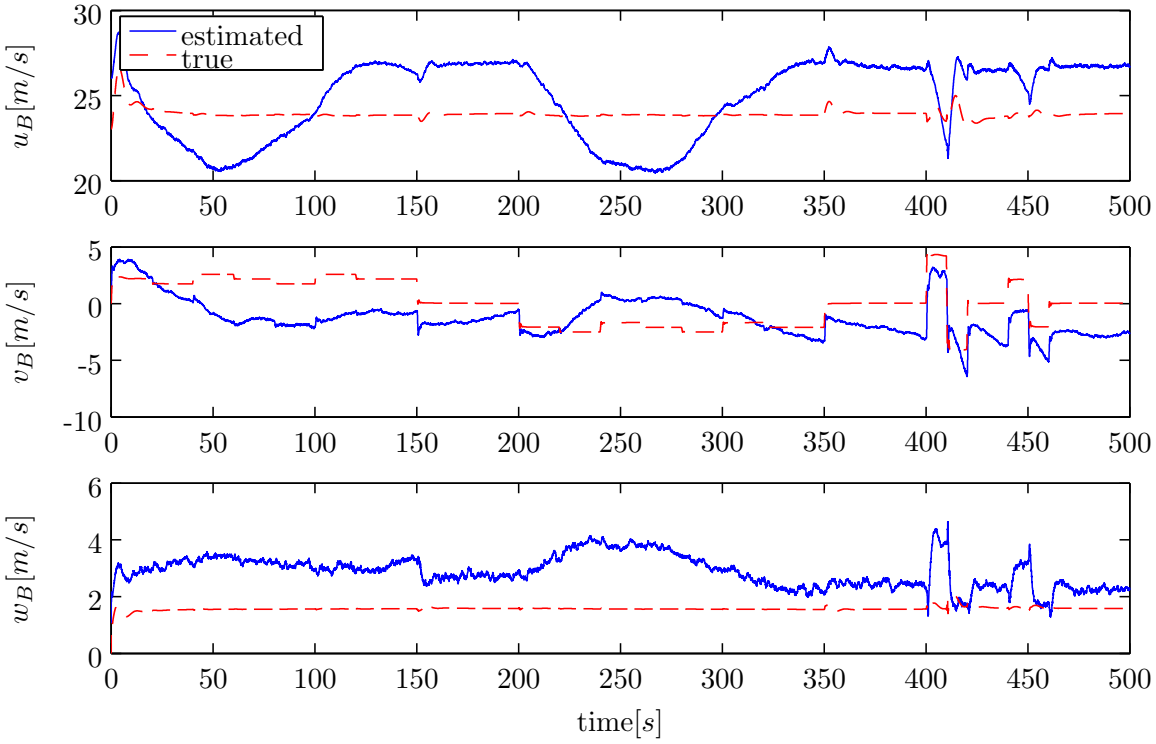

Figure D-14: Estimated velocity states EKF, generic Aerosonde UAV simulation

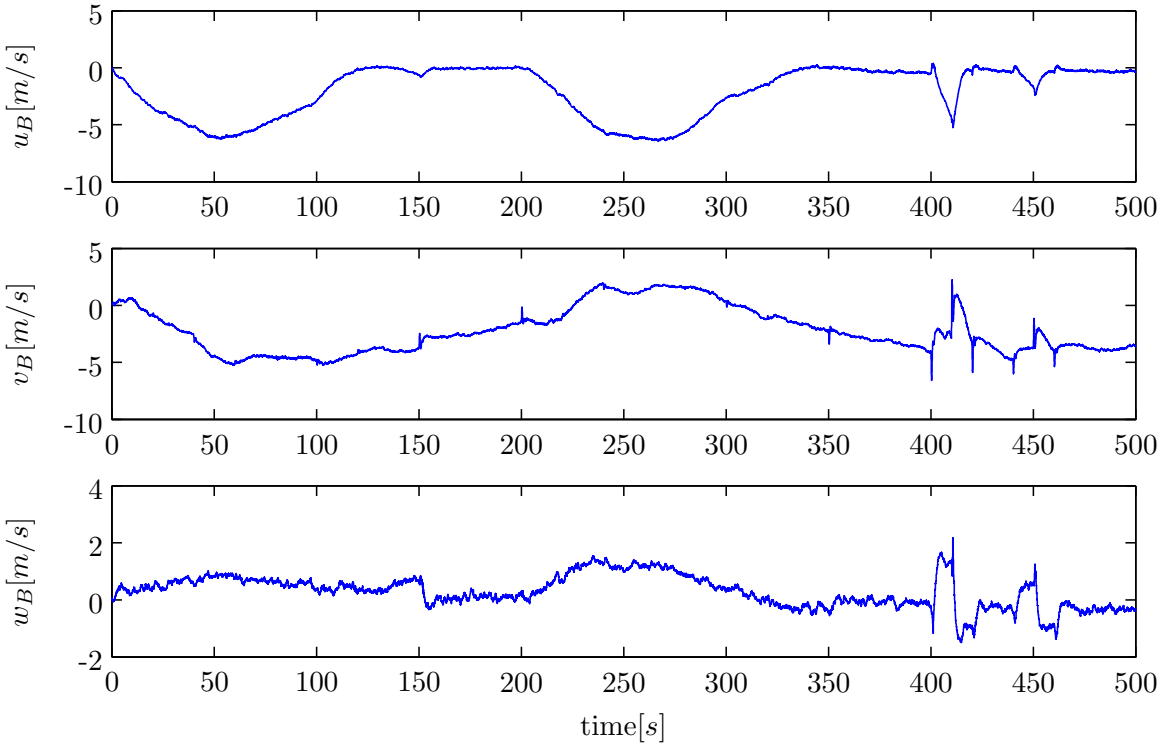

Figure D-15: Error velocity states EKF, generic Aerosonde UAV simulation

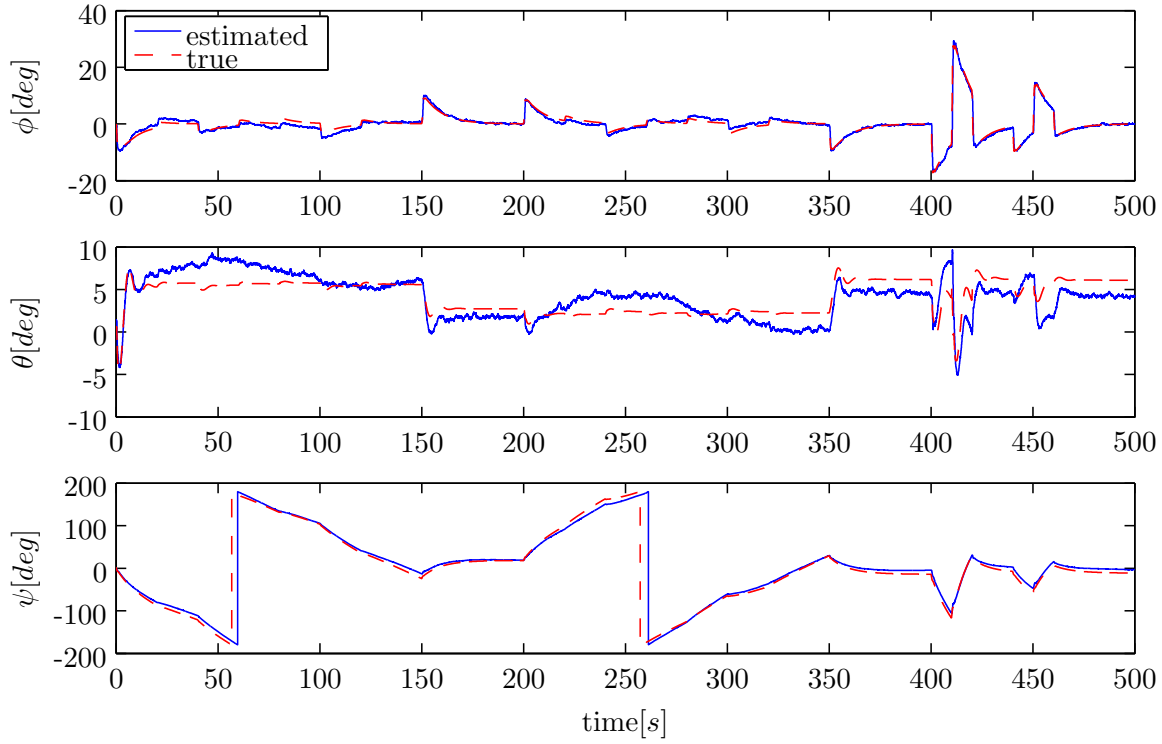

Figure D-16: Estimated Euler angle states EKF, generic Aerosonde UAV simulation

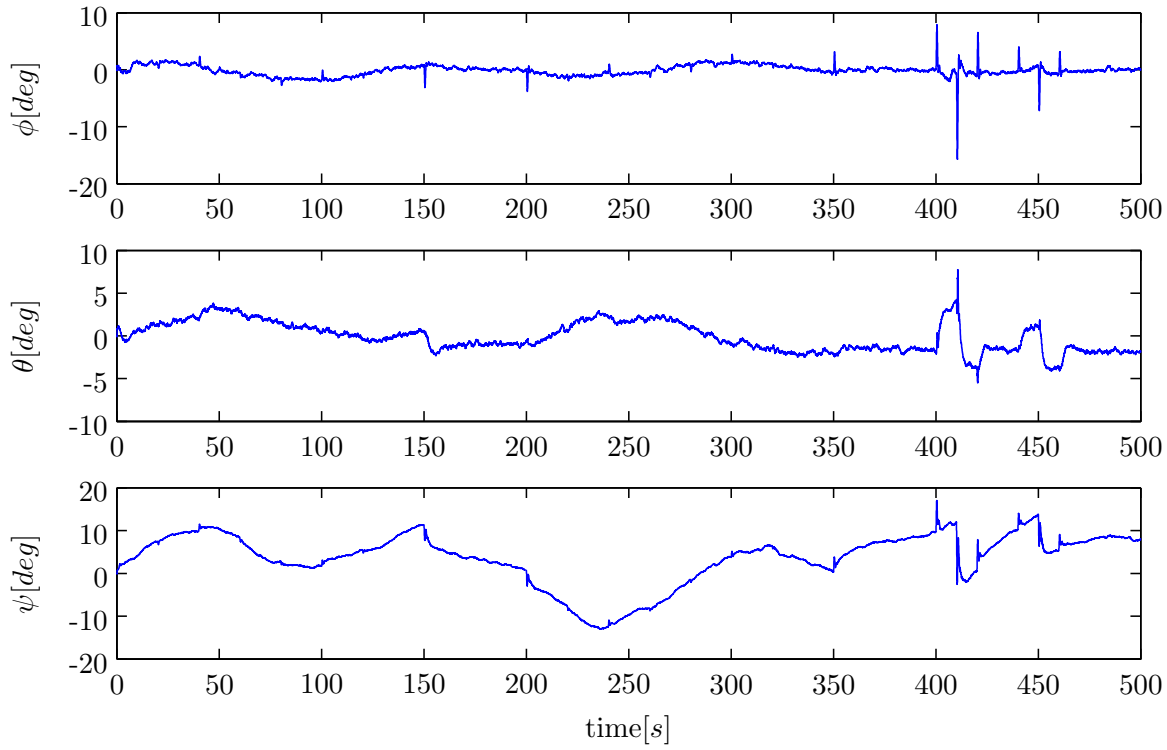

Figure D-17: Error Euler angle states EKF, generic Aerosonde UAV simulation

D-2 Results EKF Identification no Gust

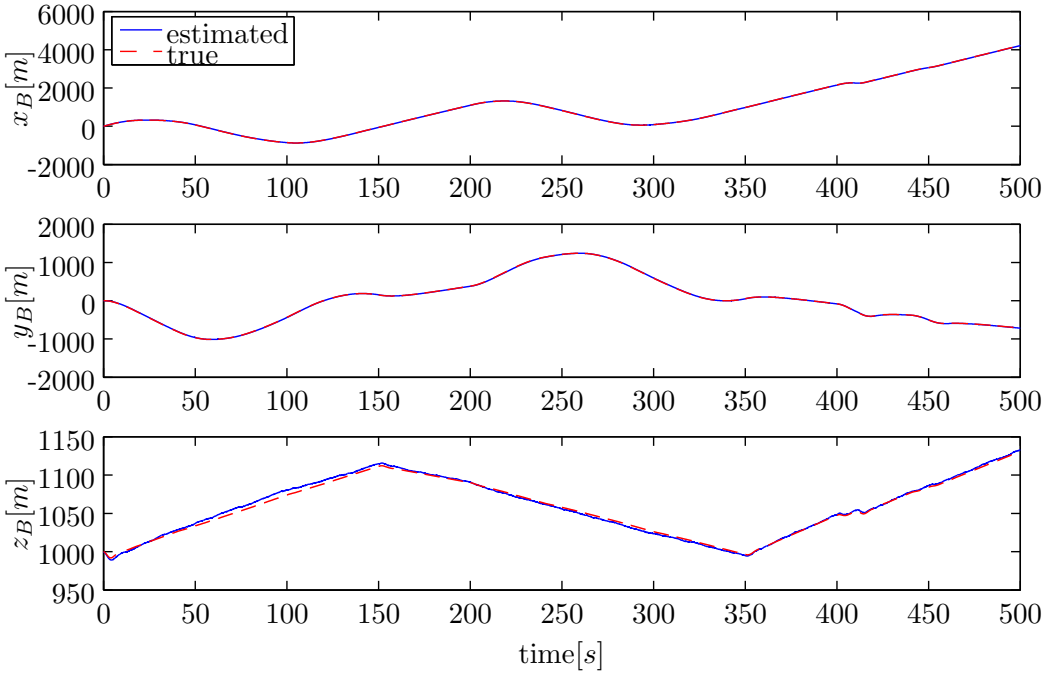

Figure D-18: Estimated position states EKF, generic Aerosonde UAV simulation

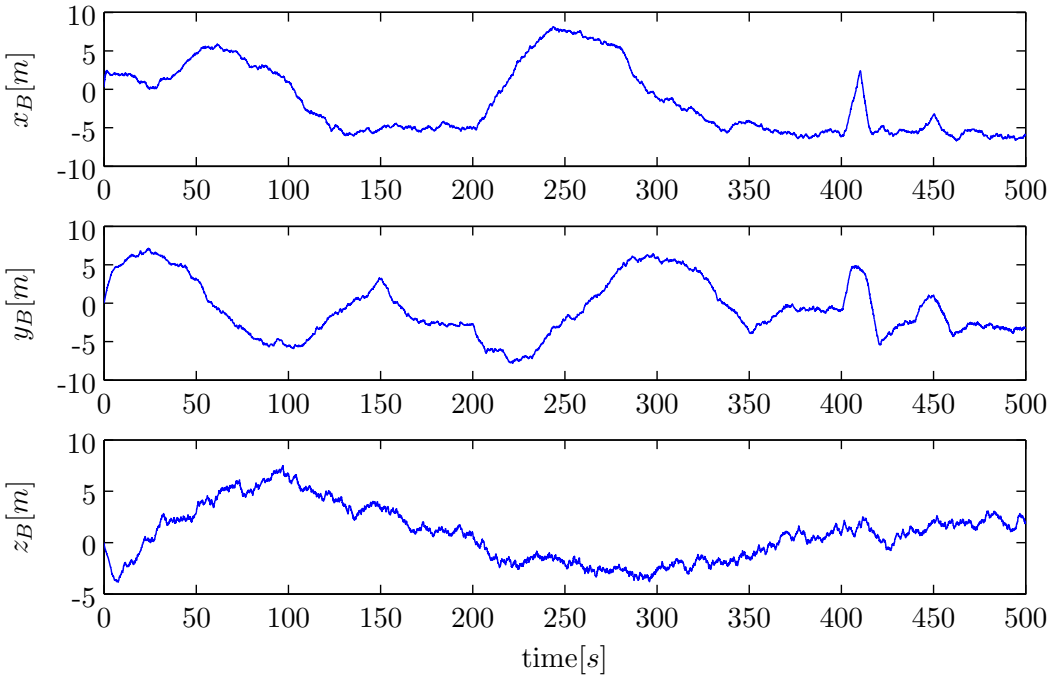

Figure D-19: Error position states EKF, generic Aerosonde UAV simulation

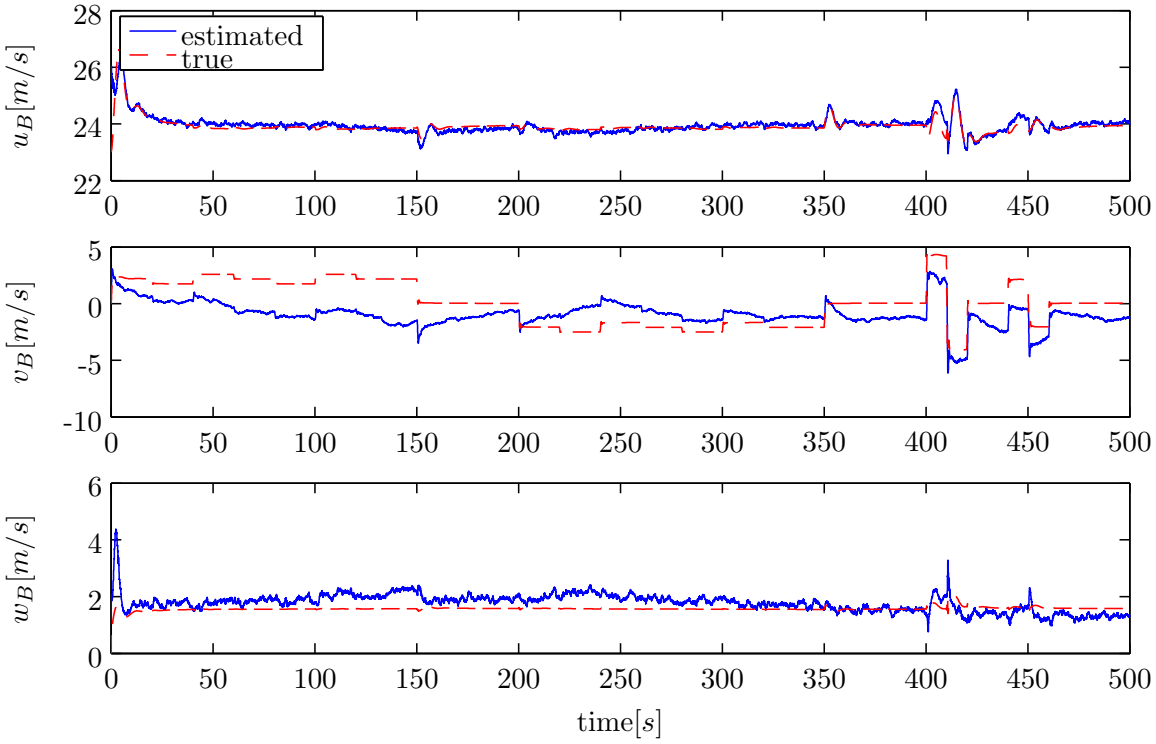

Figure D-20: Estimated velocity states EKF, generic Aerosonde UAV simulation

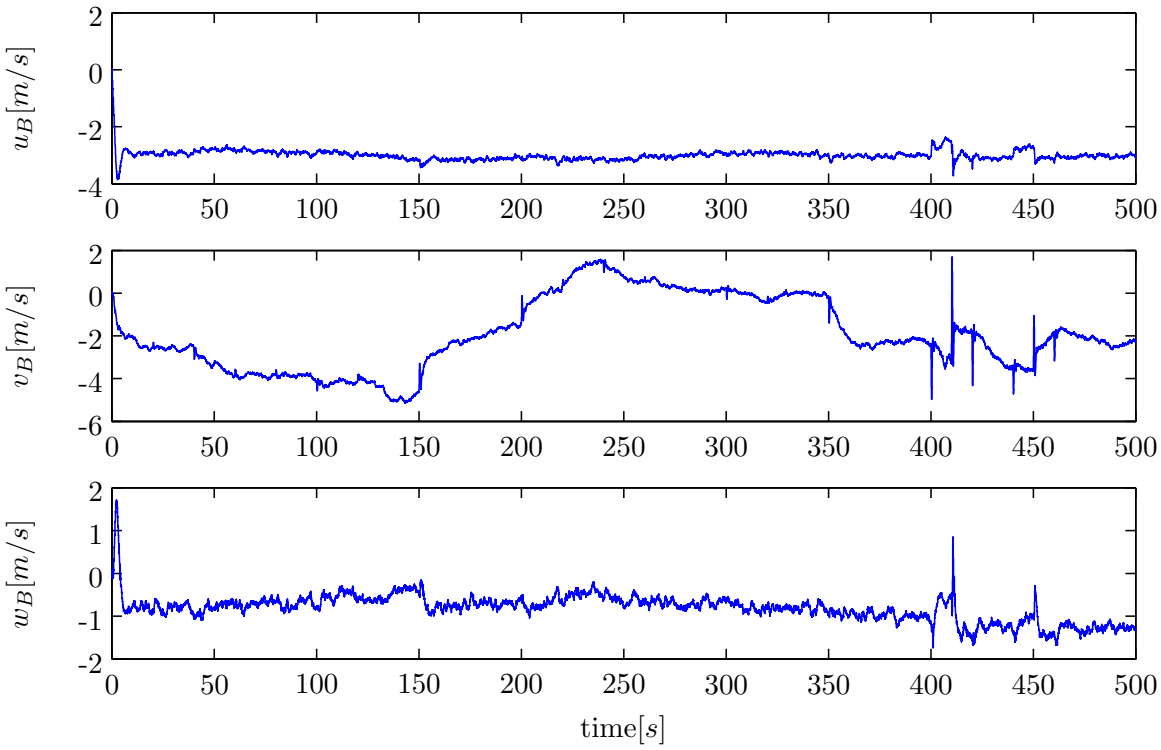

Figure D-21: Error velocity states EKF, generic Aerosonde UAV simulation

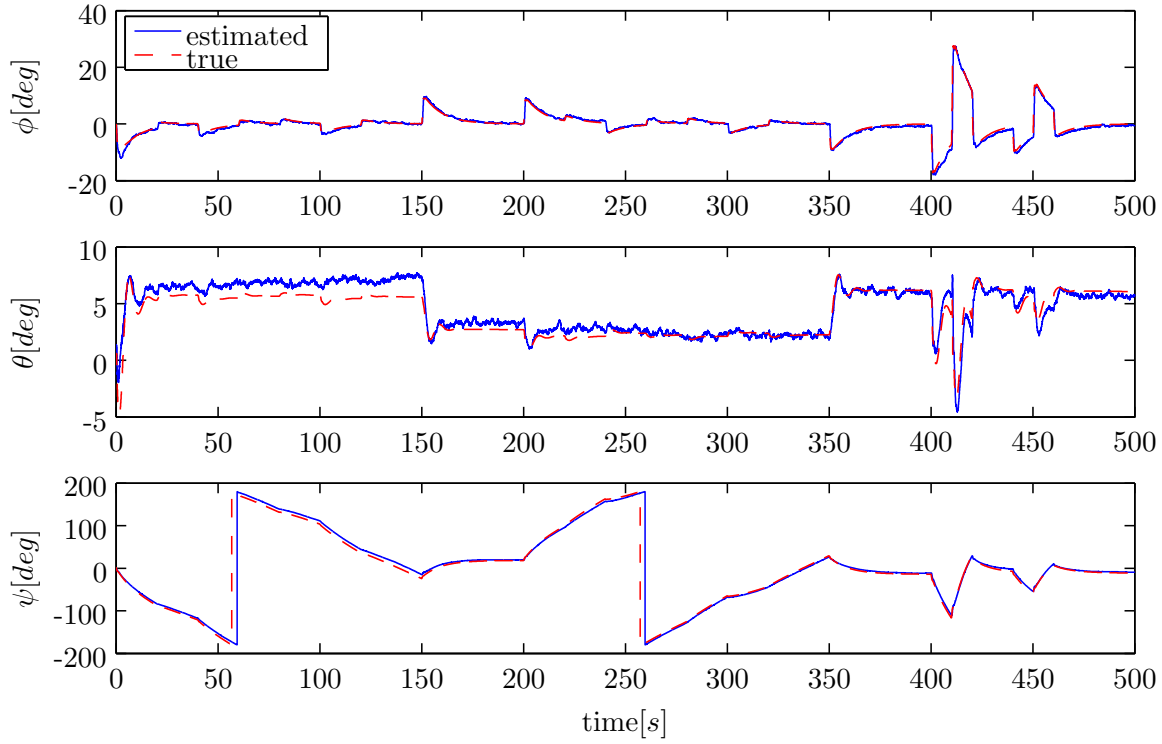

Figure D-22: Estimated Euler angle states EKF, generic Aerosonde UAV simulation

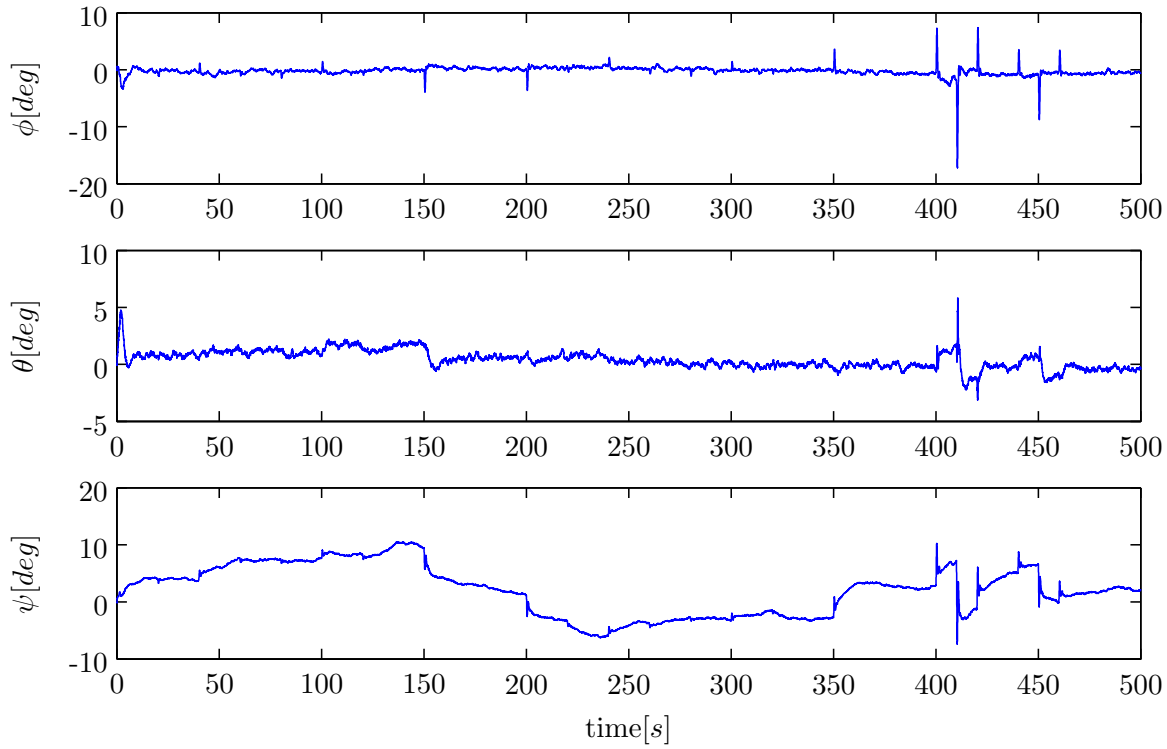

Figure D-23: Error Euler angle states EKF, generic Aerosonde UAV simulation

D-3 Results IEKF Identification

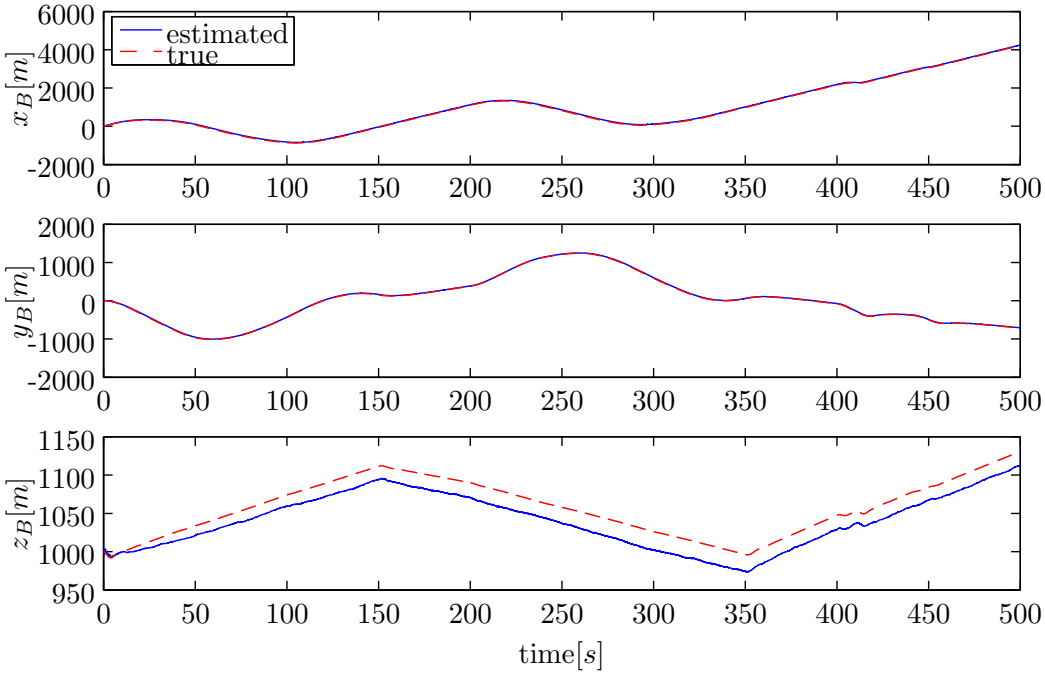

Figure D-24: Estimated position states IEKF, generic Aerosonde UAV simulation

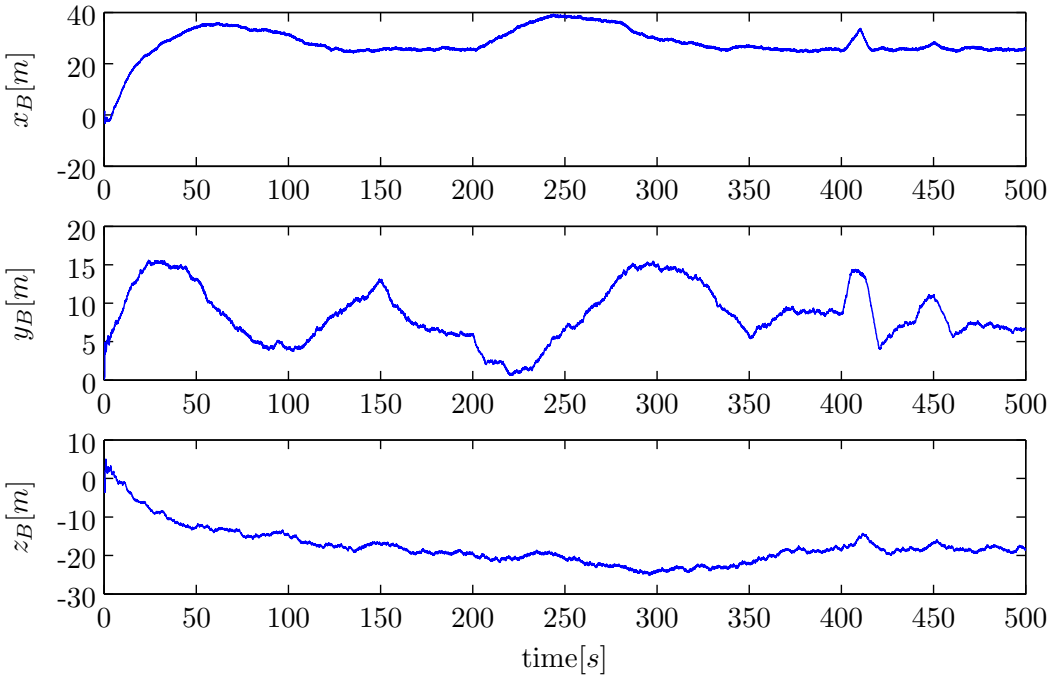

Figure D-25: Error position states IEKF, generic Aerosonde UAV simulation

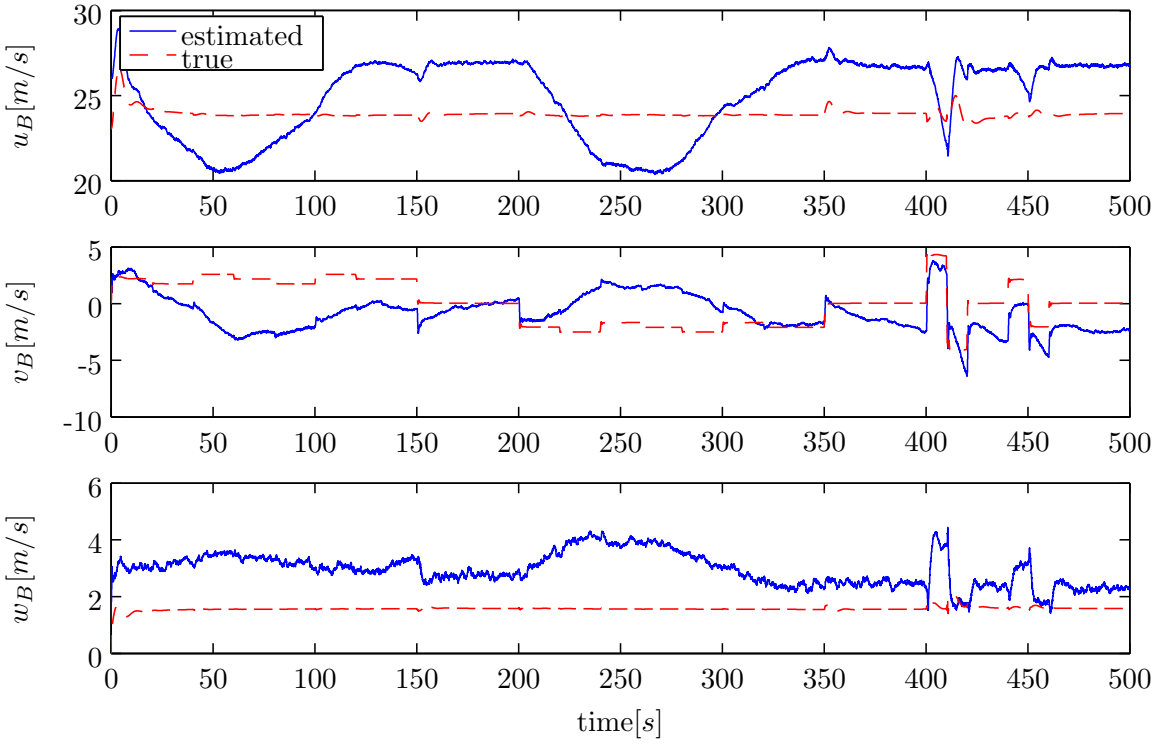

Figure D-26: Estimated velocity states IEKF, generic Aerosonde UAV simulation

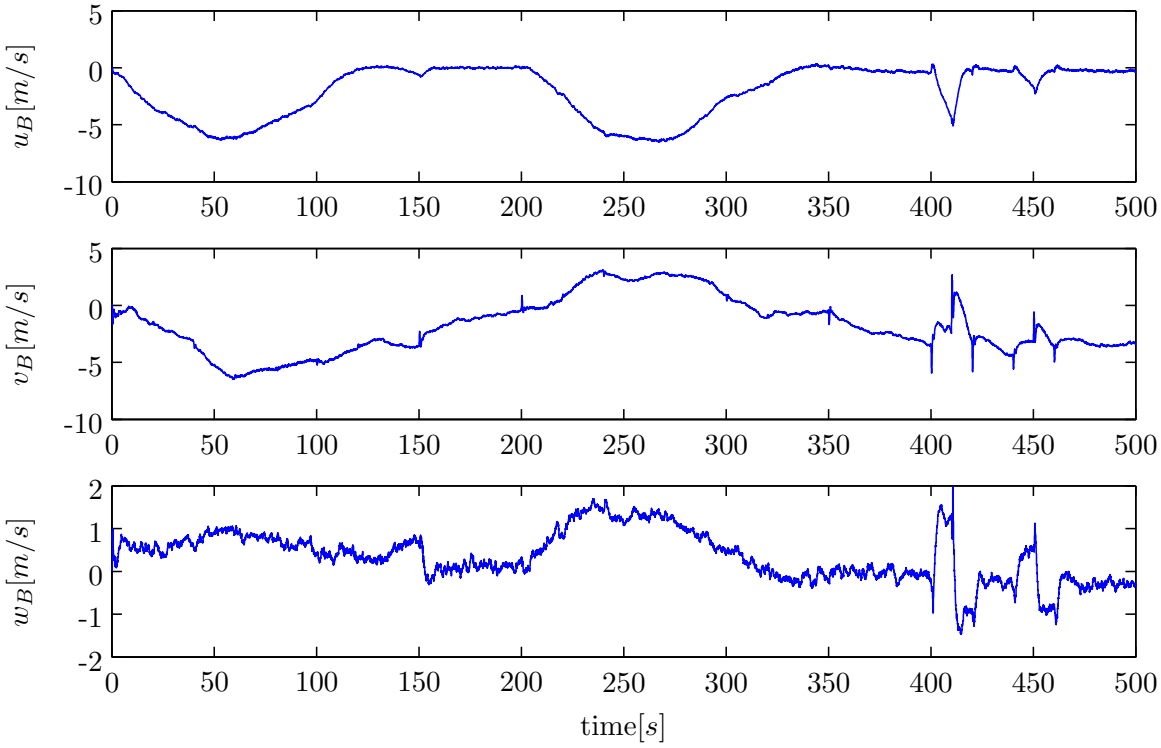

Figure D-27: Error velocity states IEKF, generic Aerosonde UAV simulation

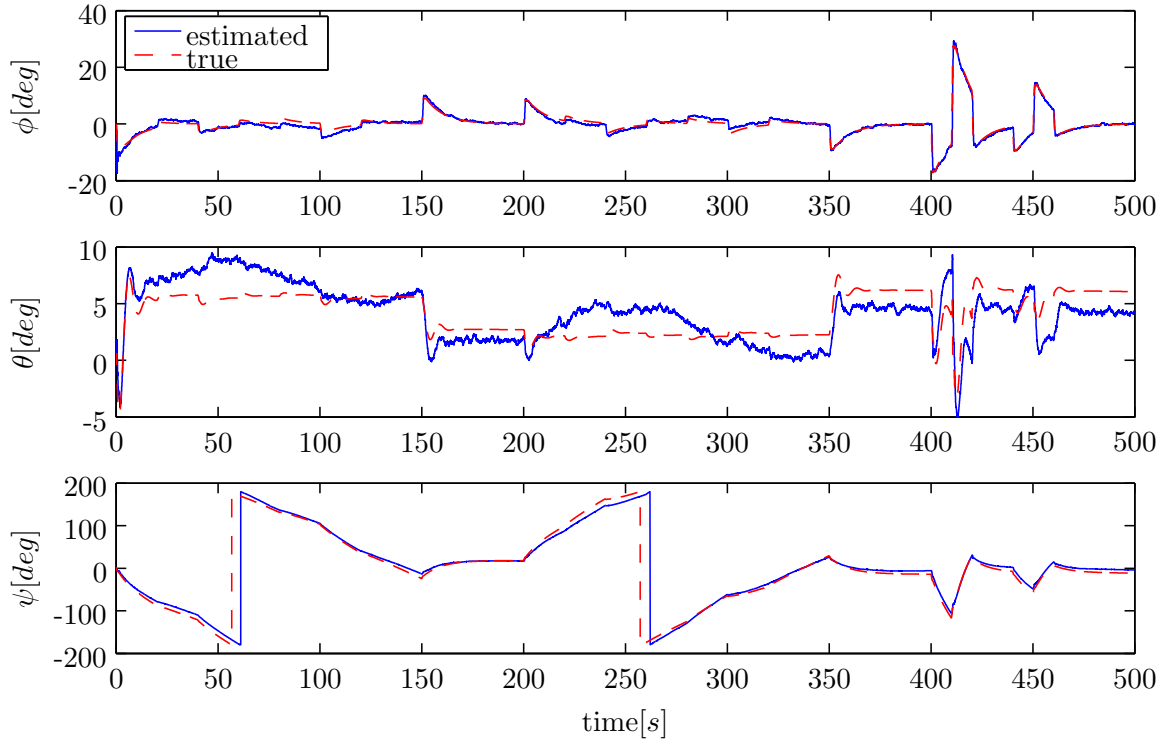

Figure D-28: Estimated Euler angle states IEKF, generic Aerosonde UAV simulation

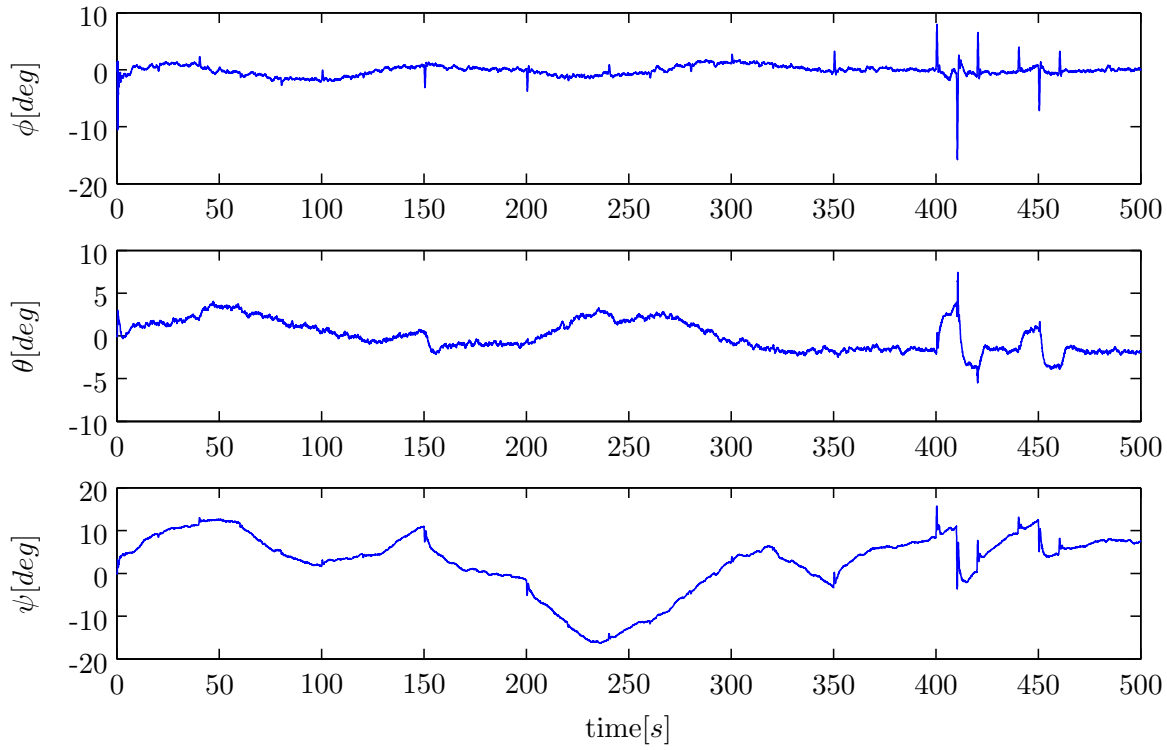

Figure D-29: Error Euler angle states IEKF, generic Aerosonde UAV simulation

D-4 Results IEKF Identification no Gust

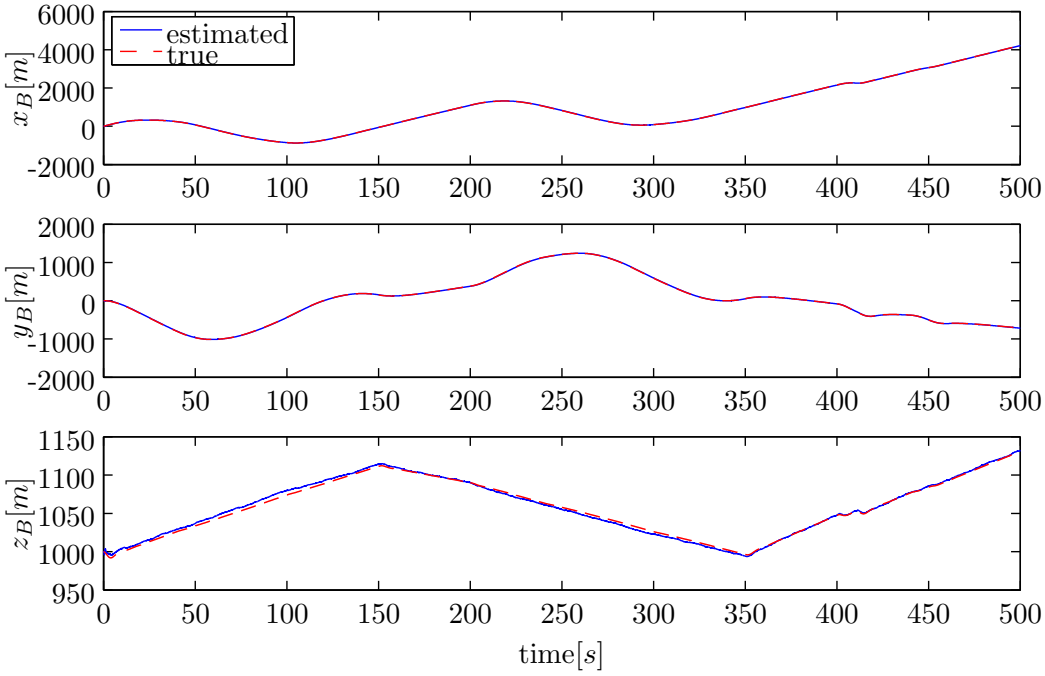

Figure D-30: Estimated position states IEKF, generic Aerosonde UAV simulation

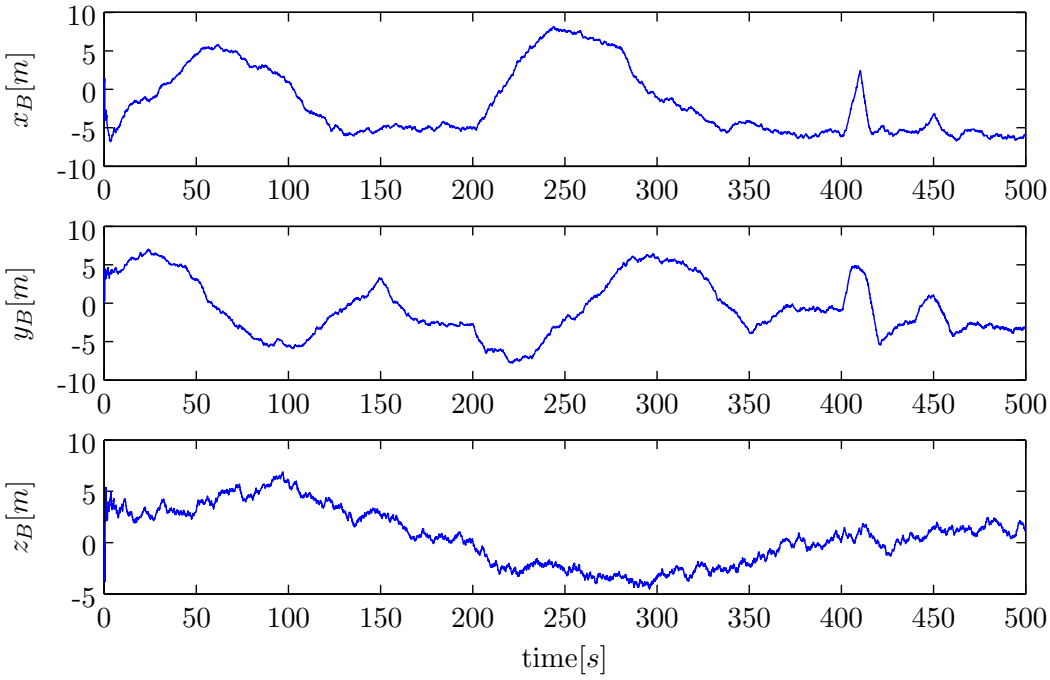

Figure D-31: Error position states IEKF, generic Aerosonde UAV simulation

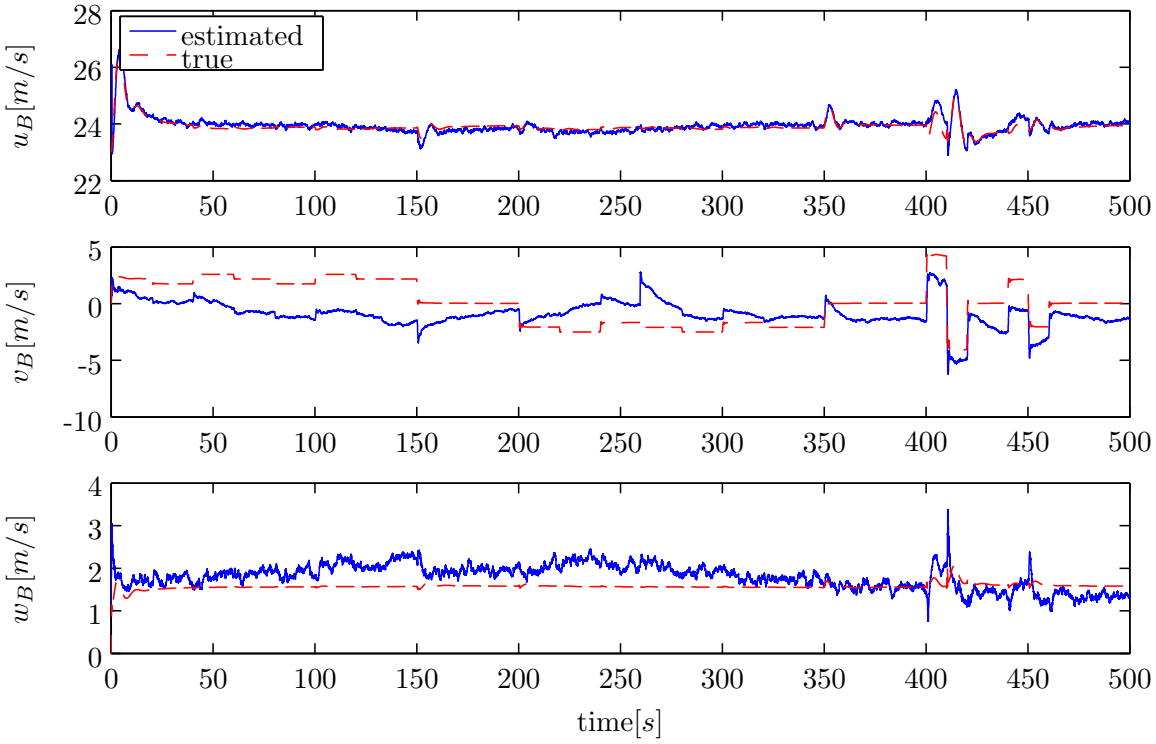

Figure D-32: Estimated velocity states IEKF, generic Aerosonde UAV simulation

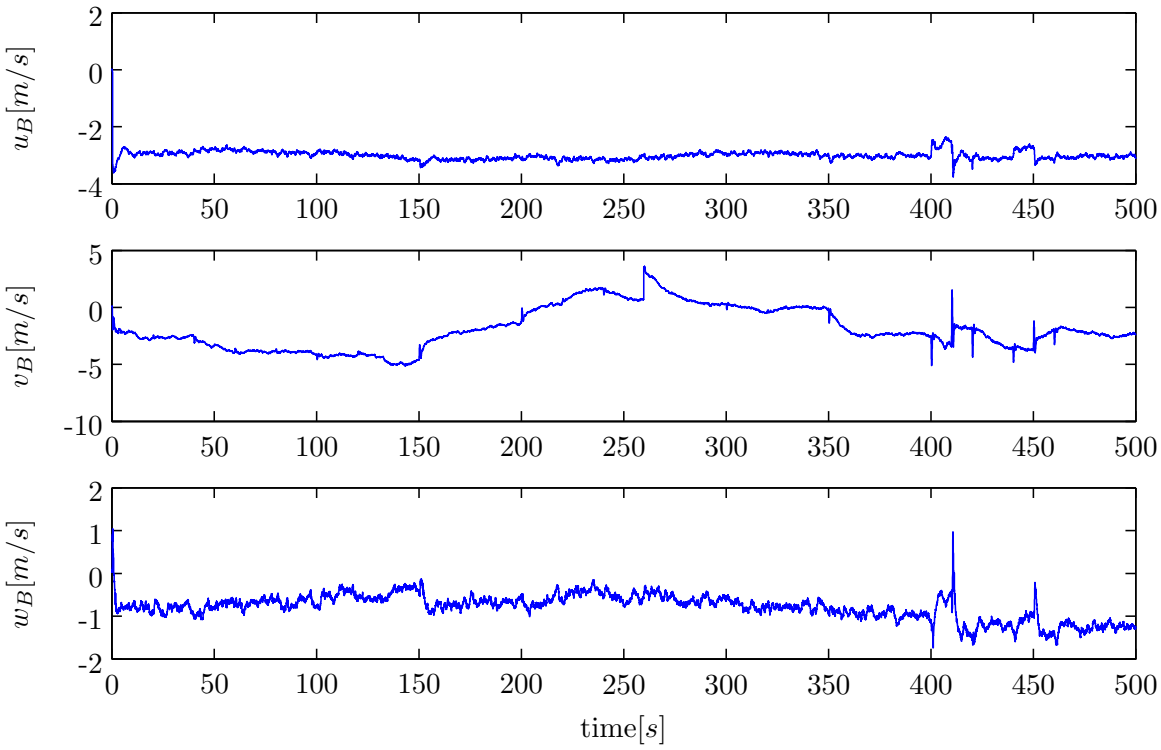

Figure D-33: Error velocity states IEKF, generic Aerosonde UAV simulation

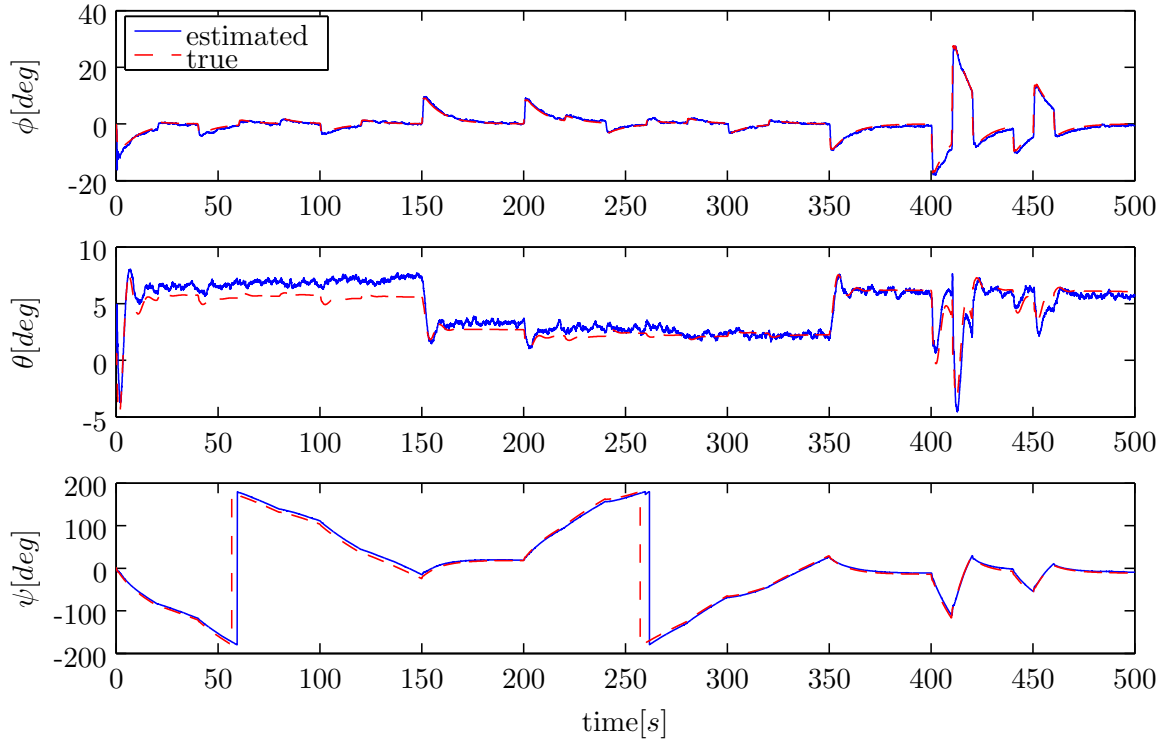

Figure D-34: Estimated Euler angle states IEKF, generic Aerosonde UAV simulation

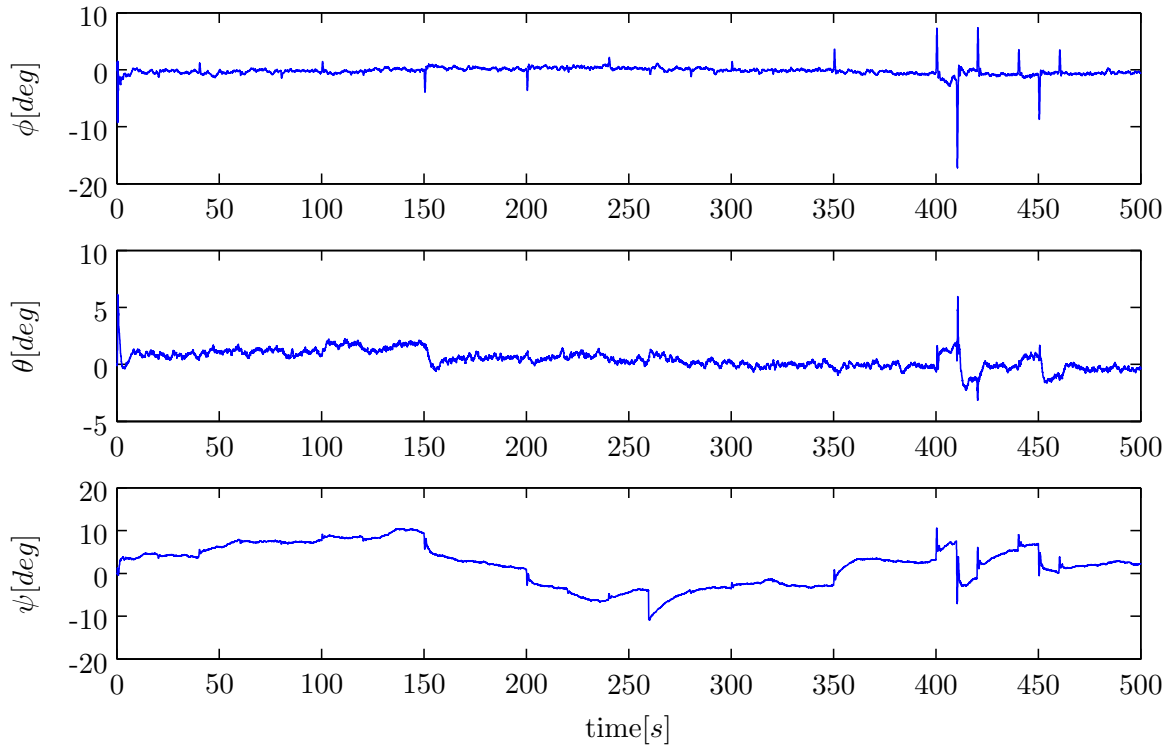

Figure D-35: Error Euler angle states IEKF, generic Aerosonde UAV simulation

D-5 Results Non-Linear SO(3) Identification

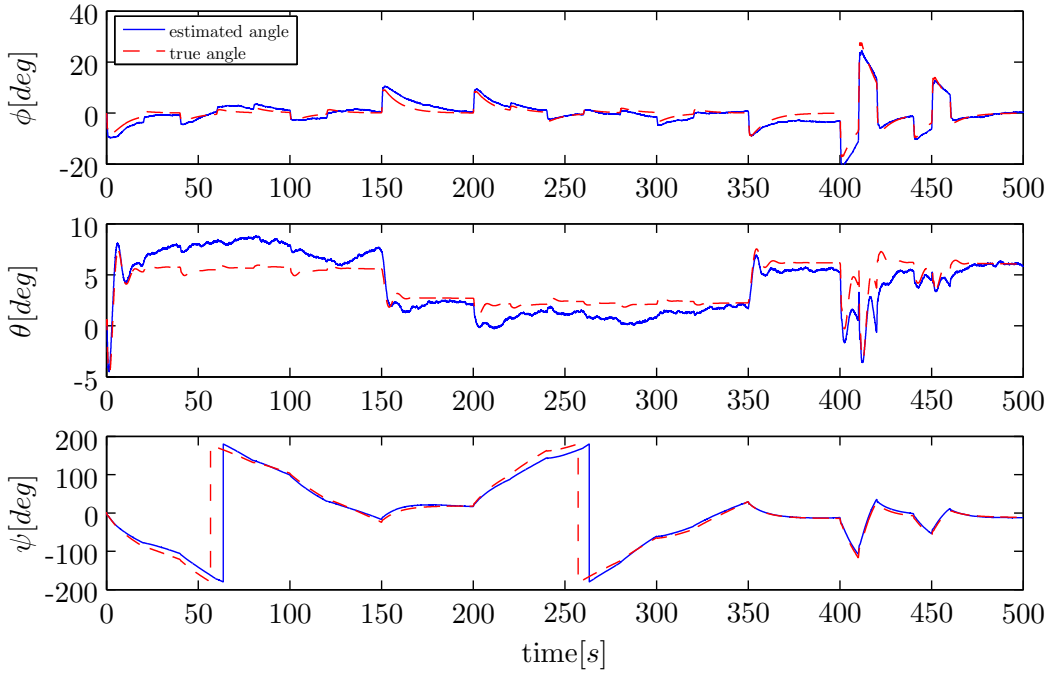

Figure D-36: Estimated Euler angles SO(3), generic Aerosonde UAV simulation

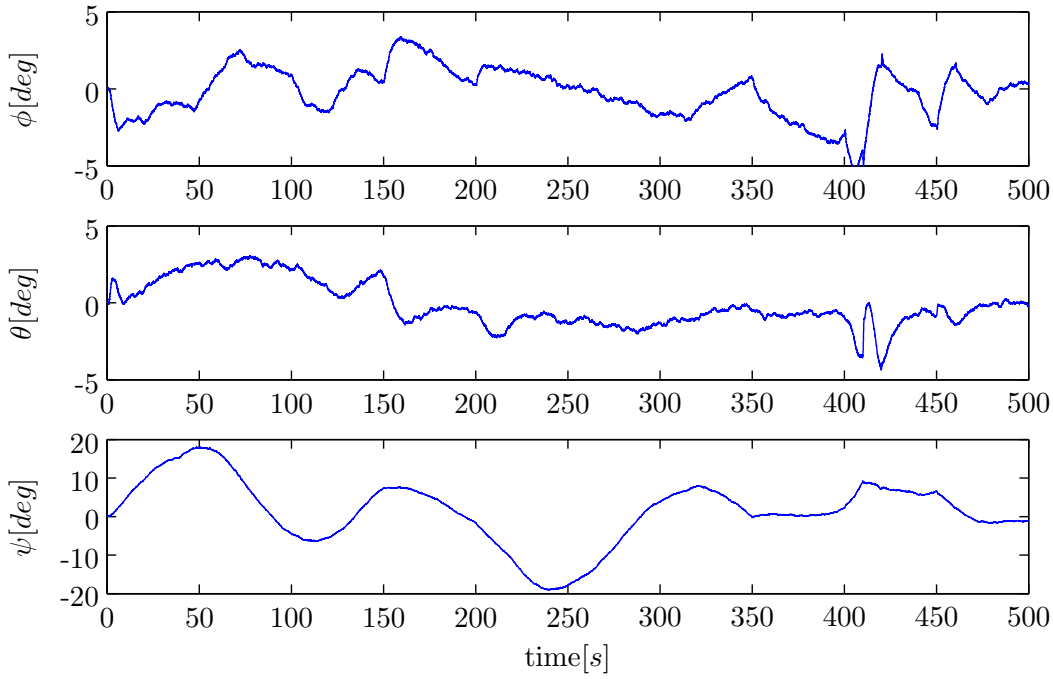

Figure D-37: Error Euler angles SO(3), generic Aerosonde UAV simulation

D-6 Results Non-Linear SO(3) Identification no Gust

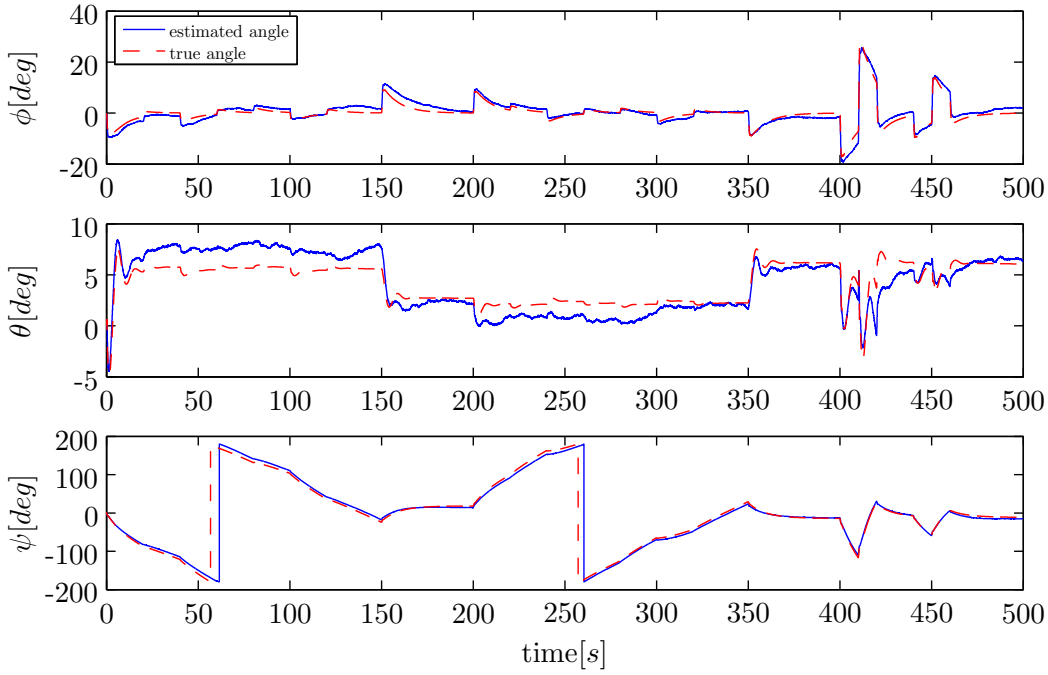

Figure D-38: Estimated Euler angles SO(3), generic Aerosonde UAV simulation

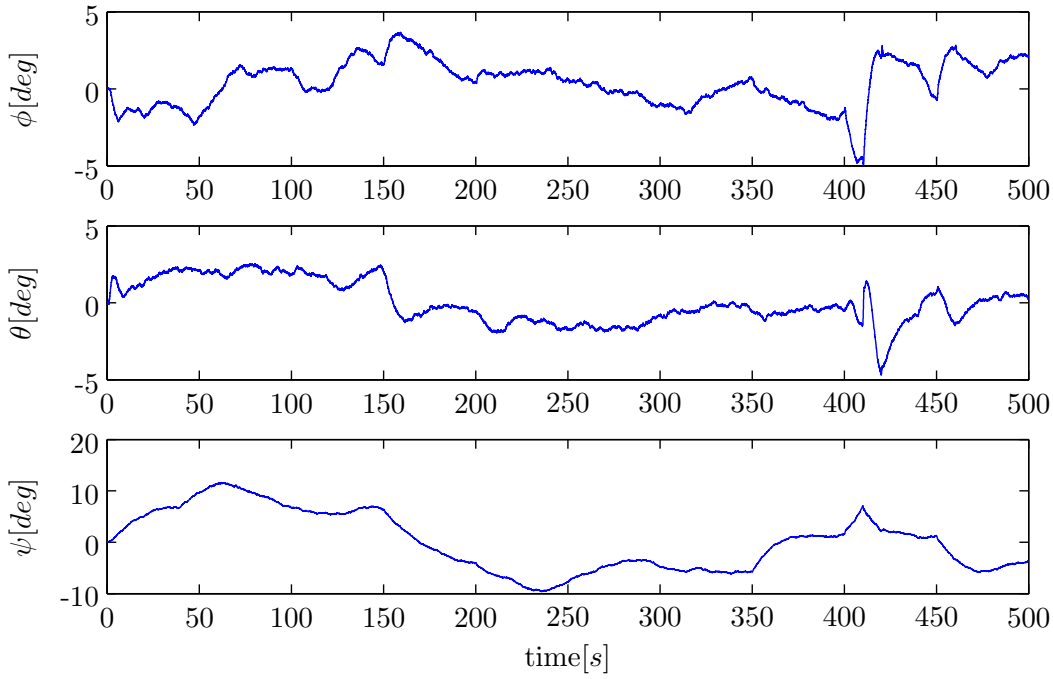

Figure D-39: Error Euler angles SO(3), generic Aerosonde UAV simulation

Appendix E

Small Turns Aerosonde UAV Simulations

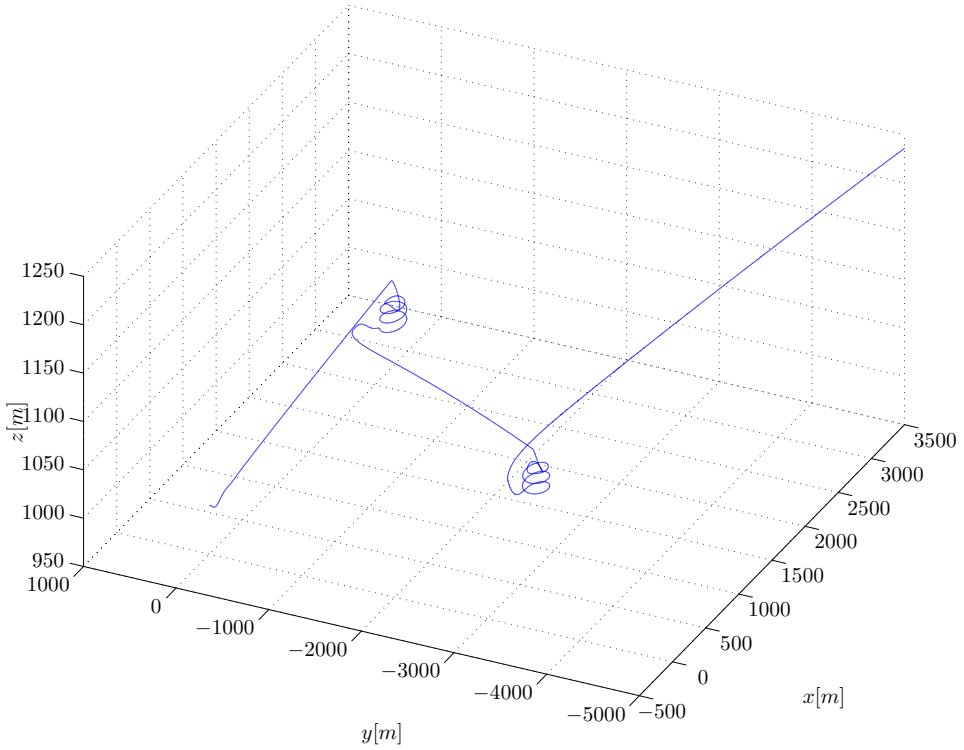

Figure E-1: 3D position, small turns Aerosonde UAV simulation

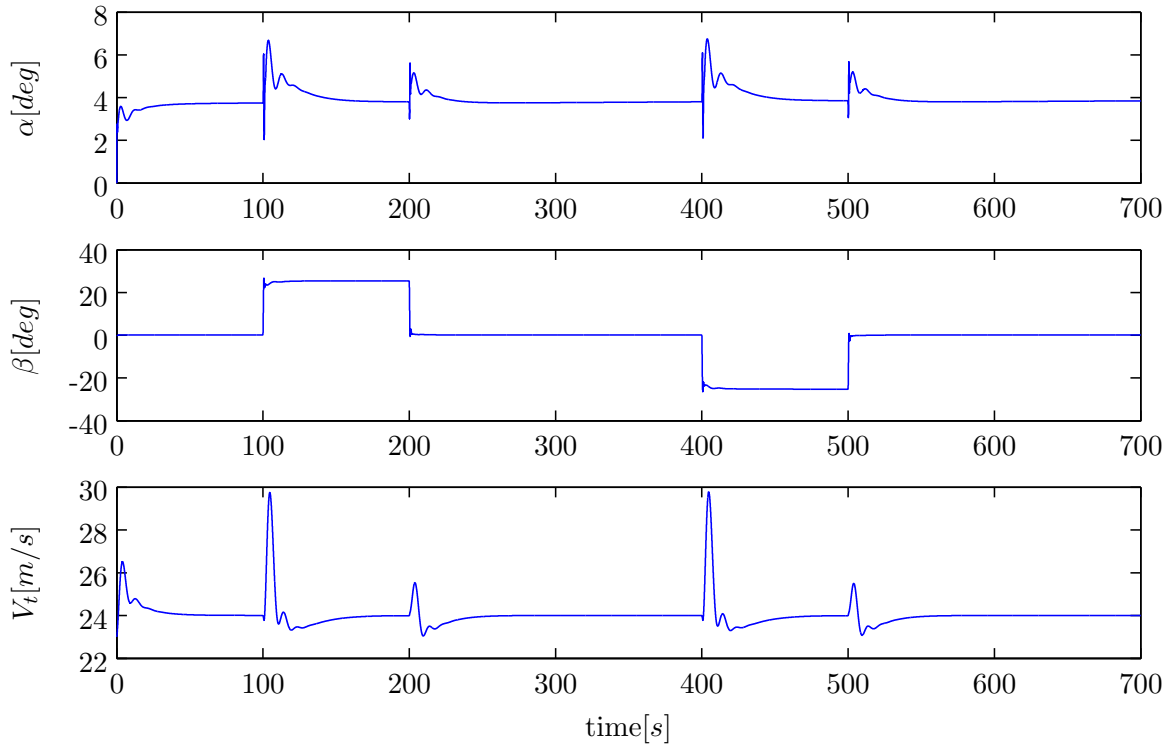

Figure E-2: Angle of attack α, side-slip angle β and true airspeed V_T

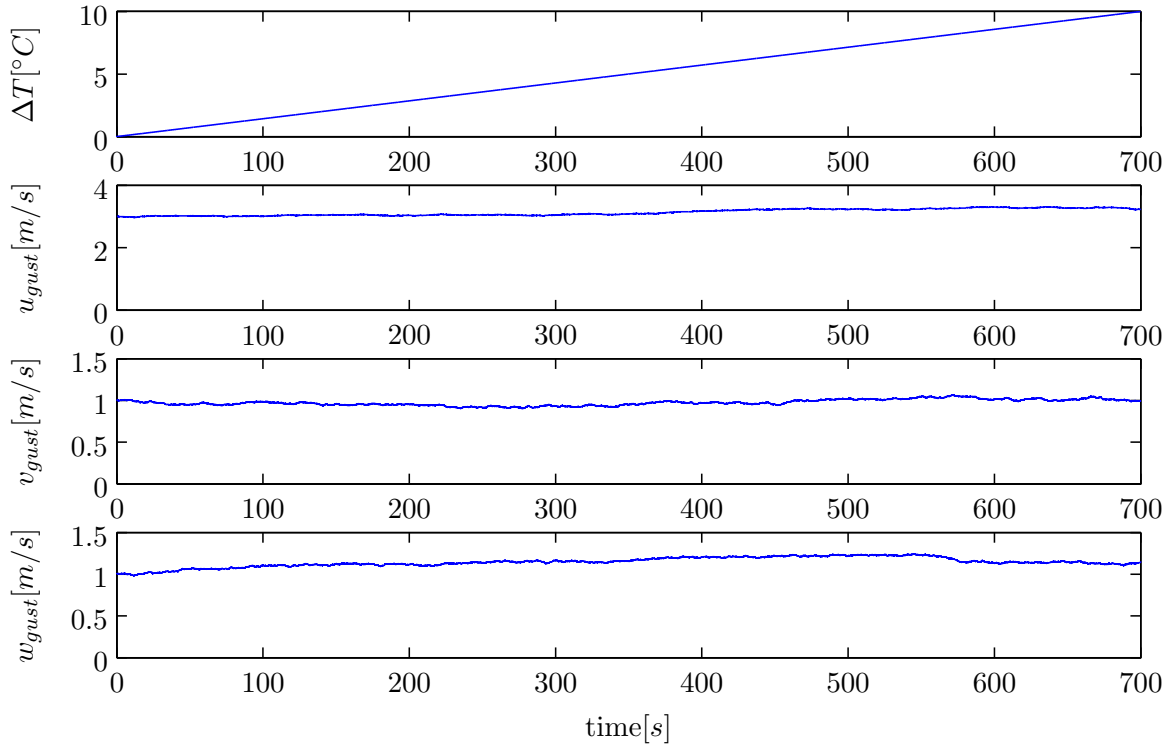

Figure E-3: Environmental properties, temperature and gust velocities in an Earth reference frame $\mathcal{F}_E$

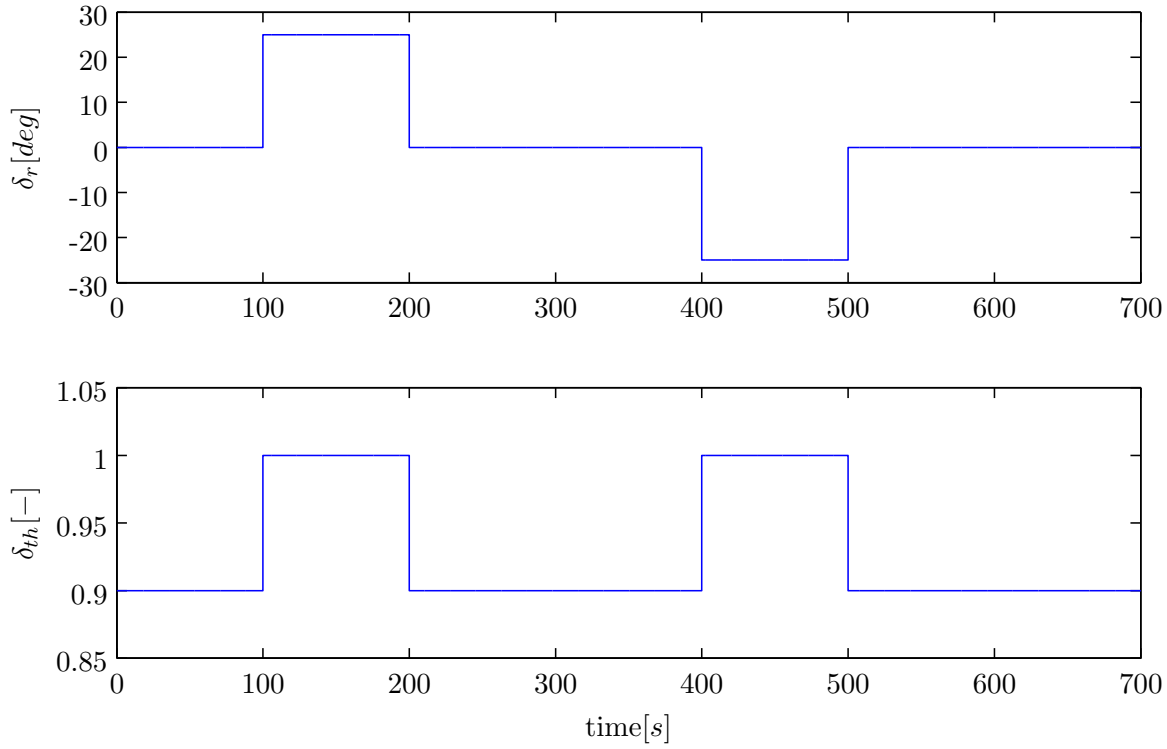

Figure E-4: Throttle and electric rudder input signal

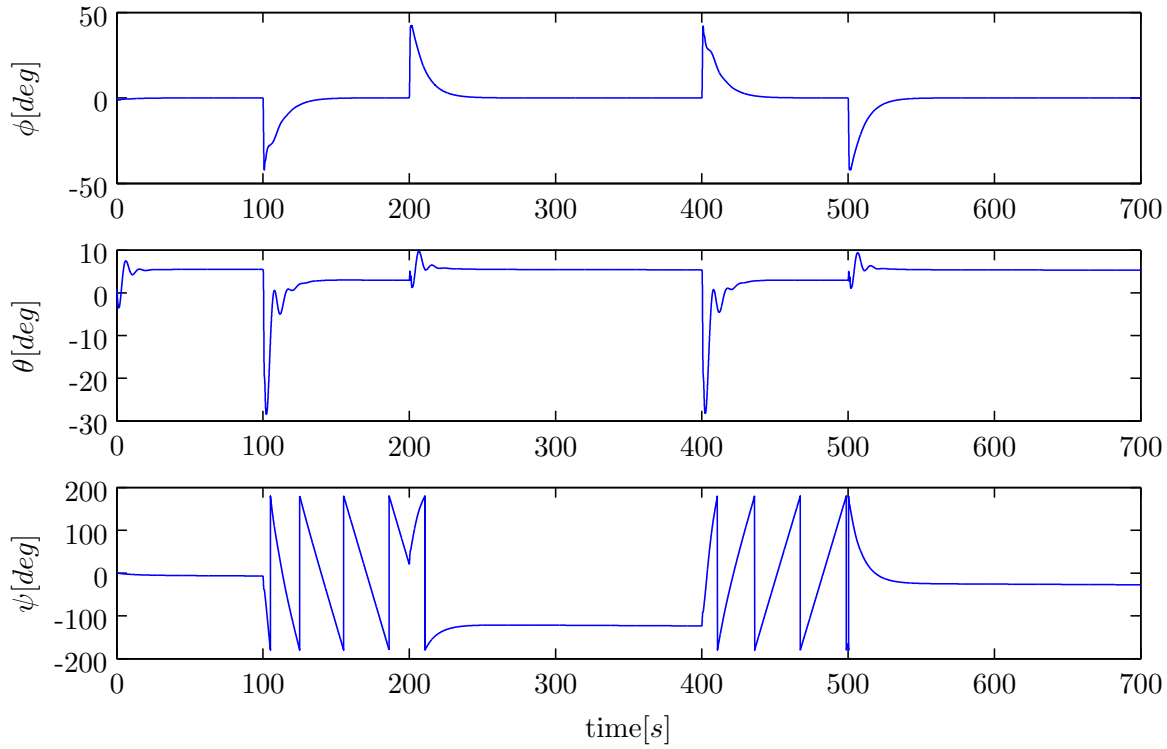

Figure E-5: Euler angles

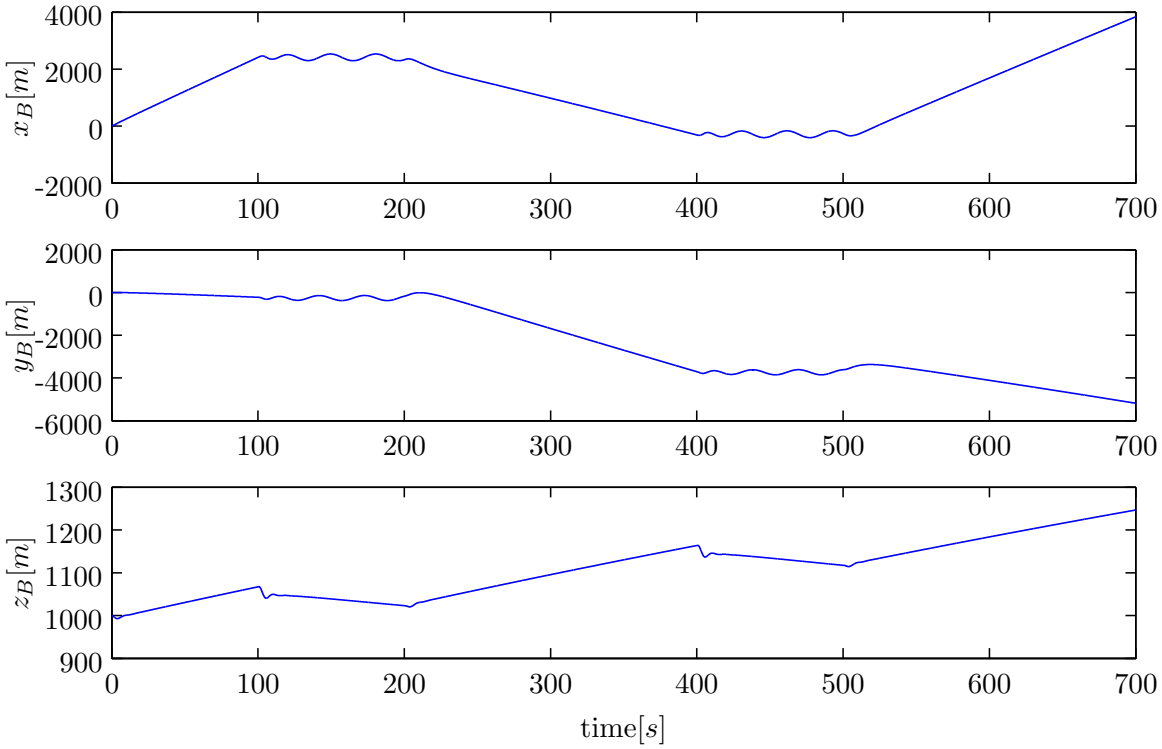

Figure E-6: Position in body-fixed reference frame $\mathcal{F}_B$

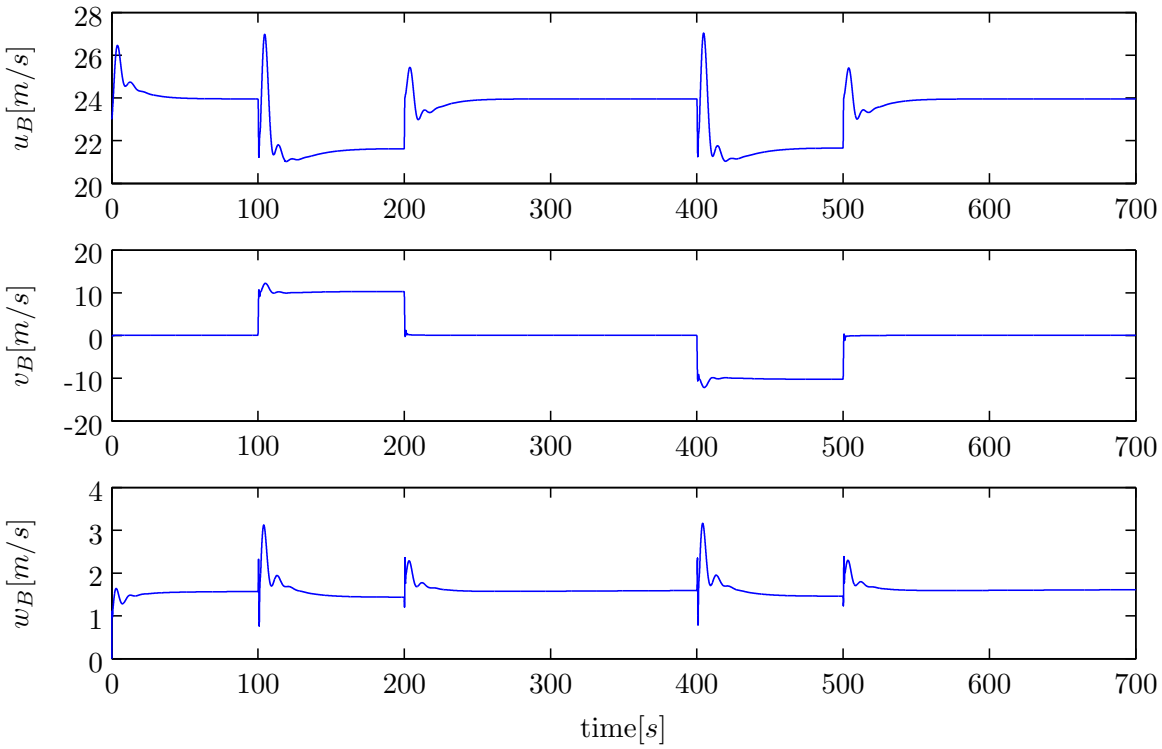

Figure E-7: Velocity in body-fixed reference frame $\mathcal{F}_B$

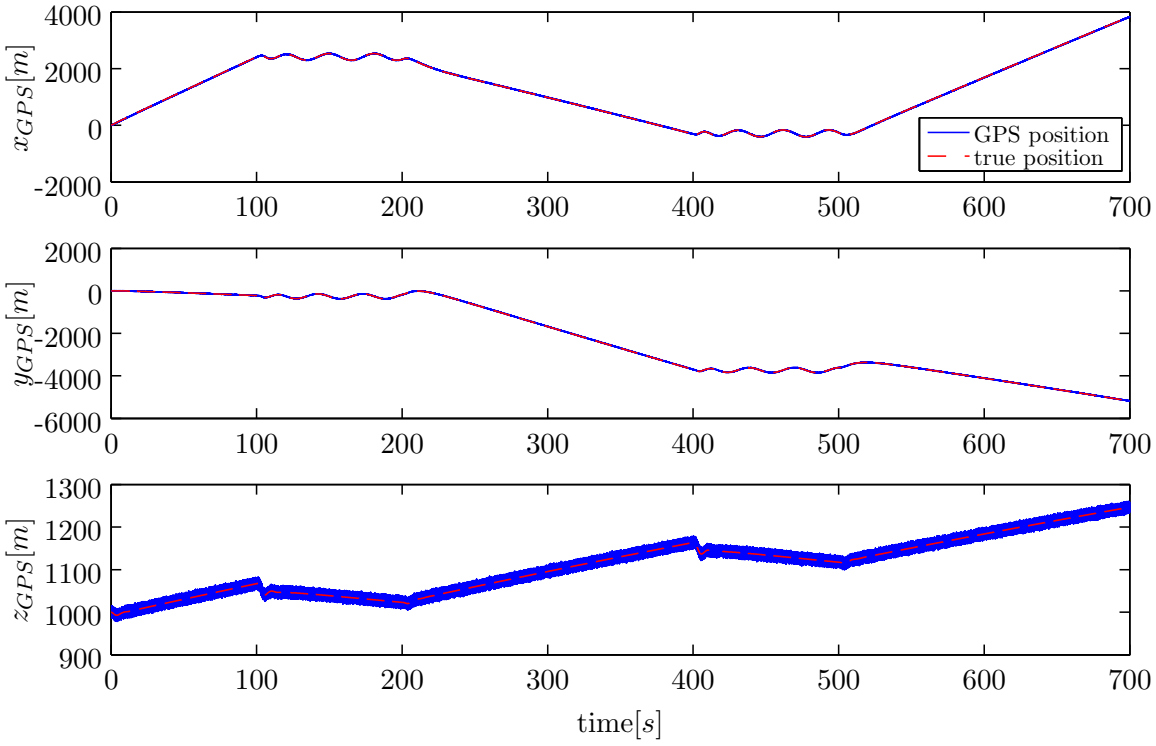

Figure E-8: GPS position in Earth reference frame $\mathcal{F}_E$

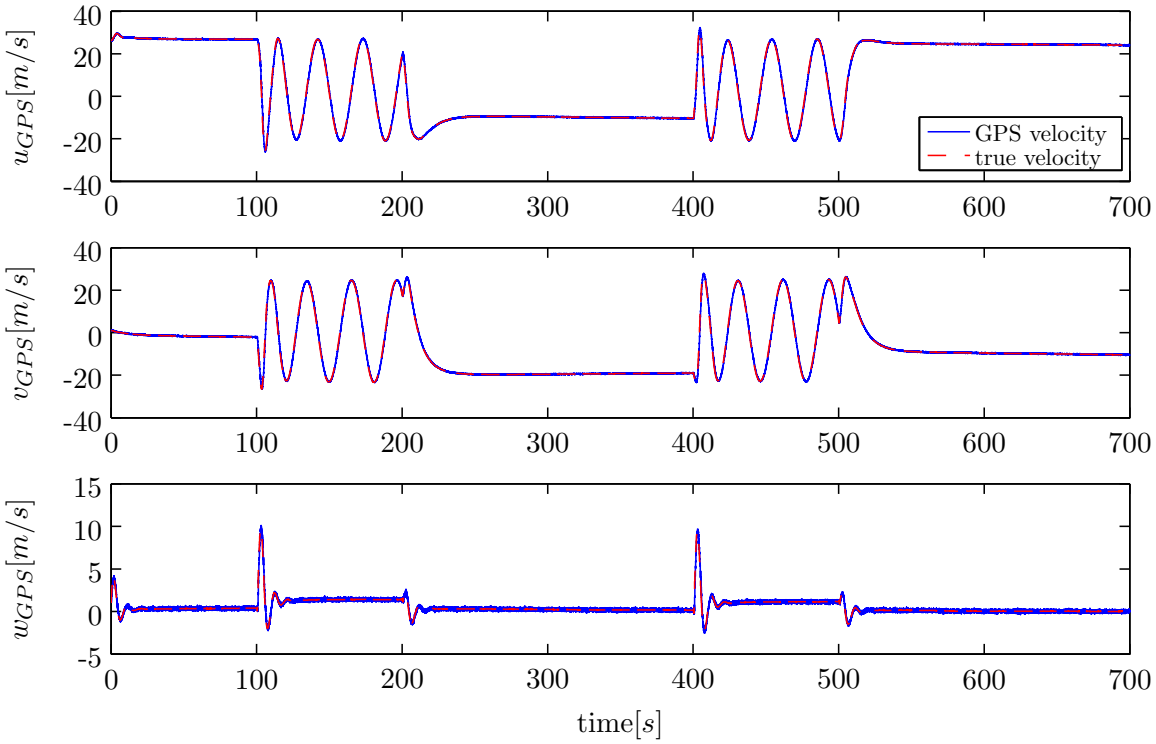

Figure E-9: GPS velocity in Earth reference frame $\mathcal{F}_E$

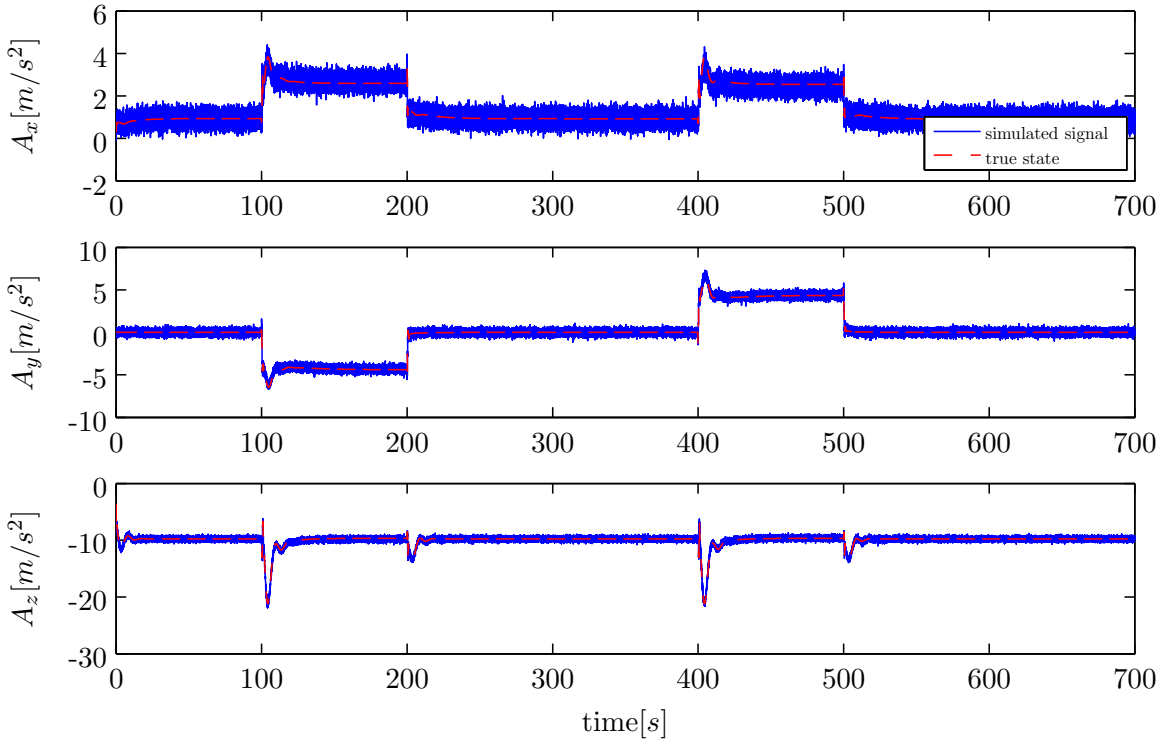

Figure E-10: Accelerometer

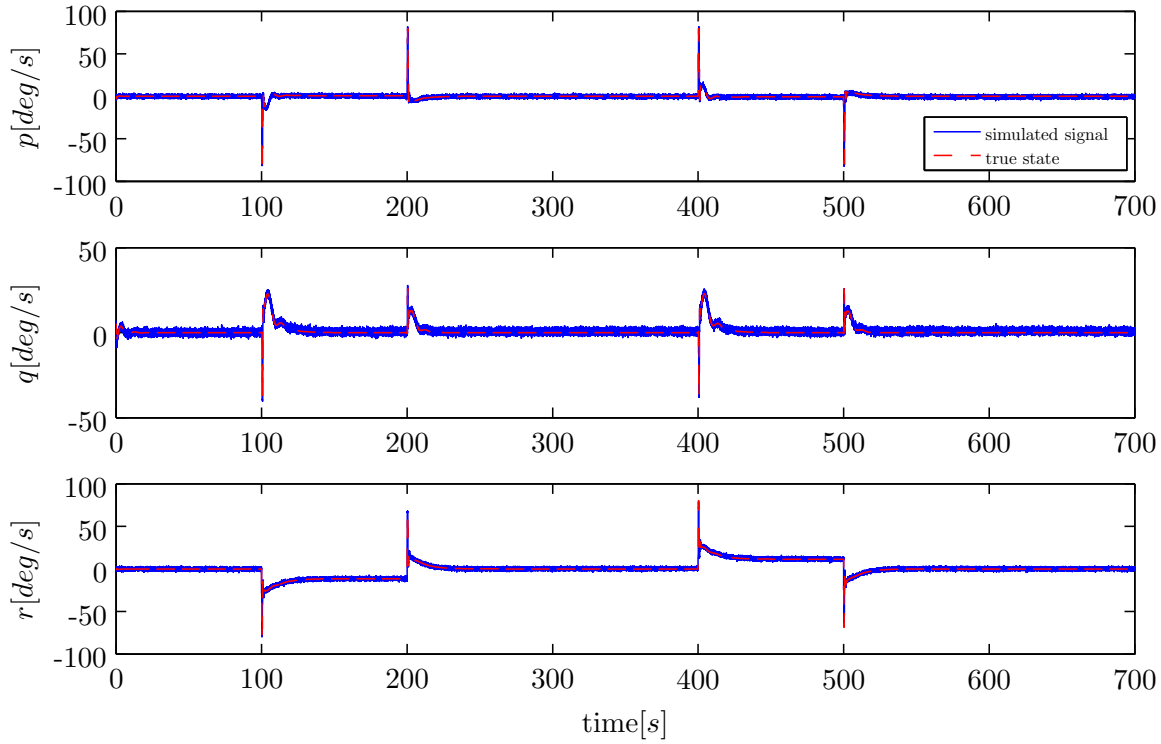

Figure E-11: Gyroscopes

E-1 Results EKF Identification

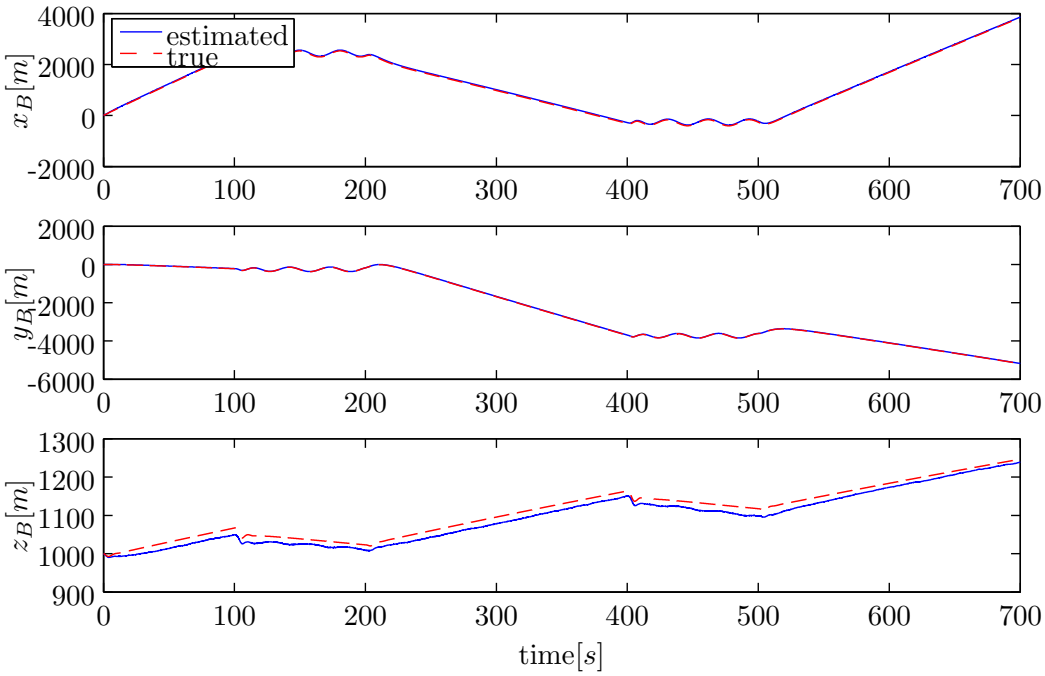

Figure E-12: Estimated position states EKF, small turns Aerosonde UAV simulation

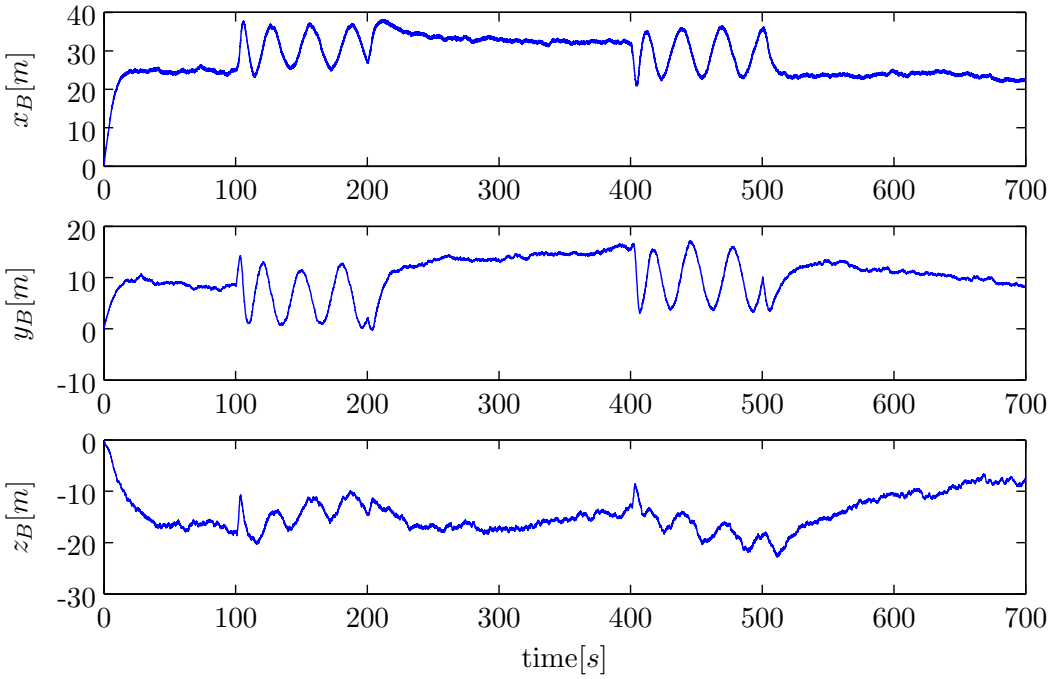

Figure E-13: Error position states EKF, small turns Aerosonde UAV simulation

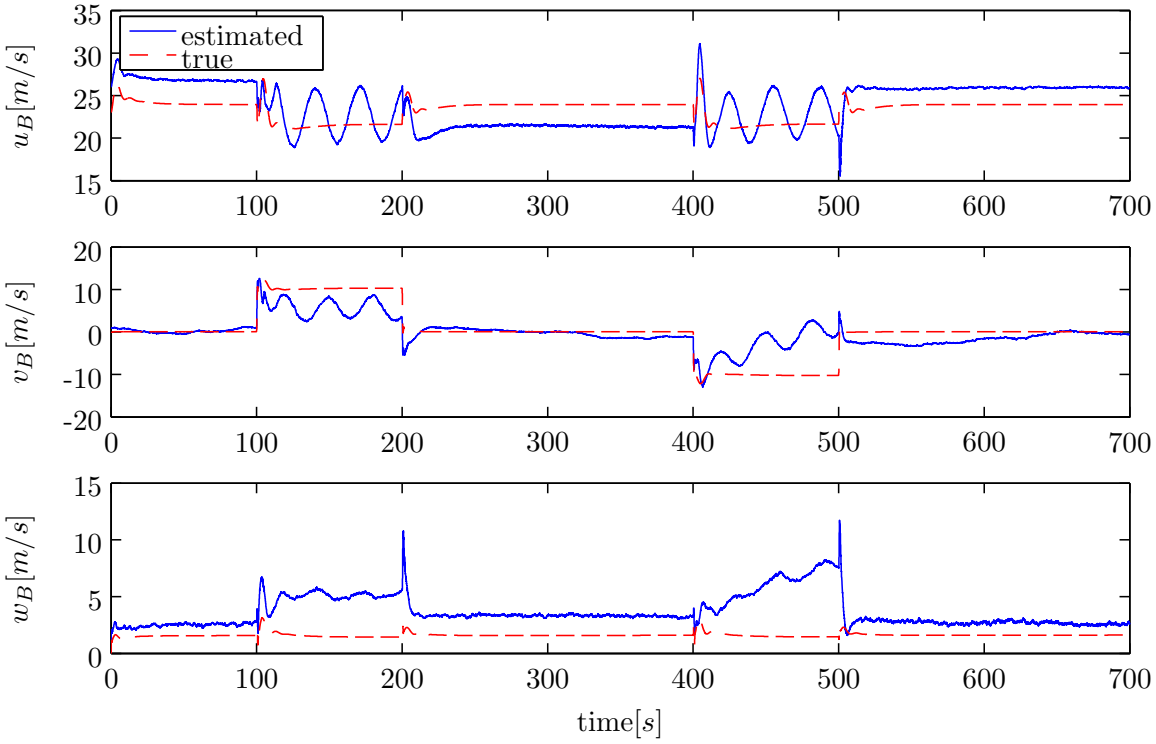

Figure E-14: Estimated velocity states EKF, small turns Aerosonde UAV simulation

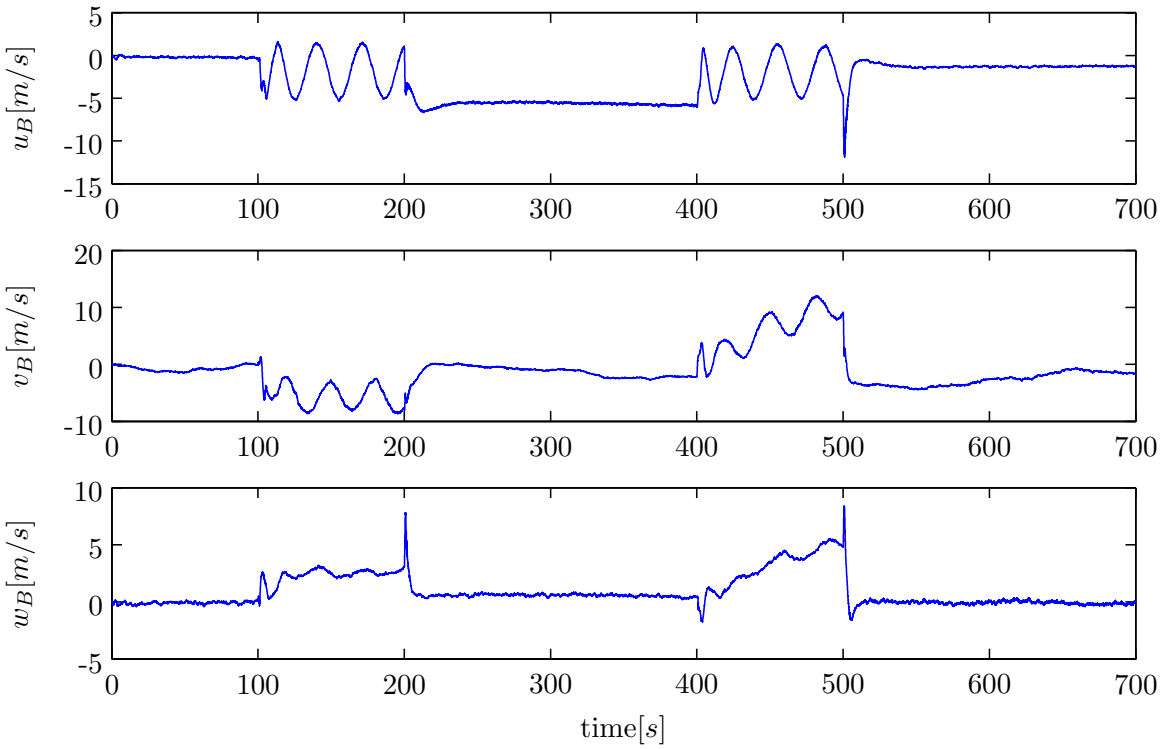

Figure E-15: Error velocity states EKF, small turns Aerosonde UAV simulation

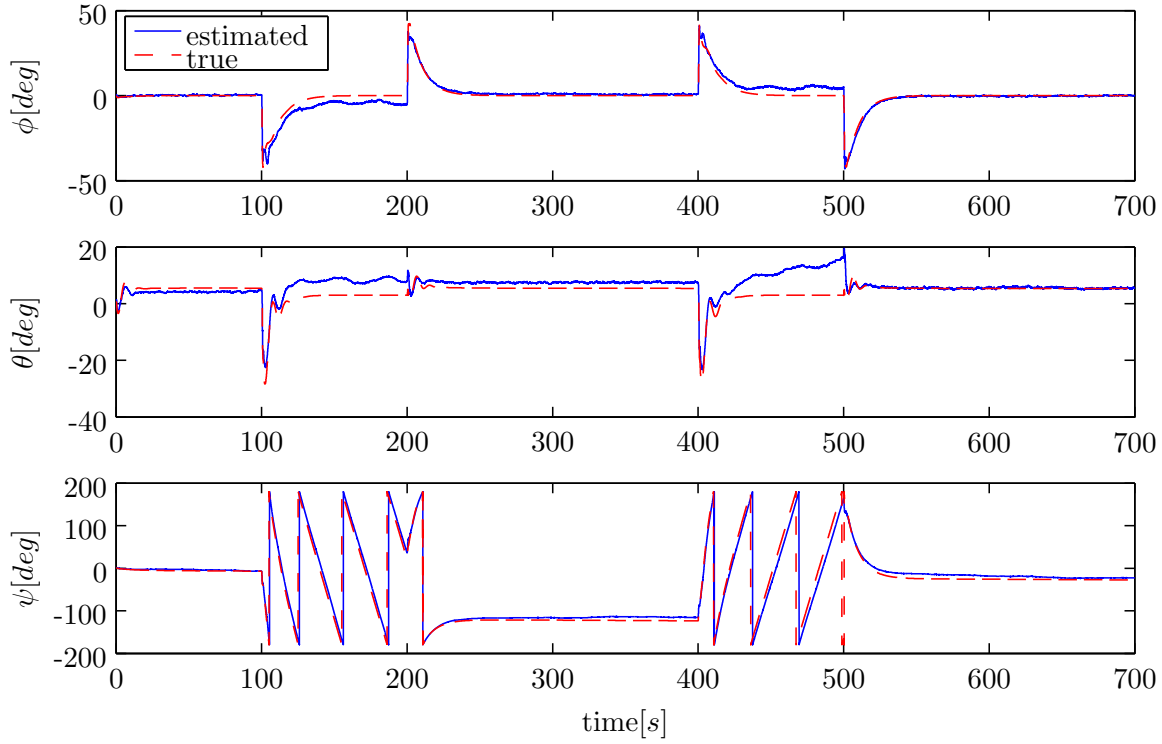

Figure E-16: Estimated Euler angle states EKF, small turns Aerosonde UAV simulation

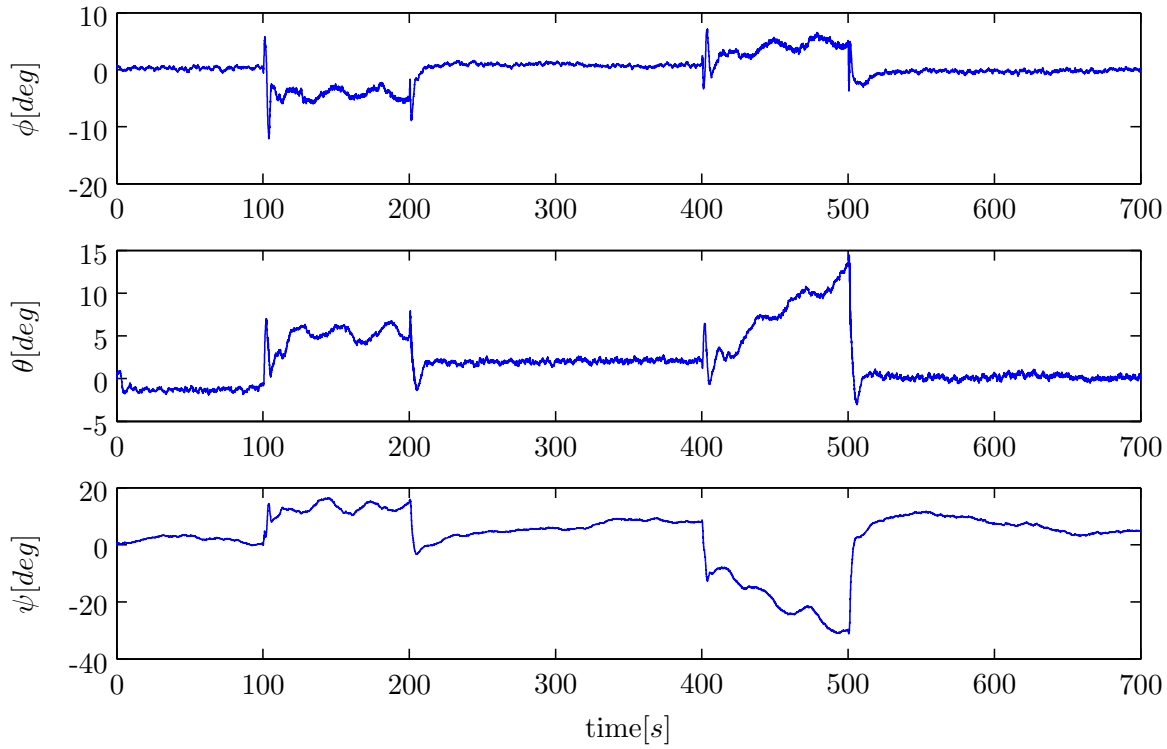

Figure E-17: Error Euler angle states EKF, small turns Aerosonde UAV simulation

E-2 Results EKF Identification no Gust

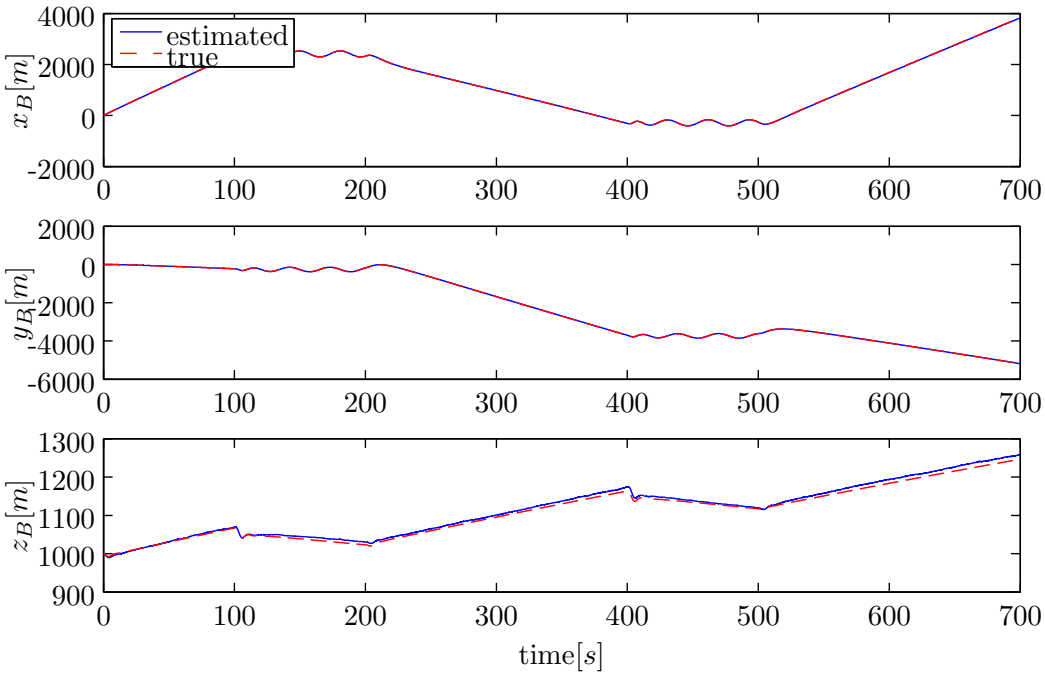

Figure E-18: Estimated position states EKF, small turns Aerosonde UAV simulation

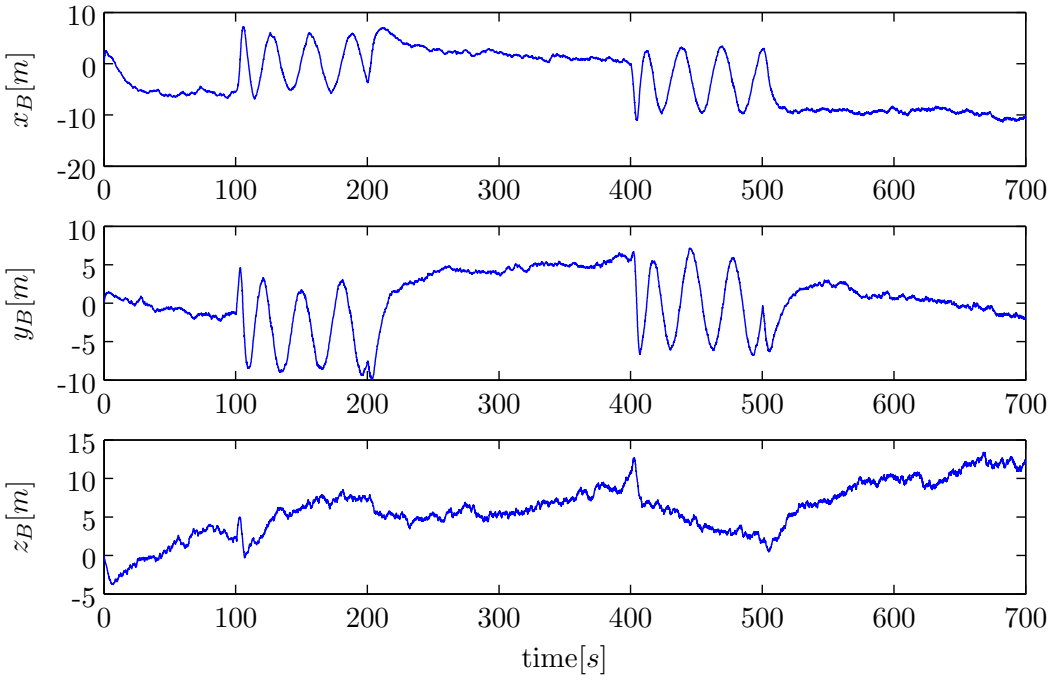

Figure E-19: Error position states EKF, small turns Aerosonde UAV simulation

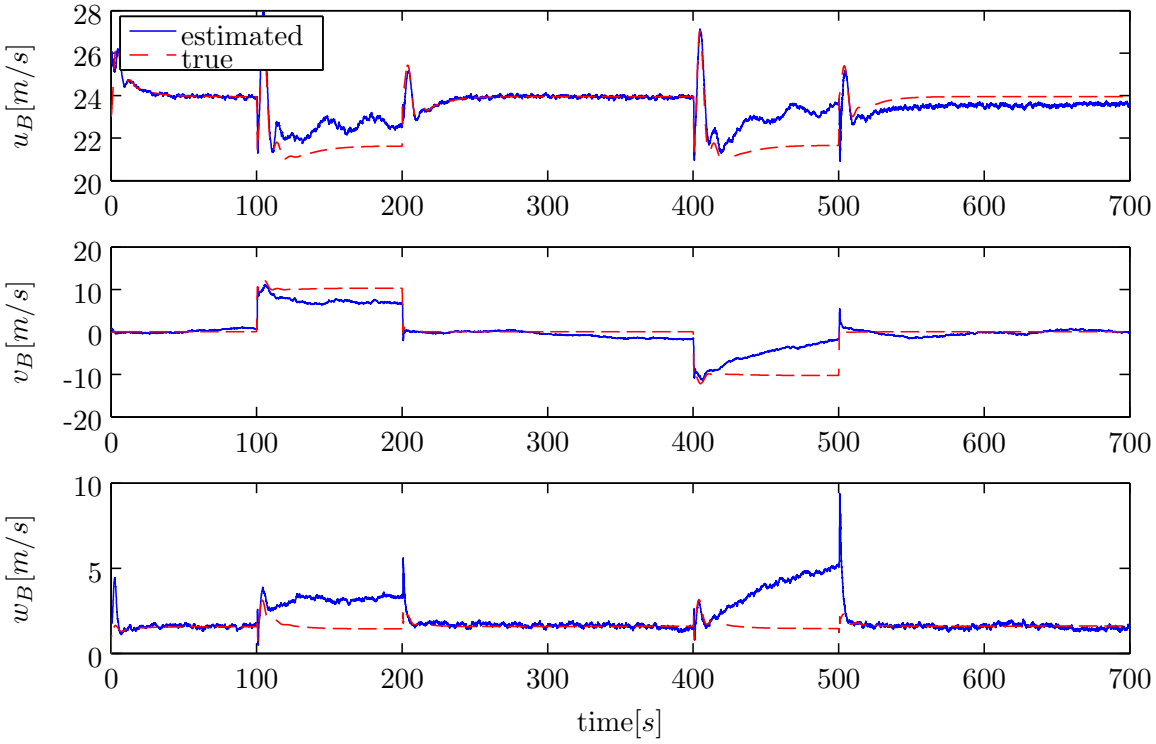

Figure E-20: Estimated velocity states EKF, small turns Aerosonde UAV simulation

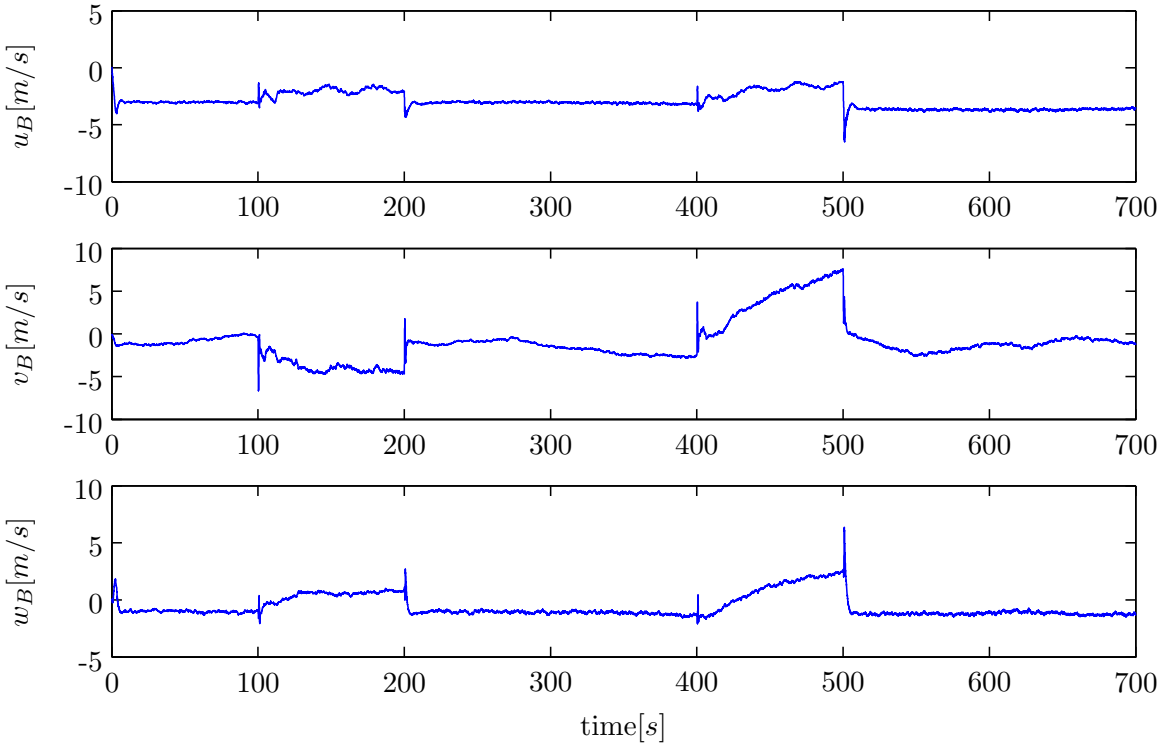

Figure E-21: Error velocity states EKF, small turns Aerosonde UAV simulation

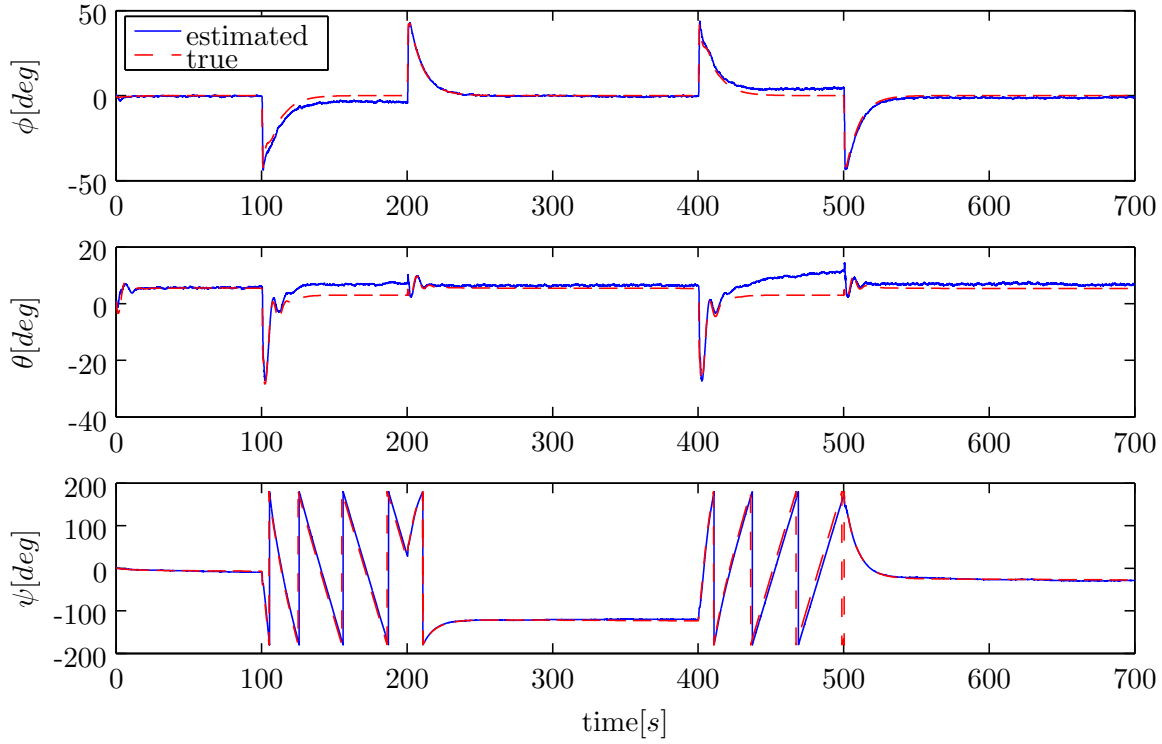

Figure E-22: Estimated Euler angle states EKF, small turns Aerosonde UAV simulation

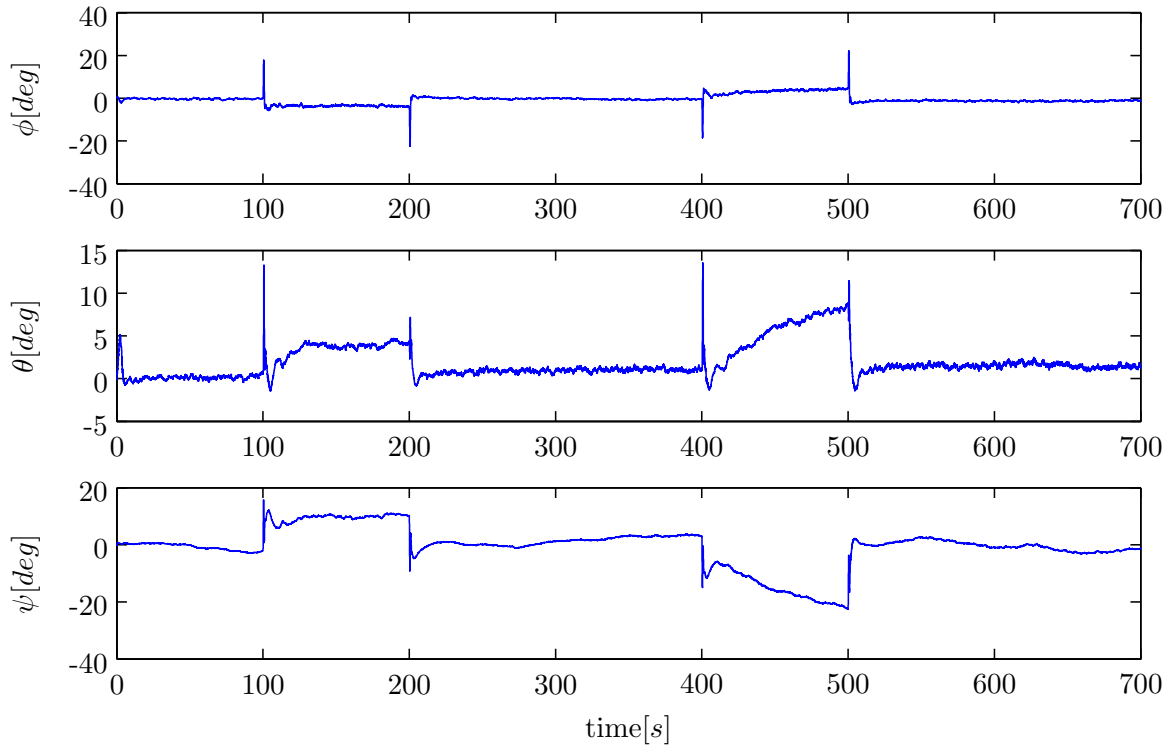

Figure E-23: Error Euler angle states EKF, small turns Aerosonde UAV simulation

E-3 Results IEKF Identification

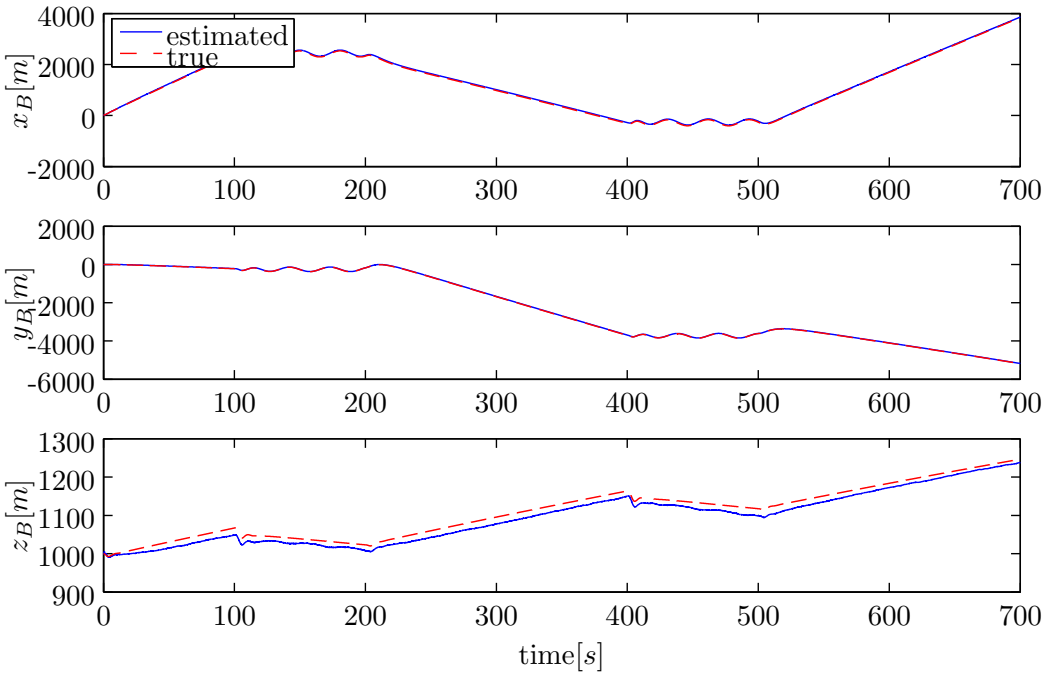

Figure E-24: Estimated position states IEKF, small turns Aerosonde UAV simulation

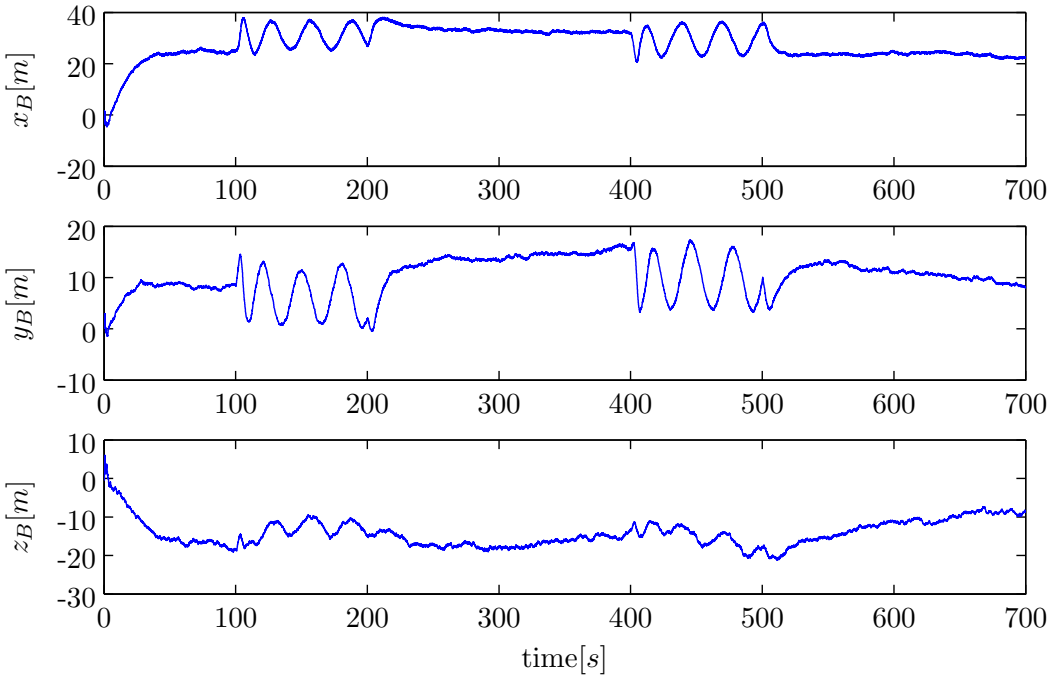

Figure E-25: Error position states, IEKF small turns Aerosonde UAV simulation

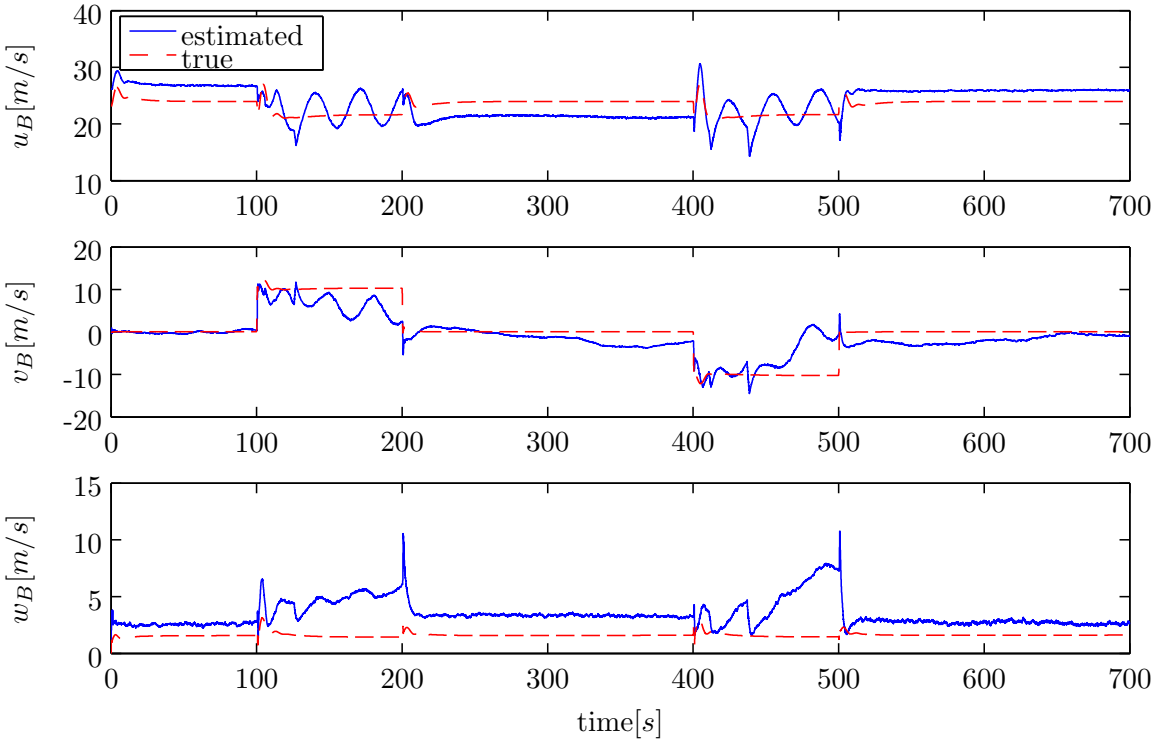

Figure E-26: Estimated velocity states IEKF, small turns Aerosonde UAV simulation

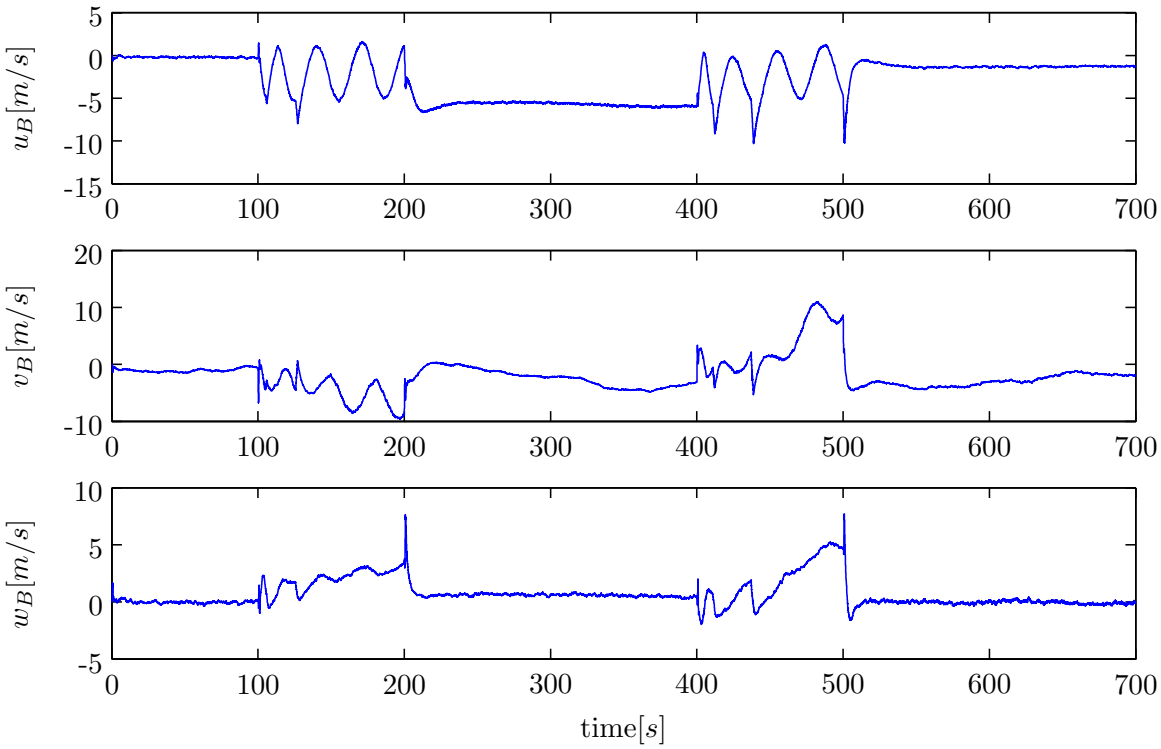

Figure E-27: Error velocity states IEKF, small turns Aerosonde UAV simulation

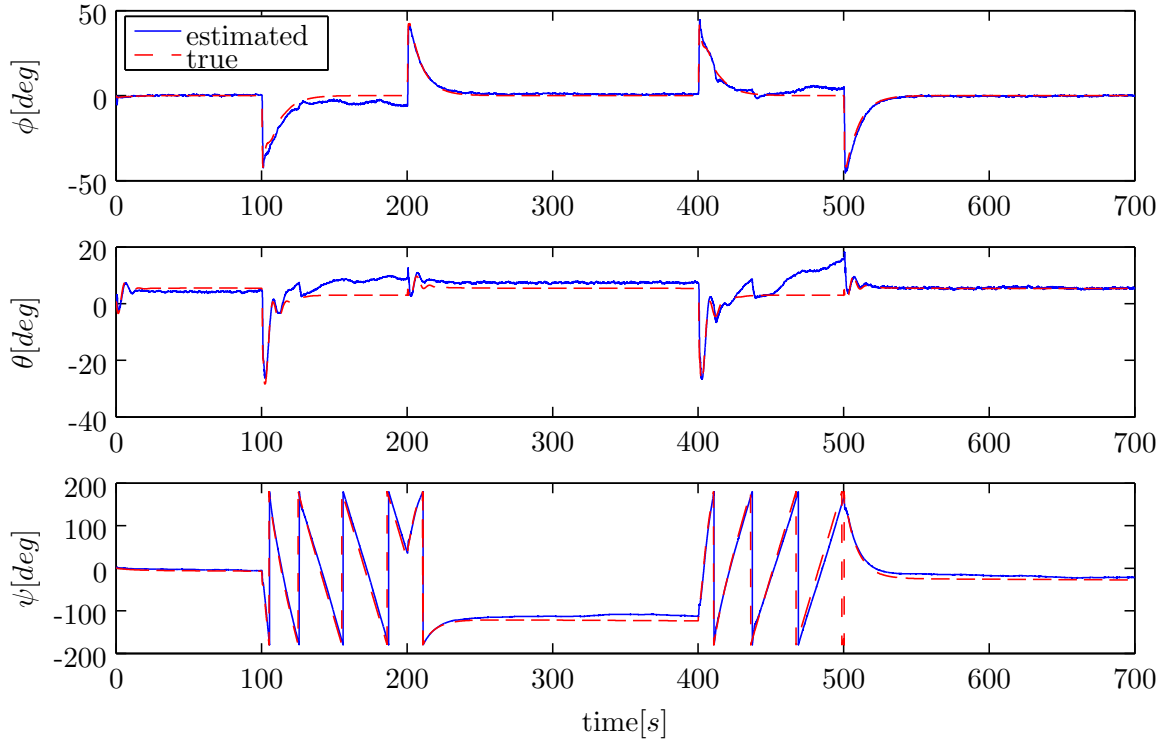

Figure E-28: Estimated Euler angle states IEKF, small turns Aerosonde UAV simulation

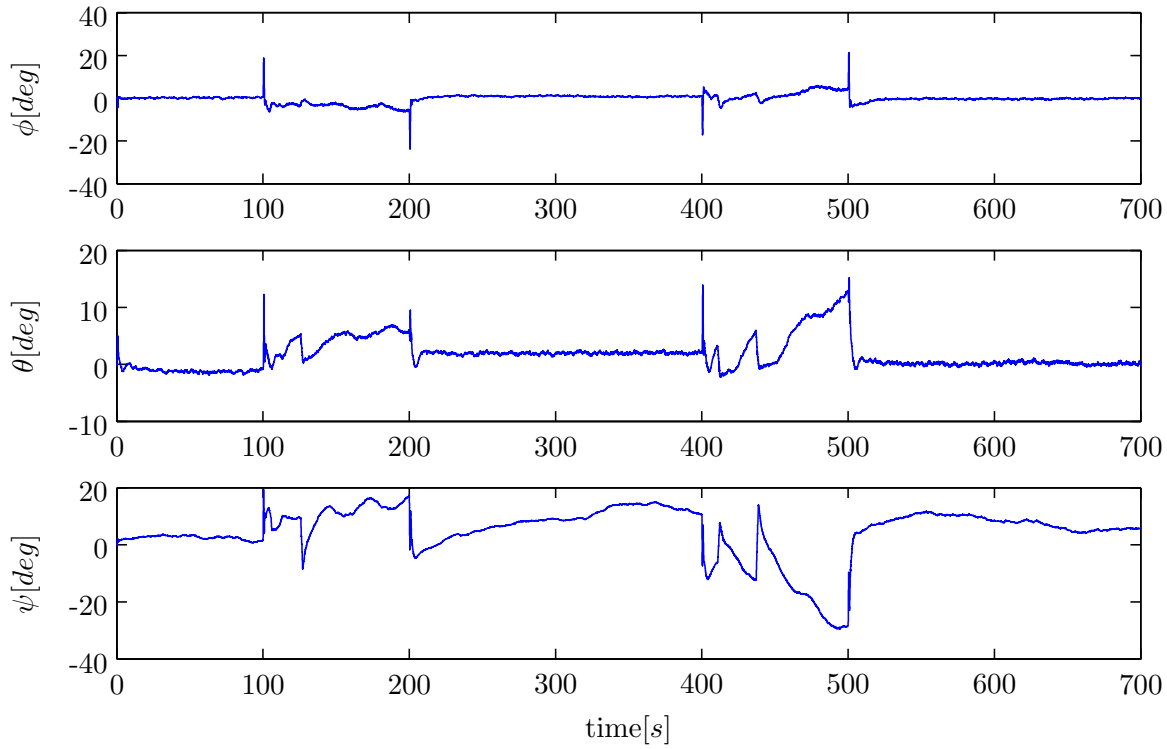

Figure E-29: Error Euler angle states IEKF, small turns Aerosonde UAV simulation

E-4 Results IEKF Identification no Gust

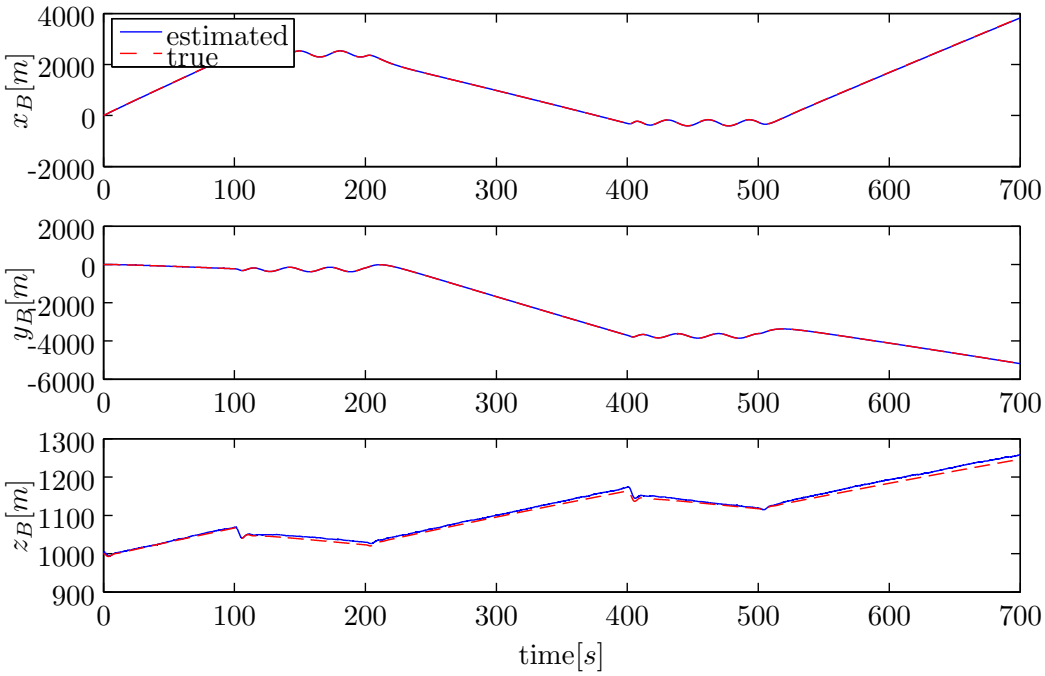

Figure E-30: Estimated position states IEKF, small turns Aerosonde UAV simulation

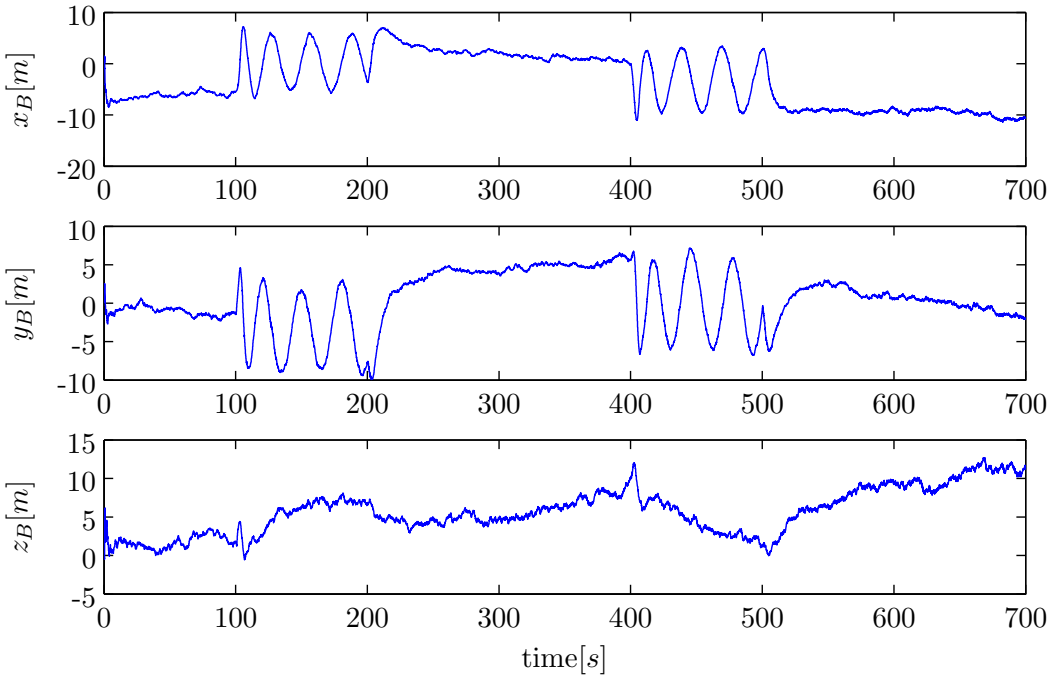

Figure E-31: Error position states IEKF, small turns Aerosonde UAV simulation

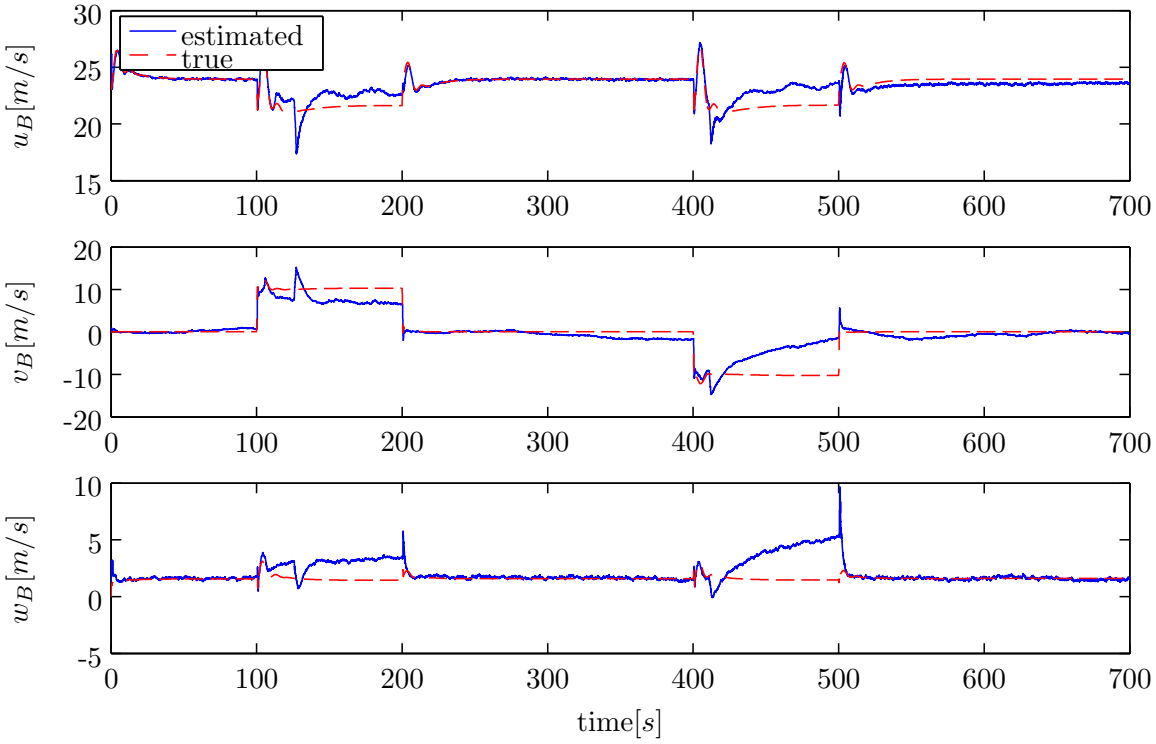

Figure E-32: Estimated velocity states IEKF, small turns Aerosonde UAV simulation

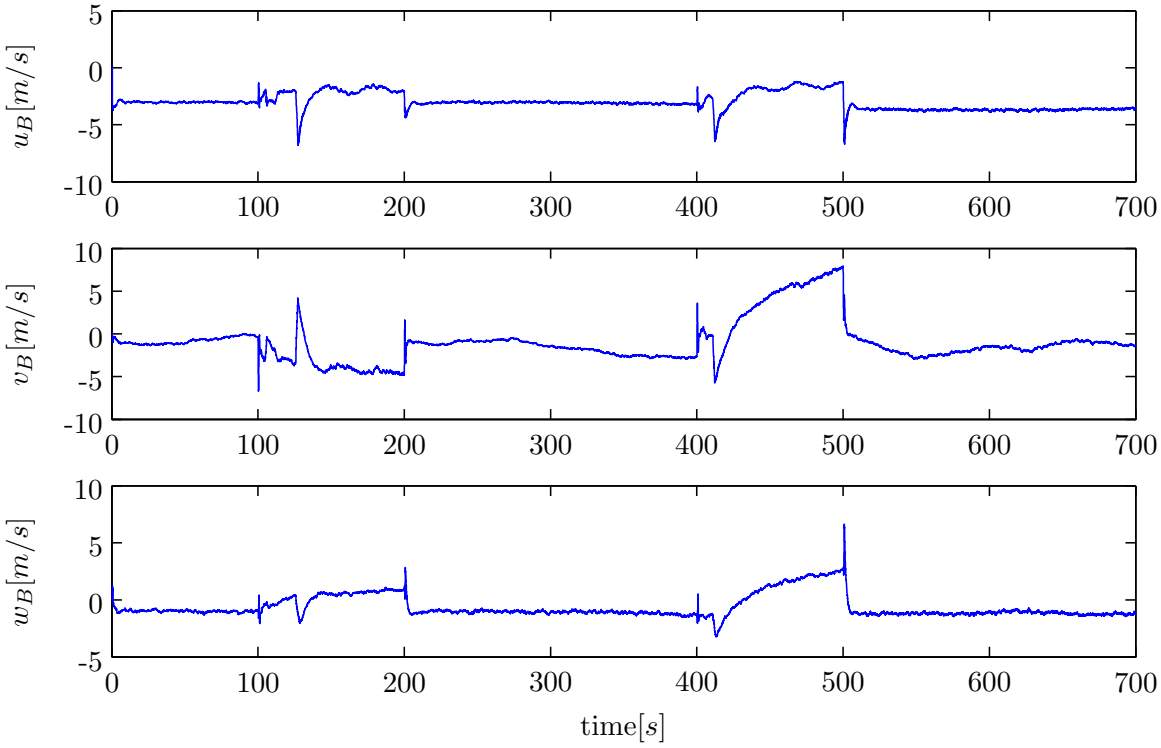

Figure E-33: Error velocity states IEKF, small turns Aerosonde UAV simulation

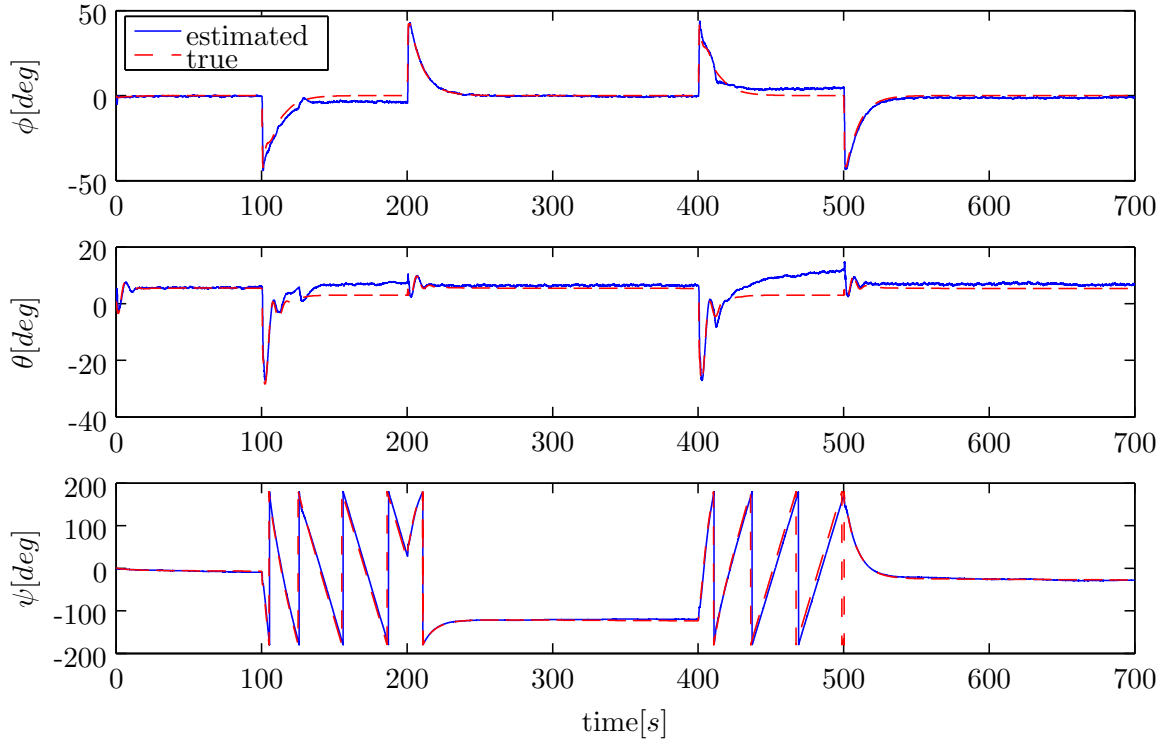

Figure E-34: Estimated Euler angle states IEKF, small turns Aerosonde UAV simulation

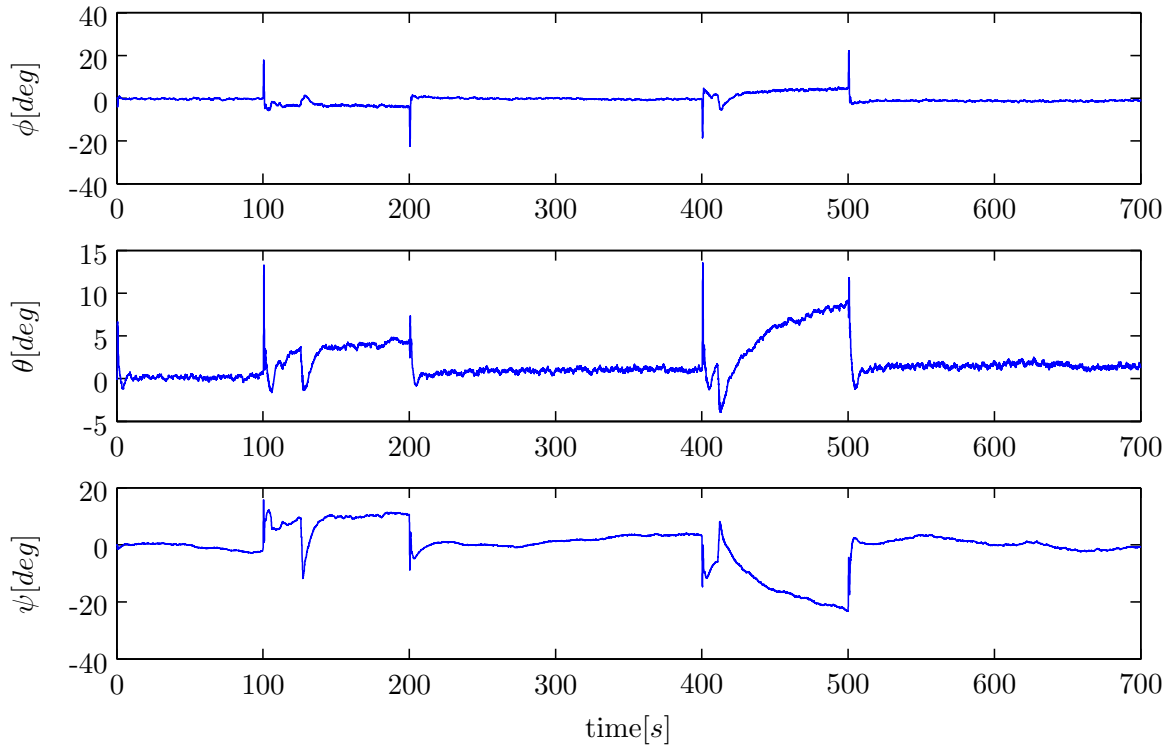

Figure E-35: Error Euler angle states IEKF, small turns Aerosonde UAV simulation

E-5 Results Non-Linear SO(3) Identification

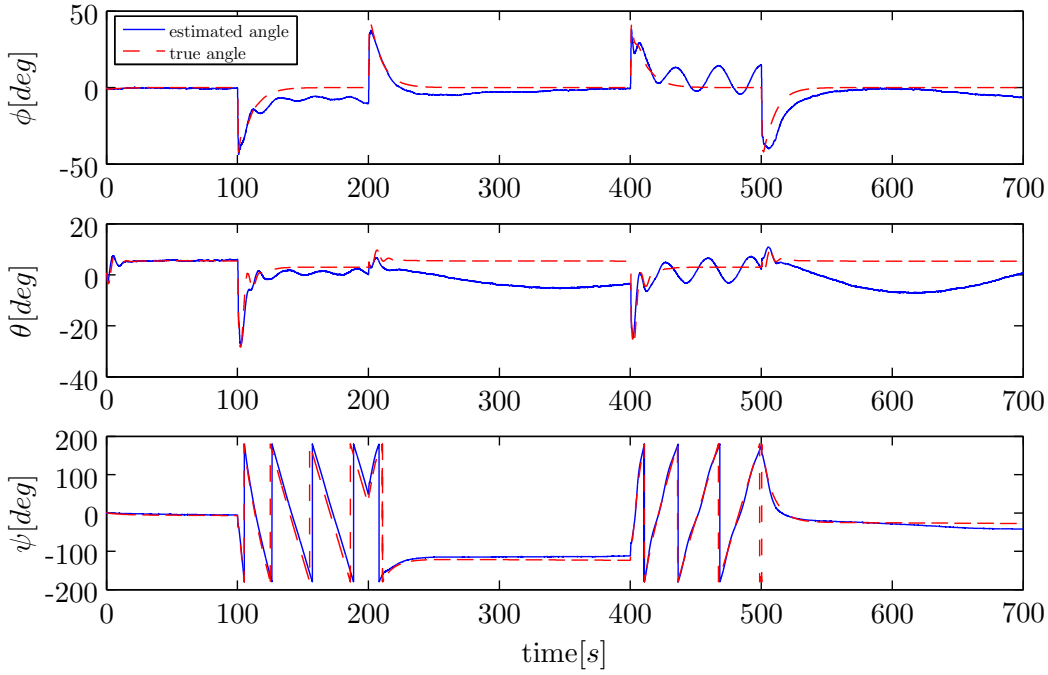

Figure E-36: Estimated Euler angles SO(3), small turns Aerosonde UAV simulation

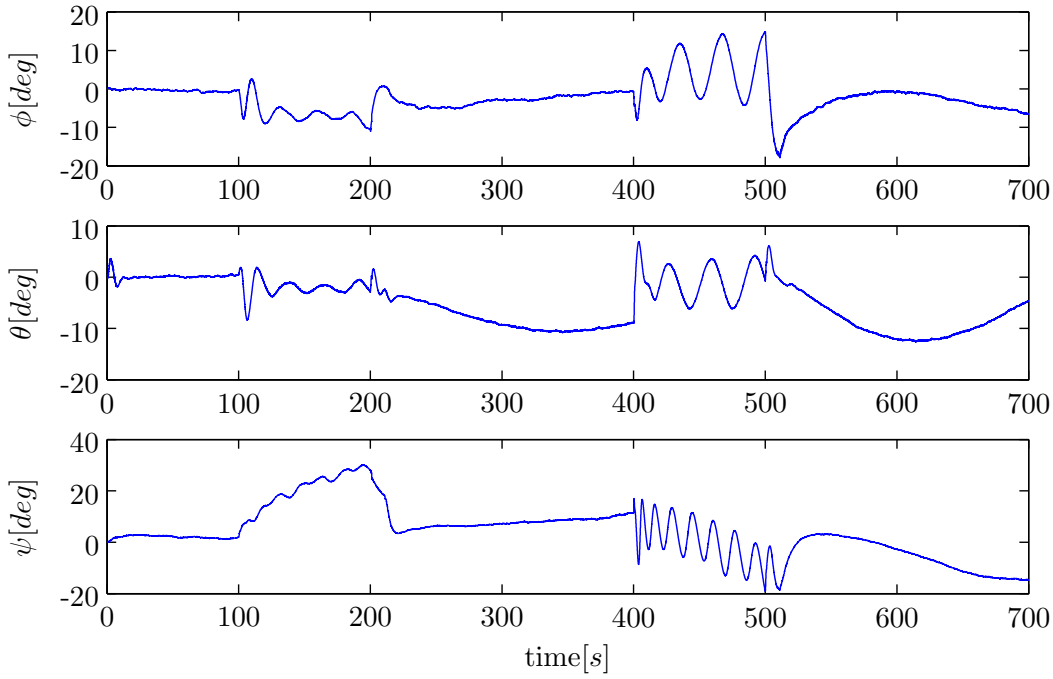

Figure E-37: Error Euler angles SO(3), small turns Aerosonde UAV simulation

E-6 Results Non-Linear SO(3) Identification no Gust

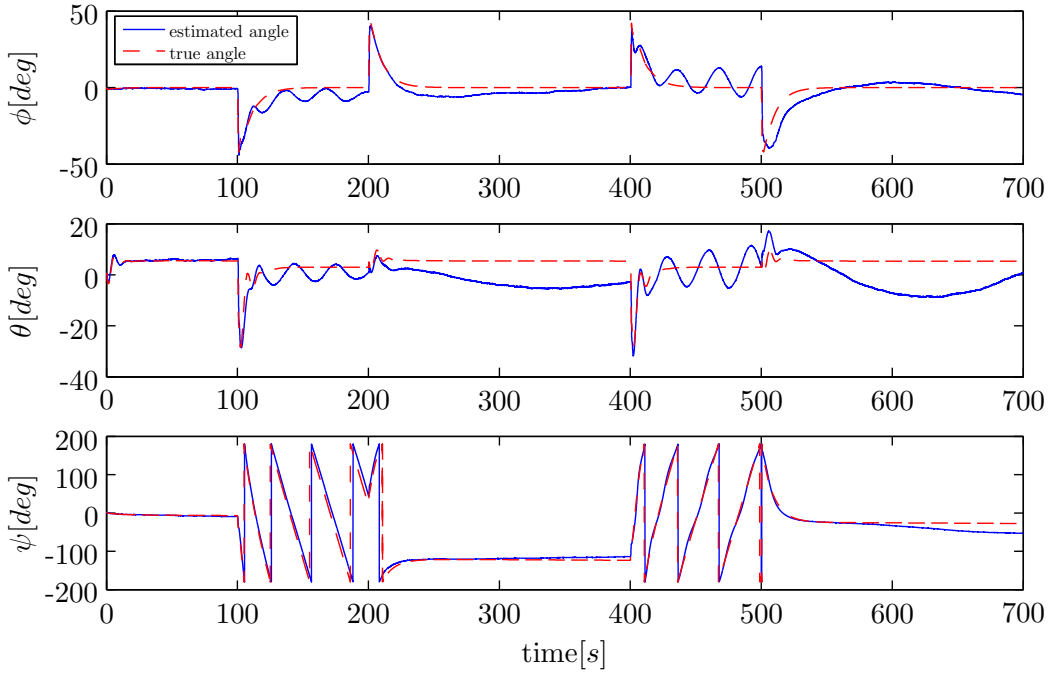

Figure E-38: Estimated Euler angles SO(3), small turns Aerosonde UAV simulation

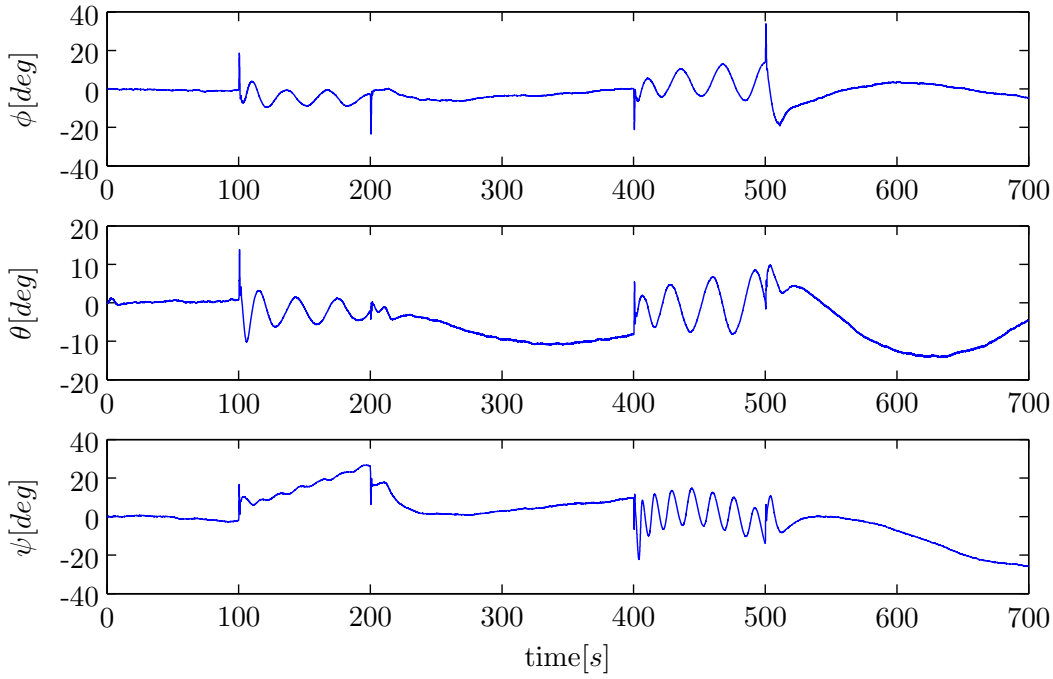

Figure E-39: Error Euler angles SO(3), small turns Aerosonde UAV simulation

Appendix F

Large Turns Aerosonde UAV Simulations

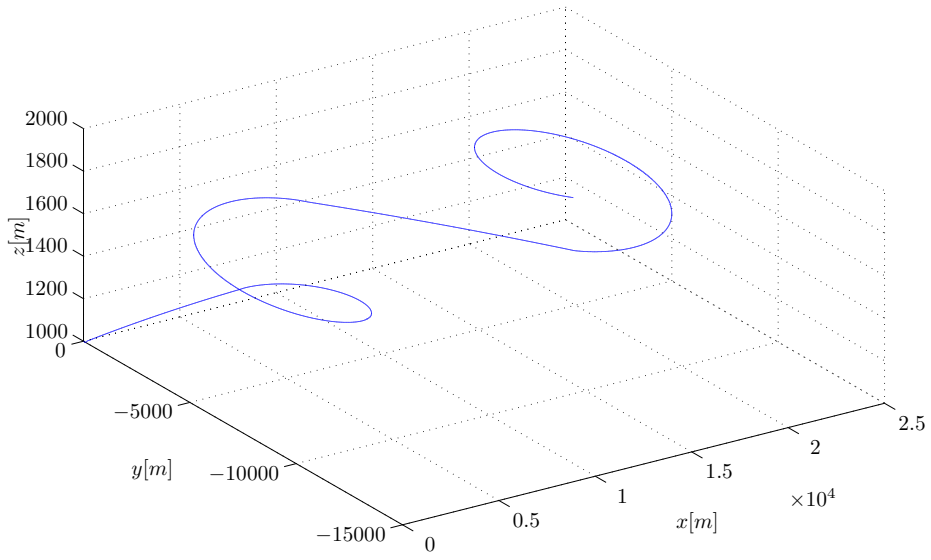

Figure F-1: 3D position, large turns Aerosonde UAV simulation

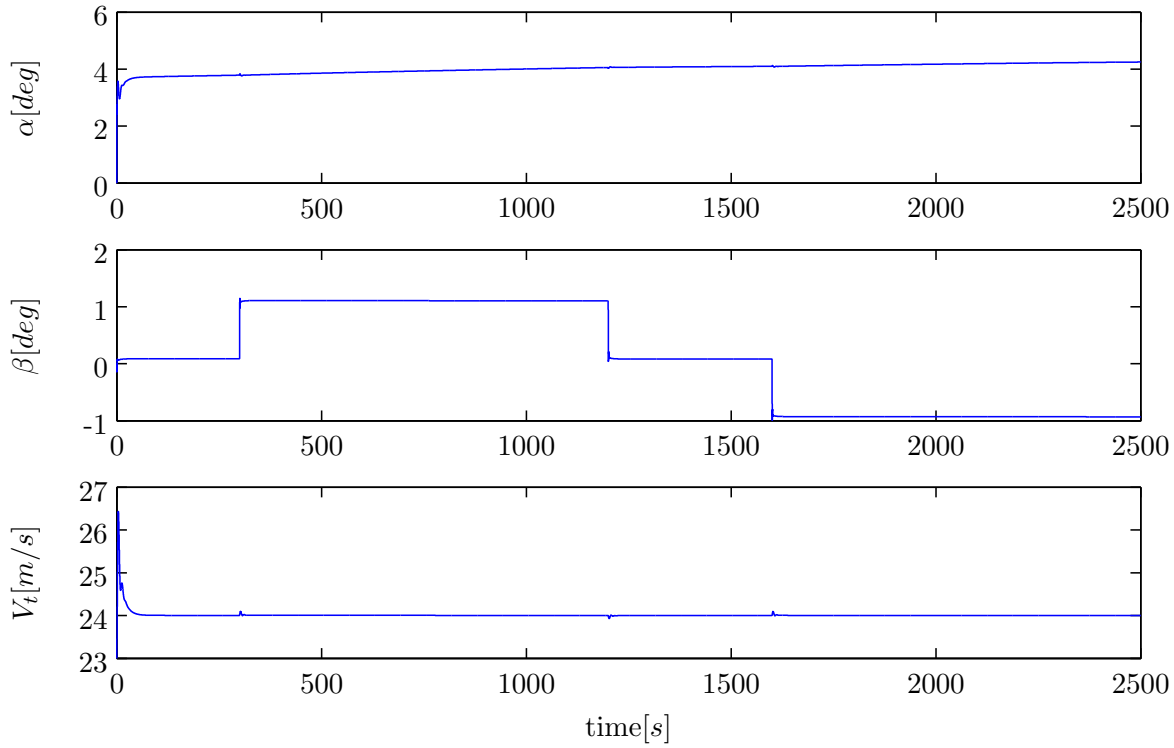

Figure F-2: Angle of attack α, side-slip angle β and true airspeed V_T

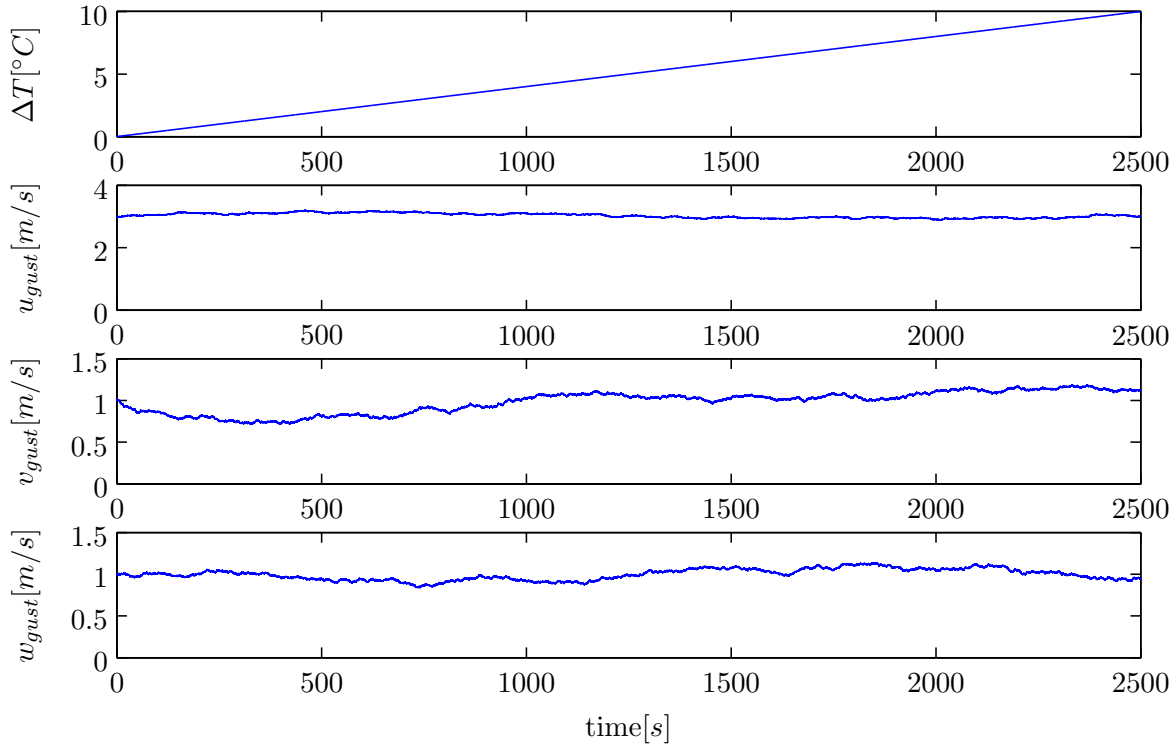

Figure F-3: Environmental properties, temperature and gust velocities in an Earth reference frame $\mathcal{F}_E$

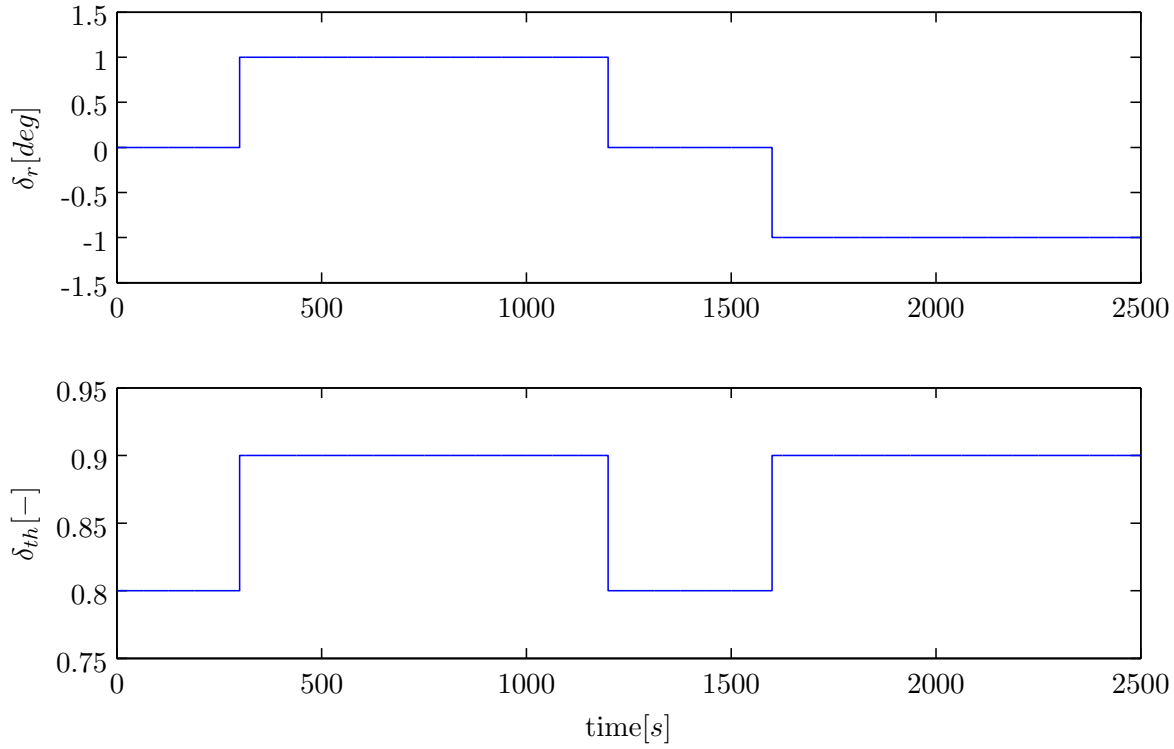

Figure F-4: Throttle and electric rudder input signal

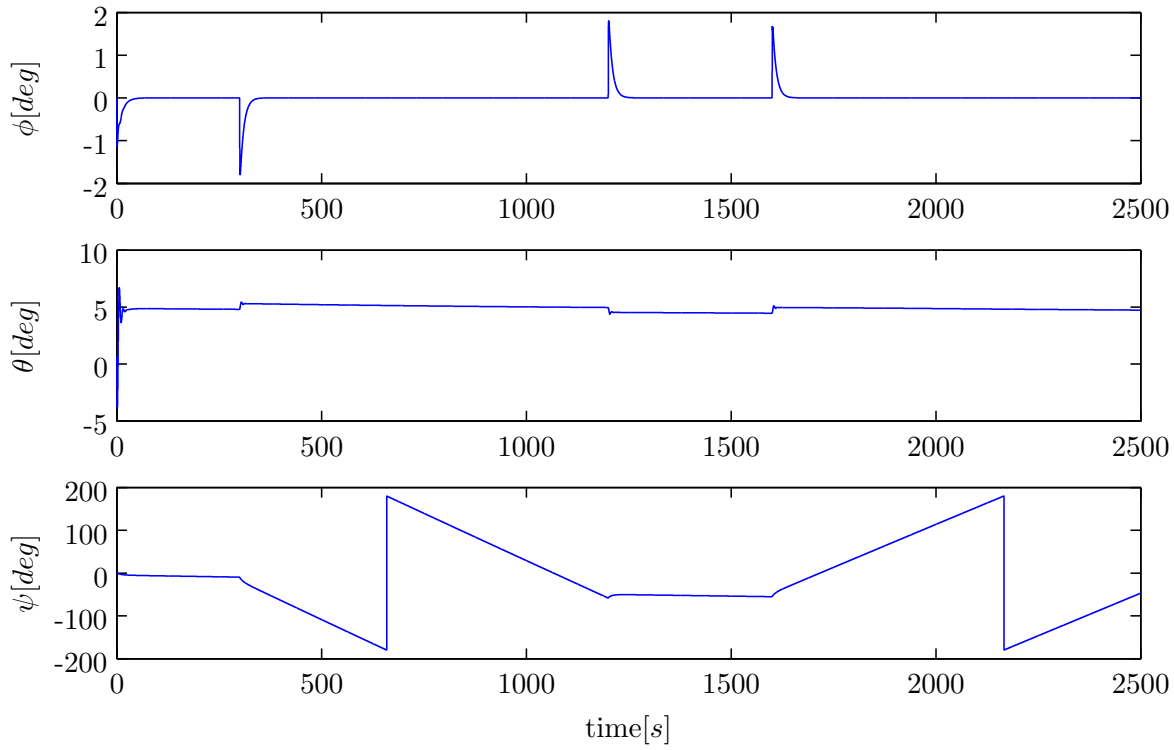

Figure F-5: Euler angles

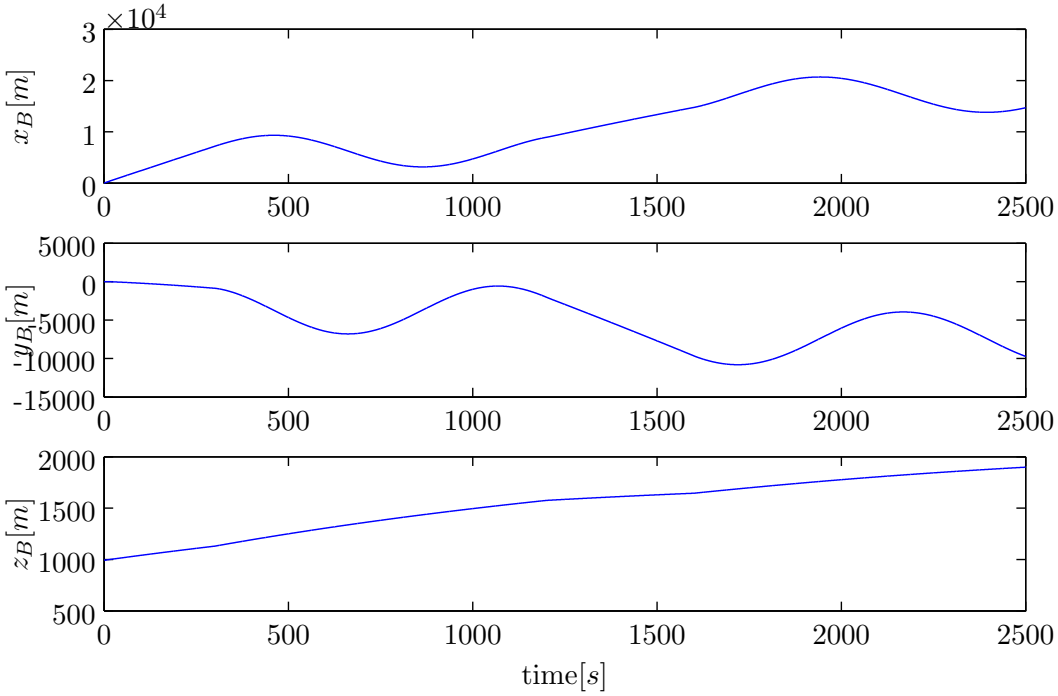

Figure F-6: Position in body-fixed reference frame $\mathcal{F}_B$

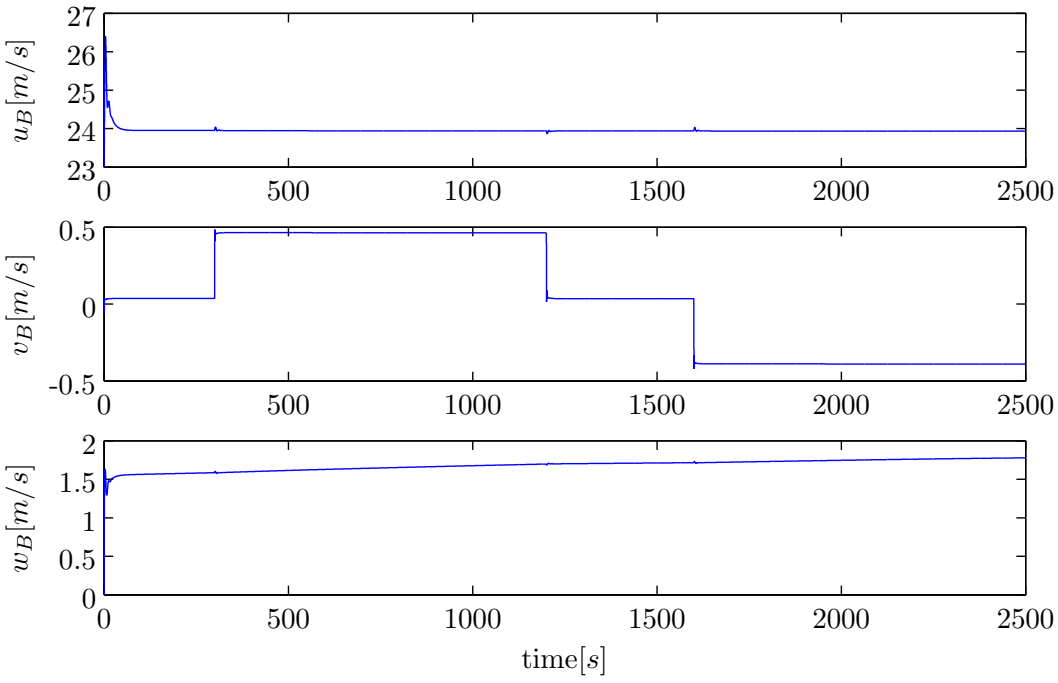

Figure F-7: Velocity in body-fixed reference frame $\mathcal{F}_B$

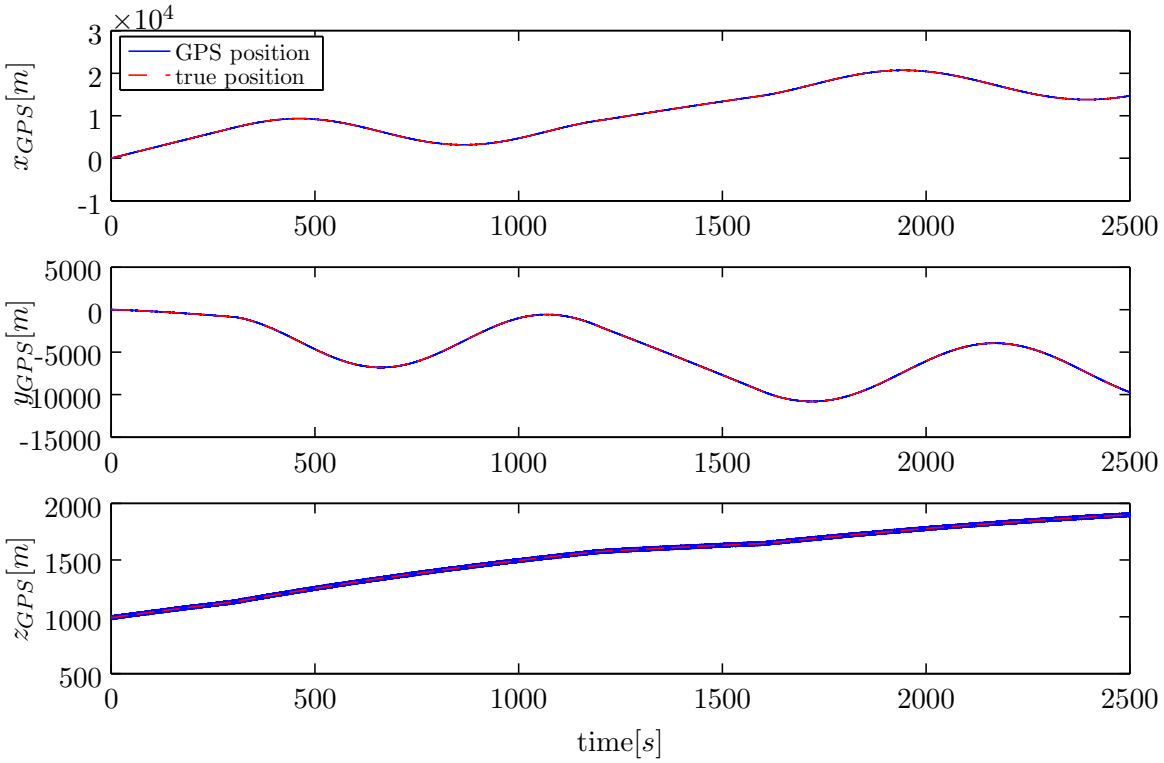

Figure F-8: GPS position in Earth reference frame $\mathcal{F}_E$

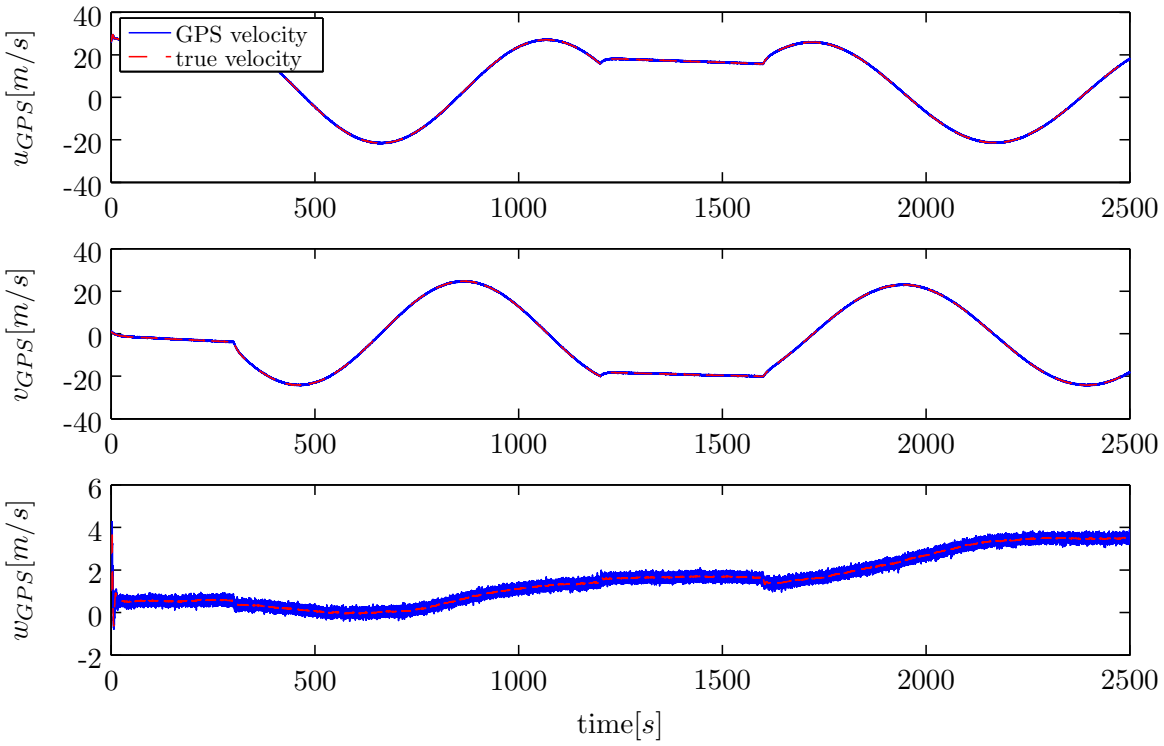

Figure F-9: GPS velocity in Earth reference frame $\mathcal{F}_E$

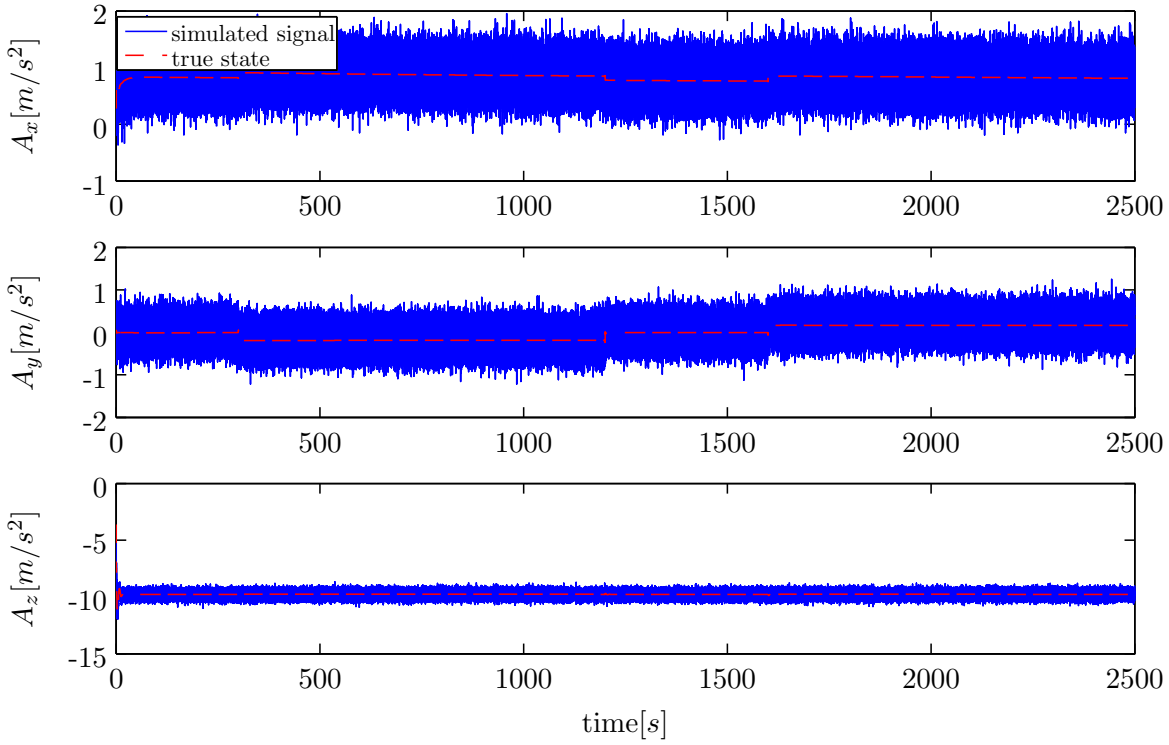

Figure F-10: Accelerometer

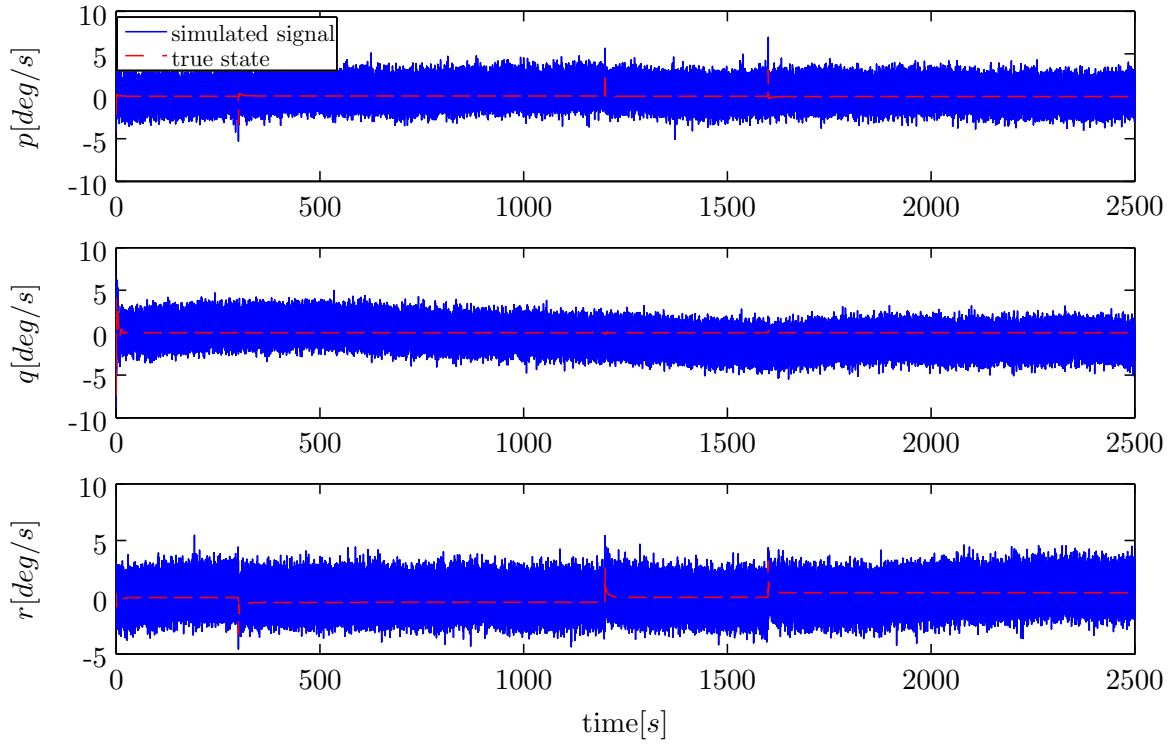

Figure F-11: Gyroscopes

F-1 Results EKF Identification

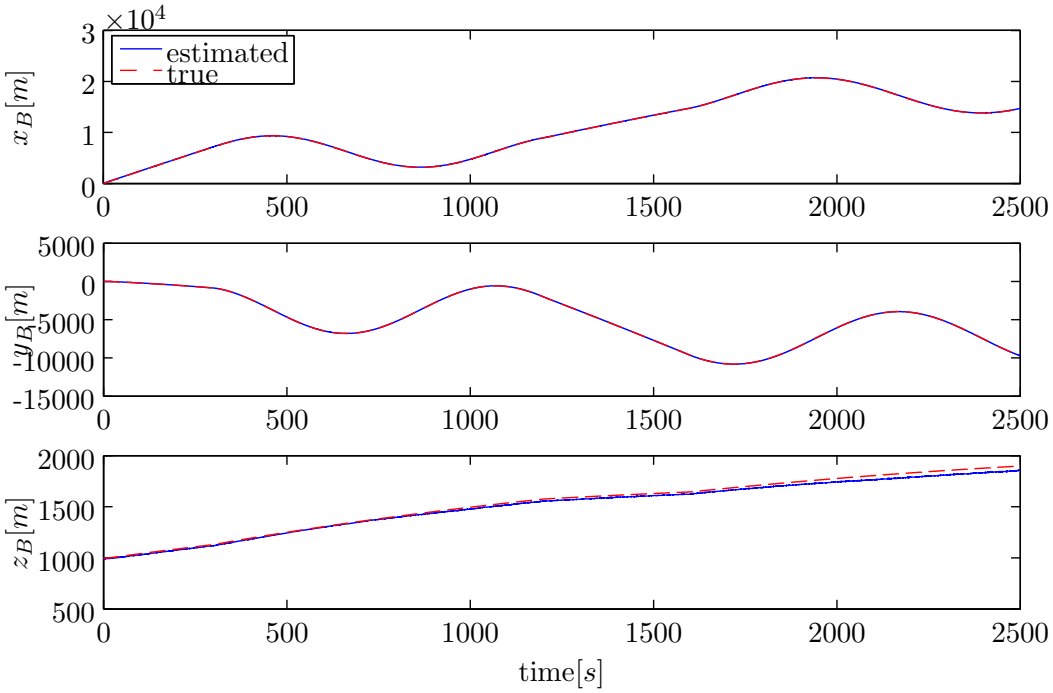

Figure F-12: Estimated position states EKF, large turns Aerosonde UAV simulation

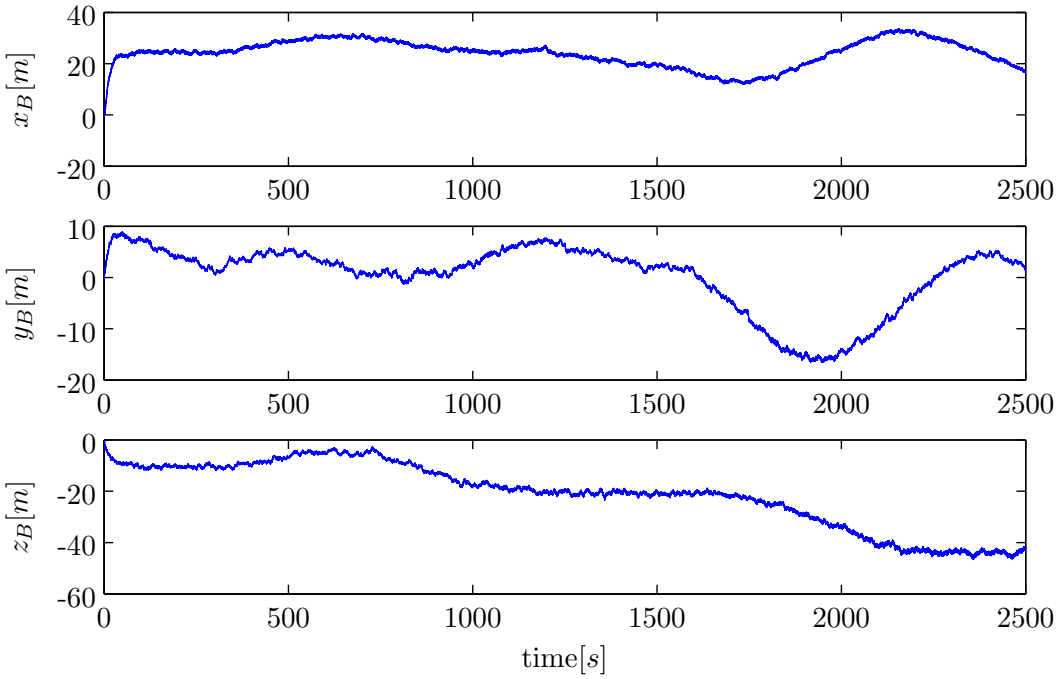

Figure F-13: Error position states EKF, large turns Aerosonde UAV simulation

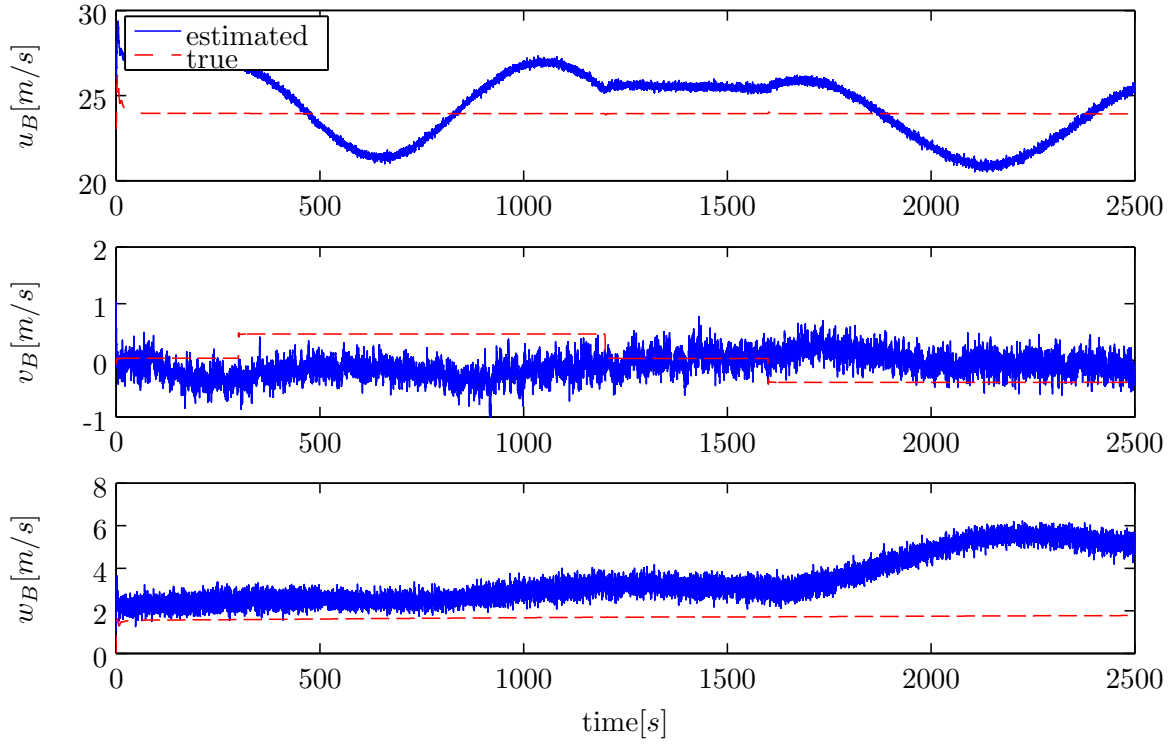

Figure F-14: Estimated velocity states EKF, large turns Aerosonde UAV simulation

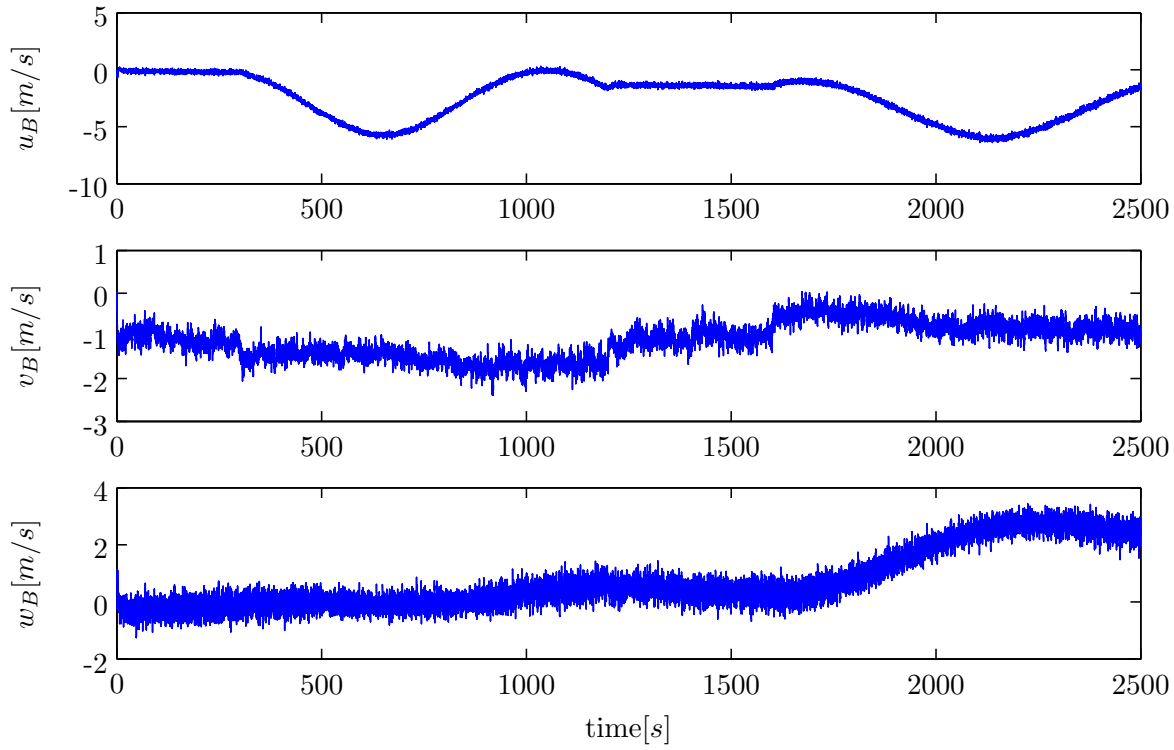

Figure F-15: Error velocity states EKF, large turns Aerosonde UAV simulation

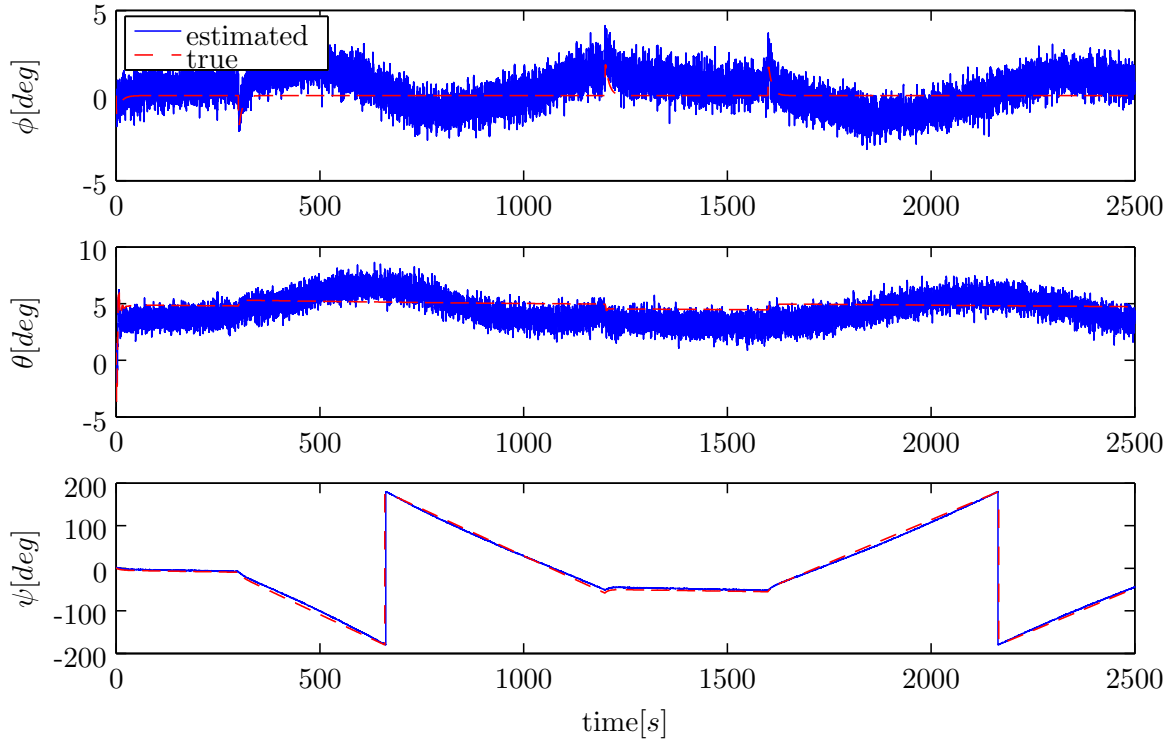

Figure F-16: Estimated Euler angle states EKF, large turns Aerosonde UAV simulation

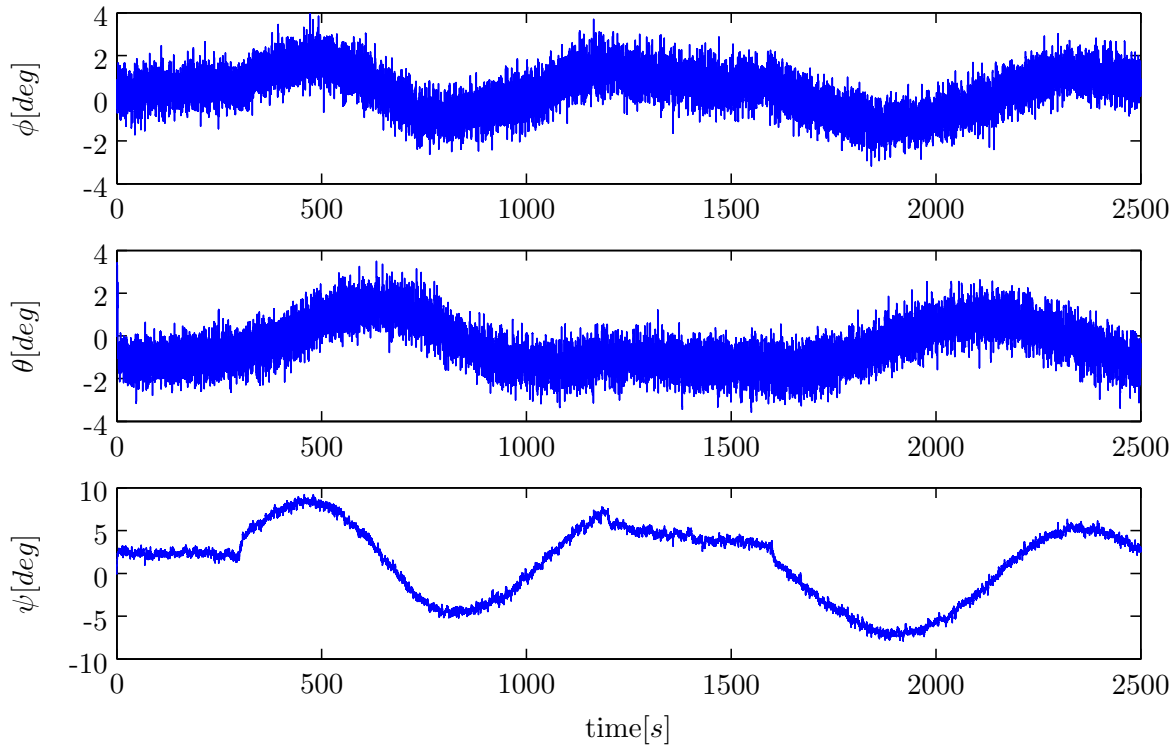

Figure F-17: Error Euler angle states EKF, large turns Aerosonde UAV simulation

F-2 Results EKF Identification no Gust

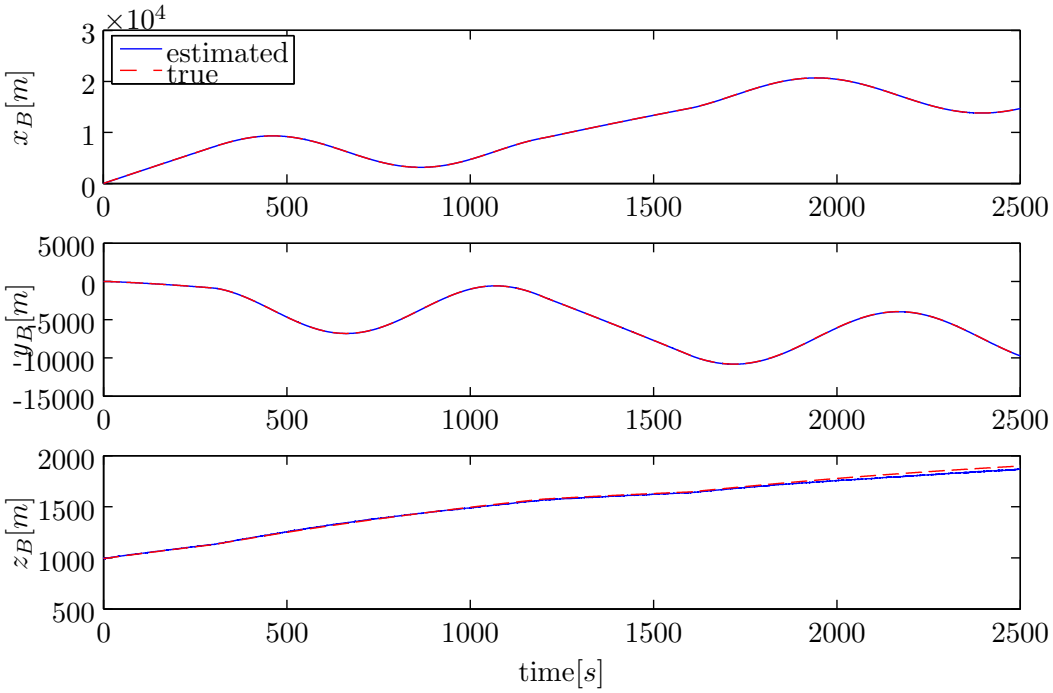

Figure F-18: Estimated position states EKF, large turns Aerosonde UAV simulation

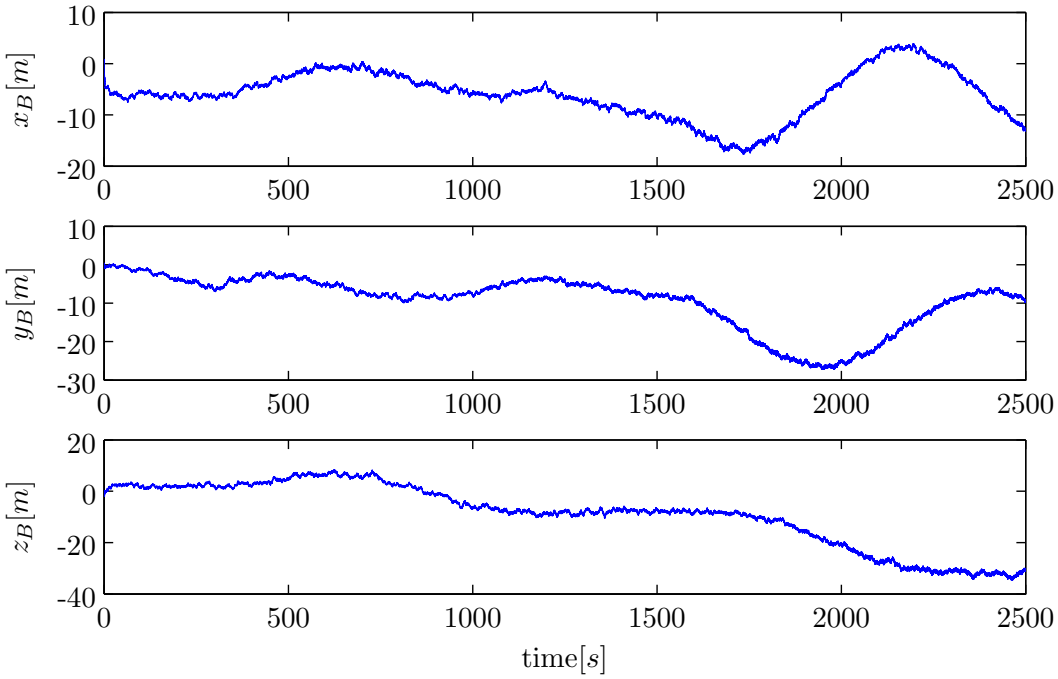

Figure F-19: Error position states EKF, large turns Aerosonde UAV simulation

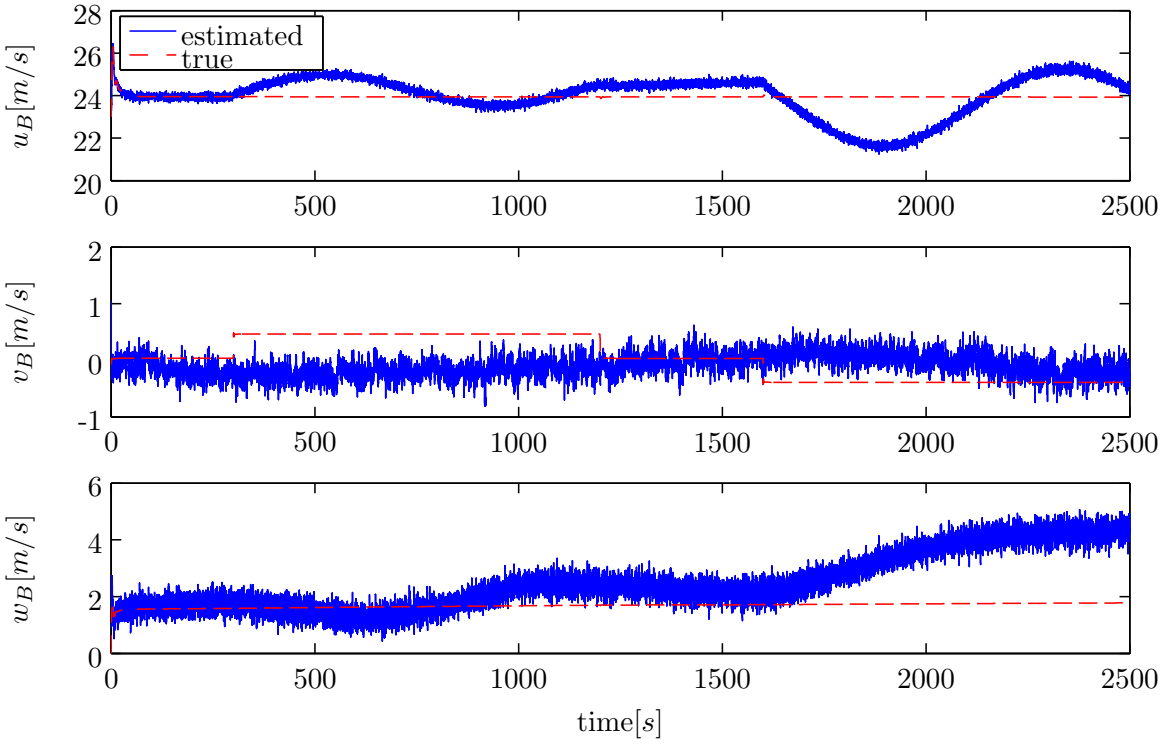

Figure F-20: Estimated velocity states EKF, large turns Aerosonde UAV simulation

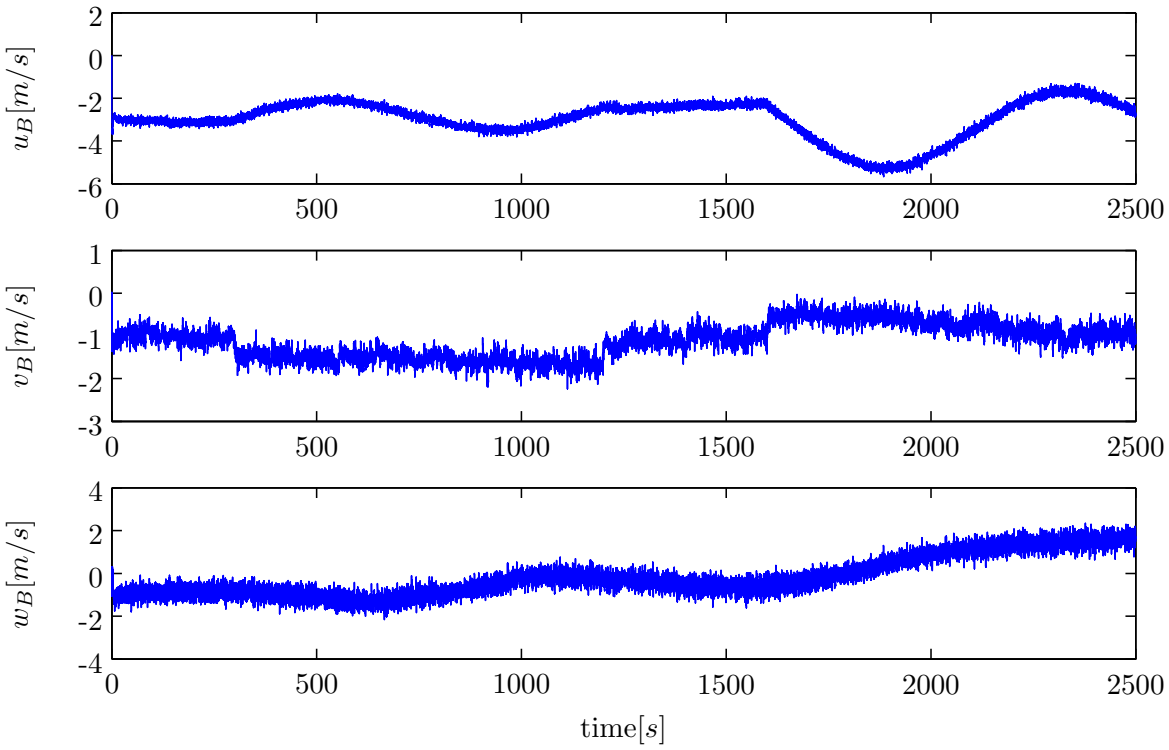

Figure F-21: Error velocity states EKF, large turns Aerosonde UAV simulation

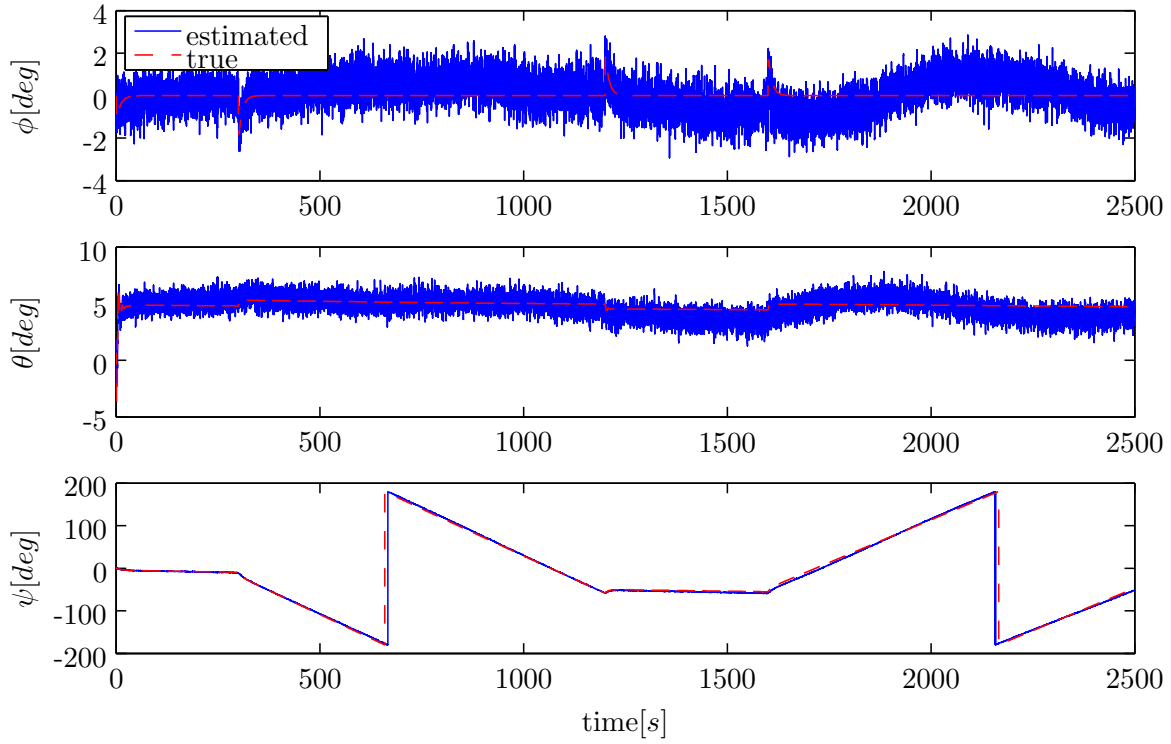

Figure F-22: Estimated Euler angle states EKF, large turns Aerosonde UAV simulation

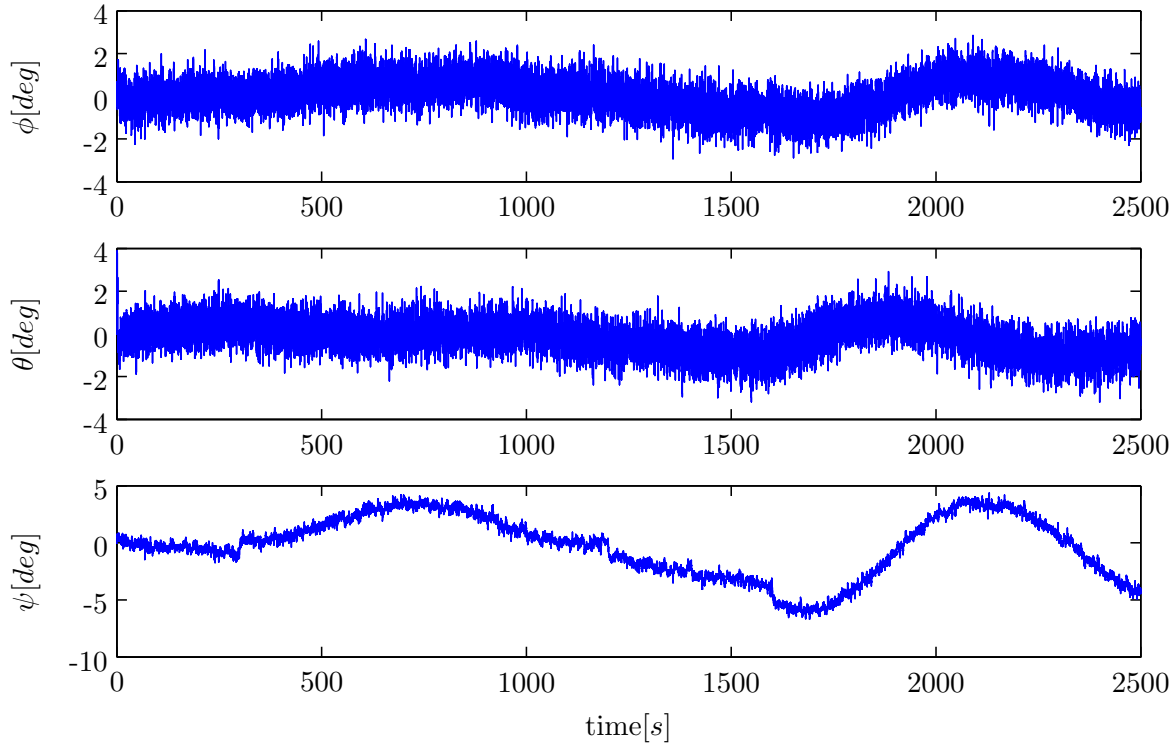

Figure F-23: Error Euler angle states EKF, large turns Aerosonde UAV simulation

F-3 Results IEKF Identification

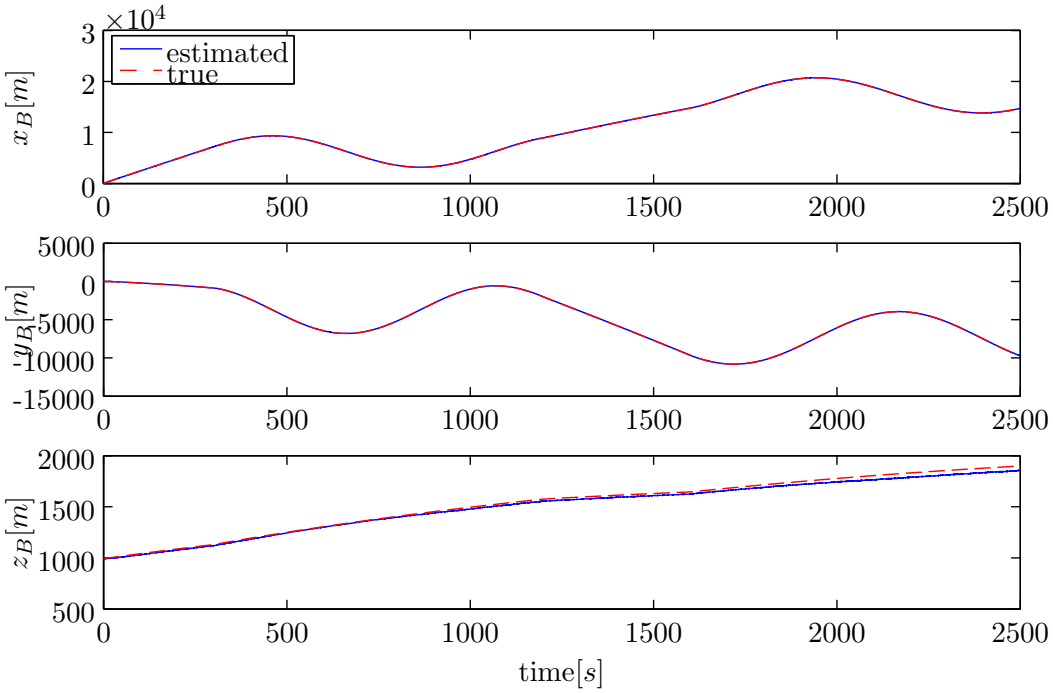

Figure F-24: Estimated position states IEKF, large turns Aerosonde UAV simulation

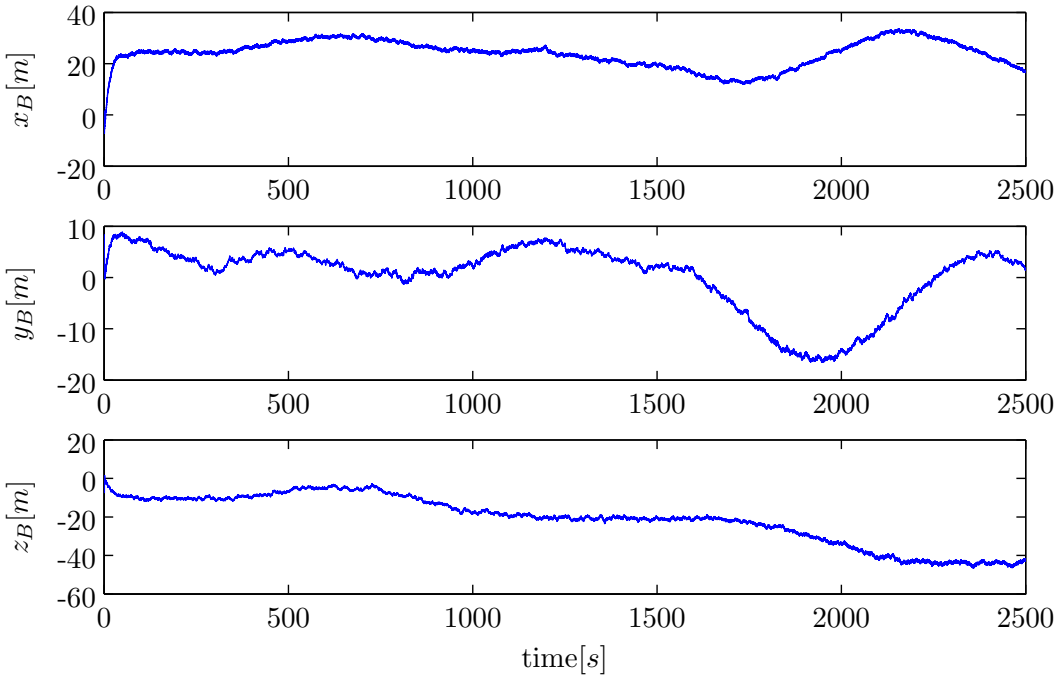

Figure F-25: Error position states IEKF, large turns Aerosonde UAV simulation

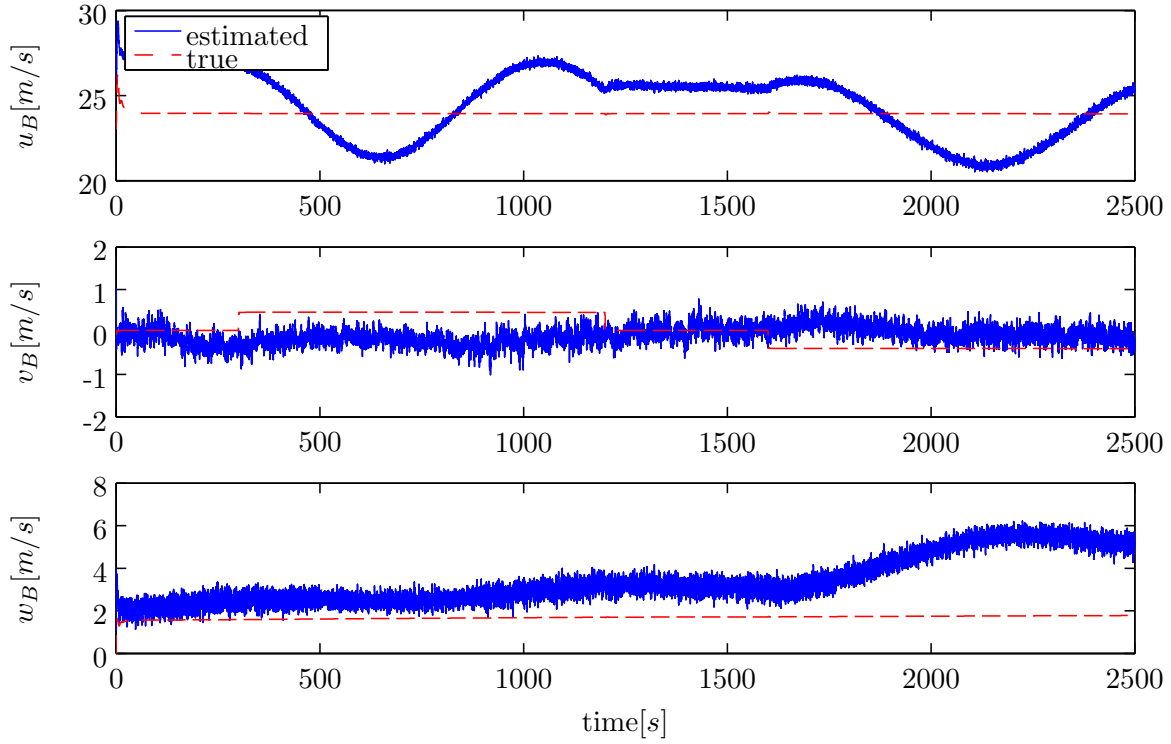

Figure F-26: Estimated velocity states IEKF, large turns Aerosonde UAV simulation

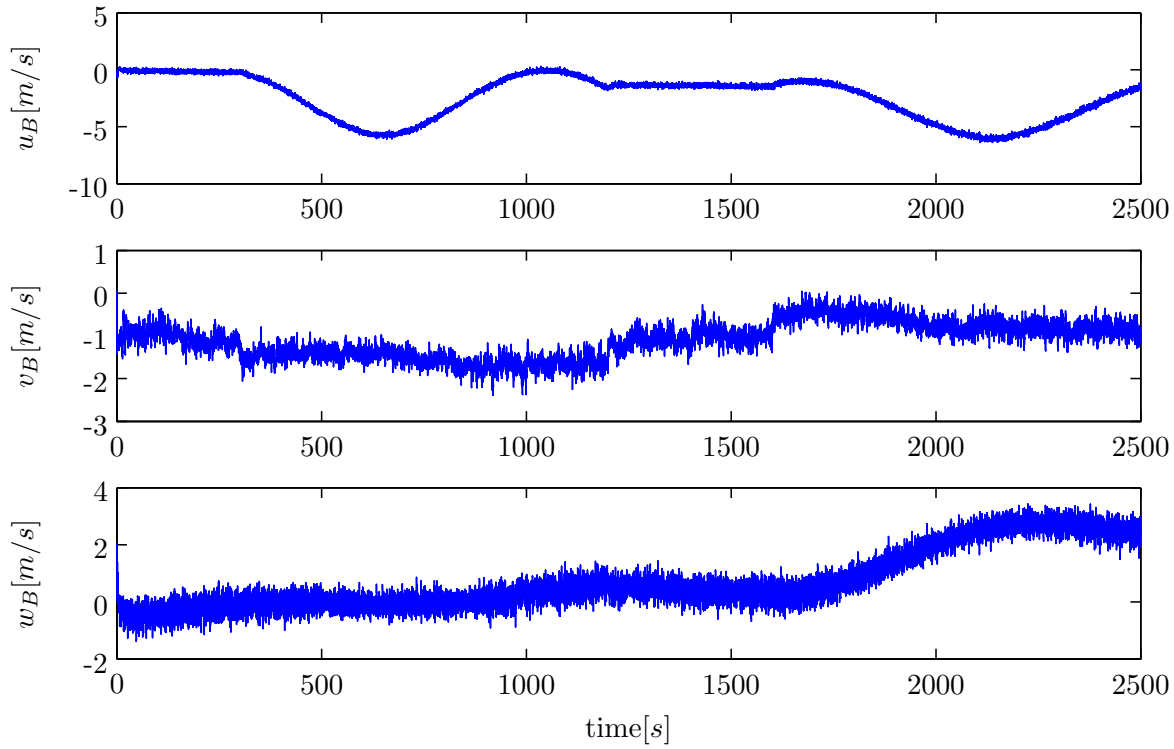

Figure F-27: Error velocity states IEKF, large turns Aerosonde UAV simulation

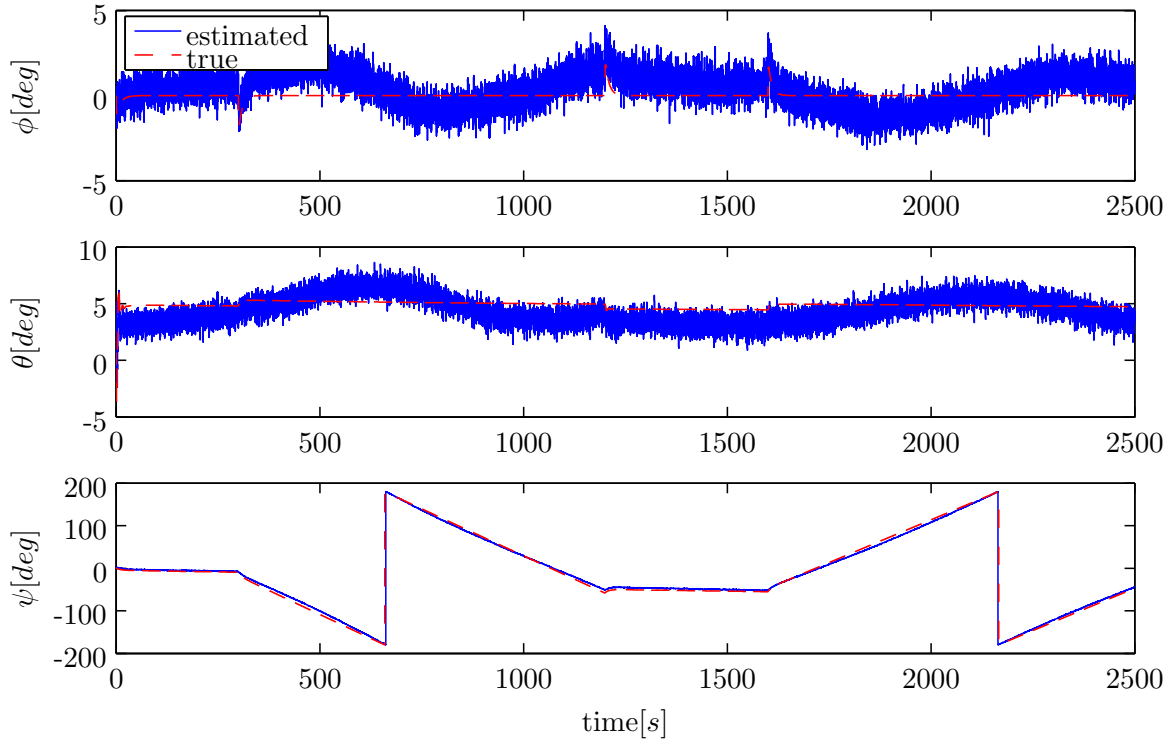

Figure F-28: Estimated Euler angle states IEKF, large turns Aerosonde UAV simulation

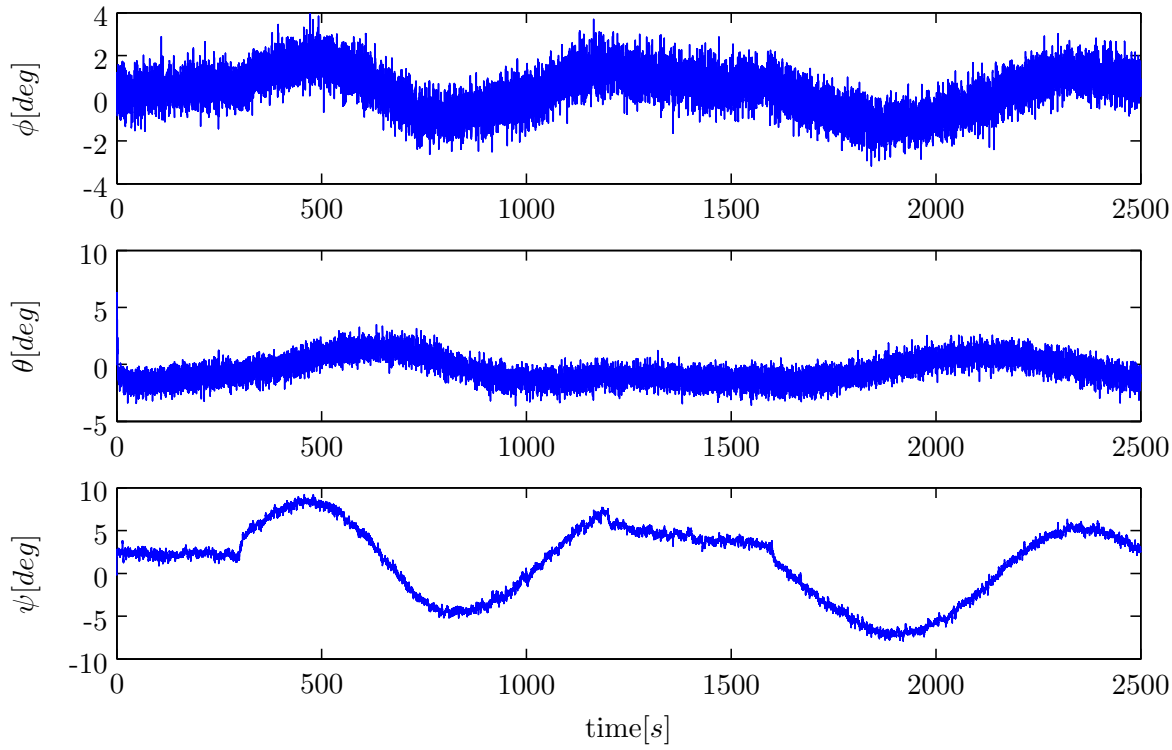

Figure F-29: Error Euler angle states IEKF, large turns Aerosonde UAV simulation

F-4 Results IEKF Identification no Gust

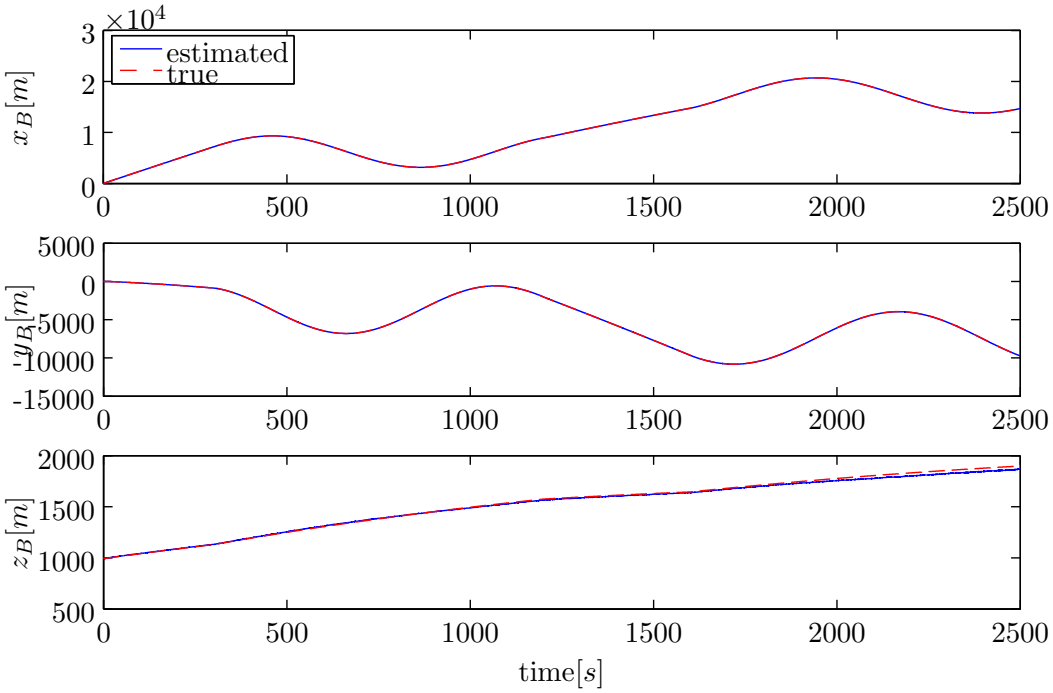

Figure F-30: Estimated position states IEKF, large turns Aerosonde UAV simulation

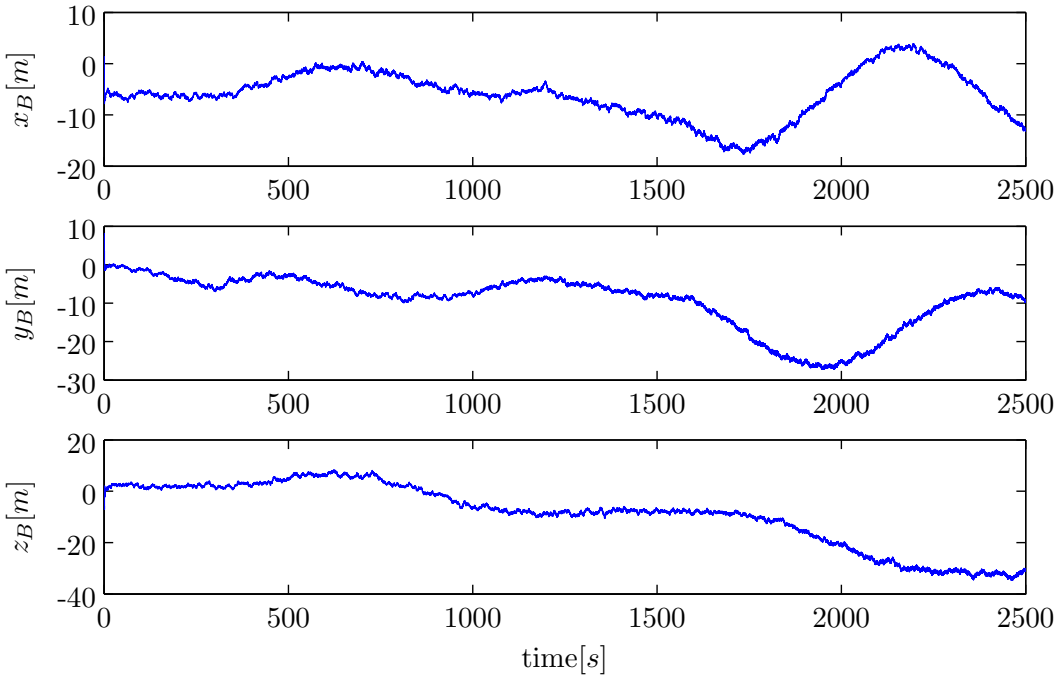

Figure F-31: Error position states IEKF, large turns Aerosonde UAV simulation

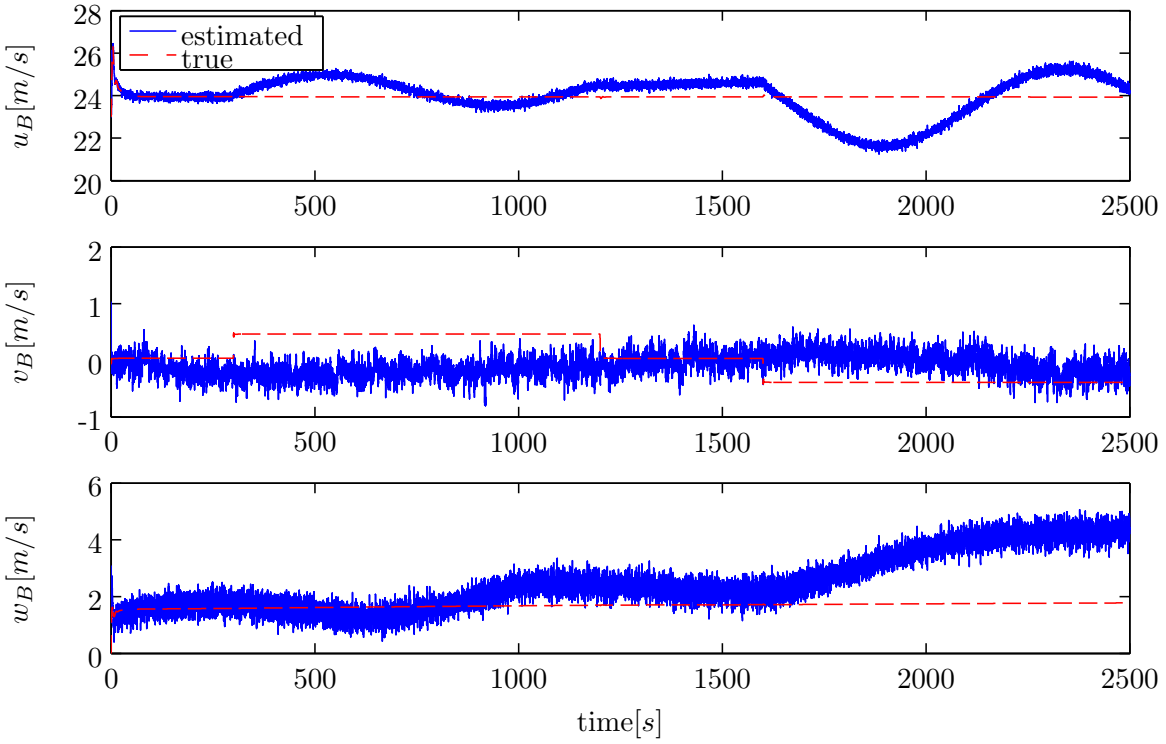

Figure F-32: Estimated velocity states IEKF, large turns Aerosonde UAV simulation

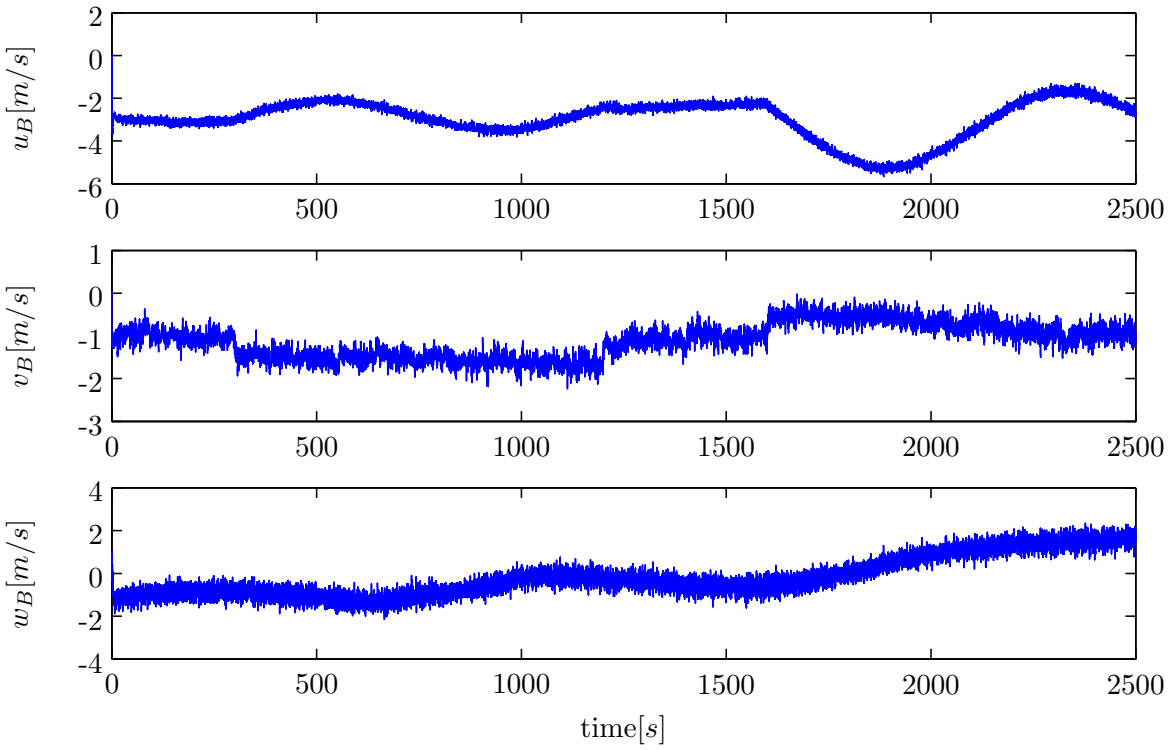

Figure F-33: Error velocity states IEKF, large turns Aerosonde UAV simulation

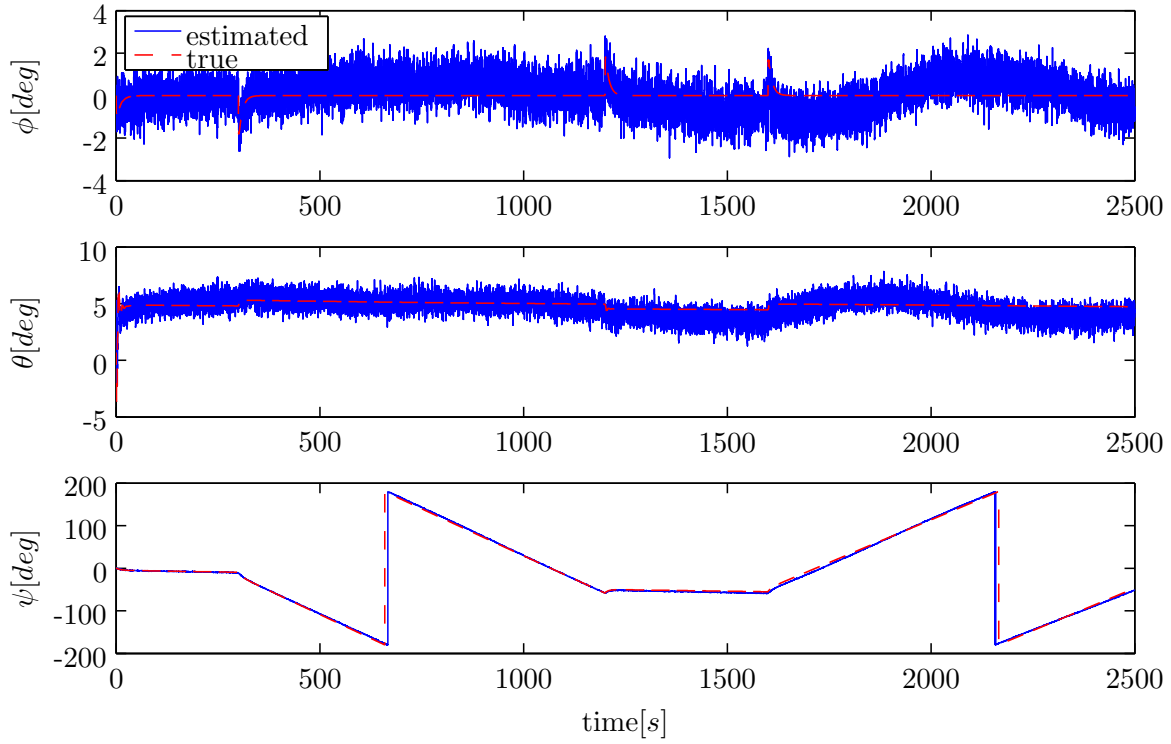

Figure F-34: Estimated Euler angle states IEKF, large turns Aerosonde UAV simulation

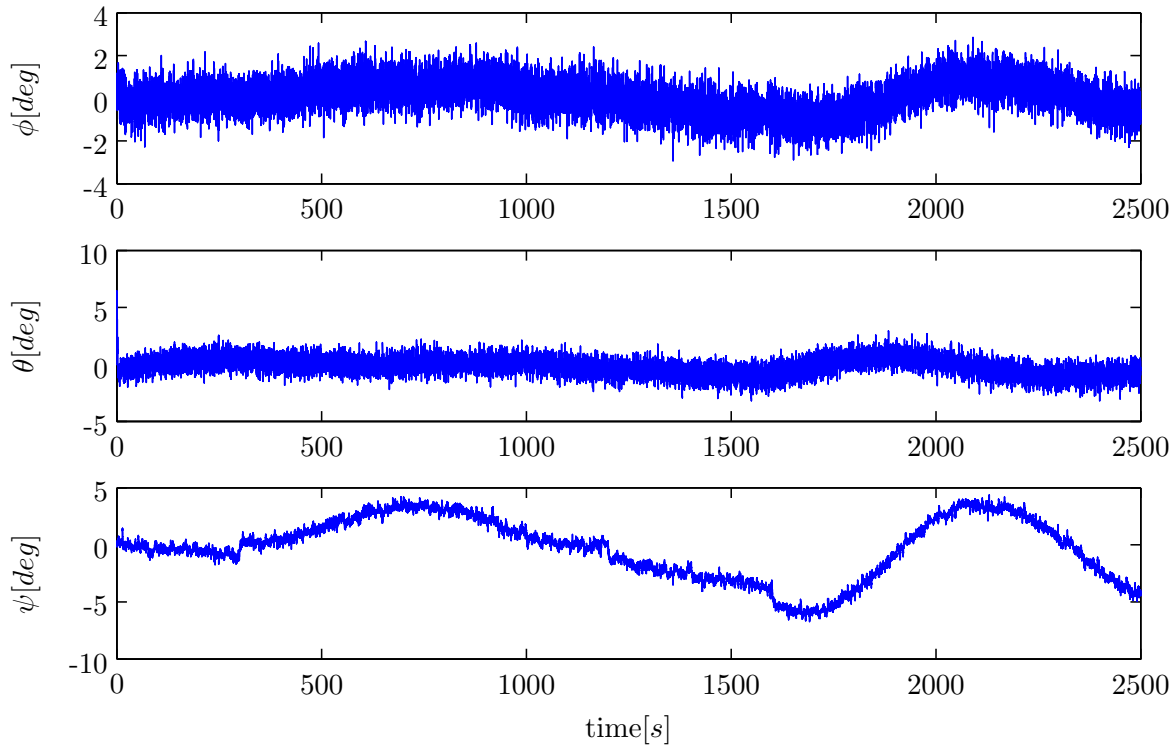

Figure F-35: Error Euler angle states IEKF, large turns Aerosonde UAV simulation

F-5 Results Non-Linear SO(3) Identification

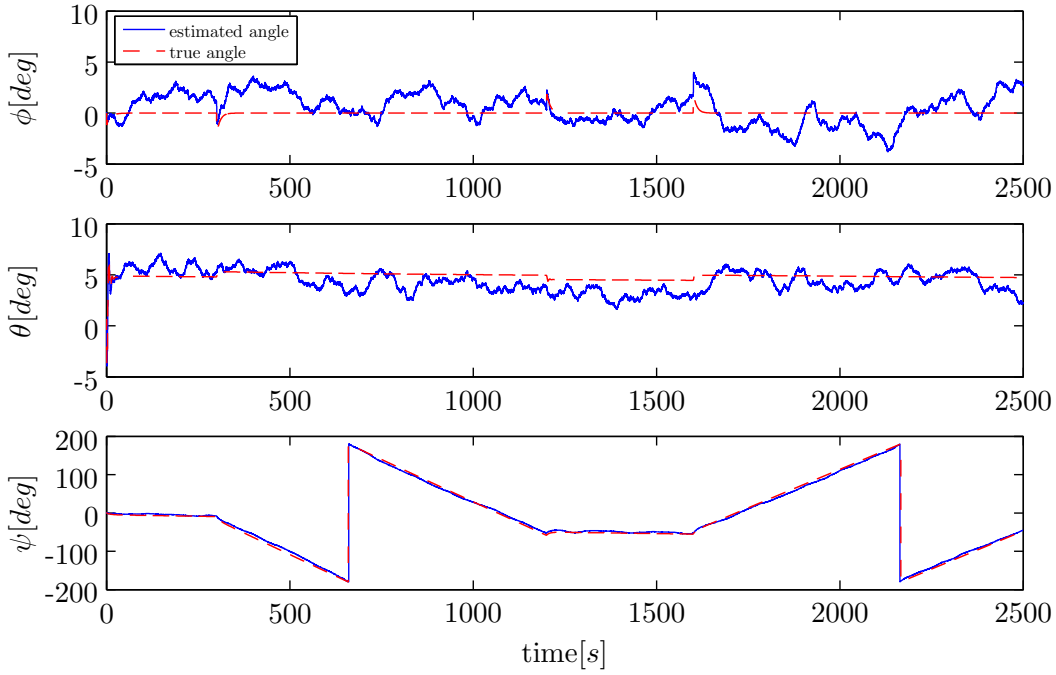

Figure F-36: Estimated Euler angles SO(3), large turns Aerosonde UAV simulation

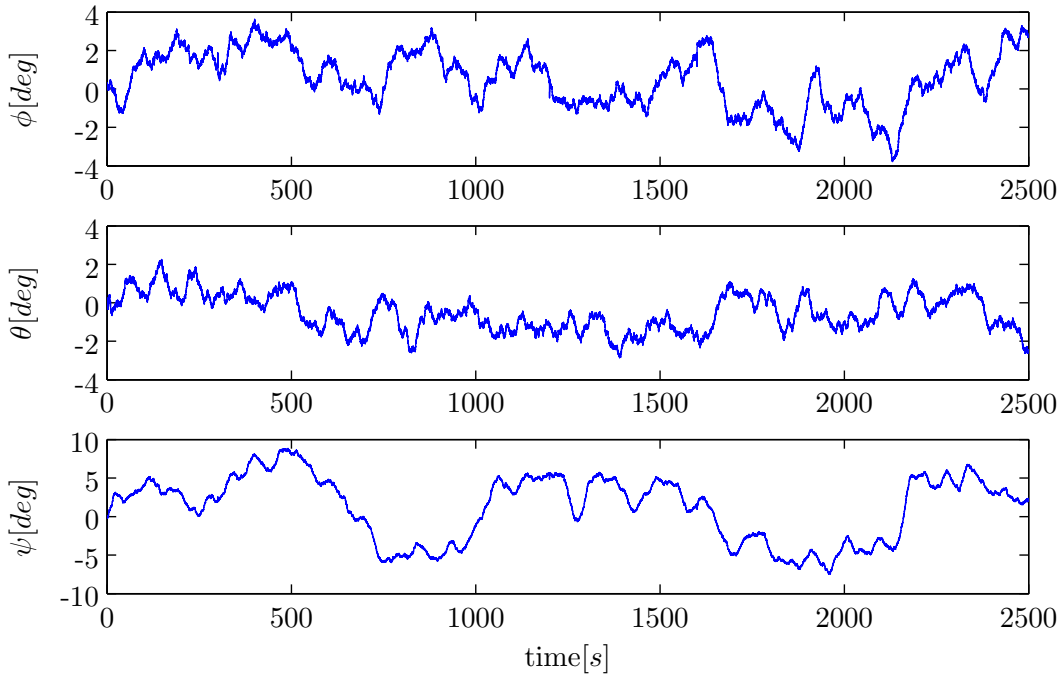

Figure F-37: Error Euler angles SO(3), large turns Aerosonde UAV simulation

F-6 Results Non-Linear SO(3) Identification no Gust

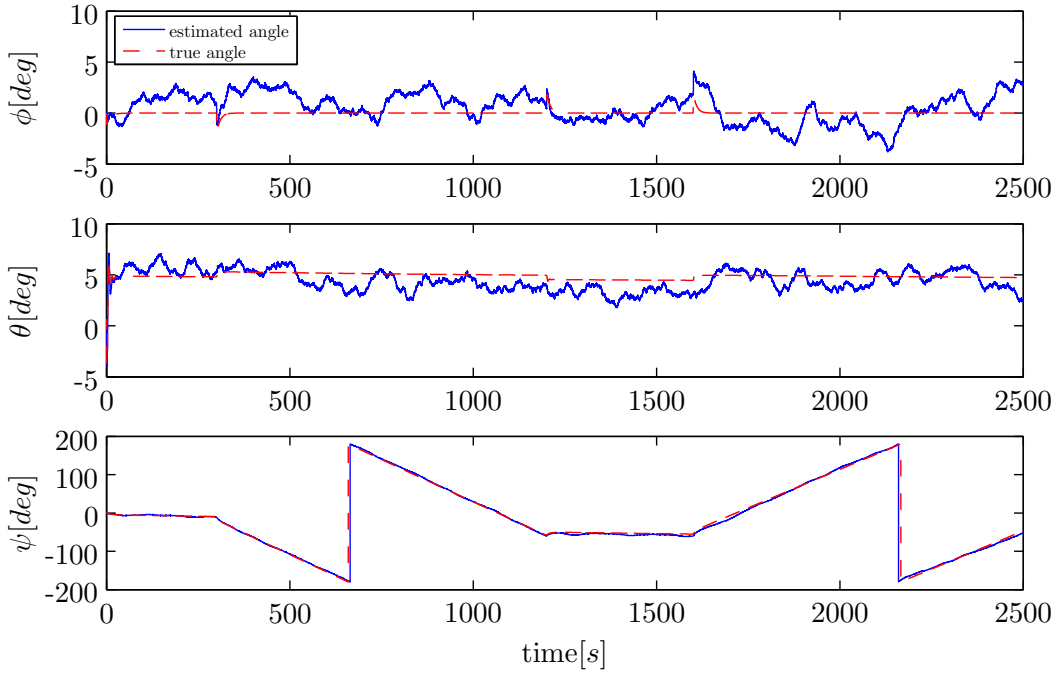

Figure F-38: Estimated Euler angles SO(3), large turns Aerosonde UAV simulation

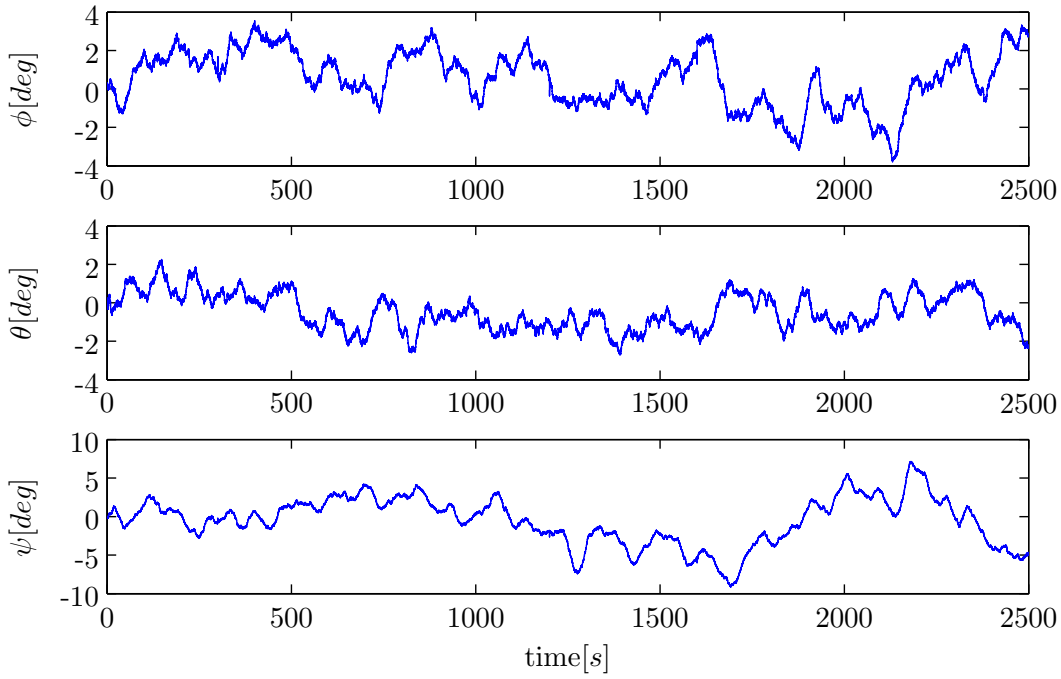

Figure F-39: Error Euler angles SO(3), large turns Aerosonde UAV simulation

Appendix G

Flight Test Data

G-1 Log-file 2010-10-05/LOG00039

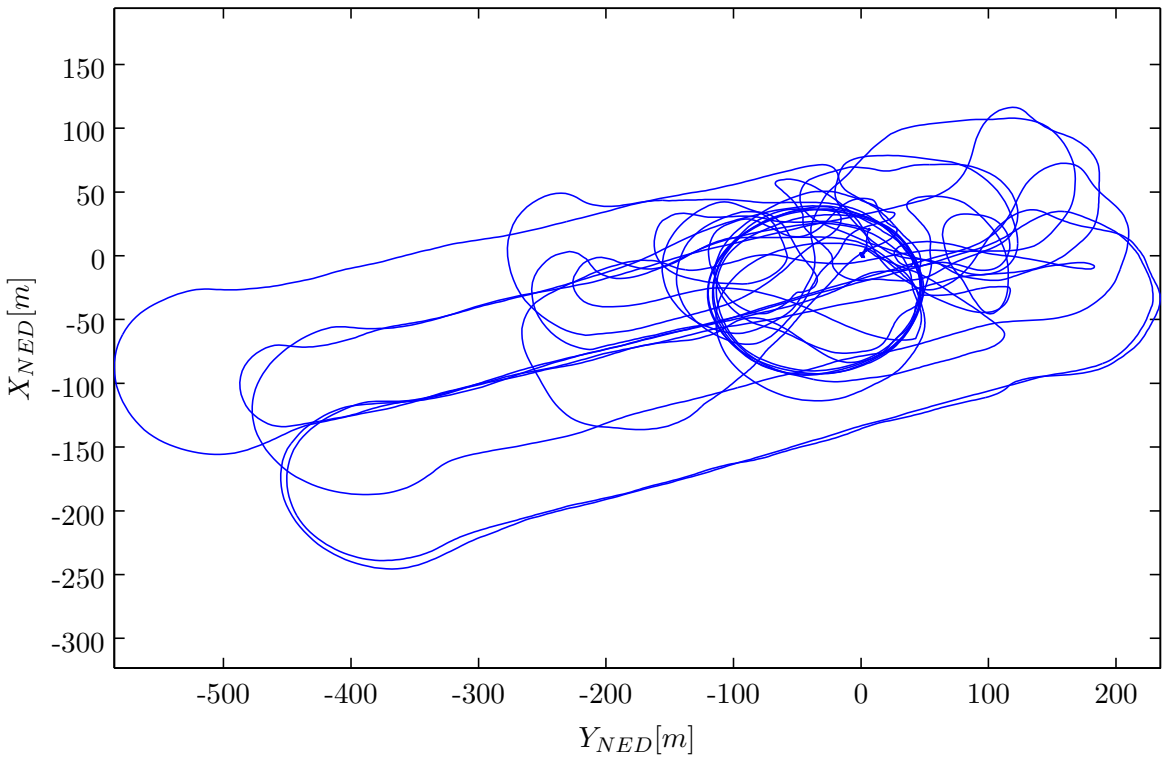

Figure G-1: Flight trajectory, LOG00039

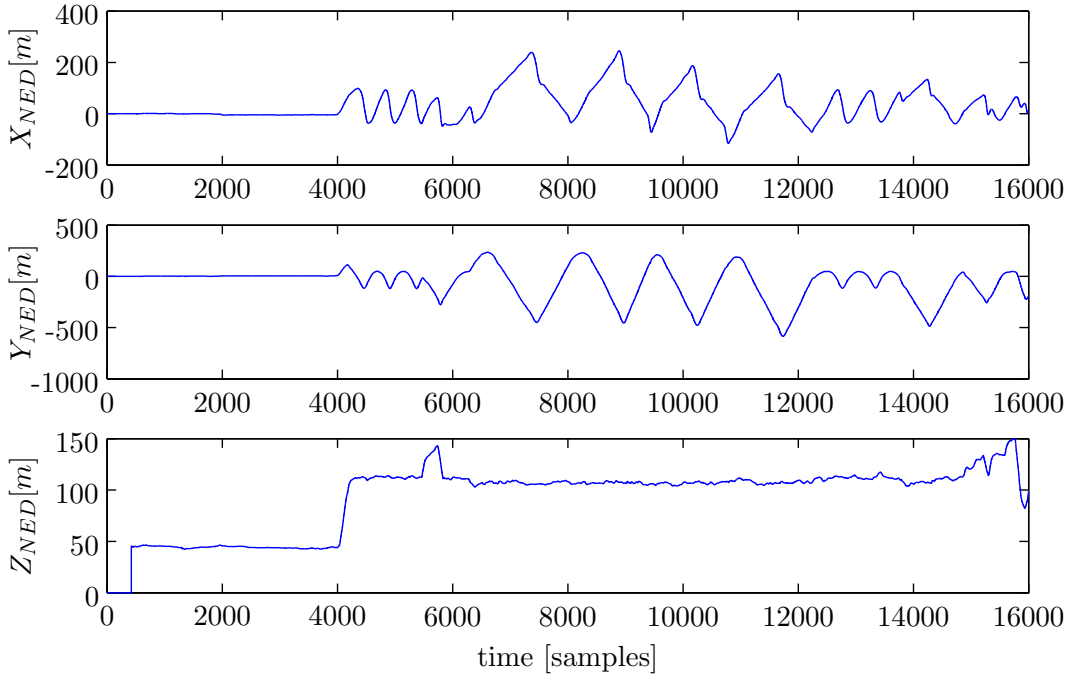

Figure G-2: GPS positions in NED, LOG00039

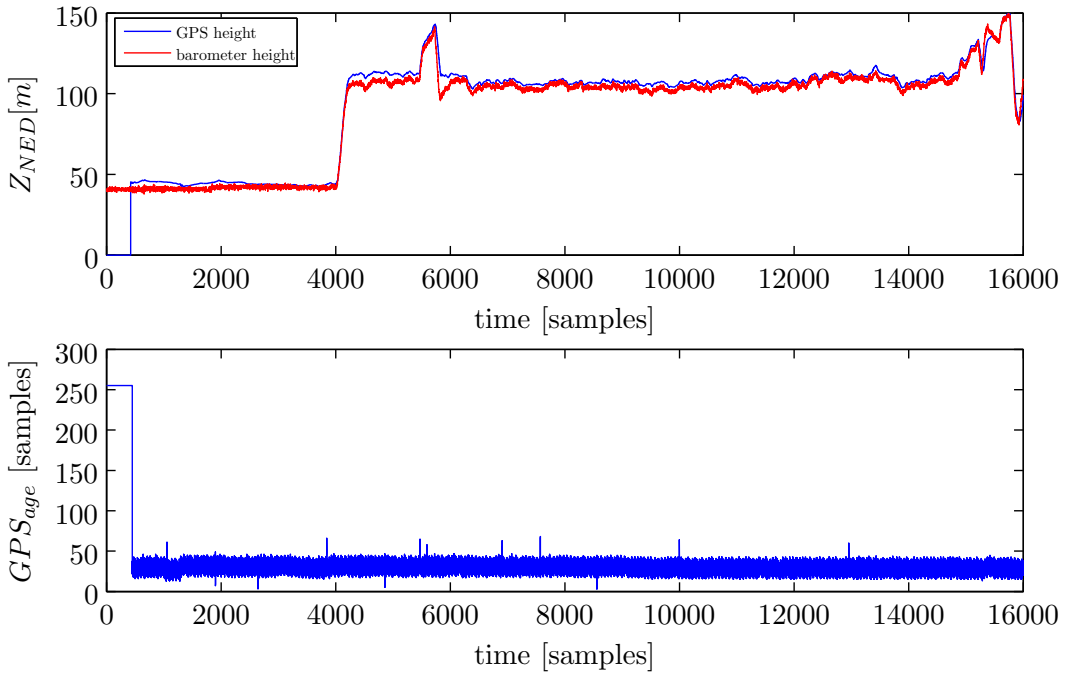

Figure G-3: GPS and barometer height in NED and GPS processing time, LOG00039

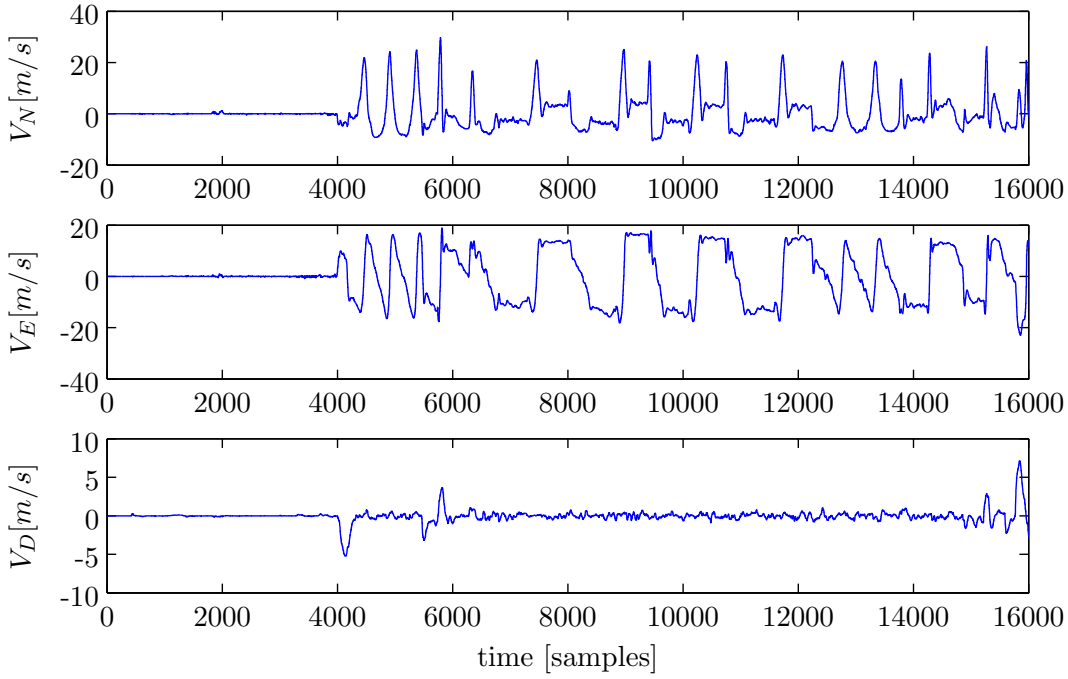

Figure G-4: GPS velocities in NED, LOG00039

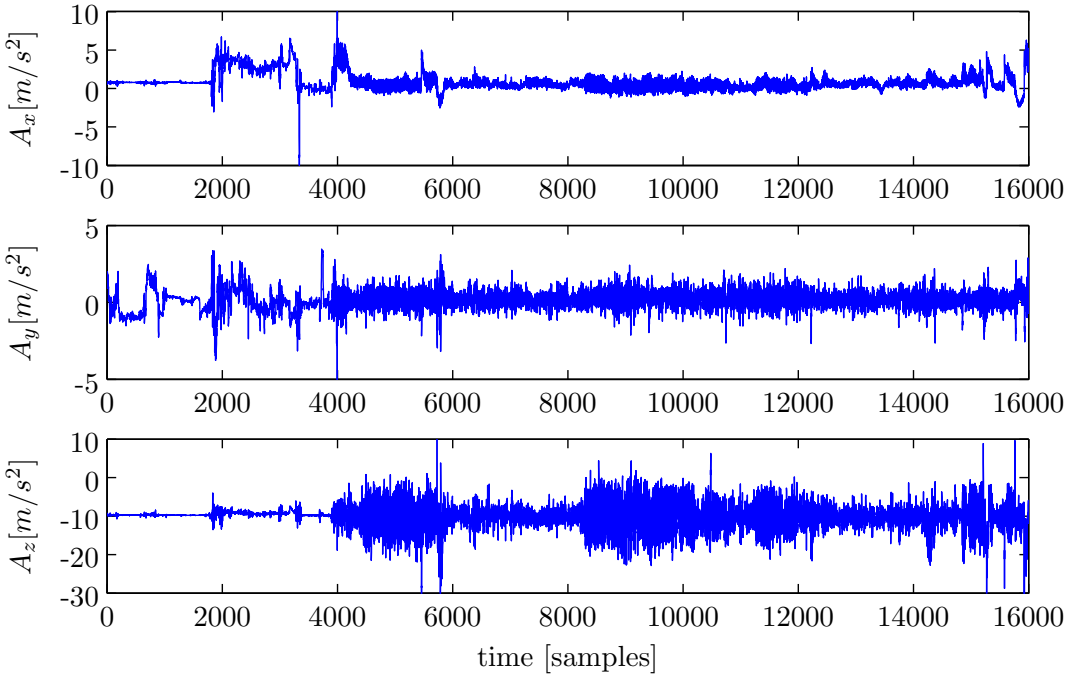

Figure G-5: Accelerometer signals in $\mathcal{F}_B$, LOG00039

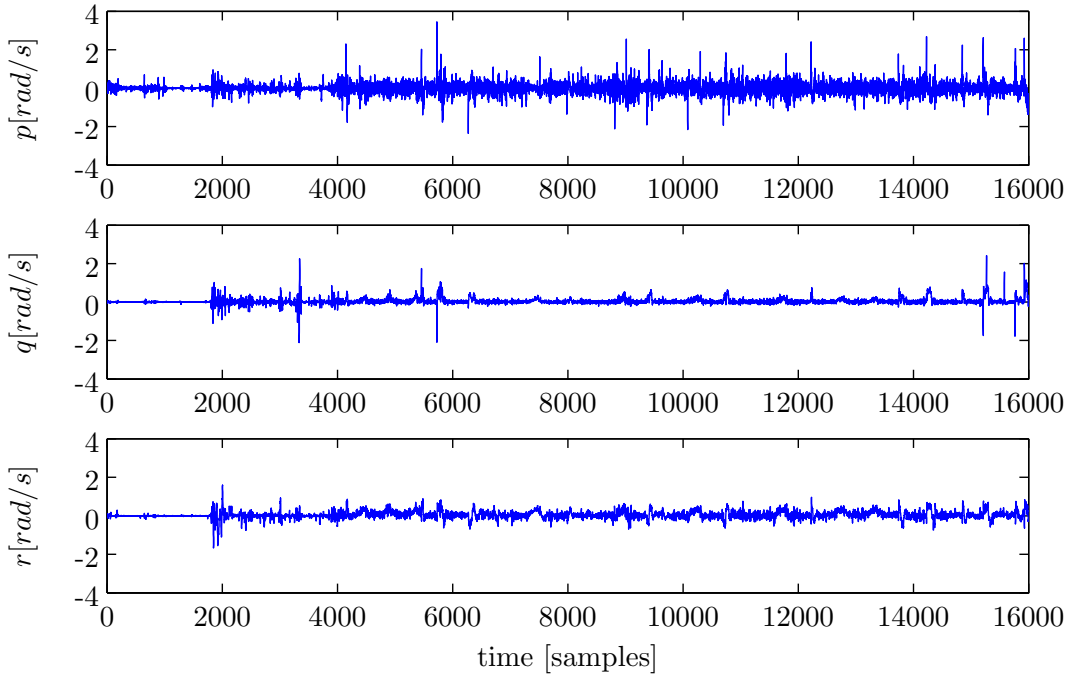

Figure G-6: Gyroscope signals in $\mathcal{F}_B$, LOG00039

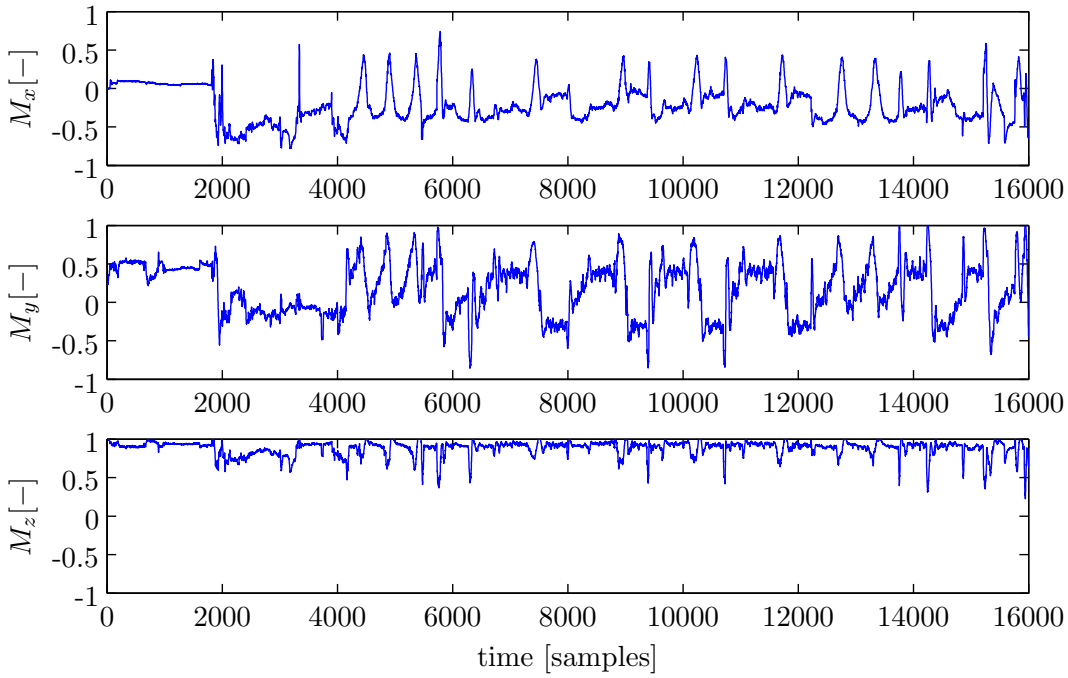

Figure G-7: Magnetometer signals, converted to unit amplitude in $\mathcal{F}_B$, LOG00039

G-1-1 Results EKF Identification

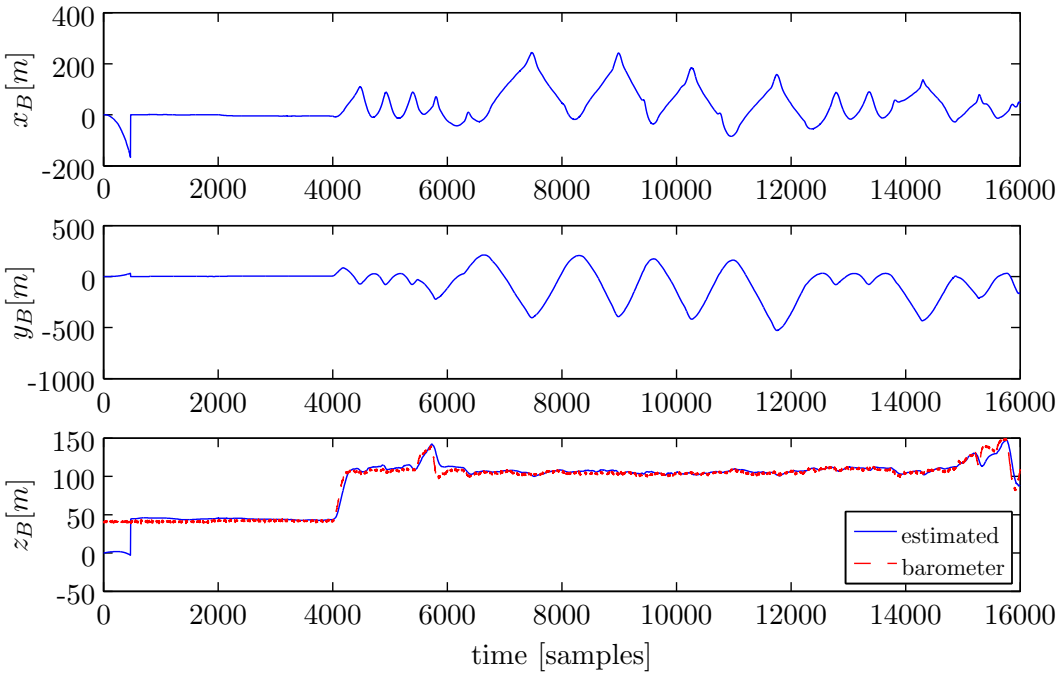

Figure G-8: Estimated position states EKF, LOG00039

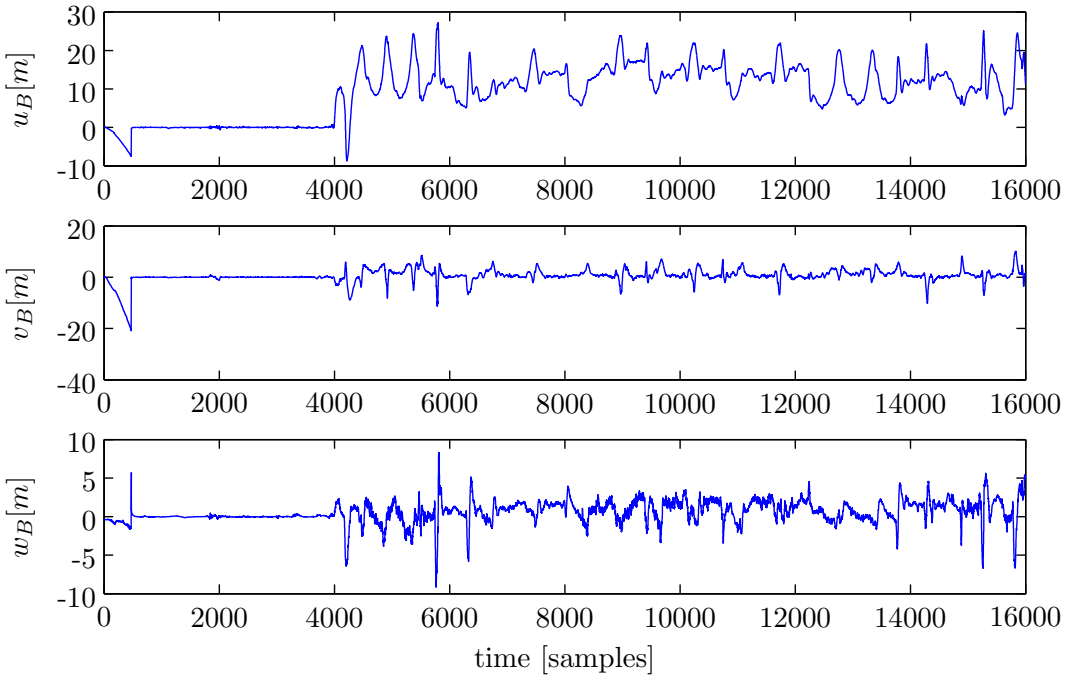

Figure G-9: Estimated velocity states EKF, LOG00039

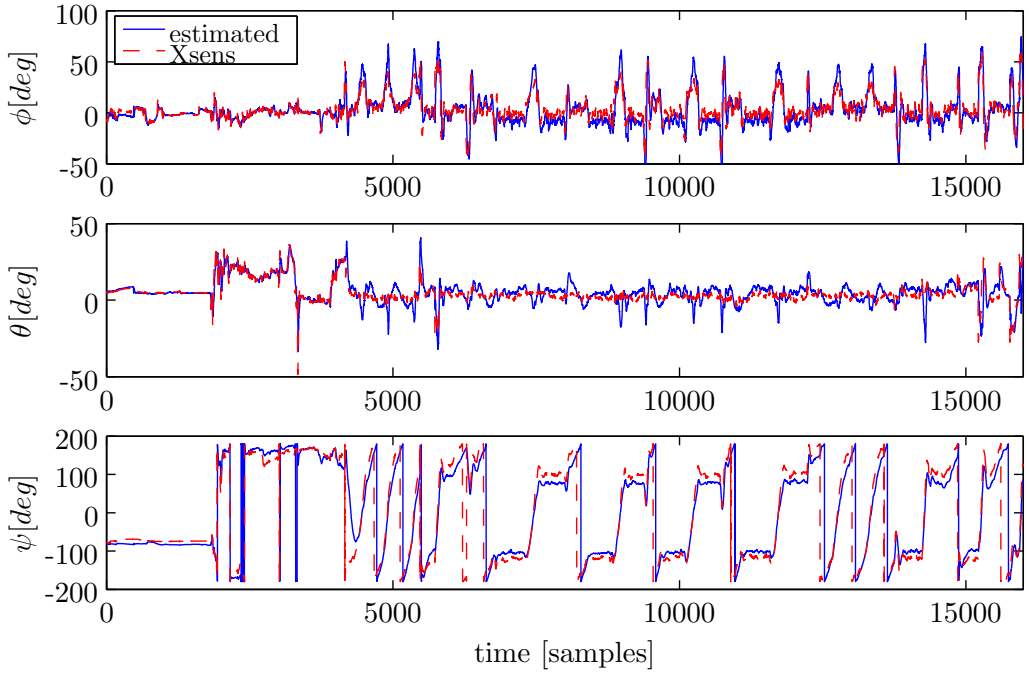

Figure G-10: Estimated Euler angle states EKF, LOG00039

G-1-2 Results IEKF Identification

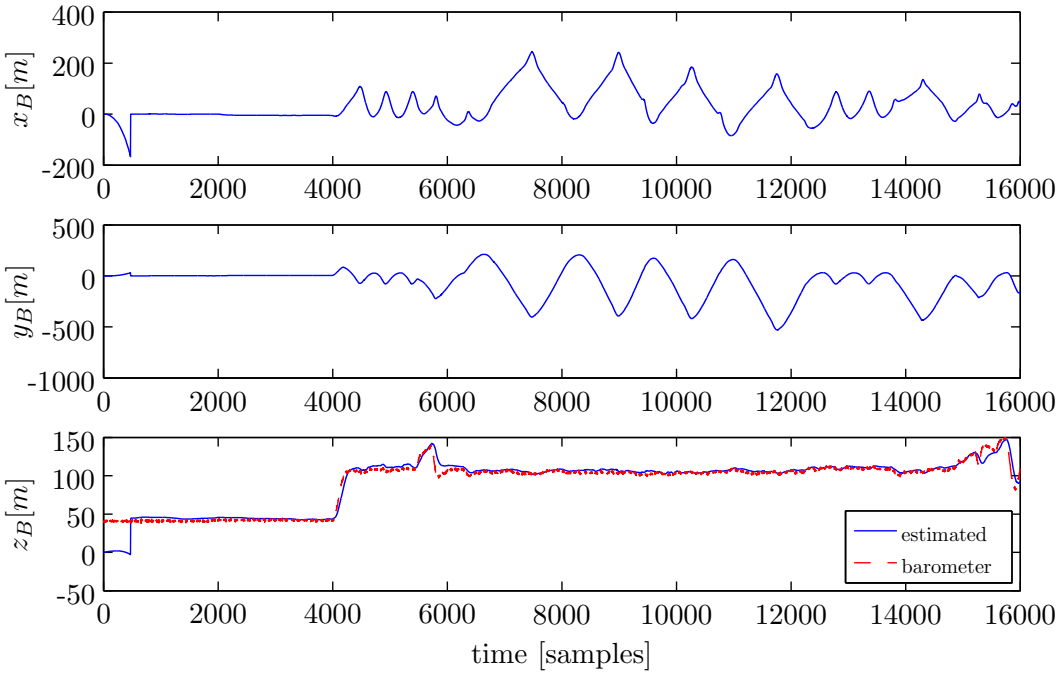

Figure G-11: Estimated position states IEKF, LOG00039

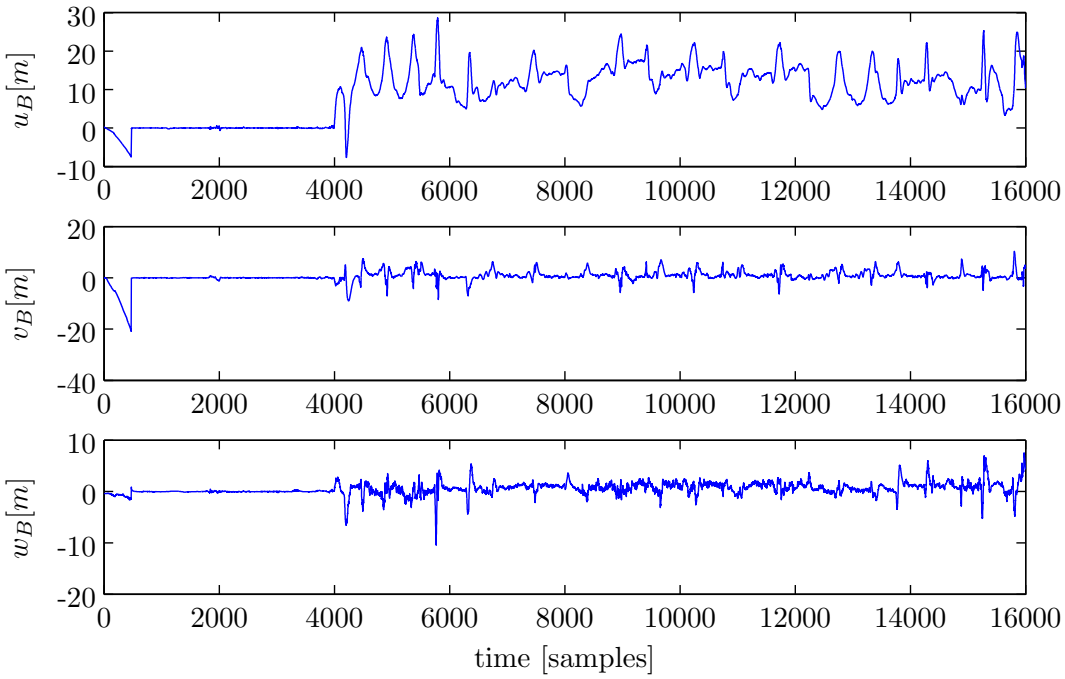

Figure G-12: Estimated velocity states IEKF, LOG00039

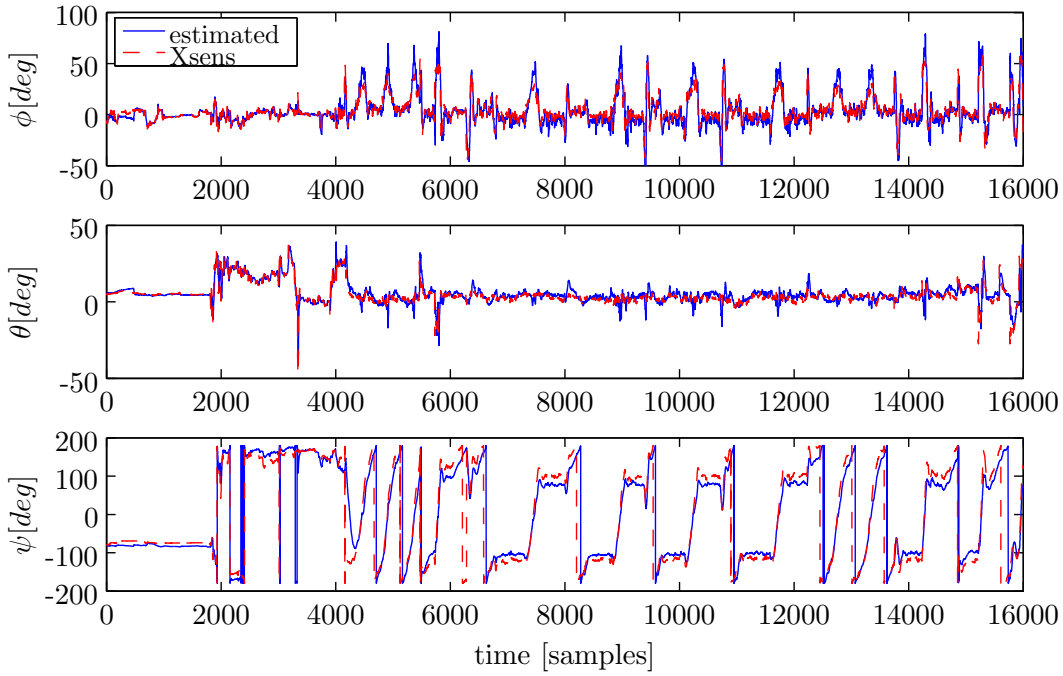

Figure G-13: Estimated Euler angle states IEKF, LOG00039

G-1-3 Results Non-Linear SO(3) Identification

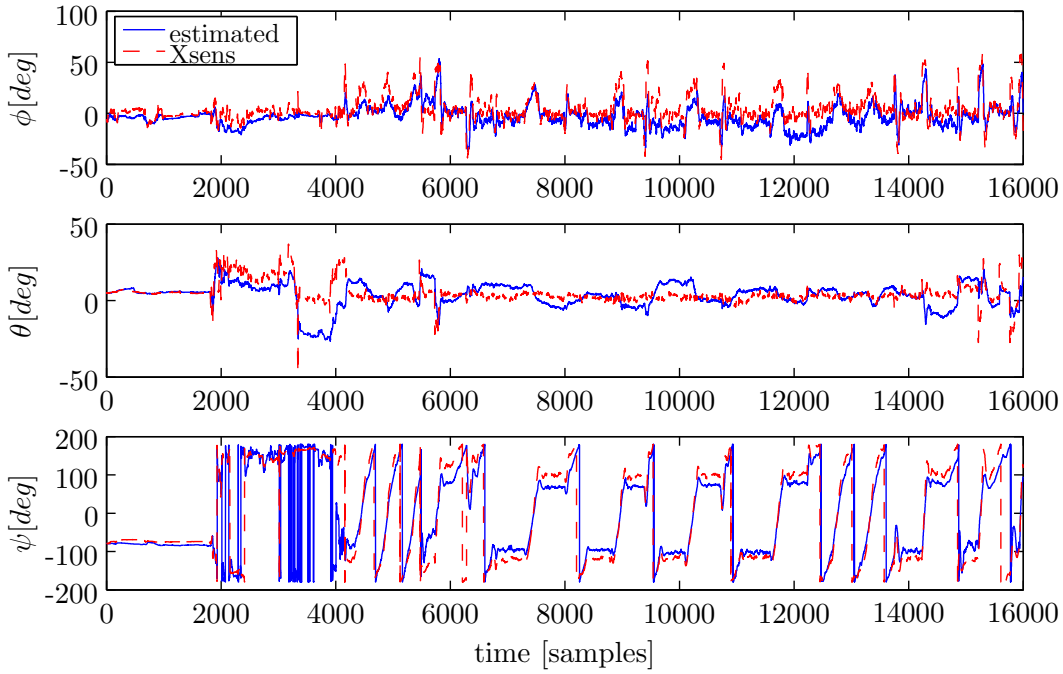

Figure G-14: Estimated Euler angle states SO(3), LOG00039

G-2 Log-file 2010-10-05/LOG00042

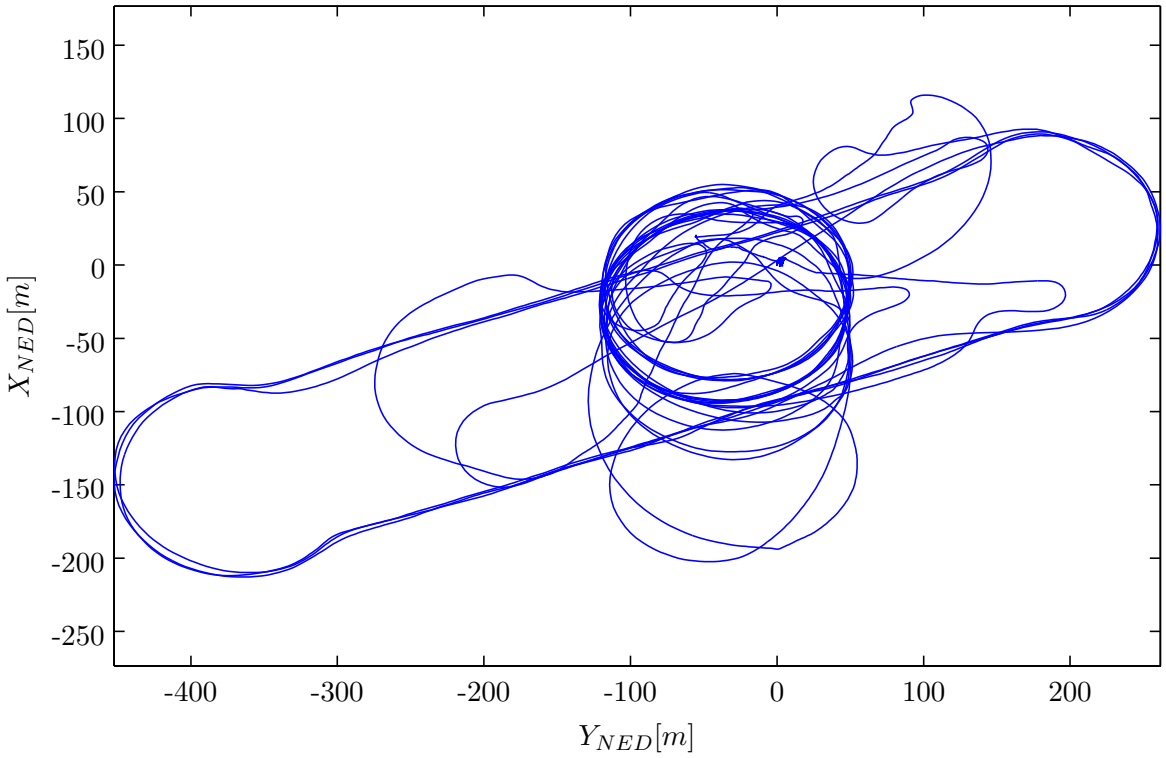

Figure G-15: Flight trajectory, LOG00042

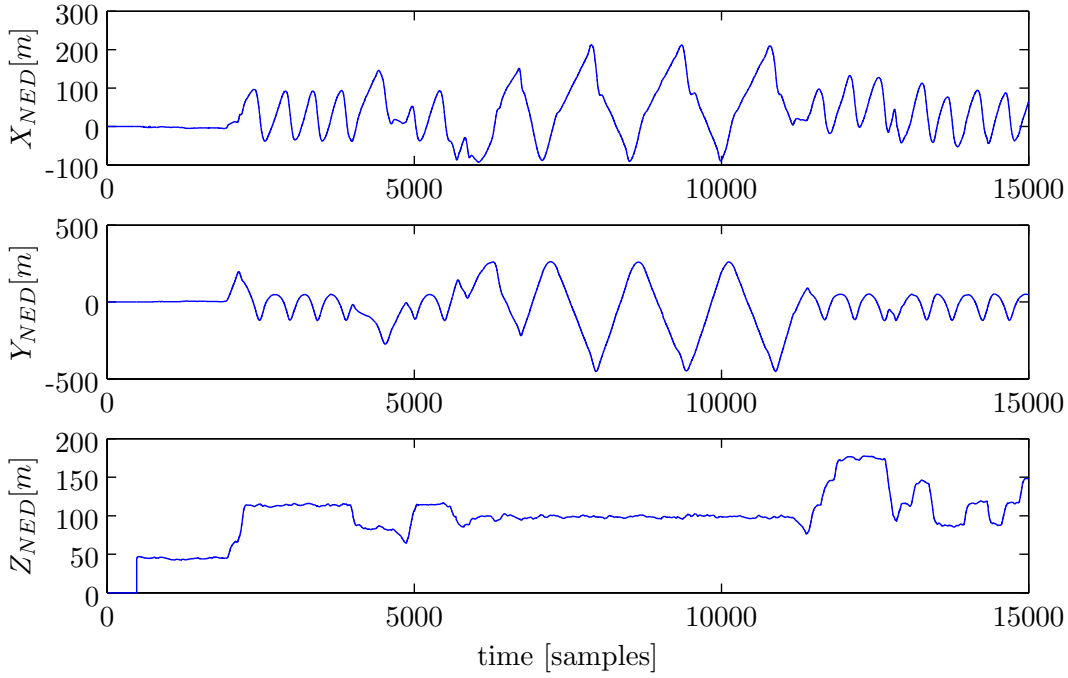

Figure G-16: GPS positions in NED, LOG00042

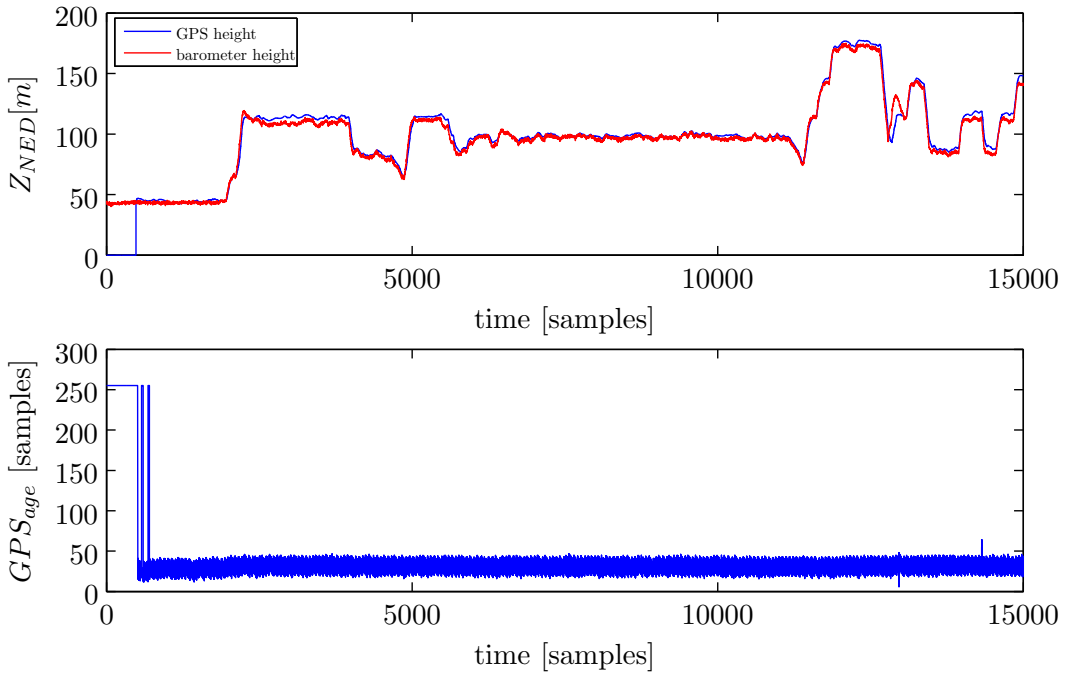

Figure G-17: GPS and barometer height in NED and GPS processing time, LOG00042

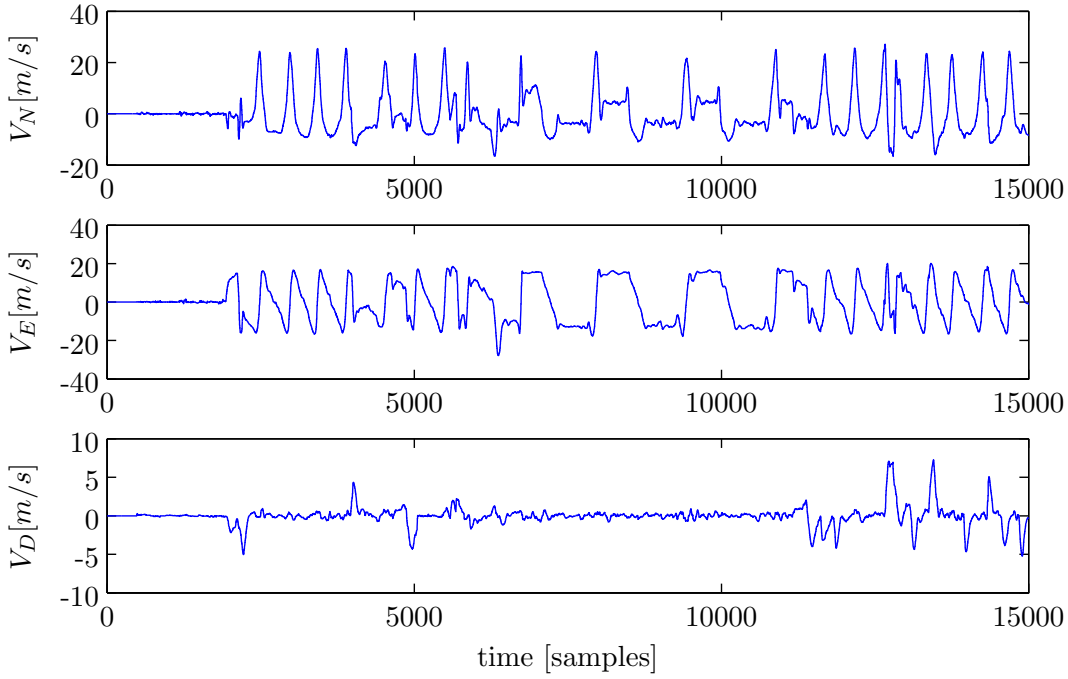

Figure G-18: GPS velocities in NED, LOG00042

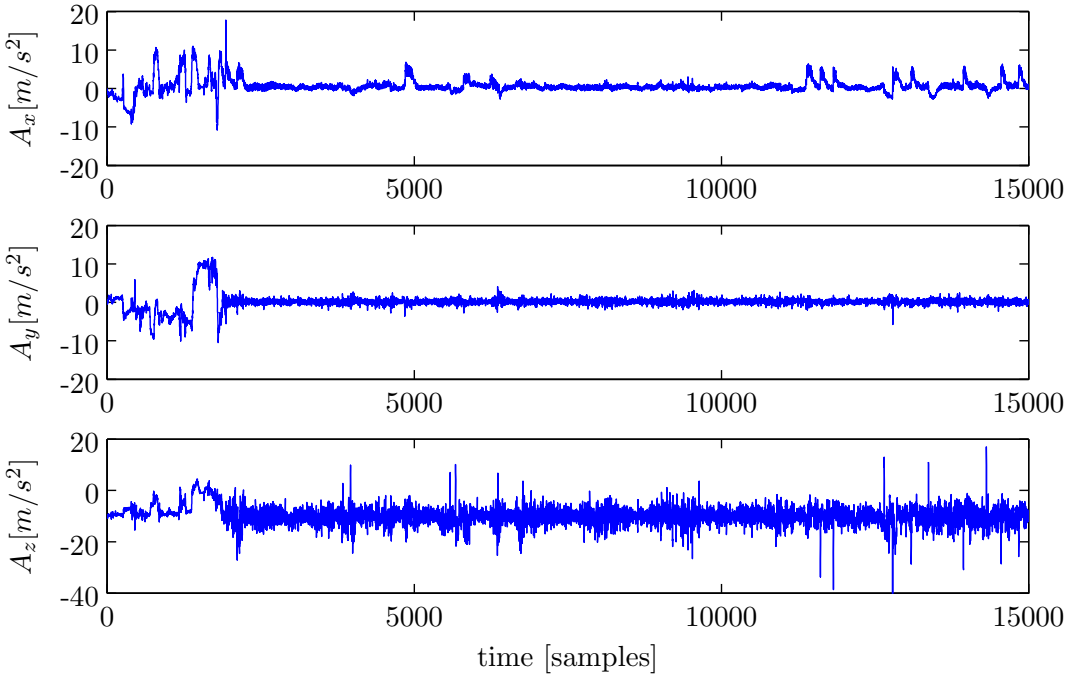

Figure G-19: Accelerometer signals in $\mathcal{F}_B$, LOG00042

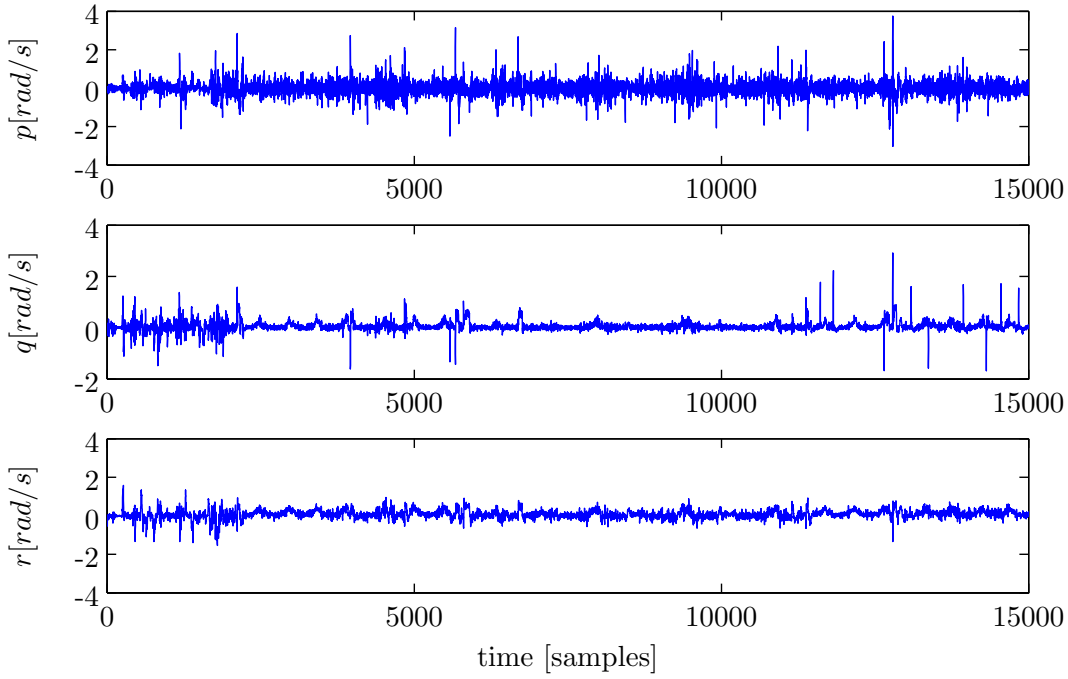

Figure G-20: Gyroscope signals in $\mathcal{F}_B$, LOG00042

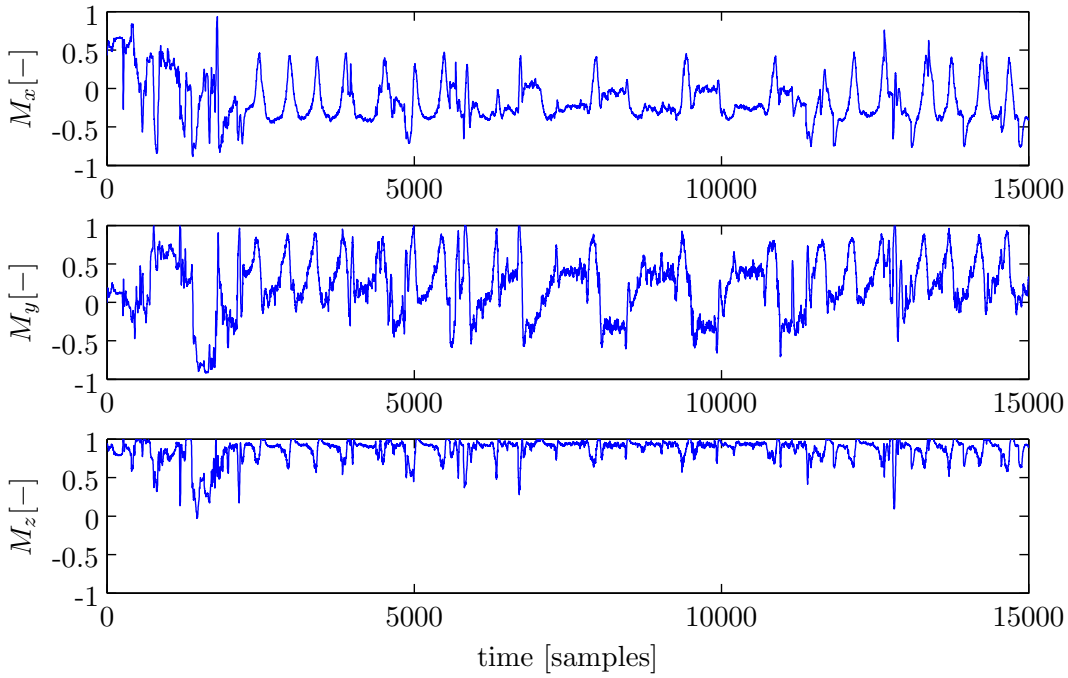

Figure G-21: Magnetometer signals, converted to unit amplitude in $\mathcal{F}_B$, LOG00042

G-2-1 Results EKF Identification

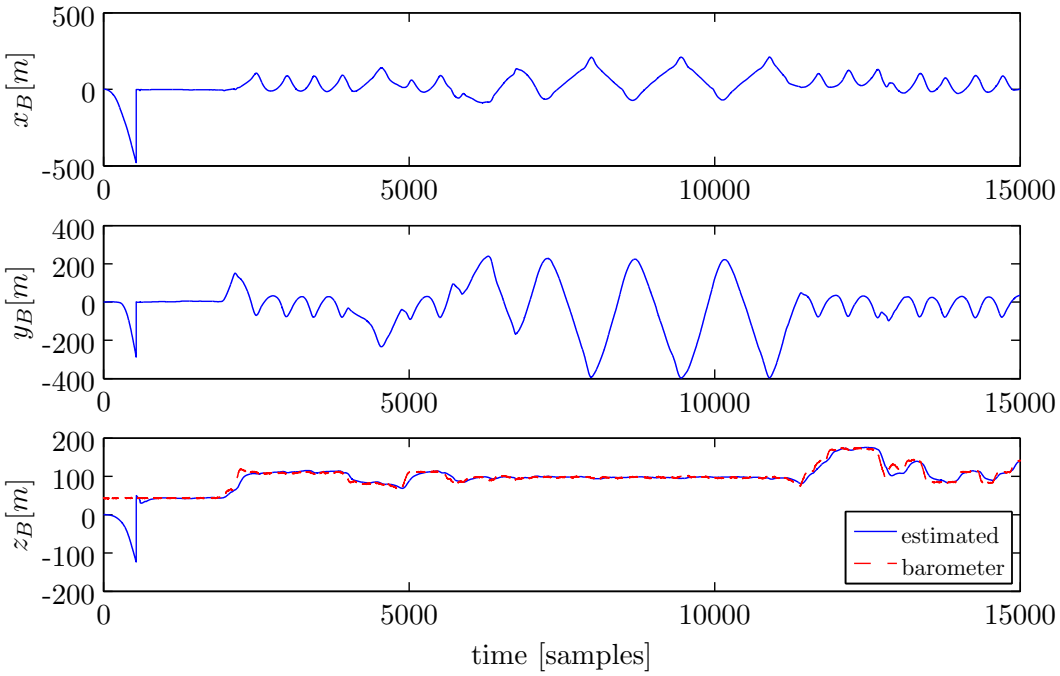

Figure G-22: Estimated position states EKF, LOG00042

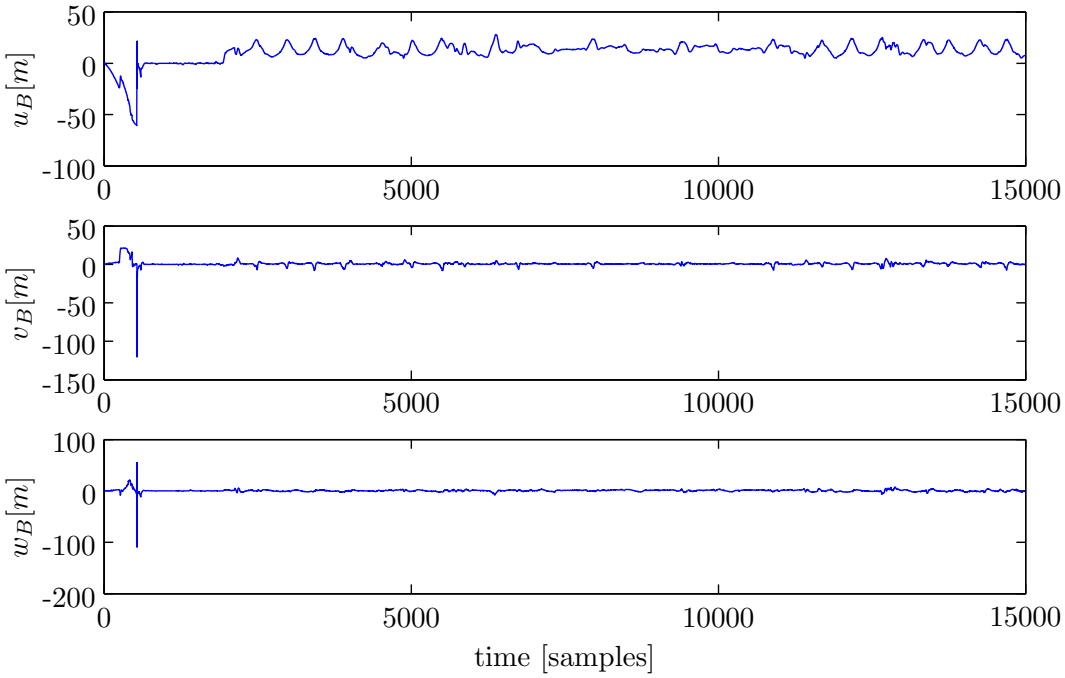

Figure G-23: Estimated velocity states EKF, LOG00042

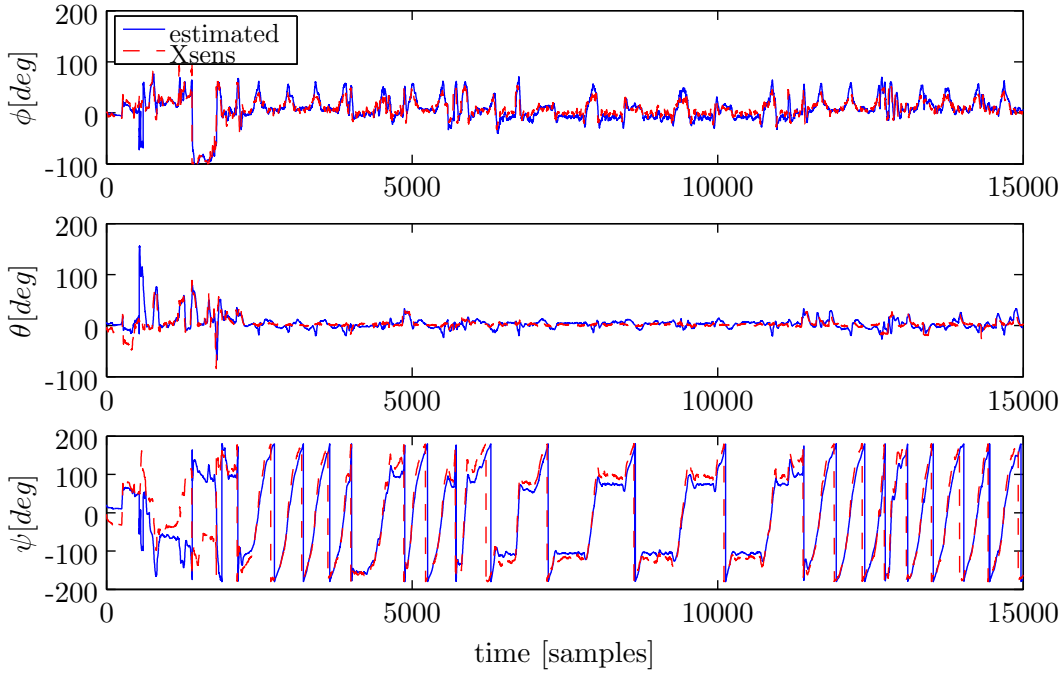

Figure G-24: Estimated Euler angle states EKF, LOG00042

G-2-2 Results IEKF Identification

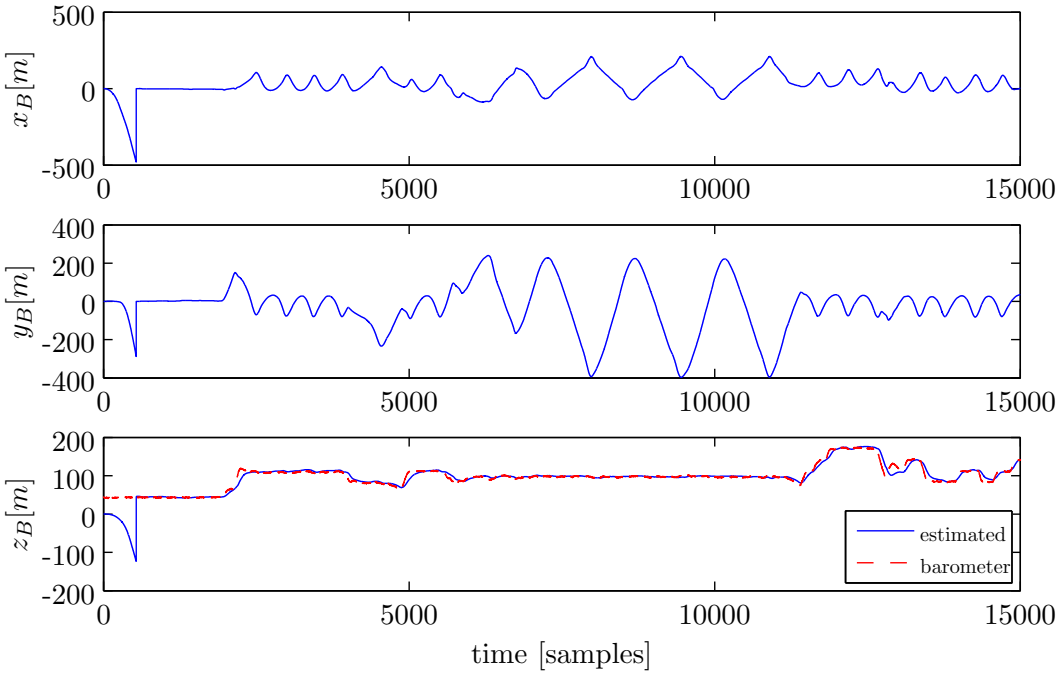

Figure G-25: Estimated position states IEKF, LOG00042

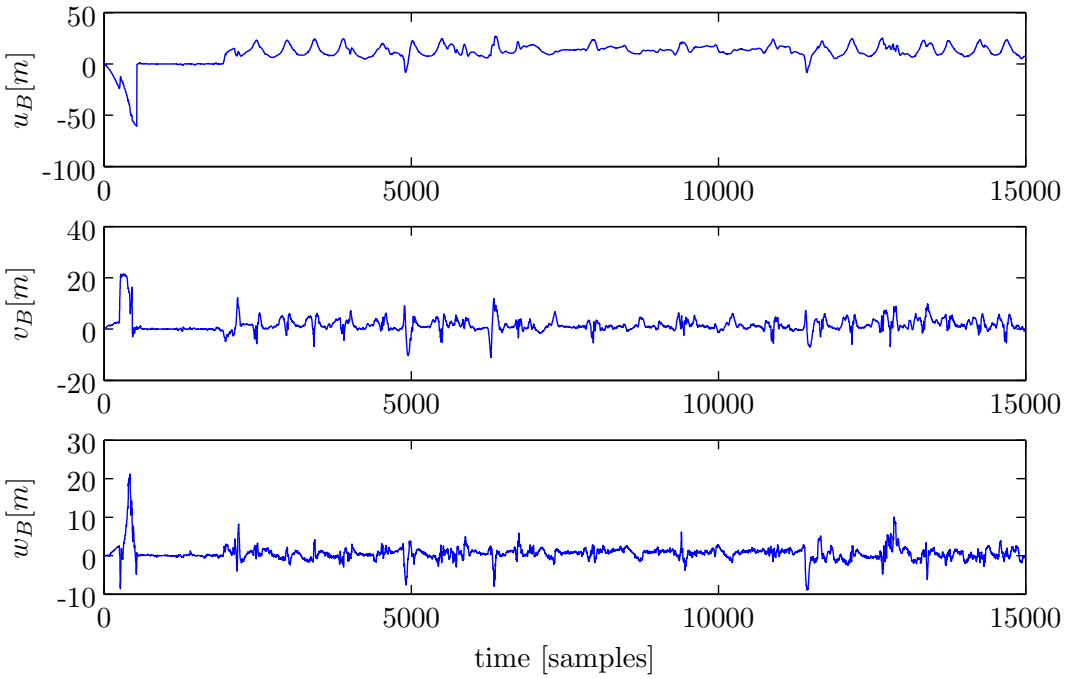

Figure G-26: Estimated velocity states IEKF, LOG00042

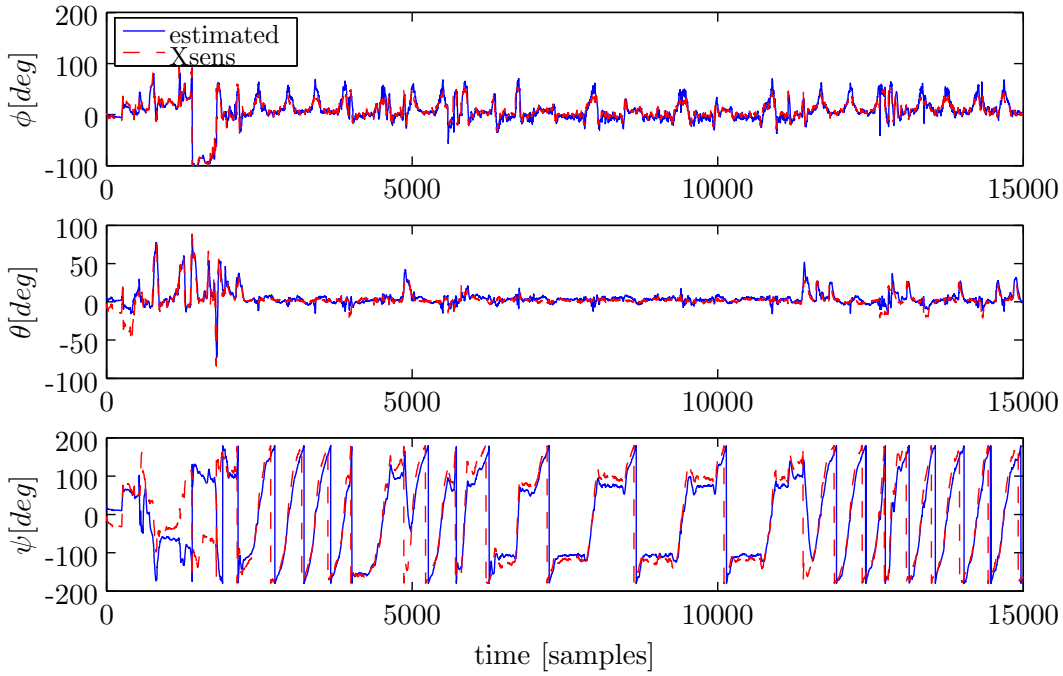

Figure G-27: Estimated Euler angle states IEKF, LOG00042

G-2-3 Results Non-Linear SO(3) Identification

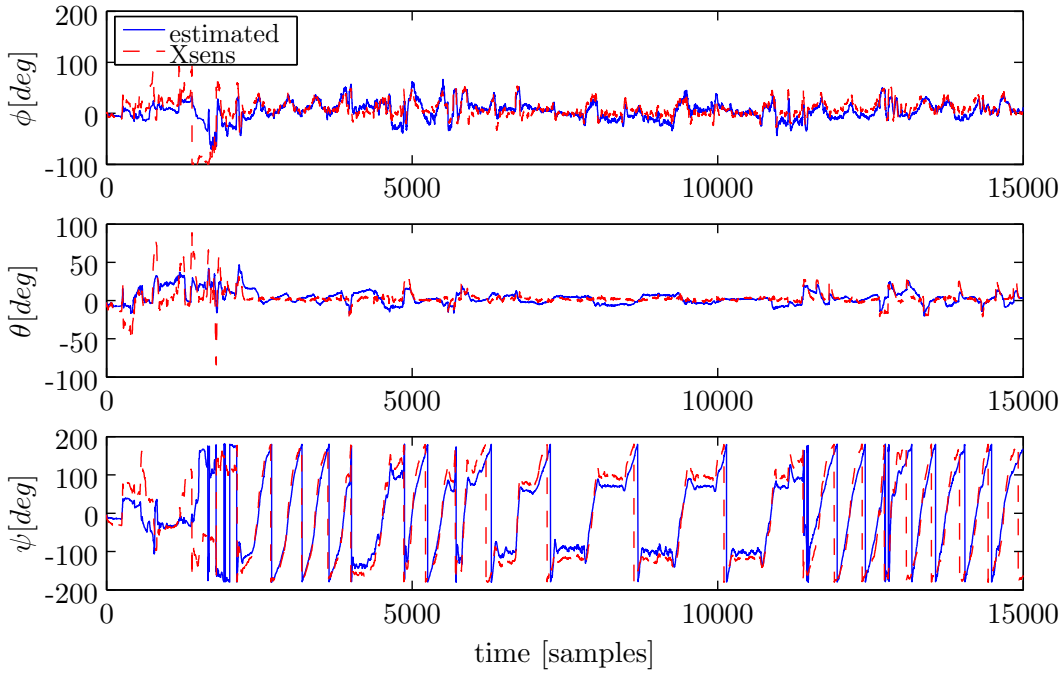

Figure G-28: Estimated Euler angle states SO(3), LOG00042

G-3 Log-file 2010-10-13/LOG00050

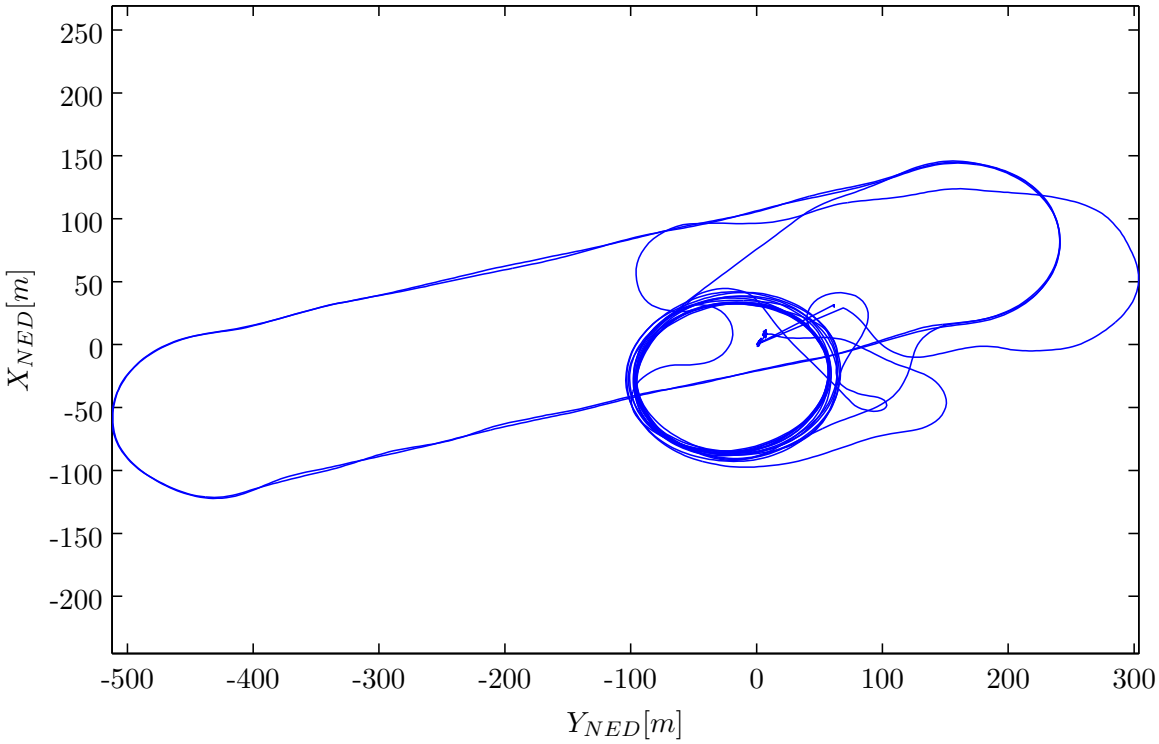

Figure G-29: Flight trajectory, LOG00050

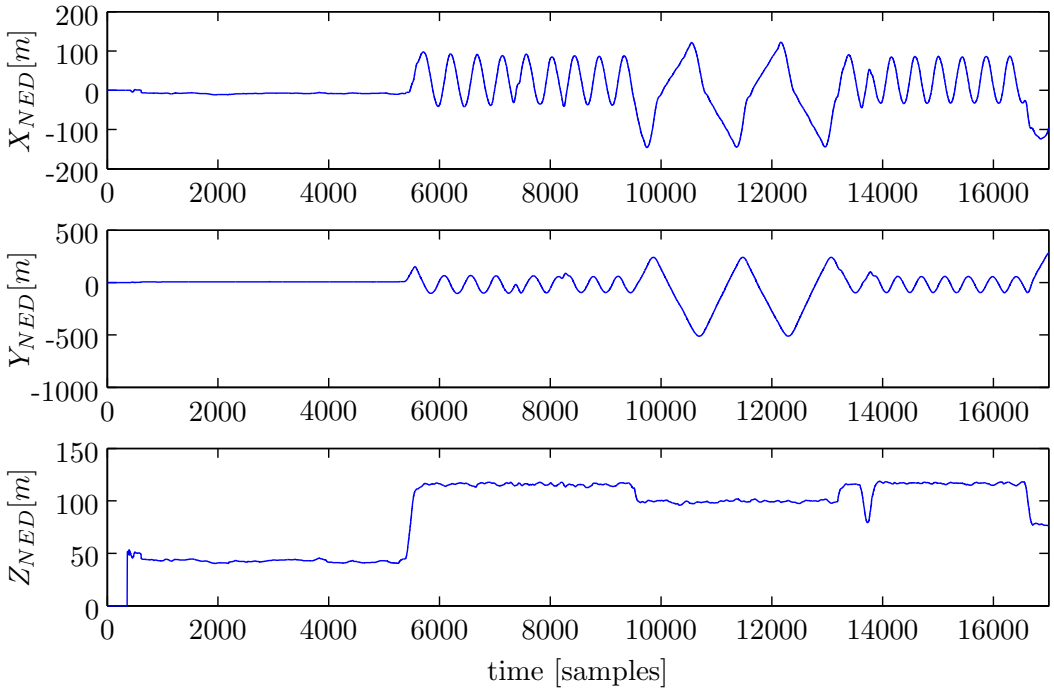

Figure G-30: GPS positions in NED, LOG00050

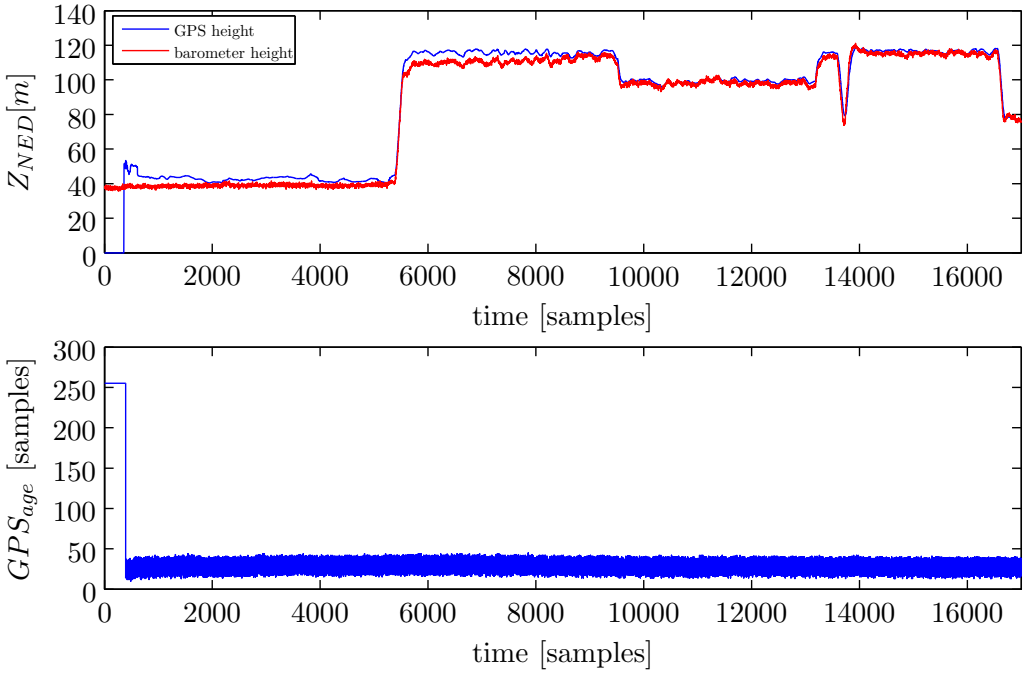

Figure G-31: GPS and barometer height in NED and GPS processing time, LOG00050

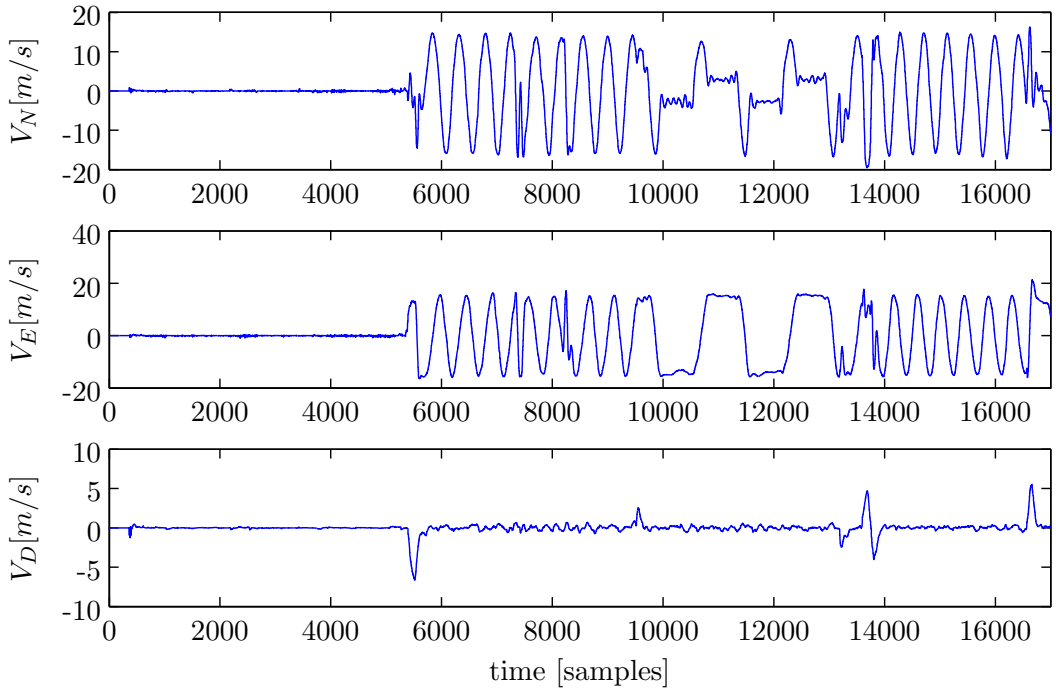

Figure G-32: GPS velocities in NED, LOG00050

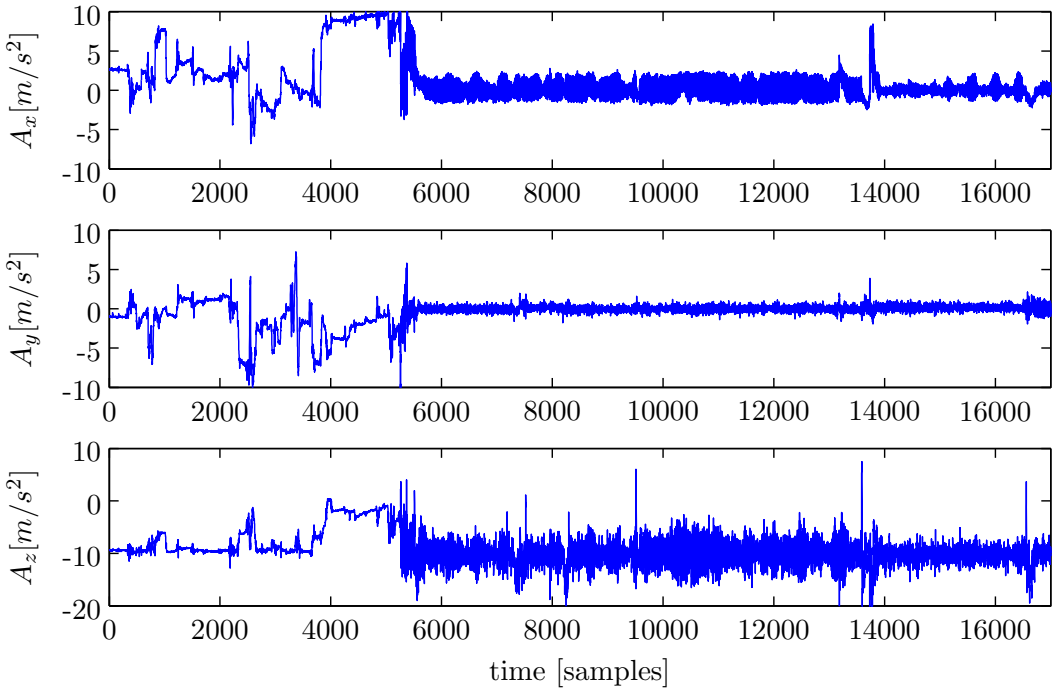

Figure G-33: Accelerometer signals in $\mathcal{F}_B$, LOG00050

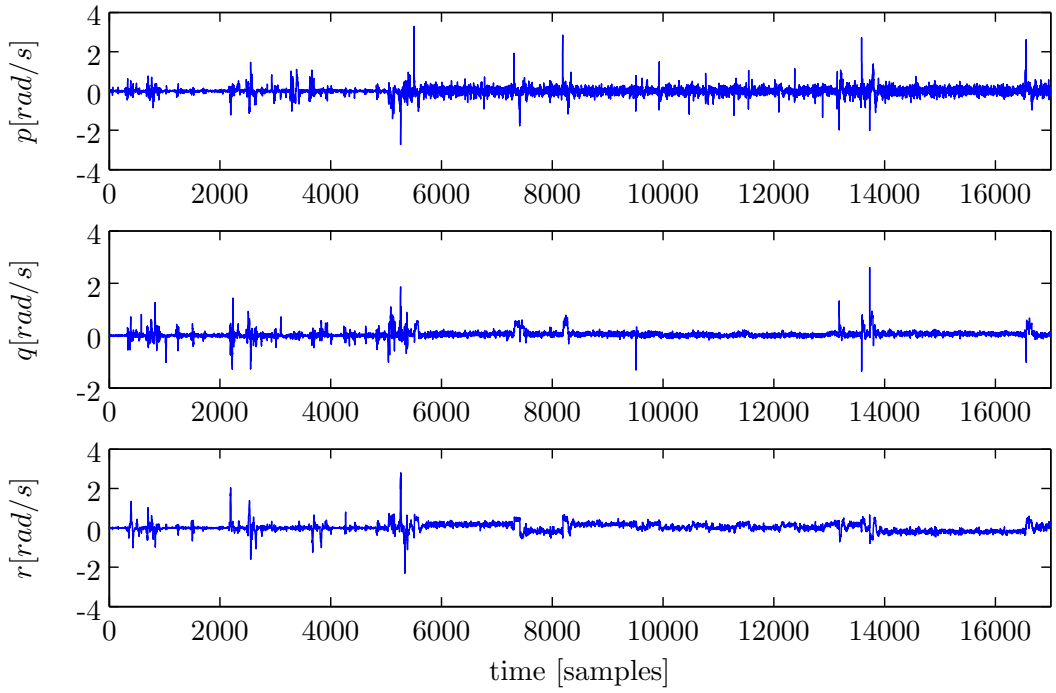

Figure G-34: Gyroscope signals in $\mathcal{F}_B$, LOG00050

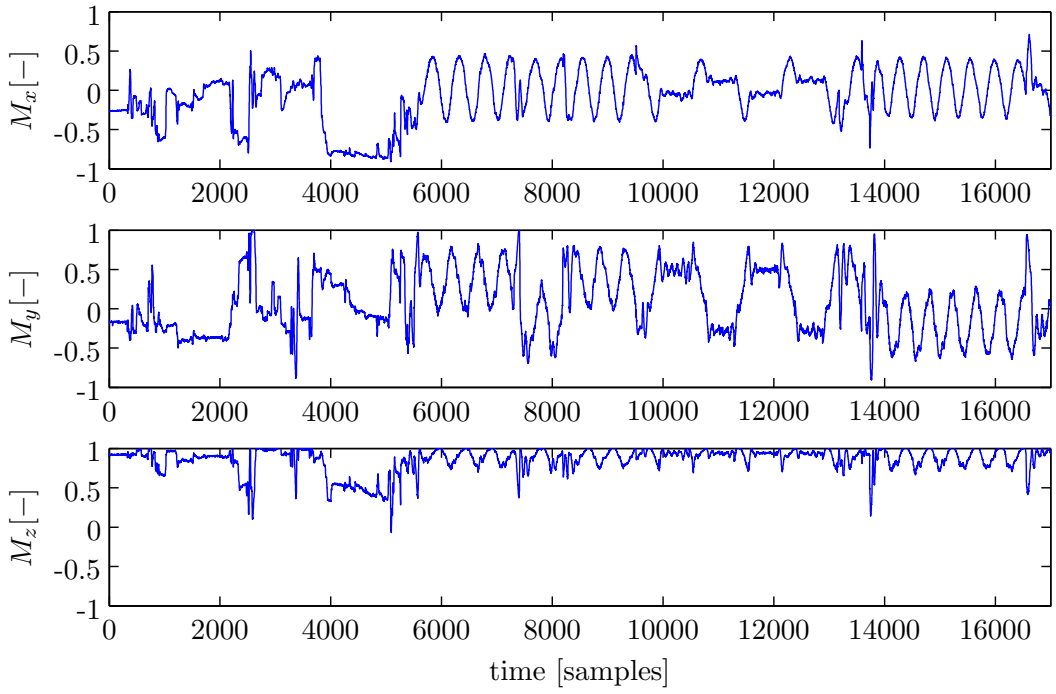

Figure G-35: Magnetometer signals, converted to unit amplitude in $\mathcal{F}_B$, LOG00050

G-3-1 Results EKF Identification

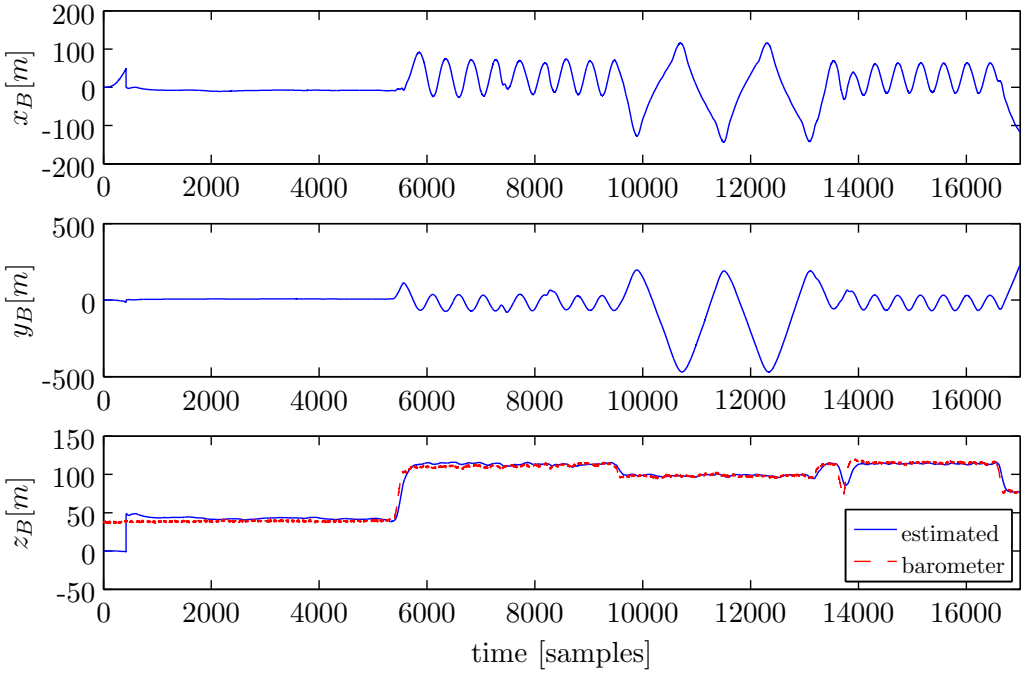

Figure G-36: Estimated position states EKF, LOG00050

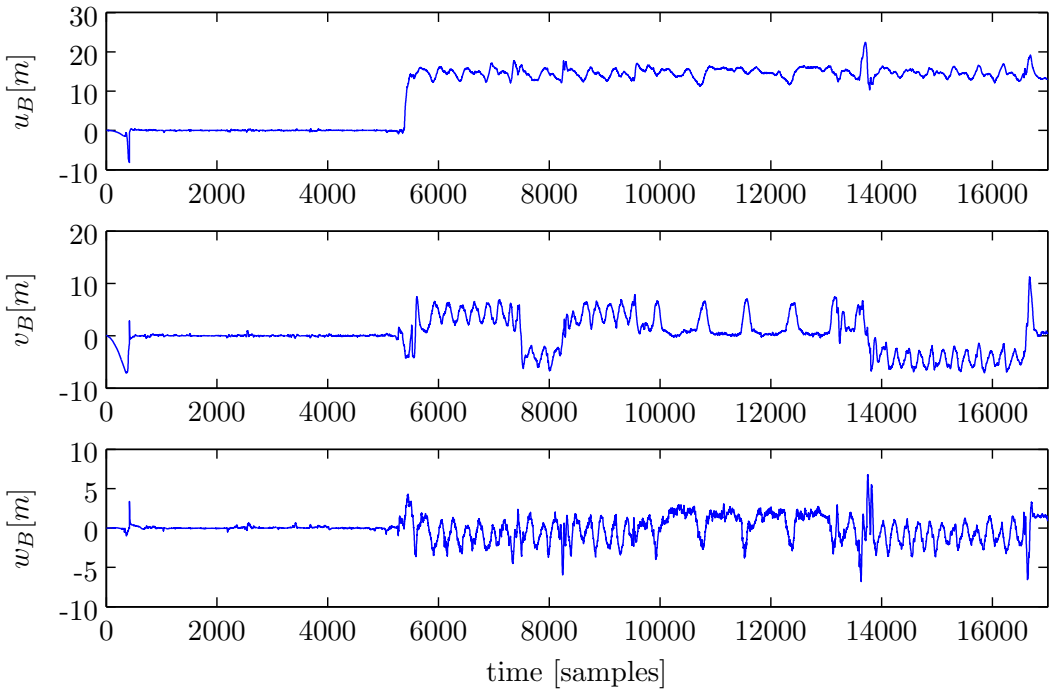

Figure G-37: Estimated velocity states EKF, LOG00050

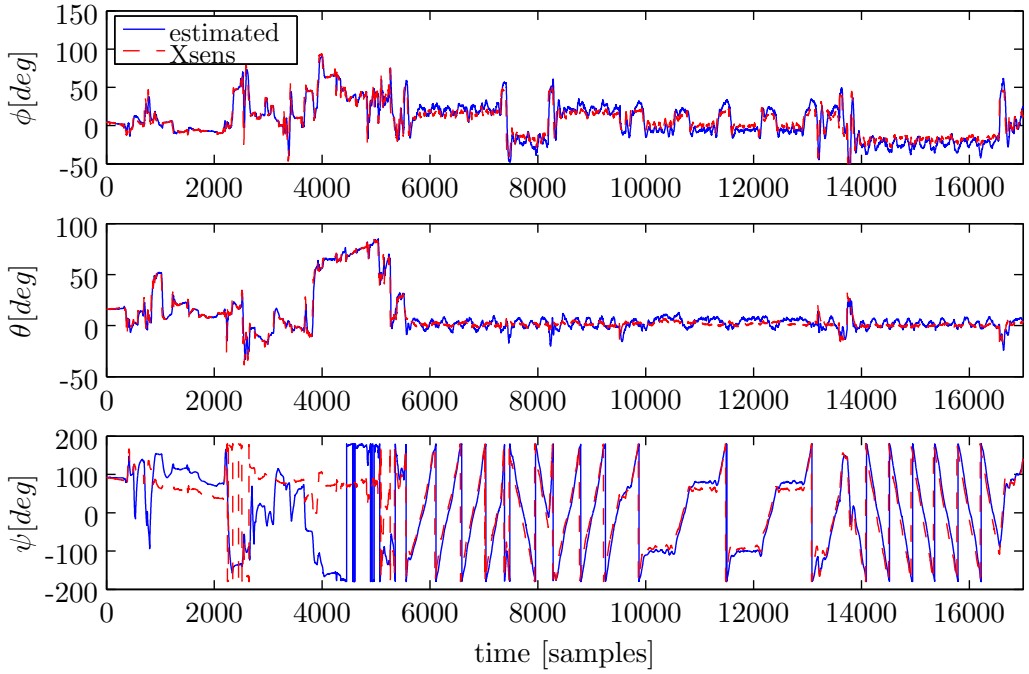

Figure G-38: Estimated Euler angle states EKF, LOG00050

G-3-2 Results IEKF Identification

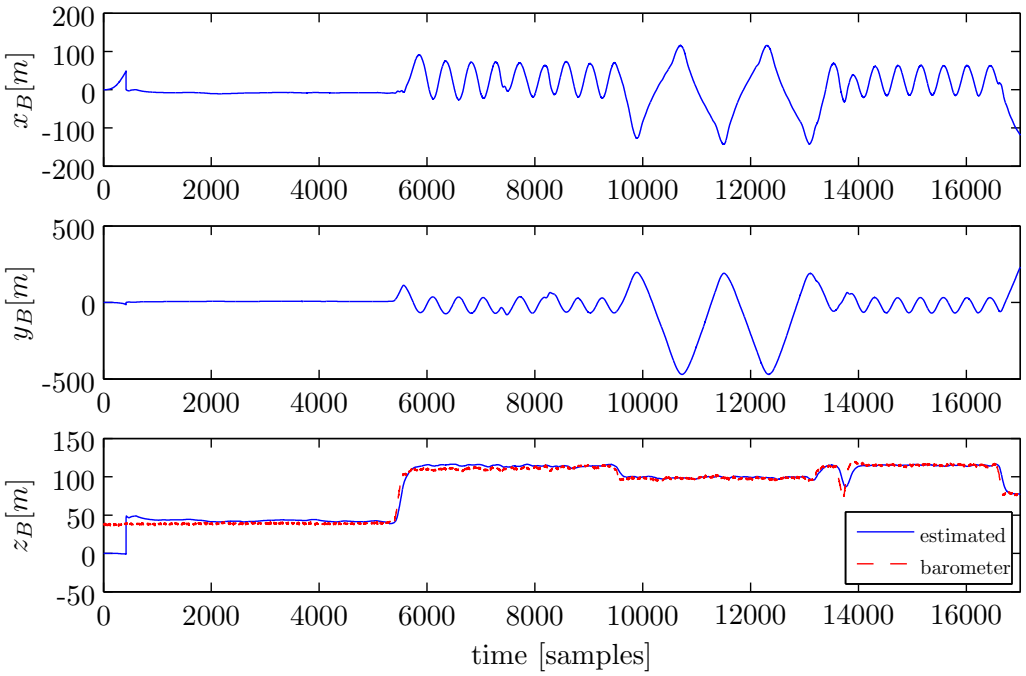

Figure G-39: Estimated position states IEKF, LOG00050

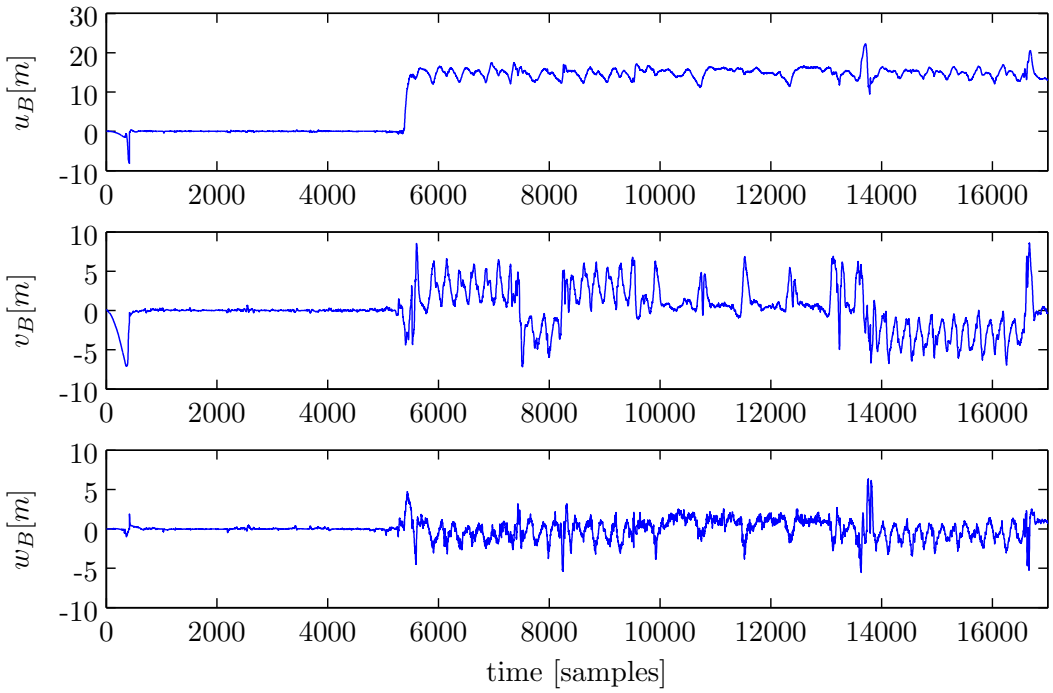

Figure G-40: Estimated velocity states IEKF, LOG00050

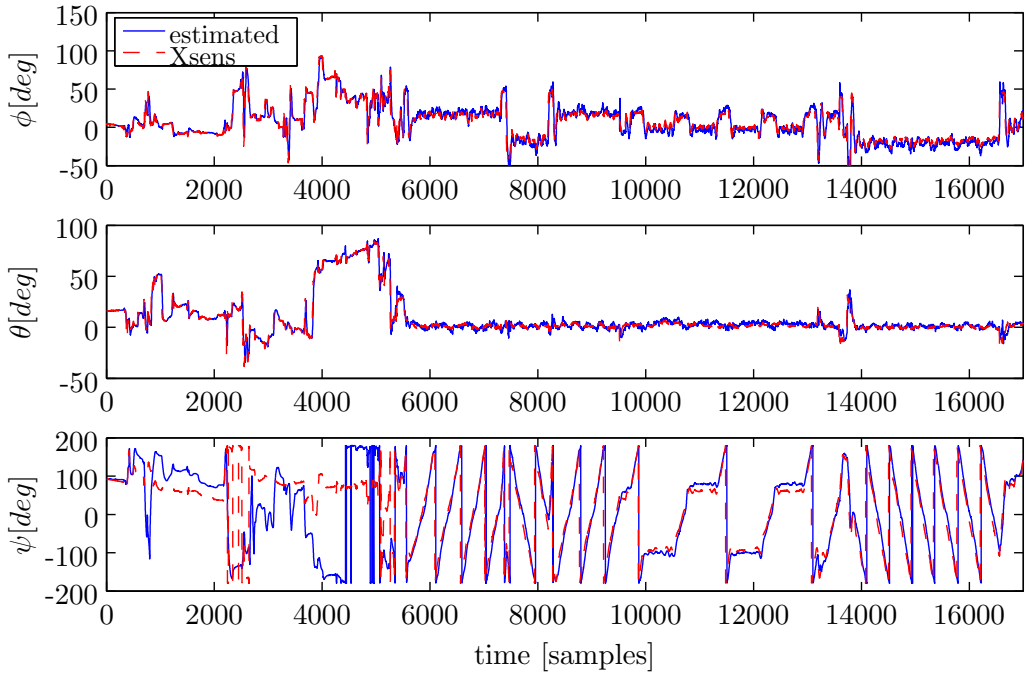

Figure G-41: Estimated Euler angle states IEKF, LOG00050

G-3-3 Results Non-Linear SO(3) Identification

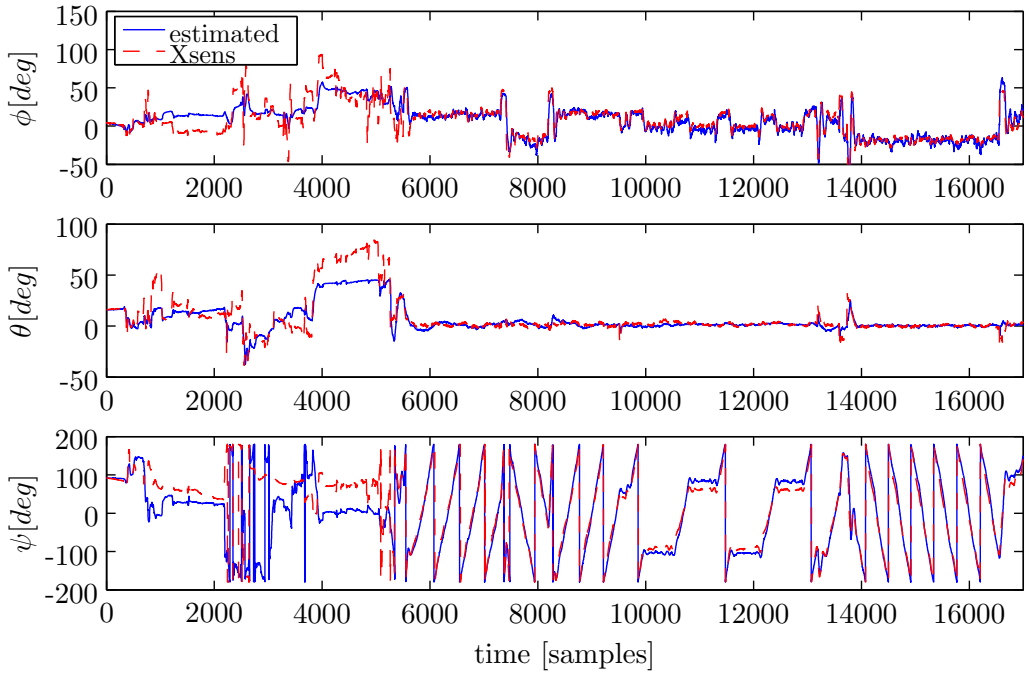

Figure G-42: Estimated Euler angle states SO(3), LOG00050

Bibliography

Abdel-Hafez, M. F. (2009). On the development of an inertial navigation error-budget system. *Journal of the Franklin Institute*, *In Press, Corrected Proof*.

Batista, P., Silvestre, C., & Oliveira, P. (2009). Necessary and sufficient conditions for the observability of linear motion quantities in strapdown navigation systems. Hyatt Regency Riverfront, St. Louis, MO, USA.

De Wagter, C. (2004, Nov). *B&A Avionics AHRS, static and dynamic calibration.*

Ding, W., Wang, J., Li, Y., Mumford, P., & Rizos, C. (2008, feb). Time Synchronization Error and Calibration in Integrated GPS/INS systems. *Electronics and Telecommunications Research Institute (ETRI)*, *12*(3).

Draper, C., Wrigley, W., & Hovorka, J. (1960). *Inertial Guidance.* Pergamon Press.

Geiger, W., & Bartholomeyczik, J. (2008). *MEMS IMU for AHRS Application.* (Northrop Grumman, Electronic Systems, LITEF GmbH, 79115 Freiburg, Germany)

Hedrick, J. K., & Girard, A. (2005). *Control of Nonlinear Dynamic Systems: Theory and Applications*. Berkeley University. (chapter 6)

Kalman, R. E. (1960). A New Approach to Linear Filtering and Prediction Problems. *Transactions of the ASME-Journal of Basic Engineering*, *82*(Series D), 35–45.

Kayton, M., & Fried, W. R. (1997). *Avionics Navigation Systems* (second ed.). John Wiley & Sons.

Lai, Y.-C., Jan, S.-S., & Hsiao, F.-B. (2010). Development of a Low-Cost Attitude and Heading Reference System Using a Three-Axis Rotating Platform. *Sensors*.

Li, D., & Wang, J. (2005, dec). Enhancing the Performance of Ultra-Tight Integration of GPS/PL/INS: A Federated Filter Approach. *GNSS*.

Long, R., Yong-yuan, Q., & Ji-chao, J. (2008, dec). Observable Degree Analysis of SINS Initial Alignment Based on Singular Value Decomposition. *IEEE International Symposium on Knowledge Acquisition and Modeling Workshop, KAM Workshop 2008*, 444-448.

Mahony, R., & Hamel, T. (2008, jun). Nonlinear Complementary Filters on the Special Orthogonal Group. *IEEE Transactions on Automatic Control*, *53*(5).

Mahony, R., Hamel, T., & Pflimlin, J. (2005, dec). Complementary filter design on the Special Orthogonal Group SO3. *IEEE Conference on Decision and Control*(44).

Markley, F. L., Crassidis, J. L., & Cheng, Y. (2005). Nonlinear Attitude Filtering Methods. *AIAA*.

Mulder, J. A., van Staveren, W. H. J. J., van der Vaart, J. C., & de Weerdt, E. (2007). *Flight dynamics*. Delft University Press. (lecture notes course AE3-302: Flight Dynamics)

Olsder, G. J., & van der Woude, J. W. (2005). *Mathematical Systems Theory* (third ed.). VSSD. (ISBN 90-71301-40-0)

Rhee, I., Abdel-Hafez, M. F., & Speyer, J. L. (2004). Observability of an Integrated GPS/INS during maneuvers. *IEEE Transactions on Aerospace and Electronic Systems*, *40, Issue 2*, 526-535.

Ruijgrok, G. J. J. (1996). *Element of Airplane Performance* (second ed.). Delft University Press.

Schmidt, G. T. (2009, May). *INS/GPS Technology Trends. in rto-en-set-116. NATO Research and Technology Organization.*

Silverman, L. M., & Meadows, H. E. (1967). Controllability and observability in time-variable linear systems. *SIAM Control*, *5, Issue 5*, 64-73.

Simon, D. (2006). *Optimal State Estimation, Kalman, h and nonlinear approaches*. John Wiley & Sons.

Skog, I., & Händel, P. (2010). Time synchronization errors in GPS-aided inertial navigation systems. *IEEE Transactions on Intelligent Transportation Systems (ITS)*.

Titterton, D. H., & Weston, J. L. (2009). *Strapdown Inertial Navigation Technology* (second ed., Vol. 207). American Institute of Aeronautics and Astronautics (AIAA).

Török, J. S. (2000). *Analytical Mechanics: With an introduction to dynamical systems*. Wiley-Interscience Publication.

Verhaegen, M., & Verdult, V. (2007). *Filtering and System Identification, a Least Squares Approach* (first ed.). Cambridge University Press.

Wendel, J., Meister, O., Mönikes, R., & Trommer, G. (2006). Time-Differenced Carrier Phase Measurements for Tightly Coupled GPS/INS Integration. *IEEE*.